ORIGIN OF GOLD MINERALIZATION IN THE BORDEN MINE AND A NEW TECTONIC MODEL FOR THE KAPUSKASING STRUCTURAL ZONE, ONTARIO, CANADA

A Thesis Submitted to the College of
Graduate and Postdoctoral Studies
In Partial Fulfillment of the Requirements
For the Degree of Doctor of Philosophy
In the Department of Geological Sciences
University of Saskatchewan
Saskatoon

By
VICTORIA R. STINSON

PERMISSION TO USE

In presenting this dissertation in partial fulfillment of the requirements for a Postgraduate degree from the University of Saskatchewan, I agree that the Libraries of this University may make it freely available for inspection. I further agree that permission for copying of this thesis/dissertation in any manner, in whole or in part, for scholarly purposes may be granted by the professor who supervised my dissertation work or, in their absence, by the Head of the Department or the Dean of the College in which my thesis work was done. It is understood that any copying or publication or use of this dissertation or parts thereof for financial gain shall not be allowed without my written permission. It is also understood that due recognition shall be given to me and to the University of Saskatchewan in any scholarly use which may be made of any material in my dissertation.

Requests for permission to copy or to make other uses of materials in this dissertation in whole or part should be addressed to:

Dean
College of Graduate and Postdoctoral Studies
University of Saskatchewan
116 Thordvaldson Building, 110 Science Place
Saskatoon, Saskatchewan S7N 5C9
Canada

Head of the Department of Geological Sciences
14 Science Place
University of Saskatchewan
Saskatoon, Saskatchewan S7N 5E2
Canada

ABSTRACT

The Kapuskasing Structural Zone (KSZ) containing high–pressure granulites is one of the best exposed mid–to–lower crustal sections in the world. However, the timing and mechanism for its formation/exhumation remain highly controversial. Previous studies of the KSZ and its neighboring Wawa Gneiss Domain (WGD) focused predominantly on Proterozoic brittle deformation in the Ivanhoe Lake Deformation Zone (ILDZ), with tectonic models restricted to political boundaries. In this study, the KSZ and WGD are proposed as a continental metamorphic core complex (MCC) with the high–grade footwall of the former exhumed in comparison to the southern Superior Province, and the latter as the hanging–wall, high–strain listric regional structure. The KSZ exposes granulite–facies ductile sinistral strike–slip shear zones and amphibolite–facies brittle–ductile sinistral and dextral shear zones that predate the ILDZ.

Neoarchean oblique collision between the Minnesota River Valley terrane and southern Superior Province formed the Pontiac subprovince accretionary prism and equivalents in the "Quiet Zone" by ca. ⩾2667 Ma. The formation and exhumation of the WGD and KSZ as a MCC were synchronous with retrograde amphibolite–facies metamorphism by at least ca. ⩾ 2630 Ma. Plutonism and continued transtension, rotation, and related folding continued to ca. 2600 Ma with magmatism ceasing by ca. 2580 Ma.

The enigmatic Borden Mine (4.17 Mt at an average grade of 6.38 g/t Au) in the Chapleau Belt within the southern KSZ is hosted in sillimanite–garnet–biotite gneisses or schists within metamorphosed mafic and felsic volcanic rocks (with mid–ocean ridge basalt and arc affinities), and banded iron formations. Laser ablation inductively coupled plasma mass spectrometry (LA–ICPMS) analysis of zircon in sillimanite–garnet–biotite gneiss from the Discovery Trench of the Borden Mine yielded three age populations: 2703.9±7.3, 2667.1±7.2 and 2590±17 Ma. The oldest population represents magmatic crystallization that formed the volcanic protolith of the sillimanite–garnet–biotite gneiss, while the latter two record prolonged high–grade metamorphism. Gold mineralization in the Borden Mine most likely formed initially as part of syn–volcanic seafloor hydrothermal alteration and was remobilized throughout prograde upper amphibolite– to– granulite–facies metamorphism during orogenesis and retrograde amphibolite–facies metamorphism during exhumation.

ACKNOWLEDGEMENTS

The foremost acknowledgement is dedicated to my thesis supervisor Dr. Yuanming Pan. Dr. Pan has provided support, insight, collaboration, and has always encouraged my development as a scientist and human. In fact, his support never wavered even when this thesis changed from a focus on the microscopic geology to the regional– to cratonic–scale tectonics.

I would like to further thank my supervisory committee members Dr. Ingrid Pickering (Chair), Dr. Mel Stauffer, Dr. Kevin Ansdell, Dr. Yansun Yao (Cognate Member), Dr. Stephen Richardson (Cognate Member), Ms. Chantal Strachan–Crossman (Graduate Secretary), and Dr. Bruce Eglington at the University of Saskatchewan for their support and guidance. I am immensely grateful to the entire examination committee (Drs. Lentz, Ansdell, Pickering, Stauffer, Yao, Walker, and Pan) for their scope and depth of questioning as it provided opportunity for growth and enriched my thesis. Special thanks to Dr. David Lentz (external examiner) for his critical review and constructive suggestions. Support for the new theories proposed in this thesis by the Ontario, Minnesota, South Dakota, Wisconsin, and Michigan geological surveys has been heartening as it reminds me that this work continues to benefit many communities. Members of the University of Saskatchewan's Geological Sciences community that have also been invaluable and include Donna Beneteau, Michelle Howe, Tim Prokopiuk, Jim Rosen, Mosa Nasreen, Dr. Douglas Milne, Dr. Sam Butler, Michael Cuggy, Tom Bonli, Blaine Novakovski, Nancy, and the Ore Gangue. Special thanks to Dr. Hua Huang and Dr. Jinyang Zhang for their insight during their Post–Doctoral work with Dr. Pan. I am grateful to have had the opportunity to work alongside and mentor Katia Jellicoe, Gleceria Gamelin, and Matthew Nadeau in the field and lab for their Bachelor theses. I am grateful for the friendships that I have made during my time at USASK and would like to thank Christine and Darcy, Paul and Madeline, Holly, Jordan, Nancy, Meagan, Michael, Stephanie, Carla, and Hoang Anh Tu (Lavie) for supporting me as a friend. Thank you to Brian Atkinson from the Ontario Geological Survey who provided us with logistical support and was always willing to discuss new ideas. Thank you to Probe Mines Ltd. and Goldcorp Inc. for their financial support, drill core, and friendly help from all their geologists.

The dearest thanks to my family who are my greatest supporters. Thank you Kerrilyn, Kathryn, Marilyn, John Paul, Lori et al., and Brandon. All diagrams have been greatly improved with the artistic care of Brandon. I love you all eternally.

TABLE OF CONTENTS

LIST OF FIGURES & MAPS

LIST OF TABLES

LIST OF ABBREVIATIONS

Abbreviation	Meaning
KSZ	Kapuskasing Structural Zone, Kapuskasing Deformation Zone, Kapuskasing Uplift, Kapuskasing Zone
WGD	Wawa Gneiss Domain, Wawa Domal Gneiss, Agawa Gneiss
ILDZ	Ivanhoe Lake Deformation Zone, Ivanhoe Lake Fault Zone
MRVT	Minnesota River Valley Terrane
GLTZ	Great Lakes Tectonic Zone
MCC	Metamorphic core complex
BIF	Banded–iron formation
SAT	Southern Accreted Terranes
BBMZ	Beartooth–Bighorn magmatic zone
MMP	Montana metasedimentary province
OTSB	Oregon Trail Structural Belt
CCW	Counterclockwise, anticlockwise
CW	Clockwise
Aug	Augite, clinopyroxene
Bt	Biotite
Ccp	Chalcopyrite
Cbrl	Chrysoberyl
Grt	Garnet
Hbl	Hornblende
Ilm	Ilmenite
Kfs	K–feldspars
Lo	Löellingite
Mag	Magnetite
Ms	Muscovite
Py	Pyrite
Po	Pyrrhotite
Sil	Sillimanite, prismatic, fibrolite
Tur	Tourmaline–group minerals, schrol

LIL	Large ion lithophile element
(H,L)FSE	(High, Low) field strength element
(H,L)REE	(Heavy, Light) Rare earth element
STEP	Subduction–Transform–Edge–Propagator fault
NaKFMASH	Na_2O–K_2O–FeO–MgO–Al_2O_3–SiO_2–H_2O system
BASH	BeO–Al_2O_3–SiO_2–H_2O system

Mineral abbreviations after Kretz (1983) and Warr (2021).

CHAPTER 1: INTRODUCTION

1.1 Purpose and objectives of research

The primary purpose and objective of research for this dissertation are (1) to document and study the gold mineralization in Newmont's Borden Mine (4.17 Mt at an average grade of 6.38 g/t Au) near Chapleau, Ontario (Fig. 1.1). The mineralization is enigmatic due to the high–grade metamorphic nature of the lithologies and the lack of notable sulphide minerals (less than 2% modally, with the exception of the semi–massive to massive, sulphide–facies banded iron formations (BIF) described in this thesis), alterations, veins, or other known features characteristic of gold deposits. Additional objectives are (2) to further understand the tectonic evolution of the study area, including the host lithologies of the enigmatic and understudied Wawa Gneiss Domain (WGD) (previously referred to the Wawa Domal Gneiss Terrane), the Chapleau Belt (also known as the Borden Belt or Borden Lake greenstone belt (Duguet and Szumylo, 2016) in the southern Kapuskasing Structural Zone, and the entire Kapuskasing Structural Zone (KSZ) adjacent to the well–studied Pontiac, Wawa and Abitibi subprovinces of the Superior Province (Figs. 1.2–1.5) to garner a deeper understanding of the development and evolution of the host lithologies, neighbouring lithologies, and tectonics of the region. The gold districts of the Wawa, Abitibi, and Pontiac subprovinces will be compared to the Borden Mine in the Chapleau Belt.

The geographical and geological context of the study is presented below. The Borden Mine, located in Chapleau, Ontario and 200 km southwest of Timmins, Ontario (Fig. 1.1), is in the Chapleau Belt, between the WGD and KSZ within the Superior Province (Figs. 1.2–1.5). Fig. 1.2 shows a general view of the Superior Province and its subdivisions. Figure 1.3 illustrates the regional geology of the Borden Mine in the context of the subprovinces, while Figure 1.4 shows the detail of the Chapleau Belt, KSZ, Shawmere Anorthosite, and ILDZ. Finally, Figure 1.5 places the major gold camps in the Wawa and Abitibi subprovinces and provides context to the domal nature of the WGD and its relationship between the Wawa subprovince and KSZ.

Figure 1.1 Geographical location of Borden Mine in the province of Ontario, Canada (Modified after LaFontaine, 2016).

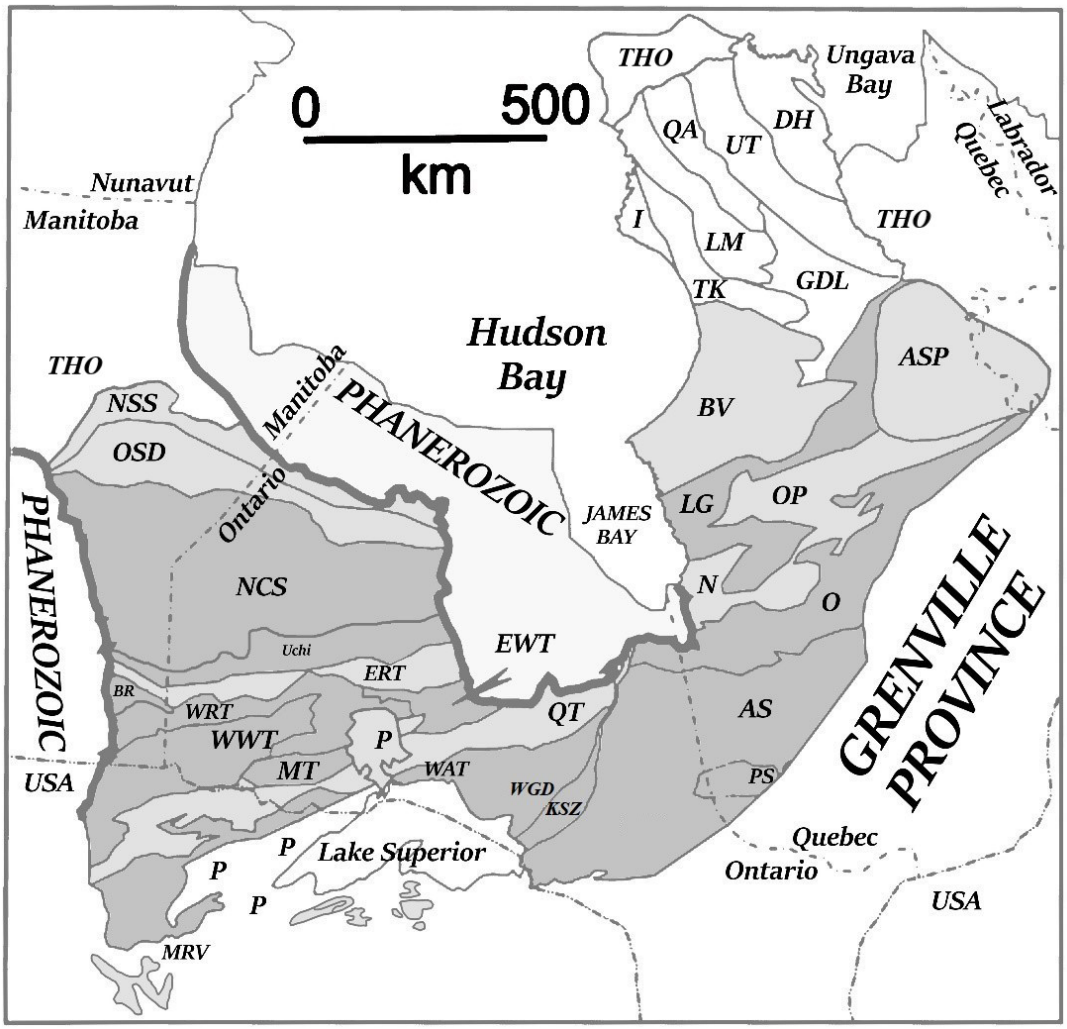

Figure 1.2: Superior Province with Archean, Proterozoic, and Phanerozoic subdivisions generalized into predominantly metavolcanic (medium grey), metasedimentary (light grey), sedimentary (lightest grey), and undifferentiated (white) lithologies (after Percival et al., 2006, and references therein) and abbreviations used: AS, Abitibi subprovince; ASP, Ashuanipi subprovince; BR, Bird River subprovince; BV, Bienville subprovince; DH, Douglas Harbour domain; ERT, English River subprovince; EwT, East Wabigoon subprovince; GDL, Goudalie subprovince; I, Inukjuak domain; KSZ, Kapuskasing Structural Zone; LG, La Grande subprovince; LM, L. Minto subprovince; MT, Marmion terrane; MRV, Minnesota River Valley terrane; N, Nemiscau; NCS, North Caribou superterrane; NSS, Northern Superior superterrane; O, Opatica subprovince; Op, Opinaca subprovince; OSD, Oxford–Stull domain; P, Proterozoic; PS, Pontiac subprovince; QA, Qalluvi–artuuq domain; QT, Quetico subprovince; THO, Trans–Hudson Orogen; TK, Tikkerutuk domain; UT, Utsalik domain; WAT, Wawa subprovince; WRT, Winnipeg River subprovince; WwT, West Wabigoon subprovince; and WGD Wawa Gneiss Domain. Note that many neighbouring Archean to Proterozoic subdivisions are below Phanerozoic cover (P, white) (Modified after Johnson, 1991; Bornhort and Johnson, 1998; Percival et al., 2012; Jirsa, 2016).

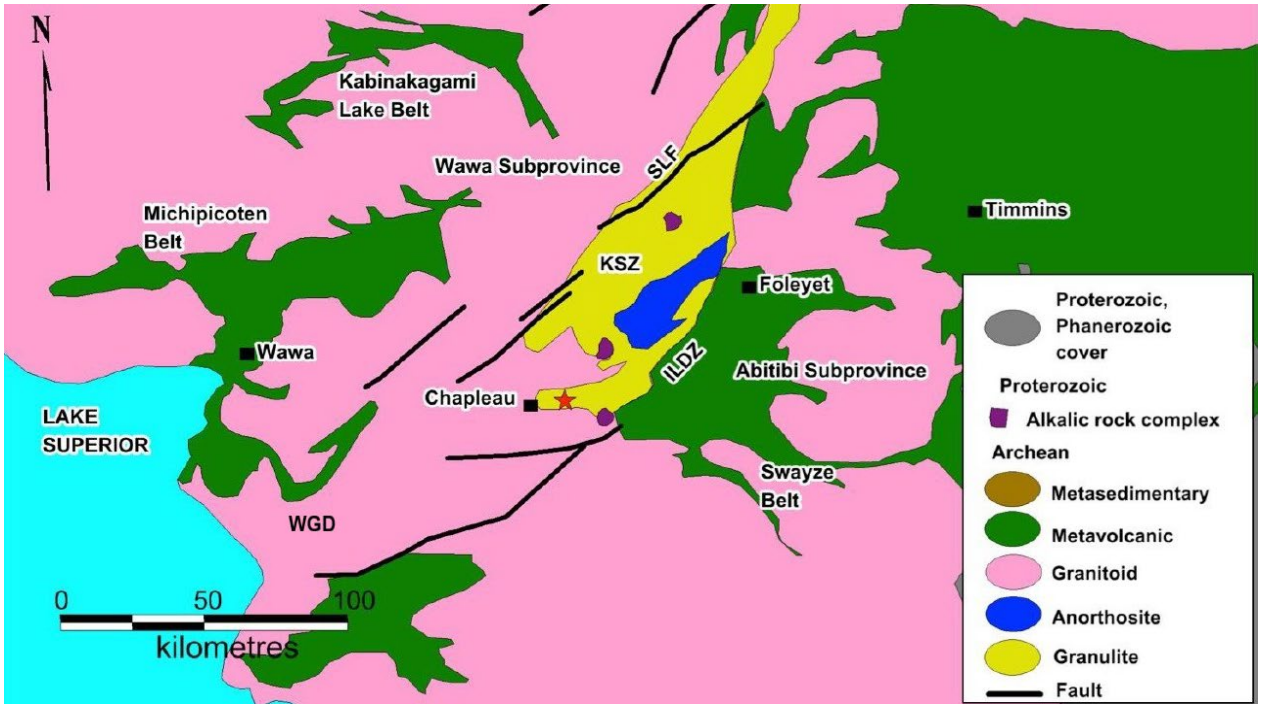

Figure 1.3: The Borden Mine (red star) and regional geology of the Wawa and Abitibi subprovinces, Wawa Gneiss Domain (WGD), Kapuskasing Structural Zone (KSZ), Ivanhoe Lake Deformation Zone (ILDZ), Saganash Lake Fault (SLF), and numerous major lithologies and structures including granulite (yellow), Shawmere Anorthosite (blue), and calc–alkaline to alkalic complexes (purple) (Modified after Percival, 1989; Moser, 1994, 1996).

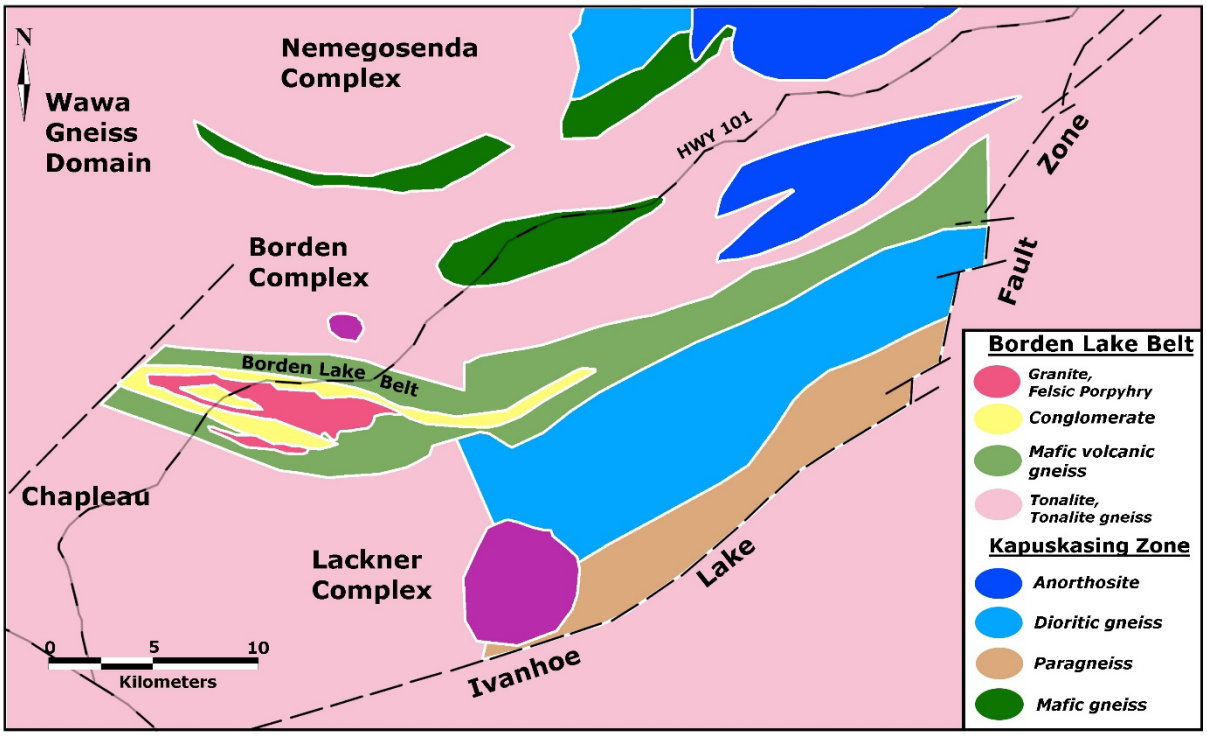

Figure 1.4: Regional geology of the arcuate Chapleau Belt (pink, yellow, and green) including major regional lithologies and the Wawa Gneiss Domain (WGD) (light pink), Ivanhoe Lake Fault (or Deformation) Zone (ILDZ), Shawmere Anorthosite (blues), and carbonatite to alkaline Lackner and Nemegosenda Complexes (purple) (after Percival, 1989; Moser, 1994, 1996).

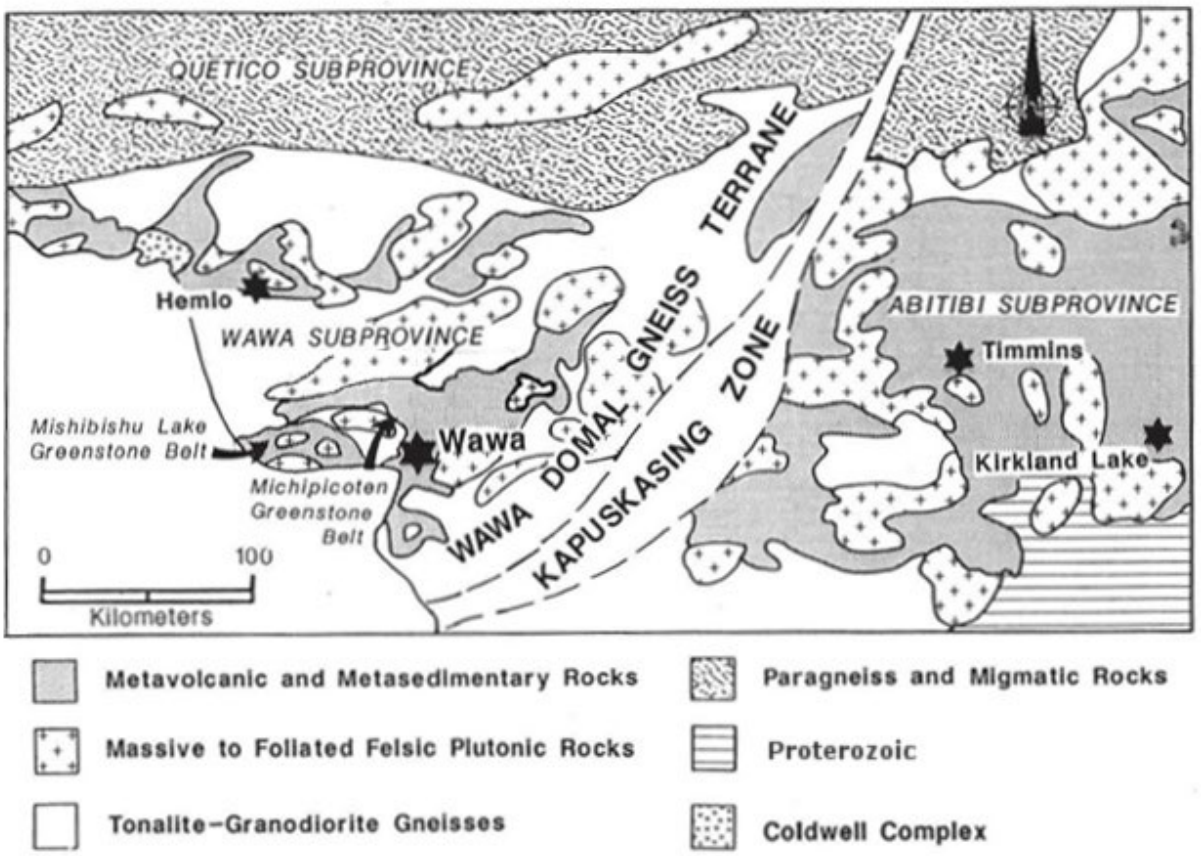

Figure 1.5: The Wawa Domal Gneiss Terrane (now the WGD) and Kapuskasing Zone (now the KSZ) share similar geometries oblique to the Quetico subprovince to the north. Note the northeast–elongated, domal gneissic nature of the WGD, western Wawa, and Quetico subprovinces. The major gold camps highlighted with stars including Hemlo, Wawa, Timmins, and Kirkland Lake (Modified after Heather and Arias, 1992).

CHAPTER 2: LITERATURE REVIEW

2.1 Literature Review

2.1.1 Literature review of gold mineralization

The study area includes numerous historic and current gold districts, camps, mines, deposits, and prospects in the Wawa, Abitibi, and Pontiac subprovinces with major focus on the recently discovered Borden gold deposit and mine in the Chapleau Belt between the high–grade KSZ and WGD metamorphic terrains in Ontario (Figs. 1.1–1.5). Gold mineralization in high–grade metamorphic lithologies is generally understudied, particularly at high temperature and pressure metamorphic grades including the amphibolite and granulite facies. Gold mineralization in the southern Superior Province is more commonly hosted in low– to medium–grade metamorphic lithologies that formed in the upper crust, including the neighbouring Timmins and Kirkland Lake gold mines in the Abitibi subprovince (Fig. 1.5) (Jemielita et al., 1990). To date there are two well–studied gold deposits hosted in granulite–facies lithologies, the Renco deposit in South Africa and the Tropicana deposit in Australia (Blenkinsop and Frei, 1996; Blenkinsop et al., 2014; Crawford and Doyle, 2016; Doyle et al., 2015; Occhipinti et al., 2017). The Borden Mine in Chapleau, Ontario is the first recognized upper amphibolite to granulite facies gold deposit in Canada. This dissertation will research the controls of gold mineralization and remobilization in the region and Borden gold mine in Chapleau, northern Ontario. The Borden Mine is characterized by its association with high–grade metamorphic lithologies, absent to trace sulphide mineralization, absence of quartz veins, and location in the underexplored WGD and KSZ between the Wawa and Abitibi subprovinces of the Superior Province (Fig. 1.3–1.5). The 2016 block 3D model of Borden Mine (Fig. 2.1) displays the shallow to moderate plunge of the gold mineralization to the north and the plan map displays the linear to "Z–shape" of the deposit. Refer to Lafontaine (2016, unpublished MSc. thesis) for more detailed work on the Borden Mine, including the collaborative drill core logging system developed by Lafontaine, Jellicoe, K., and Stinson, V.

The Borden Mine is located 9 km east–northeast of the town of Chapleau in northern Ontario, 190 km northeast of Sault Ste. Marie, and 160 km southwest of Timmins, Ontario (Fig. 1.1, 1.6). The deposit is accessible by road and Ontario Highway 101, forestry roads, and Borden Lake. The deposit is hosted in lithologies that formed in the mid–to–lower crust and may represent the possible upper limits of temperature, crustal depth, and gold mineralization and

remobilization in a natural setting. Therefore, research on the unique Borden Mine will provide new insights into gold mineralization and facilitate new exploration and mining activities in other high–grade metamorphic terrains that are generally under–explored in comparison with their low–grade counterparts.

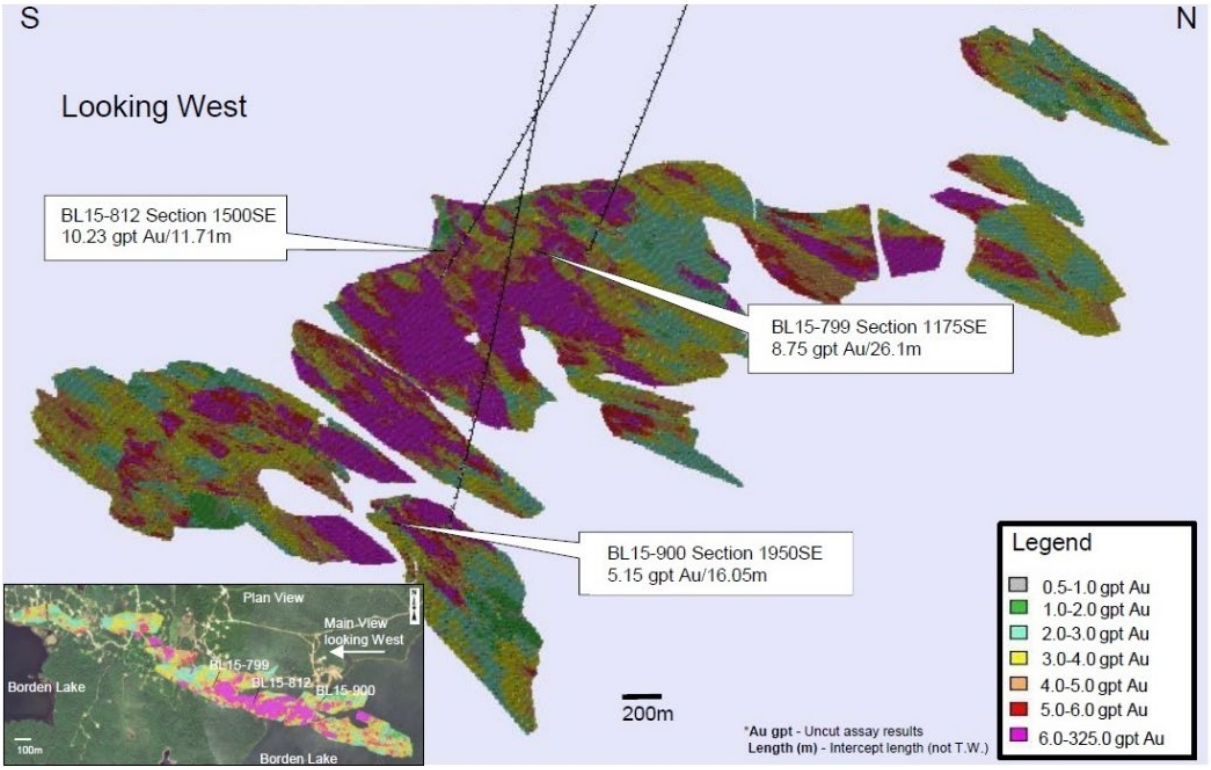

Figure 2.1: December 31, 2016 block model for Borden Mine with high–grade intercepts displayed with their drill collar and gold assay values, colour chart denoting gold assay values of the ore body, and a plan view map inset highlighting the "Z–shape" of the deposit and increased mineralization towards Borden Lake (Modified after Goldcorp Inc., 2016, www.goldcorp.com/English/portfolio/development–projects/borden).

Orogenic gold deposits, also commonly referred to as mesothermal gold, lode gold, greenstone–hosted lodes, or shear–zone–hosted gold deposits, are hosted throughout the world in Archean– to Phanerozoic–aged lithologies (Goldfarb et al., 2005). As the name suggests, orogenic gold deposits are intrinsically associated with orogenesis and are spatially, if not always temporally, linked to accretion, magmatism, metamorphism, and deformation (Kerrich and Cassidy, 1994). Although many of these deposit categories are still used today, they are generally grouped into the orogenic gold deposit category based on their proximity to orogenies (Goldfarb et al., 2005). There is a strong temporal and spatial relation of orogenic

gold deposits with the Precambrian shields throughout the world (Hagemann and Cassidy, 2000). Timing of orogenic gold deposits in Precambrian shields is generally bracketed temporally within 2800 to 2550 Ma or 2100 to 1800 Ma (Hutchinson, 1987; Goldfarb et al., 2001; Goldfarb and Groves, 2015). The sporadic or episodic nature of gold mineralization can be attested to the time required for the orogenic processes and preservation of crustal growth (Goldfarb et al., 2001).

While the majority of Precambrian orogenic gold deposits are hosted in late Archean granite–greenstone belts within orogenic settings in low– to medium–metamorphic lithologies, there is variability in the type of host lithologies, alterations, mineralogy, and other specific characteristics (Colvine et al., 1984; Dubé et al., 2007). Variability between deposits may be due to their complex geological histories with primary features modified over geological time (Colvine et al., 1984; Goldfarb et al., 2001; Goldfarb and Groves, 2015). Although orogenic gold deposits are widely studied there are still many ongoing debates, including how the deposits originally form, with a preference for a single fundamental genetic process due to the general similarities between deposits (Colvine et al., 1984; Hutchinson, 1993). The two prevailing theories are a single–stage, epigenetic model and a seafloor hydrothermal exhalative setting with extensive metamorphic reworking model (Ridler, 1970; Kerrich and Hodder, 1982; Colvine et al., 1984; Hutchinson and Burlington, 1984; Phillips et al., 1984; Stewart, 1984; Hutchinson, 1987; Hutchinson, 1993; éé et al., 2007). Many deposits have features of both models and may have overprinted one another, creating further difficulty in differentiating the two types of features characteristic of each model.

Common to the majority of orogenic gold deposits is the presenece of major structures such as shear zones and faults, or collectively referred to as deformation zones, that host mineralization. These regional structures usually have a long–lived and complex structural history with shortening, high–angle reverse faulting, and later strike–slip movement (Kerrich, 1989) or transcurrent to thrust systems (Colvine et al., 1984). The changing stress fields may cause the fluid propagation and subsequent gold mineralization during seismic activity (Goldfarb et al., 1991; Sibson et al., 1988; Cox et al., 2001). Economic gold mineralization is typically hosted outside of the main structure within secondary, anastomosing structures (Weinburg et al., 2004). Other favorable areas for gold mineralization are regional fault intersections, areas of regional anticlines, and areas of competency contrast (Groves et al., 2000).

Orogenic gold deposits typically have Au/Ag ratios of 5:1 to 10:1 and are consistent regardless of metamorphic grade (Goldfarb et al., 2005). Sulphides are typically present in quartz or quartz–carbonate veins and host wall–rock, composing 3–5% modally of the host rock (Goldfarb et al., 2005). Arsenopyrite is the most common sulphide mineral present within metasedimentary lithologies while pyrite dominates in plutonic and volcanic lithologies. In reduced hydrothermal systems 400ºC and above, pyrrhotite and löellingite are the dominant sulphides present (Goldfarb et al., 2005; Tomkins et al., 2007).

Sulphur isotopes $\delta^{34}S$ typically range from 0 ‰ to 9 ‰ (Kerrich, 1987; Peter and Golding, 1989). Anomalously high values suggest a wall rock enrichment of ^{34}S while 0 ‰ has been historically attributed to a magmatic origin, and greater ranges may be due to metamorphic and magmatic fluids mixing (Goldfarb et al., 2005). Timing of gold mineralization is most commonly syn– to post–peak metamorphism in the greenschist facies (Goldfarb et al., 2005). The greenschist facies of metamorphism has been proposed to be important to gold mineralization due to: 1) fluids being released as a product of many prograde greenschist to amphibolite facies metamorphic reactions, 2) the brittle–ductile transition in the lithosphere generally lies within pressures consistent with the greenschist facies, 3) fluids focusing and phase separation can occur during ascension in the lithosphere at depths typical of the greenschist facies, and 4) gold solubility drops significantly above the greenschist facies (Goldfarb et al., 2005). However, gold mineralization in orogenic gold deposits has been documented in lithologies that have reached a wide range of metamorphic grades from subgreenschist to granulite facies metamorphism (Groves et al., 1992).

In addition to the Borden Mine, other gold mines and deposits in northern Ontario in the Superior Province that have reached medium– to high–grade metamorphism include: Red Lake Mines, Hemlo Mine, Detour Lake Mine, historic Hardrock Mine in Geraldton, and Musselwhite Mine (Pan, 1993; Dubé et al., 2004; Stinson et al., 2009; Stinson, 2013). Remobilization of gold mineralization during metamorphism and partial melting has also been studied (Tomkins et al., 2007).

This dissertation will provide the first gold mineralization model for the Borden Mine. The model demonstrates that primary mineralization formed in the Neoarchean in a seafloor hydrothermal system and was remobilized and reconcentrated during medium– to high–grade metamorphism as an orogenic gold deposit.

2.2.1 Literature review of the study area

This study separates the Superior Province into three regions: (1) the northern Superior Province, North Caribou Superterrane, (2) the northeastern Superior Province, including the Minto, Bienville, La Grande, Ashnanipi subprovinces, and (3) the southern Superior Province, including all regions south of the North Caribou Superterrane (Figs. 2.2–2.4).

The southern Superior Province is composed of Archean, curvilinear to linear domains, subprovinces, and terranes that experienced an extensive geological history involving many episodes of compression to transpression, plutonism, and regional metamorphism in the Meso– to Neoarchean (Fig. 2.3) (Langford and Morin, 1976; Card and Ciesielski, 1986; Card, 1990; Percival et al., 2006). The usage of 'subprovince" is used in this thesis to better highlight the unique geological features of different portions of terranes and domains documented in previous studies, particularly in the Wawa, Abitibi, and Wabigoon subprovinces (or more specifically the modern terminology, the Wawa–Abitibi terrane and the Eastern and Western Wabigoon terranes). The southern Superior Province includes the following domains, subprovinces, and terranes south of the North Caribou terrane: Uchi, English River, Winnipeg River, Bird River, Wabigoon, Marmion, Quetico, Wawa, Abitibi, Opatica, Pontiac, and Minnesota River Valley (Figs. 1.2, 2.2) (Card and Ciesielski, 1986; Card, 1990; Percival et al., 2006).

In the southern Superior Province, the WGD and KSZ crosscut the curvilinear to linear domains listed above except for the Pontiac subprovince and Minnesota River Valley terrane (MRVT) (Fig. 1.2) (Percival and Card, 1983; Card and Ciesielski, 1986; Card, 1990; Percival et al., 2006). In the northeastern Superior Province, the Ashuanipi, Bienville, and LaGrande subprovince are curved to curvilinear while the Douglas Harbour Qalluvi–artuuq, Inukiuak, Tikkerutuk, Utsalik domains Goudalie and Minto subprovinces are predominantly linear (Fig. 2.2–2.4) (Percival et al., 2006). The northern Superior Province is composed of linear North Caribou Superterrane (including the Uchi subprovince along the southwestern boundary with the southern Superior province), the Oxford–Stull domain, and the Northern Superior Superterrane and is believed to be the ancient nucleus to the Superior Province (Fig. 2.2) (Percival et al., 2006).

The amalgamation of the southern and northeastern Superior Province into the present–day configuration has been previously proposed by many authors with benchmark studies conducted by Langford and Morin (1976), Sims et al. (1980), Percival (1981), Card and

Ciesielski (1986), Sims and Day (1993), Percival et al. (1994, 2012), Percival and Easton (2007). The formation of the Superior Province has also been proposed through various means of mantle flow (Bédard and Harris, 2014; Mints, 2015).

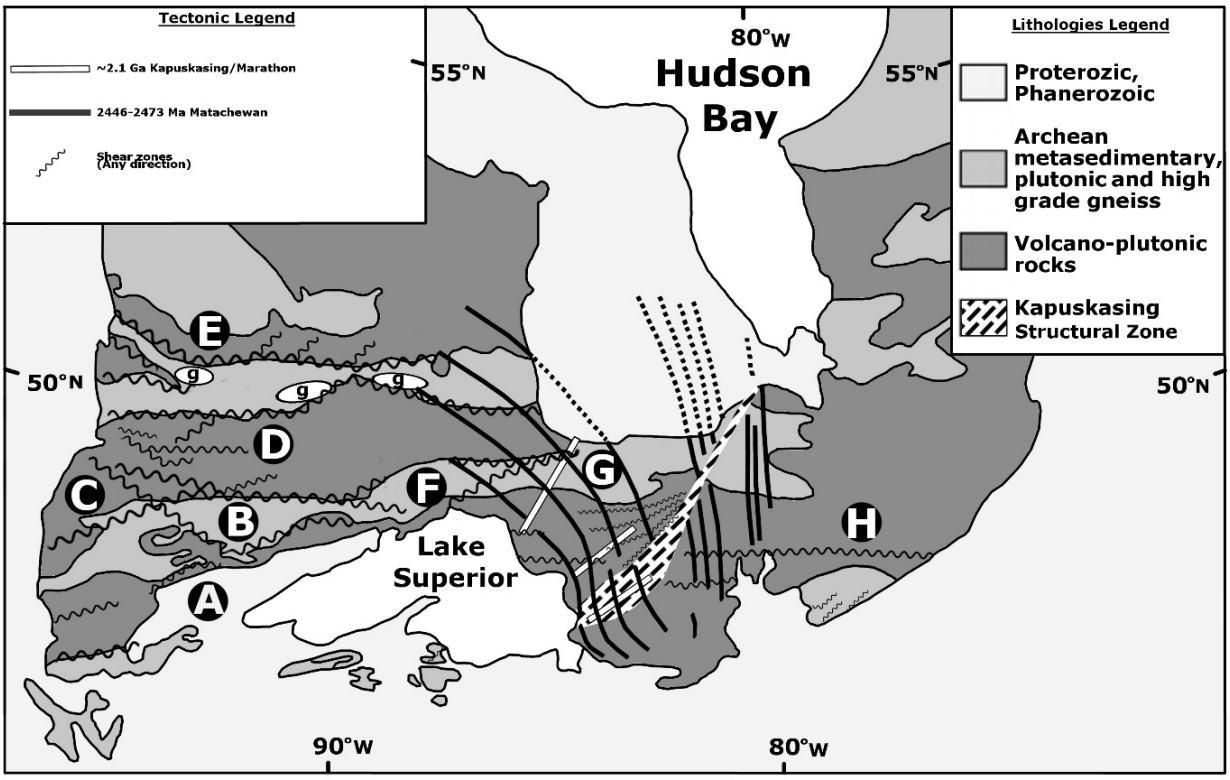

Figure 2.2: Schematic map of the regions of cratonic– to regional–scale structures referred in this thesis throughout the in the southern Superior Province and Paleoproterozoic mafic dyke swarms (A) Vermilion, Burntside, and Minnesota River Valley structures, (B) Quetico, Eye–Dasha, Finlayson structures, (C) Cameron Lake structures, (D) Miniss River, Lake St. Joseph structures, (E) Red Lake structures, (F) Beardmore–Geraldton, Hemlo–Heron Bay, and other structures, (G) Gravel and Montreal River deformation zones, Chapleau Belt and other structures in the Kapuskasing Structural Zone, (H) The Pontiac and Abitibi subprovince structures including the Procupine–Destor deformation zone, Matachewan dykes (black) with Z–folded with dextral to oblique faults that crosscut the Wawa, Abitibi, and Quetico subprovinces, and Kapuskasing/Marathon dykes (white) that are perpendicular to the folded Matachewan dykes (Modified after Card and Ciesielski, 1986; Card, 1990; Johnson, 1991; Bornhort and Johnson, 1998; Percival et al., 2012; Jirsa, 2016).

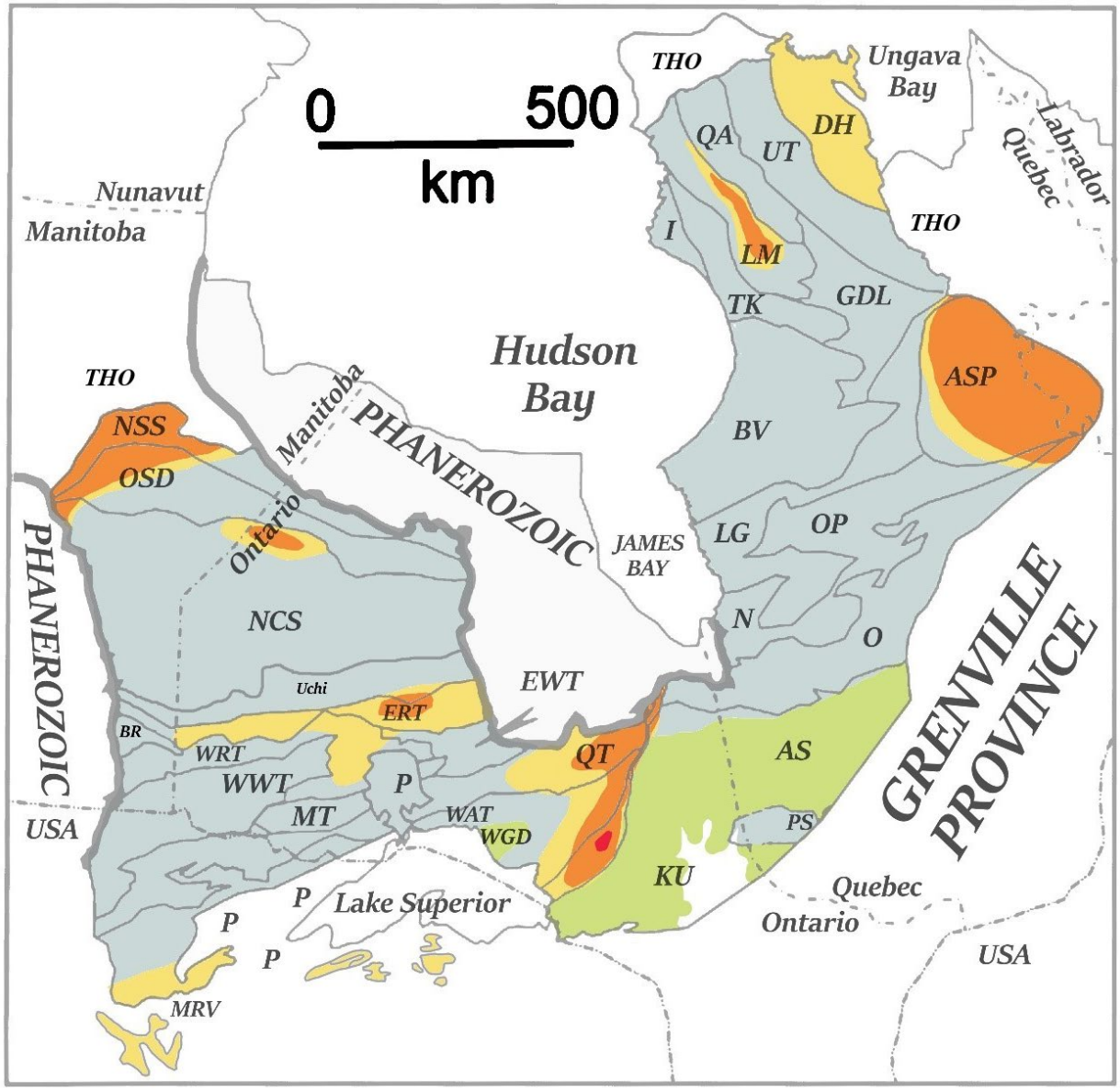

Figure 2.3: The metamorphic grades and paleopressures of the Superior Province with very–low grade metamorphism (light green), medium–grade metamorphism (grey), medium– to high–grade metamorphism (yellow), high–grade metamorphism (orange), and high–pressure and temperature metamorphism (red) (Modified after Easton, 2000; Percival et al., 2012 and references therein). Note the areas of medium– to high–pressure and temperature metamorphism in the MRV, Minnesota River Valley terrane, KU, Kapuskasing Structural Zone, QT, Quetico, ASP, Ashuanipi, WGD, Wawa Gneiss Domain, LM, L. Minto subprovince, DH, Douglas Harbour domain, PS, Pontiac subprovince, and WRT, Winnipeg River subprovince. Abbreviations are listed in Fig. 1.2.

Proposals of names, and subsequent correlations between many of these names, dates, and tectonic styles for the final or terminal Archean accretion or orogeny include: Kenorland, Algoma, Superia, Superior, Wawa, Abitibi, Minnesota, Shebandawon, Blezardian, and Pontiac with geochronological ages ranging between 2703–2400 Ma (Card and Ciesielski, 1986; Card, 1990; Phinney and Halls, 2001; Percival et al., 2006; Percival et al., 2012). Recent proposals for the timing of the final amalgamation of the southern Superior Province suggest an earlier Neoarchean amalgamation of the Wawa–Abitibi terrane, Pontiac subprovince, and the Minnesota River Valley terrane at ca. 2.68 Ma (Percival et al., 2006) or ca. 2.62 Ma and completed in the Paleoproterozoic (Bickford et al., 2006; Schmitz et al., 2006).

This dissertation will provide a new tectonic model integrating new data and previously published studies in field mapping, structural geology, geochronology, metamorphic petrology, seismic geophysics, paleomagnetism, and geochemistry.

2.2.2 North Caribou Terrane

The North Caribou terrane is located to the north of the Uchi subprovince and is thought to be a nucleus for other terranes that were accreted southward and northward (Fig. 2.2) (Thurston et al., 1991). The terrane is dominated by Mesoarchean metasedimentary lithologies and volcanic and plutonic lithologies (Stone et al., 2004). Late stage, Neoarchean granitic plutonism, common throughout the southern Superior Province, was also present in the northern Superior Province and continued to at least 2.62 Ma based on various geochronological studies using U–Pb zircon, titanite, and monazite geochronology (McNicoll et al., 2016; Van Lankvelt et al., 2016). Matachewan mafic dykes crosscut the southern Superior Province into the Uchi subprovince and North Caribou terrane (Symons et al., 1994; Evans and Halls, 2010).

2.2.3 Northeastern Superior Province

The northeastern Superior Province is primarily composed of Eo– to Neoarchean metamorphosed and migmatized volcano–sedimentary sequences in significant coeval tonalite–trondhjemite plutonic suites with crosscutting granite, granodiorite, and pyroxene–bearing plutons with ages <2.74 Ga, and high temperature, low pressure metamorphism (e.g. Percival and Skulski 2000; Leclair et al. 2001, 2003a, 2006) (Figs. 1.2, 2.2–2.4). Reconnaissance–scale field mapping designated the Minto subprovince as a granulite terrane due to metamorphic

pyroxene isograds and migmatites (Card and Ciesielski 1986; van Nostrand et al., 2016). This designation was replaced with a composite terrane dominated by plutonic rocks enclosing remnants of unevenly distributed amphibolite to granulite–facies supracrustal belts with charnockites (Percival and Skulski, 2000). Aeromagnetic anomalies in the Minto subprovince define north to northwest–striking, steeply dipping fabric and relatively young granitic–enderbitic–charnockitic plutonic massifs typically 30 to 80 km wide which define a sigmoidal geometry and oblique offsets, late transverse faults, and suggest dextral shear deformation (Pilkington and Percival, 1999). An orocline at the Ashuanipi Subprovince has been proposed to explain the strike change between the predominantly east–west striking southern Superior Province and the north–south strike of the northeastern Superior subprovinces (Fig. 2.5) (Percival et al., 2006).

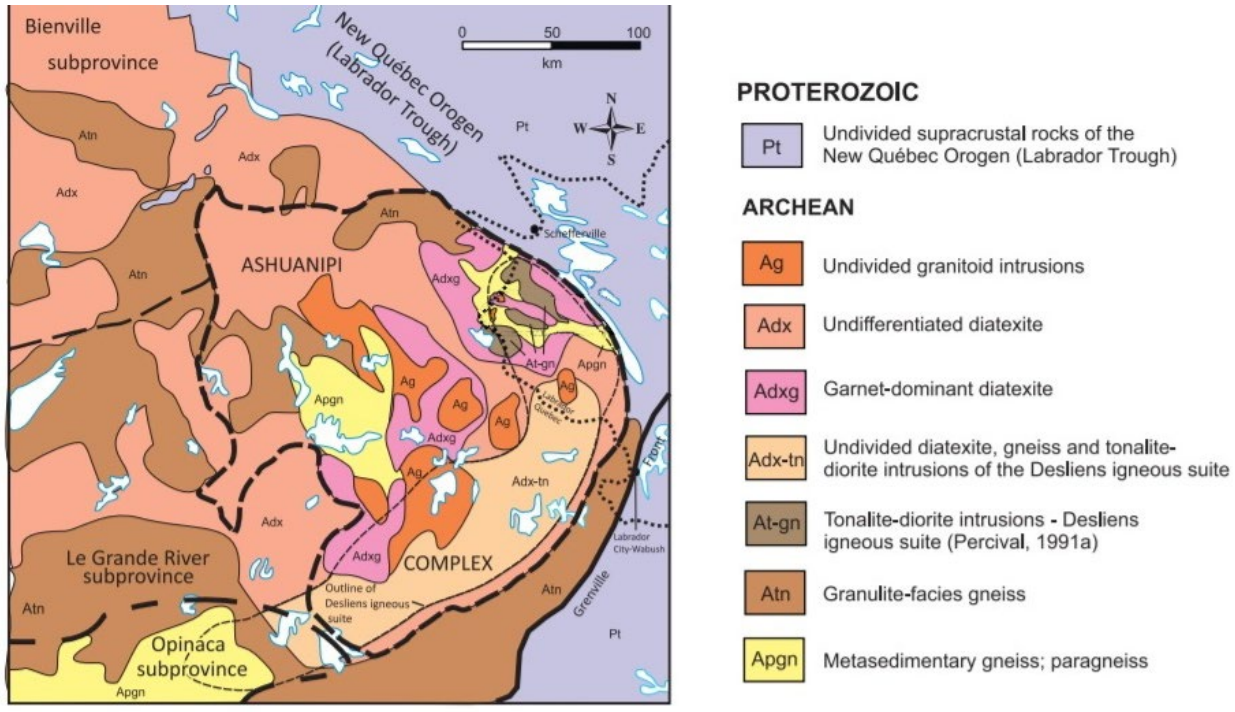

Figure 2.4: The northeastern Superior Province including the Opinaca subprovince (yellow), Le Grande River subprovince (brown), and entirety of the Ashuanipi subprovince (oranges, browns, yellows) highlighting the cratonic– to regional–scale folded geometry of granulites, migmatites, and intrusions (Card, 1990; Wheeler et al., 1996; van Norstrand et al., 2016 and references therein).

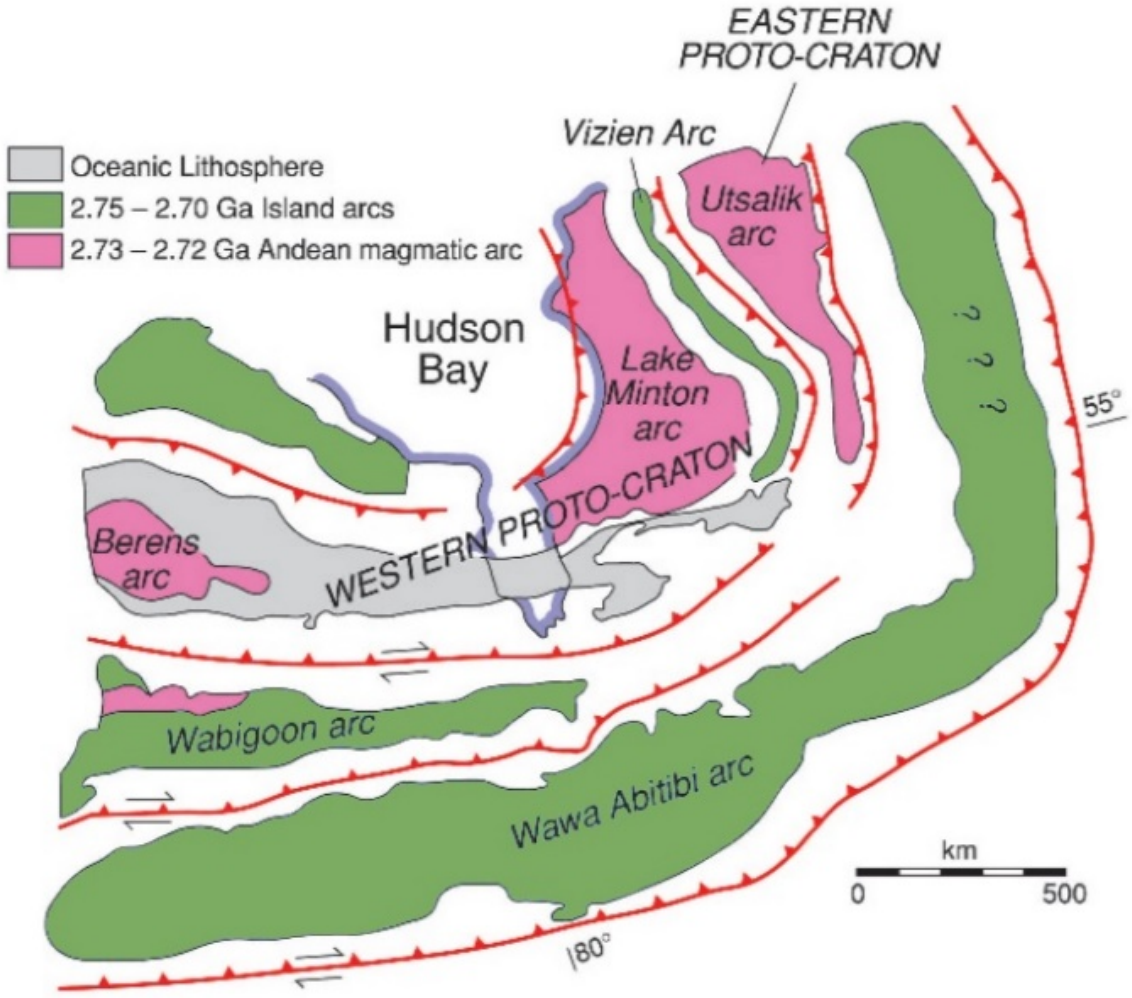

Figure 2.5: Cratonic– to regional–scale folded geometry of the southern and northeastern Superior Province with dextral–reverse and/or thrust shear zones along lithological boundaries of oceanic lithosphere, island arcs, and magmatic ars (Modified after Van der Voo, 2004).

The tectonic evolution of the northeastern Superior Province includes three distinct stages, including: (1) 2.88 to 2.74 Ga tholeiitic basalt, komatiite, felsic tuff, and iron formation, (2) 2.74–2.68 Ga transition to bimodal calc–alkaline volcanism, emplacement of syntectonic granite–granodiorite, enderbite–charnockite and mafic–ultramafic plutons in the region defining the north to northwest–striking, cratonic scale synchronous deformation and high–temperature metamorphism, and (3) culminating with 2.68–2.62 Ga granite, nepheline syenite, and carbonatite plutonism, high–temperature metamorphism and migmatization, and protracted post–metamorphic hydrothermal activity in structures (Figs. 2.3–2.4) (Percival et al. 2001; Berclaz et al. 2004; Leclerc, 2004; David et al. 2009; Maurice et al. 2009; Boily et al. 2006, 2009; van

Nostrand and Broughm, 2016). In addition, the presence of adakites in the Ashuanipi have supported additional tectonic models including from Percival et al. (2002) that involves subduction of oceanic crust beneath the southeastern corner of the Superior Province with adakite generated at ca. 2.723 Ga, continued subduction to ca. 2.700 Ga, followed by ridge–trench collision, and opening of a slab window by 2.696 Ga and was followed by granitic plutons (2.685–2.660 Ga) (Percival et al., 2002). Neoarchean cratonic– to regional–scale folded geometry of the southern and northeastern Superior Province has been proposed by Van der Voo (2004) (Fig. 2.5). Note the many similarities to the southern Superior Province, including the similarities in lithologies, geochronology, metamorphism, among others.

2.2.4 Southern Superior Province and neighbouring regions

The southern Superior Province is Archean, polydeformed and metamorphosed, with curvilinear to linear domains, subprovinces, and terranes that experienced an extensive geological history from the Meso– to Neoarchean including the southernmost Minnesota River Valley terrane (MRVT), Wawa subprovince and Abitibi subprovince (collectively the Wawa–Abitibi terrane), and Quetico (Opatica, etc.), Wabigoon, Pontiac, Winnipeg River, Bird River, English River, and Uchi subprovinces (Fig. 1.2) (Langford and Morin, 1976; Card and Ciesielski, 1986; Card, 1990; Percival et al., 2012). In the southern Superior Province, the WGD and KSZ crosscut the curvilinear to linear domains listed above except for the Pontiac subprovince and MRVT (Figs. 1.2–1.5, 2.2). The curvilinear to linear boundaries of the subprovinces, domains, and terranes in the southern Superior Province are referenced as striking east–west as a result of continuous accretion onto the northern Superior Province, although many have local– to regional–scale examples of curved to curvilinear areas that diverge from the regional, east–west strike of the boundaries (Fig. 1.2) (Langford and Morin, 1976; Card and Ciesielski, 1986; Card, 1990; Percival et al., 2012). There is a marked difference in subprovince width and metamorphic grade between the western and eastern Wawa and Abitibi subprovinces and the Quetico and Opatica subprovinces (Figs. 1.2, 2.3). The KSZ diverges from the east–west strike with an average northeast–southwest strike and curved boundaries with variable thickness (Fig. 1.2) (Langford and Morin, 1976; Percival and Card, 1983; Card and Ciesielski, 1986; Moser, 1994; Percival and West, 1994; Percival et al., 2012). A prevailing hypothesis for the

cratonic–scale boundary irregularity is indenter tectonics or similar (Sims and Day, 1993; Williams, 1991; Pan et al., 1994).

The process of amalgamation during the Archean into the present–day configuration has been previously proposed by many authors with benchmark studies including those conducted by Langford and Morin (1976), Sims et al. (1980), Card and Ciesielski (1986), Sims and Day (1993), Percival et al. (2012), Percival and Easton (2007). Numerous sets of Paleoproterozoic mafic dyke swarms crosscut the entire southern Superior Province, and include the ca. 2500–2400 Ma Matachewan mafic dykes that strike north to northwest and define gentle, upright folds, that were deformed from an undefined event during the Paleoproterozoic that caused <10º cratonic–scale rotation (Figs. 1.2, 2.2) (Vandall and Symons, 1990; Symons et al., 1994).

The majority of regional shear zones in the southern Superior Province are Archean, define the linear boundaries, strike east–west, dip steeply northward, and are ductile to brittle–ductile, dextral strike–slip (with reverse, dip–slip components) structures (Fig. 1.2, 2.2) (Card, 1990; Czeck, 2003; Czeck et al., 2006, 2009; Dyess et al., 2015). Fewer shear zones are Neoarchean to Paleoproterozoic, sinistral shear zones that are typically brittle–ductile, transpressional to transtensional, strike northeast–southwest, variable moderate dips, and are oblique to perpendicular to terrane, domain, and subprovince boundaries, except for areas of proposed indenters (Fig. 2.2) (Sims et al., 1980; Peterman and Day, 1989; Card, 1990; Sims and Day, 1993; Pan et al., 1994; Bethune et al., 2006; Erickson, 2010). Peak regional metamorphism is generally symmetrical to these boundaries with regularly spaced, linear to curvilinear metamorphic isograds (Fig. 2.3) (Easton, 2000). Variable unroofing and retrograde metamorphism has been well documented in the southern Superior Province and is defined by late Neoarchean, asymmetrical metamorphic isograds, poorly defined by subprovince boundaries with irregular localized exposure of granulites and regional–scale low–pressure metamorphism within and adjacent to these late–stage northeast–southwest–striking structures and irregular boundaries (Figs. 1.2, 2.2–2.3) (Pan et al., 1994; Pan et al., 1999; Easton, 2000; Hynes and Song, 2006; Percival and Easton, 2007). The east–west striking structures parallel to boundaries synchronous with early, prograde metamorphism throughout the southern Superior Province generally range in age between ca. >2.7 to 2.68 Ma while the sinistral shear zones and lower–pressure metamorphism and plutonism developed later ca. <2.68 Ma and into the Paleoproterozoic (Figs. 2.2–2.3) (Card and Ciesielski, 1986; Corfu, 1988; Percival and Williams,

1989; Peterman and Day, 1989; Kamineni et al., 1990; Southwick, 1991, 2014; Pan et al., 1994; Pan and Fleet, 1998; Pan et al., 1999; Hanes et al., 2003; Smith et al., 2004; Valli et al., 2004; Bethune et al., 2006; Hrabi and Cruden, 2006; Hynes and Song, 2006; Kremer and Lin, 2006; Duguet et al., 2009; Percival and Easton, 2007; Stone, 2010; Percival et al., 2012; Zhou et al., 2016). In addition, granulites, gneissic plutons, domes, and the Pontiac metamorphic core complex have been exhumed in this time frame within these curvilinear boundaries and sinistral shear zones (Pan et al., 1994; Sawyer and Barnes, 1994; Percival and Easton, 2007; Liodas, unpublished MSc. thesis, 2010).

The Superior Province lithosphere and mantle have remained stable since the Neoarchean based on electrical and seismic anisotropy studies using magnetotelluric and teleseismic data (Boerner et al., 2000; Frederiksen et al., 2013; Ferré et al., 2014). The western and eastern Superior Province differ in their lithospheric and mantle properties between the Wawa subprovince and Abitibi subprovince boundary, at the transition between the WGD and KSZ with the western Superior Province having ENE–WSW fast directions and the eastern portion having an east–west orientation (Frederikson et al., 2007, 2013). Shear wave splitting measurement data indicate north–northwest to northwest measurements in the western Superior Province and west–northwest to east–west directly east of the KSZ (Frederiksen et al., 2007). Heat flow has also been documented to be lower in the eastern Abitibi subprovince compared to the western Wawa–Abitibi (Jaupart et al., 2014). A preserved slab of oceanic lithosphere has been interpreted at 40 to >60 km depth in the upper mantle north of the Wawa–Abitibi and Quetico subprovince suture with a northeast dip (Sol et al., 2002; Musacchio, 2004; Frederiksen et al., 2007). Gravity, aeromagnetic, and seismic refraction geophysical studies provide evidence of >50 km overthickened lithosphere and a complex lithosphere–mantle boundary indicative of uplift of lower–crustal material (Cook, 1985; Percival and West, 1994; Darbyshire et al., 2007).

The final amalgamation of the Superior Province has been suggested by many authors to have been completed by the Neoarchean (Card and Ciesielski, 1986; Card, 1990; Percival et al., 2006). The central to southern Superior Province, including the Wabigoon, Marmion, Winnipeg River, English River, Quetico, Opatica subprovinces, Wawa–Abitibi terrane, and WGD, KSZ, are all well–exposed and studied, however their tectonic histories individually and as a whole, with respect to the construction of the Superior Province, require further study. Each subsequent subprovince and/or terrane affected the next one to amalgamate onto the southern Superior

Province, similar to a domino effect (Langford and Morin, 1976; Card and Ciesielski, 1986; Card, 1990; Percival and Easton, 2007). Although the boundaries of the central and southern subprovinces, terranes, and domains are commonly described as east–west striking and linear to curvilinear there are important differences in size, shape, and boundary geometries that differ significantly from average. In particular, the Winnipeg River, Bird River, English River, Eastern and Western Wabigoon, Quetico and Opatica subprovinces, Marmion domain, WGD, and KSZ, and Wawa and Abitibi subprovinces have subprovince boundaries with pronounced differences between the adjacent subprovince that differ in size, shape, and geometeries along their strike and require additional tectonic interpretations to better explain their current sizes, shapes, and geometries (Fig. 1.2). The subdivisions of the southern Superior Province will be described below from geographical north to south and with characteristics relevant to this thesis highlighted.

2.2.5 Uchi Subprovince

The Uchi subprovince is commonly included in either the North Caribou Superterrane or the southern Superior Province, however for this thesis it will be included in the southern Superior Province to highlight its characteristics (Fig. 1.2). The Uchi subprovince is dominated by metamorphosed mafic volcanic, felsic plutonic, and minor metasedimentary lithologies (Stott, 1996). The deformation zones define the Uchi–English River subprovince boundary with dextral, transcurrent shear zones and mylonites (Figs. 2.2, 2.6) (Osmani and Stott, 1988; Stott, 1996). The Sydney Lake–Lake St. Joseph Fault Zone is continuous for at least 440 km from Lake Winnipeg to Pashkokogan Lake where it connects to the Miniss River and Pashkokogan Lake–Kenoji Lake Faults (Fig. 2.6) (Stott, 1996). Granitoid batholiths in the northern portion of the subprovince have long axes defining a northeast–southwest geometry (Stott, 1996). Early regional subgreenschist facies to amphibolite facies metamorphism occurred throughout the Uchi subprovince, predominantly along the regional, east–west to northeast–southwest to northwest–southeast striking, Lake St. Joseph Deformation Zone with significant retrograde metamorphism (Figs. 2.3, 2.6) (Goodwin, 1965; Ayres, 1978; Chipera and Perkins, 1988; Borowik, 1998). World–class gold mines and deposits in the Uchi subprovince host gold mineralization that formed between ca. 2712 Ma to ca. 2702 Ma and remobilized between 2.66 Ga and 2.63 Ga

during regional, thermal events documented by ^{39}Ar–^{40}Ar cooling ages in hornblende, muscovite, and biotite (Dubé et al., 2004).

2.2.6 English River Subprovince

The English River subprovince boundaries are generally linear except in the central region which is indented at the southern boundary (Figs. 1.2, 2.2, 2.6). Along the southern margin there is a 1 to 3 km wide, dextral to transcurrent brittle–ductile shear zone that has approximately 30 km of dextral, strike–slip displacement and 2.5 km dip–slip displacement with the south side up (Stone, 1982). The English River subprovince experienced multiple metamorphic events, including prograde amphibolite to granulite facies metamorphism and was exhumed relatively rapidly between 2.705–2.691 Ga (Figs. 2.3, 2.6) (Corfu, 1988; Pan et al., 1999; Smith et al., 2004; Hynes and Song, 2006). A metamorphic event occurred at 2.669 Ga and subsequent pegmatites and hydrothermal formed around 2.65 Ga (Corfu, 1988; Corfu et al., 1995; Pan et al., 1999; Smith et al., 2004). Regional structures coincide or postdate the migmatitic layering after 2.69 Ga and exhumation along brittle structures, such as the Sydney Lake –Lake St. Joseph fault have been interpreted to have formed much later at 2.5–2.4 Ga (Fig. 2.6) (Hanes et al., 2003; Hrabi and Cruden, 2006). The tectonic setting has been interpreted as a fore–arc basin (Langford and Morin, 1976), an accretionary prism (Breaks and Bond, 1993), and a back–arc basin (Pan et al., 1998). The timing of sedimentary deposition has been bracketed by the youngest detrital zircon U–Pb age of 2.713 Ga in the southern margin (Stott et al., 2002) and a 2.698 Ga crosscutting diorite–granodiorite intrusion providing a U–Pb age from igneous zircon (Corfu, 1988; Corfu et al., 1995).

2.2.7 Bird River Subprovince

The English River, Bird River, and Winnipeg River subprovinces intersect in a triple–junction boundary zone that is dominated by ductile thrust, high–angle reverse, and dextral and sinistral strike slip structures (Figs. 1.2, 2.2, 2.6) (Hynes and Song, 2006; Duguet et al., 2009). The northern and southern subprovince boundaries are straight and taper to a point in the southeastern boundary of the subprovince, where it is dominated by plutonic lithologies and zones of cataclasis with the metamorphic grade between greenschist and amphibolite facies (Fig. 2.3) (Černý et al., 1981; Beakhouse and McNutt, 1991). Felsic plutonic and pegmatitic

lithologies, including complex pegmatites, occur in this boundary zone and have U–Pb zircon ages as young as 2646 Ma (Wang, 1994; Smith et al., 2004; Gilbert, 2006; Kremer and Lin, 2006).

2.2.8 Winnipeg River Subprovince

The Winnipeg River subprovince is irregular in shape with curved to curvilinear boundaries around the southern Wabigoon subprovince and Marmion domain, and tapers to a point in the eastern boundary like the Bird River subprovince (Figs. 1.2, 2.2, 2.6). Significant Neoarchean plutonism is located throughout the terrane that crosscuts the older Paleo– to Meosarchean gneisses (Corfu, 1988; Tomlinson and Dickin, 2003; Melnyk et al., 2006). Multiple episodes of deformation and metamorphism affected the subprovince as documented in U–Pb zircon and titanite geochronological studies, including amphibolite to granulite facies metamorphism at 2680 Ma and localized, retrograde greenschist facies metamorphism between 2640 to 2520 Ma (Corfu, 1988). Sinistral transpression is restricted to the Miniss River Deformation Zone that defines the eastern boundary of the Winnipeg River terrane (Figs. 1.2, 2.2, 2.6) (Bethune et al., 2006). The Winnipeg River–English River subprovince boundary involves both dextral and sinistral strike–slip and high–angle reverse and thrust ductile deformation (Hynes, 1998).

2.2.9 Wabigoon Subprovince

The Wabigoon subprovince is commonly separated into the western and eastern Wabigoon subprovinces with the Marmion terrane dividing the two sides (Figs. 1.2, 2.2, 2.6–2.7) (Card, 1990; Percival et al., 2006). The Wabigoon subprovince may have been deposited upon the older Winnipeg River terrane and Marmion domain (Tomlinson et al., 2004; Melnyk et al., 2006). The Wabigoon subprovince is composed predominantly of mafic volcanic lithologies and tonalitic plutons (Corfu and Davis, 1991; Ayer and Davis, 1997; Wyman et al., 2000). The oldest, volcanic lithologies were formed between 2.775 and 2.70 Ga (Stott et al. 2002; Sanborn–Barrie and Skulski, 2006) and felsic plutons, some with sanukitoid affinity, circa 2.698–2.690 Ga, also occur in the subprovince (Stern et al., 1989; Percival et al., 2006).

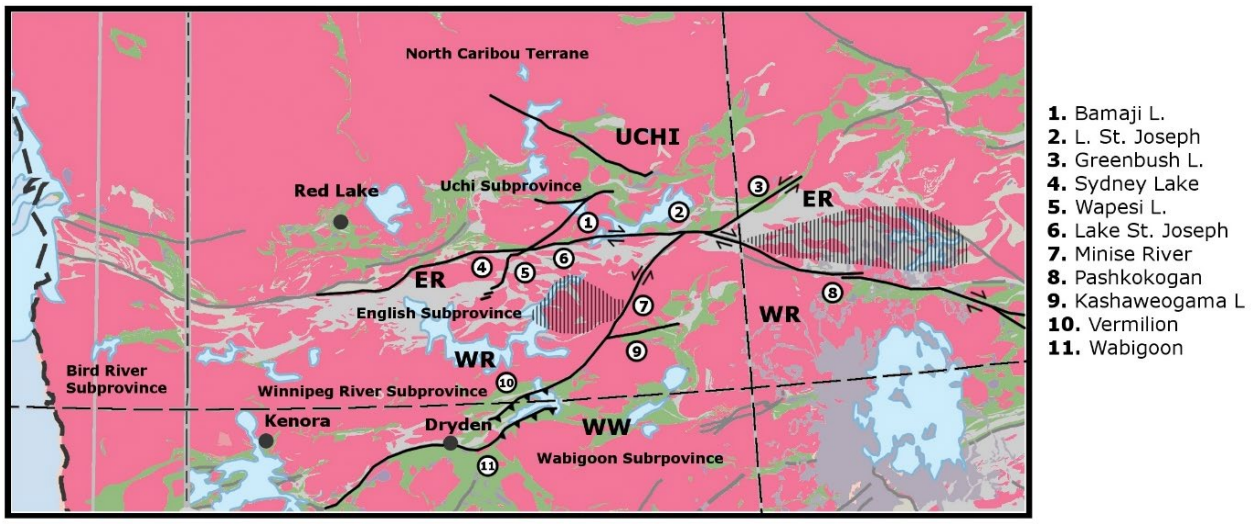

Figure 2.6: Regional–scale areas of exposed granulite facies lithologies (striped) are highlighted with adjacent regional– to cratonic–scale structures (black lines, numbered) within the western Wabigoon (WW, pink and green), English River (ER, light grey and pink), Uchi (pink and green), Winnipeg River (WR, pink), and Bird River (pink) subprovinces (Modified after Montison, et al., 2018).

Metasedimentary lithologies are younger than the metavolcanic and plutonic lithologies and were deposited <2.702 Ga (Fralick et al., 2006). A lower limit on the age of east–west striking, dextral transpressive shear zones in the area is 2.694 Ga (Stott et al., 2002) and oblique–ramp structures have similar approximate ages (Edwards and Stauffer, 1999) (Figs. 2.2, 2.6). Anorthosites in the Wabigoon subprovince intruded into the Wabigoon–Quetico subprovince boundary between 2716 ± 18 Ma and 2649 ± 17 Ma using U–Pb zircon geochronology in granitic lithologies and geochemical data which are consistent with syn– to post–collisional, extensional settings after intra–oceanic subduction zone settings (Zhou et al., 2016).

East–west striking, steeply–dipping northward shear zones in the eastern Wabigoon have $^{40}Ar/^{39}Ar$ geochronological ages extending from ca. 2690–2950 Ma in hornblende, 2660–2560 Ma in muscovite, and 2650–2600 Ma in biotite (Figs. 1.2, 2.2, 2.6) (Culshaw et al., 2006). Northeast–striking structures are younger than 2685 Ma as the few hundreds of meters width structures, including mylonite and cataclasite, offset earlier plutons (Stone, 2010; Stinson, 2013, MSc. thesis). The regional deformation zones, such as the Miniss River Deformation Zone, are sinistral strike–slip structures that are oblique to the most common dextral structures in the Wabigoon subprovince (Figs. 2.2, 2.5) (McWilliams, 1998; Bethune et al., 2006; DeWolfe et al., 2007). The deformation zones are typically mylonitic to schistose with pegmatites and migmatitic leucosomes that define the ductile, sinistral strike–slip structure and were active at

least to 2.65 Ga and offset the Quetico and Wabigoon subprovince boundaries (Fig. 2.7) (Percival and Williams, 1989; Williams, 1989). There are also crenulation cleavage and schistosity that exhibit evidence of sinistral, extensional movement with steep to shallow plunges east and west, and a secondary kink in foliation and crinkle in lineation (Williams, 1989). The metamorphic grade increases from lower greenschist facies in the western Wabigoon and most eastern Wabigoon to upper amphibolite facies and migmatization in the far eastern Wabigoon subprovince and along the Wabigoon–Quetico subprovince boundary immediately west of the KSZ (Stinson, 2013).

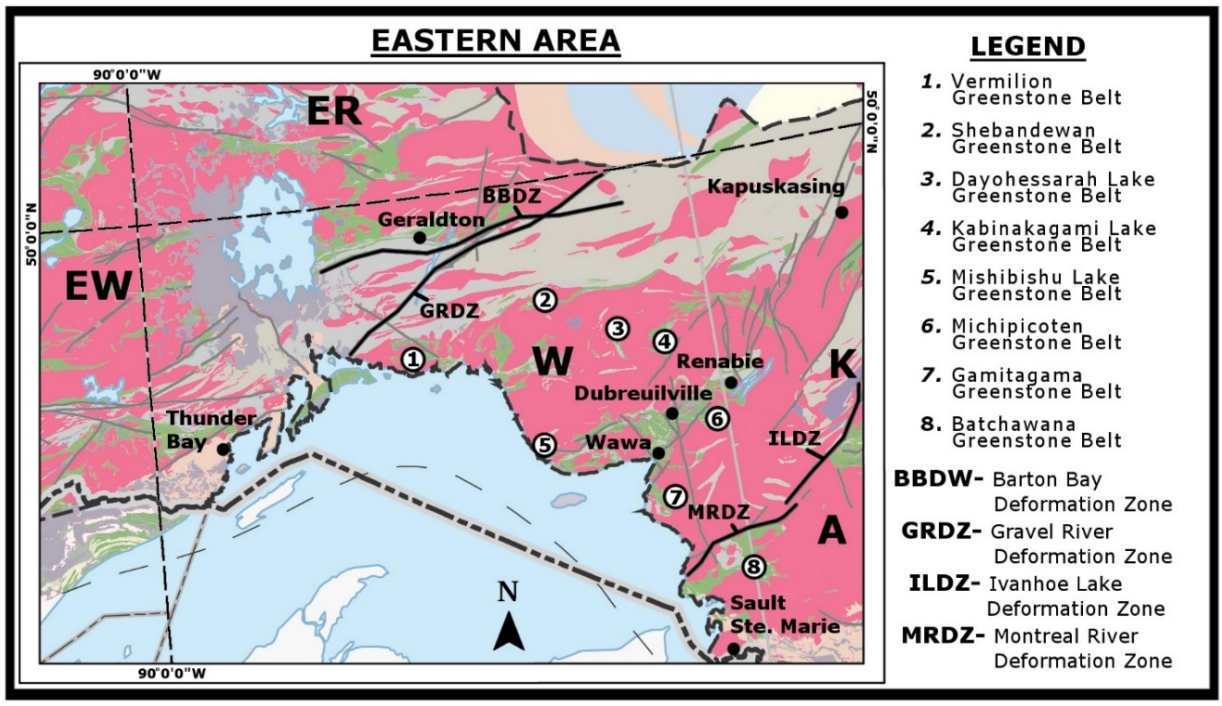

Figure 2.7: The greenstone belts (numbered) of the eastern Wawa subprovince (W, lower pink and green), major gold camps and cities (black dots), Quetico subprovince in the middle of the map (Q, grey), eastern Wabigoon subprovince in the north (EW, pink and green), English River in the far northwest (ER, grey), Abitibi in the east (A, pink and green), Kapuskasing Structural Zone (K, pink, grey, purple, and green), Wawa Gneiss Domain (WGD, grey), regional structures (dark grey, bold font), and Proterozoic cover (light grey and light peach). Note the structures in the KSZ extend to at least Lake Superior in the MRDZ and the northeast– and east–west striking plutons and supracrustal belts in the WGD (Modified after Montison, et al., 2018).

2.2.10 Marmion Domain

The Marmion Domain is predominantly 3.01 to 2.999 Ga tonalite with smaller, younger greenstone belts throughout ranging in ages from 2.99 to 2.78 Ga (Figs. 1.2, 2.2, 2.7) (Davis and

555 Jackson, 1988; Tomlinson et al., 2004). Regional, ductile sinistral strike–slip occurred in the
556 Miniss River Deformation Zone circa 2.685 Ga followed by brittle reactivation (Figs. 2.1, 2.6)
557 (Bethune et al., 2006) as well as strike slip and dip–slip motions along the terrane boundary with
558 neighbouring terranes (Gower and Clifford, 1981). The Eye–Dashwa pluton experienced
559 significant northeast–striking, dextral strike–slip and thrust components with mylontitic to
560 cataclastic deformation after its crystallization age of 2665 Ma that continued into the
561 Proterozoic (Fig. 2.7) (Kamineni et al., 1990).
562
563 **2.2.11 Quetico and Opatica Subprovinces (± Nemiscau subprovince)**
564 The Quetico, Opatica, and Nemiscau subprovinces are commonly identified separately in
565 literature, although many workers have proposed the thicker, eastern Opatica ± Nemiscau
566 subprovinces as the continuation of the thinner, more sinuous, western Quetico subprovince
567 (Figs. 1.2, 2.2, 2.6–2.7) (Card and Ciesielski, 1986). In this thesis the Quetico subprovince refers
568 to all three unless stated otherwise. The Quetico subprovince boundary with the western
569 Wabigoon subprovince is well defined along the Seine River–Rainy deformation zone, whereas
570 east of Lake Nipigon the boundary with the eastern Wabigoon has been defined as an imbricate
571 zone with an earlier history of structural telescoping (Figs. 1.2, 2.6–2.7) (Devaney and Williams,
572 1989; Tomlinson et al., 1996). The Wabigoon–Quetico subprovince boundary is also marked
573 sporadically by coarse metasedimentary lithologies with detrital zircon ages of ca. <2.690 Ga
574 (Davis et al., 1989; Zaleski, 1999; Fralick et al., 2006). The Quetico subprovince is composed of
575 metasedimentary lithologies, migmatite, and granite that is steeply dipping, polydeformed, and
576 has experienced variable metamorphism (Percival and Williams, 1989). Seismic reflection
577 profiles indicate north–dipping reflectors of a deformed, metasedimentary basin (Percival et al.,
578 2006).
579 Metamorphism in the Quetico subprovince reached amphibolite facies to local, low–
580 pressure granulite facies in the central region at 2.67–2.65 Ga (Figs. 2.3, 2.6) (Pan et al., 1994;
581 Pan and Fleet, 1998) and greenschist facies at the subprovince boundary (Percival, 1989).
582 Prograde regional metamorphism occurred at 2698–2689 Ma in the staurolite zone and 2689–
583 2671 Ma in the sillimanite zone, followed by retrograde metamorphism during south–southeast
584 compression at 2671–2667 Ma using U–Pb monazite geochronology (Valli et al., 2004). Late–
585 tectonic granitic plutons and pegmatites have zircon ages in peraluminous granite of 2.67 Ga and

biotite granite of 2.63 Ga (Southwick, 1991) and monazite U–Pb ages from ca. 2671± 2 to 2641 Ma (Percival and Sullivan, 1988; Percival and Williams, 1989). Batholiths and adjacent plutons are interpreted to have formed from partial melting of the migmatitic terrane and the second plutonic event represents double distillation of melt from a predominantly sedimentary parent lithology (Southwick, 1991).

Regional structures along the Wabigoon–Quetico subprovince boundary include the Quetico Deformation Zone that is predominantly ductile to brittle–ductile with dextral, strike–slip components that deformed into the Paleoproterozoic (Figs. 2.2, 2.6–2.7) (Peterman and Day, 1989). As much as 100 km of dextral strike–slip displacement has been estimated for the Quetico Deformation Zone (Mackasey et al., 1974). The numerous structures crosscut the Quetico subprovince at oblique angles, are ductile, mylonitic, sinistral shear zones and faults (e.g. Miniss River structures) (Williams, 1989; Bethune et al., 2006). Gneissic domes occur in the western portion of the subprovince and have experienced deformation during and after emplacement (Borradaile and Gauthier, 2003). Northeast–striking, sinistral, late structures crosscut the early, regional metamorphic isograds strike and lower temperature and pressure minerals outcrop and define the lineation, including cordierite after staurolite, sillimanite after kyanite (Pirie and Mackasey, 1978; Williams, 1989; Stinson, 2013). The easterly plunge of high–grade metamorphic minerals defining isograds do not coincide with the differential uplift of granulite facies in the central subprovince (Williams, 1989).

There are two sets of foliation throughout the Quetico subprovince, particularly near the Quetico Deformation Zone, with one at 080° north northeast and another, which is less developed, is 055° northeast (McWilliams, 1998). The northeast–striking structures include portions of the Quetico and Seine Deformation Zones near the Quetico–Wabigoon subprovince boundary. There are schistose lithologies up to several hundreds of metres wide with mylonite, cataclasite, and pseudotachylite throughout (Stone, 2010). The Quetico Deformation Zone was active well into the Proterozoic with a Rb–Sr isochron age of 1947 ± 23 Ma (Figs. 2.2, 2.7 (Peterman and Day, 1989).

The Quetico subprovince has been proposed as a forearc and the depositional ages (2.698–2.690 Ga) are coeval with the Wabigoon terrane late arc magmatism, perhaps followed by slab breakoff following collision with the Wawa and Abitibi subprovinces (Langford and Morin, 1976; Percival and Williams, 1989; Fralick et al., 2006; Percival et al., 2006). Card

(1990) suggested other possible extensions of the Quetico and Opinaca subprovinces include the English River and Nemiscau subprovinces. Indeed, petrologically and geochemically they may represent one, large accretionary prism as defined by Doyon (2004). Different degrees of metamorphism have been previously studied with an increase from the Quetico to the Opinaca subprovince to the east and may be explained by differential uplift (Percival, 1989; Guernina and Sawyer, 2003). Moukhsil et al. (2003) proposed volcanic and plutonic formation in the Nemiscau subprovince between 2697 and 2674 Ma from studying U–Pb in zircons in paragneisses. Regional high temperature, low pressure metamorphism occurred in the Nemiscau and Opinaca subprovinces after 2670 Ma and was attributed by a break in the lithosphere to produce deep, partial melting and metamorphism (Moukhsil et al., 2003). Structurally the subprovinces are complex as they consist of complex folds that formed in a compressive regime (Percival, 1989; Williams, 1990) and extensional features, such as a back–arc basin (Moukhsil et al., 2003).

2.2.12 Wawa and Abitibi Subprovinces

The Wawa and Abitibi subprovinces (Figs. 1.2–1.4, 2.6–2.10) are commonly considered as one larger terrane (i.e. the Wawa–Abitibi terrane) but for the purpose of this thesis they are described separately in order to highlight their differences (Ludden et al., 1986; Percival and West, 1994). The southern boundaries of the Wawa and Abitibi subprovinces are currently being researched as they outcrop and have been reached in drill core in Minnesota, Wisconsin, and Michigan (Fig. 2.10) (Sims and Peterman, 1992; Bornhorst and Johnson, 1998; McCormick, 2010). The division between the western Wawa subprovince and eastern Abitibi subprovince is marked by the WGD and KSZ in the centre of the Superior Province. The Quetico–Wawa subprovince boundary is curvilinear boundary with indents into the western and centre of the terrane into the Quetico subprovince. The Wawa subprovince is also markedly narrower in plan view than the Abitibi subprovince. The southern boundary between the Wawa subprovince and MRVT is sharp while the southern Abitibi subprovince boundary with the Pontiac subprovince is more irregular. The greenstone belts within the Wawa and Abitibi subprovince parallel the subprovince boundaries. The western Wawa subprovince includes many Archean greenstone belts, including the Mitchipicoten, Mishibishu, Gamitagama, Batchawana, Hemlo–Schreiber, Manitouwadge, Shebandowan, Vermilion greenstone belts, among others, while the eastern Abitibi subprovince includes greenstone belts including the Abitibi (including the Swayze and

Batchawana) (Figs. 2.6–2.10) (Card and Ciesielski, 1986). The long axes of the western Wawa and eastern Abitibi greenstone belts are predominantly have east–west geometries, however the central greenstone belts adjacent to the WGD have long axes between northeast–southwest to north–south (Card, 1990).

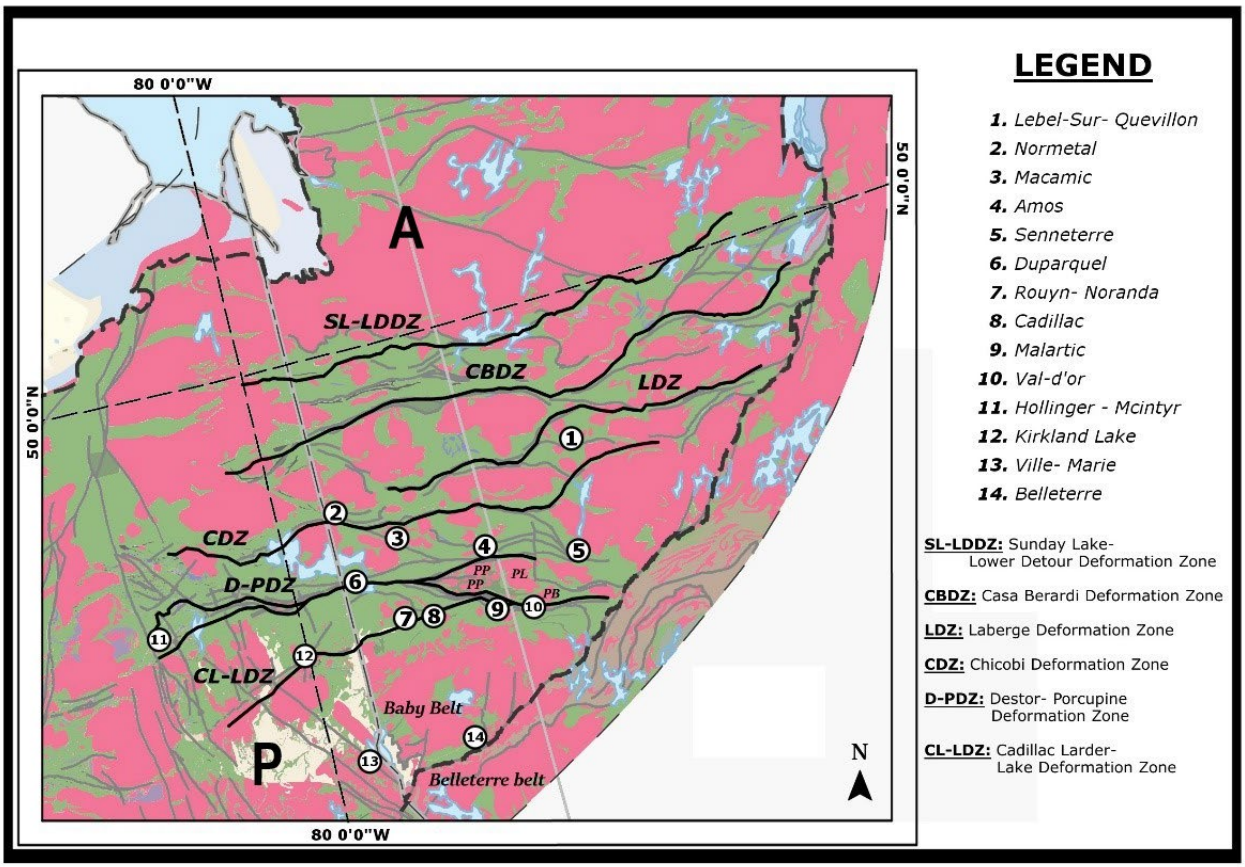

Figure 2.8: The Abitibi (A, green and pink) and Pontiac (P, pink and yellow) subprovinces highlighting the major regions and gold camps (numbered and/or named) and regional–, subprovince– and cratonic–scale structures (named and/or highlighted in black) (Modified after Montsion, et al., 2018).

Structures in the Wawa and Abitibi subprovinces can be categorized into east–west striking and northeast–southwest striking and generally parallel the geometry of the subprovince and greenstone belt boundaries (Figs. 1.2, 2.2, 2.6–2.10). Ductile, east–west striking, subvertical to vertical, dextral strike–slip transpressive shear zones were active at ca. 2.685 Ga in much of the terrane, including the Larder–Cadillac and Porcupine–Destor deformation zones (Figs. 2.2, 2.8)(Corfu and Stott, 1986, 1996; Leclair et al., 1993; Bursall et al., 1994; Peschler et al., 2006). Northeast–striking shear zones are located around Lake Superior to the north, including the Vermillion and Burntside shear zone and among others that crosscut the entire Wawa and Abitibi

subprovinces and parallel the adjacent WGD and KSZ (Sims et al., 1980; Card and Ciesielski, 1986; Leclair et al., 1993). A seismic reflection survey suggested that many of these shear zones may also continue across Lake Superior (Milkereit et al., 1988). The shear zones in the Wawa subprovince strike northeast to north–northeast near the town of Wawa and continue east towards the WGD and the KSZ. Paleomagnetic data collected from Matachewan dykes suggest the Wawa subprovince has not been rotated or translated ≥ 8º relative to the adjacent Abitibi subprovince (Fig. 2.2) (Vandall and Symons, 1990; Symons et al., 1994). Cratonism of the Wawa subprovince has been proposed as occurring at a high angle to the east–west striking lithologies and is related to the northeast–striking steep cleavages and upright folds (McGill, 1992). Local extension between 2680 and 2670 Ma may have been a result of oblique plate collision after subduction along the southern Superior Province (Ayer et al., 2002).

The metamorphic grade varies from low–grade prenhite–pumpellyite to lower greenschist in the western and eastern extremes of the Wawa and Abitibi subprovinces to medium– to high–grade in the center adjacent to the WGD and KSZ (Fig. 2.3) (Powell et al., 1993, 1995; Pan and Fleet, 1995; Easton, 2000). The juxtaposed metamorphic low–grade and medium– to high–grade are defined by the numerous late–stage northeast–southwest striking deformation zones and subprovince–scale indentations that affect and crosscut earlier east–west structures and isograds, and include the Burntside Fault and Vermilion Fault in the west, the Gravel and Montreal River deformation zones in the central region, and the ILDZ (Figs. 2.3, 2.7–2.10) (Sims et al., 1980; Percival and Card, 1983; Sims and Day, 1993a; Willams, 1989; Easton, 2000; Goldner, 2013).

The Wawa and Abitibi subprovinces are predominantly Neoarchean in age with limited remnants of the Mesoarchean crust occur as tonalitic gneiss and mafic volcanic lithologies, however much of the subprovinces are younger (Turek et al., 1992; Moser, 1994). The Southern Volcanic Zone of the Abitibi greenstone belt has experienced one continuous cycle of volcanism and plutonism (Pacaud, Deloro, Stoughton–Roquemaure, Kidd–Munro, Tisdale, Blake River, Kinojevis, Porcupine, Timiskaming assemblages), ca. 2.70 to 2.75 Ga, whereas the Michipicoten and Mishibishu greenstone belts have experienced at least three cycles, ca. 2.70, 2.75, and 2.89 Ga, with a potential fourth cycle at ca. 2.68 Ga (Ludden et al., 1986; Turek et al., 1990a; Ayer et al., 2005).

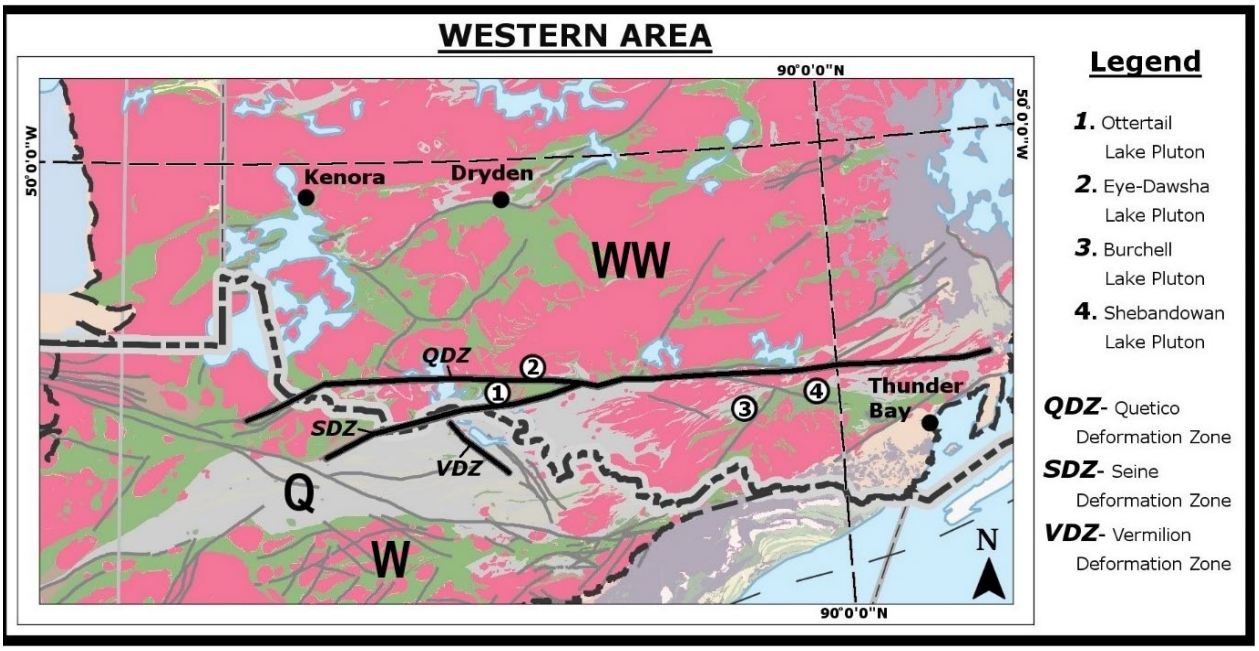

Figure 2.9: The western Wabigoon (WW, green and pink), central Quetico (Q, lightest grey and pink), and southern Wawa (W, pink and green) subprovinces with regional–scale to cratonic–scale structures (named and highlighted in black) and late Neoarchean plutons (numbered) (Modified after Montsion, et al., 2018).

Geochemically the Wawa subprovince is dominated by two volcanic successions with the older association dominated by tholeiitic basalts with near–flat REE patterns and komatiities and a younger bimodal association of arc basalts and dacites to rhyolites with adakites forming the bimodal arc volcanic sequence (Polat et al., 1998; Polat and Kerrich, 2000). The Abitibi assemblages also predominantly range from komatiitic and tholeiitic to more calc–alkaline (Ayer et al., 2005). The lithologies formed in the Michipicoten (including Mishibishu and Gamitagama) greenstone belt contain bimodal basalt–rhyolite with only the earliest 2.89 Ma cycle with komatiites (Bennett and Thurston, 1977; Krogh and Turek, 1982; Williams, 1989; Turek et al., 1992, 1990a; Sage et al., 1996; Turek et al., 1996b). Younger volcanism and plutonism continued to at least ca. 2.67 Ga in the southern Abitibi and Wawa subprovinces (Corfu and Stott, 1986; Corfu and Grunsky, 1987; Corfu et al., 1989a, 1991; Corfu and Stott, 1996; Krogh and Turek, 1982; Turek et al., 1996a, 1990b). Calc–alkaline lamprophyres and breccia intrude all of the metavolcanic lithologies in the Wawa and Abitibi subprovinces and some host macro– and micro–diamonds (Lefèbvre et al., 2005; Wyman et al., 2006; Stachel et al., 2006). Zircon and titanite U–Pb ages of diamond–bearing lithologies are ca. 2.67 Ga (Vaillancourt et al., 2004; Wyman et al., 2006). Magnesium–rich basalts, andesites, and adakites

718 created through slab melting in an arc setting have also been identified in the Wawa subprovince
719 (Polat and Kerrich, 2001). There are ongoing debates on the role of tectonic and/or mantle plume
720 settings in the Wawa and Abitibi subprovinces and adjacent Pontiac subprovince (Wyman and
721 Kerrich, 2010; Mole et al., 2021).
722 The oldest Abitibi subprovince assemblages, including the 2750 to 2735 Ma Pacaud
723 assemblage, is predominantly tholeiitic volcanic lithologies with minor calc–alkaline
724 intermediate and felsic volcanic lithologies and minor komatiite (Ayer et al., 2002; Ayer et al.,
725 2005). The Deloro assemblage is 2730 to 2724 Ma and is dominated by calc–alkaline volcanic
726 lithologies and banded iron formations. The next oldest assemblage is the Stoughton–
727 Roquemaure and has crystallization ages between 2723 to 2720 Ma and is dominated by mafic
728 volcanic lithologies and minor felsic volcanic lithologies, komatiites, and BIF. The Kidd–Munro
729 assemblage is 2723 to 2711 Ma and is dominated by intermediate to felsic calc–alkaline volcanic
730 lithologies in the lower portion of the assemblage and mafic to felsic tholeiitic volcanic
731 lithologies, komatiite, and graphitic sedimentary lithologies. The younger Tisdale assemblage is
732 2710 to 2704 Ma and is predominantly tholeiitic mafic volcanic lithologies with local komatiite,
733 intermediate to felsic calc–alkaline volcanic lithologies and banded iron formation in the lower
734 part with the upper part dominated by calc–alkaline felsic to intermediate volcanic lithologies
735 and volcaniclastic sedimentary rocks. The Blake River assemblage is 2704 to 2701 Ma in the
736 lower part with predominantly tholeiitic mafic volcanic lithologies and isolated tholeiitic felsic
737 volcanic and turbiditic sedimentary lithologies including conglomerate, banded iron formation,
738 and an unconformable graphitic argillite (Ayer et al., 2002; Ayer et al., 2005; Wyman and
739 Kerrich, 2010). The upper portion of the Blake River assemblage is 2701 to 2696 Ma and is
740 predominantly calc–alkaline basalt and andesite with local bimodal tholeiitic basalt and rhyolite
741 (Ayer et al., 2005; McNicoll et al., 2014). The Porcupine assemblage is 2690 to 2685 Ma and is
742 composed predominantly of metamorphosed Bouma sequences of wacke, siltstone, and
743 mudstone with minor volcanic units including the Krist formation consisting of calc–alkaline
744 felsic fragmental volcanic lithologies with crystallization ages of 2687.5 ± 1.3 and 2687.3 ±1.6
745 Ma, consistent with regional subvolcanic intrusions. The youngest assemblage is the 2676 to
746 2670 Ma Timiskaming assemblage and is composed of clastic sedimentary rocks and alkaline to
747 calc–alkaline volcanic lithologies (Ayer et al., 2005). Metamorphism in the Abitibi subprovince
748 is bracketed between 2677 to 2643 Ma (Powell et al., 1994). 40Ar–39Ar geochronological

studies conducted in the Abitibi greenstone belt indicate that regional metamorphism occurred at ca. 2.68 Ga using metamorphic amphibole, whereas muscovite from a gold–bearing quartz veins in the Timmins gold camp yielded ages of 2579 ± 9 Ma and 2607 ± 10 Ma, respectfully (Hanes et al., 1992a).

The Batchawana greenstone belt is located in the most southwestern area of the Abitibi subprovince, crosscut by the eastern KSZ (Figs. 1.2, 2.2, 2.8–2.9). The Batchawana greenstone belt is subdivided into predominantly metamorphosed volcanic and volcaniclastic lithologies and metasedimentary lithologies with ages between 2730 to 2670 Ma (Corfu and Grunsky, 1987; Siragusa, 1986). The metamorphosed volcanic lithologies include tholeiitic mafic lithologies, calc–alkaline mafic to felsic lithologies with a sharp nonconformity with banded iron formations, staurolite–garnet schists and gneissic metasedimentary lithologies (Corfu and Grunsky, 1987; Siragusa, 1986). Zircon and titanite U–Pb geochronological ages of metavolcanic lithologies range from ca. 2729 Ma in the western portion of the belt to ca. 2711 to 2698 Ma in the eastern portion, and plutons and gneisses have zircon U–Pb ages of 2673 ± 5 Ma, 2674 ± 3 Ma, 2668 ± 2 Ma (Corfu and Grunsky, 1987). Two populations of titanite U–Pb ages of 2661 ± 2 Ma and 2646 ± 3 Ma were attributed to later regional metamorphism (Corfu and Grunsky, 1987).

The most eastern extension of the Wawa subprovince adjacent to the WGD are the Michipicoten, Mishibishu and Gamitagama greenstone belts in the Wawa subprovince which developed from 2900 to 2660 Ma and are commonly grouped together (Turek et al., 1992). Three cycles of volcanism occurred in the belt ca. 2900, 2750, and 2703 Ma and included ultramafic komatiites to mafic and intermediate high–iron and magnesium tholeiites, banded iron formations, and felsic to intermediate calc–alkaline rhyolite and dacite tuffs and breccias (Turek et al., 1992). The Mishibishu greenstone belt may also have a younger 2677 Ma felsic volcanic event (Turek et al., 1990b, 1992). Each volcanic cycle is topped with metasedimentary lithologies (including carbonate–, sulphide–, and oxide–facies banded iron formations) and all lithologies are intruded by gabbroic to quartz dioritic sills and dikes (Turek et al., 1992).

Although the primary lithologies and gold mineralization of the Wawa and Abitibi subprovinces are mapped as continuous or analogous, the metamorphic and structural histories of the Wawa and Abitibi subprovinces are markedly different (Easton, 2000). The two subprovinces host world–class gold districts and mines (e.g. Timmins district and Hemlo Mine) and the structural, metamorphic, and tectonic research in these regions is ever evolving, driven

780 particularly by gold exploration and mining (Fig. 1.5). Generally, gold mineralization in the
781 Wawa subprovince is hosted predominantly hosted in east–west to northeast–southwest striking
782 and boudinaged structures in medium– to high–grade metamorphic lithologies (e.g. Hemlo
783 Mine) while mineralization in the Abitibi subprovince is hosted in very–low grade to low–grade
784 metamorphic lithologies in east–west striking structures (Reid and Reilly, 1987; Roberts, 1987;
785 Colvine et al., 1988; Hodgson, 1989, 1993; Poulson and Robert, 1989; Callan, 1991; Heather and
786 Arias, 1992; MacDonald, 1992; McCauig and Kerrich, 1994; Turek et al., 1996a; Samson et al.,
787 1997; Bornhorst and Johnson, 1998; Bornhorst et al., 1999; Lin, 2001; Muir, 2003; Ayer et al.,
788 2005).

789 The age of gold mineralization throughout the Wawa and Abitibi subprovinces (and
790 common throughout the southern Superior Province) has been defined as a "100 Ma timing
791 paradox" as gold mineralization has been dated between ca. 2700 to 2579 Ma (Jemielita et al.,
792 1990; Kerrich and Kyser, 1994). The primary mineralizing event in the Abitibi and Wawa
793 subprovinces are documented by zircon U–Pb and Pb–Pb ages to ca. 2700 to 2680 Ma (Kerrich
794 and Kyser, 1994; Mercier–Langevin et al., 2007). Rutile and titanite U–Pb, scheelite Sm–Nd,
795 and muscovite $^{40}Ar/^{39}Ar$ ages between 2630 to 2579 Ma are considered a long–lived event or
796 secondary event associated with reactivation along structures (Kerrich and Kyser, 1994). Similar
797 ages have been documented throughout the Wawa and Abitibi subprovinces, including in the
798 northern Porcupine–Destor deformation zone U–Pb zircon dated at ca. 2685 and 2676 Ma and a
799 Re–Os age of molybendite at 2672 ± 7 Ma and 2670 ± 10 Ma (Ayer et al., 2005), the southern
800 region in the Marquette/Ishpeming greenstone belt with a zircon U–Pb age of 2668.4 + 2.1/– 1.8
801 Ma crosscut by a 2585 Ma granite (Sims and Peterman, 1992; Bornhorst and Johnson, 1998; and
802 western Hemlo Mine mineralization bracketed between 2678 Ma to 2632 Ma (Fig. 1.5) (Corfu
803 and Muir, 1989; Pan and Fleet, 1995). The timing of gold mineralization is an ongoing, current
804 debate in the Wawa and Abitibi subprovinces.

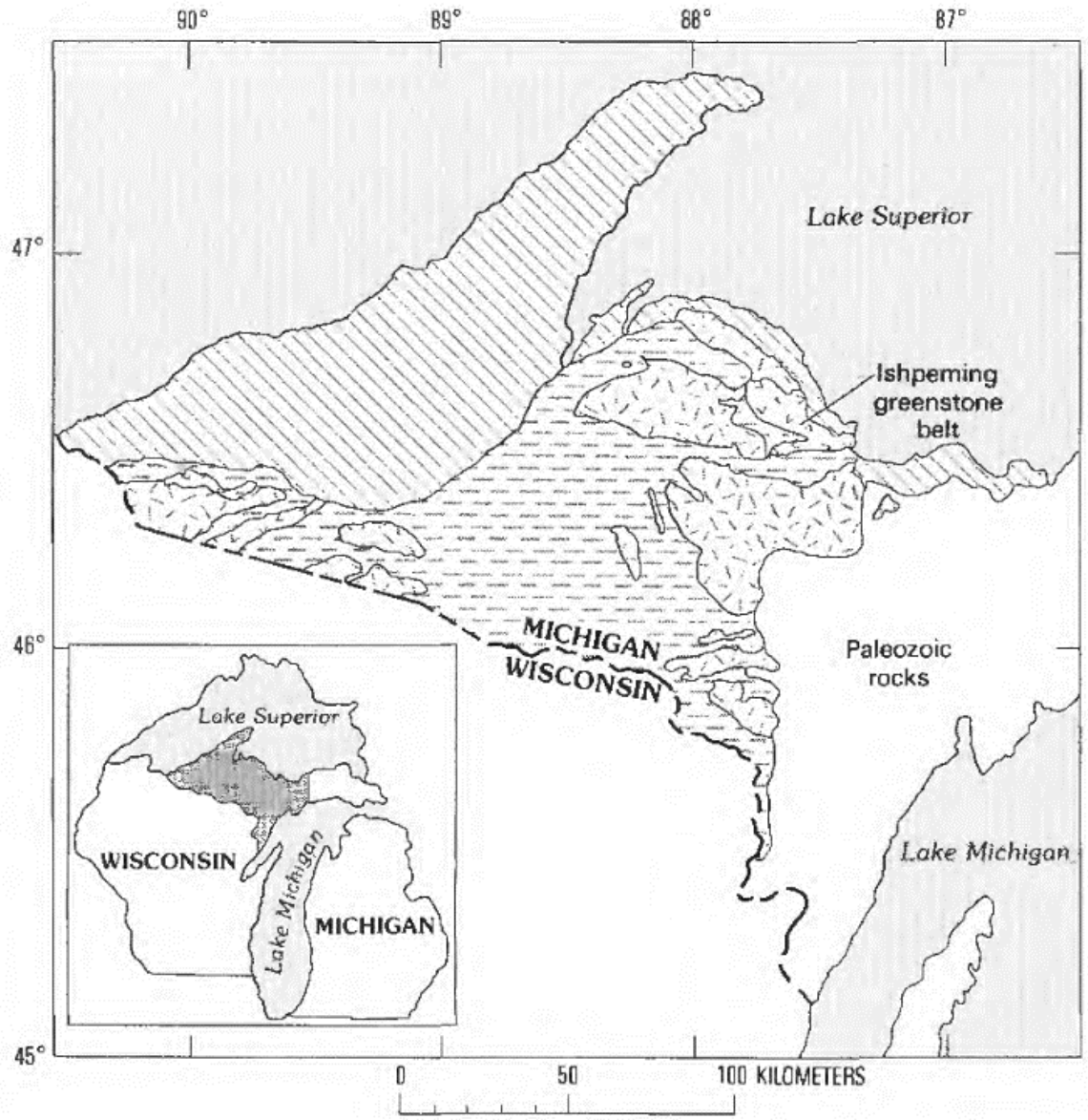

Figure 2.10: The southern extension of the Wawa subprovince in the Ishpeming/Marquette greenstone belt with minor outcrops of MRVT granulite and gneisses is not present on modern maps of the Superior Province and is included in all maps in this study (random hatching denotes MRVT in Proterozoic and Phanerozoic straight lines and hatching) (Johnson, 1991).

2.2.13 Pontiac Subprovince

The Pontiac subprovince is exposed between the southern Grenville Province, the northern Abitibi subprovince, and its western boundary is truncated by the eastern extent of the KSZ (Figs. 1.2, 2.2, 2.6–2.9). The Pontiac subprovince has been proposed to have accreted onto the southern Superior Province at ca. 2.68 Ga during the collision with the MRVT from the south

(Percival et al., 2012) as well as the Abitibi–Pontiac collision (Feng and Kerrich, 1991; Feng et al., 1992). The Pontiac subprovince is commonly categorized by the northern, metasedimentary lithologies and ultramafic to mafic volcanic lithologies at low to medium metamorphic grades, the central area with a MCC, intrusions, pegmatites, and medium to high–grade paragneisses, ca. 2684 to 2681 Ma, low–grade metavolcanics, ca. 2690 to 2682 Ma, metasedimentary lithologies, ca. <2683 Ma, and metamorphism bracketed between 2668.5 ± 0.9 and 2663.0 ± 0.9 Ma (Mortensen and Card, 1993; Sawyer and Barnes, 1994).

The earliest regional metamorphic isograds strike parallel to the northern boundary with the Abitibi subprovince with a later retrograde metamorphism and irregular isograds (Fig. 2.3) (Camiré and Burg, 1993; Morin et al., 1993; Benn et al., 1994; Easton, 2000; Frieman et al., 2017). Most shear zones are dextral, ductile and strike–slip that parallel the northern boundary with a few sinistral shear zones striking northeast–southwest and crosscut the regional metamorphic isograds, and MCC (Figs. 2.2, 2.7, 2.9) (Camiré and Burg, 1993; Benn et al., 1994; Sawyer and Barnes, 1994; Daigneault et al., 2002; Bedeaux et al., 2018) and NE–SW crenulation cleavage is present in both the Abitibi terrane and Pontiac subprovince (Desrochers and Hubert, 1996; Daigneault et al., 2002; Lafrance, 2015). Thrusting has also been proposed in response to NE–SW to N–S regional compression (Camiré and Burg, 1993). The early metamorphic event of intermediate–pressure, greenschist facies in the Pontiac subprovince has been bracketed to occur between 2690 and 2667 Ma, while the later, higher grade metamorphic event that resulted in migmatization occurred between 2660–2630 Ma (Feng and Kerrich, 1990, 1991).

The Pontiac subprovince is commonly categorized by the northern, metasedimentary lithologies at low to medium metamorphic grades; the central area that is composed of the Decelles batholith, intrusions, pegmatites, and medium to high–grade metamorphic paragneisses; and the low–grade, Belleterre metavolcanics and metasedimentary lithologies in the south. The metasedimentary and metavolcanics lithologies of the northern and southern areas consist of turbidites (Mortensen and Card, 1993). The Pontiac Group is approximately 3 km thick with local lenses and layer rich in amphiboles (Holubec, 1972) and has been suggested to have derived from andesitic to dacitic volcaniclastic lithologies (Rocheleau and Dimroth, 1985).

The Baby and Belleterre metavolcanic belts are composed of komatiites, basaltic komatiites, tholeiitic basalts, calc–alkaline dacites, conglomerates, and wacke (Imreh, 1973). The Angliers felsic volcanic flow has ^{207}Pb–^{206}Pb zircon crystallization ages between 2680.1 ± 2.5 to

2685.3 ± 1.1 Ma, the Belleterre felsic volcanic breccia between 2709.4 ± 1.3 to 2702.3 ± 0.9 Ma, and the Belleterre quartz–feldspar porphyry between 2707.4 ± 1.0 to 2684.8 ± 1.3 Ma (Mortensen and Card, 1993). The Lac Frechette quartz syenite has 207Pb–206Pb zircon crystallization ages between 2679.5 ± 0.9 to 2666.4 ± 0.9 Ma, the Lac Remigny quartz syenite between 2679.2 ± 0.9 to 2645.9 ± 1.1 Ma and a titanite age of 2676.1 ± 1.6, and the Lac Frechette quartz syenite between 2682.6 ± 1.1 to 2634.4 ± 1.3. The Decelles batholith and other plutons, batholiths, and gneisses include dioritic, granodioritic, monzonitic, and syentitic intrusions and partially melted metasedimentary gneisses and peraluminous pegmatites (Mortensen and Card, 1993). The pegmatites formed from partial melting of metasedimentary lithologies were emplaced at 2668.5, 2666.5, and 2663 + 0.9 Ma using U–Pb monazite geochronology (Mortensen and Card, 1993).

The earliest prograde regional metamorphic isograds strike parallel to the northern boundary with the Abitibi subprovince with a later, retrograde isograds oblique to the boundary (Fig. 2.3) (Camiré and Burg, 1993; Easton, 2000). The majority of shear zones are dextral, ductile and define the northern boundary while the few sinistral shear zones and MCCs crosscut the entire subprovince, strike northeast–southwest and also crosscut the regional metamorphic isograds (Camiré and Burg, 1993; Benn et al., 1994a; Sawyer and Barnes, 1994; Daigneault et al., 2002; Mueller et al., 1985; Lafrance, 2015; Bedeaux et al., 2018). On the smaller scale, northeast–southwest crenulation cleavage is present in both the Abitibi terrane and Pontiac subprovince (Desrochers and Hubert, 1996; Daigneault et al., 2002; Lafrance, 2015). Thrusting has also been proposed in response to NE–SW to N–S regional compression (Camiré and Burg, 1993). The early metamorphic event of intermediate–pressure, greenschist facies in the Pontaic subprovince has been bracketed to occur between 2690 and 2667 Ma, while the later, higher grade metamorphic event that resulted in migmitization occurred between 2660–2630 Ma (Feng and Kerrich, 1991, 1990). Dextral, strike–slip shear zones along the Kirkland Lake–Cadillac Fault facilitated differential uplift in the Pontiac and Abitibi subprovinces and deformed the metamorphic isograds (Camiré and Burg, 1993; Morin et al., 1993; Benn et al., 1994a; Frieman et al., 2017).

2.2.14 Wawa Gneiss Domain

The WGD, formally Wawa Domal Gneiss Terrane, and KSZ (described below) crosscut the southern Superior Province (Figs. 1.2–1.5, 2.2, 2.9, 2.11). The WGD is a gradual, linear zone immediately east of the Wawa subprovince and west of the KSZ with boundaries that extend towards the northeast to southwest (Figs. 1.2–1.5, 2.2, 2.9, 2.11). The WGD parallels the northeast–southwest to north–south geometries of the eastern greenstone belts in the Wawa subprovince as well as the KSZ (Card, 1990). The WGD is composed of deformed, domal plutonic gnessies and supracrustal lithologies that formed between 2.9 and 2.66 Ga, and that were metamorphosed between 2660 and 2640 Ma (Krogh and Turek, 1982; Corfu and. Grunsky, 1987; Frarey and Krogh, 1986; Turek et al., 1990b, 1992; Moser, 1994; Turek et al., 1996a). Lead isotopes from whole rock in the WGD plot on a 2.48 ± 0.02 Ga isochron (Smith et al., 1992). The metamorphic grade increases from amphibolite facies in the western WGD and transitions into granulite facies in the KSZ in the east (Bennett and Thurston, 1977; Percival, 1981; Hartel and Pattison, 2003). The plutons in the WGD are predominantly tonalitic to granodioritic forming regional domes and deformed domes that intruded after granulite metamorphism (Moser, 1994; Liodas, 2010; Beakhouse et al., 2011). Regional extensional and ductile sinistral strike–slip shear zones and faults are located throughout the domain (Moser, 1994). Currently the WGD lacks a tectonic mechanism for its formation, although it is regularly grouped into the formation of the KSZ and/or Wawa subprovince (Percival, 1989; Moser, 1994, 1994; Percival et al., 2012).

2.2.15 Kapuskasing Structural Zone

The KSZ is a 150 km wide by 500 km long, curvilinear exposure of middle to lower crust that crosscuts northeast–southwest across the generally east–west striking Wawa, Abitibi, Quetico, and Opatica subprovinces of the southern Superior Province and parallels the WGD (Figs. 1.2–1.5, 2.2, 2.9, 2.11)(Card and Ciesielski, 1986; Percival and West, 1994). The KSZ exposes high–grade metamorphic schists, gneisses, migmatites, gabbros and the Shawmere anorthosite complex of the middle to lower crust and is sharply truncated along its eastern boundary with the Abitibi subprovince along a major regional structure named the ILDZ (and more minor Montreal River deformation zone) (Percival and West, 1994). The ILDZ divides the upper amphibolite to granulite facies regional metamorphism of the KSZ and subgreenschist to

greenschist facies in the Abitibi subprovince (Powell et al., 1993; Easton, 2000; Hartel and Pattison, 2003). The ILDZ in the KSZ may have been active as late as ca. 2630 Ma (Krogh and Moser, 1994). The WGD (also known as the Wawa Domal Gneisses, Val Rita Block, Agawa migmatite terrain, or Algoma gneisses) defines the gradational and domal western boundary of the KSZ with the eastern extent of the Wawa subprovince (Bennett and Thurston, 1977; Sims et al., 1980; Percival and McGrath, 1986; Moser, 1994). The southern boundary has not been defined and could include the Pontiac subprovince and/or MRVT.

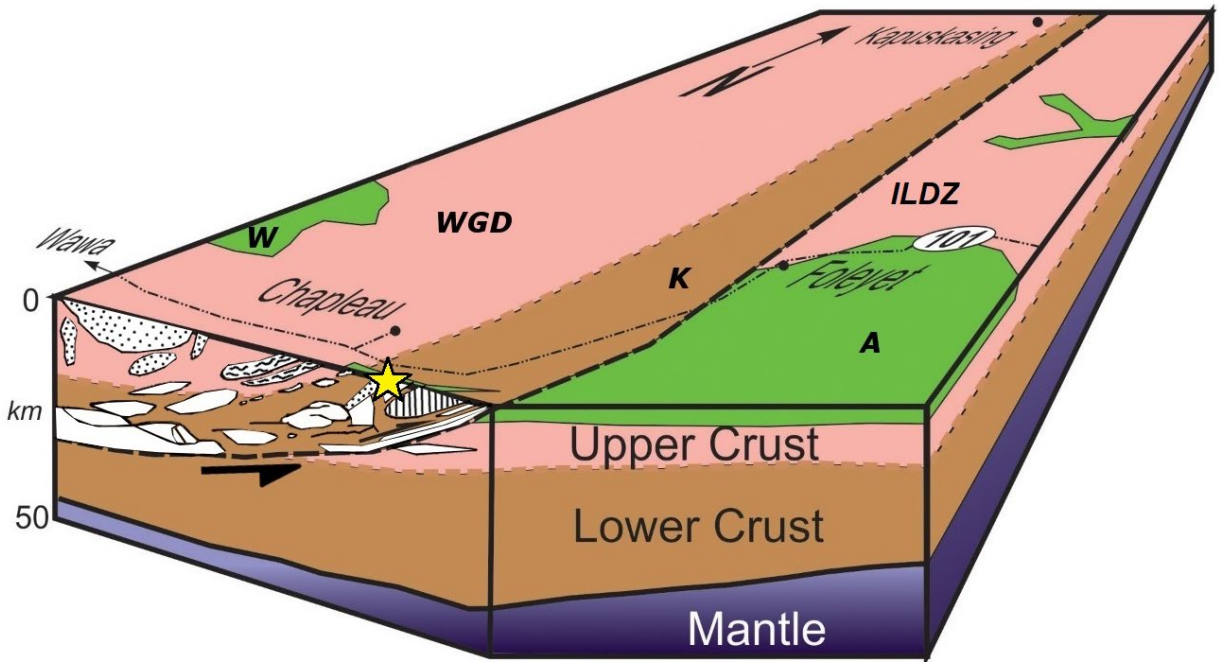

Figure 2.11: A 3D seismic block model of the study area. The western Wabigoon subprovince (W, green, dots and undifferentiated), Wawa Gneiss Domain (WGD, pink, dots, curved lines and undifferentiated), Kapuskasing Structural Zone (KSZ, brown, dots, stripes, and undifferentiated), Ivanhoe Lake Deformation Zone (ILDZ, black dashed lines and arrow), and Abitibi subprovince (A, green) subprovinces. The star marks the Borden Mine (Modified after Percival, 1994 and references therein).

Prevailing hypotheses for the bisection of the Superior Province and exhumation of the mid– to lower–crustal exposure of the KSZ include: (1) intracratonic uplift due to dextral thrust faults and dip–slip faults (Percival and Card, 1983; Ernst and Halls, 1984), (2) a suture (Gibb, 1978), (3) sinistral, strike–slip faults (Watson, 1980), and (4) a positive flower structure (Goodings and Brookfield, 1992; Halls and Zhang, 1998; Nitescu and Halls, 2002) but lack a tectonic hypothesis for the WGD. Also, previous studies did not resolve contradictory geological and geophysical data nor provide a tectonic mechanism for their formation. Structural and geophysical interpretations on the local scale include the northernmost exposed area of the KSZ

to be a set of thrust faults (Percival and McGrath, 1986) or a positive flower structure (Goodings and Brookfield, 1992). The centre has been interpreted to have a listric normal fault in the west of the block as well as a thrust fault (Percival and McGrath, 1986), a dip–slip fault (Percival and McGrath, 1986), or a sinistral, transpressive strike–slip basin (Goodings and Brookfield, 1992). The Chapleau Belt is the southernmost identified block and transitions into the WGD to the south and southwest with tectonic interpretations including a positive flower structures from dextral shear along left–stepping, en echelon faults (Halls and Zhang, 1998; Nitescu and Halls, 2002). Other interpretations include en echelon, sinistral transcurrent structures with local thrusting components (Nitescu and Halls, 2002) or sagduction (Lin et al., 2013). Another interpretation for the KSZ involves the formation of a plume–generated, failed–arm of a triple junction (Burke and Dewey, 1973), and local sagduction (Lin et al., 2013). New mapping projects have commenced in the area and new work should produce more data (Duguet and Szumylo, 2016).

The igneous crystallization history of the KSZ, except for the emplacement of the large Shawmere anorthosite complex at ca. 2.66 Ga (Dr. Hua Huang, unpublished zircon U–Pb data), is similar to the Wawa and Abitibi subprovinces, however it has a substantially longer metamorphic history documented in metamorphic zircon, monazite, and garnet (Frarey and Krogh, 1986; Percival, 1989b; Corfu et al., 1989a; Turek et al., 1992; Moser, 1994; Krogh and Moser, 1994a; Moser et al., 1996a, 1996b, 2008; LaFontaine, 2016; Kendrick et al., 2019). An enigmatic, long–lasting high–temperature magmatic and metamorphic history has been used to explain the approximately 80 Ma metamorphic anomaly between 2660 Ma to 2585 Ma (Moser, 1994; Krogh and Moser, 1994a; Moser et al., 1996a, 2008; LaFontaine, unpublished MSc. thesis, 2016; Kendrick et al., 2019). While the high–temperature anomaly is long–lived, the dominant mode of the zircon, monazite, and titanite ages in the study area is 2.66 Ma (Krogh, 1993; Krogh and Moser, 1994b), coinciding with the emplacement of the Shawmere anorthosite complex (Dr. Hua Huang, unpublished zircon U–Pb data). Structural and tectonic interpretations of the long–lived high–temperature anomaly include underplating across a zone of crust–mantle delamination, approximately 50 Ma after 2703 Ma volcanism (Krogh, 1993).

Regional mapping and U–Pb zircon geochronology have been used to propose five stages for the formation of the WGD and KSZ: 1) between 2703–2680 Ma the lithologies were tightly folded and thrusted, 2) 2680–2667 Ma continued folding and thrusting occurred, including

960 sedimentary lithologies, 3) all lithologies between 2667–2660 Ma were underthrust to depths of
961 30 km with a stable upper crust, 4) 2660–2637 Ma east–west extension and granulite
962 metamorphism produced gently dipping shear zones overprinting earlier structures, and 5) 2630–
963 2580 Ma east–west shortening with potential fault reactivation in the KSZ (Moser, 1994; Moser
964 et al., 2008). The crosscutting felsic plutons and dykes have igneous zircon crystallization U–Pb
965 ages as young as 2585 Ma in the study area (Corfu and Grunsky, 1987; Krogh, 1993; Krogh and
966 Moser, 1994a; Moser, 1994; Moser et al., 2008) and a strain shadow is dated to 2603 ± 2 Ma
967 (Krogh, 1993). Moser et al. (2008) stated that analyses conducted in the region have lower
968 intercepts of discordant arrays near 0 Ma and therefore there is no evidence of ancient lead loss
969 and the U–Pb isotopic ages may be treated as close approximations of true U–Pb isotopic ages
970 (Moser et al., 2008). The Shawmere anorthosite has similar major and minor trace element
971 geochemistry to the Abitibi tholeiitic basalt (Simmons et al., 1980) and a K–Ar hornblende age
972 of 2519 Ma (Watkinson et al., 1972). The previously described field mapping studies have
973 focused primarily on the ILDZ, particularly to define the uplift of the KSZ and WGD. The
974 majority of earlier studies focused primarily on the brittle structures, although brittle–ductile and
975 ductile structures, generally overprinted by brittle structures, have also been documented
976 (Bursnall, 1990a; Percival and Peterman, 1994). More recent studies have identified and mapped
977 brittle–ductile and ductile structures, although they have not been the primary focus for
978 geochronology of the ILDZ (Moser, 1994; Moser et al., 1996a; Swoffer et al., 2011).
979 The ILDZ was active as early as ca. 2630 Ma using U–Pb zircon geochronology (Krogh
980 and Moser, 1994b). $^{40}Ar/^{39}Ar$ geochronology in amphiboles place an upper limit on the time of
981 uplift to 2.52–2.46 Ga and biotite dates of 2.45–2.40 Ga support the hypothesis of >15–20 km
982 uplift (Hanes et al., 1994). Fault reactivation and dyke emplacements in the ILDZ are also
983 documented by micas, feldspar, and whole–rock analyses with 40Ar/39Ar age populations of
984 2.30–2.25 Ga and <2.1 Ga (Hanes et al., 1994). Rb–Sr in biotite and whole–rock geochronology
985 document isochron ages between >2.5 to 1.93 Ga (Percival and Peterman, 1994) and K–Ar in
986 biotite yields 2.44–2.28 Ga ages (Easton, 1986). Similar Ar–Ar and K–Ar ages using micas and
987 amphiboles between 2.48–2.25 Ga are located in the Abitibi subprovince, and Gravel River and
988 the Miniss River deformation zones in the Quetico and Wabigoon subprovinces have ages of
989 2.28 Ga (Figs. 2.2, 2.6–2.9) (Easton, 1986; Hanes et al., 1992b, 1994; Hanes and Archibald,

1998). These radiometric ages provide evidence of active regional structures across the southern Superior Province during low–grade metamorphism and alteration well into the Proterozoic.

Extensive geophysical studies, including seismic reflection, gravity, aeromagnetic, and paleomagnetism surveys have been conducted in the KSZ to better describe the nature of the high–grade metamorphic lithologies exposed at surface (Gibb, 1978b; Geis et al., 1990; Clowes et al., 1996; Halls and Zhang, 1998; Borradaile et al., 2003). Seismic, gravity, and magnetic studies have been used to interpret the structures particularly where it is covered by Phanerozoic lithologies in the north or plutonic lithologies in the WGD (Halls and Zhang, 1998; Evans and Halls, 2010). LITHOPROBE seismic reflection studies have identified the KSZ as a west–dipping, 20 km thick intracrustal decollement which was created from 55–70 km thrusting (Percival, 1994 and references therein). The deformation is inferred to have formed a 200 km wide and 12 km thick crustal root. Lozenge–shaped geometry of various densities (inferred lithologies) have been identified between the more isotropic WGD, high–density KSZ, and low–density Abitibi subprovince. The ILDZ is identified as either shallow– to moderately–dipping along the main structure or vertical (Percival, 1994 and references therein).

Geochronological studies described previously supported by seismic and paleomagnetic studies have identified two stages of uplift in the KSZ with the first ca. 2500–2454 Ma and the second ca. 1950–1850 Ma (Vandall and Symons, 1990; Symons et al., 1994; Halls and Zhang, 1998; Borradaile et al., 2003; Ernst and Bleeker, 2010a; Evans and Halls, 2010).

The majority of the paleomagnetism studies have focused on the Matachewan mafic dyke swarm that strikes predominantly northwest–southeast and crosscut the KSZ by at least 2.51 Ma (Heaman et al., 1988; Heaman, 1997) and has a Pb isochron age of 2479 ± 20 Ma (Fig. 2.2) (Smith et al., 1992). Lower–crustal xenoliths place the initiation of rifting and emplacement by 2.52 Ga (Moser and Heaman, 1997). The oldest mafic dykes are linear to curvilinear and strike north to northwest with steep to near–vertical dips (Percival and Card, 1983). In the WGD and KSZ the dykes that were emplaced during retrograde metamorphism preserved a normal paleomagnetic polarity (with blue–green amphibole and clouded feldspar), whereas those exhumed from shallower depths, have reverse polarities in response to faster cooling (Halls and Zhang, 1998). The baked–margins of the Matachewan dykes provide further evidence of their emplacement before and after crustal uplift in temperatures greater than 580ºC, or the Curie point of magnetite (Halls and Palmer, 1990). In addition to mafic dykes, the granulite and anorthosite

host lithologies in the KSZ also have the same palomagnetic remanence direction, thus implying they were uplifted and acquired a remanence through their unblocking temperatures during deformation (Halls and Palmer, 1990). Limited areas in these lithologies, including the east side of the Shawmere anorthosite, were chemically remagnetized ca. 1.86 Ga potentially along brittle structures (Martinez and York, 1990; Vandall and Symons, 1990). Aeromagnetic geophysical surveys have identified regional–scale deformation in the Matachewan dykes creating a rounded, Z–shaped pattern (Bates and Halls, 1991b; West and Ernst, 1991). Many paleotectonic models have been proposed to reconstruct the region and many have non–unique solutions, most involving translation or rotation of the region (Ernst and Halls, 1984; Bates and Halls, 1991b; West and Ernst, 1991; Ernst and Bleeker, 2010a). However, the most often cited paleomagnetic models of the KSZ include: 1) the paleomagnetism of the mafic dyke swarm suggest that <10º relative motion has occurred between the western and eastern Superior Province since ca. 2.65 Ga based on the declination differences between the paleomagnetic data from dykes and host lithologies (Symons et al., 1994), 2) at least 55 km of crustal shortening has been reported (Geis et al., 1990), and 3) 70 km of dextral translation occurred (West and Ernst, 1991). However even these studies must be used with caution as reference points, including plutons in the Wawa Subprovince, may also have been rotated about a vertical axis clockwise between 5–10º (Bates and Halls, 1991a). The most recent paleomagnetic reconstruction has been proposed by (Evans and Halls, 2010) using a quantitative plate–tectonic model predicted 90 km of dextral displacement, approximately half that amount was absorbed by simple shear and rotations of 23º ("domino–style"), and the other half by NE–verging transpression along the ILDZ. They also gave the caveat that the distributed shear is likely more complex than that used for the model and they discourage use of paleomagnetic poles from that region when constructing apparent polar wander paths prior to 1870 Ma, which they attempted to do (Evans and Halls, 2010).

The magnetic fabrics in the KSZ in igneous plutonic and metamorphic schists and gneiss in regional– and local–scale structures have been studied using AMS (anisotropy of low field magnetic susceptibility) and AARM (anisotropy of anhysteretic remanence magnetism), and an age of 2.55 Ga is proposed with consideration to the dip of the lithologies, the magnetic blocking temperatures (500–600ºC), and the neighbouring Wawa and Abitibi subprovinces (Vandall and Symons, 1990; Borradaile and Lagroix, 2000). Borradaile and Lagroix (2000) stated that the magnetic fabric postdates the silicate fabrics, which makes the 2.55 Ga age a minimum date.

2.2.16 Minnesota River Valley Terrane

The MRVT, composed of Paleo– to Neoarchean gneisses and granites, is located in the southwestern corner of the Superior Province and continues southwest to at least South Dakota at depth (Figs. 1.2, 2.12–2.14) (Bickford et al., 2006; Schmitz et al., 2006; McCormick, 2010). The proposed suture between the MRVT and the southern Superior Province is the Great Lakes Tectonic Zone (GLTZ), which is amphibolite to granulite facies in grade, and is generally northeast striking, steeply southeast dipping, and a north–verging suture (Sims et al., 1980; Sims and Day, 1993a). The structure of the GLTZ varies along strike from northwest–striking in South Dakota and Minnesota to steeply dipping to the southwest in northern Wisconsin at an indentation, and marks the southern extension of the undefined "Quiet Zone" which extends to the southern Wawa subprovince boundary (Figs. 2.12–2.14) (Sims and Day, 1993; Southwick, 2014). The MRVT has a complex history with numerous Paleoarchean to Mesoarchean U–Pb zircon and monazite igneous crystallization ages and Neoarchean metamorphic ages (Bickford et al., 2006; Schmitz et al., 2006). The eastern extension of the MRVT in Wisconsin and Michigan have similar crystallization and metamorphic ages (Craddock et al., 2007). The terrane is commonly separated into distinctive regions defined by ductile, dextral strike–slip shear zones called the Morton, Montevideo, and Benson blocks (Figs. 2.12–2.14) (Sims et al., 1980; Sims and Day, 1993a). In the Morton and Benson blocks late–kinematic monzogranites have a crystallization age of 2603 ± 1 Ma, crosscutting syenogranites and aplitic dykes are 2591 ± 2 Ma, and granulite metamorphism is constrained between 2609 to 2595 Ma (Bickford et al., 2006; Schmitz et al., 2006).

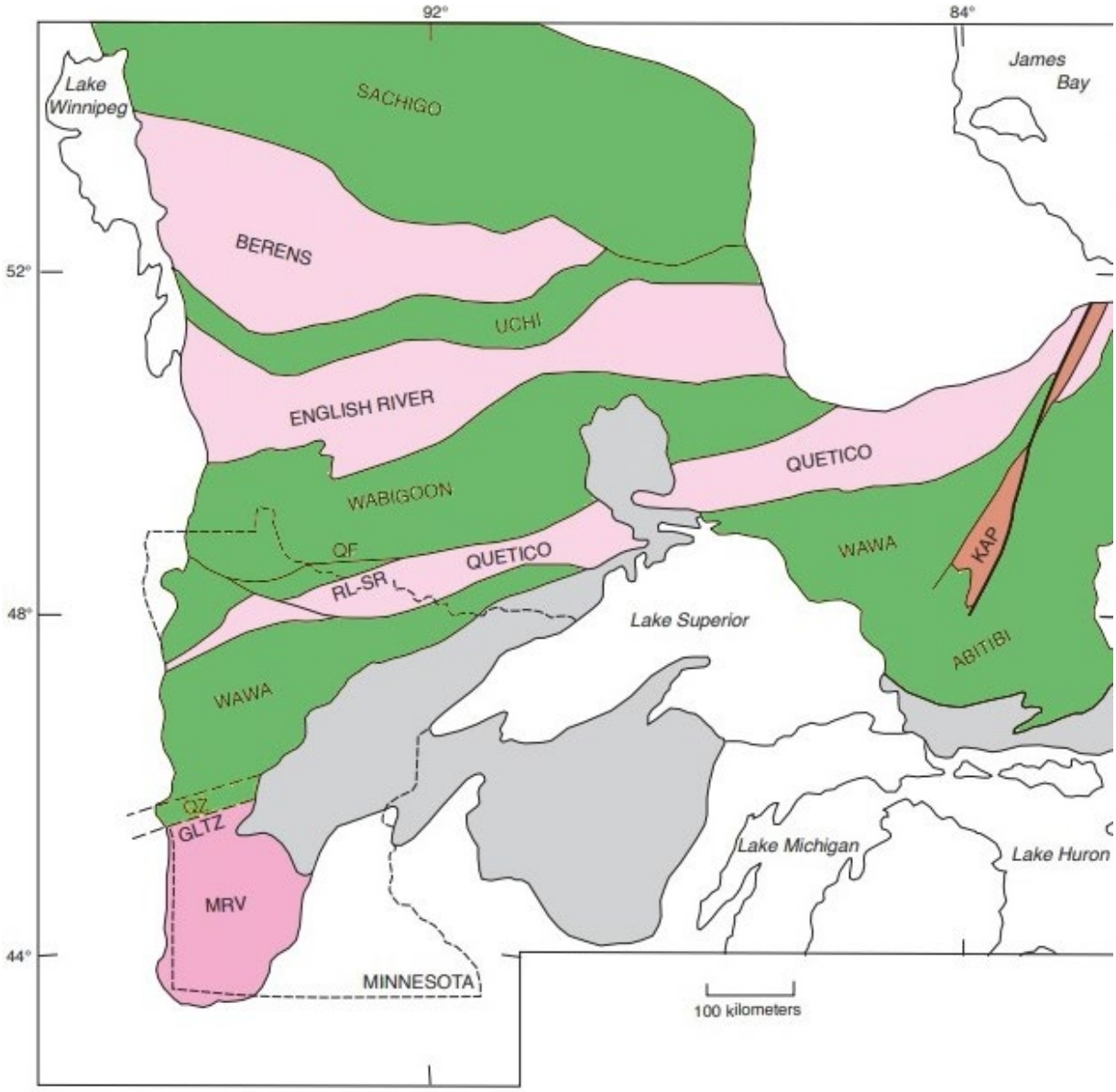

Figure 2.12: Plan view map of the Quiet Zone (QZ) and Great Lakes Tectonic Zone (GLTZ) between the Minnesota River Valley terrane (dark pink) and the Wawa subprovince (green) and other similar subprovince–scale structures highlighted at the Wawa–Quetico subprovince boundary (including the Rainy Lake–Seine River Deformation Zone (RL–SR) and Quetico Fault (or Deformation Zone (QF)). The Kapuskasing Structural Zone (orange) crosscuts the Wawa and Abitibi subprovinces. The Proterozoic cover is displayed in grey (Modified after Southwick, 2014).

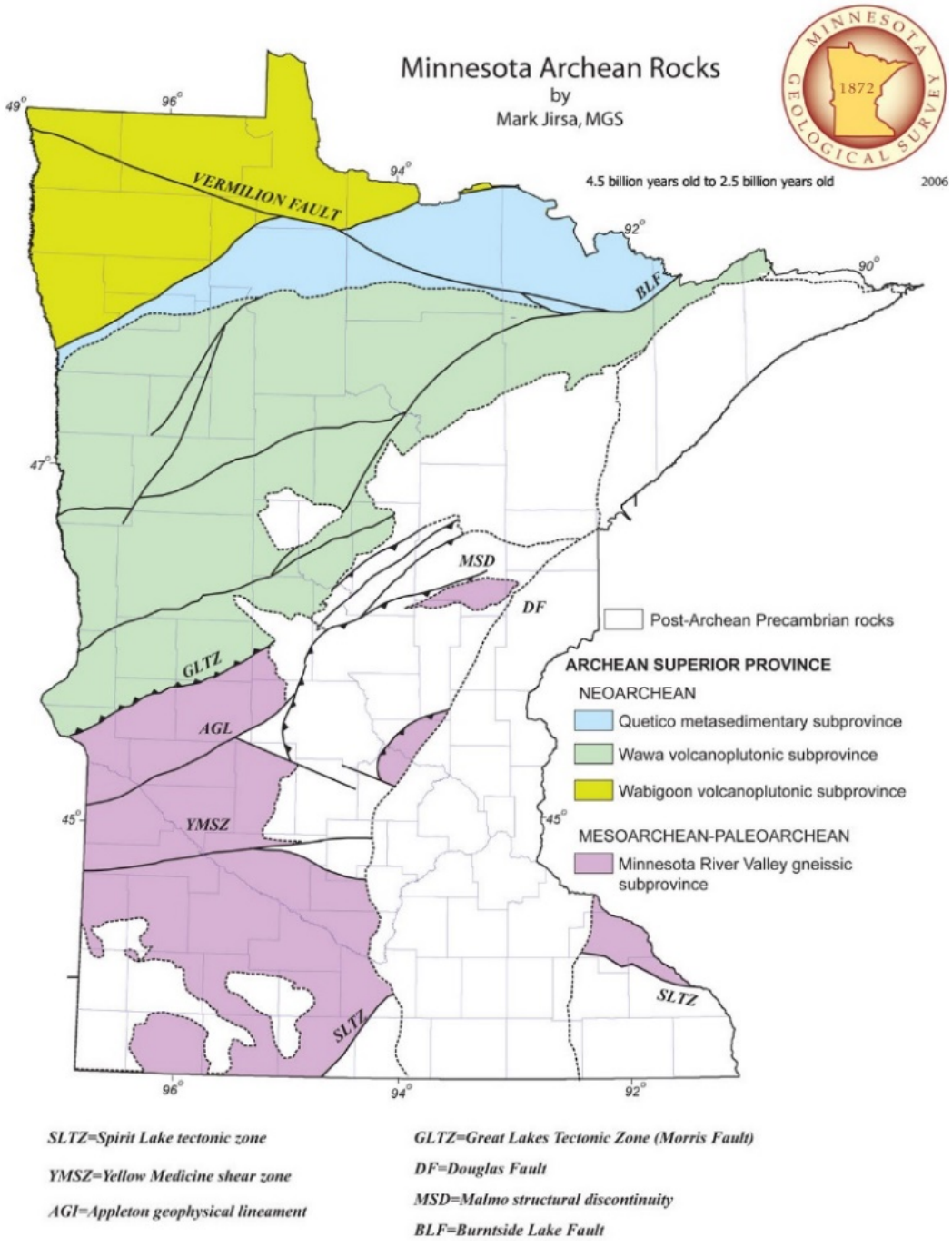

Figure 2.13: The regional–, subprovince– and cratonic–scale structures are highlighted within the Minnesota River Valley terrane (gneissic subprovince) in purple, the Wawa subprovince (green), tapered Quetico subprovince (blue), and Wabigoon volcanoplutonic subprovince (yellow) including the northern dipping thrust fault of the Great Lakes Tectonic Zone (GLTZ) and the predominantly dextral, strike–slip Vermillion Fault, Burntside River Fault (BLF), and Yellow Medicine shear zone (YMSZ) (Modified after Mark Jirsa, 2016 and personal communication, 2016).

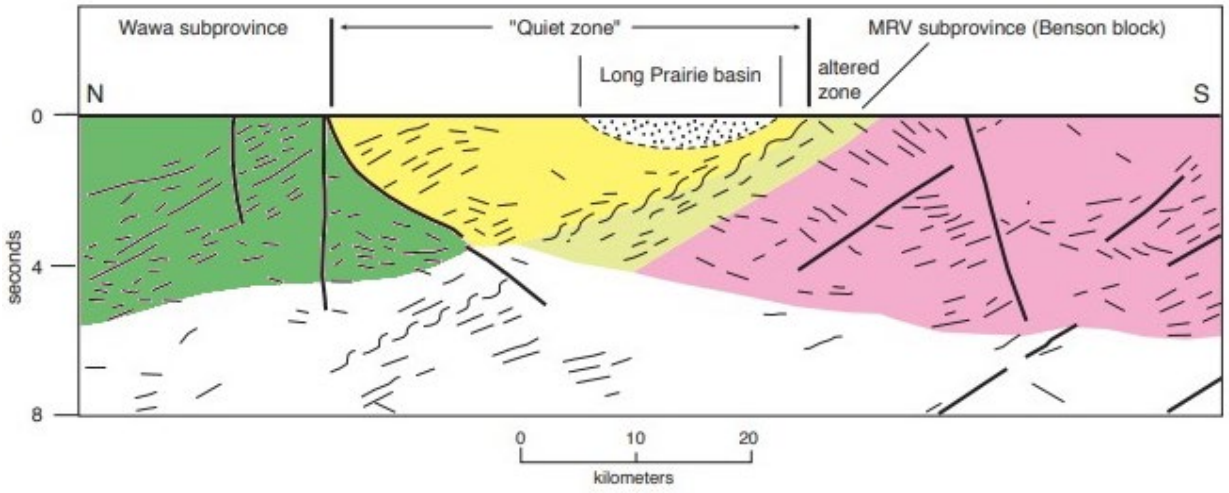

Figure 2.14: Cross section of seismic interpretation of the north–dipping Great Lakes Deformation Zone along the northern MRVT (Benson block), the "Quiet Zone" including the "altered zone", and the south dipping boundary of the Wawa subprovince and structures therein (modified after Southwick, 2014).

2.2.17 Huronian/Marquette Supergroup

The Proterozoic Huronian/Marquette Supergroup outcrops along the southern Superior Province boundary (Fig. 1.2) (Card, 1990). The current hypotheses of the early Huronian/Marquette Supergroup tectonic setting(s) include an elongate pull–apart basin related to oblique subduction (Long, 1984), a south facing continental margin developed by rifting and rotation (Roscoe and Card, 1993), a transform segment of a complex continental margin (Long and Lloyd, 1983), transpression to sinistral transtension (Long, 2004). The prevailing tectonic hypothesis for the later sedimentation in the Huronian/Marquette Supergroup is a passive margin (Long, 1995). Key lower stratigraphic markers include the uranium– and gold–rich quartz–pebble conglomerate of Elliot Lake and has been correlated to other cratons, including the Wyoming and Karelian cratons (Ojakangas et al., 2001a,b). Detrital zircon U–Pb ages collected in the Matinenda Formation in contact with the Archean basement yield concordant ages between 2776 to 2620 Ma. The local felsic metavolcanic lithologies are dated at 2687 ± 2 Ma and the granitic plutons are 2667 to 2620 Ma (Easton and Heaman, 2011).

2.2.18 Wyoming Province

Neighbouring the Superior Province to the southwest is the Wyoming Province, which is exposed predominantly in South Dakota, Wyoming, and Montana U.S.A., and is composed of

Paleo– to Mesoarchean gneisses and supracrustal lithologies that record high grades of metamorphism and Neoarchean gneisses and felsic plutons (Fig. 2.15) (Frost and Frost, 1993). Earlier geological processes are obscured by Neoarchean tectonics, including metamorphism, deformation, and pulses of calc–alkaline magmatism between 2.72–2.67 Ga, 2.63–2.60 Ga, and 2.55–2.50 Ga along an active continental margin (Mueller et al., 1985; Frost et al., 2006; Frost and Frost, 1993; Chamberlain et al., 2003; Grace et al., 2006; Souders and Frost, 2006; Krogh et al., 2011). The Sweetwater subprovince of the Wyoming Province includes the Teton and Wind River ranges that experienced retrograde amphibolite after granulite facies metamorphism and were deformed between 2680 to 2667 Ma due to east– to northeast–directed subduction forming calc–alkaline magmatism and preserve peralkaline, felsic magmatism with ages between ca. 2.65–2.63 Ga (Chamberlain et al., 2003; Frost et al., 2006; Grace et al., 2006; Dragovic et al., 2016). Mafic magmatism, including dykes and plutons, were emplaced throughout the Wyoming Province and may extend into the Superior Province by ca. 2480 Ma (Dahl et al., 2006).

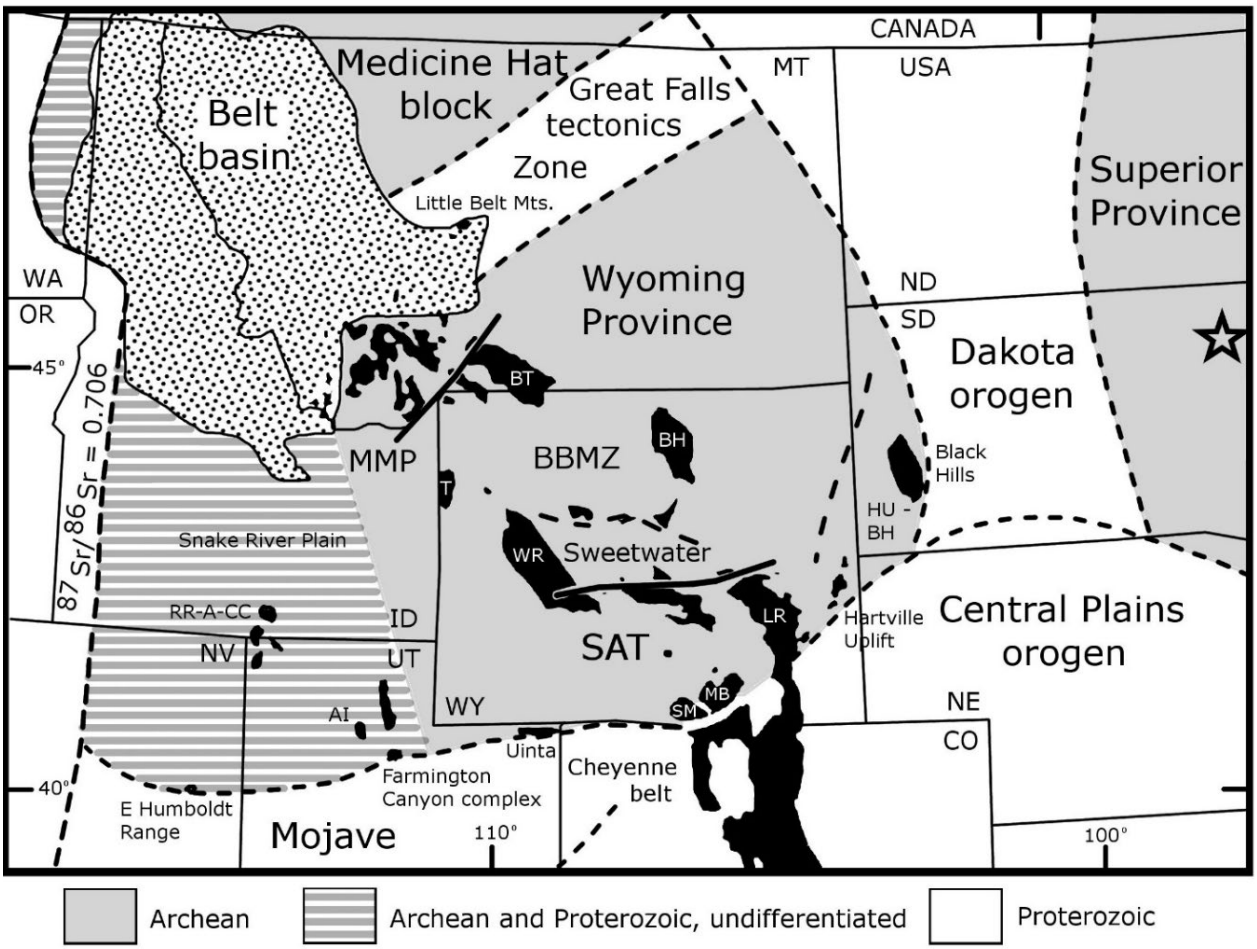

Figure 2.15: Regional map of the western extension of the Superior Province, Dakota Orogen, and Wyoming Province with AI, Antelope Island; BH, Bighorn Mountains; BT, Beartooth Mountains; LR, Laramie Range; MB, Medicine Bow Mountains; RR–A–GC, Raft River – Albion–Grouse Creek Mountains; SM, Sierra Madre; T, Teton Range; WR, Wind River Mountains; Great Falls Tectonic Zone; SAT, Southern Accreted Terranes. The Beartooth–Bighorn magmatic zone (BBMZ) and Montana metasedimentary province (MMP) were cratonized by ca. 2.80 Ga. The Sweetwater subprovince was metamorphosed and deformed in the late Archean and the SAT accreted by ca. 2.63 Ga and cratonized by 2.50 Ga. Staurolite–schist (open star) was intersected in drill core with a staurolite–biotite schist with Rb–Sr whole rock date of 2560 ± 55 Ma between a fault bounded Wawa subprovince to the north and the GLTZ to the south; the Oregon Trail Structural Belt (OTSB, black line), and the Snowy Pass Supergroup (white line between Archean craton (grey) and Proterozoic (white)) (Modified after Sims et al., 1991; Chamberlain et al., 2003; Foster et al., 2006; Mueller and Frost, 2006; McCormick, 2010).

CHAPTER 3: METHODS

3.1 Field Data and Petrography

Seven seasons of field and underground mapping were conducted prior to this study by the author in mines and deposits throughout the Superior Province (including the Wawa, Abitibi, Quetico, Wabigoon, and Uchi subprovinces, Marmion domain, and North Caribou terrane). Therefore, effort was taken to test hypotheses on gold mineralization by other workers as well as those proposed earlier by the author in previous studies and theses: (1) the regional– to microscopic–scale structures that host gold mineralization in the southern Superior Province are ductile to brittle–ductile shear zones that have a penetrative, anastomosing, tightly–spaced schistose foliation and may have a mylonitic fabric adjacent to rheologically competent lithons (Hill et al., 2011; Stinson, 2013), (2) the strike and dip of the shear zones is dependent on rheology, although it is typically parallel to oblique to the terrane or subprovince boundary or suture zone, (3) the property–scale structures that host gold mineralization are folded, mylonitized, and boudinaged quartz veins; shear–related early, late, and complex folds; folded fault breccia, and pressure shadows of rigid minerals within schistose to mylonitic fabric (Stinson, 2010; Stinson, 2013), (4) on the microscopic scale gold mineralization is located in areas of micro–folds, micro–boudins, folded micro–fault breccia, undulatory extinction, mylonites with grain size reduction along irregular grain boundaries, subgrain boundaries, folded healed fractures, fractures in competent minerals, and in pressure shadows within areas of strain heterogeneity, and (5) microstructures that host gold mineralization are minerals that display evidence for brittle deformation synchronous or overprinted by dislocation or diffusion creep during both prograde and retrograde metamorphism (Stinson et al., 2009; Hill et al., 2010; Stinson, 2010; Stinson, 2013).

The field work conducted for this study includes twenty–four weeks of reconnaissance, trench, outcrop, and detailed mapping in the Wawa and Abitibi subprovinces, WGD, KSZ, and MRVT as a Ph.D. student. The first field season focus was on the Borden Mine and adjacent properties, however reconnaissance mapping with outcrop mapping and sampling occurred throughout the study area. Field data and structural data collected on the cratonic– to microscopic– scale includes planar data (including strike and dip of foliation, gneissosity, schistosity, mylonities, pseudotachylites, cataclasites, faults, shear zones, boudins, boudin necks, foliation boudins, S–C fabrics, spacing of fabrics, etc.), linear data (plunge and trend of

lineations including intersecting planes, clast/bomb/block/lapilli lineation, mineral lineation, boudin necks, intersecting lineations, mullions, etc.), interpreted to be previously planar or linear (deformed stratigraphic contacts, igneous dykes and sills, etc.), folds (cratonic– to microscopic– in scale, measurements of limbs, plunge, fold axis, axial trace, description of shape, interlimb angles, etc.), shear sense (S–C fabrics, mineral fish, etc.), rotation (measurement of plastic distributed deformation and/or rigid block rotation interpreted paths in plan view and when available, cross section, or oblique, particularly in foliation boudins and dykes), strain ellipses (using dense, isotropic minerals including garnet, less rigid minerals including quartz eyes in felsic volcanic lithologies, mineral rotation, rotated lamellae in minerals, boudins and foliation boudins, and polymictic metaconglomerate clasts, identification of potential deformation mechanisms in porphyroblastic minerals (grain size reduction, myrmekitic textures, fractures, etc. that were confirmed in thin section), interpretation of competency (fabric spacing, types of foliation and mylonites, width of mylonites and cataclasites, relationship between fabrics, differences in boudin types and end members present in each rock type, etc.), and interpretation of the sequence of events (using the principles of geology, although due to the high–grade metamorphism and high–temperature deformation many of these features are ambiguous).

Over 10 000 lithological and mineralogical descriptions and structural measurements were taken and two hundred sixty–seven samples of all visually distinct, or hypothesized to be distinct at the microscopic scale (i.e., mineralogy, texture, morphology, alteration, mineralization, and structure), were collected from the field, trenches, and drill cores. Seventy polished–thin sections were prepared at Lakehead University by Victoria Stinson and Anne Hammond as well at the University of Saskatchewan by Blaine Novakovski. The samples and petrography are described in Appendices. Samples were collected for petrography to test the mineralogy, lithology, alteration, structure, metamorphism, mineralization, and geochemistry at the Borden Mine and throughout the study area. Samples collected for mineralogy, lithology, and metamorphism had useful index minerals (or pseudomorphs of index minerals) and retrograde minerals overprinting earlier minerals. Samples for structure included those with low–grade, high–grade or potential for mineralization. Samples collected for alterations and retrograde metamorphism were collected based on presence of potential minerals present in the sample and how they appear to overprint earlier mineralogies. Samples collected for geochemistry were collected outside of the ore zones, alteration, and for general “freshness”. Exceptional field

assistance was completed by Katia Jellicoe (2013), Gleceria Gamelin (2014), and Matthew Nadeau (2015) who also conducted mapping and sample collections for their own Bachelor's honours theses. Regional, reconnaissance mapping was conducted in the southern KSZ, WGD, Wawa and Abitibi subprovinces and more detailed mapping, including trench mapping and core logging at Wawa, Chapleau, and Timmins gold mines, was conducted in the southern KSZ, southern WGD, and Chapleau Belt. All geographic data were collected using the Geodetic Datum NAD 83 in UTM Zone 16 N unless otherwise specified. Mathematical conversions were used to convert UTM data to latitude and longitude and may have introduced minor errors.

3.2 Zircon U–Pb geochronology and Hf–isotopic analysis

Fifty kilograms of rock samples of sillimanite–garnet–biotite gneiss and schist were collected from the predominantly amphibolite Discovery Trench (16N 5303686/0330311) at the Borden Mine property with low–grade gold mineralization. The samples were hammered and cleaned to remove any weathered or contaminated surfaces in Dr. Shannon Zurevinski's laboratory at Lakehead University, Thunder Bay, Ontario.

The sample was then crushed in a clean jaw crusher and further milled in a tungsten–carbide disc mill. A Wifley Table was then used to separate finer materials. Magnetic separation included the use of a hand magnet, rare–earth magnets, and Franz magnetic and paramagnetic separators. Gravity separation by lithium metatungstate was conducted at the Saskatchewan Isotope Laboratory. Nitric acid was then used to dissolve excess pyrite in the sample. The samples were then placed in Petri dishes with ethanol for random, handpicking using a binocular microscope. Grain selection was random however zircon chosen for analyses was based on clarity, crystal integrity that are euhedral, transparent, and fracture and inclusion free as many orange, metamict zircons were originally selected randomly and were not suitable for analyses. All zircon grains were <200 μm, on average 50–100 μm along the c–axis, predominantly a combination of {100} prism ({100} >> {110}) and {101} pyramid forms ({101} >> {211}), predominantly prismatic to subrounded, and are broken fragments of crystals or intact crystals. Approximately 10% of the total population of zircon grains has twins parallel to the c–axis. Two populations can be distinguished based on colour and transparency from the 200 zircon grains picked. The first population, representing approximately 50% of the grains, is euhedral, translucent to cloudy, brown–orange, pitted crystal faces, and moderately to severely metamict

and not selected for further study. The second population, approximately the other 50%, is euhedral, transparent to translucent, pink to pink–brown to brown, smooth crystal faces, distinct cleavage planes, generally lacked inclusions and fractures, and was selected and used in the study. From the 100 zircon crystals from the second population only 50 spots were analyzed from 45 grains. Cathodoluminescence (CL) imaging highlights the bright, oscillatory growth zoning in the zircon grains, which is consistent with igneous crystallization, and the dark, fir tree– and nebulous–zoned patterns, characteristic of metamorphic zircons (Fig. 3.1). Thicker zones were analyzed to test for metamorphic rims or igneous zoning present in spots 6 and 7, 8 and 9, 10 and 11, 40 and 39, and 43 and 44.

Zircon fractions for analysis were handpicked under a binocular microscope and subsequently mounted in epoxy along with zircon reference materials OG1 (Stern et al., 2009) at the Canadian Centre for Isotopic Microanalysis (CCIM), at the University of Alberta. The mounted grains were gold coated and imaged using a Zeiss Evo 50 scanning electron microscope at CCIM, and Secondary Electron (SE), Back–Scattered Electron (BSE) and CL images were taken of each grain to reveal internal features such as zoning, fractures, internal domains (cores) and alteration (Fig. 3.1). U–Pb data on zircon crystals were acquired using a Nu–Plasma MC–ICP–MS (Nu Instruments, UK) coupled to a frequency quintupled (= 213 nm) Nd:YAG laser ablation system (NewWave Research, USA) at the RIF, University of Alberta, Edmonton, Canada. The collector configuration consists of 12 Faraday 'buckets' and three ion counters, allowing for the simultaneous acquisition of ion signals ranging from mass ^{203}Tl to ^{238}U, with the ^{207}Pb, ^{206}Pb and ^{204}Pb (+^{204}Hg) ion beams measured on the ion counting channels. Detailed information regarding the nature of the ion counters, calibration and data reduction can be found in Simonetti et al., (2005). A 30 s blank analysis prior to ablation is performed for determination of ^{204}Hg contribution and is followed by ablation for another 30 s. The ablation is Tl–doped to correct instrumental mass bias using ^{205}Tl/^{203}Tl. Internal standards [LH94–15 (Ashton et al., 1999) for zircon crystals from Khan mine pegmatite (Simonetti et al., 2006)] were used for correction of instrumental drift and the standard was analyzed after every 12 unknown zircon grains. Common lead correction is readily possible from ^{204}Pb measurements and data reduction for error propagation was performed using an in–house spreadsheet. U– Pb/Lu–Hf isotope measurements were collected simultaneously, measured on the ion–probe spots, using the laser ablation split–stream protocol (LASS) coupled with LASS–specific data reduction software

(Fisher et al., 2017). The LASS analyses were screened according to the following criteria: (i) pristine CL/BSE structures; (ii) Integration Time ≥ 15 s; (iii) Uncertainty in the $^{207}Pb/^{206}Pb$ date <1%; (iv) 95% ≤ Concordance ≤ 105%; (v) Uncertainty in the εHfi ≤3 ε; (vi) common Pb ≤0.1%. For a total of 50 analyses that met these criteria. Uncertainties reported hereafter are at a coverage factor of 2 (Committee Guides Metrology, 2008; Ickert, 2013), i.e., ca. 95.5% confidence level. Uncertainty in the $(176Hf/177Hf)_{initial}$ value includes uncertainty in the measured $^{176}Hf/^{177}Hf$ value, uncertainty in $^{176}Lu/^{177}Hf$, uncertainty in the assigned age and uncertainty in the decay constant (Soderlund et al., 2004) and is reported in the last decimal place. Uncertainty in the $\varepsilon^{176}Hf_{initial}$ value is calculated following model–1 of Ickert (2013) and includes uncertainty in the $(^{176}Hf/^{177}Hf)_{initial}$ uncertainty in the CHUR model of Bouvier et al., 2008, and long–term variance of validation reference materials. MSWD and ρ (rho) values reported in this study correspond to the mean squared weighed deviation (MSWD or reduced chi–squared) and probability of fit provided by Isoplot (Ludwig, 2012).

3.3 Microstructural and fabric analysis

After detailed petrographic analyses were conducted using a transmitted and reflected light microscope (data summarized in Appendix D) further microstructural and fabric analyses were conducted in samples from ductile to brittle–ductile shear zones, rotated boudins, rotated foliation boudins, and faults in the field and massive samples. Oriented samples of BIF, amphibolites, granulites, gabbros, and anorthosites were collected from the field in areas of no observable SPO (shape–preferred orientations) in areas of lowest–strain and in areas of observable SPO defining foliations, lineations, boudins, foliation boudins, pinch–and–swell, mullions, and chocolate tablet structures. The samples were collected perpendicular to the primary foliation and boudin direction (inferred to as the greatest stretching direction), and parallel to the primary and secondary lineations and prepared as polished–thin sections. Polished–thin sections were studied using transmitted and reflected–light microscopy and EMPA (electron microprobe analyzer) to analyze the relationship between gold mineralization and microscopic structures. CPO (crystallographic–preferred orientation) was identified on a transmitted light microscope using a lambda plate, and was studied further using a universal stage, G50 Fabric Analyzer, and G60 Fabric Analyzer (http://www.russellheadinstruments.com). The latter two instruments determine the c–axis orientation of uniaxial crystals such as quartz at

each pixel in the field of view (Wilson et al., 2007). CPO data were consistent between the methods, including manually selected computer–operator selected crystals. Numerous lineations were also determined in retrograde minerals, particularly in boudin necks. Indeed, retrograde minerals including blue–green amphibole define two or more lineations in boudin necks suggesting they formed and continued to grow in a changing strain regime in the low–pressure boudin neck. Black hornblende and prismatic sillimanite defines a horizontal to shallow lineation outside of the boudin neck and within the boudin neck a subvertical to vertical lineation is defined by blue–green amphibole. Fibrolite sillimanite commonly defines a lineation parallel to the greatest stretching direction in boudin necks. Pseudo–hexagonal tourmaline defines a lineation perpendicular to extension in boudin necks. Gneissosity is generally defined by prograde stable metamorphic mineral assemblages including ortho– and clinopyroxenes, garnet, black to brown hornblende, titanite, plagioclase, biotite, and alkali feldspars. Schistosity commonly overprints earlier gneissosity and is defined by retrograde mineralogy, including muscovite, biotite, and chlorite.

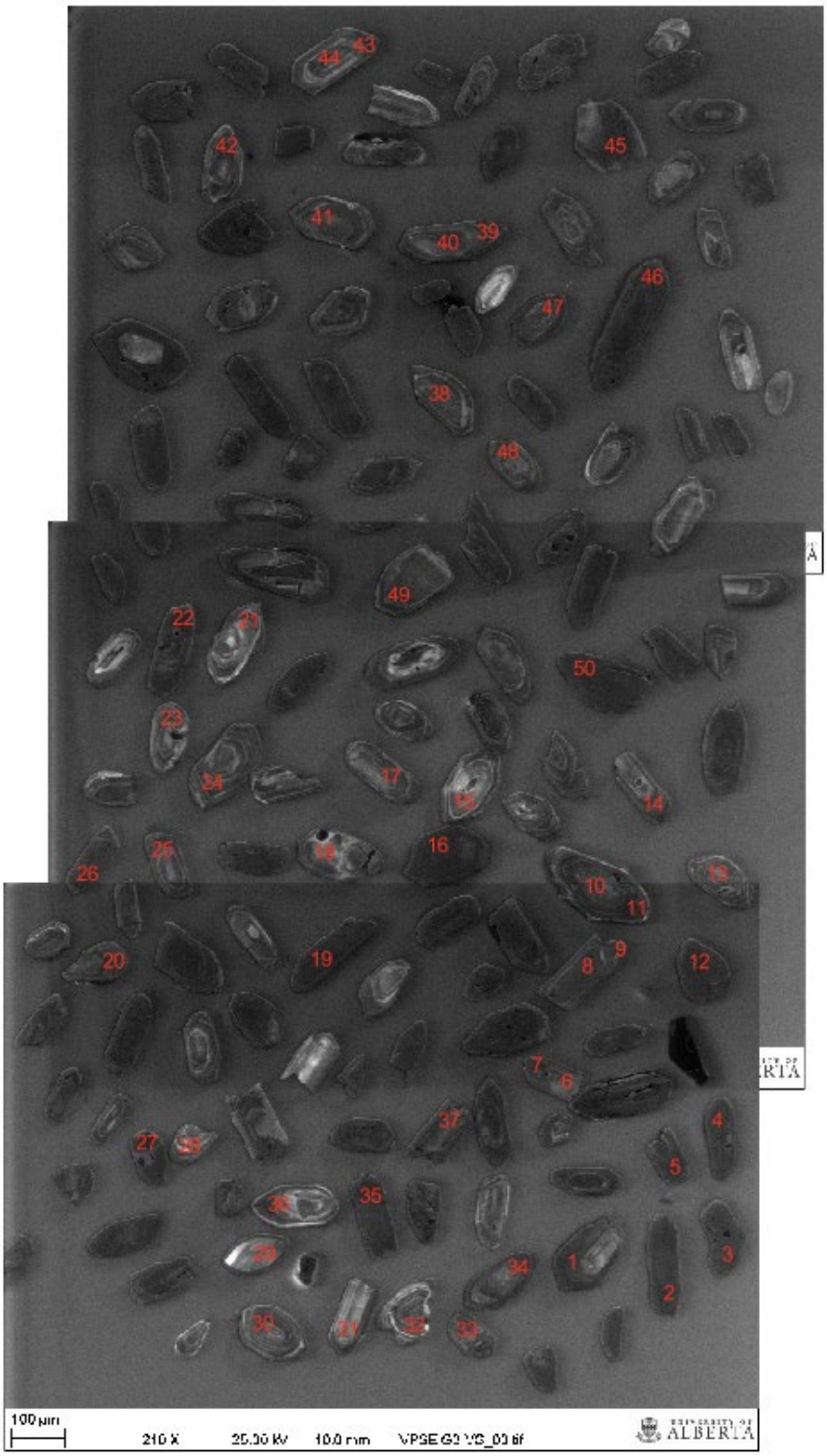

Figure 3.1: CL image of the second population of zircon crystals with the red numbers indicating sample number, spot location, and size with CL imaging highlighting the bright, oscillatory growth zoning consistent of igneous crystallization and darker fir tree– and nebulous–zoned patterns, characteristic of metamorphic zircons. Spots 6 and 7, 8 and 9, 10 and 11, and 39 and 40 were tested for metamorphic rims or igneous zoning.

3.4 Whole rock and trace element geochemistry

Fresh samples without visible surface weathering or hydrothermal alteration were collected from the field and drill cores for whole–rock and trace–element geochemical analysis to ascertain the lithologies, protoliths, alterations, and potential for gold mineralization in the study area. Whole–rock and trace element geochemistry was performed before further sulphur and lead isotope geochemistry was conducted. The selected samples were powdered using a tungsten carbide disc mill at the University of Saskatchewan and were then shipped to the Activation Laboratories Ltd. (Actlabs) in Thunder Bay, Ontario for analysis.

Whole rock analyses at Actlabs were conducted using the lithium metaborate/tetraborate fusion method combined with inductively coupled plasma mass spectrometry (ICP–MS), for which the detection limit was 0.01% with standards NIST 694, DNC–1, GBW 07113, W–2a, SY–4, and BIR–1a Measured and Certified with splits and blanks every 30 samples and duplicates every 15 samples. Briefly, a 0.2 g sample is mixed with a mixture of lithium metaborate/lithium tetraborate and fused in a graphite crucible. The molten mixture is poured into a 5% nitric acid solution and shaken until dissolved (~ 30 minutes). The samples are run for major element oxides and selected trace elements on a Varian Vista ICPMS. Calibration is achieved using a variety of international reference materials. Independent control standards are also analyzed. A 0.25 g sample is digested with four acids beginning with hydrofluoric, followed by a mixture of nitric and perchloric acids, heated using precise programmer–controlled heating in several ramping and holding cycles which take the samples to dryness. After dryness is attained, samples are brought back into solution using hydrochloric acid. An in–lab standard (traceable to certified reference materials) or certified reference materials are used for quality control. Samples are also analyzed using a Varian Vista ICPMS. Additional INAA that was also required for trace element geochemistry used a 1 g aliquot that is encapsulated in a polyethylene vial and irradiated with flux wires and an internal standard (1 for 11 samples) at a thermal neutron flux of 7 x 1012 n cm–2 s–1. After a 7–day period, to allow Na–24 to decay, the samples are counted on a high purity Ge detector with resolution of better than 1.7 KeV for the 1332 KeV Co–60 photopeak. Using the flux wires, the decay–corrected activities are compared to a calibration developed from multiple certified international reference materials. The standard present is only a check on accuracy and is not used for calibration purposes. From 10–30% of the

samples are rechecked by re–measurement. One standard is run for every 11 samples. One blank is analyzed per work order. Duplicates are analyzed when samples are provided.

3.5 Sulphur isotope analysis

Samples for sulphur isotope analysis were collected from fresh drill core at Borden Mine site and unaltered, unweathered samples from the field in the northern Chapleau Belt of the KSZ (listed and described in Appendix D). Samples were collected based on lithology, texture/structure (coronas, boudins, disseminated, massive), mineralogy (suphides, oxides, and graphite), and gold mineralization (barren, ore, or high–grade ore) before Pb–isotopes and geochronology were conducted.

The $\delta^{34}S$ values of sulfide minerals are denoted in parts per thousand enrichment or depletions relative to a known standard and are calculated by: (in ‰) = (Rsample/Rstandard – 1)1000, where "R" is the ratio of $^{34}S/^{32}S$ in the sample or standard. The more enriched (or higher) or more positive the material, in respect to the standard, the heavier isotope the sample contains compared to the standard. Equilibrium and kinetic chemical reactions, including biological reactions, may cause sulfur isotopic fractionation.

Sulphur isotopic analysis was conducted by the G. G. Hatch Stable Isotope Laboratory at the University of Ottawa in Ottawa, Canada. Twenty–nine samples of sulfide separates were analyzed with three duplicates and one blind duplicate. Sulphide samples were separated from rock samples collected from the field in outcrops and drill cores based on gold mineralization, lithology, structures, and igneous and metamorphic textures. Pyrite, pyrrhotite, and an intergrown mixture of pyrite and pyrrhotite were sampled as they are present in most lithologies with numerous textures, easily identifiable by core–logging geologists, and present in unmineralized samples, mineralized, and high–grade ores. Sulfide samples were hand–picked and powdered using a pestle and mortar. Samples were weighed into tin capsules with a minimum of twice sample weight of tungsten oxide (WO_3). Samples were loaded into a Vario Micro Cube (Elementar, Germany) elemental analyzer and flash combusted at 1800ºC. Released gases were carried by helium through the EA to be cleaned and separated by “trap and purge”. The separated SO_2 gas was carried by helium into the Delta XP IRMS via a Conflo IV to the isotope ratio mass spectrometer (ThermoFinnigan, Germany) for analysis. Analytical precision is ± 0.2 ‰. The blind standard measured –0.44‰, n= 6, and a standard deviation of –0.21‰ with

the known sample = –0.62‰. The standards used by the lab include IAEA–S–2 which is a silver sulphide (with a starting material of gypsum) prepared by the B. W. Robinson, Department of Scientific and Industrial Research, Lower Hutt, New Zealand with a value of +22.7‰ and a standard deviation of 0.2‰. IAEA–S–1 is a silver sulphide (with a starting material of sphalerite) prepared by S. Halas, Maria Curie–Sklodowska University, Lublin, Poland with a value of –0.30‰ and is defined in respect to VCDT and therefore bears no associated uncertainty. A lab standard of AG–2 is the third standard used. The 34S data collected was normalized to these standards and IAEA–S–2 was measured 22.7‰, IAEA–S–1 was measured –0.3‰, and AG–2 was measured –0.71‰. All methods followed those by Robinson (1995); Stichler et al.(1995) and Wagner et al. (2004).

3.6 Lead isotope analysis

Lead isotopic analyses were conducted after sulphur isotopes were determined. Samples for lead isotope analysis were collected from fresh drill core at Borden Mine site and unaltered, unweathered samples from the field in the northern Chapleau Belt (listed and described in Appendix D). The lead isotopic analyses were conducted using the Multi–Collector ICP–MS (MC–ICP–MS; Finnigan Neptune, Thermo Electron Corp.) at the Saskatchewan Isotope Laboratory, University of Saskatchewan. Pyrite, pyrrhotite, and magnetite separates were handpicked and crushed by hand using an agate pestle and mortar, decomposed in 8 N HNO3, and taken to incipient dryness. Decomposed samples were dissolved in HBr for Pb column separation using standard anion exchange techniques (Cousens, 1996). For analyses via MC–ICP–MS, samples were Tl–doped to facilitate corrections for instrumental mass bias based on an exponential dependence on mass law (e.g. Zhu et al., 2000). Corrections were based on values obtained for several aliquots of Tl–doped NIST 981 solution run before, during (every 4 samples) and after the sample sequence. Results were first standardized for Tl fractionation for the NIST SRM 997 standard, then restandardised using accepted values for NIST SRM 981 (Todt et al., 1984). Analytical uncertainties for repeat analyses of standards are better than 0.01% (1 sigma), but a conservative estimate of 0.05% (1 sigma) has been used for sample analyses based on replicates with varying contents of Pb and mineralogy. Error correlations between $^{207}Pb/^{204}Pb$ and $^{206}Pb/^{204}Pb$ and between $^{208}Pb/^{204}Pb$ and $^{206}Pb/^{204}Pb$ were calculated from the repeat analyses of NIST 981. NIST 981 is commonly used or a combination of external reference

and internal isotope pairs (^{203}Tl and ^{205}Tl are commonly used because their mass numbers are close to that of Pb) to correct the mass discrimination of MS, so as to achieve an accuracy of analysis that is approaching TIMS measurement using double or triple spikes (Taylor et al., 2015). Raw data were processed with the program GEODATE (Eglington and Harmer, 1999).

CHAPTER 4: RESULTS & DISCUSSION

4.1 Lithologies

Four generalized lithological categories in the study area include: mafic, felsic, and sedimentary protoliths, and crosscutting mafic dykes. The general tectonostratigraphy is presented below, however further work is required to subdivide the lithologies (Fig. 4.1). The most common lithologies, mineralogy, and structures in the Borden Mine, Chapleau greenstone belt, WGD, and KSZ are described below along with photographs, photomicrographs, and petrographic descriptions (Figs. 4.2–4.18). Refer to Jellicoe (2014, unpublished Honours BSc. thesis) and Lafontaine (2016, unpublished MSc. thesis) for detailed descriptions on types of amphibolite lithologies in the Borden Mine. Field data is presented in stereonets as well as trench and regional maps (Figs. 4.19–4.45).

4.1.1 Ultramafic to mafic (and minor felsic) lithologies

Ultramafic, mafic, and intermediate plutonic (plutons and dykes) and volcanic rocks, interlayered with minor sillimanite–garnet–biotite schists and gneisses and oxide– and sulphide–facies BIF, are the lowest lithologies stratigraphically and structurally at the Borden Mine, Chapleau Belt, and KSZ in the study area. The lowest, and most porphyroblastic and garnet–rich amphibolite is commonly referred to “footwall” amphibolite and above is the finer–grained “hangingwall” amphibolite. At this contact are BIF and sillimanite–garnet–biotite schists and gneisses. The schists and gneisses are in contact with the BIF and mafic lithologies and have been interpreted based on these relationships to have a mafic protolith. Stratigraphically and structurally above the ultramafic to intermediate lithologies (Figs. 4.2, 4.5) are intermediate to felsic volcanic (Figs. 4.3–4.4) and volcaniclastic lithologies, with minor mafic volcanic blocks and breccia.

Tectonostratigraphy

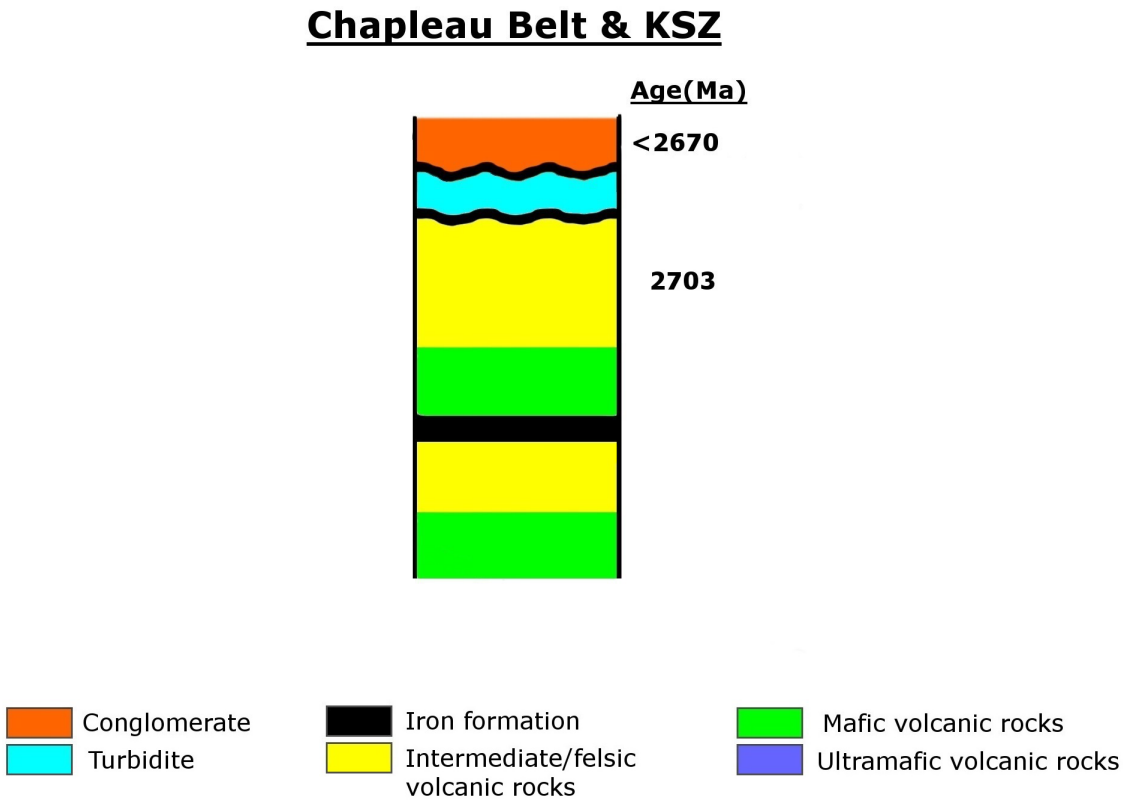

Figure 4.1: Proposed tectonostratigraphy in the Chapleau Belt, western WGD, and southern KSZ, including the Borden Mine. The "footwall" amphibolites have a gradational upper contact with felsic lithologies, including sillimanite–garnet–biotite gneiss and and BIF therein. The "hangingwall" amphibolite has a sharper contact with metavolcanic and volcaniclastic felsic lithologies. Topping the sequence are metasandstones and metaconglomerates. Ages are described in this study and by those of Krogh (1993) and Moser (1996, 2008).

Figure 4.2: Amphibolite (dark grey to black) is the predominant mafic lithology in the western study area and has variable mineralogy, textures, and host numerous types of structures (porphyroblastic “leopard print” amphibolite with foliation boudins) (UTM 16N 5305232/0320828, Boudin Outcrop).

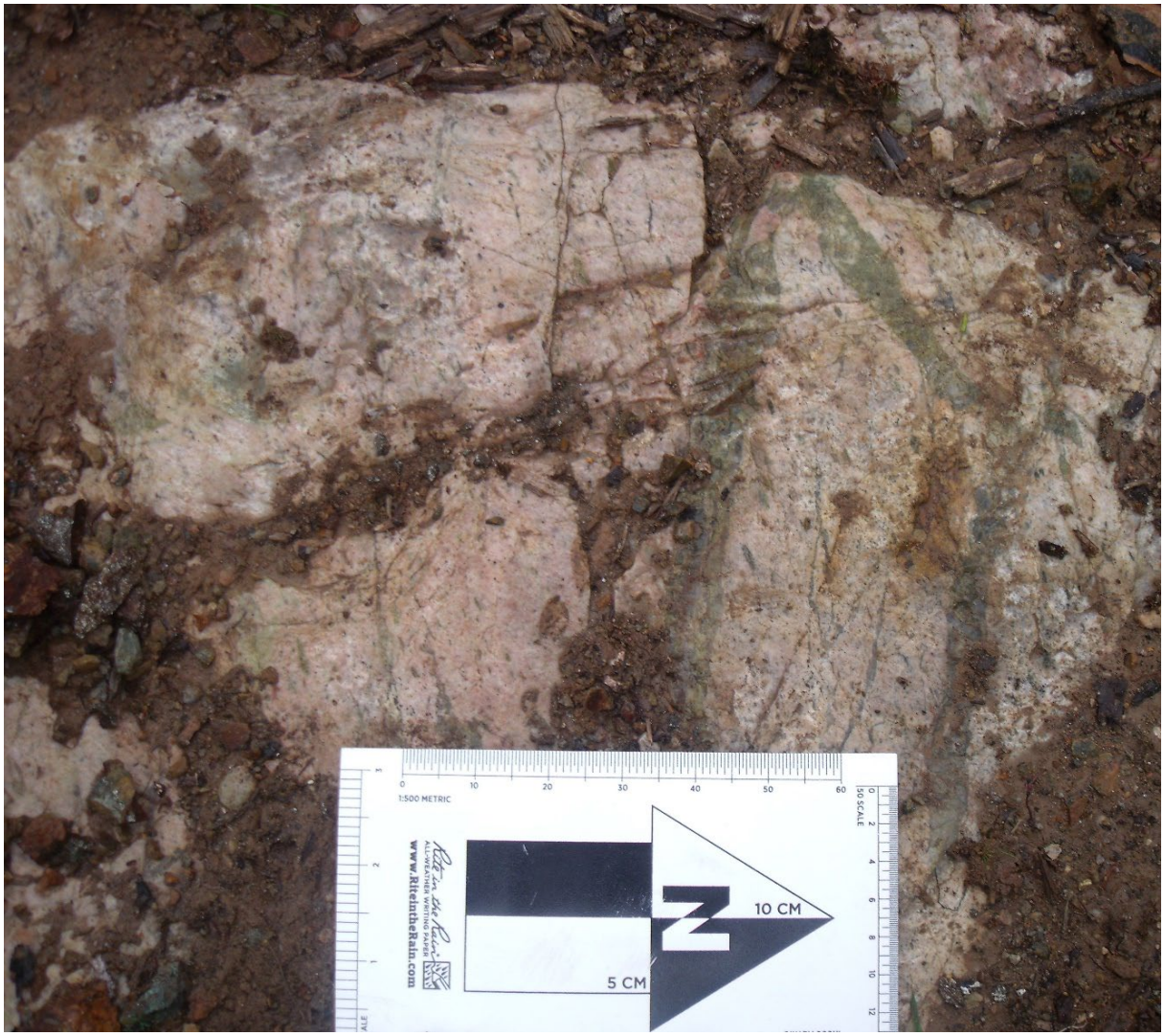

Figure 4.3: Felsic metavolcanic and volcaniclastic lithologies (pink and light green) (UTM 16N 5306367/0327107).

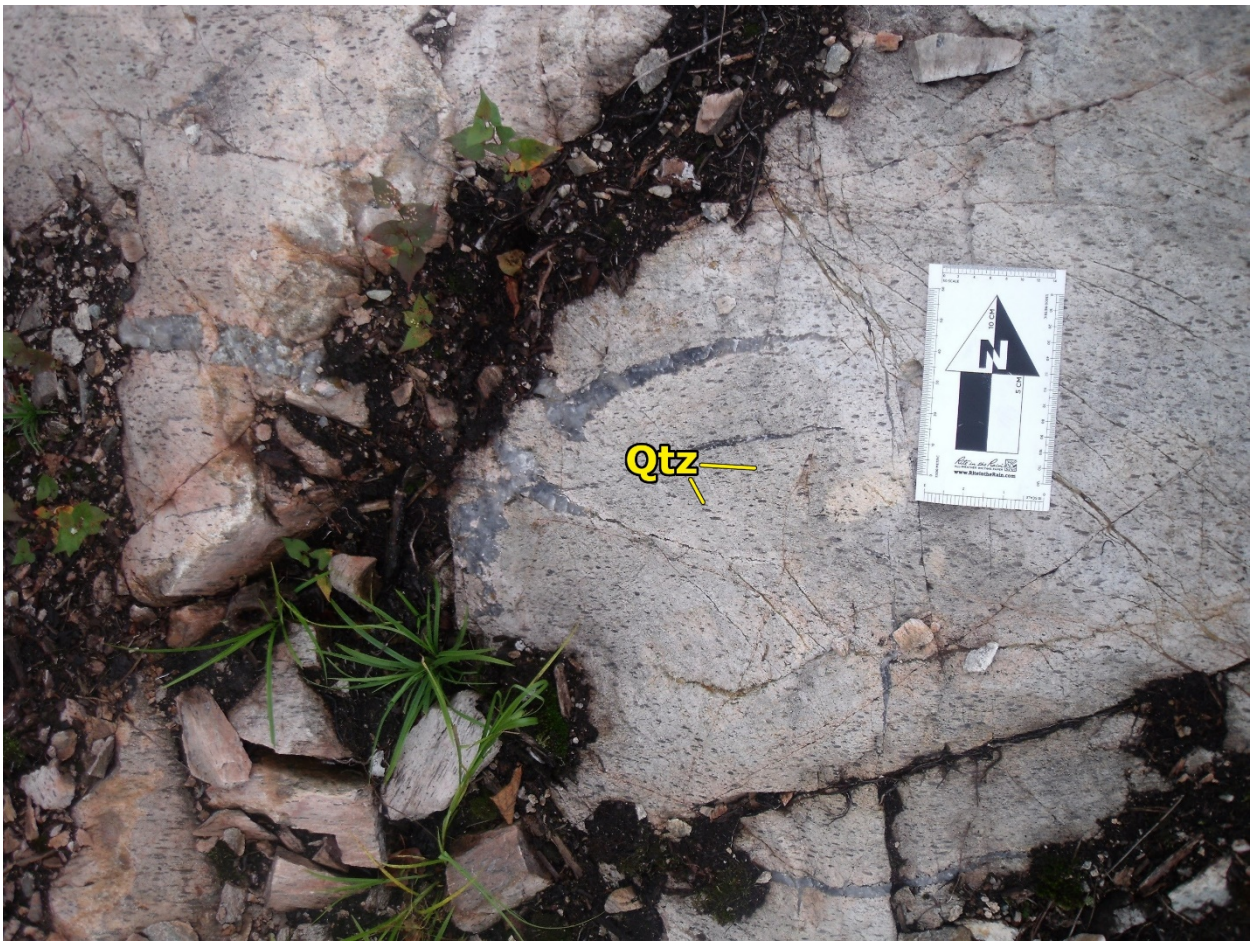

Figure 4.4: Felsic (pink to beige) metavolcanic (± subvolcanic) lithologies commonly host prophryoblasts of quartz (Qtz) (UTM 16N 5306367/0327107)

Ultramafic to mafic intrusive lithologies are black to dark green in colour, medium to coarse–grained and range from mafic to ultramafic due to variability of plagioclase present. The fine– to coarse–grained, porphyroblastic mafic to intermediate lithologies have been described as "leopard print" by some Borden Mine workers (Fig. 4.2). In low–strain regions, from the microscopic scale to regional scale, these ultramafic to mafic intrusive lithologies are composed of 50% plagioclase, 50% diopsidic pyroxene, garnets, orthopyroxene, and hornblende. In areas of the greatest strain there are mafic to ultramafic lithologies up to 100% mafic minerals (including assemblages of pyroxenes, garnet, rutile and lacking plagioclase) and up to 100% plagioclase (An % 70–100) in low–strain boudin necks within these generally high–strain zones. Observation of labradoresence in the field is uncommon, with only three such observations, due to the calcic nature of the plagioclase. In areas of more moderate strain the plagioclase–rich leucosome can be traced back to the mafic restite along open to gently folded migmatitic

neosome dykes. On the regional scale the Shawmere anorthosite complex is located in relatively lower–strain areas in the KSZ (Figs. 1.3–1.4, 4.14 D).

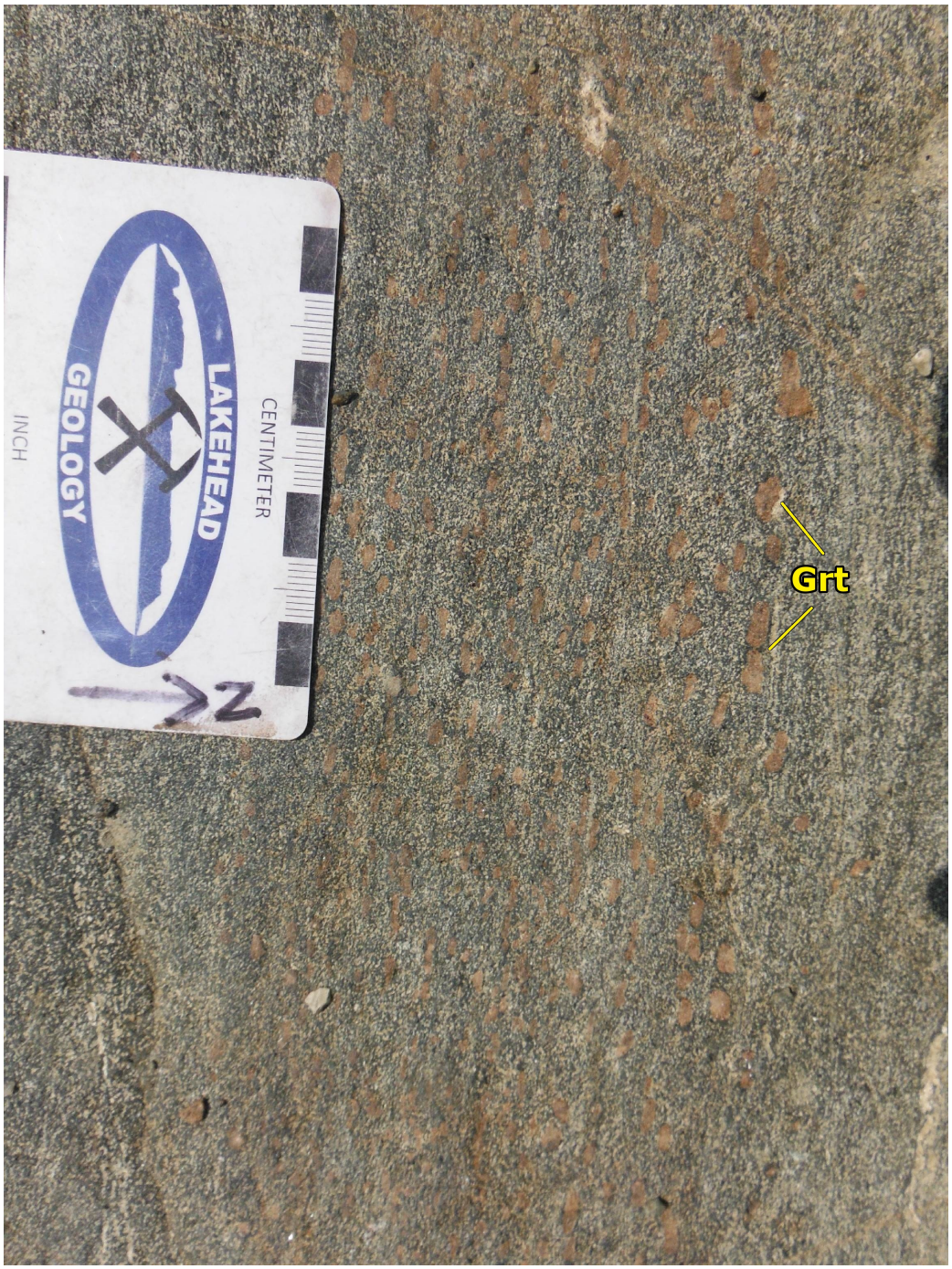

Figure 4.5: Medium– to coarse–grained garnet amphibolite with elongated garnet (red–brown minerals, Grt) defining the lineation (UTM 16N 5306478/0328477).

There is variability in mafic to intermediate regions with augite, plagioclase, scapolite, hornblende, titanite, chlorite, biotite, and prehnite present in deformed and migmatized mafic

lithologies and plagioclase, hornblende, biotite, chlorite, carbonate, and quartz in the intermediate lithologies. Modally the granulite is composed of plagioclase (30–60%), orthopyroxene (10 to 25%), clinopyroxene (5 to 25%), garnet (5 to 15%), titanite (trace to 5%), and scapolite (trace to 5%). Spinel, sapphirine, and cordierite were not observed. The amphibolite had the greatest variability due to the amount of retrograde minerals present. Modally the average amphibolite is composed of plagioclase (30–60%), hornblende amphibole (30–50%), clinopyroxene (trace to 20%), garnet (trace to 15%), biotite (0–15%), chlorite (0–15%), prehnite (0–10%), scapolite (second order birefringence, marialite) (0–15%), titanite (0–10%), pyrite (0–5%), pyrrhotite (0–5%), magnetite (0–5%), rutile (0–5%), actinolite (0–3%), carbonate (0–3%), quartz (0 to 3%), microcline (trace to 3%), and chalcopyrite (trace). Lamprophyre is composed of 15–45% partially to completely altered volcaniclastic fragments, 20–40% phlogopite, chlorite 10–30%, carbonate 15–30%, and riebeckite amphibole 5–15%.

In high–strain areas adjacent to the orthopyroxene isograd mapped by Percival (1981, 1989) the orthopyroxene is partially to fully–replaced by diopside and hornblende. Inside the orthopyroxene isograd orthopyroxene grains have not been retrograded but display undulose extinction, plagioclase displays deformation twins, and augite displays deformation twins and simple twins. Garnet in areas of lower strain (or lithons) in the clinopyroxene isograd have coronas of plagioclase or symplectic coronas of plagioclase and clinopyroxene. As such, the previously mapped isograds and newly proposed mineral–out and migmatitic “isograds” are displayed as clearly marked, sharp boundaries when in fact they are more jagged and irregular in nature. Metatexites to diatexite migmatites of ultramafic to mafic compositions could be classified as igneous, metamorphic, or migmatitic lithologies (Figs. 4.6 B, 4.23). Restites of clinopyroxene, orthopyroxene, hornblende, titanite, rutile, garnet, and sulphides can be described in lower–strain zones as igneous lithologies, such as gabbronorite or pyroxenite, with massive to cumulate textures or appear tectonized in shear zones and classified as metamorphic lithologies with hornfels to gneissic to migmatitic textures (Fig. 4.8). This study uses primarily metamorphic terminology with minor migmatitic terminology when significant, however, in many instances the use of igneous terminology is perfectly acceptable.

In sharp contact with the intermediate, mafic to ultramafic migmatized plutonic lithologies are ashy grey–blue to medium blue–grey, very–fine grained to fine–grained massive

to porphyritic basalt with euhedral, medium grained, plagioclase phenocrysts to massive amphibolite in the amphibolite facies and medium– to coarse–grained granulite in the granulite facies. The mineral assemblages of the mafic lithologies are hornblende, augite, garnet, orthopyroxene, scapolite, biotite, chlorite, prehnite and plagioclase with quartz and potassium feldpsars in the intermediate lithologies. Stratigraphically above the mafic metavolcanic lithologies with plagioclase phenocrysts is an increase in progressively more felsic metavolcanic lithologies (Fig. 4.7 A–C). Modally the felsic lithologies are composed of alkali feldspars (40–60%), quartz (40–50%), and muscovite (0–15%). In the package of mafic metavolcanic lithologies are minor felsic, intermediate, and ultramafic volcanic (± subvolcanic) and volcaniclastic lithologies, including lamprophyres, and sulphide– and oxide–facies BIF in gradational contact with the mafic metavolcanic lithologies. The sulphide–facies BIF are the only lithologies with appreciable sulphide minerals (dominantly euhedral, cubic pyrite with trace pyrrhotite and chalcopyrite) with textures ranging from stringer to semi–massive to massive locally. The felsic lithologies are light pink, cream, to very light green in colour, very fine grained to fine grained, and include volcaniclastic lithologies including volcanic breccia, blocks, bombs, and lapilli (Figs. 4.3–4.4, 4.6, 4.7 A–C). The volcanic breccia is defined by angular blocks composed of smoky quartz and light pink, cream, or very–light green alkali feldspars with two sets of mutually intersecting fractures at 60º and 120º (Figs. 4.3–4.4, 4.7 A–C). The blocks and bombs are composed of smoky quartz and alkali feldspars with colours of light cream, light pink, light green, and light grey (Figs. 4.7 A–C). Lapilli are light cream to light grey and the matrix of finer particles (particles smaller than crystal tuff including ash) is dark grey to light grey with a rusty–red matrix (hematite) (Fig. 4.7 A–C).

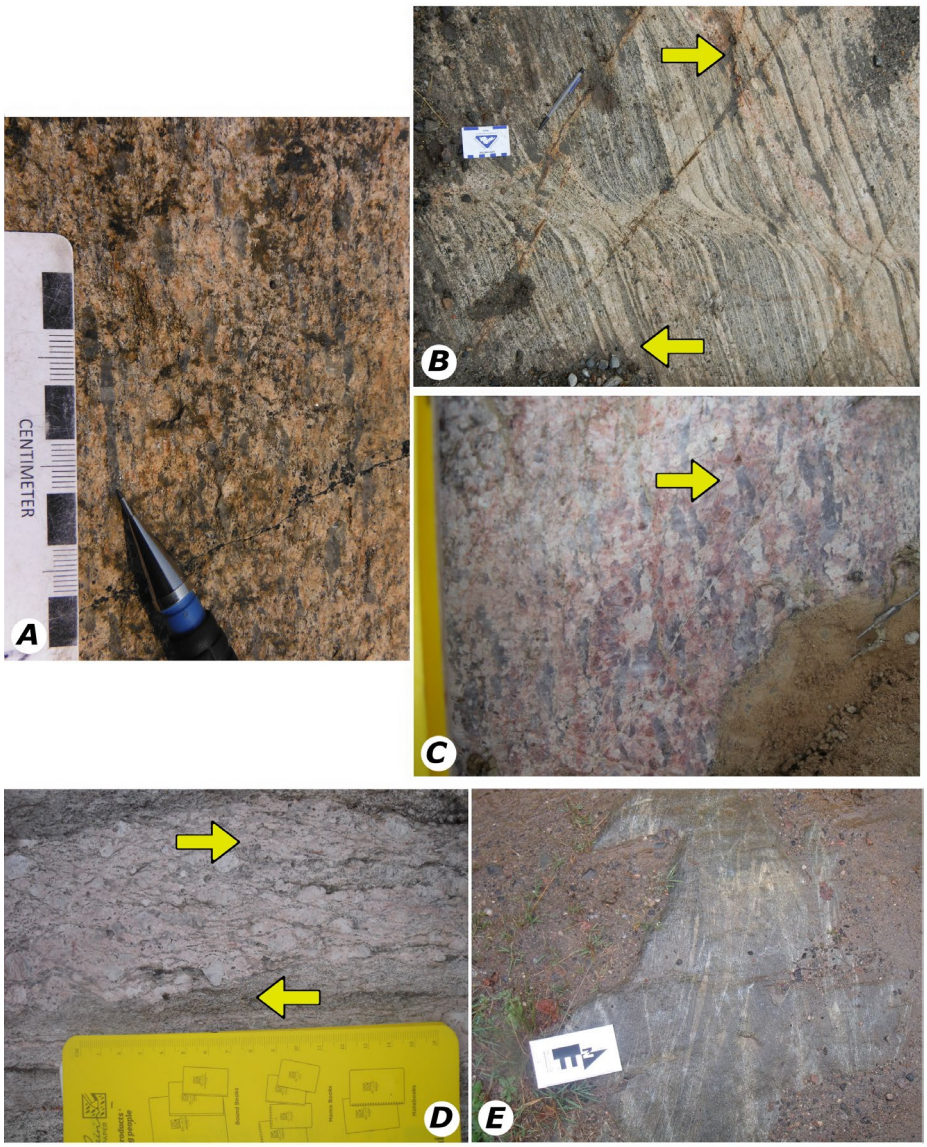

Figure 4.6: Common lithologies and structural fabrics in the eastern and central Chapleau Belt and adjacent WGD (A) Elongated, smoky quartz ribbon defining vertical lineation in metamorphosed dacite to rhyodacite crystal to lapilli tuff common in mafic lithologies (16N 5302878, 032590), (B) Ductile, sinistral, near vertical shear zone defined by alkali feldspar, hornblende, and biotite in a schileric diatexite migmatite and very common in the WGD east, north, and south of the Chapleau Belt (16N 5301990/0325477), (C) Quartz, alkali feldspars, and plagioclase ribbons define a subvertical foliation and lineation in the WGD demonstrating even in the most coarse–grained plutonic lithologies the feldspars and quartz deformed at or above amphibolite facies temperatures (16N 5307674/0328131), (D) Plan view of pegmatitic, alkali feldspar augens defining subhorizontal to horizontal mineral fish in ductile, sinistral shear zones in the WGD along the northern boundary with the Chapleau Belt (16N 5307831/0328839), (E) Patchy metatexite of mafic to intermediate metavolcanic lithologies defining isoclincal folds in the western Chapleau Belt (16N 5304122/0319683).

Primary, volcaniclastic structures include coarsening upwards in the lapilli layer as well as a general coarsening upwards sequence (ash to lapilli to blocks) and suggest younging to the south (Fig. 4.7 A–C). The proposed lower contact of the volcaniclastic breccia has <10% mafic blocks in addition to the intermediate to felsic blocks and may provide evidence of weaning mafic volcanism and felsic volcanism predominating. Overprinting schistosity, boudinage, and lineations typically destroy most primary features. The felsic volcanic and pyroclastic lithologies have a penetrative schistosity and subvertical to vertical lineation. The east–west strike of the 45º angles of the fractured breccia suggest it failed during north–south compression. Blebs to stringers of very–fine grained to medium–grained, anhedral chalcopyrite and euhedral pyrite occur throughout the felsic volcanic protolith. The intermediate and ultramafic lithologies are minor and are in gradational contact within the mafic metavolanic lithologies. The intermediate lithologies are modally composed of 50–60% plagioclase, 15–40% hornblende amphibole, 5–20% biotite, and 0–15% titanite. The ultramafic units are difficult to assess modally as they are composed primarily of chlorite after other ferromagnesian minerals. The sulphide–facies BIF are typically 5–15 cm thick composed of lenses of coarse–grained, euhedral pyrite within the massive, mafic metavolcanic lithology. Modally they are composed of 80–90% pyrite in low–strain zones and 40–60% pyrite, 0–20% quartz, 10–20% pyrrhotite, 10–30% magnetite, and 0–5% chalcopyrite in high–strain zones. In areas of highest strain, the pyrrhotite is present as partially to complete coronas around the pyrite and defines a foliation. The oxide–facies BIF are typically 15–30 cm thick with magnetic, medium grey quartz–rich layer alternating with garnet and biotite–rich layer. Modally the unit is composed of 30–60% quartz, 10–50% magnetite, 10–15% hornblende amphibole, 5–15% garnet, and trace biotite. The felsic lithology is light salmon to very light green, very–fine grained to fine grained, and composed of alkali feldspar and quartz. Breccia is present in the felsic volcanic lithology and due to the angles of breccia it appears it failed during north–south compression (Fig. 4.3). Blebs to stringers of very–fine grained to medium–grained, anhedral chalcopyrite and euhedral pyrite occur throughout the felsic volcanic protolith. In sharp contact with the metavolcanics lithologies are the metasedimentary lithologies. In areas of high strain in the amphibolite or granulite facies these lithologies appear as white and grey–blue to black lit–par–lit gneisses and may be magnetic due to the presence of magnetite and pyrrhotite. In areas of lower strain primary textures are discernable. The mafic and felsic metavolcanics and pyroclastic lithologies and banded iron formations are steeply plunging

to vertical, steeply–inclined to upright, tight, isoclinal to sheath folded (dextral and sinistral) and boudinaged towards the east–west (mm to 20 m spacing between boudins) and up–down the z– or vertical–axis (mm to m); garnet and plagioclase ribbons in metavolcanics near boudins; garnet, plagioclase, hornblende, clinopyroxenes, and quartz eyes define mineral lineations; foliation boudinage; sinistral asymmetrical shear boudins and extension fractures including: rectangular, parallelogram–shaped, unicorn–shaped, and fish–mouth shaped boudins. Plagioclase and garnet define mineral lineations and are elongated in foliation boudins and parallel to the last sinistral, oblique movement (up and to the east based on strike and dip, trend and plunge) in areas of high strain boudinage but typically defines a horizontal lineation and northeast (Fig. 4.4).

4.1.2 Intrusive intermediate to felsic lithologies

Crosscutting the metavolcanic and metasedimentary lithologies are plutons and dykes of intermediate to felsic intrusive rocks (Fig. 4.6, A, C, D). The intrusive lithologies appear to have partially to completely assimilated the host rock, typically mafic lithologies, and in areas of assimilation the mineralogy and geochemistry is intermediate (hornblende, biotite, and plagioclase), commonly referred to as “Wawa Gneiss” (Fig. 4.6 B). The majority of the crosscutting, intrusive lithologies are more felsic including some areas of assimilation (muscovite, biotite, and garnet). In areas of highest strain, the crosscutting relationships between the host rock and the intrusions cannot be discerned, in fact many intrusive lithologies experienced intense volume change due to boudinage or pseudo–boudinage and may pinch out entirely in areas of highest strain. It is in these areas of highest strain that many plutons appear as dykes. Felsic intrusive lithologies are coarse grained to megacrystic, pegmatitic plutons and dykes that commonly define many varieties of structures, including dykes defining open to tight, ptygmatic folds and pseudo–boudins or have been boudinaged, or intruded into boudin necks on all scales. The felsic intrusive lithologies are composed modally of alkali feldspars 30–60% (perthite, microcline, orthoclase), quartz 30–60% (± graphitic texture), ± albite (up to 10%), ± muscovite (up to 20%), ± biotite (up to 10%), ± garnet (up to 5%). The latest felsic dykes crosscut all lithologies and are pegmatitic, with alkali feldspar megacrysts, and strike northwest–southeast (or perpendicular to the direction of greatest strain). Quartz and feldspar ribbons occur in the felsic intrusive lithologies and have kinematic indicators of predominantly sinistral, strike

slip movement (Figs. 4.6 C–D). Due to the boudinage of the felsic intrusive lithologies there are two predominant structures in the Borden Lake gold deposit: horizontal to low angle structures and vertical to moderate structures. Sinistral asymmetrical shear boudins including parallelogram–shaped and lens (lenticular)–shaped boudins are prevalent throughout all lithologies. Mullions are present along the edges of boudinaged, felsic intrusive dykes in contact with the mafic lithologies.

4.1.3 Metasedimentary lithologies

The metasedimentary lithologies have a sharp, angular unconformity with the metavolcanic and metaplutonic lithologies (Fig. 4.16 C). The metasedimentary lithologies are not migmatized and include light grey greywacke with 10–15 cm thick lenses of white to light grey lenses and layer of arenite and <5 cm thick lenses of white arkose. The modal mineralogy of the units is fairly basic with arkosic units composed of 25–75% feldspars, 25–75% quartz, and trace biotite and zircon. The arenite is composed predominantly of quartz (40–100%), feldspars (10–20%), muscovite (5–10%), and biotite (1–10%). The greywacke or immature sandstones are composed of quartz (25–40%), feldspars (25–50%), biotite (10–35%), muscovite (10–20%), garnet (1–5%), and pyrite (trace). Younging directions in these deformed metasedimentary lithologies is generally ambiguous however fifteen instances of moderately–well preserved normal grading, scour (sole) marks, and crossbedding suggest the younging direction is to the north to northwest similar to preliminary studies conducted by the Ontario Geological Survey (Atkinson et al., 2014). Metasedimentary clasts are composed of all lithologies previously described. The clasts define a clast lineations, which are most commonly flattened and elongated, except in areas of greatest extension where they are prolate, and extremely elongated in areas of greatest schistosity where they are oblate. The metaconglomerate clast lineation typically defines a horizontal to sub–horizontal lineation except in areas of regional boudinage where the lineations define moderate to vertical lineations suggesting oblique (sinistral–normal) movement.

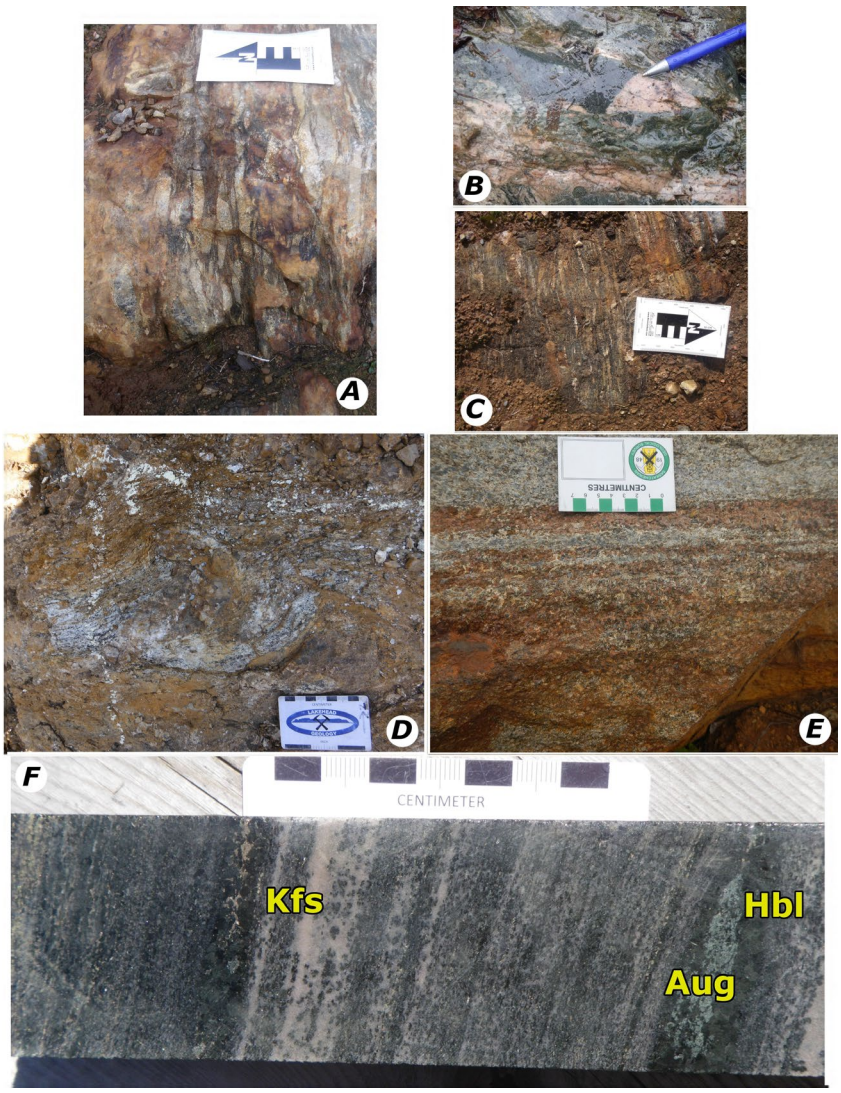

Figure 4.7: Common lithologies in the Chapleau Belt to the southern Kapusasking Structural Zone (A) Flattened and elongated felsic to intermediate volcaniclastic blocks defining vertical clast lineations within minor felsic volcanic lithologies in predominantly mafic volcanic lithologies, (16N 5306367/0327107), (B) Schistose, flattened and elongated felsic volcanic breccia with mafic volcanic clast demonstrating the progression from predominately mafic to more felsic volcanism and preservation of some volcanic textures after subsequent deformation and metamorphism (16N 5303137/327720), (C) Flattened and elongated felsic to intermediate volcaniclastic lapilli and tuff in a dark, mafic matrix that may have been ash to tuff prior to deformation and metamorphism (16N 5306378/0327095), (D) Borden Mine garnet–muscovite amphibolite ore in outcrop, note the visible muscovite (Garnet–biotite Gneiss Trench F), (E) Amphibolite and banded iron formation outside of the ore zone, banded garnet–rich and –poor layer, common to zones of early seafloor alteration and banded iron formations (Discovery Trench 16N 5303686/0330311), (F) Stromatic metatexite (or migmatized amphibolite) displaying zone of alkali–feldspar leucosome with metastable hornblende (left) and zone of black hornblende and medium green, clinopyroxene restite (right) (DDH# BL12–256 at 229.8 m).

4.1.4 Intrusive felsic, pegmatitic lithologies

The felsic intrusive lithologies are composed of alkali feldspars (perthite, microcline, orthoclase), quartz (± graphitic texture), ± albite, ± muscovite, ± biotite, ± garnet, ± pseudohexagonal tourmaline, ± sillimanite, ± beryl, and ± chrysoberyl (Figs. 4.6). The earliest pegmatites are located in low–strain areas as leucosomes in migmatized mafic lithologies and are composed predominantly of alkali feldspars with minor quartz, chrysoberyl, albite, and biotite (Fig. 4.6 D; 4.7 F; 4.8 A). Modally they are commonly composed of 40% microcline, 30% perthite, 5% orthoclase, 5% albite, 5% quartz, 5% biotite, 5% chrysoberyl, and 5% quartz. No muscovite has been noted in these pegmatites. Later pegmatites are composed modally of equal feldspars (40–50%) and quartz (40–50%), muscovite (5–30%), tourmaline (trace to 10%), and beryl (trace to 10%). The last pegmatite phase is quartz and beryl (aquamarine) (Fig. 4.8 A). The youngest felsic pegmatite dykes crosscut all lithologies and are pegmatitic, megacrystic, and strike northwest–southeast (or perpendicular to the direction of greatest strain, with a strike of east–west to northeast–southwest). The pegmatitic dykes are commonly sinistrally boudinaged or rotated ~10–30º counterclockwise and least commonly, in regional to local, "M– and Z–shape" boudin–controlled folds they are rotated 10–30º clockwise (Figs. 4.17 B, C, F) (similar to folds mapped by Moser, 1994 and Bursall, 1990).

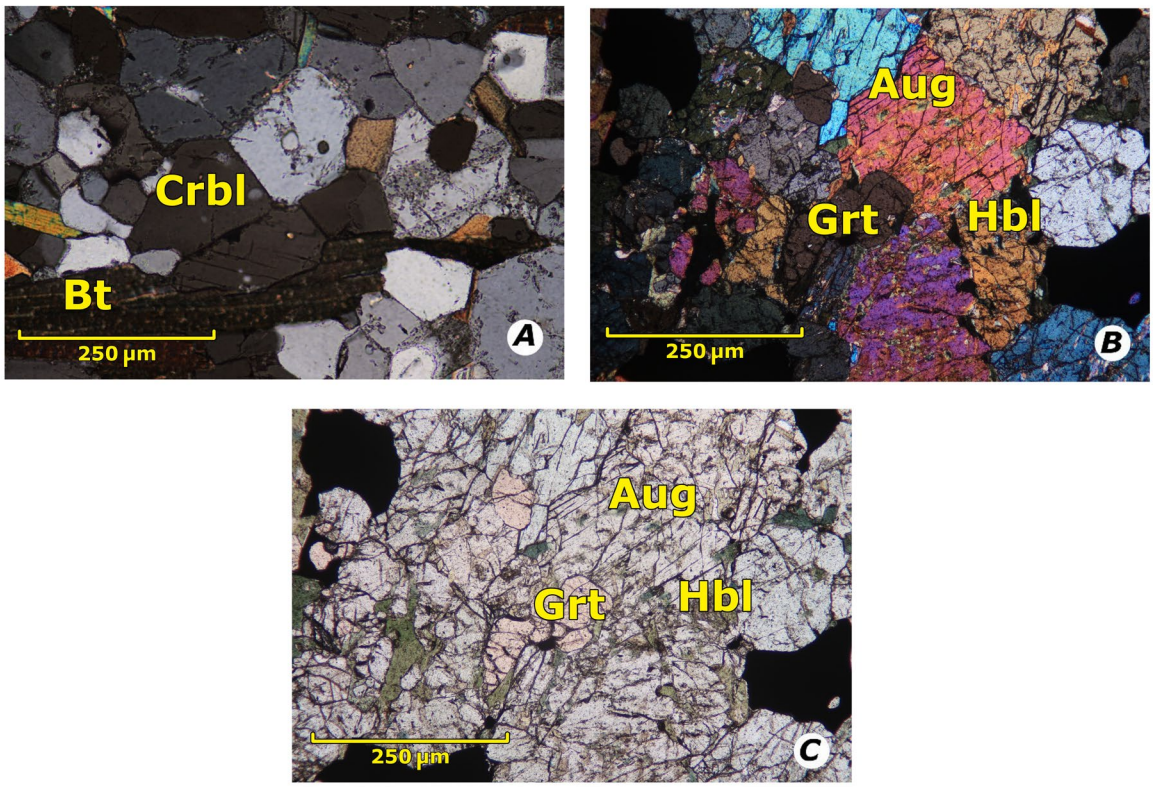

Figure 4.8: Migmatitic mineralogies in study area (A, XPL, PVS021) neosomes of amphibolite and granulite metatexite in ore zones contain Be–rich minerals including chrysoberyl (Crbl, dusty appearance, low–order birefringence with common penetration twins), along with alkali feldspars, quartz, biotite, tourmaline, and beryl, (B, XPL and C, PPL, PVS055) restites of amphibolite and granulite metatexite to diatexite are composed of Garnet–Clinopyroxene–Rutile ± Hornblende ± Orthopyroxene ± Pyrrhotite (and plagioclase–free) and neosomes are composed entirely of high–Ca plagioclase .

4.1.5 Matachewan mafic dykes

Mafic dykes attributed to the Matachewan mafic dyke swarm are present in the study area and have two populations of strikes: parallel to regional foliation and perpendicular to boudinage or extension. The dykes range from <1 m to >2 m in width within the study area at Borden Mine. Mafic dykes are diabase, dark blue to dark grey, aphanitic to fine–grained and have textures ranging from massive to subophitic to ophitic. Modally they are 50–75% pyroxene and 25–50% plagioclase. Secondary black to blue–green amphibole is located along baked margins. The shape of dykes ranges between straight boundaries to curved boundaries with instances of sinistral, faults displacing the dykes. They commonly occur perpendicular to boudinage. Many display counterclockwise rotation of about 10°–20° in relation to the rest of the Superior Province with Paleoproterozoic ages including U–Pb baddeleyite ages of 2459 ± 5 Ma (Fig. 2.1) (Heaman, 1997; Halls et al., 2005).

4.1.6 Ore geology

The ore zones of the Borden Mine are located in ductile to brittle–ductile shear zones with foliated, boudinaged, and migmatized upper amphibolite to granulite facies mafic to felsic schists and gneisses, including metavolcanic and BIF lithologies, and pegmatite in sinistral–oblique boudin necks and mullions with alkali feldspars, quartz, muscovite, biotite, tourmaline, garnet, sillimanite, beryl, and chrysoberyl (Figs. 4.9–4.12). The ore zones in the field and drill cores are identified by sillimanite–garnet–biotite schists and gneisses (+ leucosomes) and BIF along the contact between coarse–grained, garnet porphyroblastic hornblende (“footwall” amphibolite) and fine–grained amphibolite (“hangingwall” amphibolite) with tightly–spaced foliation (< 0.2 mm, defined by micas) and two lineations (defined by amphiboles, pyroxenes, and garnet) overprinting early gneissosity, defining rotated boudins and mullions (Figs. 4.9–4.11). In thin section, the economic gold mineralization is located in healed, folded fractures and cataclasites within overprinting schistose to mylonitic fabrics, sulphide melts, mineral inclusions, and along grain boundaries, subgrain boundaries, and deformation twins (Figs. 4.10–4.12, 4.44 A–C).

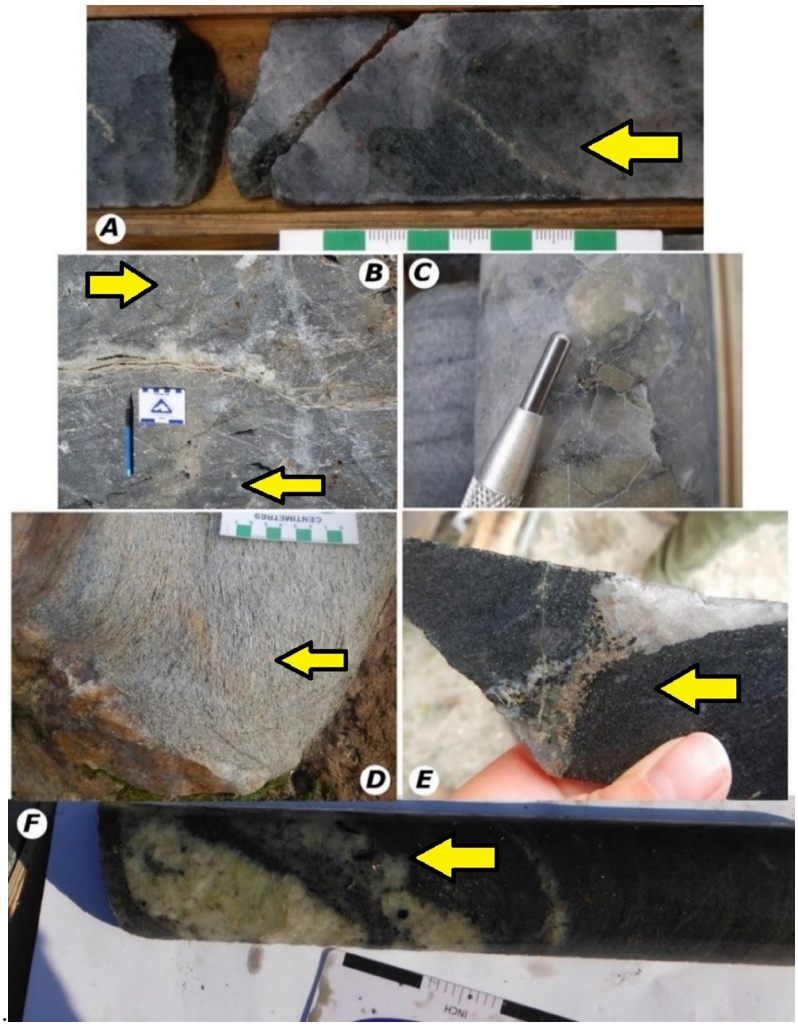

Figure 4.9: Mineralization styles in the Borden Mine (A) Mullions (arrow) and chocolate–tablet structures in oxide–facies banded iron formation in garnet–clinopyroxene amphibolite (metatexite migmatite) with pyrite, pyrrohite, and gold in gently folded fracture providing evidence for remobilization of gold from BIF to brittle–ductile (micro)fractures in sinistral, ductile shear zones, DDH# BL12–256 at 337.2 m, (B) Sinistral, strike–slip fault with horsetail splay (arrows) in barren amphibolite filled with epidote, clinozoicite, carbonate, and prehnite postdate gold mineralization (16N 5306514/0327567), (C) Coarse–grained anhedral pyrite mineral fish with pyrrhotite in boudin neck (arrow) ore zone mirror the Z–shape of the rotated ore body and demonstrate that pyrrhotite is after earlier pyrite (DDH# BL15–853–72, 313.04 m), (D) Obliquely eroded intermediate intrusive lithology (top to centre of photo) and rusty, quartz boudin neck (bottom of photo) display the control boudinage has on lineation, with subvertical to vertical blue–green amphibole (arrow) defining lineation adjacent to rigid boudins (Northeastern Discovery Trench), (E) Pyrrhotite, pyrite, magnetite, and gold in neck of quartz boudin (arrow) in an amphibolite and BIF ore zone, DDH# BL12–222, 322–323 m depth, (F) Visible gold (arrow) in albite–alkali feldspar leucosome of metatexite amphibolite demonstrating remobilization is at least partially controlled by high–grade deformation and metamorphism (DDH# BL13–479, 482.5–482.7 m).

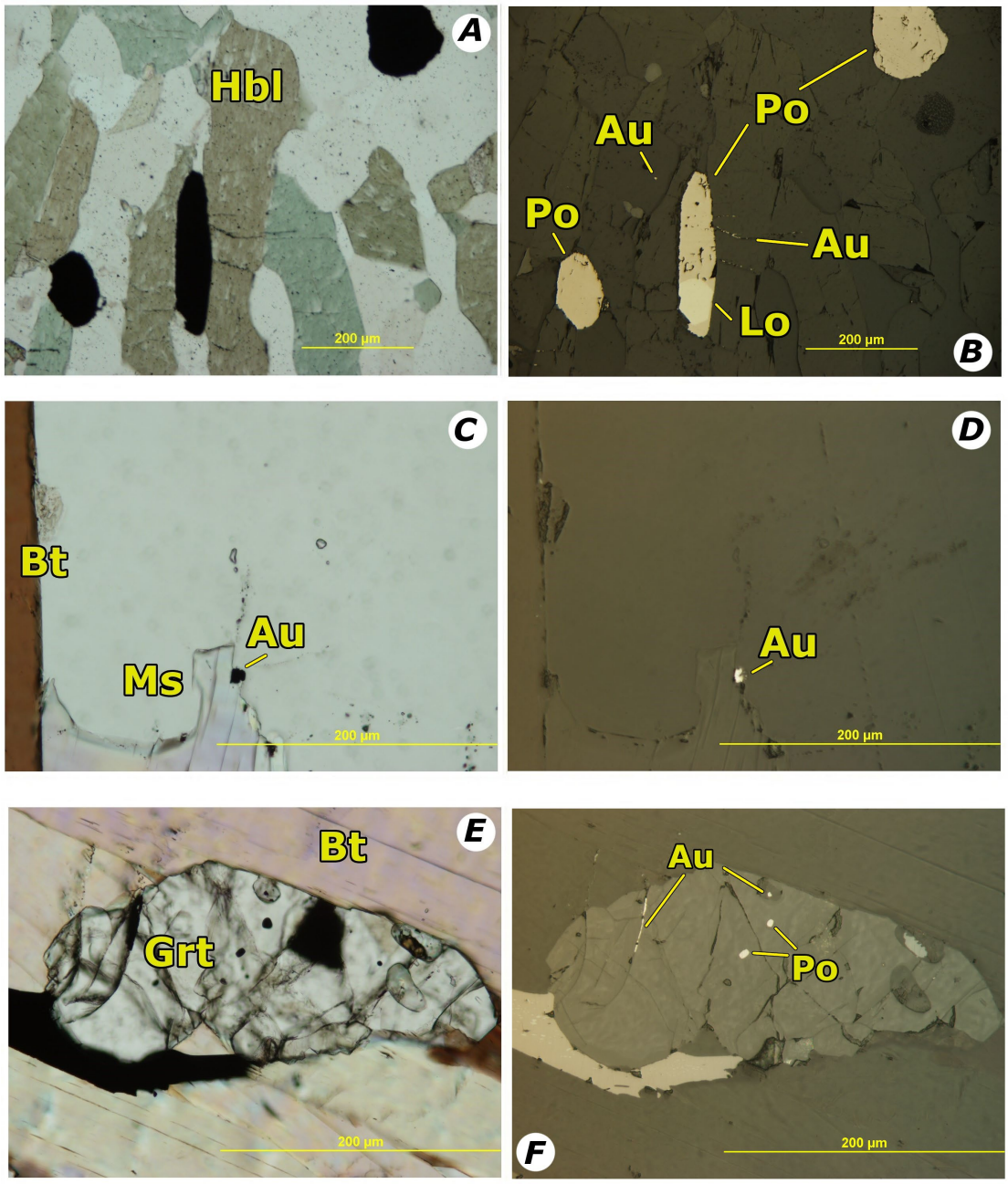
A
Hbl
200 µm
B
Au
Po
Po
Au
Lo
200 µm
C
Bt
Au
Ms
200 µm
D
Au
200 µm
E
Bt
Grt
200 µm
F
Au
Po
200 µm

1735

Figure 4.10: Photomicrographs of mineralization (A, Plane–polarized light (PPL) and B, Reflected–light (RL), PVS029). Brown–green hornblende and pyrrhotite define foliation and lineation in amphibolite with pyrite and gold inclusions in pyrrhotite and healed fractures in hornblende, demonstrating gold remobilization during high–grade metamorphism and deformation, (C, PPL and D, RL, PVS035) Gold touching muscovite and quartz in garnet–muscovite amphibolite ore zone demonstrating the relationship between remobilization of gold and retrograde amphibolite metamorphism, (E, PPL, and F, RL, PVS037) Garnet and biotite defining foliation with inclusions of pyrrhotite, sphalerite, and a healed fracture in garnet hosting gold, providing evidence for early ore mineralization and remobilization.

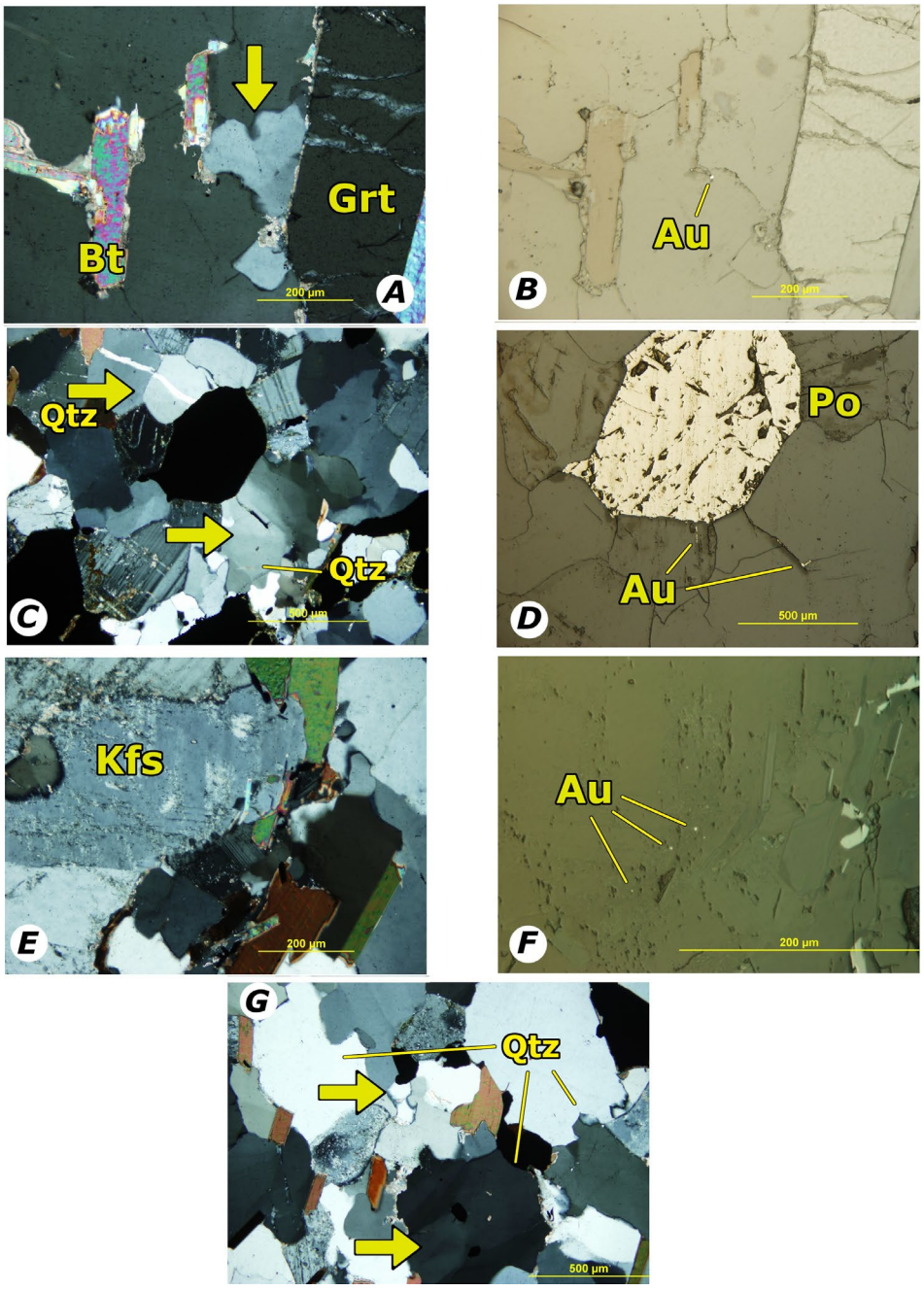

Figure 4.11: Photomicrographs of mineralization (A, XPL and B, RL, PVS035) Biotite and elongated garnet in recrystallized, polyhedral quartz vein with gold and carbonate along folded fracture adjacent quartz displaying evidence of grain bulging (arrow), thereby providing evidence for fracture and dislocation creep in quartz during gold remobilization ,(C, XPL and D, RL, PVS037) Gold along healed and folded micro–fractures (top and bottom arrows) and faults in plagioclase and quartz, displaying undulatory extinction and subgrains (bottom arrow), and radiating from anhedral pyrrhotite (bottom arrow) in amphibolite suggest brittle–ductile deformation during gold remobilization (perhaps after pyrite to pyrrhotite due to radial fractures present), (E, XPL, and F, RL, PVS037) Gold located along deformation twins in plagioclase, suggestive of gold remobilizing during temperatures at amphibolite facies temperature or higher, (G, XPL, PVS037) Quartz microstructures provide evidence of subgrains (top arrow), bulging (top arrow), and chessboard recrystallization (bottom arrow) in medium– to coarse–grained felsic plutonic lithologies which are diagnostic of dislocation creep during at least amphibolite to granulite facies temperatures.

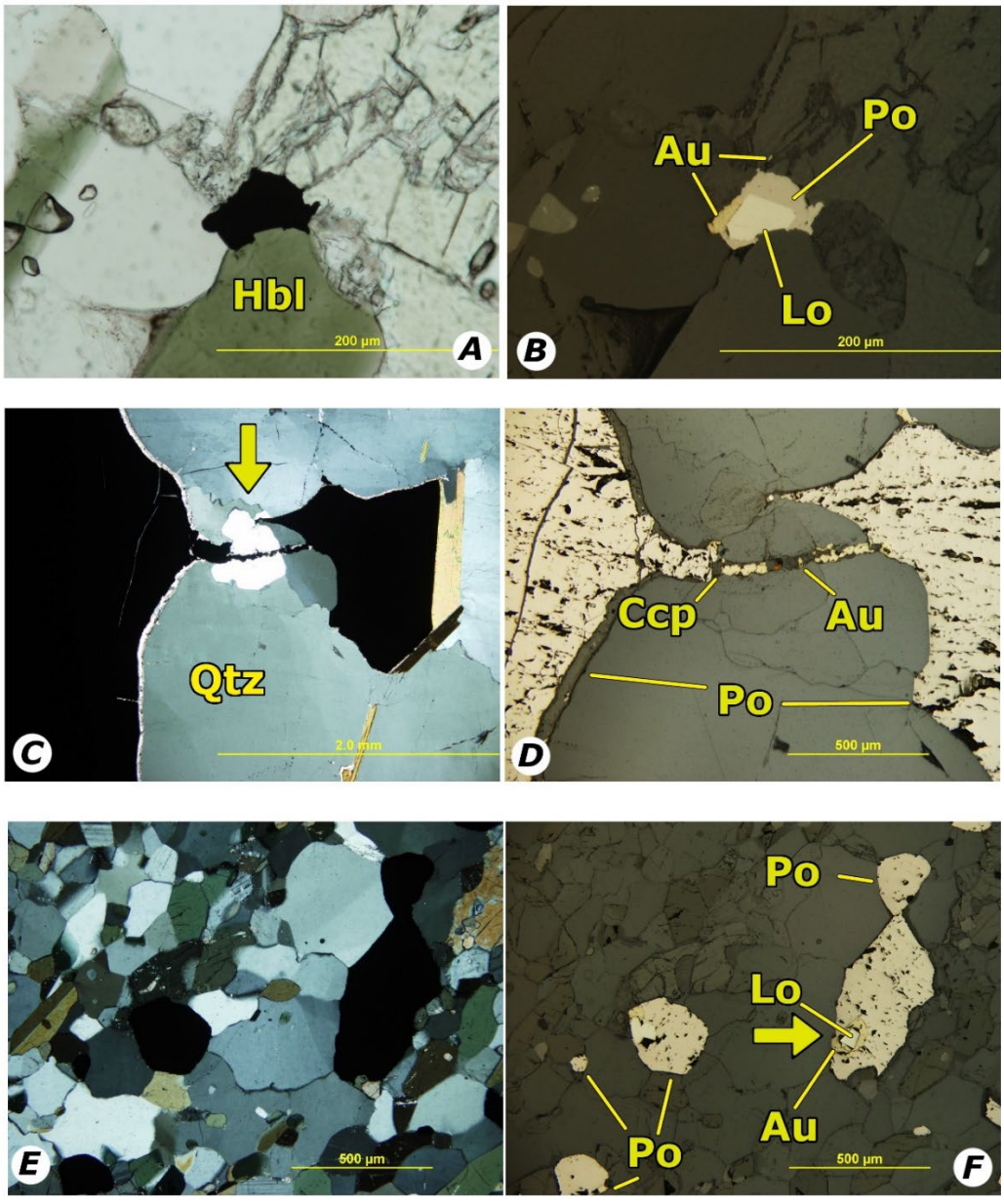

Figure 4.12: Mineralization styles in Borden Mine and study area (A, PPL and B, RL, PVS029) Amphibolite (metatexite migmatite) with sulphide melts between green–brown hornblende, clinopyroxene, and plagioclase with euhedral, daughter löllengite with partial anhedral gold and pyrrhotite corona, suggestive of both sulphide and silicate migmatization during metamorphism and subsequent remobilization of gold mineralization, (C, XPL and D, RL, PVS035) Boudinaged and fractured pyrrhotite with chalcopyrite and gold in boudin neck (arrow)within finer–grained quartz displaying irregular grain boundaries in coarse–grained, polyhedral, recrystallized quartz vein with carbonate at the pyrrhotite–quartz vein boundary which is indicative of boudinage reconcentrating the ore minerals at the Borden Mine, (E, XPL and F, RL, PVS029) Sulphide melts (arrow) with euhedral pyrite daughters and partial to complete coronas of anhedral gold and pyrrhotite within a quartz boudin of BIF in amphibolite (metatexite migmatite). The presence of sulphide melts (arrow) along the BIF–amphibolite boundary supports the hypothesis that gold remobilized from partial to complete melting of sulphides during metamorphism and deformation.

Outside of the ore zones these lithologies are barren except in sulphide–facies BIF within massive amphibolite and granulite, which locally contain subeconomic gold (100–200 ppb Au). The boudin necks and mullions also host economic to subeconomic gold mineralization in foliated, intermediate to felsic volcanic and pyroclastic lithologies, migmatized mafic intrusive and volcanic lithologies, and pegmatites throughout these lithologies. The metaconglomerate and metasandstones are structurally and stratigraphy above the subeconomic to economic ore–hosting lithologies and host no mineralization. The youngest, straight, megacrystic felsic pegmatites and mafic dykes crosscut all lithologies and host no gold mineralization.

Ore minerals include pyrite, pyrrhotite, löllengite, arsenopyrite, and magnetite with ilmenite, rutile, sphalerite, and chalcopyrite in economic, subeconomic, to barren ore zones. Additional studies are required to assess the economic potential of diamond (in lamprophyres) as well as chrysoberyl and beryl (in leucosome pegmatites). Primary ore mineralogy and textures are not preserved, however inclusions of pyrite, native gold, sphalerite, chalcopyrite, pyrrhotite, and scheelite are present in the higher–grade metamorphic minerals and healed fractures providing evidence of an earlier mineralization. For example, inclusions of pyrite, pyrrhotite, löllengite, magnetite, native gold, ilmenite, rutile, sphalerite, chalcopyrite, and scheelite have been identified in garnet, pyroxenes, and hornblende porphyroblasts. The ore mineralogy has been significantly affected by high–grade metamorphism as sulphide melt inclusions define foliation and lineation. Sulphide melts are anhedral with euhedral, daughter mineral(s) of pyrite ± arsenopyrite, ± löllengite surrounded by partial to complete coronas of native gold with defining foliation in quartz ± carbonate boudin necks (Figs. 4.10–4.12). High–grade ore zones have the highest modal percentage of coarse–grained, euhedral pyrite with pyrrhotite, löllengite, and gold coronas as well as gold in microscopic fractures within porphyroblastic and porphyroclastic minerals in schistose fabrics.

4.2 Field mapping and structural geology

4.2.1 Field mapping

The common structures in the field are displayed in Figures 4.13–4.18 and have been incorporated into the regional and trench maps. Regional maps include the lithological map (Fig. 4.19), regional structures presented in stereonets (Fig. 4.20), regional–scale structures in plan view (Fig. 4.21), regional–scale structures in cross–section (Fig. 4.22), regional–scale metamorphism and migmatization map (Fig. 4.23), local–scale map of the high–grade zone at Borden Mine (Fig. 4.24), regional–scale compilation map (Fig. 4.25), and locations of trenches (Fig. 4.26) in the Chapleau Belt and southern KSZ. The most detailed regional map is located in Appendix E.

Subprovince–scale boundaries and structures in the study area vary. There is no marked boundary between the southern Superior Province (including the Wawa subprovince) and the WGD although it is roughly defined by a diffuse decrease in brittle–ductile shear zones, increase in metamorphic grade, and increase in strike–slip and horizontal ductile shear zones, and overprinting felsic to intermediate plutonic and migmatitic lithologies near the longitude at the western extension of the Michipicoten (Mishibishu, Gamatigama) greenstone belt. The WGD and Chapleau Belt (of the southern KSZ) boundary is irregular with overprinting, assimilated plutonic lithologies with both sinistral strike–slip and horizontal shear zones. There is no marked boundary between the Chapleau Belt with the southern KSZ as the lithologies and structures are continuous, albeit higher temperature and pressure equivalents into to the KSZ. The boundary between the northern, central, and southern KSZ with the southern Superior Province (including the Abitibi subprovince) is sharply defined by brittle–ductile to ductile strike–slip shear zones and overprinting faults. Note the marked difference in types of boundaries between the diffuse, plutonic to assimilated migmatites, with horizontal shear zones in medium– to high–metamorphic grade lithologies between the southern Superior Province and WGD versus the sharp, moderately to steeply–dipping boundary between the high–metamorphic grade KSZ and lower–metamorphic grade southern Superior Province.

Regional structures in the study area include: (1) ductile shear zones ranging meters to kilometers in width, commonly mylonitic, steeply dipping northward (with fabrics of sinistral, sinistral–reverse and sinistral–normal kinematics), (2) subhorizontal to horizontal, ductile shear zones with the kinematic direction to the northeast (and transfer shear zones therein), and (3) upright– to moderately–plunging, tight “Z–folds” that define regional rotated boudins (and more localized “M”–folds), and an upright– to steeply–plunging, open orocline (Figs. 4.19–4.33, Appendix E). Similar shear zones and folds were identified in the WGD and KSZ from previous, detailed mapping by Bursnall (1990), Bursnall et al. (1994) and Moser (1994). The ductile shear zones, foliation boudins, boudins, and

antithetic shear bands are overprinted by brittle–ductile shear zones, faults, and pseudotachylites (Percival, 1981).

Similarly, the three populations of regional– to outcrop–scale ductile and brittle–ductile shear zones identified in the field and thin section include: (1) east–west to northeast–southwest striking, moderately– to steeply–dipping northward, sinistral strike–slip to oblique ductile shear zones (sinistral–reverse and dextral–reverse), (2) ductile to brittle–ductile shear zones, northeast–southwest striking, gently– to steeply–dipping north (in folds there is variability), and (3) ductile, subhorizontal to horizontal, top to the northeast, shear zones (connected to ductile, sinistral strike–slip to oblique (sinistral–normal or extensional, listric, and transfer) shear zones). The strike–slip shear zones are upwards of 100s of kilometers in length and kilometers in width to the microscopic scale, while the ductile, horizontal and sinistral–normal and brittle–ductile, steeply dipping, dextral–reverse shear zones are at least meters to 10s of meters in length and width to the microscopic scale. The three populations of shear zones occur together and the subhorizontal to horizontal, sinistral–normal or extensional shear zones, with mylontitic to gneissic fabrics can be referred to as detachment zones that are connected by transverse, sinistral–reverse strike–slip ductile to brittle–ductile shear zones, and have accommodated transfer motion between the areas of detachment. Dextral shear zones are local to regional antithetic shear bands in the fold axes in the rotated boudins that define "M– and Z–folds" (Figs. 4.25, 4.27, 4.29).

The northern and southern boundaries of the Chapleau Belt with the WGD are defined by ductile, sinistral shear zones and the boundaries define a large–scale sigmoidal (or "Z–shape") in plan view, which is repeated on smaller scales (Fig. 4.25). The north, central, and southeastern portions of the regional map denoted by metaconglomerate (yellow) define a regional sigmoidal "Z–shape" (and local "M–shapes), in plan view which we will be further defined in the trench maps below. Sinistral and counterclockwise rotation is evident in numerous types of boudins and small–scale folds. A regional–scale boudin neck in ductile, near vertical shear zones, is present above Borden Lake (Figs. 4.21, 4.24). This regional boudin neck is mineralized with >15% muscovite (modal percentage) and is also the location for the high–grade ore zone of Borden Mine. Mineral and clast lineations range between horizontal, shallow, moderate, to vertical. Generally, the highest strain in shear zones also have shallow lineations, moderate strain has moderate lineations, and in areas of local boudinage on the meter to 100s of meter scale the lineation is vertical and defined by retrograde, lower–amphibolite facies metamorphic minerals (Fig. 4.9 D). Perpendicular to oblique to foliation, schistosity, gneissosity and all metamorphic fabrics are early quartz veins, late boudins, very late pegmatite dykes, and the southern KSZ are presented in their own stereonets in Figs. 4.31–4.33. Foliation and gneissosity define a regional orocline that extends from the eastern Chapleau Belt into the eastern KSZ, parallel to the ILDZ. The orocline is

defined by moderate to vertical to periclinal striking fabrics, commonly plunging to the west to northwest, including schistosity, gneissosity, and lineations in amphibolite, granulite, gneisses, and migmatites. Internal to the orocline are the belt–scale to regional–scale "Z–, S–, and M–folds" with variable boudinage. The CCW rotation in the WGD and adjacent western KSZ may also have controlled the oroclinal nature of the eastern KSZ. Both perpendicular and parallel to metamorphic fabrics are the Matachewan mafic dykes. These mafic dykes have also experienced brittle–ductile deformation along dextral shear zones and faults.

The regional and trench mapping conducted for this study has produced significant map changes since the earlier mapping studies and most importantly the early ductile sinistral strike–slip shear zones, rotated boudins, foliation boudins, and antithetic dextral brittle–ductile shear zones that predate the ILDZ (Percival, 1981; Bursnall, 1990b; Moser, 1994; Bursnall et al., 1994). The Chapleau Belt is now extended linearly and extends further west than the town of Chapleau, Ontario as the belt is present, albeit assimilated in the granitic WGD. Metaconglomerate, coarse–grained ultramafic to mafic intrusive, and mafic to felsic metavolcanic and volcaniclastic lithologies can be continuously mapped through the eastern Chapleau Belt to the southern extent of the KSZ (Fig. 4.19). Similar lithologies are also identified in the eastern WGD, east of the town of Wawa, Ontario.

Additional lithologies recognized in the study area include: oxide– and sulphide–facies BIF, graphitic schist, sillimanite–garnet–biotite schists and gneisses, mafic and felsic metavolcanic and volcaniclastic breccia, lapilli, and tuff, migmatites including ultramafic pyroxenites or restites, complex pegmatites, and calc–alkaline lamprophyres. The WGD extends into the Chapleau Belt which itself extends into the southern and central KSZ, however with increasing metamorphic grade and partial melting. New isograds, isograd–outs, and migmatite types are provided in the regional maps (Fig. 4.23). Note the increase in metamorphic grade from the WGD and Chapleau Belt into the KSZ as well as the increase in higher–temperature and higher–strain migmatitic textures. Indeed, the least strained migmatites with the lowest amount of partial melting is present in the eastern WGD at the transition into the Chapleau Belt and the greatest is in the transition from the eastern Chapleau Belt to the KSZ. Diatexites are pervasive throughout the southern KSZ (Fig. 4.23). Previous mapping identified numerous folds with complex lineations in the region and interpreted them to be a regional syncline, however this study has identified these folds to be related to regional boudin necks and regional to local "Z–folds" (and more localized "M" folds) and not a single syncline (Moser, 1994) (Figs. 4.21–4.25). Additionally, the moderate– to steeply–dipping foliation in the western Chapleau Belt and southeastern KSZ define an orocline and the horizontal–, gently–, and shallowly–dipping foliation define an extensional shear zone (Figs. 1.3–1.5, 2.2, 4.30–4.31).

The general strike and dip of schistosity, gneissosity, and mylonites are presented in equal area stereonets with arrows to the general areas these measurements were taken. The change in strike from predominantly east–west to northeast–southwest and northwest–southeast is evident from west to east and continues into the eastern KSZ and defines a regional fold (Fig. 4.30–4.33). As dip is moderate to vertical there is a significant range between north– and south–dipping metamorphic fabrics. The anastomosing nature of the shear zones is also evident in the stereonets as they display a range of strike and dips around a similar average.

The metasedimentary lithologies are interpreted to have deposited in basins that formed during regional, sinistral–oblique shear zones or faults and subsequently deformed. Due to the access to drill cores for logging this study also proposes significant reverse–sense shear zones in the study area as stratigraphy could be assessed. Sinistral–reverse ductile to brittle–ductile shear zones in felsic, intrusive lithologies with quartz defining subvertical to vertical lineations have exposed these instances of repeating stratigraphy (Fig. 4.22). Note the regional, ductile to brittle–ductile, sinistral strike–slip shear zones at the boundaries of the WGD and the Chapleau Belt affect the interior of the Belt, however they are most pronounced at the boundaries. The more local, dextral, oblique–reverse shear zones are located in the felsic, plutonic lithologies, particularly in areas of greatest rotation. The younging directions in the metaconglomerate and metasedimentary lithologies are truly limited as significant metamorphic fabric overprints these features. Younging direction in the mafic to felsic metavolcanics and volcaniclastic lithologies has been better preserved than the metasedimentary lithologies, however there is still some ambiguity in these features. The lack of migmatization in the metaconglomerates and the difference in younging direction compared to the mafic and felsic lithologies suggest the metaconglomerate lithologies are younger than the other lithologies and were deposited in a different setting. Younging to the north in the metaconglomerate and metasedimentary lithologies is consistent with reverse–sense structures hosting these lithologies, however is not a unique solution. On the regional scale the size of clasts in the metaconglomerate and metasedimentary lithologies generally increases to the north (Atkinson, 2013) which this study supports. Additionally, the general thickness of lithologies, without taking in account volume change, generally decreases to the north.

Boudinage on the microscopic– to meter–scale is documented in sinistral–reverse strike slip shear zones and on the 10s to 100s of meter scale in extensional shear zones (Figs. 4.6 B–D; 4.21, 4.25). Regional– to local–scale shear zones and boudins and rotated boudins control the variability in strike, dip, and thickness of the lithologies in the study area as areas of highest–strain are tightly–spaced and have reduced lithological thickness and areas of sinistral, counterclockwise rotation and boudinage are thickest. Volume loss and gain has been inferred but not mathematically studied.

Many types of boudins on all scales have been identified in the study area and boudin block geometry includes shearband, drawn, and torn boudins with object, single–layer, and foliation boudinage to describe the material layeredness, and foliation–parallel and foliation–oblique boudin trains (Figs. 4.2, 4.9 D–E, 4.11 C–D, 4.12 D–F, 4.13 F; 4.14 A, B, E, G, H, 4.15 A–E, 4.16 B–E, 4.17, and 4.18) (Goscombe et al., 2004). Qualitative, comparative competency contrasts were determined based on the boudin types in each lithology. The medium– to coarse–grained ultramafic and mafic lithologies have predominantly fish–mouth torn boudins they required the greatest amount of vein infill with limited host inflow and therefore had the greatest potential for competency contrasts and remobilization of vein and fluid materials (Goscombe et al., 2004). The mafic and felsic metavolcanic and banded iron formation lithologies have domino, straight–faced boudins that are termed blocky boudins with host inflow and vein infill (Goscombe et al., 2004). Felsic, coarse–grained and pegmatite dyke boudins range between blocky and tapering boudins which are predominantly host inflow only and limited vein infill (Goscombe et al., 2004). Sigmoidal–gash boudins and dilatational domino boudins are present in areas of schistose fabrics and flattened fabrics and may also supply limited vein filled and host inflow (Goscombe et al., 2004). Therefore, based on boudin morphologies the most competent boudins are as follows: medium– to coarse–grained ultramafic to mafic lithologies > mafic and felsic metavolcanics and banded iron formation lithologies > coarse–grained to pegmatitic pegmatites > schistose and flattened lithologies. Brittle–ductile, sinistral–dextral shear zones are also overprint boudin necks and foliation boudins with northeast–southwest long axes, as antithetic shear bands and have accommodated the predominantly asymmetrical, sinistral or CCW (minor CW) rotation. Rotated boudins define the regional "Z–shape" folds.

Evidence of vorticity is also identified in the schistose, flattened, and boudinaged lithologies. Vorticity has been measured in the field on rigid–body rotation of minerals, clasts, boudins, and semi–rigid–body rotation of foliation boudins in the ductile to brittle–ductile shear zones. Areas of greatest flattening in schistose fabrics have the greatest components of measured vorticity, typically 15º–30º counterclockwise or clockwise. Areas of plane strain have measured vorticity between 10º–15º counterclockwise or clockwise. Measurements <5º may not have been identified in the field and further work is necessary to mathematically assess vorticity. The areas of greatest counterclockwise–rotation also correspond to the presence of muscovite after alkali feldspar as muscovite defines the schistosity in these areas. The areas of greatest counterclockwise (CCW) vorticity are located in the local to regional, northern limb of the "M– and Z–shape" boudin–controlled folds while the areas of greatest clockwise vorticity are located in dextral shear zones in areas of greatest compression, the southern fold limb, in the regional "M– and Z–shape" folds. These folds mapped by Bursnall (1990), Moser (1994), and the

author are a result of the sinistral strike–slip shear zones and rotational boundinage along the WGD–Chapleau Belt and Chapleau Belt–KSZ boundaries and many are overprinted by the ILDZ. The structures bounding the Chapleau Belt and KSZ are predominantly sinistral, with minor dextral components, and define the proposed KSZ orocline. The upright to vertical folds in the mafic dykes, which formed synchronously during amphibolite retrograde metamorphism, mirror the internal, rotated folds in the Chapleau Belt and KSZ.

The relationship between structure, metamorphism, and migmatization is complex is described below. As evidenced by high–temperature and pressure mineralogy, plane strain occurred during early, prograde upper amphibolite to granulite facies during reverse–sinistral strike–slip deformation, including those with muscovite–out reactions in felsic, pelitic lithologies, including Mus + Qtz = Kfs + Sil (var. prismatic) + H_2O (Fig. 4.23). Muscovite–out reactions may also be noted geochemically and mineralogically with the abundance Be and Be–minerals in silicate, migmatitic leucosomes without muscovite (Fig. 4.8 A). The presence of abundant Be and Be–minerals are important indicators for felsic, pelitic lithologies that underwent partial melting during migmatization and plane strain. Accompanying the silicate partial melts, partial melting of sulphides is also documented in amphibolite to granulite facies lithologies. Coronas of magnetic, pyrrhotite around pyrite, gold, and löllengite are present in mineralized samples, providing evidence of partial melting during high–grade metamorphism (Figs. 4.10 A–B, 4.12 A, B, E, F) (Tompkins et al., 2007). Inclusions of gold and other sulphides are also hosted within high–grade metamorphic minerals, including garnet and pyroxenes.

However, areas that were most affected by retrograde amphibolite facies metamorphism, particularly in brittle–ductile shear zones with mylonitic fabrics, experienced greater flattening strain in areas with well–developed, tightly spaced (< 0.2 mm) M–domains defined by muscovite after feldspars and fibrolite after prismatic sillimanite (Figs. 4.45 B, C). The metamorphic mineral assemblages in the tightly–spaced schistosity and mylonites are consistent with retrograde amphibolite facies reactions including Sil (var. fibrolite) + Mus + Grt + Fluid formed at the expense of lower granulite facies mineral assemblages (i.e. Sil (var. prismatic) + Alkali feldspars + Grt). Flattening and the formation of a more schistose fabric due to the presence of white mica increased the rheological differences in the lithologies and enhanced boudinage and counterclockwise rotation. In boudin necks intrusions of pegmatites and leucosomes were emplaced and supplied additional fluid into the retrograde metamorphic system with the introduction of additional white mica, biotite, and tourmaline. Zones of greatest vorticity also have the greatest volume of migmatization, felsic intrusions, Be– and Be–minerals, tourmaline, and gold mineralization. In areas of highest strain within retrograde amphibolite facies mineralogy are porphyroblasts of pyrite, arsenopyrite, and magnetite not in equilibrium with sulphide melts. Inclusions

of gold and sulphides are present in retrograde minerals, including amphiboles and white micas, supporting remobilization of gold mineralization.

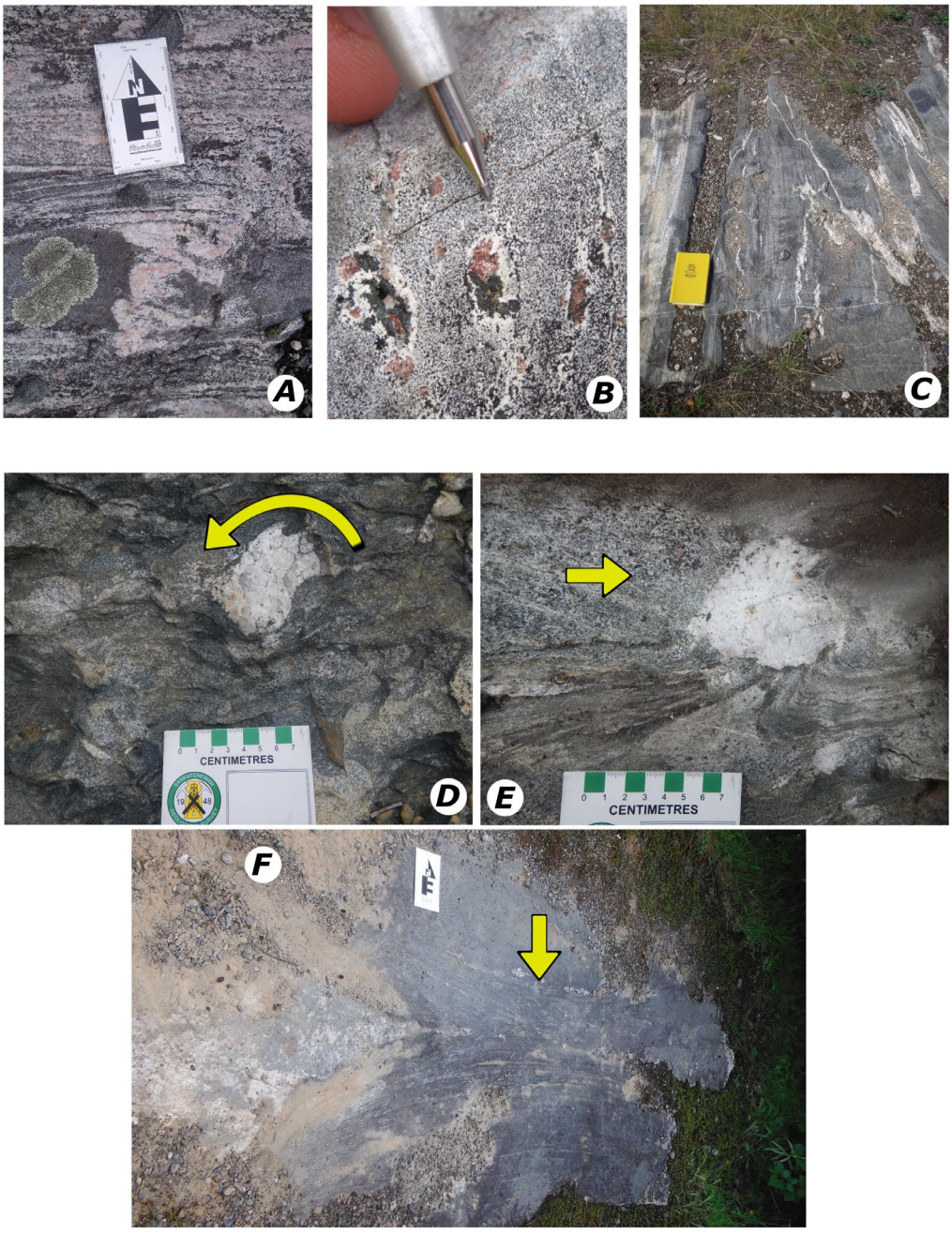

Figure 4.13: Common structural features in the Chapleau Belt (A) Flattened pegmatitic leucosome in boudinaged amphibolite at the boundary with the Wawa Gneiss suggestive of flattening (16N 530463/0325189), (B) Areas of lowest strain near the Cpx isograd display plagioclase coronas which are present in patchy metatexite migmatites throughout the central Chapleau Belt (16N 5306733/0327877), (C) Isoclinal folds in net–textured metatexite amphibolite nearing the Cpx isograd and corresponds to the orocline in the southern Chapleau Belt and Kapuskasing Structural Zone (16N 5297955/0321041), (D) Quartz foliation boudinage in metaconglomerate defining typical ~15ºCCW rotation (arrow) (16N 5305250/0330179), (E) Quartz boudin neck and foliation boudinage (arrow) displaying evidence of asymmetric, higher strain in western boudin boundary forming "Z–shape" in foliation and is consistent with a similar vorticity to D (16N 5305158/0330420), (F) 2–m–wide spacing between boudin necks (arrow) in pegmatite dykes (with mullions therein) in amphibolite with the boudin necks defining open folds which is typical within the Cpx–In isograd (16 N 5302768/0339747).

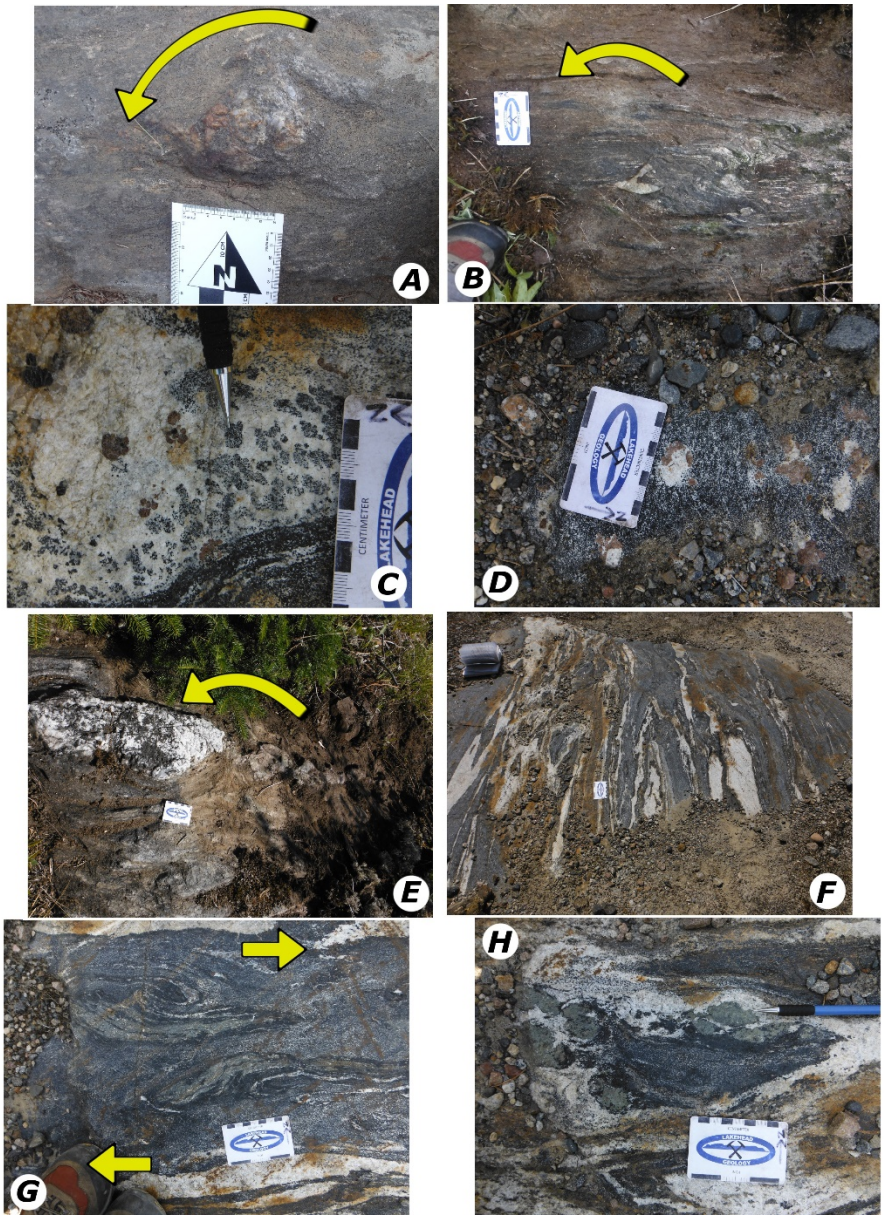

Figure 4.14: Common structural features in the Chapleau Belt (A) Quartz foliation boudinage in amphibolite rotated CCW defining sigma–shaped kinematic indicator (arrow), (16N 5302336/0331634), (B) Metatexite amphibolite with domino foliation boudinage rotated into "Z–shape" (arrow), mirroring the regional Z–shape boudin–controlled fold (16N 5302662/0340607), (C) Leucosomes in the Cpx isograd exhibit Hbl–out reactions with Grt stable and define the transition from metatexite–only to the appearance of diatexite migmatites (16N 5302672/0340129), (D) In areas of lower strain, patchy migmatites have formed with large Gt formed in the leucosomes (16N 5302645/0340260), (E) Pegmatitic dyke in amphibolite defining asymmetrical, shear–bound boudin train that defines CCW rotation (arrow) (16N 5302676/0341224), (F) Isoclinal folds in amphibolite well into the Cpx isograd and "Hbl–out" in leucosomes (16N 5302468/0341749), (G) Sinistral, ductile, near vertical strike–slip shear zone (arrows) in shearband foliation boudin in amphibolite (with retrograde green–blue amphibole) demonstrating that sinistral, strike–slip shear zones and boudinage continued into retrograde amphibolite facies during exhumation (16N 5302457/0341408), (H) Lecosomes in the blue–green amphibole pseudo–isograd have porphyroblastic blue–green amphibole that overprints black Hbl (16N 5302468/0341749).

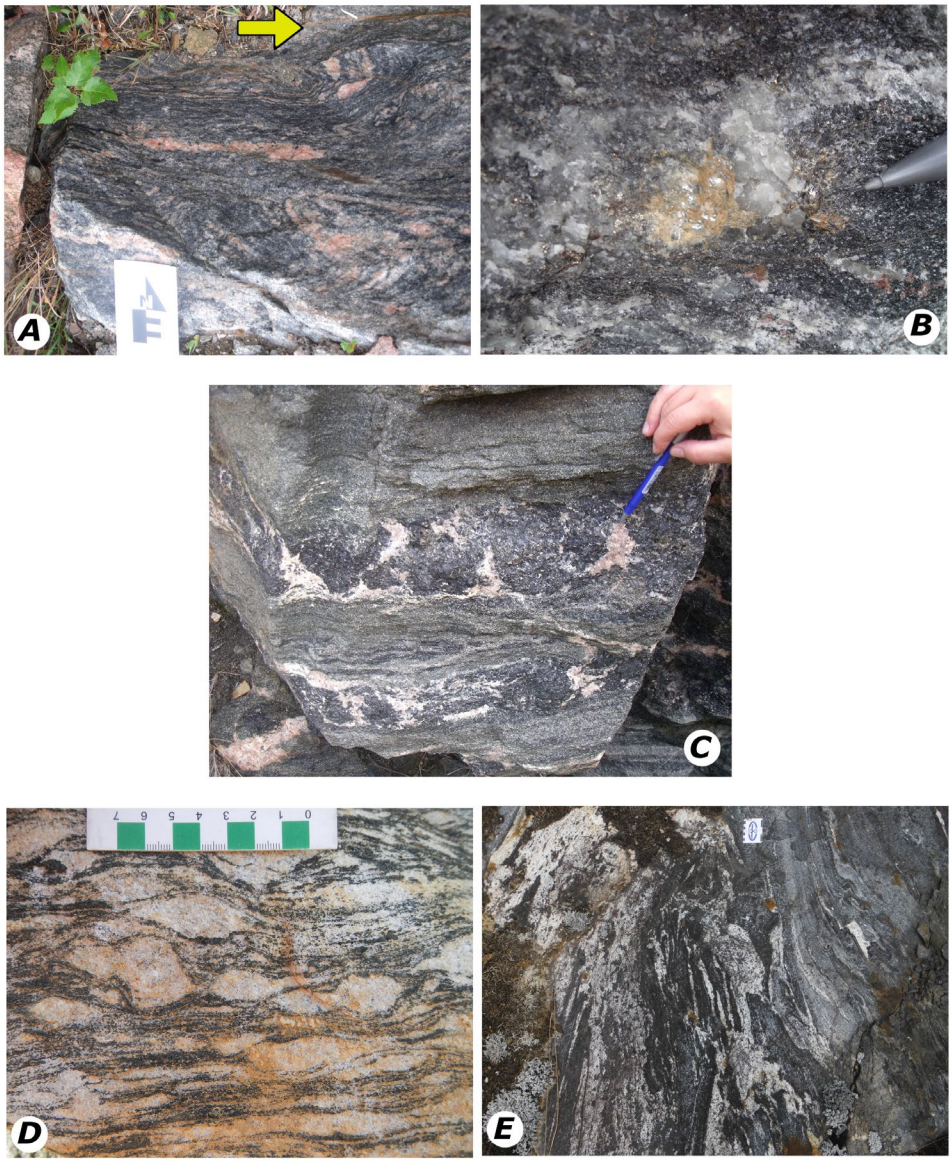

Figure 4.15: Common structural features in the KSZ and Shawmere anorthosite (A) Horizontal, mylonitic and gneissic shear zone typical in green–blue amphibole isograd, this one defining reverse sense kinematics (top–to–the–right movement) which is consistent with the regional, horizontal shear zones in the study area (arrow) (16N 5302010/0332679), (B) Quartz and muscovite in Cpx–Grt restite boudin necks, suggestive that metasomatism occurred during retrograde metamorphism in all types of high–grade migmatites (16N 5303109/0326195), (C) Alkali feldspar in Cpx restite boudin necks between subhorizontal shear zones demonstrate that restite–rich zones of migmatites are more likely to boudinage while leucosome–rich zones are more likely to deform along subhorizontal shear zones during retrograde metamorphism (16N 5298015/0321030 and 5310163/0340518), (D) Plagioclase (An % >70) in Shawmere leucogabbro and anorthosite as flattened and elongated, sinistral kinematic indictors provide evidence that the anorthosite underwent ductile deformation similar to the rest of the KSZ (16N 5332243/0374509), (E) Cpx restites and plagioclase leucosomes in metatexite amphibolite near the Opx–In isograd have greater zones of diatexites (16N 5302590/0342582).

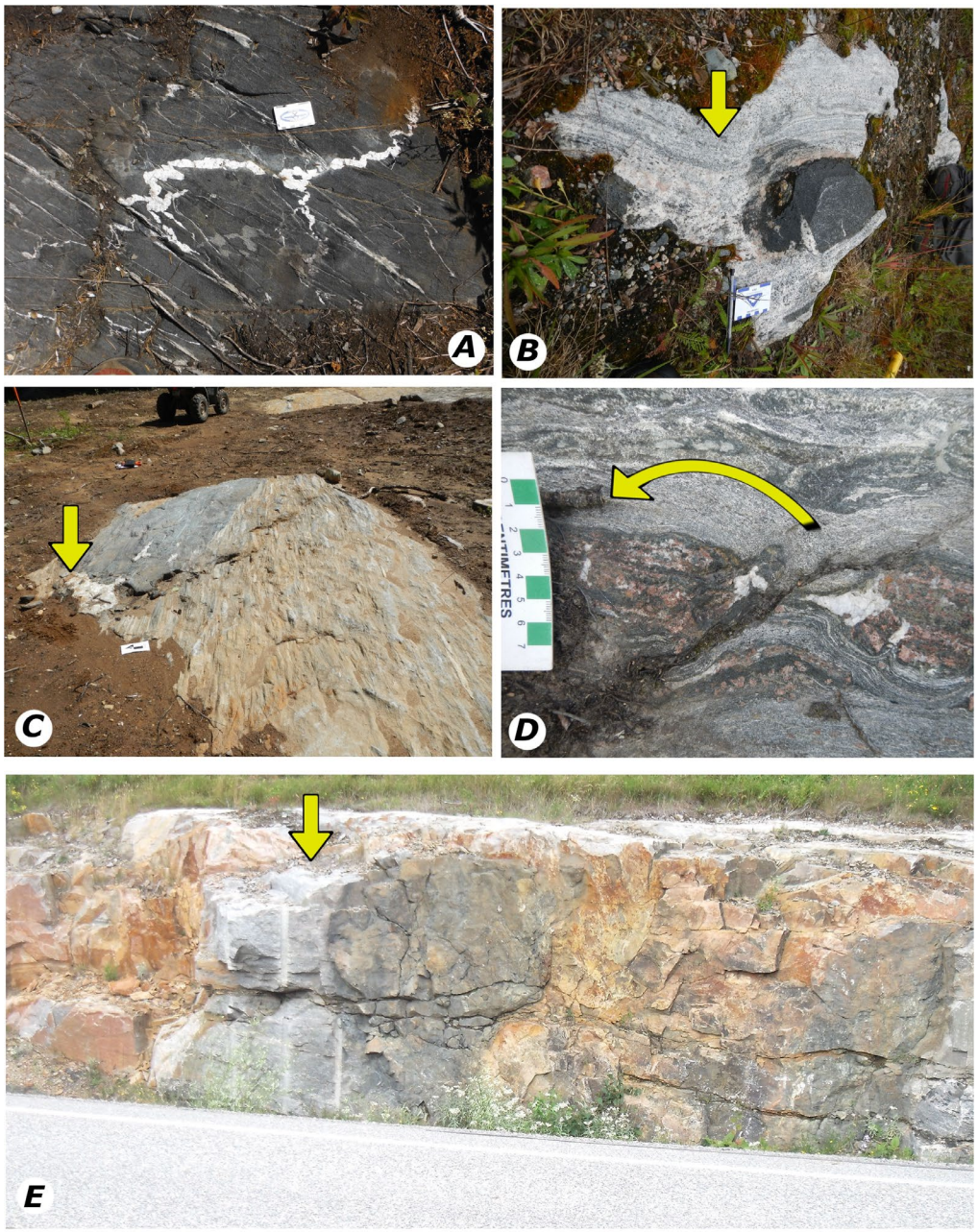

Figure 4.16: Common structural features in the Chapleau Belt and KSZ (A) Isoclinal folds of leucosomes and quartz veins in prograde amphibolite (16N 5306478/0328477), (B) Boudinaged east–west amphibolite restite has north–south crosscutting granitic dyke (arrow)(16N 5302082/0325338) (C) Looking north, amphibolite in metaconglomerate boudinaged northwest–southeast in regional "Z–shape" (arrow), CCW or dextral fold (Metaconglomerate Trench B), (D) Deformed quartz boudin necks (arrow) in garnet–rich amphibolites defining a very limited "Z–shape", CCW or dextral fold involving sinistral extension (Boudin Outcrop, 16N 5304869/0329109), (E) Amphibolite, concave boudin with >2 m–wide boudin necks (arrow) and 15–18 m–long amphibolite boudin train over 100s of metres (visible from Highway 101 from 16N 5307348/0327392 to 5298294/0321138).

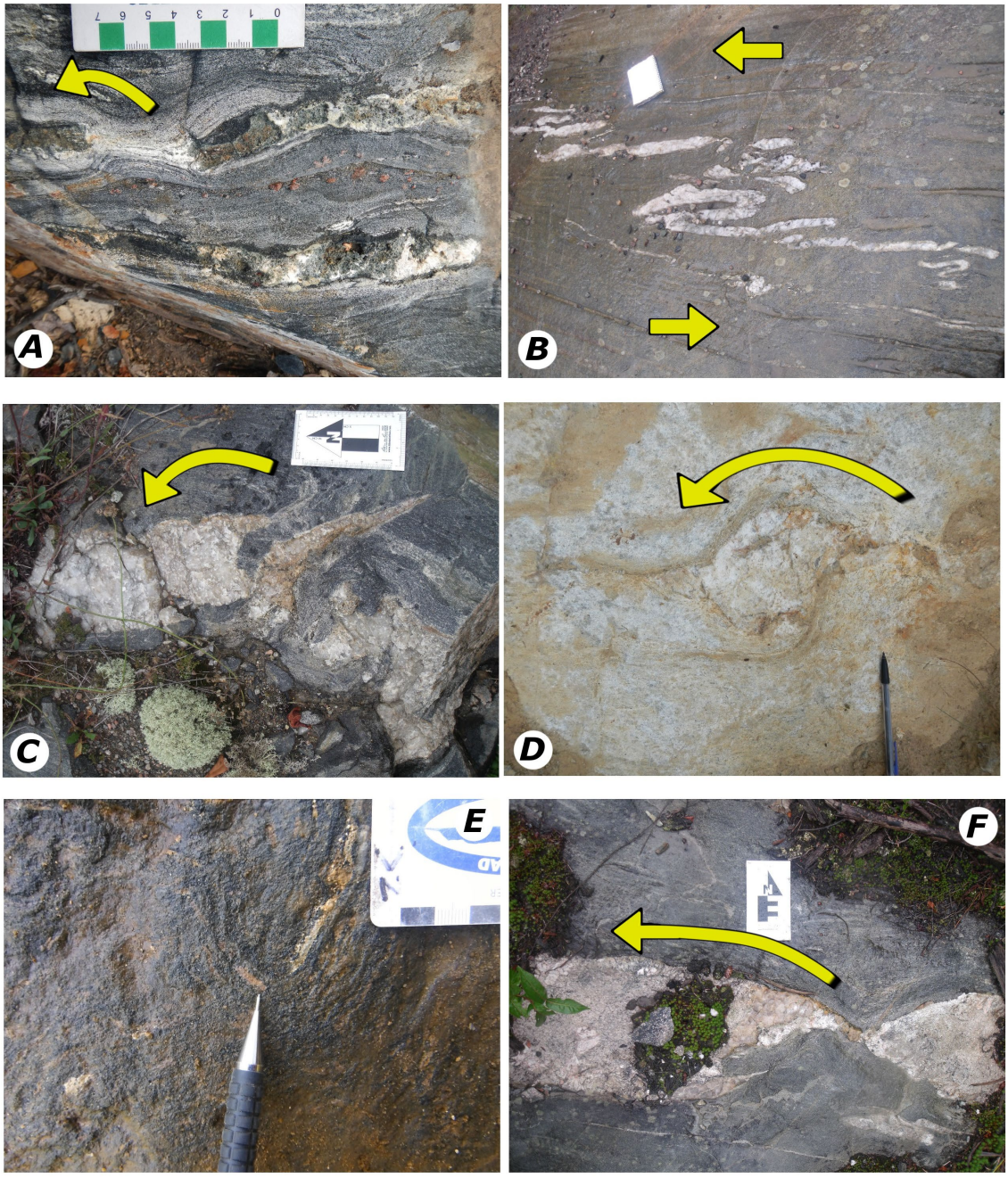

Figure 4.17: Common structural features in the Chapleau Belt (A) Cpx–Grt boudins in amphibolite defining sinistral boudinage and CCW rotation (arrow) with plagioclase–rich leuscomes filling the boudin necks, (Boudin Outcrop, 16N 5304869/0329109), (B) "Z–shape" fold (arrows) in quartz–rich BIF in amphibolite (16N 5302713/0328057), (C) Coarse–grained felsic dyke defining CCW rotation (arrows)(16N 5302751/0328311), (D) Quartz foliation boudin (arrow) in muscovite–quartz pegmatite defining CCW rotation (Large Pegmatite F and area), (E) Elongated Grt defining foliation boudinage in amphibolite, demonstrating that garnet continued to deform during retrograde metamorphism (16 N 5302772/0337424), (F) Pegmatite dyke in amphibolite defining dilatational domino, sinistral–boudinage and CW rotation (arrow) which is expected in some of the region to accommodate the regional "Z–fold" (16N 5302600/0328143).

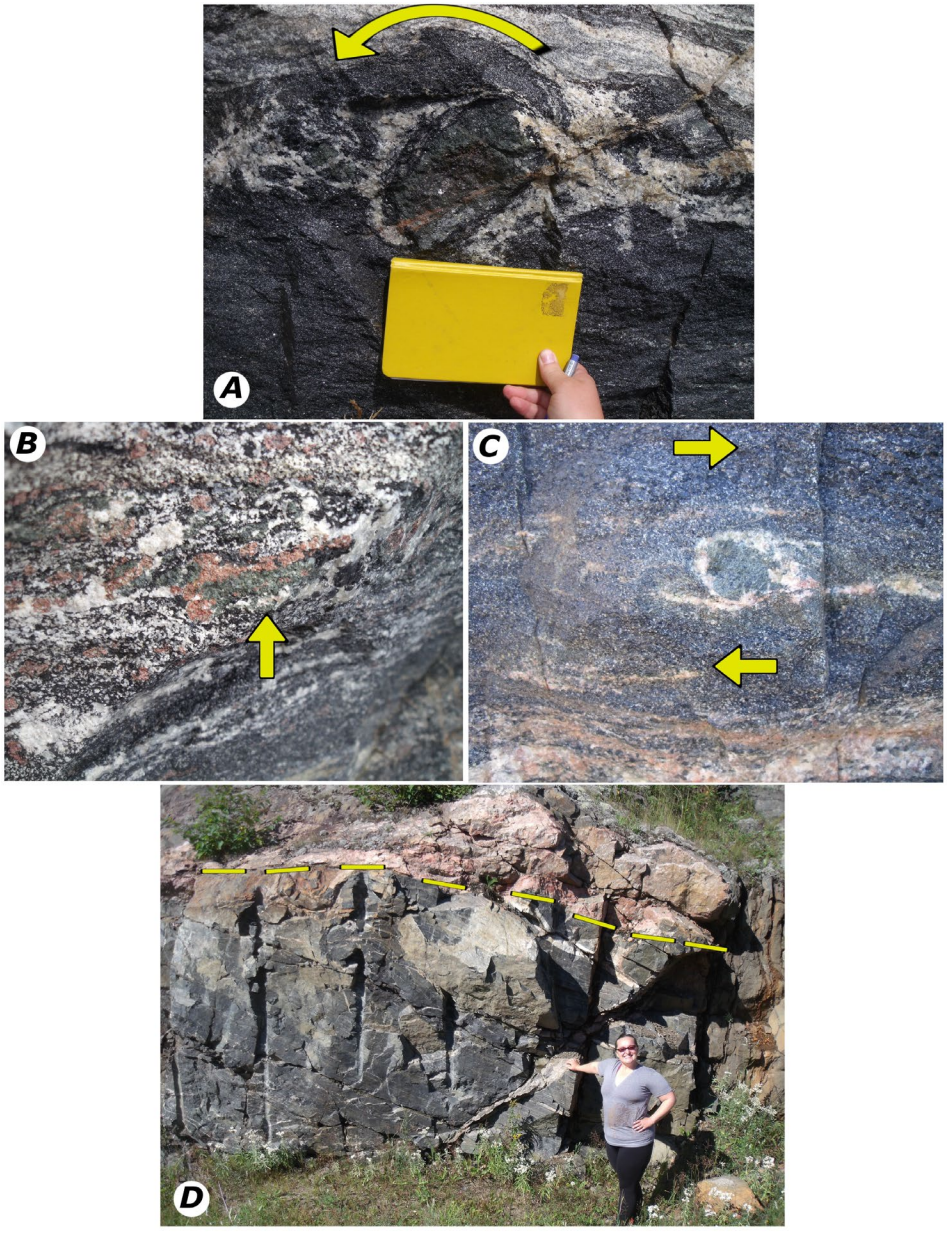

Figure 4.18: Common structural features in the KSZ (A) Cpx restite with Hbl rim in horizontal, shear zone in leucosome–rich boudins necks in amphibolite, rotated ~45º towards vertical (arrow), which demonstrates the rigid body rotation of the restites in the region while the leucosome–rich zones accommodate mainly planar, subhorizontal strain in the form of shear zones (16N 5310098/0340404), (B) Elongated Cpx + Grt in horizontal, ductile shear zone (arrow), suggestive of the garnet and clinopyroxene continuing to deform in the crystal plastic regime during retrograde metamorphism (16N 5297159/0321303), (C) Horizontal shear zone defining planar, subhorizontal strain (top–to–the–right movement, arrow) in Cpx restite in alkali feldspar leucsome, demonstrating the rigid restites (centre) will deformed differently than the leucosome–rich zones (below) (17 5304361/0327571), (D) Tapering, symmetrical boudin of amphibolite and granulite with localized, extensional, subhorizontal shear zone in pegmatite (top, arrow) anastomoses around the more rigid amphibolite, granulite, and restite lithologies providing evidence that the rigid boudins rotate after formation during retrograde metamorphism while the less rigid leucosome–rich lithologies form horizontal shear zones along the top and bottom of boudins (16N 5298014/0321029 to 5297988/0321035 and 5310163/0340518, Highway 101).

The tectonic history presented in this thesis takes into account the previous studies as well as the new field mapping presented in this chapter. The subprovince– to regional–scale strike–slip sinistral structures previously defined by previous workers are the most prominent structures in this study area. The strike–slip dextral structures were present and documented (including the ILDZ), however they are predominantly brittle–ductile to brittle features and more localized, particularly in the Chapleau Belt. The rotation previously proposed by other authors in the southern Superior Province has been documented in this thesis and supports earlier work.

Based on the literature review and new field mapping, the extensional shear zones are ductile and subhorizontal to horizontal and are predominant in the WGD and KSZ, particularly the western axes of the KSZ orocline, and are defined by prograde metamorphic mineral assemblages. The extensional shear zones also define CCW rotation which mirrors the KSZ orocline and could therefore have formed synchronously. The shear zones that bound the southern and northern Chapleau Belt and KSZ are predominantly ductile and sinistral strike–slip (oblique and transfer) with areas of transpression and transtension at subprovince– to local–scale fold axes that formed during boudinage (including the "Z–shape" boudin–controlled fold due to rotation during boudinage in the internal Chapleau Belt and KSZ orocline). The late stage, dextral strike–slip brittle–ductile shear zones and overprinting faults, including the ILDZ, define the same geometry as the antithetic shear bands in the regional– to outcrop–scale boudins formed during the same event. The sinistral strike–slip shear zones are defined by both prograde amphibolite to granulite facies metamorphic mineral assemblages as well as retrograde amphibolite facies mineralogy. The dextral strike–slip shear zones are defined by retrograde amphibolite facies metamorphic mineral assemblages, while the dextral strike–slip faults (± oblique) have greenschist and below assemblages. Therefore, there are three predominant styles of structures: (1) extensional and

transfer ductile shear zones, top to the northeast, that deformed during prograde metamorphism, (2) ductile to brittle–ductile sinistral strike–slip structures that deformed during prograde and retrograde metamorphism, and (3) brittle–ductile to brittle, sinistral and dextral strike–slip (± oblique) shear zones and faults that formed during retrograde metamorphism. These three structural types affected the WGD, Chapleau Belt, KSZ, and entire southern Superior Province. Previous studies have not accounted for all of these types of structures and metamorphic events in one hypothesis, while this study will purpose a new tectonic hypothesis that incorporates all features in the next section.

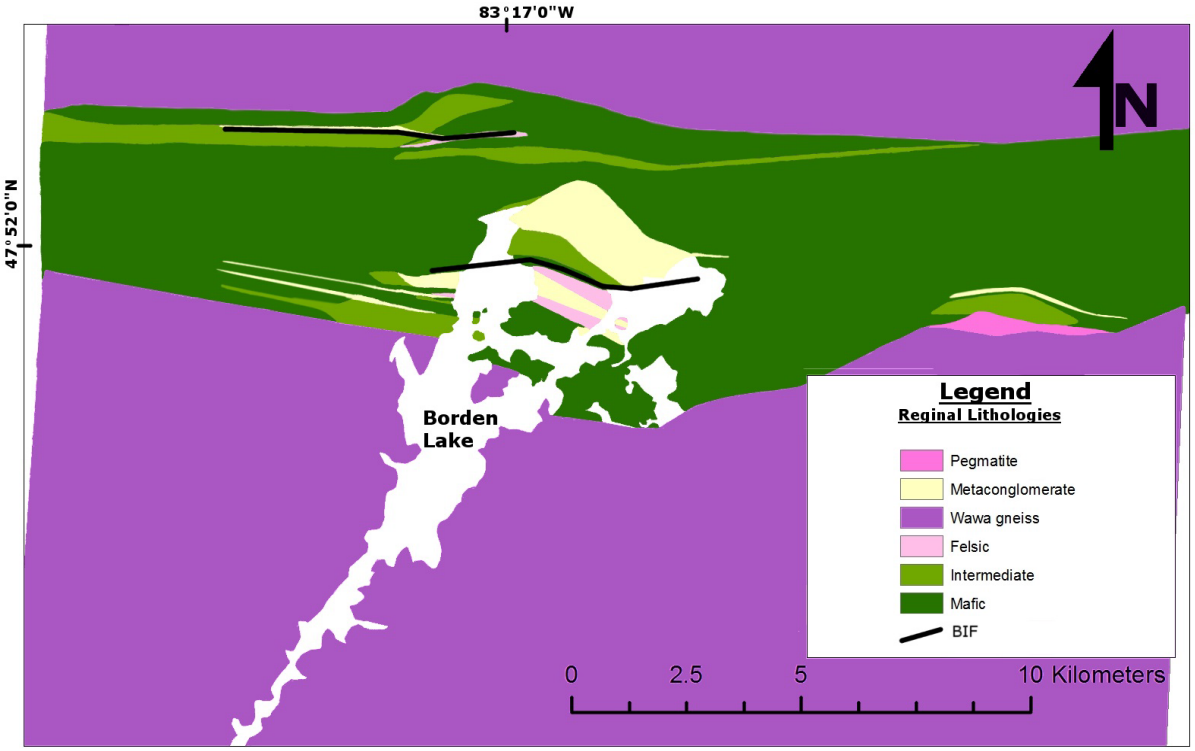

Figure 4.19: Regional lithological map of the Chapleau Belt and southern KSZ displaying major, regional lithologies including banded iron formation (BIF, black, not to scale), mafic metavolcanic lithologies (including minor metamorphosed BIF and mafic to felsic volcanic, volcaniclastic, plutonic lithologies), intermediate metavolcanic lithologies, felsic metavolcanic and plutonic lithologies (including minor metaconglomerate and mafic metavolcanic lithologies), Wawa Gneiss (assimilated metaplutonic felsic to intermediate lithologies), metaconglomerate (including minor metasandstone to metasiltstone and mafic metavolcanic lithologies), and pegmatites.

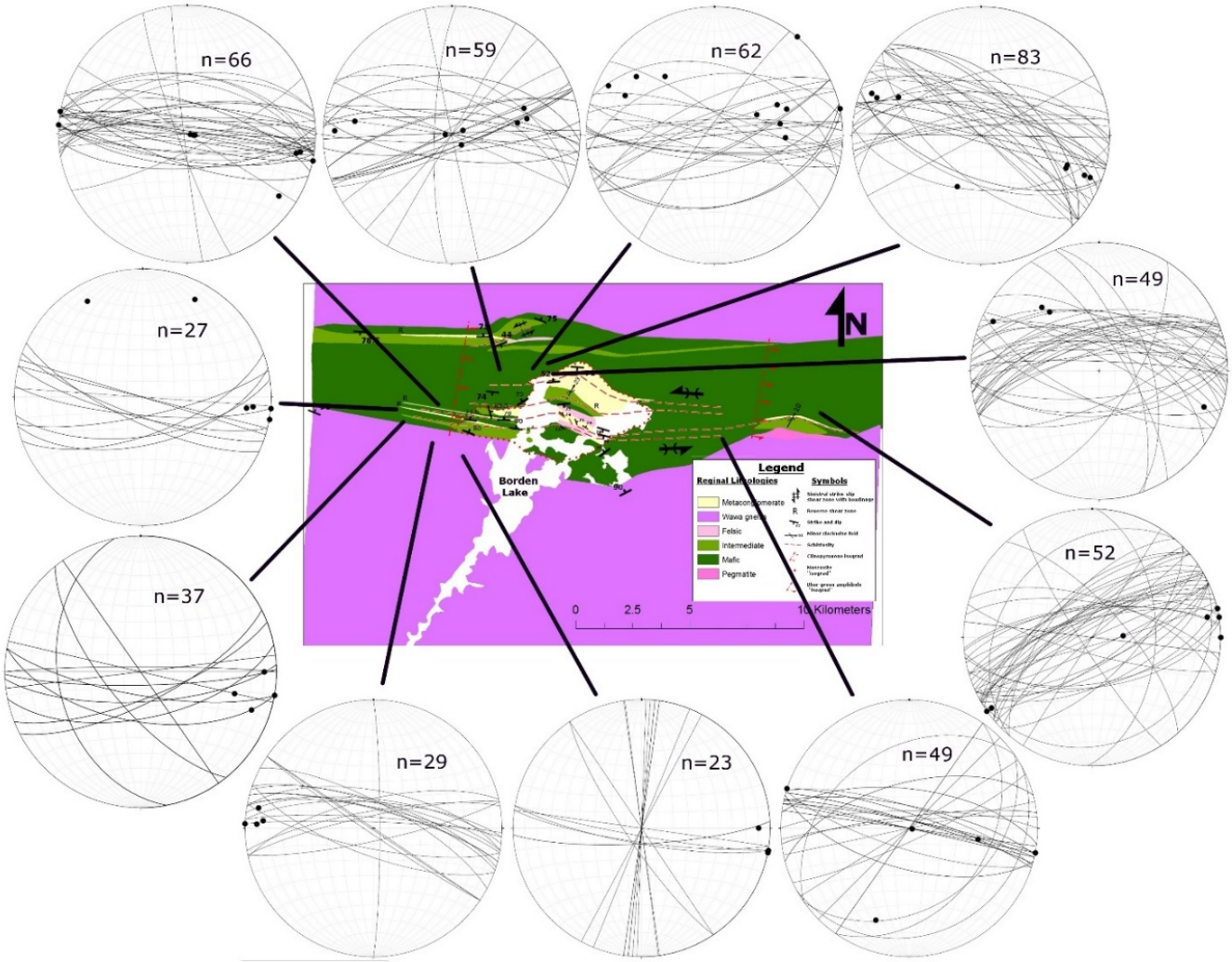

Figure 4.20: Stereonets of Chapleau Belt, KSZ collected from regional field mapping (planes denote lithological contacts, foliation, schistosity, gneissosity, and mylonitic fabrics and points denote lineations of minerals and clasts). Note the prevalence of east–west striking fabrics outside of regional folds and boudins in the centre and far west of the regional map. Note the fabrics dip both north and south in regional shear zones, particularly in regional boudins. Oblique to perpendicular fabrics are crosscutting pegmatites and are common throughout the Chapleau Belt and Kapuskasing Structural Zone, particularly in regional folds and boudins. Lineations are east or west plunging except in regional to local boudins where they are steeply dipping to vertical due to changes in local strain. The transition from the Chapleau Belt to the KSZ is visible with a change to northeast–southwest striking fabrics and is characteristic of the Kapuskasing orocline.

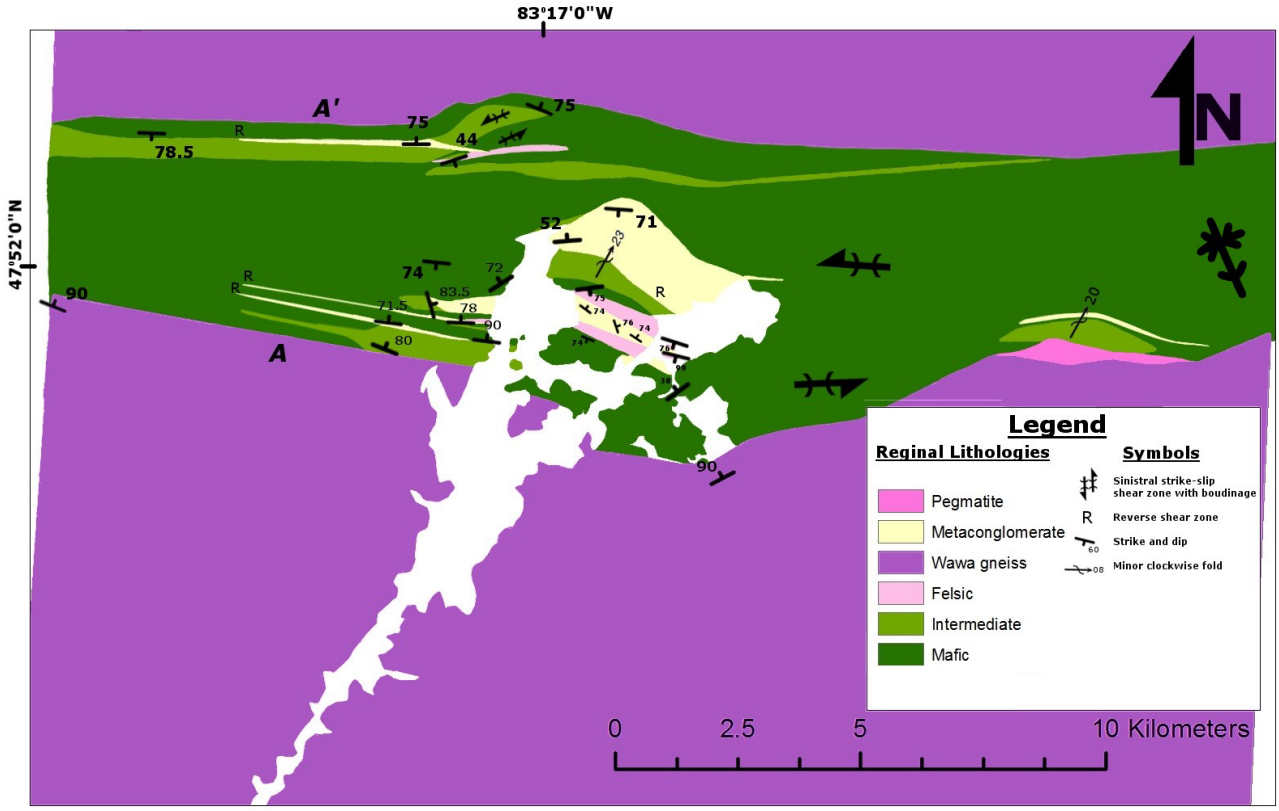

Figure 4.21: Regional structural map of the Chapleau Belt and southwestern KSZ collected from regional field mapping. Note the prevalence of east–west striking fabrics outside of regional folds and boudins in the centre and far west of the regional map. Note the gneissic, schistose fabrics dip both north and south in regional shear zones, particularly in regional, rotated boudins (Borden Lake, white). Lineations are east or west plunging except in regional to local boudins where they are steeply dipping to vertical due to changes in local strain. The transition from the Chapleau Belt to the KSZ visible with a change to northeast–southwest striking fabrics and is characteristic of the Kapuskasing orocline and denoted with the symbol for a fold with near–vertical limbs and half–circle denotes direction of closure. The northern and southern boundaries with the WGD are ductile, sinistral strike–slip ± oblique shear zones that define the belt–scale sigmoidal shape.

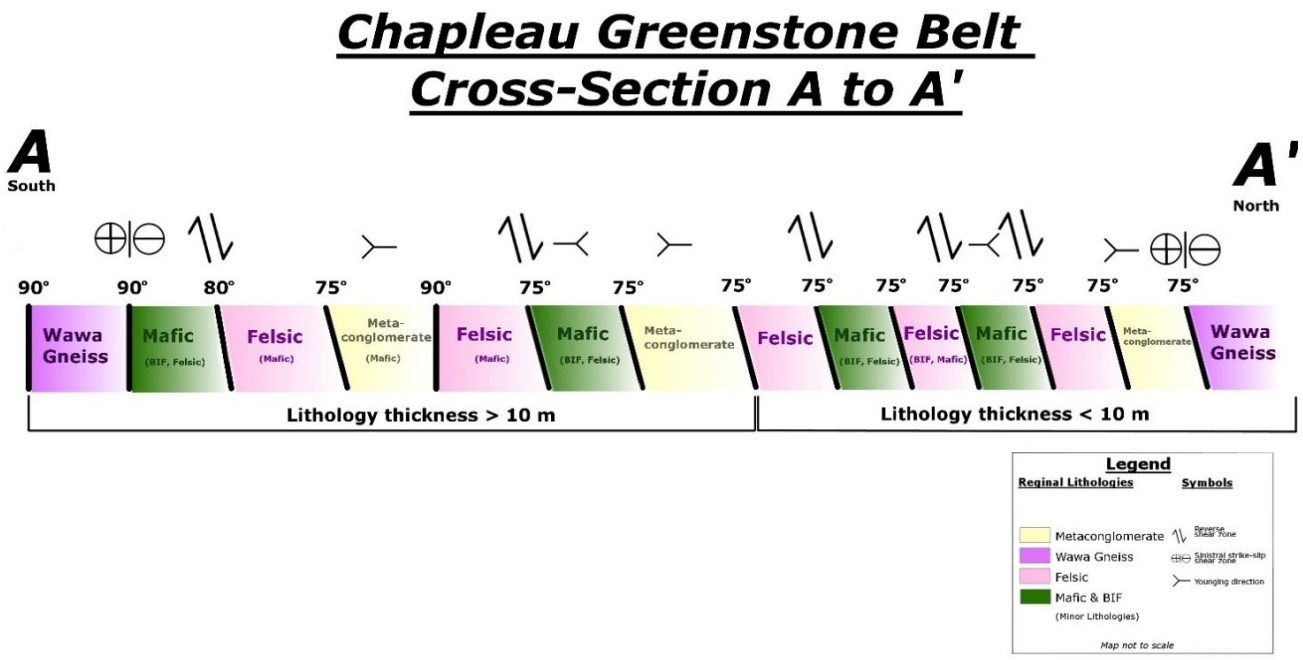

Figure 4.22: Cross–section (A to A', Fig. 3.20) schematic of the regional lithologies and structures across the Chapleau Belt near Borden Lake highlighting the strike–slip and reverse shear zones, potential preserved younging directions, and average thicknesses of the lithological units in the region. The greater dip, additional felsic lithologies and thickness in the south corresponds to additional gold mineralization adjacent to Borden Mine. The ductile, sinistral strike–slip (± oblique) shear zones that define the boundaries with the WGD also define the sigmoidal shape of the Chapleau Belt.

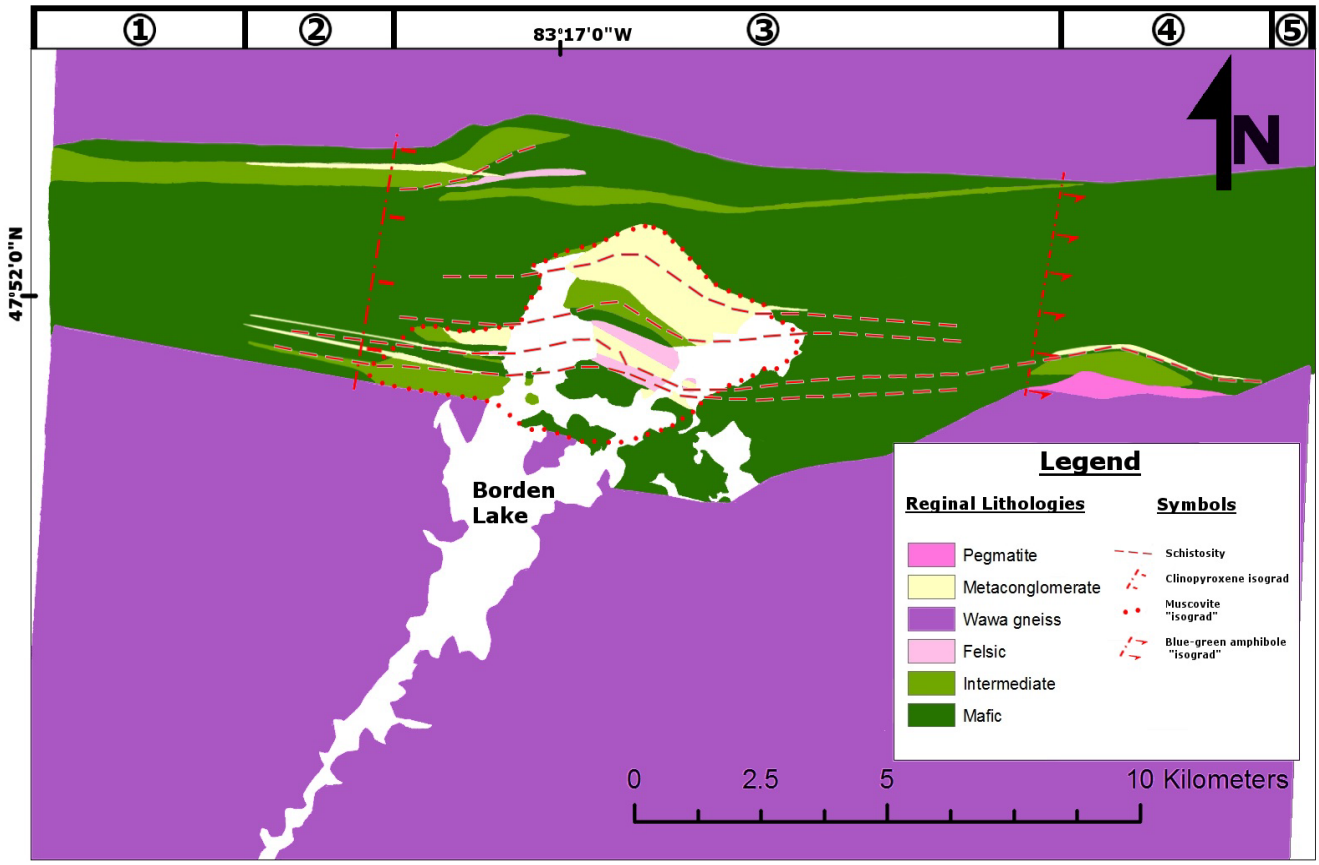

Figure 4.23: Regional metamorphic and migmatite map of the Chapleau Belt and southern KSZ highlighting the increasing grade from amphibolite facies in the west to granulite facies in the east. The clinopyroxene isograd (rectangles) is located in the western Chapleau Belt, the muscovite "isograd" (is located in the central Chapleau Belt), and the blue–green amphibole "isograd" is in the eastern Chapleau Belt and southern Kapuskasing Structural Zone. Migmatization and related structures also increase from west to east the most common migmatite structures in the mafic and intermediate metavolcanic protoliths are denoted 1 (least deformed and/or lower temperature) to 5 (most deformed and/or higher temperature). The migmatitic structures include: 1) metatexite, patchy and dilation, 2) metatexite, net texture, and dilation, 3) metatexite, dilation, stromatic, and vein, 4) metatexite, dilation, stromatic, 5) diatexite, schollen, schlieric, and metatexite dilation (Sawyer, 2008). The WGD in the region (purple) is predominantly felsic plutonic lithologies, assimilated gneiss, and schollen diatexite.

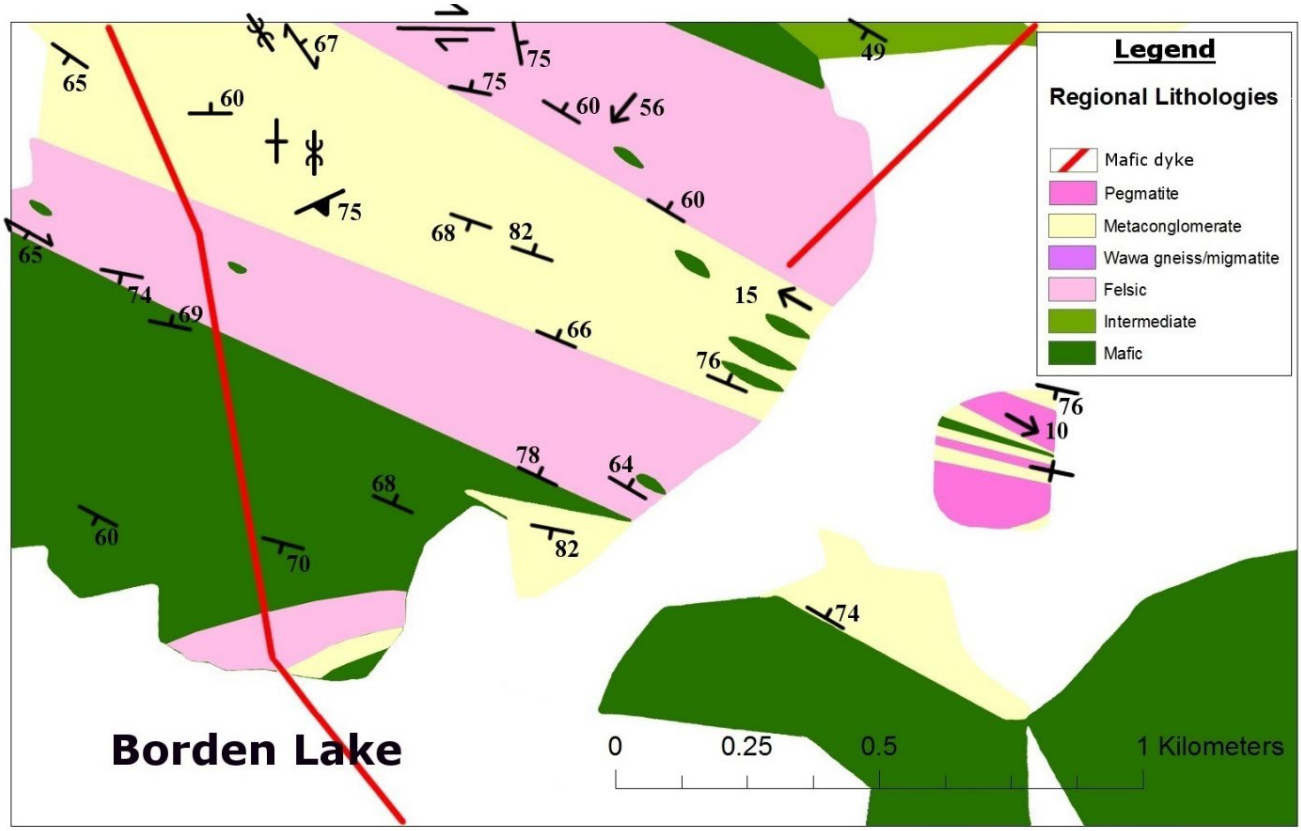

Figure 4.24: Borden Mine high–grade ore zone defines a regional boudin neck at the northeastern section of Borden Lake (white). Note the extreme change in lithology thickness along strike due to boudinage and an increased strain gradient. Boudinage and dip directions vary depending on the regional "Z–shape" fold. The mafic dyke in the west mirrors the regional "Z–fold" and the mafic dyke in the northeast is perpendicular to boudinage. Refer to trench maps for additional data.

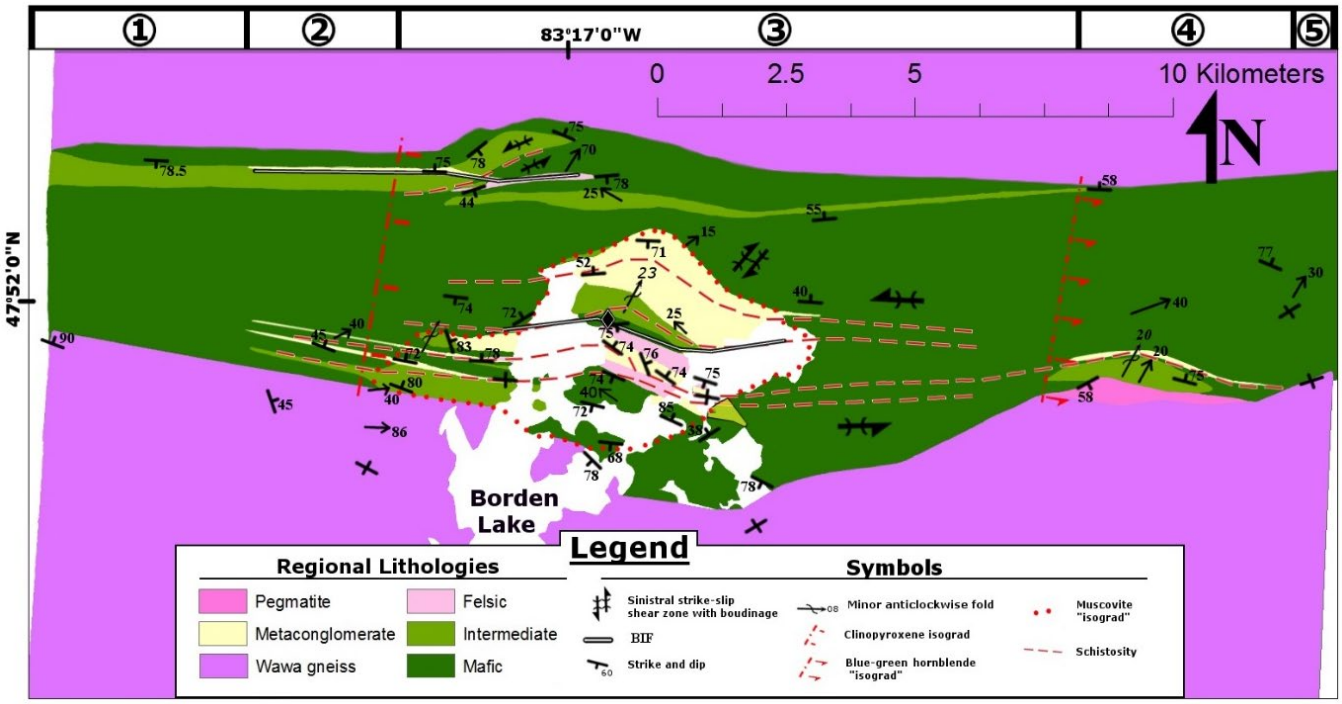

Figure 4.25: Regional map of the Chapleau Belt and southern KSZ (printed fold–out version is located in back pocket of thesis in Appendices) with regional lithologies, structures, and isograds highlighted. The rotation and boudinage are highlighted in the centre of the map as well as in the north and eastern areas of the region as they are the major mineralization controls at Borden Mine and regionally. Note the tightness of spacing in foliation bands), and the presence of coarse–grained pegmatite at the regional boudin neck. The variable strike and dip is due to the regional "Z–shape" fold. The highest strain and vertical to southerly dip is concentrated above Borden Lake (white) at the high–grade ore zone.

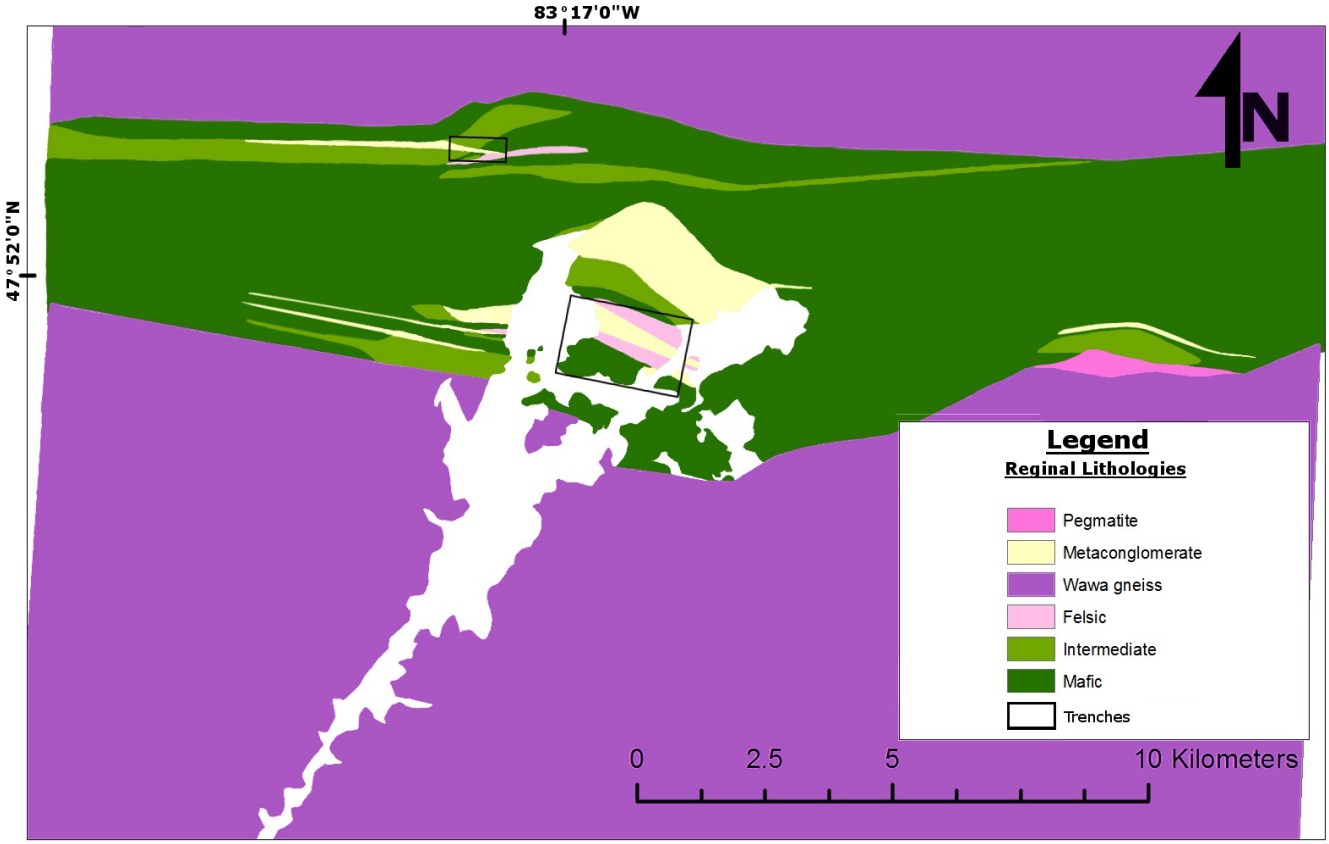

Figure 4.26: Regional map highlighting areas of trenches (black boxes).

Equal area stereonets or Schmidt nets are displayed in Figs. 4.27–4.33 and highlight regional data. The smaller–scale data are also presented in stereonets and include boudinaged lithologies, presented as their general strikes and projected as poles to planes to simplify their orientation as they have extremely variable dips, trends, and plunges. The stereonet of boudin extension closely mirror the regional east–west foliations. The stereonet of quartz veins displays a northeast–southwest strike, which is oblique to parallel to regional foliation (Fig. 4.32). The pegmatite dykes are most similar to the east–west foliation and similar to the boudins (Fig. 4.33).

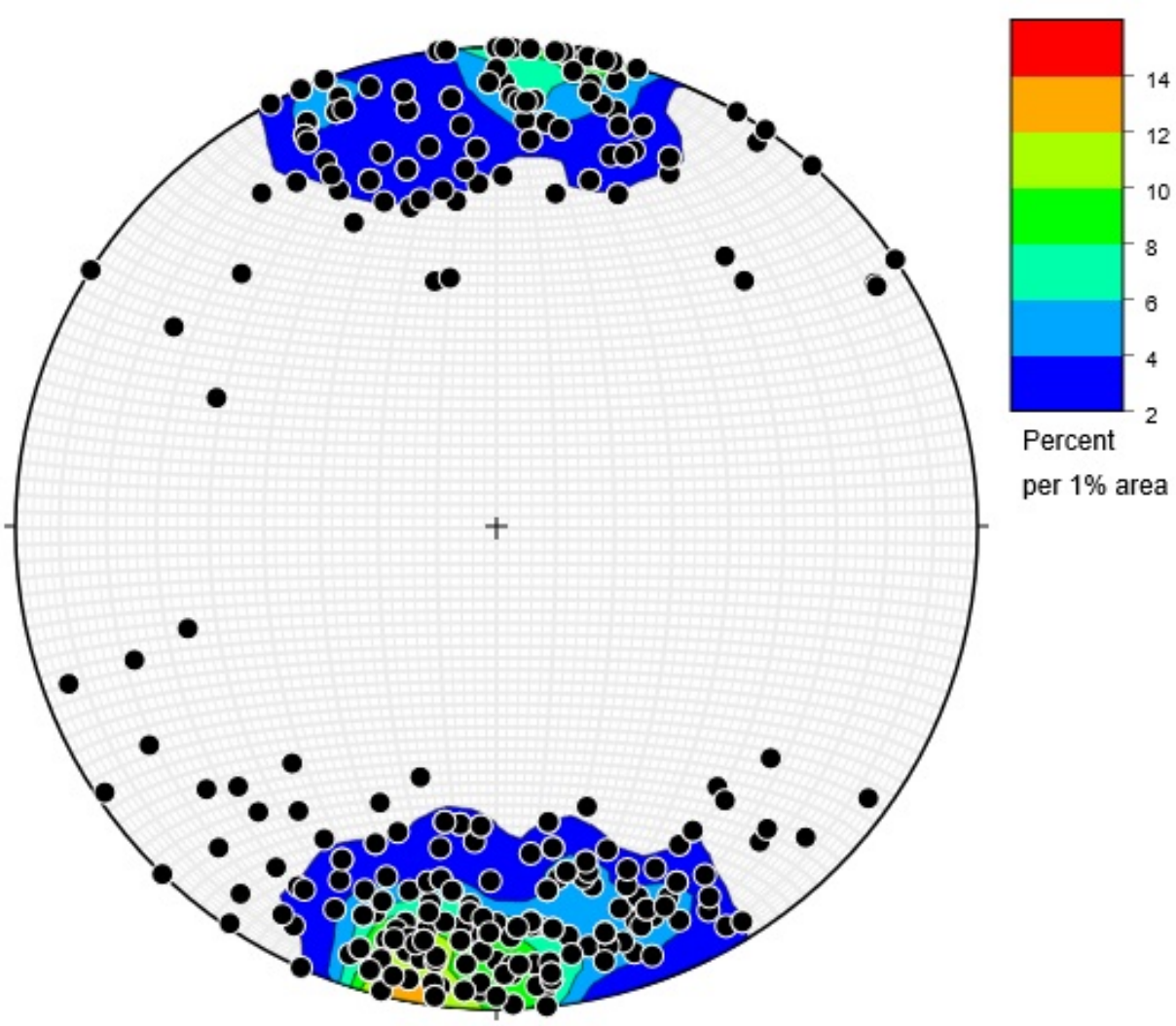

Figure 4.27: Contoured (percent per 1% area) poles to planes stereonet of the western WGD and Chapleau Belt presents the prevalence of east–west striking fabrics outside of regional folds and boudins in the centre and far west of the regional map. The fabrics dip both north and south in regional shear zones, particularly in regional boudins. Oblique to perpendicular fabrics are crosscutting pegmatites and are common throughout the Chapleau Belt and KSZ, particularly in regional folds and boudins.

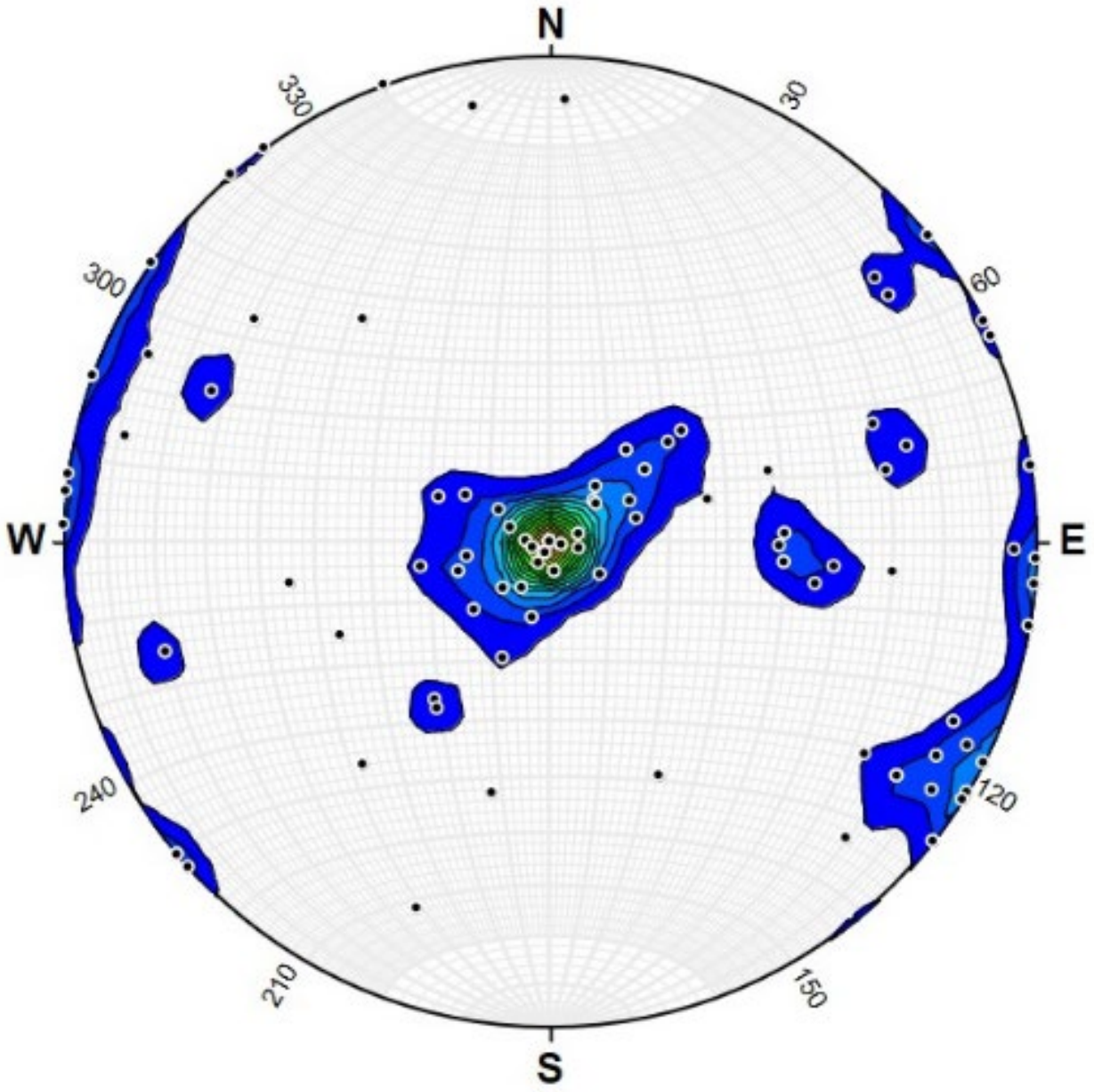

Figure 4.28: Contoured (percent per 1% area) poles to planes stereonet of lineations (mineral, clast, and minor fold, n=57) of the western WGD and Chapleau Belt generally have a shallow to moderate plunge to the east or west, except in boudin necks where elongate, retrograde minerals define subvertical to vertical plunge.

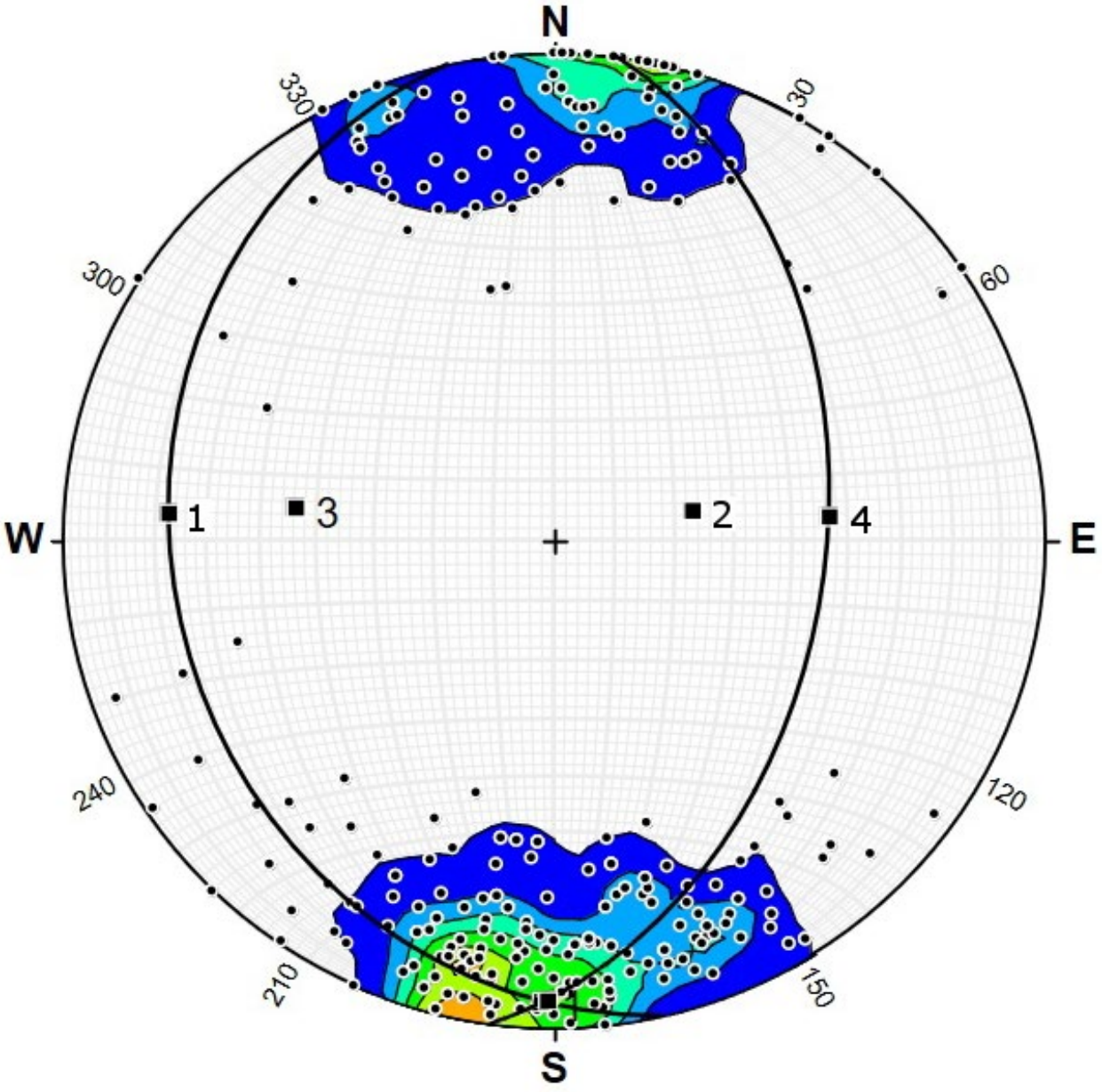

Figure 4.29: Contoured (percent per 1% area) poles to planes stereonet of the boundin–controlled "Z–shape" fold in the Chapleau Belt that formed from CCW rotation during boudinage (great circles and points 1–4 define the fold axes and their poles). The northern boudin (or "limb") (1 and pole, 2) has a fold axis (or boudin neck) plunge and trend of 67º/078º and an axial plane (or median schistosity) of 89º/077º S. The southern boudin (or "limb") (4 and pole 3) has a fold axis (or boudin neck) plunge and trend of 49º/279º and an axial plane (or median schistosity) of 90º/279º N.

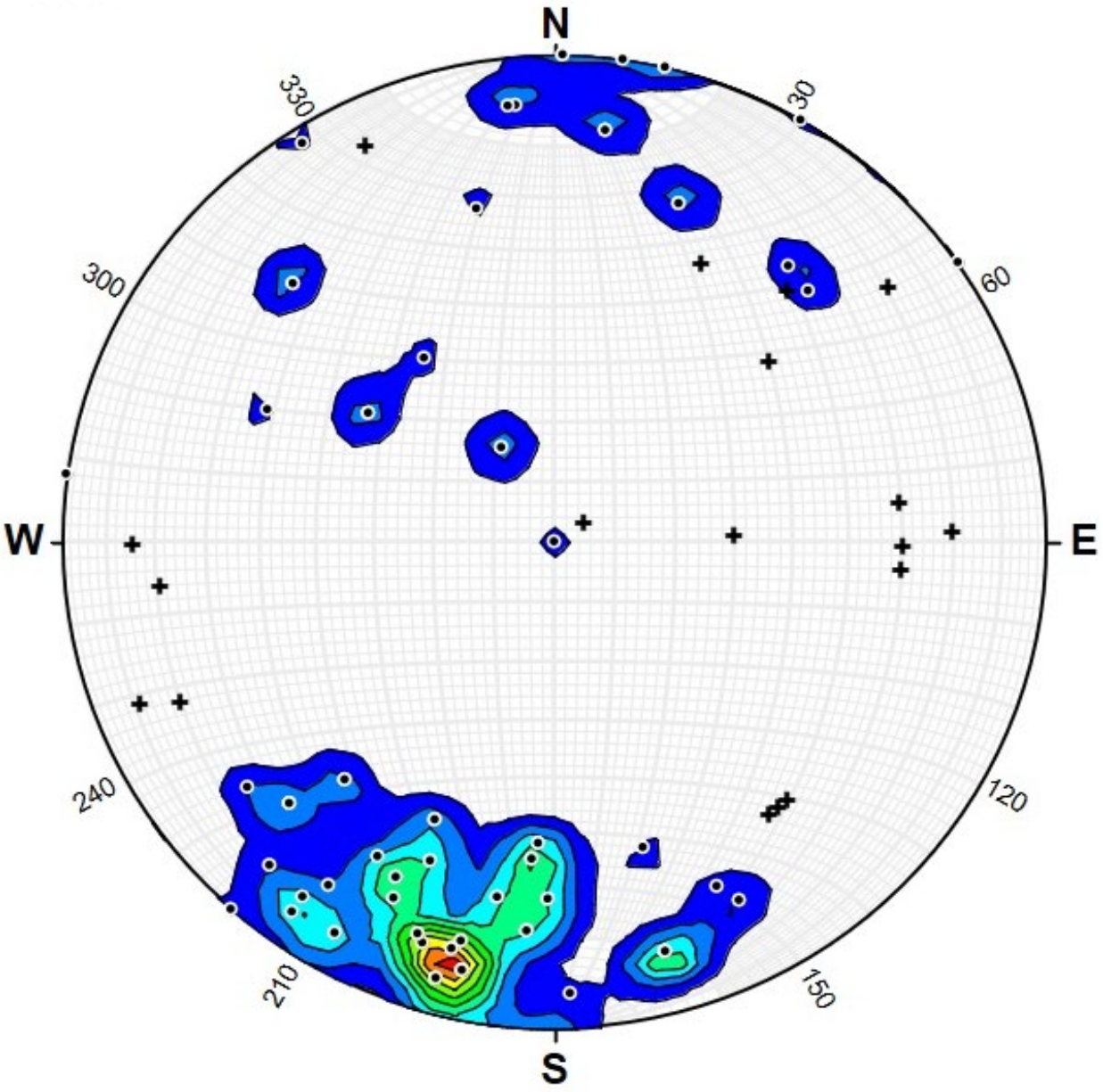

Figure 4.30: Contoured (percent per 1% area) poles to planes stereonet of the southern KSZ gneissosity and lineations (black crosses). Northeast–directed horizontal extensional shear zones are perpendicular to the gneissosity. The change in fabric from the east–west striking WGD and Chapleau Belt to the northwest–southeast strike of the southwestern KSZ defines the southern extension of the KSZ orocline that overprints the ILDZ.

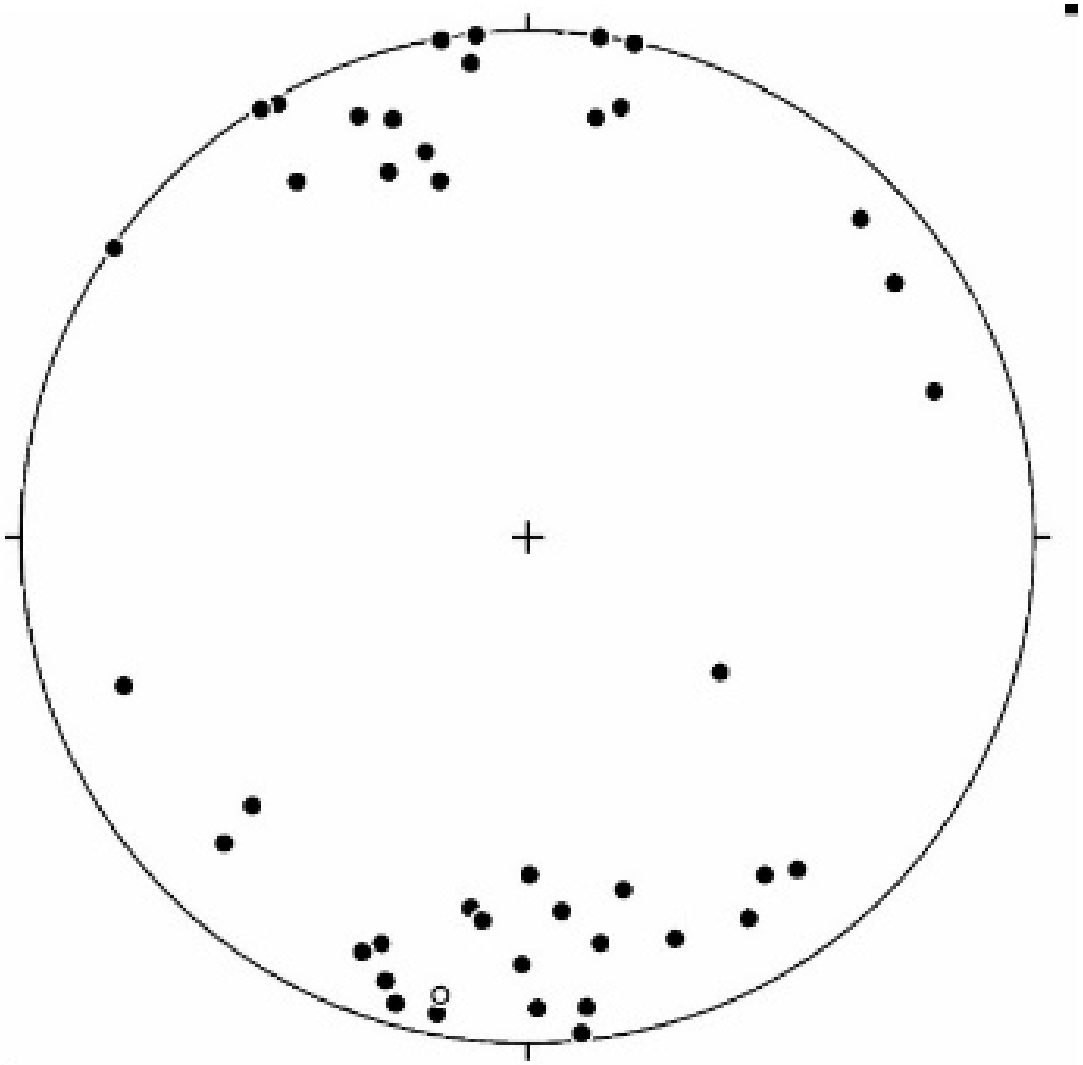

Figure 4.31: Poles to planes stereonet of schistosity and gneissosity in boudinaged lithologies in the trenches, Chapleau Belt and southern KSZ and separated from the main data set in Fig. 3.16 to highlight their difference from the main population (poles to planes, n=43). Due to the variability of the asymmetrical boudins and foliation boudins only the poles to planes of the foliation and gneissosity measurements are presented as they better display the data. The boudin axes are perpendicular to these poles and define predominant extension east–west to northeast–southwest.

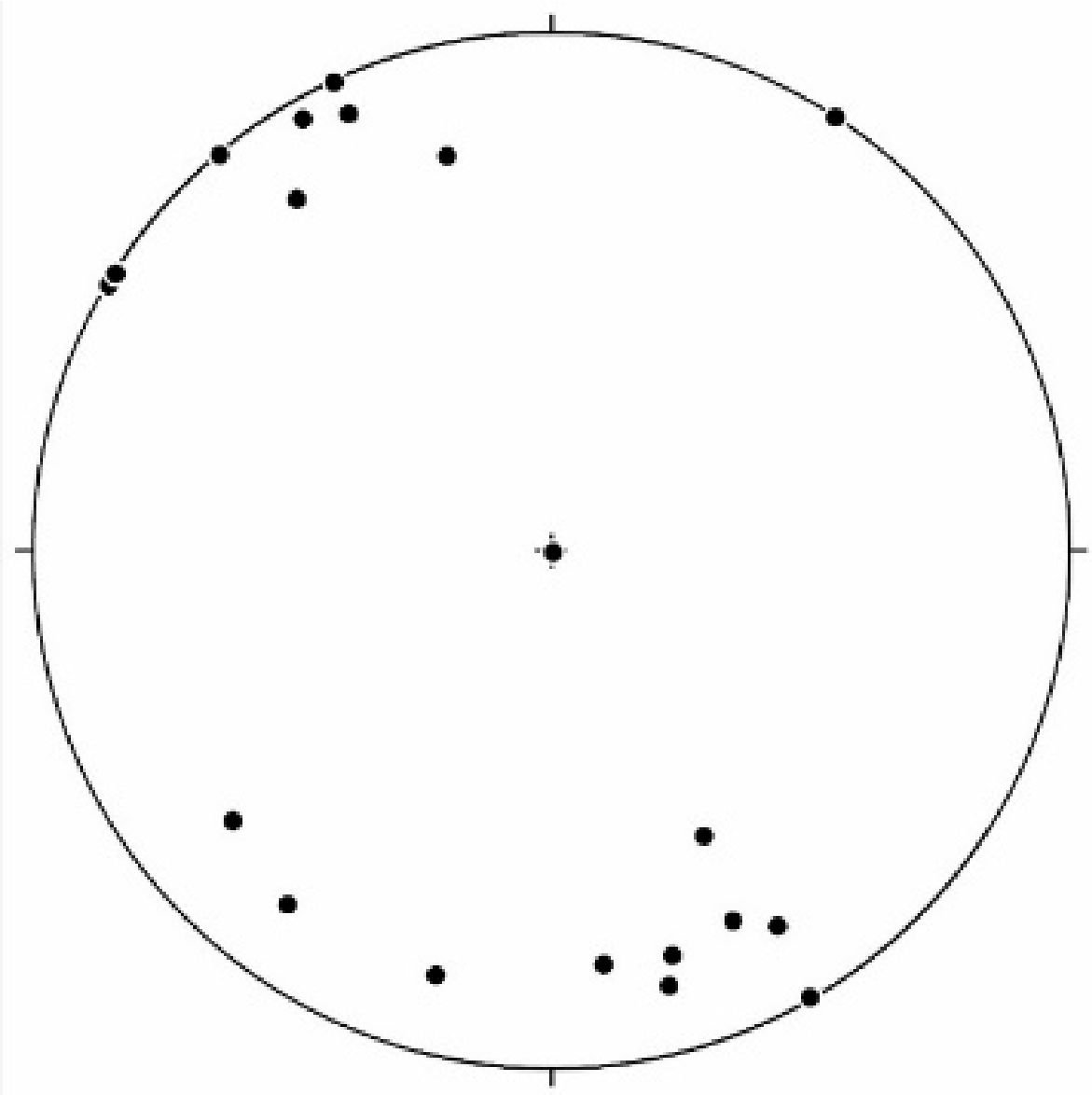

Figure 4.32: Stereonet of strikes of quartz veins from the Chapleau Belt and southern KSZ (poles to planes, n=19, black dots). The northeast–southwest strike of the quartz veins demonstrates the change from predominantly east–west striking lithologies to the subsequent regional rotation to a strike of northeast–southwest.

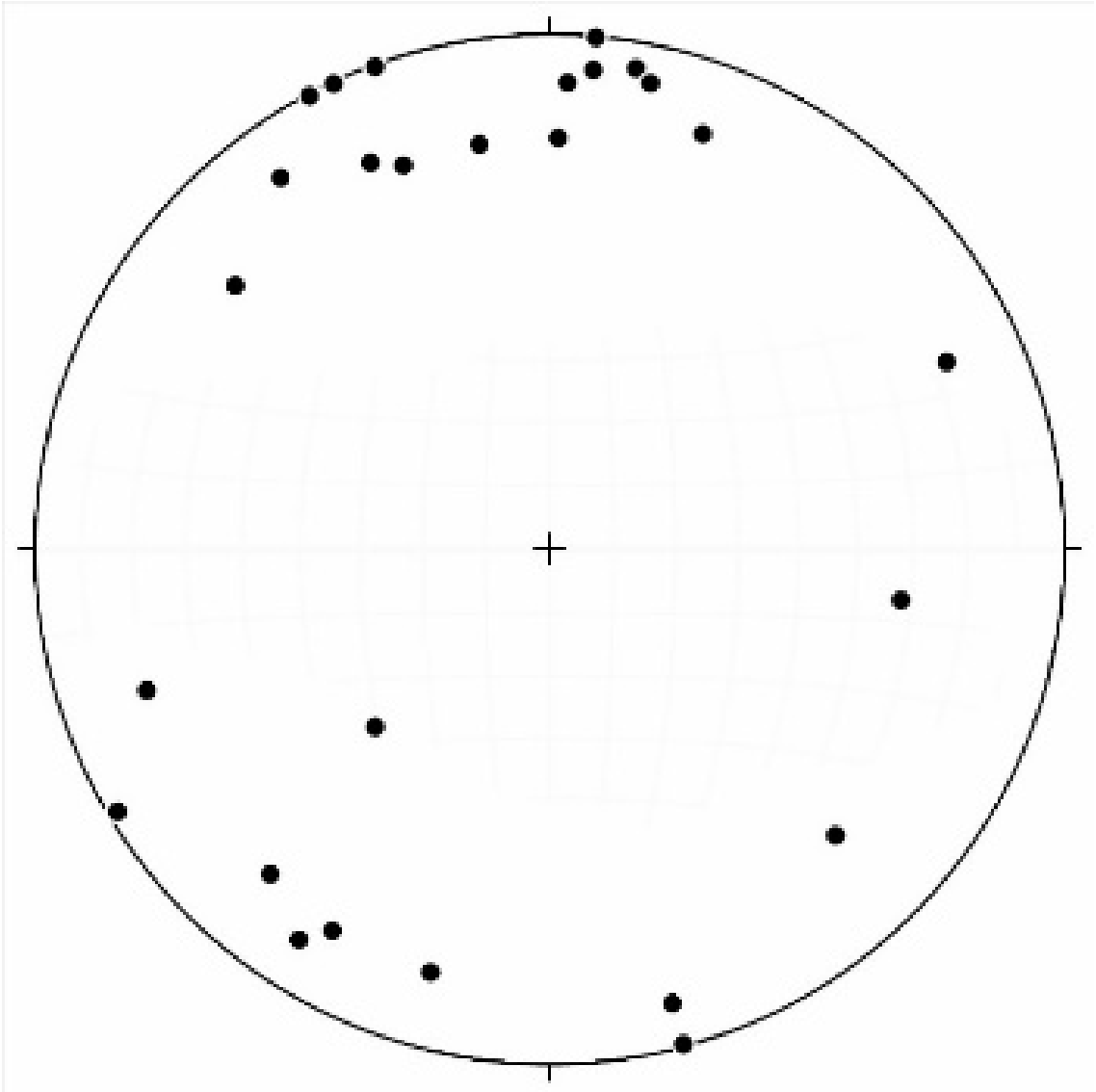

Figure 4.33: Stereonet (poles to planes) of strikes of pegmatitic dykes in the trenches, Chapleau Belt, WGD, and KSZ (poles to planes, n=27, black dots). The pegmatitic dykes provide evidence that the zones of dilation have some similarity to the boudinaged lithologies except for the oblique to perpendicular dykes. The pegmatite dykes parallel to the regional fabrics provide supporting evidence for dilation in the region, including ore zones, and the perpendicular pegmatite dykes providence evidence of extension.

The Chapleau Belt defines a sigmoidal shape and the KSZ defines an arcuate shape that plunges to the west (Figs. 1.2–1.5, 2.11, 4.25). Regional schistosity and gneissosity are defined by sinistral strike–slip ductile to brittle–ductile shear zones that strike east–west with moderate to steep northerly dips and moderate to steep plunges (Figs. 4.27–4.28). These structures continued to deform or were later reactivated during boudinage with regional CCW rotation and local CW rotation with pegmatite dykes perpendicular to extension (Figs. 4.31, 4.33). The CCW rotation during belt–scale to microscopic–scale boudinage and foliation boudinage created the sigmoidal shape of the Chapleau Belt and the arcuate shape of the southern KSZ. The CCW rotated boudinage is displayed as regional folds, the "Z–shape" fold, in the Chapleau Belt and the northernmost boudin neck (or "limb") (1 and pole, 2) has a fold axis (or axis of the boudin neck) plunge and trend of 67º/078º and an axial plane (or median schistosity) of 89º/077º S (Fig. 4.29). The southern boudin (or "limb") (4 and pole 3) has a fold axis (or axis of boudin neck) plunge and trend of 49º/279º and an axial plane (or median schistosity) of 90º/279º N (Fig. 4.29). There are numerous smaller–scale boudins throughout the belt but this regional–scale boudin has affected the geometry of the entire belt.

Ductile to brittle–ductile sinistral and dextral strike–slip shear zones formed during CCW rotation and are defined by antithetic shearbands with outcrop–scale examples displayed in trench maps in the following section. The dextral strike–slip shear zones and faults have the same geometry as the rotated foliation boudins, east–west to northeast–southwest striking and shallowly to moderately dipping to the west to northwest. These structures represent the earliest stage of deformation in the thrust, normal, and reverse faults previously identified in the southern KSZ within the ILDZ (Percival, 1989). Extensional (horizontal to subhorizontal ductile shear zones towards the northeast) and transfer structures (ductile to brittle–ductile sinistral and dextral shear zones) accommodated the boudinage and rotation. The Chapleau Belt and KSZ have similar mineral and clast lineation as they are both affected by regional boudinage with lineation moderately plunging to vertical in boudin necks and horizontal to subhorizontal in early sinistral strike–slip shear zones and extensional and transfer shear zones. Additional field mapping is required in the less accessible, northern KSZ Zone in addition to detailed, ground–based geophysical studies as this study focused on the more accessible southern and central regions of the KSZ.

4.2.2 Trench mapping

Trench mapping was conducted at the Borden Mine near Chapleau, Ontario in the centre of the study area at the metre–scale to assess details (Figs. 4.34–4.43). Other areas with well–exposed outcrop not mapped at 1 m–trench scale include: Discovery trench (16N 5303686/0330311) mapped

synchronously during our mapping seasons by LaFontaine (unpublished MSc. thesis, 2016), Boudin outcrop (5306514/0327567), and the Highway exposure (Highway 101, 5304271/0327720 area also known as D. Moser's Hill outcrops in Moser (1994, 1996) (Figs. 4.16 E, 4.18 D). Trenches A, B, C, and D are predominantly composed of metaconglomerate (yellow), metasediment (brown), and amphibolite (green) lithologies. The general foliation strikes east–west with a steep dip to the north or south. Foliation anastomoses around quartz veins, boudinaged quartz veins, and quartz foliation boudins and two, 10–cm–long, brittle–ductile shear zones have dextrally offset two of the quartz foliation boudins and quartz boudins in the metaconglomerate. Clast lineation is apparent throughout the trenches and is shallowly plunging to the northwest. Boudinage and pinch–and–swell structures are apparent in the metaconglomerate and amphibolite but not the metasedimentary lithologies. Quartz boudins and quartz–foliation boudins have been rotated on average 10º counterclockwise and the antithetic shear bands have been overprinted by dextral brittle–ductile shear zones. The regional "Z–shape" fold is clearly observed between trenches due to the change in strike, dip, and plunge.

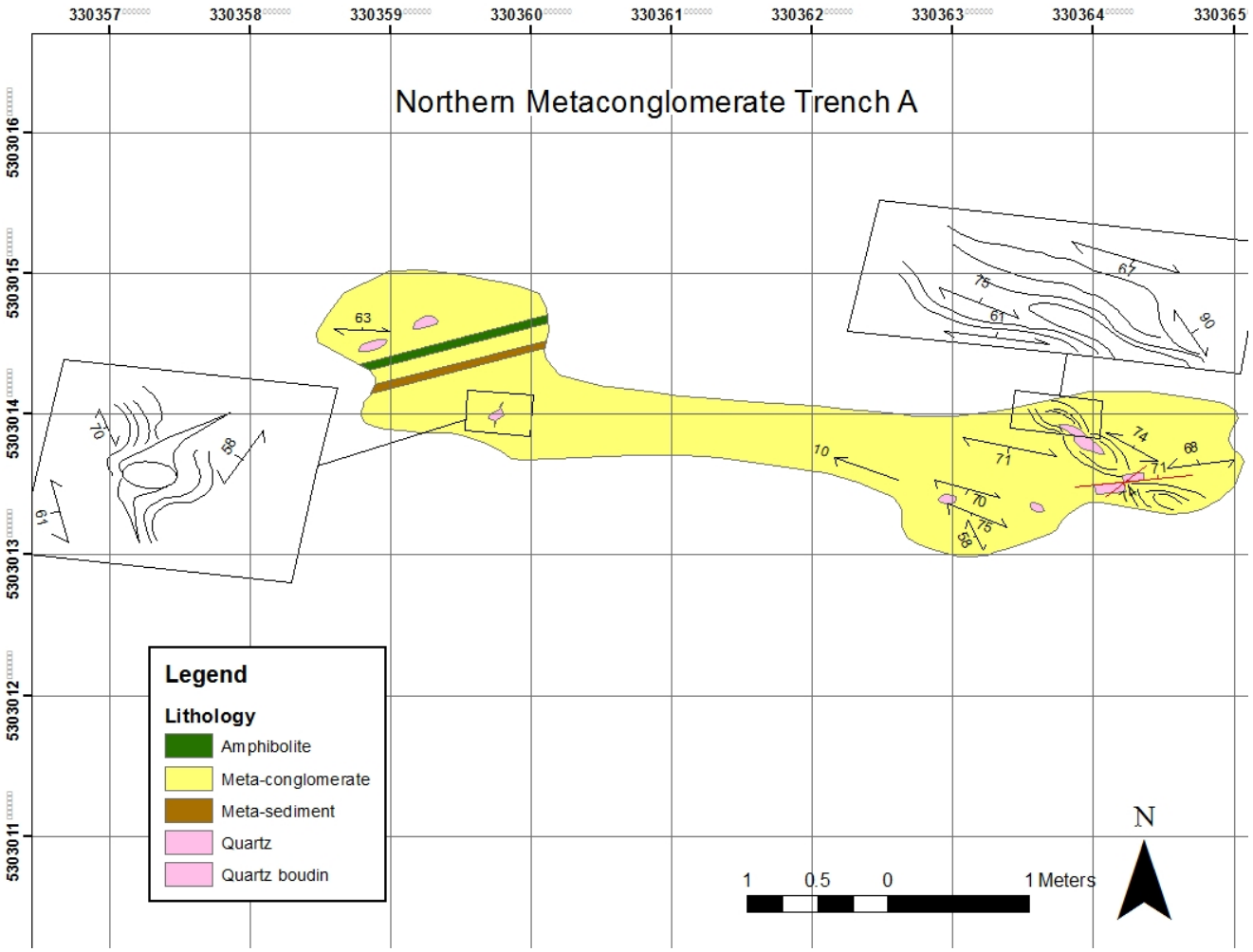

Figure 4.34: Trench map of Northern Metaconglomerate A. The mafic and metasedimentary lithologies in the metaconglomerate strike east northeast with a moderate dip north, subhorizontal plunge to the east. The metaconglomerate strikes predominantly east–west with a steep, southern dip and shallow plunge west, consistent with the regional "Z–shape" fold. The quartz boudins have been rotated CCW and have been offset by dextral, brittle–ductile shear zones in antithetic shear bands. The regional shear zones anastomose around the rigid quartz boudins and dip to the north and south.

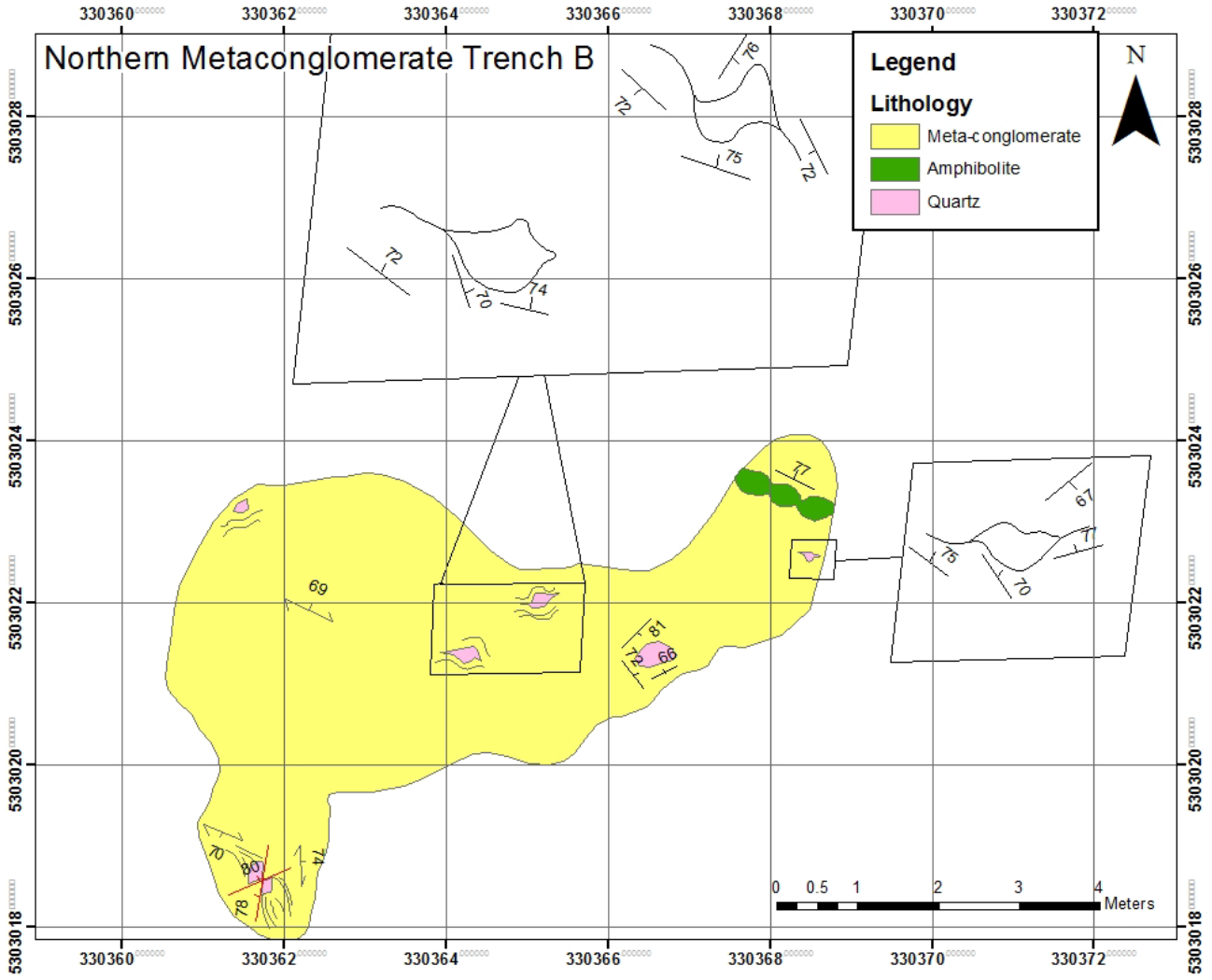

Figure 4.35: Trench map of Northern Metaconglomerate B. The metaconglomerate and amphibolite strike east southeast–west northwest with a north and southward steep dip, consistent with the regional "Z–shape" fold. The amphibolite pinches and swells. Quartz boudins have been predominantly rotated CCW and offset by dextral, brittle–ductile shear zones overprinting antithetic shear bands. The regional shear zones anastomose around the rigid clasts and dip to the north and south.

The Trenches A–D are predominantly composed of metaconglomerate (yellow), metasediment (brown), and amphibolite (green) lithologies (Figs. 4.34–4.37). They strike northeast–southwest to northwest–southeast with both a southern and northern dip in the trenches. Boudinage and pinch–and–swell structures are apparent in the metaconglomerate and amphibolite but not the metasediment lithologies. Quartz boudins and quartz–foliation boudins have been rotated on average 10º counterclockwise and define antithetic shear bands overprinted by dextral brittle–ductile shear zones. A quartz and biotite–filled boudin neck is located in the middle of Metaconglomerate A. The amphibolite defines a tapered boudin as is typical in the fine–grained mafic metavolcanics lithologies. The amphibolite is a patchy– to vein–metatexite migmatite and the leucosomes are folded and define the

tapering as well. A quartz vein inside the amphibolite has a pinch–and–swell structure and has not been as greatly boudinaged. The foliation in Metaconglomerate B trench strikes northwest–southeast and is inferred to be the greatest amount of strain in the regional "Z–shaped" fold. Rotation in quartz veins, foliation boudins, and boudins is $<5^{0}$ counterclockwise. Folding and boudinage is inferred from Trench C to D due to the change in strike and dip in the amphibolite. The biotite schist (or biotite lens) in Trench C is located in the quartz boudin neck in amphibolite. Various ptygmatic folds are also present in the amphibolite and appear as white in the trench map.

The Micaceous Quartzofeldspathic Gneiss Trench E (A and B) (Figs. 4.38–4.39) are predominantly composed of muscovite–rich quartzofeldspathic gneisses and assimilated felsic metavolcanic lithologies with quartz porphyroclasts (or "quartz eyes"). The northwest–southeast strike and steep to vertical dip to the south or north is inferred to define the fold axis of the regional "Z–shape" boudin–controlled fold. Mylontitic fabric (or high–strain zone) and quartz boudins also define this axis. Perpendicular to boudinage are minor, northeast–striking, mafic dykes.

The Large Pegmatite Trench F is composed of quartzofeldspathic lithologies, including biotite– and muscovite–quartzofeldspathic gneisses (Fig. 4.40). Areas of assimilation have been visually identified. Quartz–alkali feldspar pegmatite is very–coarse grained to megacrystic. Graphitic and myrmekitic textures have been identified in the pegmatites and are sinistral kinematic indicators. The Large Pegmatite Trench F is inferred to be the location of a regional boudin neck in the mafic and felsic lithologies.

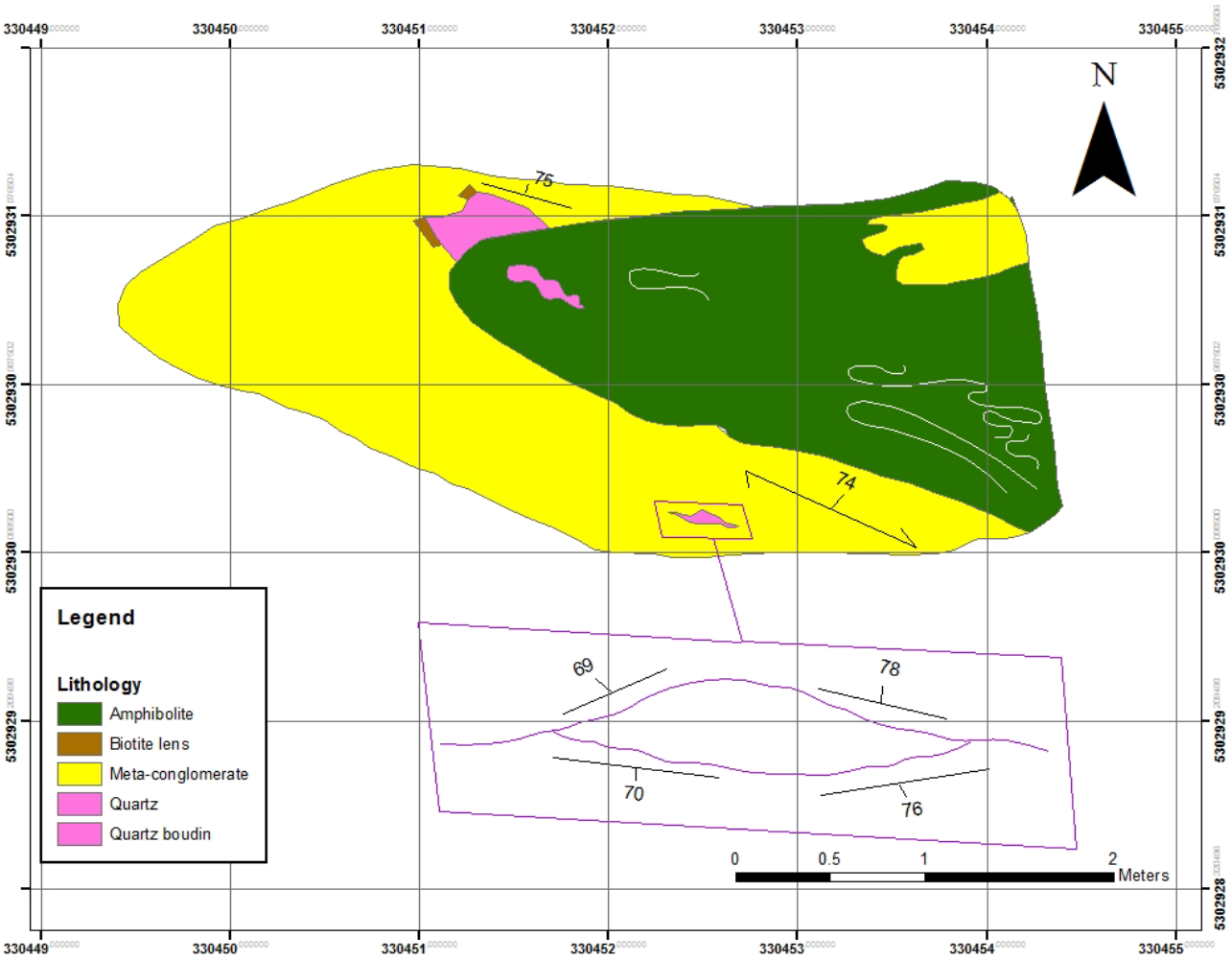

Figure 4.36: Trench map of Metaconglomerate C. The metaconglomerate and amphibolite strike east–west with a northern, steep dip consistent with the centre of the regional "Z–shape" fold. The amphibolite boudin has metaconglomerate, quartz boudins, and biotite–rich lenses in the tapered boudin neck. Quartz and biotite are common in amphibolite boudins in the area, as are complex folds within the amphibolite drawn in white. The direction of local, greatest extension is northwest–southeast in this trench and is consistent with the regional "Z–shape" boudin–controlled fold. Minor isoclinal folds in the amphibolite plunge moderately north to northwest. The greatest boudinage extension is northwest–southeast and defined by biotite–quartz boudins. The quartz foliation boudins have long axes striking east–west.

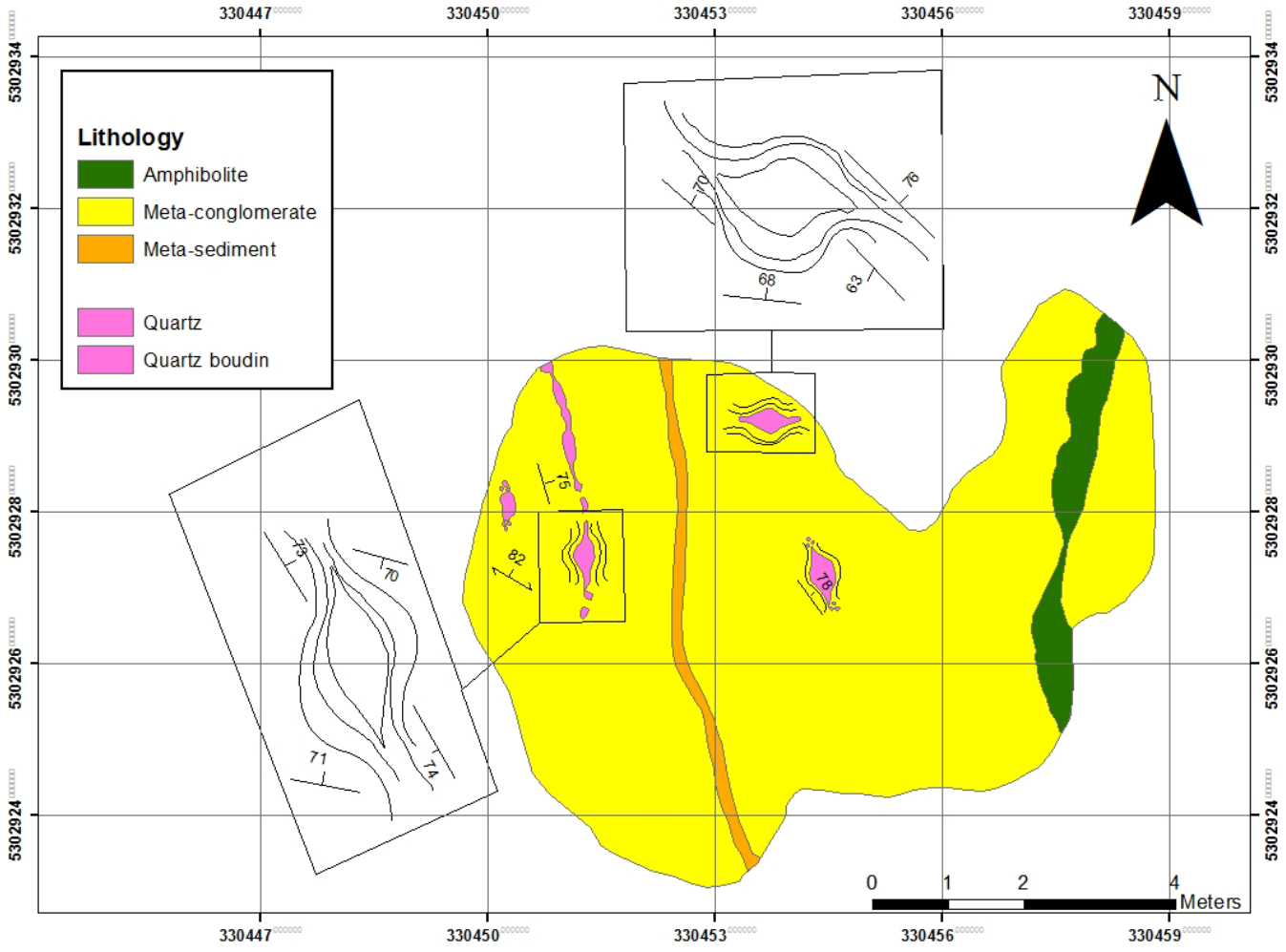

Figure 4.37: Trench map of Metaconglomerate D. The metaconglomerate and amphibolite strike nearly north–south with a northeastern, steep dip consistent with the centre of the regional "Z–shape" fold. The amphibolite has been boudinaged north–south. The quartz boudins have been boudinaged similarly to the amphibolite and a few are rotated CCW.

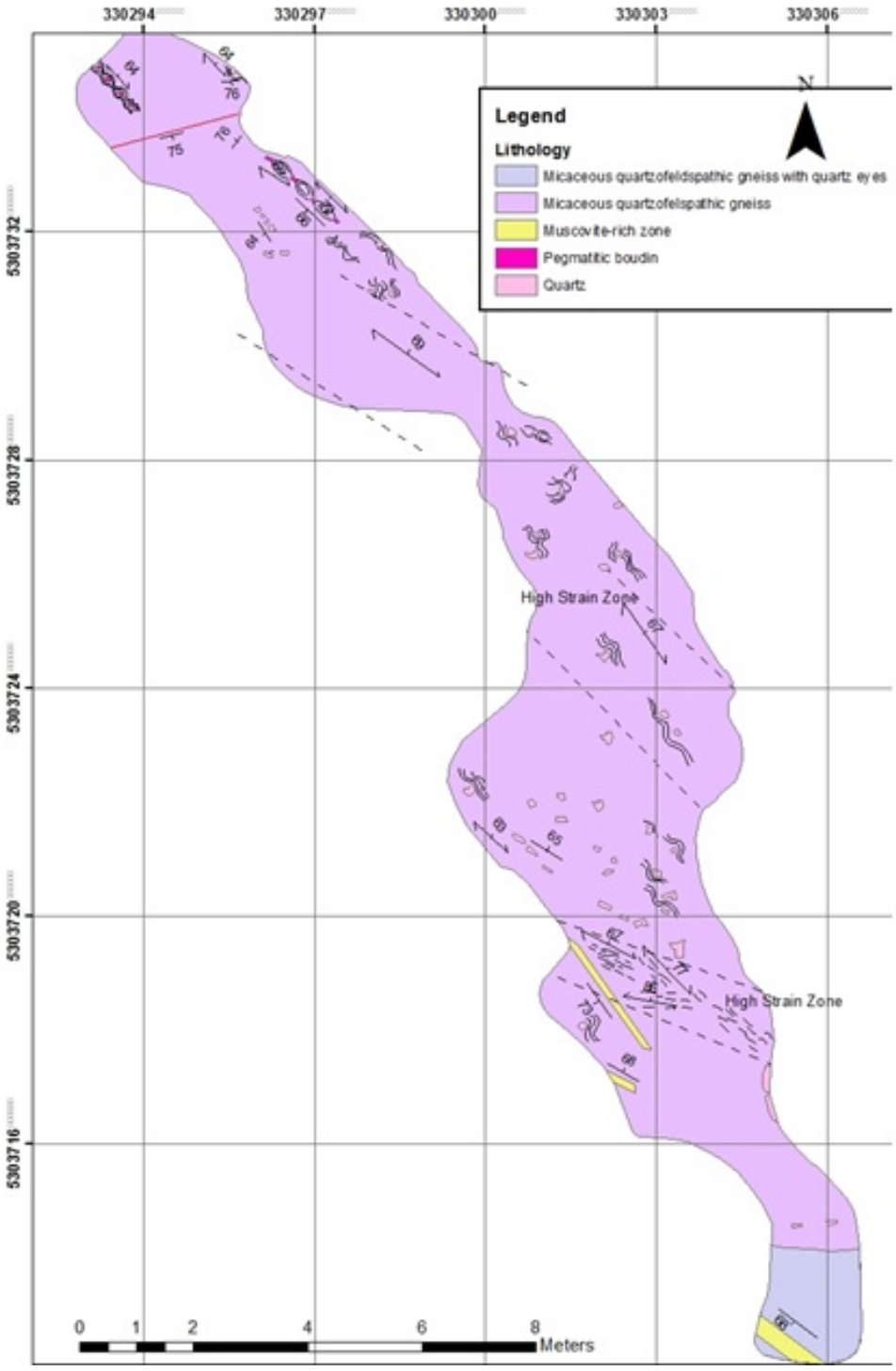

Figure 4.38: Trench map of Micaceous Quartzofeldspathic Gneiss E (A). The quartzofeldspathic gneiss has muscovite–rich zones, areas of high–strain visually based on grainsize reduction in quartz and feldspars, tightness of foliation spacing, and numerous quartz and pegmatite boudins rotated CW and CCW. The mafic dyke has intruded perpendicular to extension. Quartz boudins have been rotated both CW and CCW.

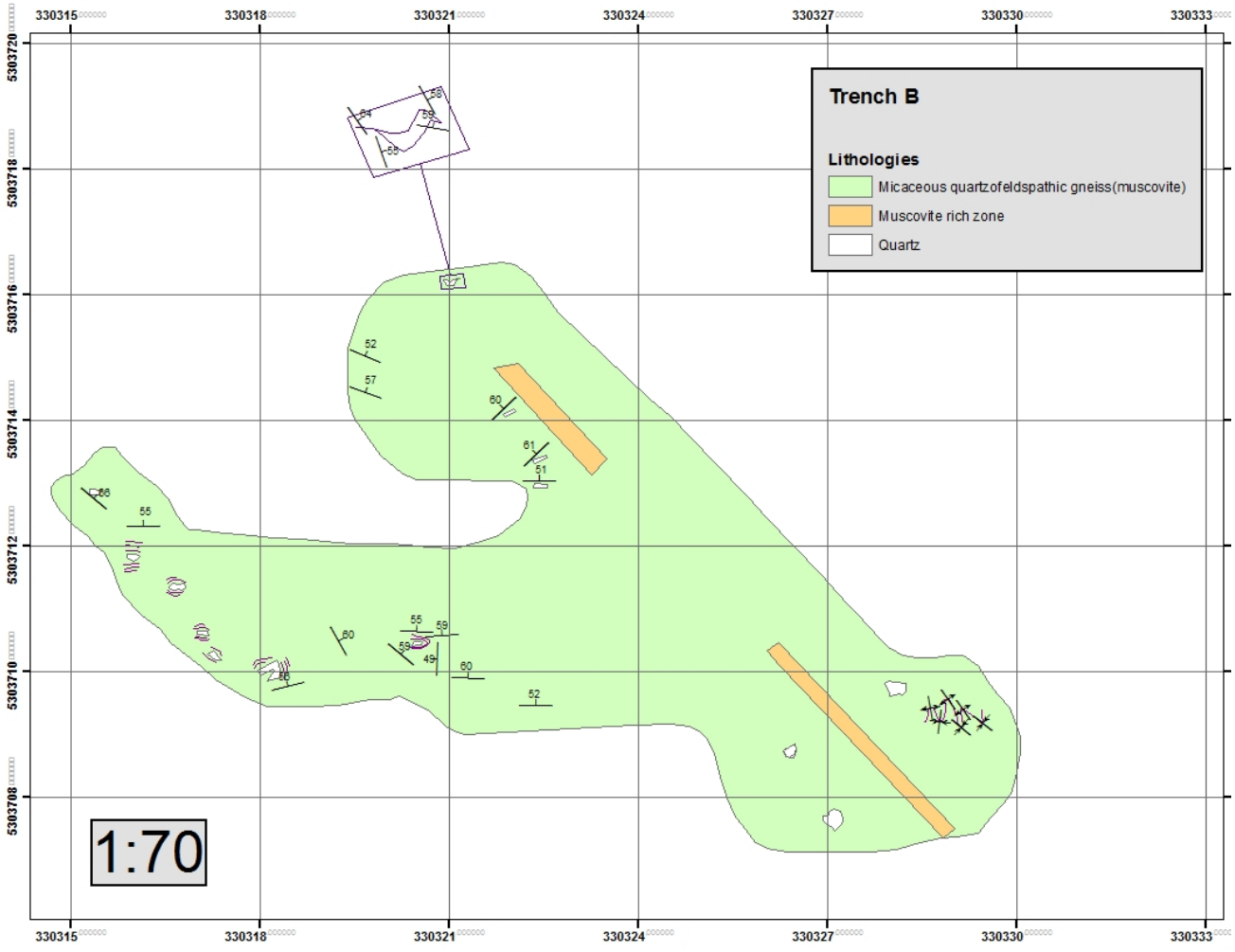

Figure 4.39: Trench map of Micaceous Quartzofeldspathic Gneiss E (B). The Trench map of Micaceous Quartzofeldspathic Gneiss E (A). The quartzofeldspathic gneiss has muscovite–rich zones that strike northwest–southeast and dip north and numerous CCW rotated quartz boudins and foliation boudins.

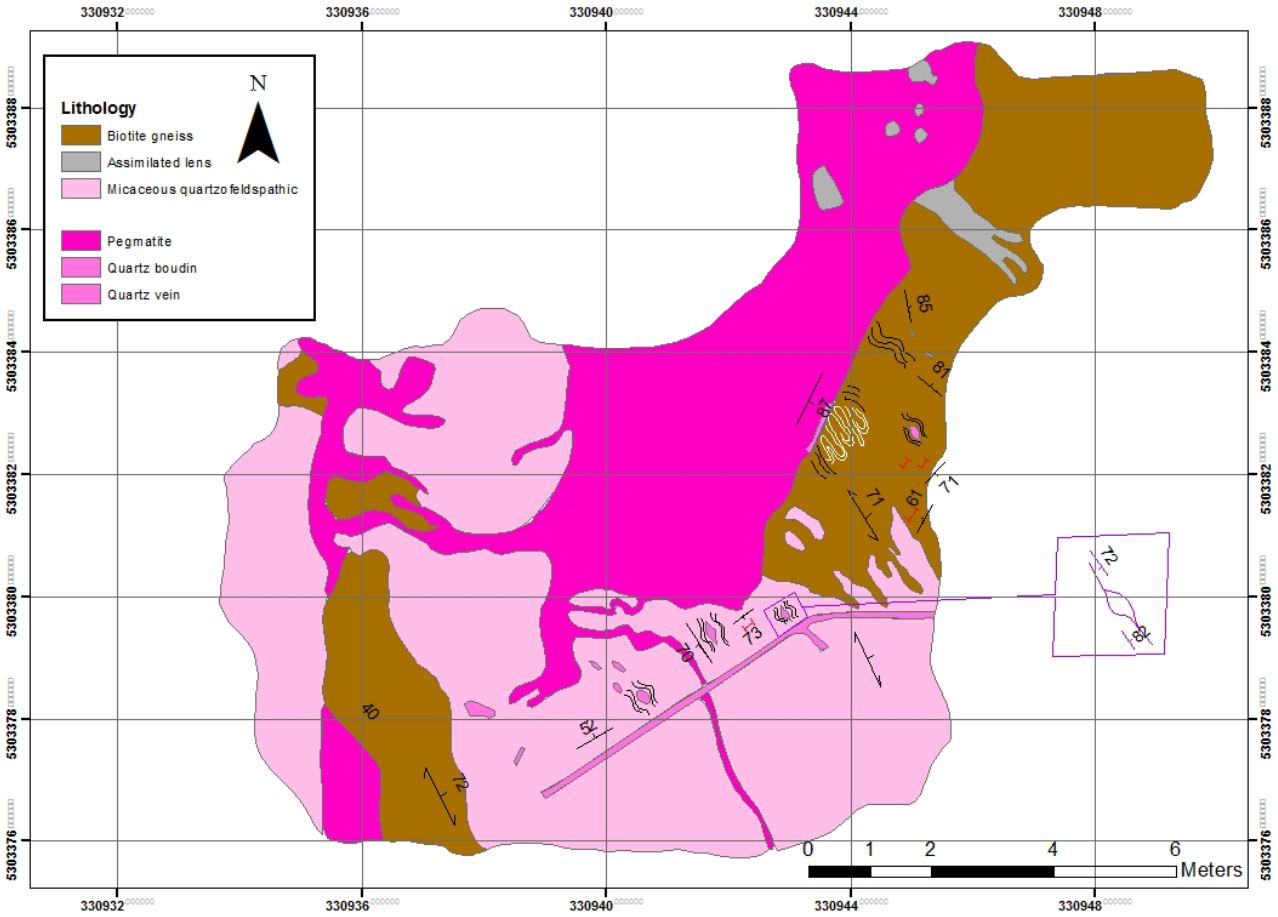

Figure 4.40: Trench map of Large Pegmatite F. The strike is generally northwest–southeast with steep dips to the northwest as well as southeast. The biotite gneiss has experienced dextral strike–slip, subsolidus deformation. The quartzofeldspathic gneiss has muscovite–rich zones while the biotite gneiss lacks muscovite. Partially assimilated lenses of quartzofeldspathic gneiss with muscovite are in both the pegmatite and biotite gneiss. The boudins and potassium feldspar lamellae have been unrotated CW and CCW.

The Garnet–biotite Gneiss Trench G hosts subeconomic gold mineralization and continues to the Borden Mine ore zone at depth (Fig. 4.41). Amphibolite (green), biotite schist (brown), muscovite–quartzofeldspathic gneiss (purple), garnet–hornblende–biotite–muscovite schist (orange), pegmatite (pink), and a mafic (diabase) dyke (grey) are the lithologies present in this trench. The presence of trace pyrrhotite at only one location in the trench clearly represents the low percentage of sulphides present at the Borden Mine and surrounding area. The muscovite–defining schistosity and overprinting gneissosity in amphibolite with pegmatite is characteristic of gold mineralization in the Borden Mine (Atkinson, 2013). Along the boundary of muscovite–quartzofeldspathic gneiss the amphibolite transitions into biotite schist and both strike west–northwest and dip 80º to the south. The mafic dyke strikes perpendicular to foliation and boudinage direction.

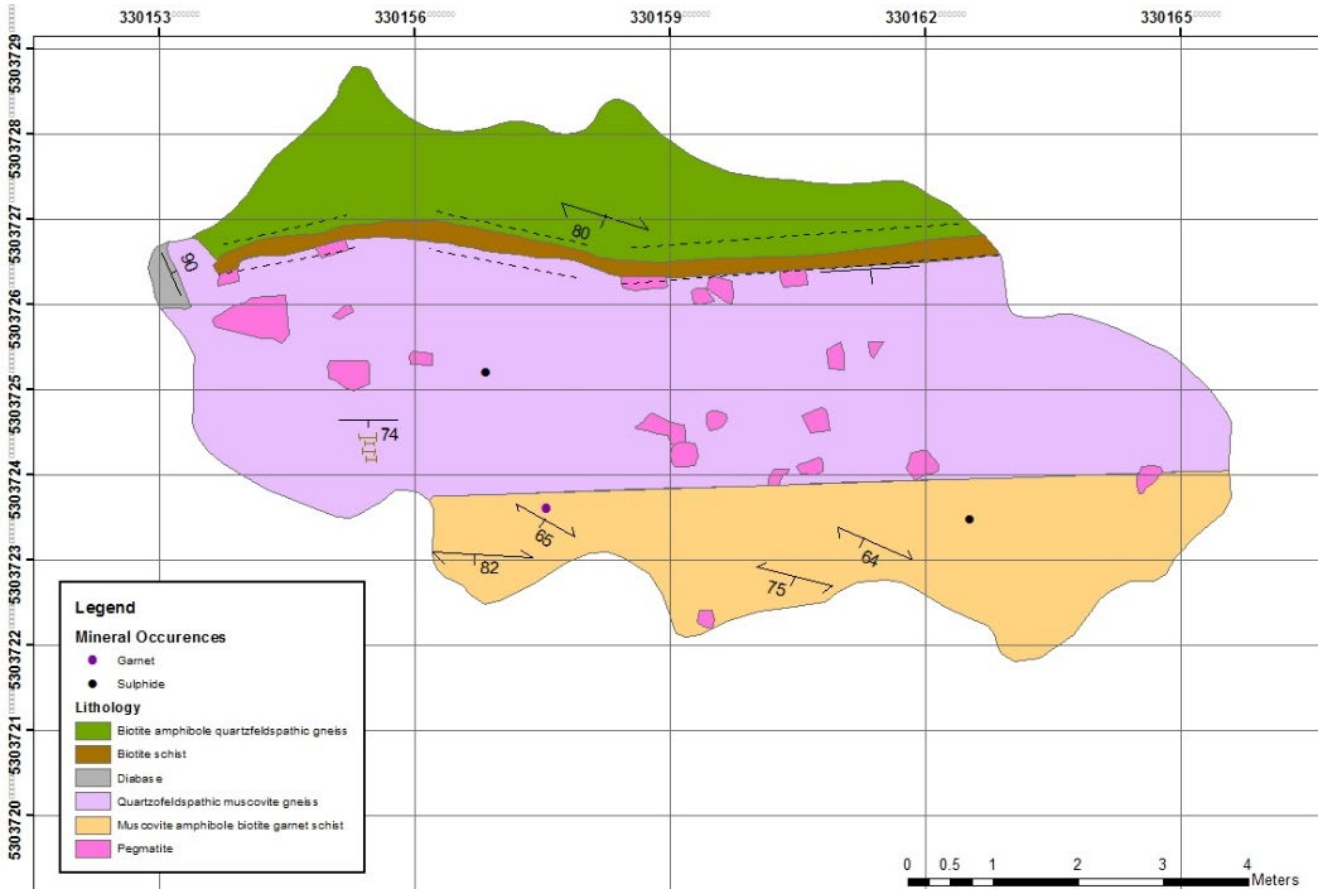

Figure 4.41: Trench map of Garnet–biotite gneiss G. The muscovite–amphibole–garnet–biotite gneiss and schist (low–grade ore zone) in the lower portion of the trench has an overprinting, northwest–striking, southerly dipping schistosity defined by muscovite and is the only lithology with sulphide (magnetic pyrrhotite) mineralization in the trench. The biotite–amphibole–quartzofeldspathic gneiss (migmatized amphibolite) at the top of the map transitions into highly strained biotite schist at the muscovite–rich quartzofeldspathic gneiss. Numerous boudins of pegmatite are located throughout the quartzofeldspathic gneiss and the low–grade ore zone of muscovite–rich garnet–amphibolite schist. The northwest–striking schisosity is consistent with the regional "Z–shape" fold. The mafic dyke has intruded perpendicular to boudinage.

The Folded Metaconglomerate H and I trench maps expose more of the regional "Z–shape" fold (Figs. 4.4–4.43). Slivers of amphibolite, metaconglomerate, quartzofeldspathic gneiss, and pegmatite are folded and define boudin and pinch–and–swell structures and plunge 56º towards the southwest. Mafic dykes strike perpendicular to boudinage.

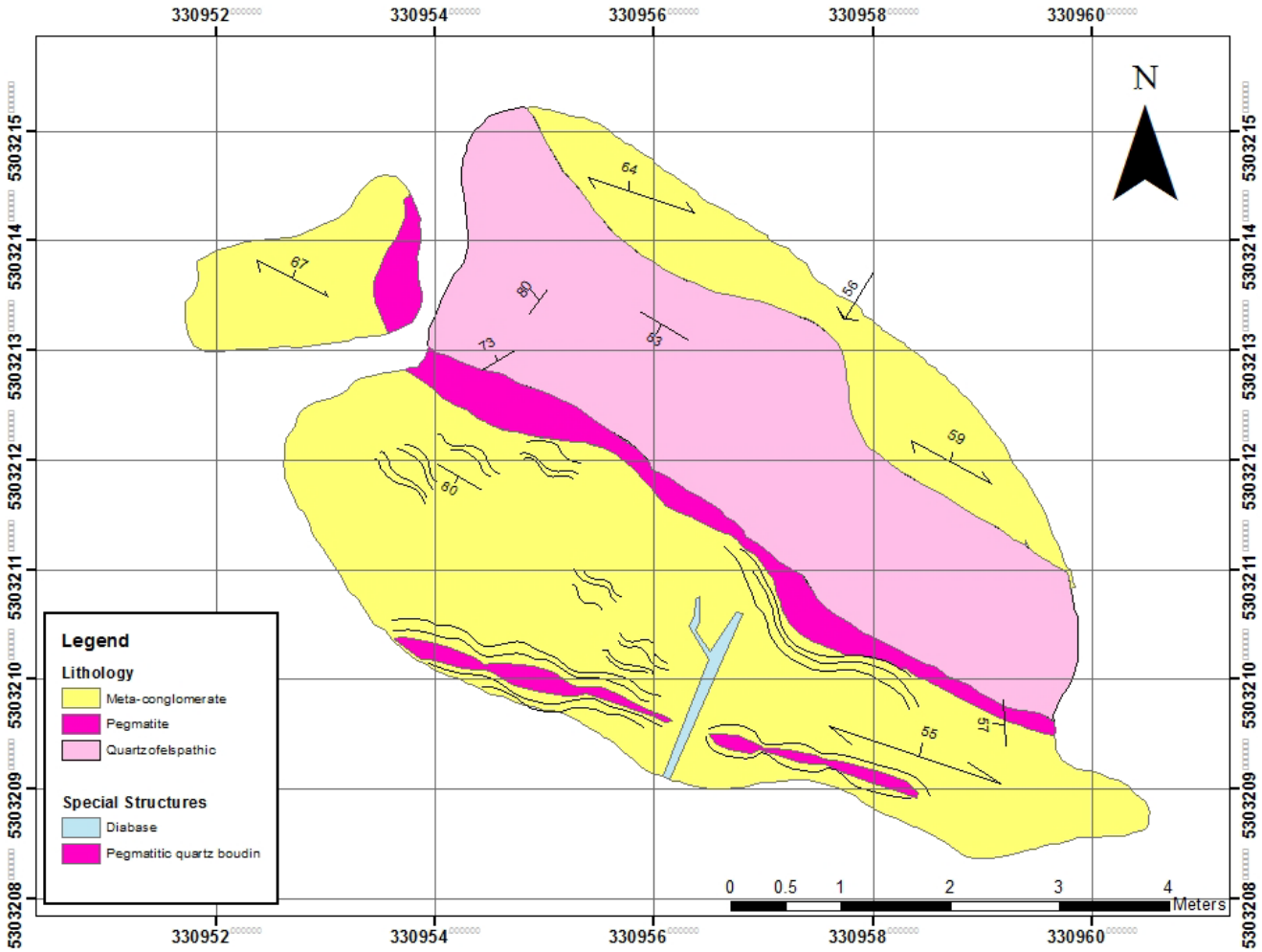

Figure 4.42: Trench map of Folded Metaconglomerate H. The metaconglomerate is characteristic of the region with infilled pegmatite and quartzofeldspathic lithologies. The general strike is northwest–southeast to northeast–southwest with a northern dip and moderate fold hinge towards the southwest. The clast lineation is horizontal to subhorizontal. The youngest lithologies of pegmatite and quartzofeldspathic gneisses have been boudinaged and display pinch–and–swell structures. The pinch–and–swell has a moderately plunging, gentle fold lineation which is like the ore zone. The diabase outcrops perpendicular to boudinage and is well displayed in this trench.

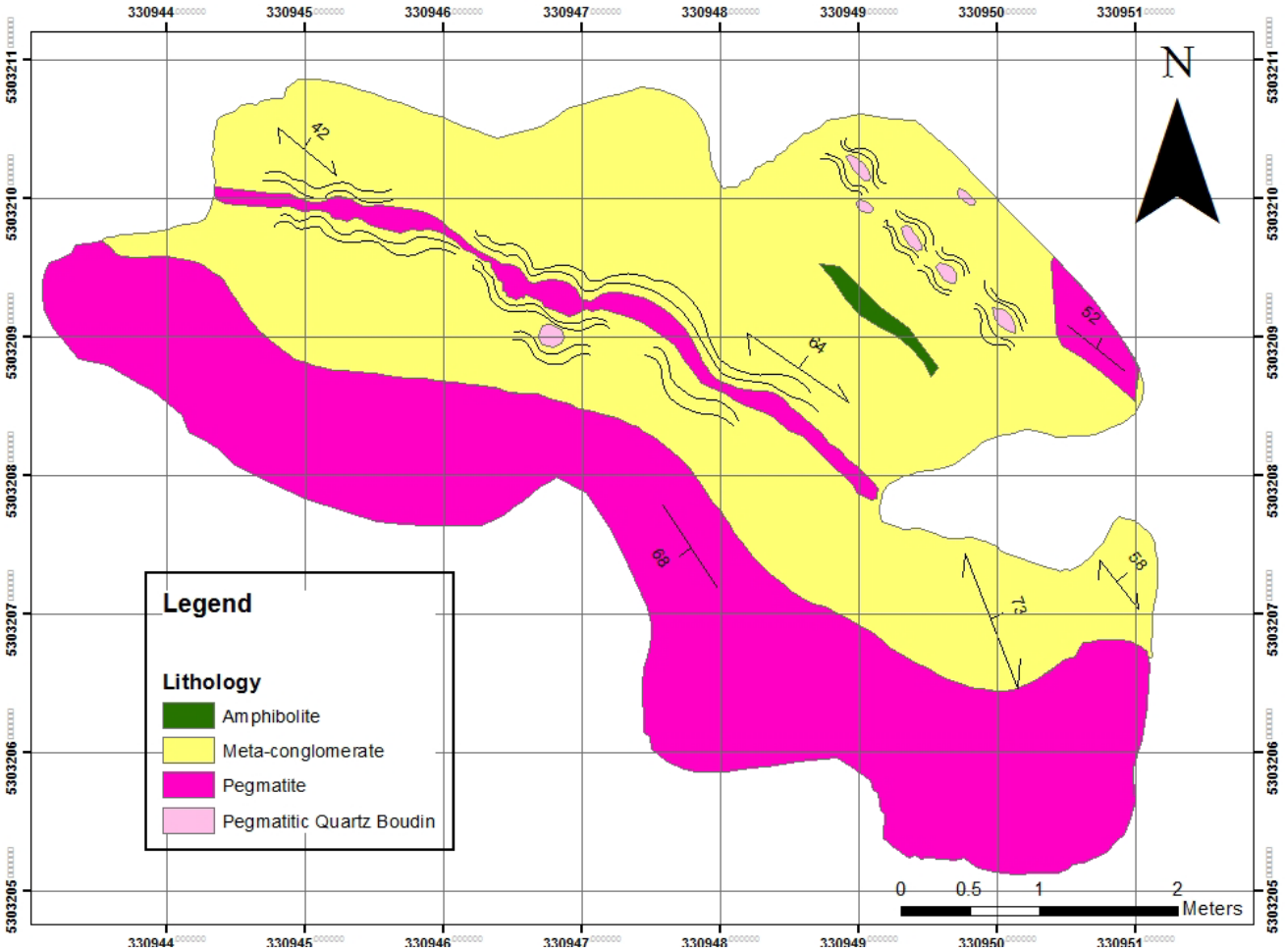

Figure 4.43 Trench map of Folded Metaconglomerate I. The metaconglomerate is characteristic of the region with infilled pegmatite and quartzofeldspathic lithologies. The northwest–southeast striking foliation and northern and southern dip is consistent with the centre of the regional "Z–shape" fold. The youngest lithologies of pegmatite and quartzofeldspathic gneisses have been boudinaged and display pinch–and–swell structures. The symmetrical, unrotated quartz boudins are extended northwest–southeast.

Two populations of plagioclase, microcline, garnet, hornblende, pyroxenes, and quartz microscopic structures were identified in thin section. An earlier population of microscopic structures displays evidence of partially to fully recrystallized and recovered grains and grain boundaries in upper amphibolite facies to granulite facies stable metamorphic mineral assemblages and a later population lacking significant dynamic recrystallization and recovery with numerous features of crystal–plastic deformation features (i.e., deformation twins, undulatory extinction, sutured grain boundaries, subgrain formation, grain boundary bulging, subgrain rotation, patchy– to chessboard–extinction textures, ribbons, boudins, mineral fish, etc.) in lower amphibolite (formally epidote–amphibolite facies) and lower metamorphic mineral assemblages (Figs. 4.8, 4.9–4.12, 4.44–4.45). The earlier, recrystallized population includes much smaller, subgrains with regime 1 microstructures in quartz while the later,

least recrystallized population includes regimes 2 and 3 microstructures in quartz (Tullis, 1992). Garnet and perthite feldspar also define microstructures similar to the second population of quartz with subgrain formation, ribbons, boudins, and mineral fish. Perthite lamallae are visible in hand sample and thin section, commonly defining upright folds the have been rotated CCW and CW. In thin section the perthitic lamallae is most commonly flame lamallae. Therefore, high–temperature deformation occurred during prograde and retrograde metamorphism as well as late–stage plutonism in the subsolidus.

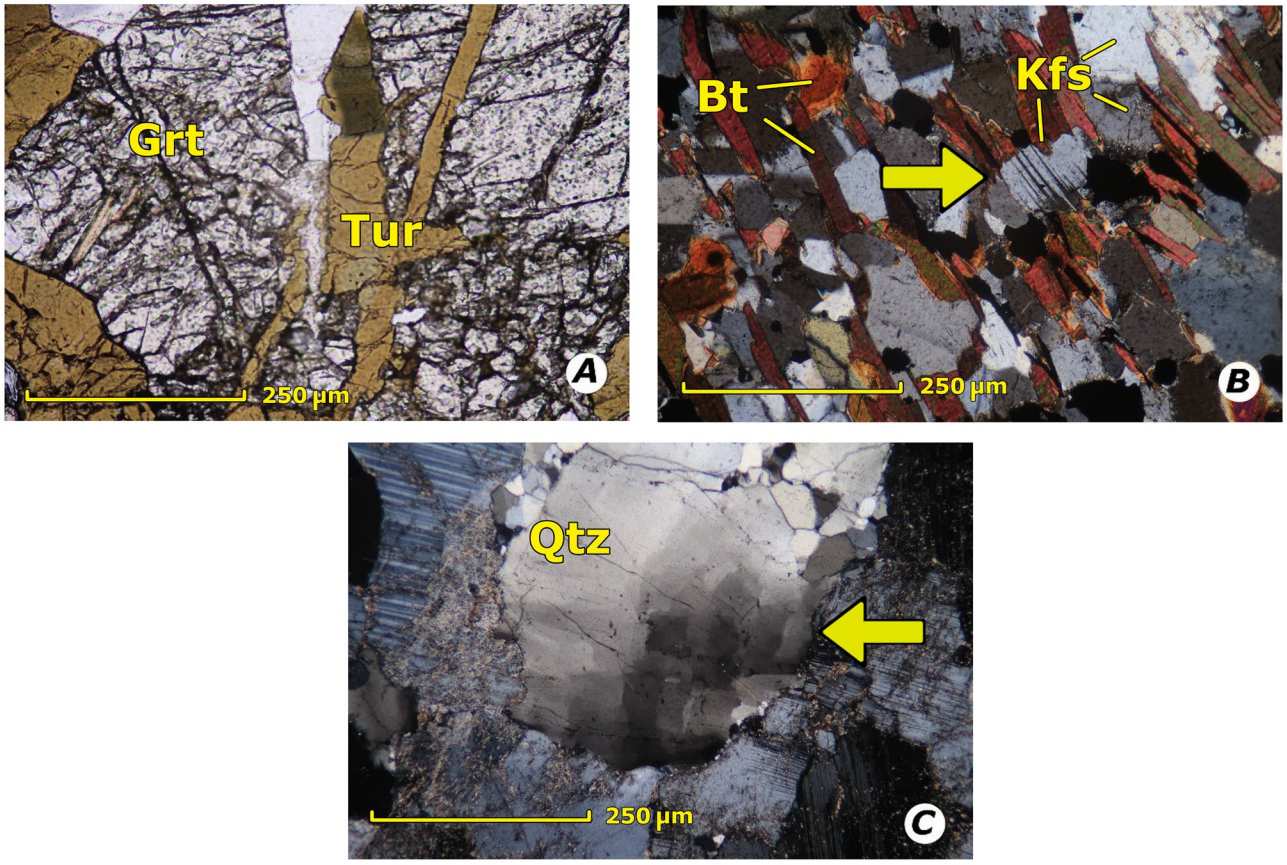

Figure 4.44: Common microstructures in high–grade ore zones at Borden Mine (A, PPL, PVS022) healed, quartz–tourmaline fractured garnet in overprinting schistose fabrics in garnet–amphibolite and granulite boudins in amphibolite which provide evidence for failure in rigid minerals during overall regimes of crystal plastic deformation, predominately fracture during dislocation creep and diffusion creep, (B, XPL, PVS032) Mylonites in amphibolite display dynamic recovery and recrystallization in plagioclase with minimal deformation twins and subgrains (arrow), (C, XPL, PVS065) Boudinaged quartz in BIF with checkerboard microstructures (arrow) indicating dislocation creep at granulites–facies temperatures.

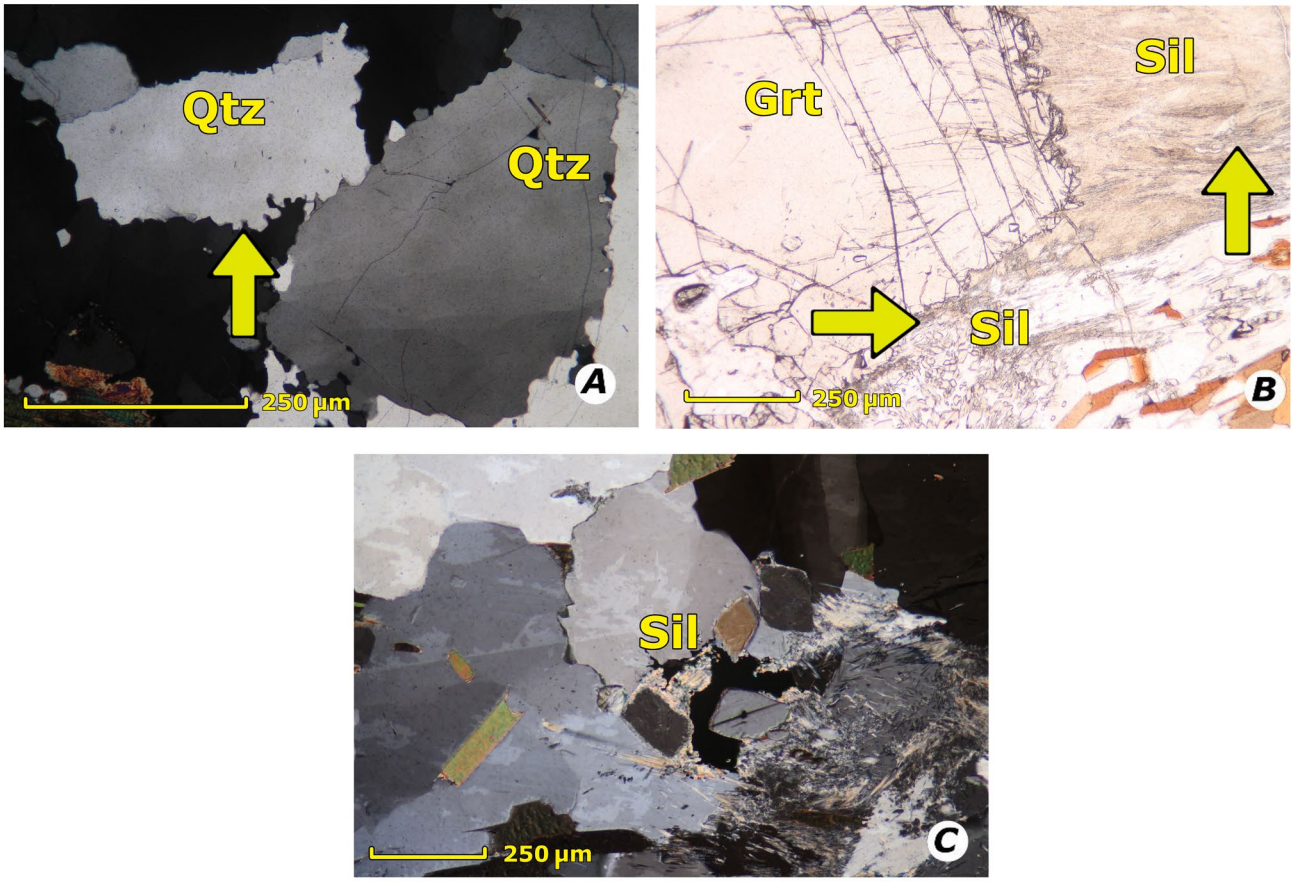

Figure 4.45: Common microstructures in high–grade ore zones at Borden Mine (A, XPL, PVS067) Quartz and quartz boudins from BIF directly outside of high–grade ore zones in subeconomic ore display evidence of a lack of recovery and recrystallization with serrated, irregular grain boundaries and subgrains (arrow) present compared to those directly within the ore zone, (B, PPL, PVS024), Fibrolite sillimanite defines the lineation in the garnet boudin necks (top left, upwards arrow) and prismatic sillimanite is replaced by fibrolite in matrix (bottom centre, sideways arrow) which are typical retrograde amphibolite reactions after to granulite facies in structures which may accommodate the new crystal growth (perpendicular to lineation), (C, XPL PVS219), Prismatic sillimanite and microcline replaced by fibrolite sillimanite and muscovite adjacent to quartz boudin throughout the photomicrograph denote amphibolite reactions after prograde granulite metamorphism.

Quartz CPO (crystallographic preferred orientation) data is presented below in an equal–area projection, lower hemisphere stereonet projections oriented normal to the predominant foliation and parallel to the predominant lineation (Fig. 4.46). Point and contoured data are presented together with number of crystals measured (n= 705) with data that had greater than 90% geometric quality and retardation quality used. The dark contours denote the highest density data and provides evidence of basal <a> and prism [c] slip in quartz and are consistent with early, prograde sinistral kinematics and continued, high–temperature simple shear to non–coaxial simple shear (dextral) and flattening consistent with regional– to trench–scale structural mapping (Wilson et al., 2007; Festa, 2009; Barth et al., 2010).

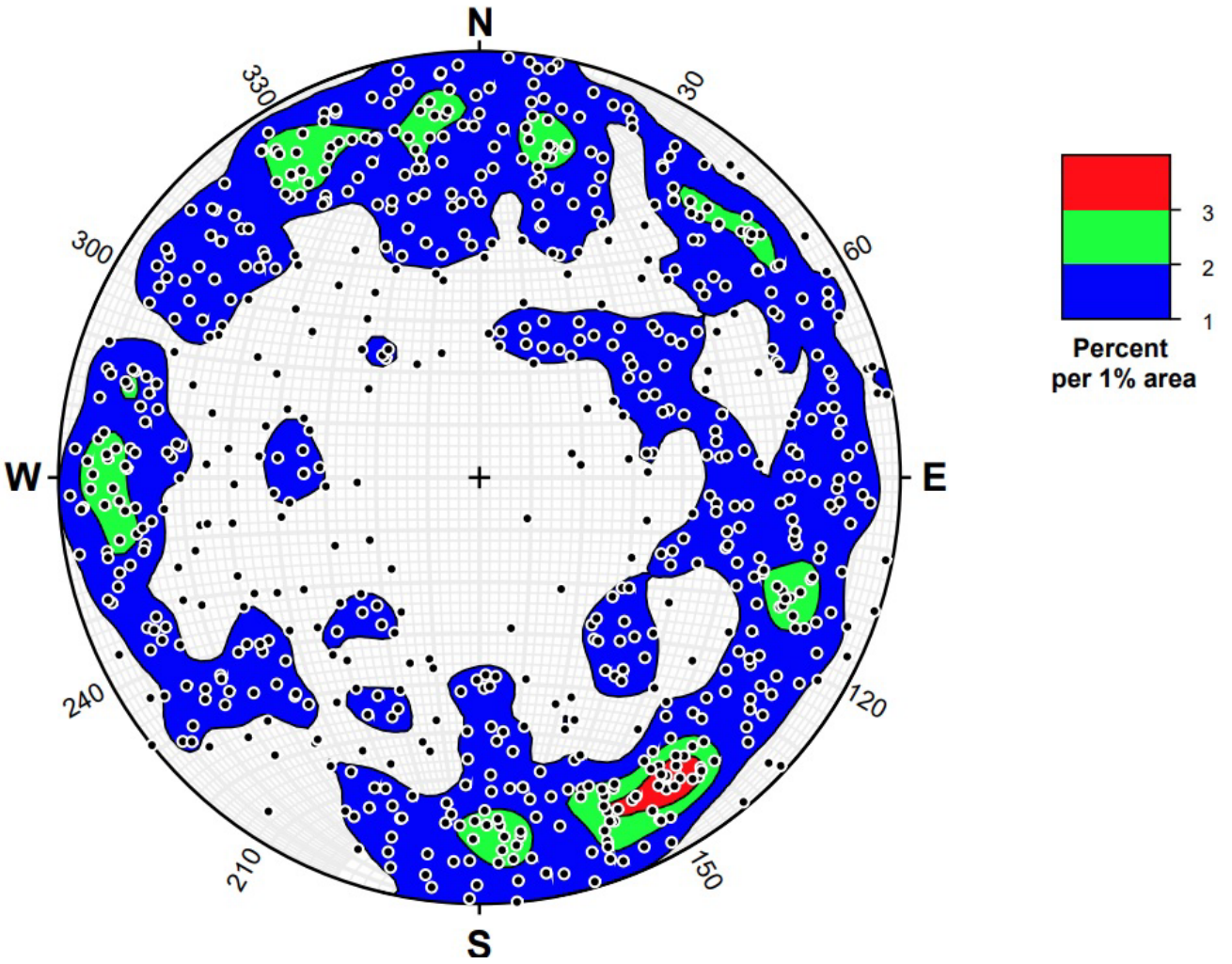

Figure 4.46: Equal area stereonet showing crystal preferred orientation (C–axis CPO, n= 705) of quartz in garnet–augite gneiss (UTM 16N 5302031/0330452). Black points denote samples with increasing population with 20% contour gradient. Data that had greater than 90% geometric and retardation quality were used. No points with greater than 260 nm retardation were used to ensure selections were quartz. The red and green contours indicate an asymmetrical pattern that is consistent with predominantly prism [c] slip during plane strain, under sinistral, non–coaxial shear deformation, and high–temperatures consistent with grain boundary migration.

4.3 Geochemistry

4.3.1 Geochemistry of mafic lithologies

Whole rock geochemistry further defines the lithologies described in the field and drill cores (Appendix C) and thin section (Appendix D). The whole rock geochemistry samples were collected based on textures and proximity (or potential) to gold mineralization. The least altered lithologies collected from the field, trenches, and drill cores in the Borden Mine, Chapleau Belt, WGD, and KSZ can be generally categorized into ultramafic, mafic, intermediate, and felsic using whole rock and trace element geochemistry with the aid of petrography. Within each category the predominant differences in geochemistry are controlled by modal percentages of each mineral, presence of minor to trace minerals, and textures (e.g. porphyritic versus aphanitic) and not related to differences in location. Further study is required to assess differences between geographical locations.

As all lithologies experienced metamorphism and alteration to some degree, element mobility was assessed in the least–altered samples from this study and by Gamelin (unpublished BSc. thesis, 2015) (Figs. 4.47–4.48). Samples used for geochemistry collected in this study include: PVS001–004, PVS009–011, PVS014, PVS019, PVS023, PVS025–027, PVS029, PVS043–047, PVS158, PVS166. Samples collected by Gamelin include GG009, GG013–015, GG018–019. Samples with gold mineralization generally display the greatest element mobility (Figs. 4.47–4.48, grey dots), and have been removed from some geochemistry analyses as they may be considered outliers.

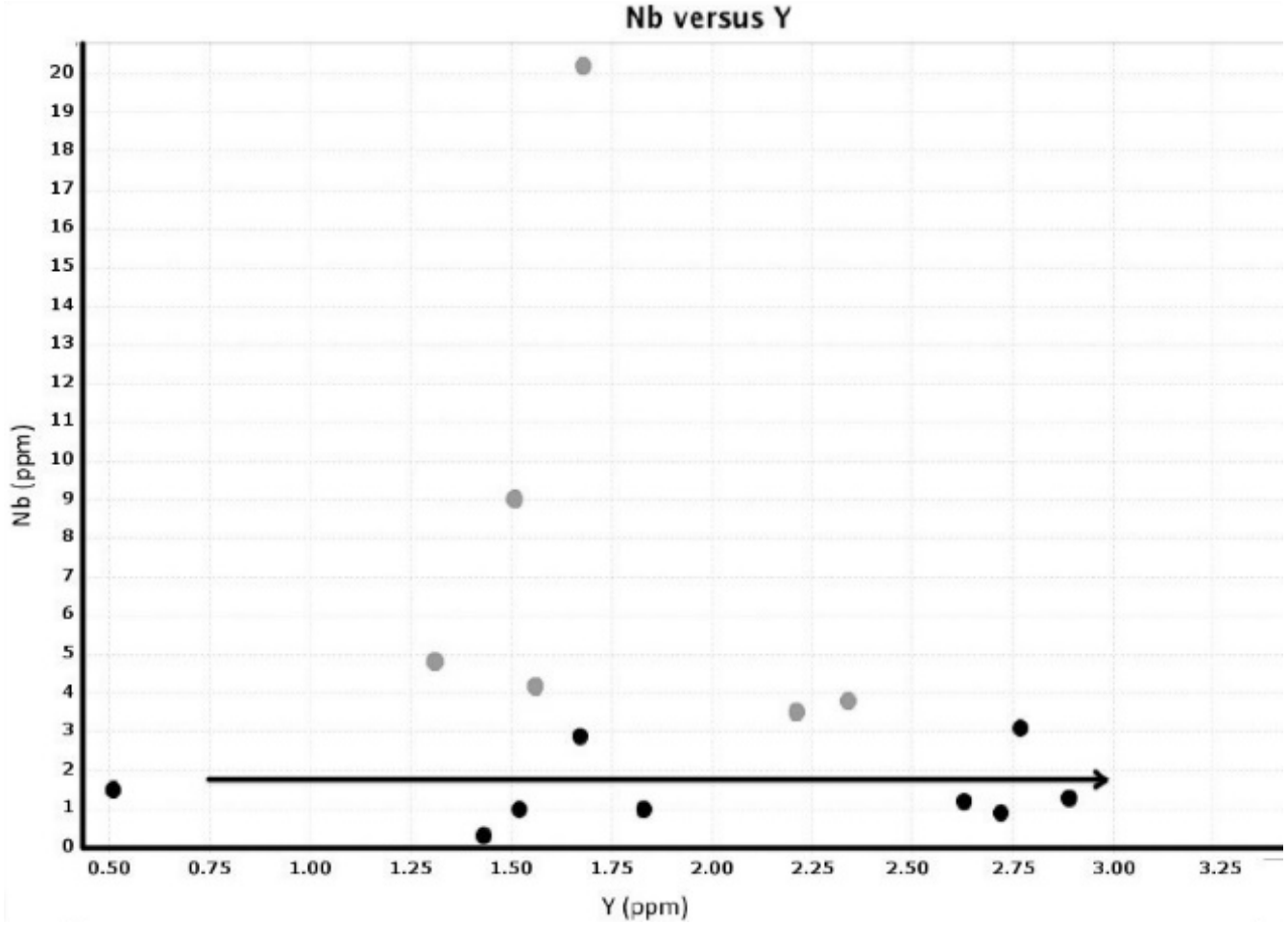

Figure 4.47: Representative sample of mafic lithologies to test trace element mobility using a Nb versus Y diagram discrimination diagram. Note the barren samples (black dots) have the least mobility while the mineralized samples have the most mobility (grey).

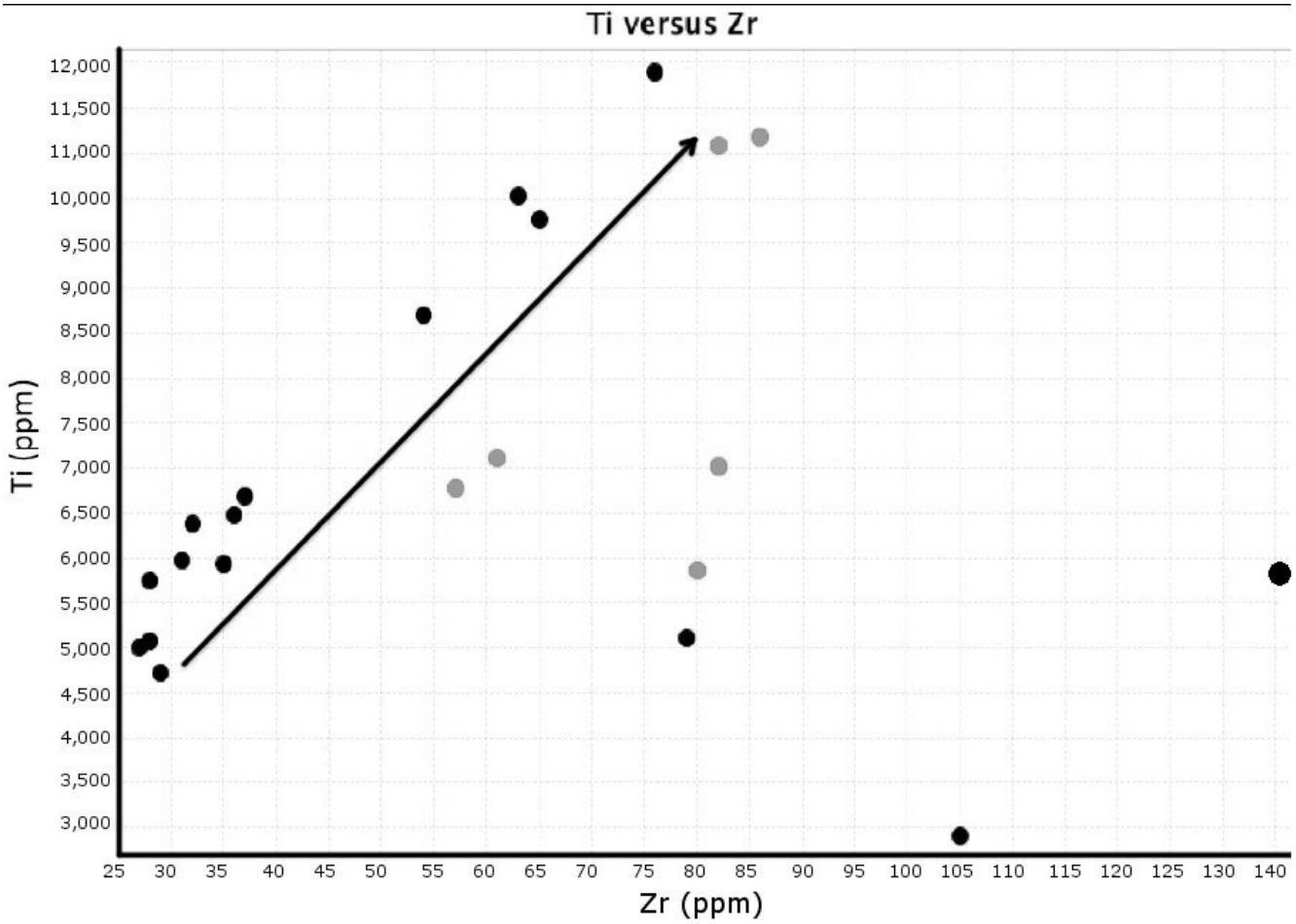

Figure 4.48: Representative sample of mafic lithologies to test trace element mobility using a Ti versus Zr diagram discrimination diagram. Note the barren samples (black dots) have the least mobility while the mineralized samples have the most mobility (grey).

The IUGS classification using total silica to classify the lithologies in the study is generally sufficient due to element mobility. The total silica versus alkali diagram (TAS) generally is able to categorize the lithologies but is affected by mobility of alkali elements, noted in Ti/Zr and Nb/Y (Figs. 4.47–4.50) (Gamelin, G., unpublished BSc. thesis, 2015).

Therefore, total silica in combination with elevated Mg, Ni, and Cr is generally sufficient to classify the majority of the least–altered lithologies. Ultramafic lithologies are chlorite–rich samples with <40% SiO_2 with variably elevated Mg, Ni, and Cr. The mafic lithologies are typically ~50% SiO_2, 15–2.5% Mg, and pronounced Ni and Cr. Intermediate and felsic lithologies are defined by 60% SiO_2, <2.5% Mg and 70% SiO2 with insignificant Mg, respectfully. Pelitic geochemistry was determined from the presence of elevated silica, aluminum, alkalis, and similar to the classic study by Shaw (1956).

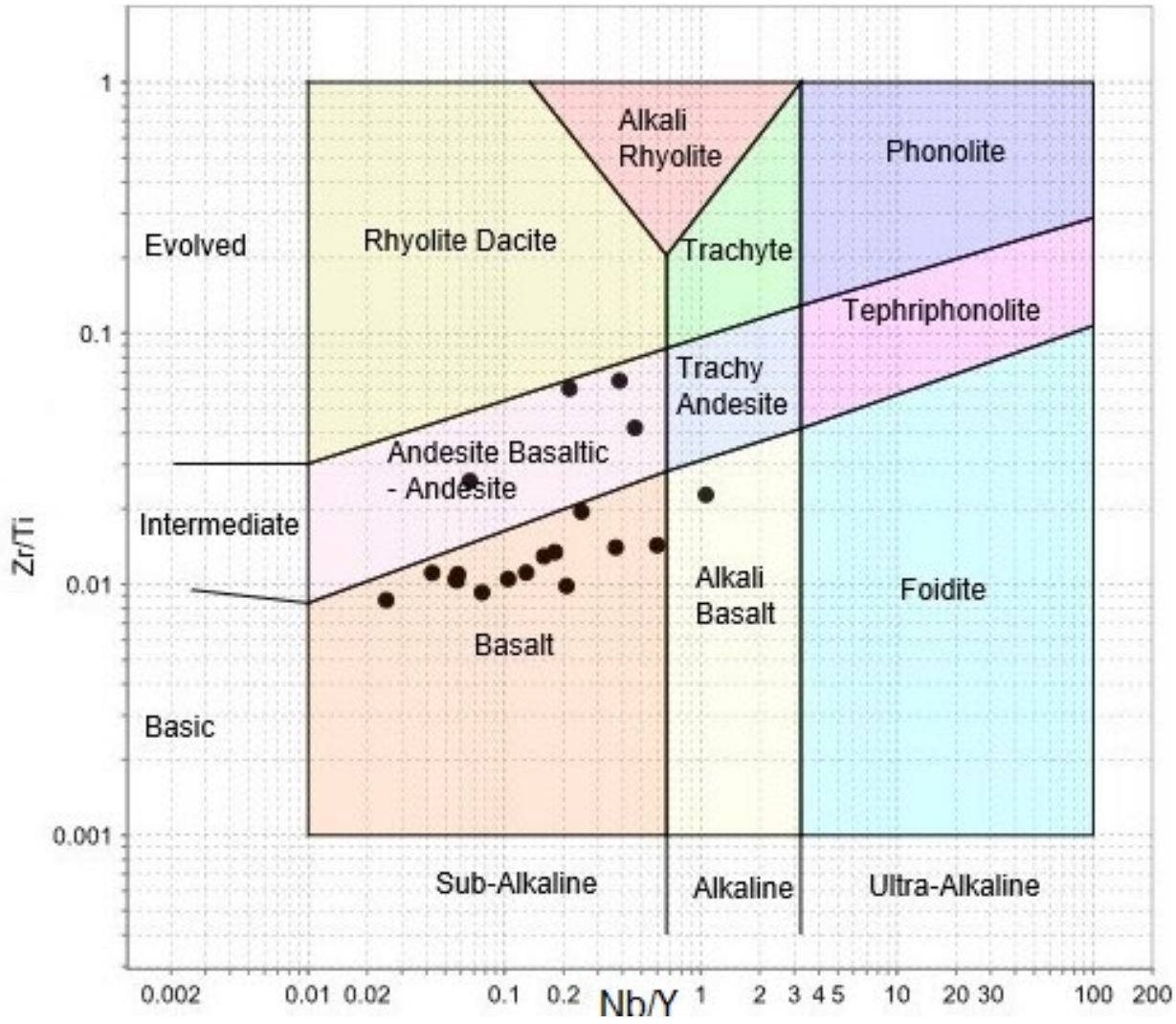

Figure 4.49: Trace element proxy TAS diagram (Zi/Ti versus Nb/Y). Note the mafic lithologies plot predominantly in the basaltic field with a few samples in the andesite basaltic – andesite field and only one sample in the alkali basalt field (Pearce, 1996).

To account for the alkali mobility, a Pearce element ratio diagram is presented, with Zr/Ti on the Y–axis acting as a proxy for silica, and Nb/Y on the X–axis acting as a proxy for total alkali content (Figs. 4.49). The proxy elements are used due to the increased mobility of major and some minor elements during high–grade metamorphism and deformation. The black circles represent the least–altered mafic samples collected from the Chapleau Belt. The majority of samples plot in the sub–alkaline region and are classified as basalt with some as intermediate.

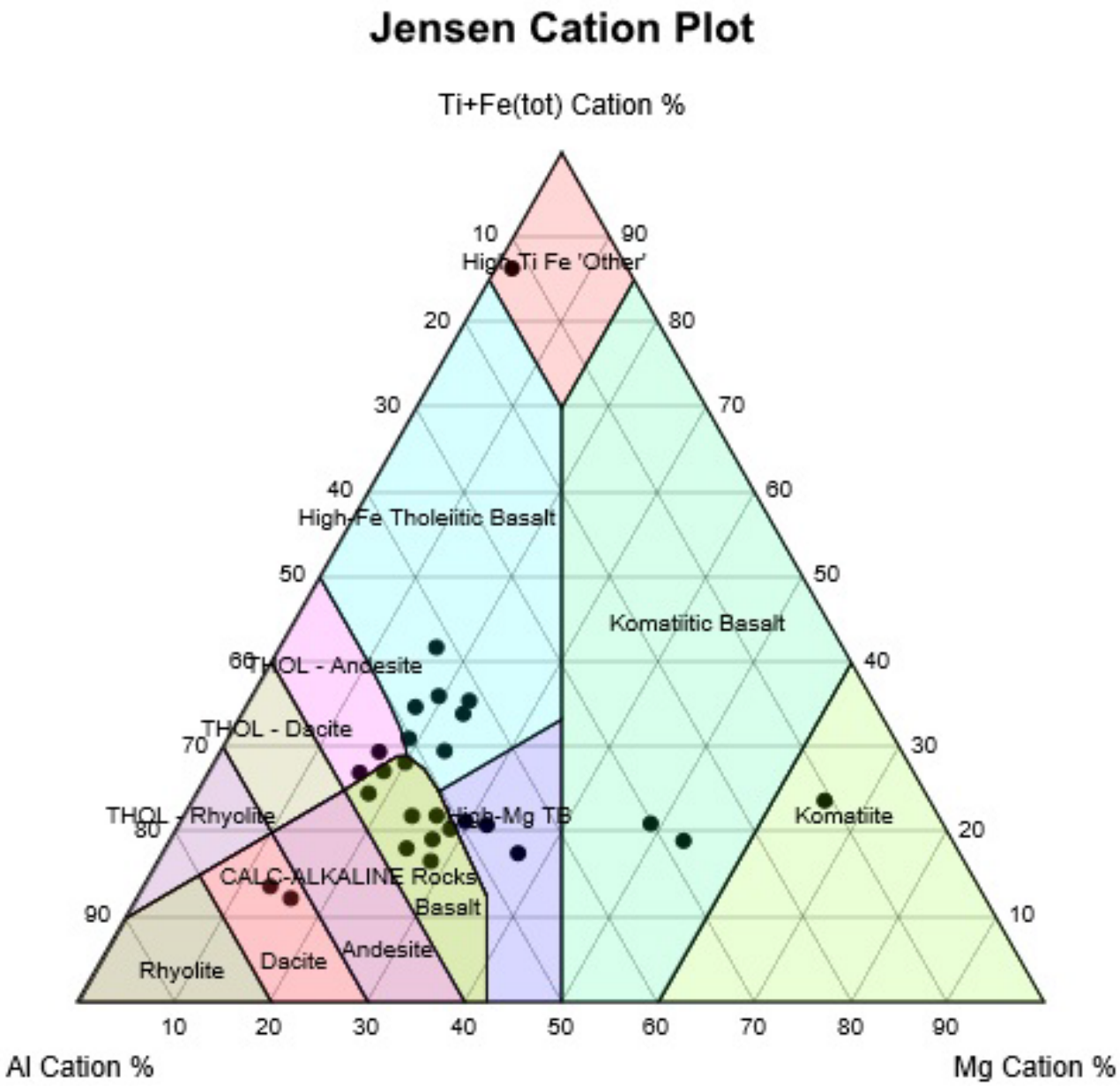

Figure 4.50: The Jensen cation plot categorizes the ultramafic to intermediate samples into the tholeiitic and calc–alkaline series with samples plotting mainly in ultra mafic to intermediate fields (Jensen, 1976).

The Jensen cation plot categorizes the least–altered ultramafic and mafic samples into calc–alkaline, tholeiitc, and komatiitic series (Fig. 4.50). The calc–alkaline samples plot in the high–Mg basalt, basalt, and dacite fields while the tholeiitic samples plot in the high–Fe and andesite fields. The mafic to ultramafic samples plot as komatiitic basalt and komatiite.

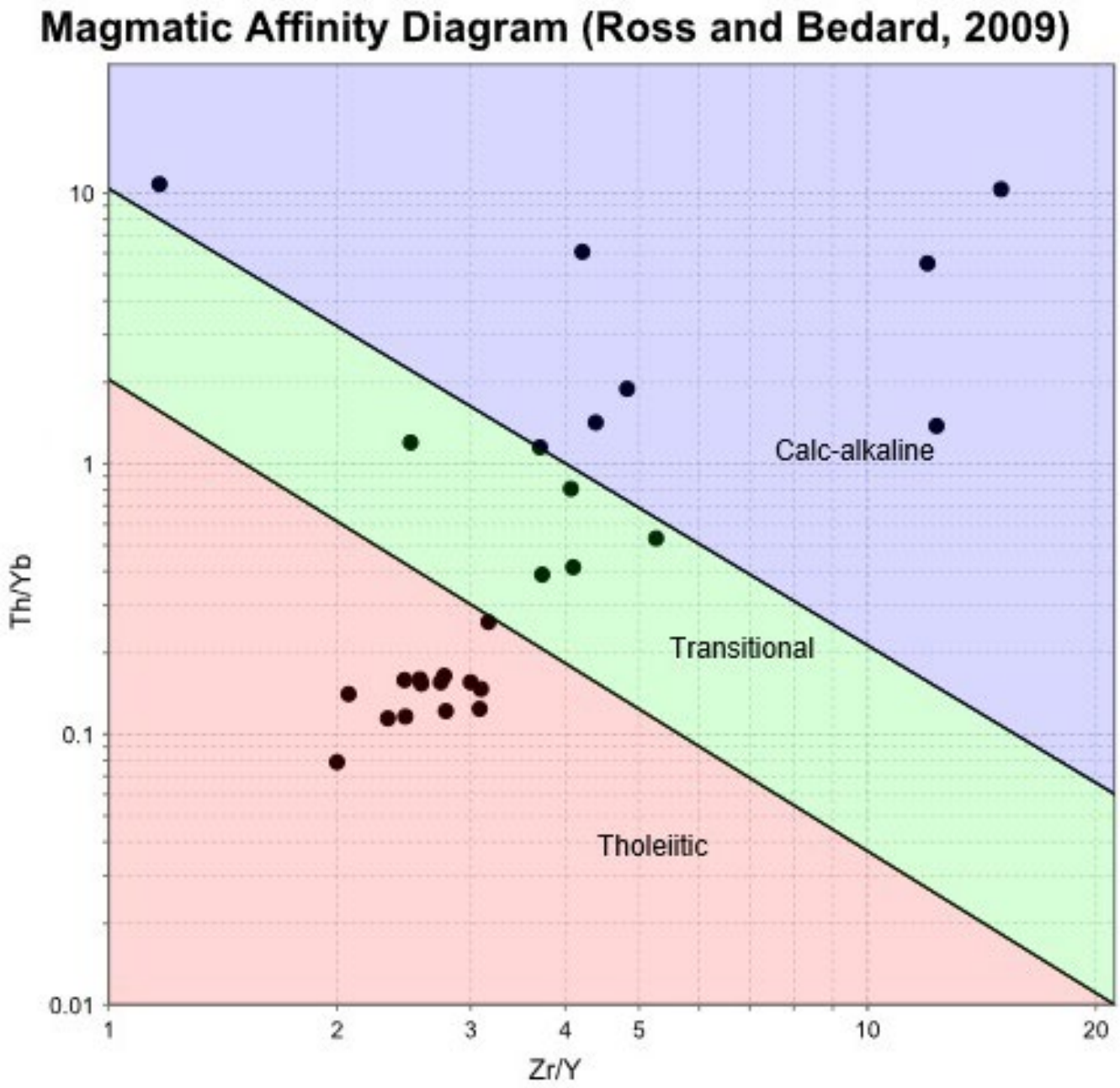

Figure 4.51: The magmatic affinity diagram comparing Th/Yb versus Zr/Y displays the range of lithologies from tholeiitic to calc–alkaline (Ross and Bedard, 2009).

Further classification comparing Th/Yb versus Zr/Y is presented in a magmatic affinity diagram (Fig. 4.51) (Ross and Bedard, 2009). Note the tight cluster of samples in the tholeiitic region, scattered samples in the calc–alkaline region, and five samples within the transitional region.

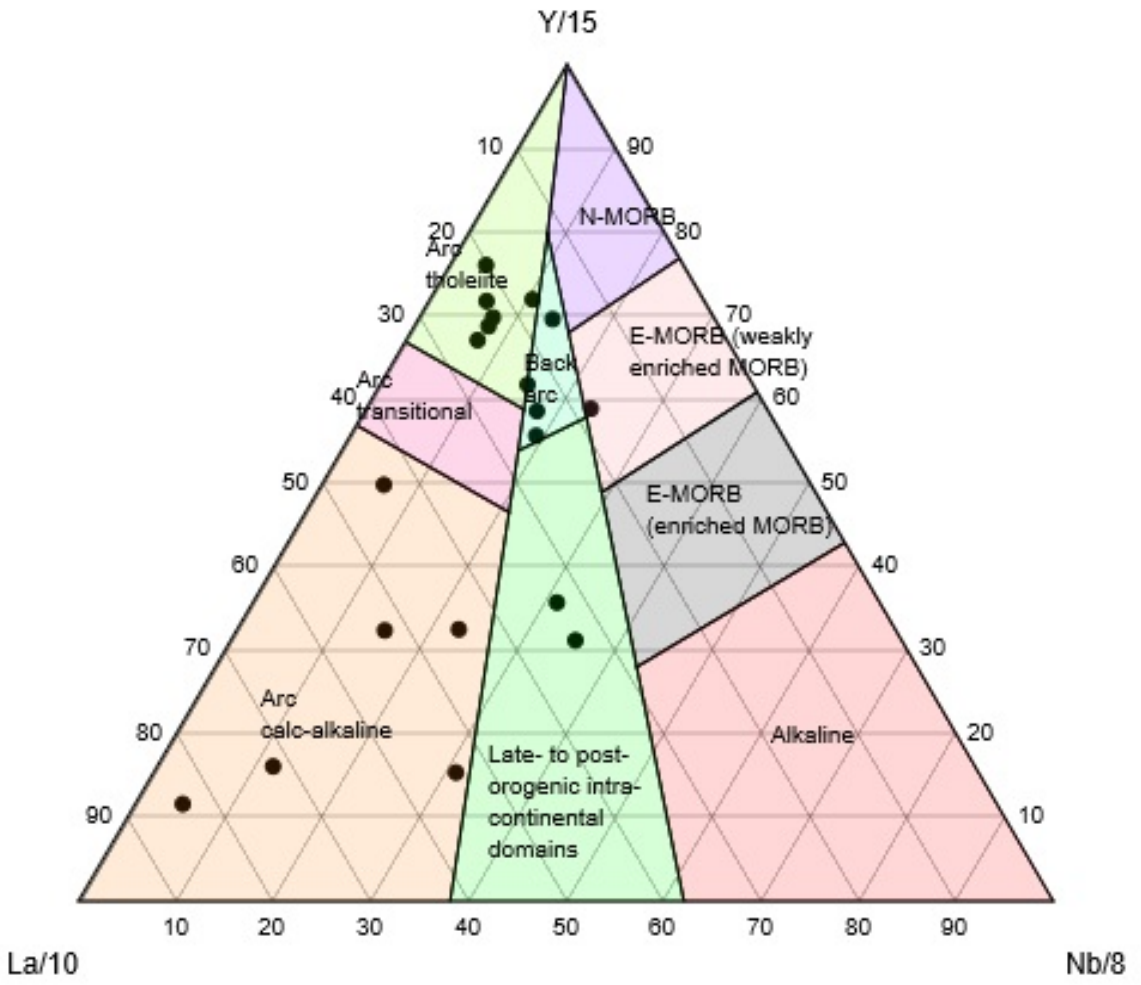

Figure 4.52: The tectonic classification of mafic igneous rocks classifies the samples by tectonic setting, including tholeiite, backarc, arc calc–alkaline, and late– to post–orogenic intra–continental domains (Cabanis and Lecolle, 1989).

Additional discrimination diagrams were used to better constrain the potential tectonic environments in which these mafic lithologies were formed. The tectonic classification of mafic igneous rocks (Cabanis and Lecolle, 1989) displays the wide range in potential tectonic regimes (Fig. 4.52). There is a clustered population in the arc tholeiite and backarc fields and more spread in the arc calc–alkaline field. Two samples plot in the late– to post–orogenic intra–continental domains.

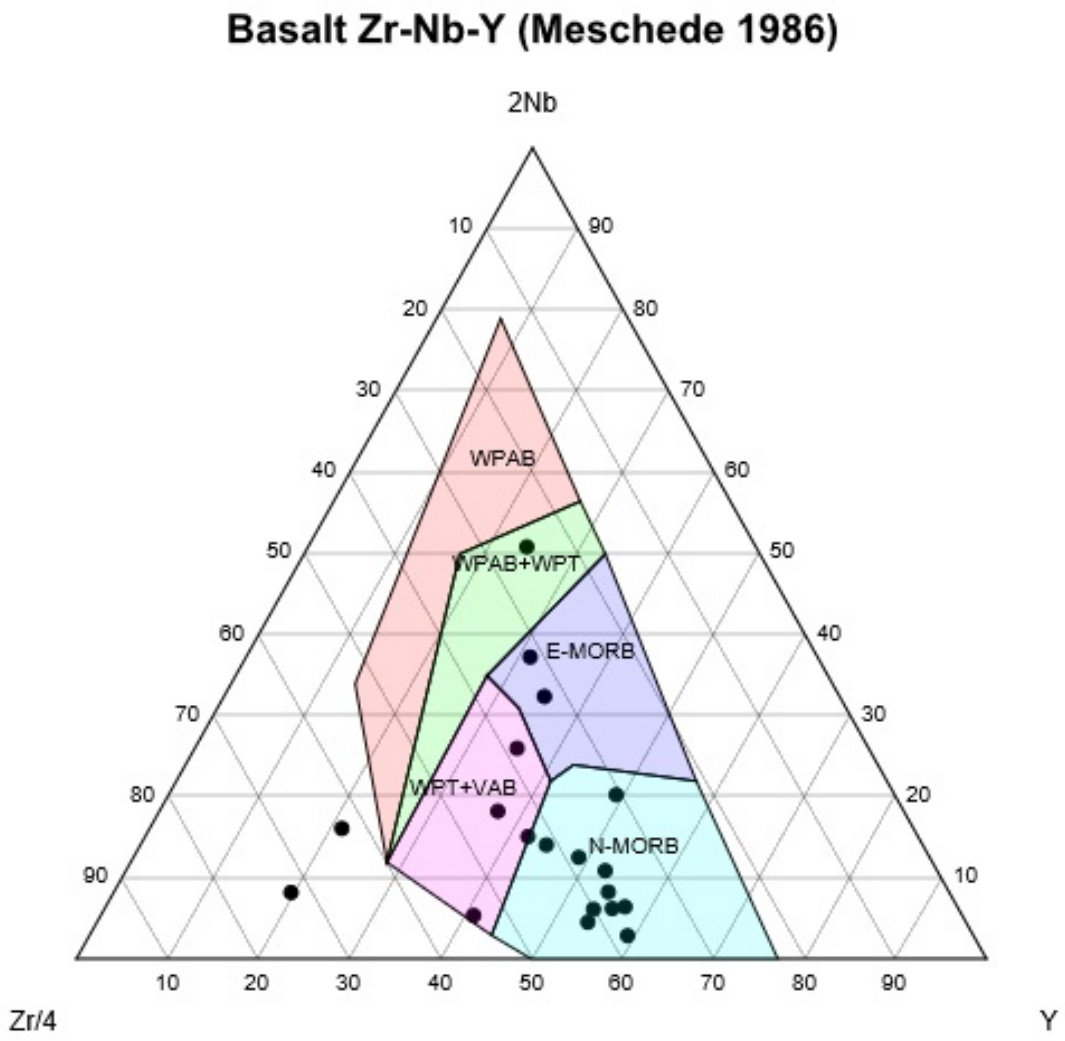

Figure 4.53: The basalt Zr–Nb–Y discrimination diagram classifies the mafic samples as within–plate alkali basalts (WPAB), within–plate alkali basalts and tholeiites (WPAB+WPT), E–type MORBs, N–type MORBs, within–plate tholeiites, and volcanic arc basalts (WPT+VAB) (Meschede, 1986).

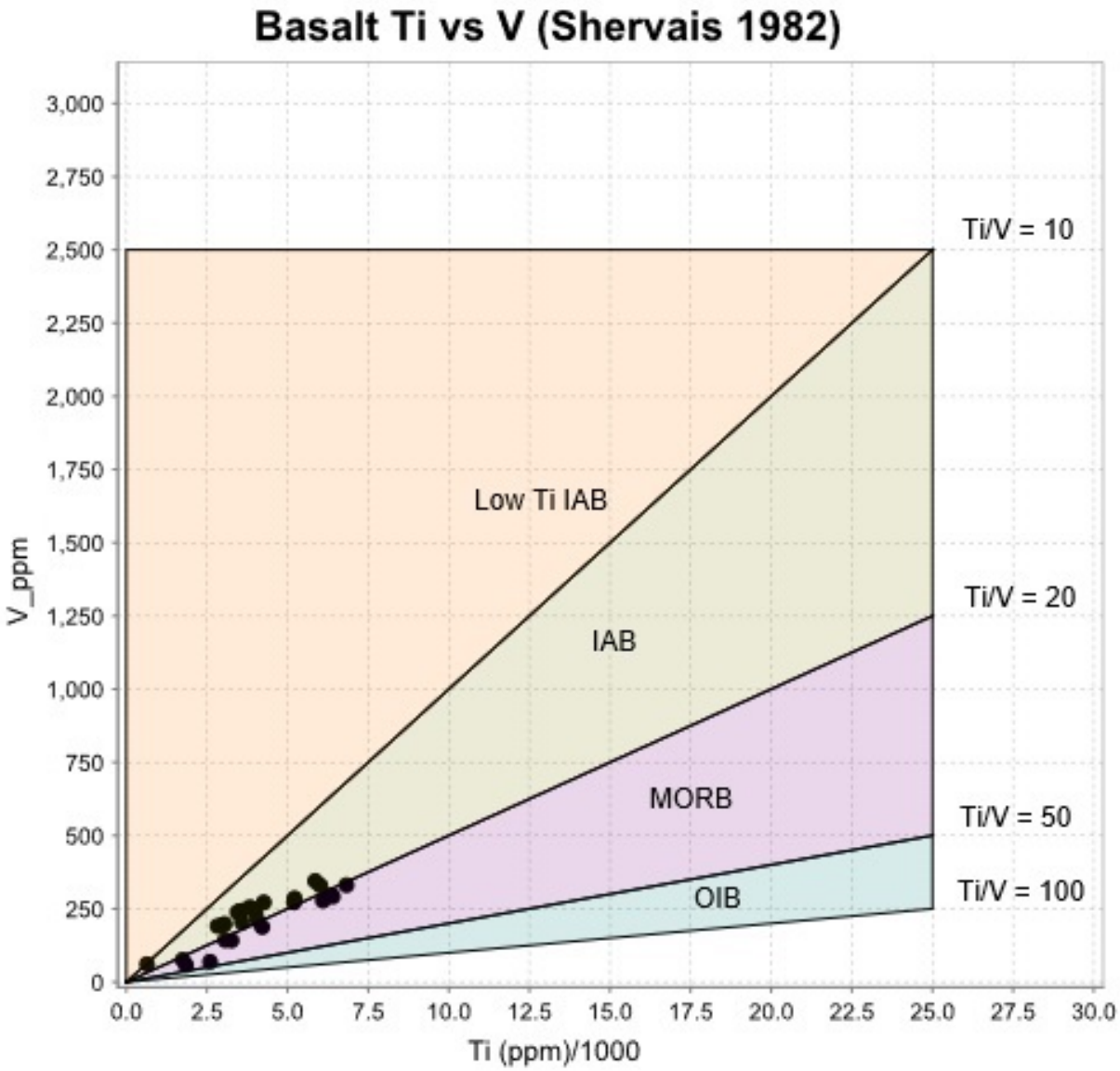

Figure 4.54: The basalt Ti versus V discrimination diagram classifies the mafic samples between the MORB and IAB (island arc basalt) fields (Shervais, 1982).

The basalt Zr–Nb–Y (Meschede, 1986) classification scheme has one cluster of samples in the N–MORB field, two in the E–MORB field, three in the within–plate tholeiites and volcanic arc basalt field, one sample in the within–plate alkali basalt and within–plate tholeiite field, and two samples that do not plot within any field on the diagram (Fig. 4.53). The classification of basalt (Shervais, 1982) defines a much tight cluster along the linear trend between MORB and IAB (island arc basalt) boundary (Fig. 4.54). The samples are clustered near the origin as the concentration of V and Ti are low in all of the samples.

The two discrimination diagrams by Wood (1980) display some similarity to one another (Figs. 4.55–4.56). The basalt Th–Hf–Ta diagram displays one population in the VAB CAB (volcanic arc

basalt, calc–alkaline basalt) field and a more scattered population in the E–MORB WPT with a number of samples plotting in neighbouring regions including N–MORB and N–MORB WPT. The basalt Th–Zr–Nb diagram (Wood, 1980) plots the majority of samples in the arc fields (VAB IAT, VAB CAB). Only two samples fall outside these fields with one in the transitional N–MORB WPT field and the other in the transitional E–MORB WPT field. Both discrimination diagrams divide the samples into arc and MORB settings.

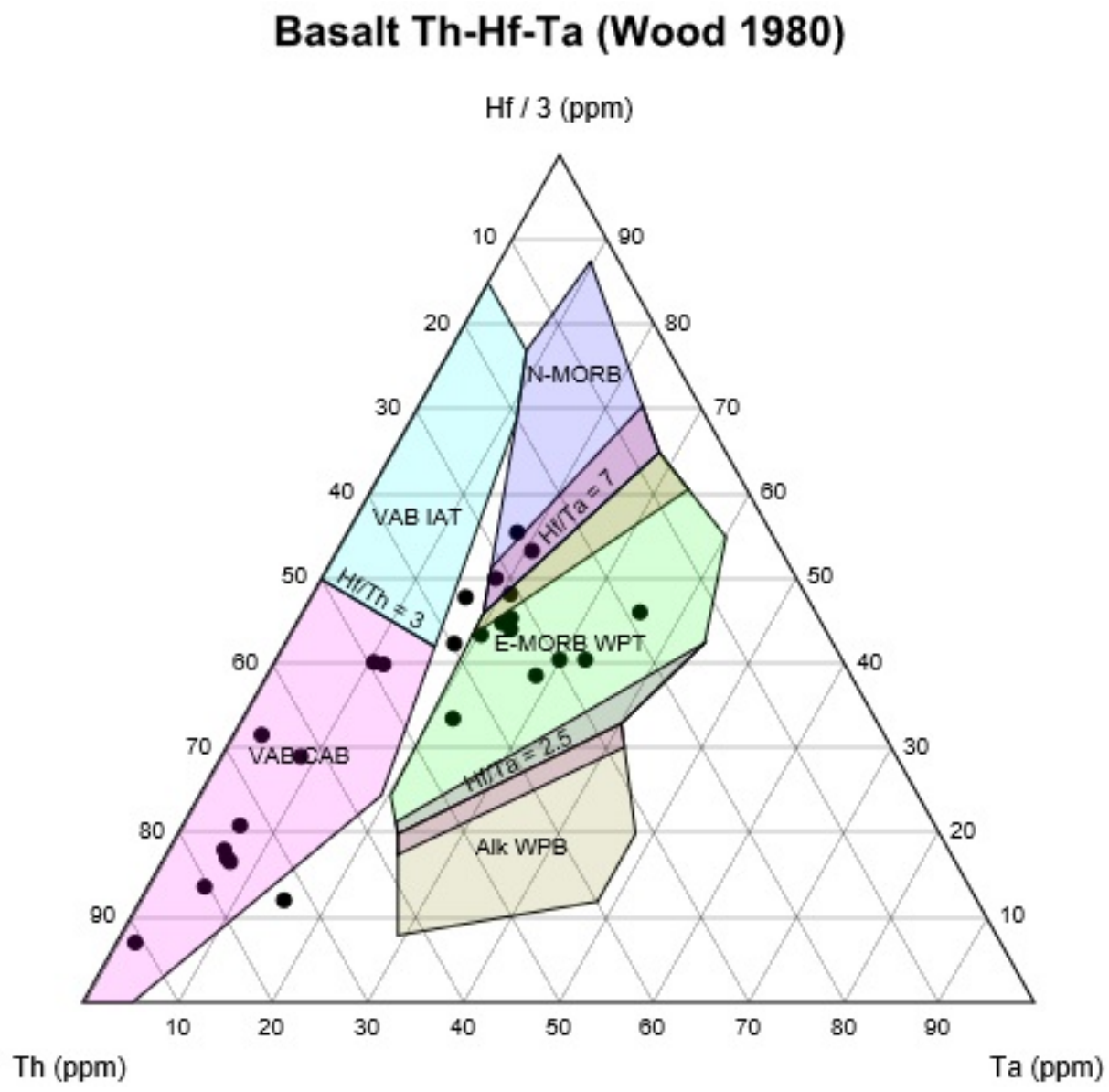

Figure 4.55: The basalt Th–Hf–Ta discrimination diagram plots the mafic samples into MORB (predominantly E–MORB and a few in N–MORB) as well as volcanic arc basalt and calc–alkaline basalt (VAB CAB). Two samples are in the boundary between MORB and VAB (Wood, 1980).

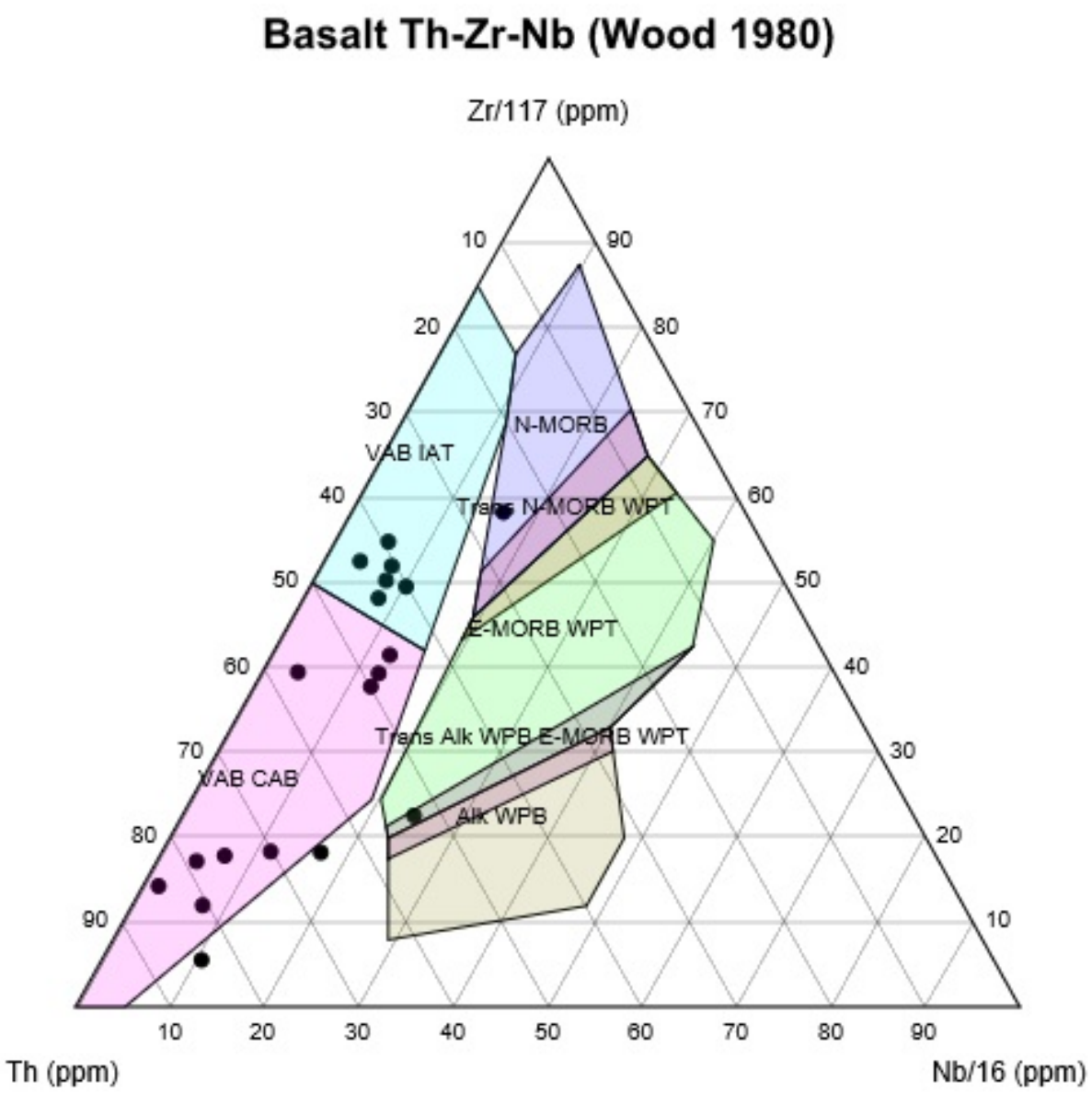

Figure 4.56: The basalt Th–Zr–Nb discrimination diagram plots the mafic samples into N–MORB, E–MORB, CAB, and island–arc tholeiite and volcanic arc basalt (Wood, 1980).

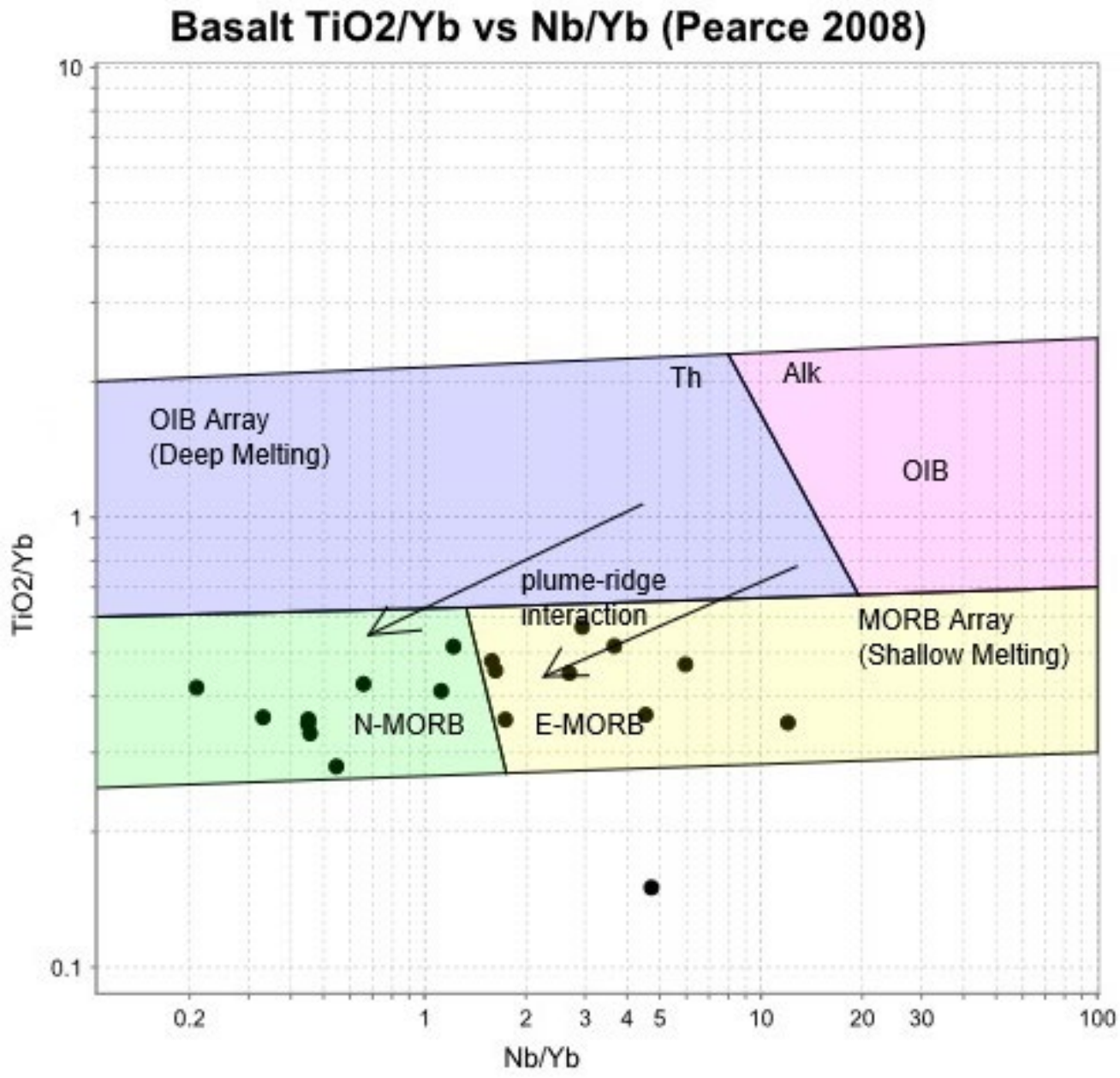

Figure 4.57: The basalt TiO_2/Yb versus Nb/Yb discrimination diagram plots the mafic samples into the MORB array in the N–MORB and E–MORB regions (Pearce, 2008).

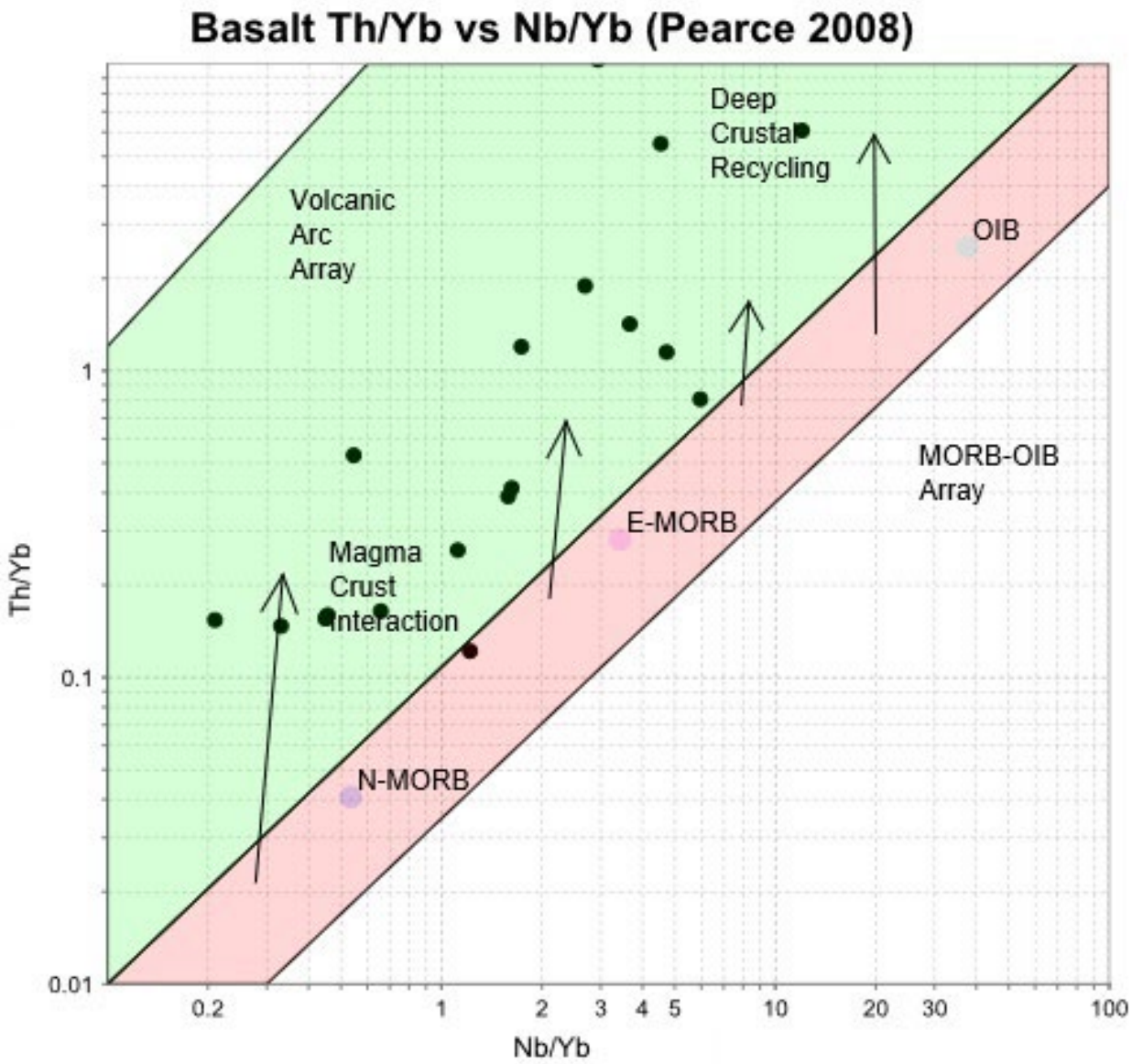

Figure 4.58: The basalt Th/Yb versus Nb/Yb discrimination diagram plots one sample in the MORB–OIB array, in the N–MORB region and the majority of samples in the volcanic arc array near the MORB–OIB boundary. The majority of samples are in the magma crust interaction region and a couple samples are in the deep crustal recycling region (Pearce, 2008).

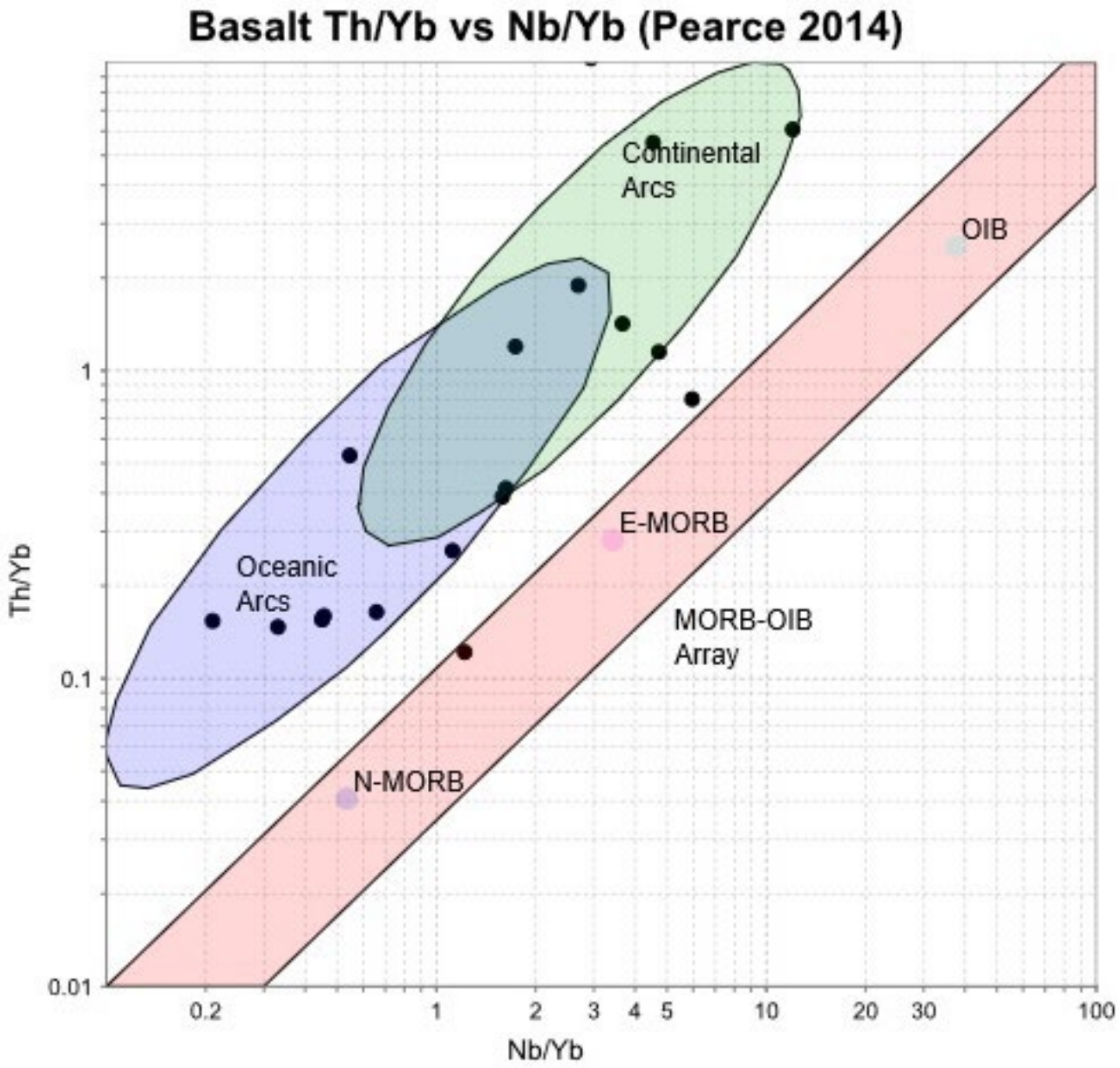

Figure 4.59: Basalt Th/Yb versus Nb/Yb variation diagram from Pearce (2014) plots the mafic samples into the N–MORB, oceanic and continental arc regions, with one sample near the E–MORB region (Pearce, 2014).

The basalt diagrams by Pearce (2008, 2014) are used to constrain the tectonic affinity and involvement of the continental crust in the samples (Figs. 4.57–4.59). The samples plot throughout the oceanic, continental, and transitional arcs setting with one sample in the N–MORB section of the MORB–OIB array and one adjacent to the E–MORB section. These results support magmatic crustal interactions and/or the potential for deep crustal recycling. The basalt TiO_2/Yb versus Nb/Yb and Th/Yb versus Nb/Yb diagrams from Pearce (2008, 2014) are used to classify the tectonic affinity using basalt and the processes that form them. The diagrams generally agree that the samples range between MORB and arc, however there are some discrepancies between the diagrams. The mafic samples were then further

categorized based into their location in the Borden Mine and textures, including samples from the hangingwall, footwall, samples with hornblende porphyroblasts, and ore zone (Figs. 4.60–4.78).

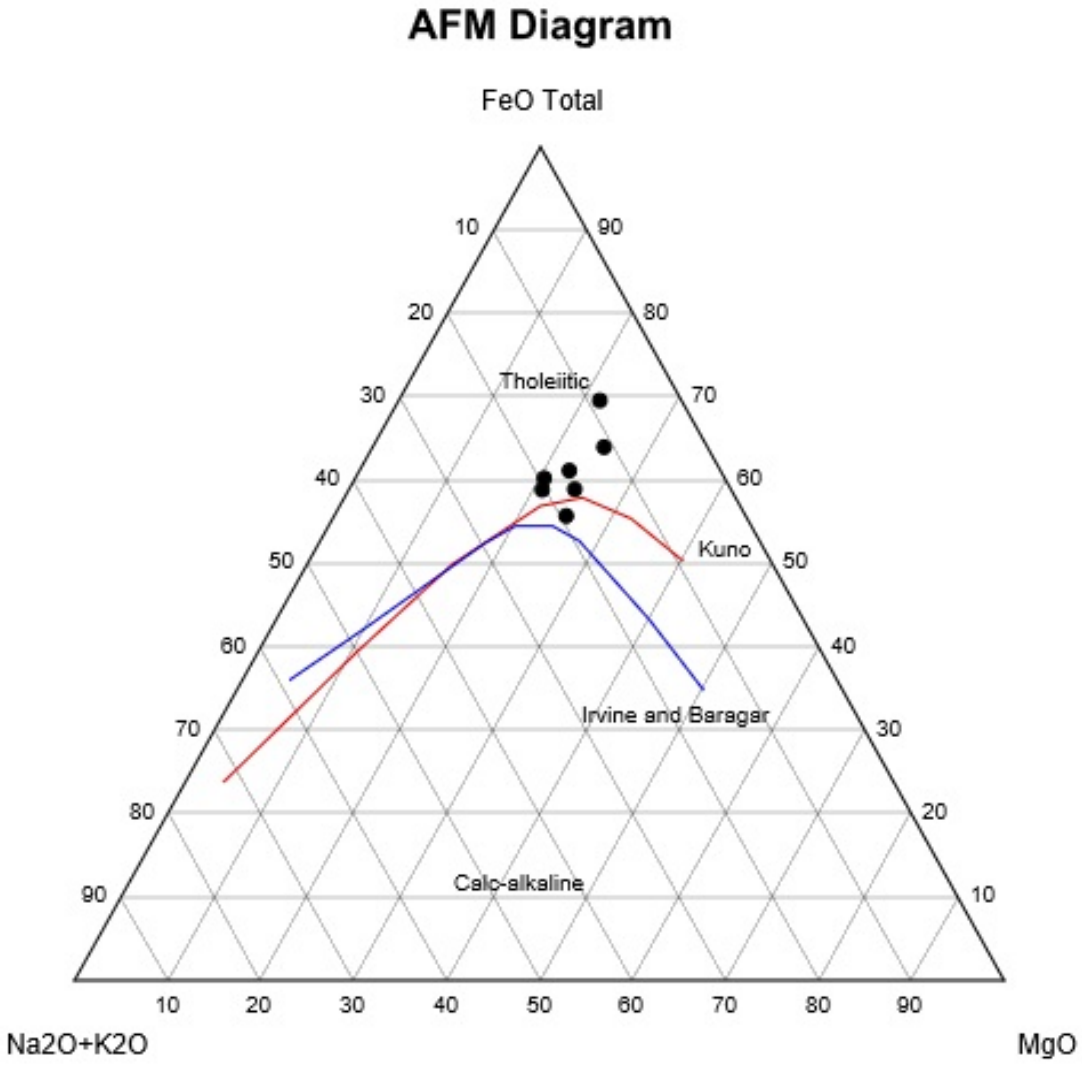

Figure 4.60: AFM diagram to classify mafic footwall samples in Borden Mine into the tholeiitic series (Irvine and Baragar, 1971).

Mafic samples collected from below the ore zone in Borden Mine, in the mine footwall, are characterized as a massive to gneissic coarse– to medium–grained black amphibole and black to green clinopyroxene with interstitial plagioclase amphibolite. The footwall samples plot in the tholeiitic area in the AFM plot with one sample classified as calc–alkaline (Fig. 4.60). Given the alkali mobility this calc–alkaline classification may be unwarranted. The Jensen cation plot further subdivides these samples into both tholeiitic and calc–alkaline and they include classification as calc–alkaline basalt, tholeiitic andesite, and high–Fe tholeiitic basalt.

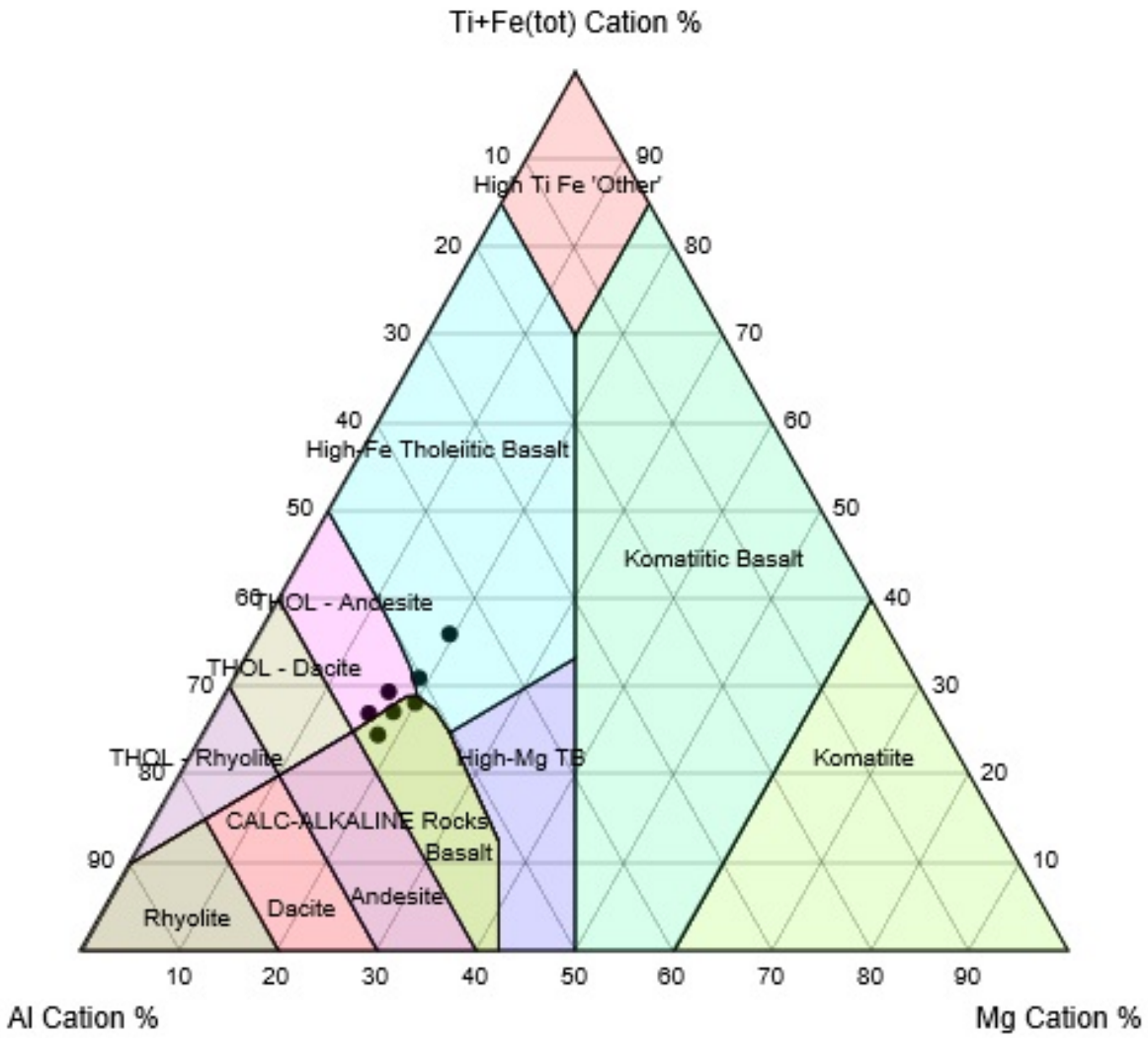

Figure 4.61: The Jensen cation plot categorizes the mafic footwall samples into tholeiitic andesite and high–Fe basalt and calc–alkaline basalt (Jensen, 1976).

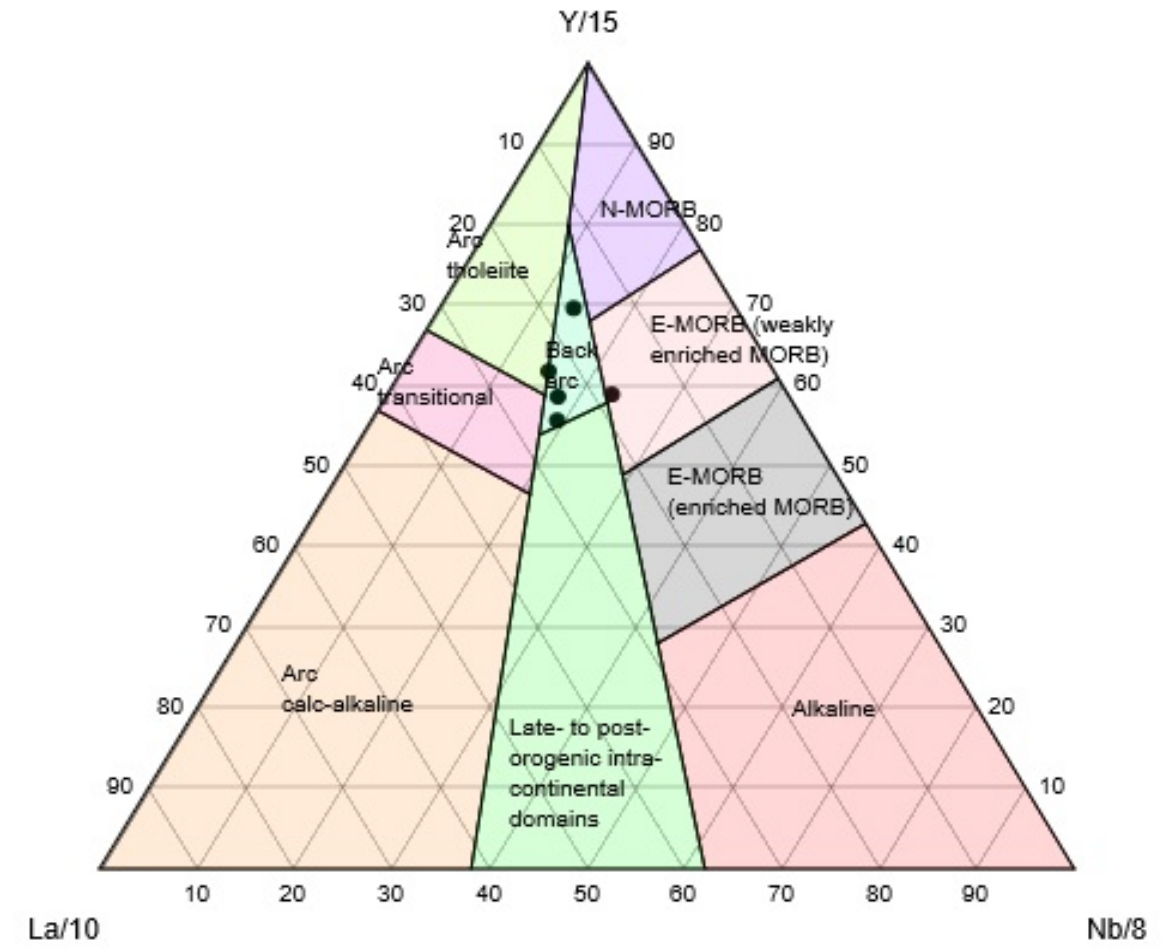

Figure 4.62: The tectonic classification of mafic igneous rocks classifies the mafic footwall samples from Borden Mine into the backarc region (Cabanis and Lecolle, 1989).

The Jensen cation plot categorizes the mafic footwall lithologies into the tholeiitic and calc–alkaline series into calc–alkaline basalt, tholeiitic andesite, and high–Fe tholeiitic basalt (Fig. 4.61). The mafic footwall samples of the Borden Mine define a tight cluster in the backarc field of the tectonic classification of mafic igneous rocks diagram (Fig. 4.62) (Cabanis and Lecolle, 1989).

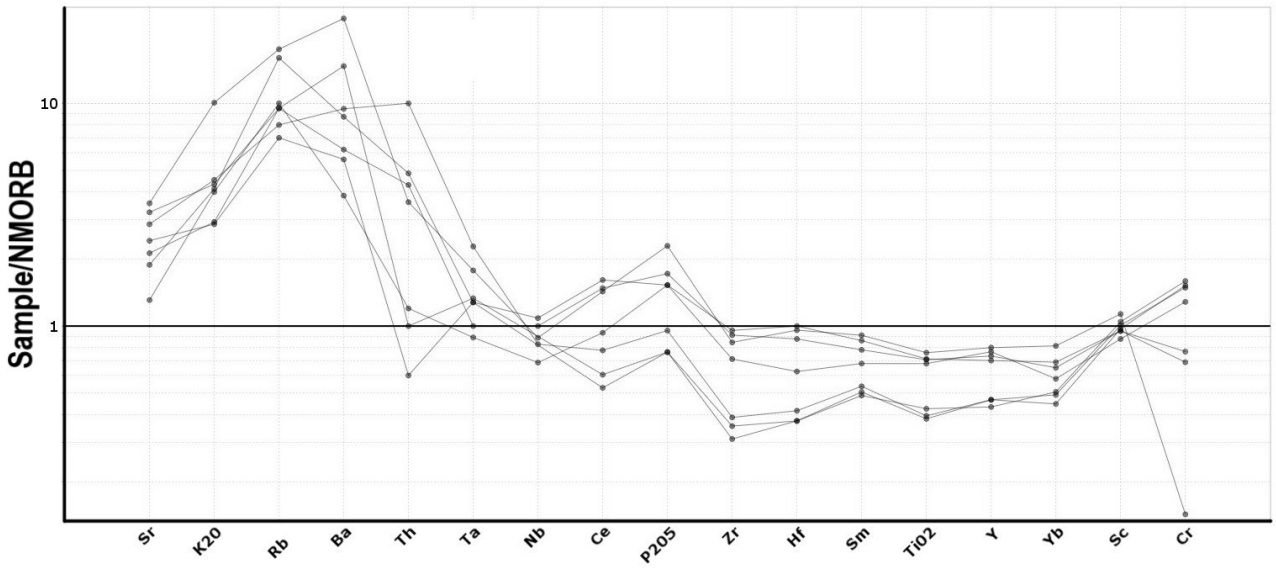

Figure 4.63: MORB–normalized multi–element diagram illustrating the whole–rock and trace element concentrations of the footwall mafic lithologies (Pearce, 1983).

The MORB–normalized multi–element diagram of MORB–normalized multi–element diagram of hanging wall mafic lithologies clearly displays the enrichment of the most mobile elements (large ion lithophile (LIL) elements such as Sr, K_2O, Rb, Ba) and/or low field strength elements (LFSE such as Rb, K, Ba, Sr, Th) and relative to a depleted, flat pattern in the HFS (high field strength) elements (Nb, Ta, Zr, Hf, Ti, P) (Fig. 4.63). To account for potential enrichment of LIL and/or LFSE from alteration Th may be represented the LFSE and defines a flat pattern relative to HFSE and REEs. All samples have low normalized abundances of Nb and Ta relative to LFSE and one samples has a Nb/Ta anomaly of 0 and the other samples are similar, consistent with a primitive geochemical signature (Li et al., 2017). There is minor variability in P_2O_5 and Cr as half of the samples plot above and below the MORB standard. Enrichment in Sr, K_2O, Rb, Ba, and Th paired with a flat pattern in the HFSE are consistent with both MORB and arc settings, as is common in back–arc basin basalts (Taylor and Martinez, 2003). This is consistent with the previous Cabanis and Lecolle (1989) classification. However, the identification of back–arc basin basalts (BABB) is markedly difficult and signatures of arc and MORB may be present as numerous processes in the BABB setting may affect magmatism (Saunders and Tarney, 1984; Taylor and Martinez, 2003). The MORB normalized multi–element REE patterns for footwall mafic lithologies use normalization values from Sun and McDonough (1989) (Fig. 4.64). The REE pattern is flat with minor enrichment in light rare earth elements (LREEs) and by less than a factor of 1. Of note there is no Eu anomaly and flat heavy rare earth elements (HREEs).

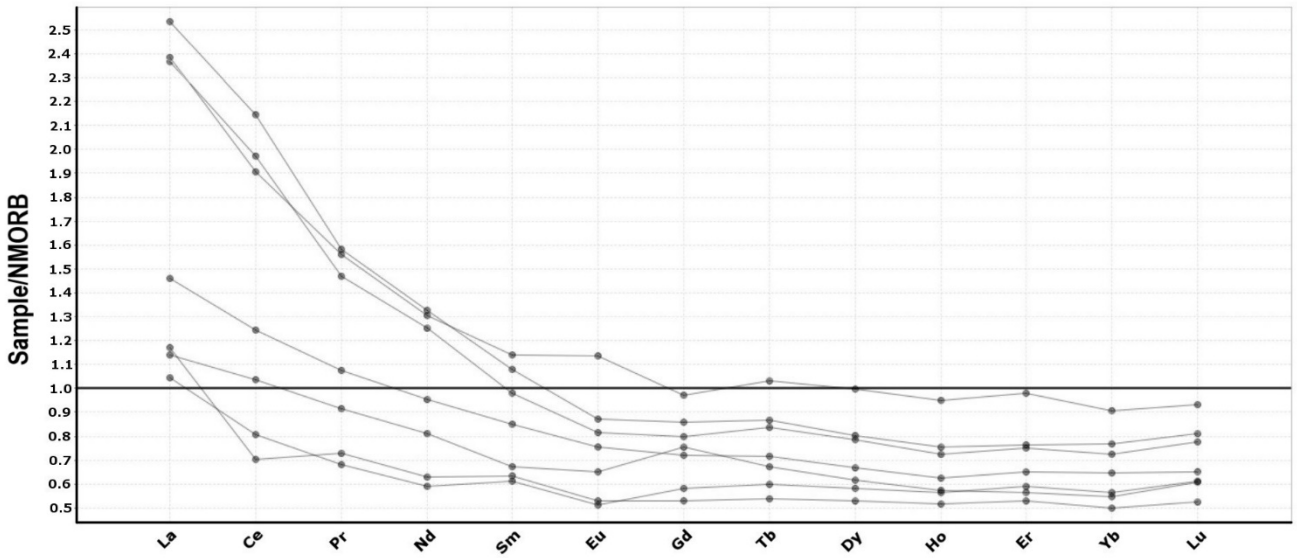

Figure 3.64: MORB–normalized rare earth element patterns in the footwall mafic lithologies (Sun and McDonough, 1989).

The visually and petrographically identical hangingwall samples located above the ore zone in Borden Mine and are characterized as a garnet–hornblende amphibolite with schistose to gneissic to migmatitic textures with coarse– to very–fine grained black and green amphibole, garnet, and interstitial plagioclase. The hanging wall samples plot in both the tholeiitic and calc–alkaline series in the AFM plot (Fig. 4.65). The Jensen cation plot further subdivides these samples into High–Fe and high–Mg tholeiitic basalts, komatiite, and calc–alkaline basalt and dacite. The hangingwall mafic lithologies have more scatter than the footwall lithologies. This spread could be primary and/or due to the variability of textures and fabrics present in this group, as opposed to the more massive footwall lithologies. Outliers include one ultramafic and intermediate sample. The komatiite sample was collected as it visually appeared to have a protolith of komatitic basalt. The dacite sample is a lighter grey than the other mafic lithologies and has a greater modal percentage of plagioclase porphyroclasts (hypothesized to be primary phenocrysts). The Jensen cation plot categorizes the mafic hangingwall lithologies as komatiite, high–Fe tholeiitic basalt and calc–alkaline high–Mg basalt, basalt, and dacite (Fig. 4.66)

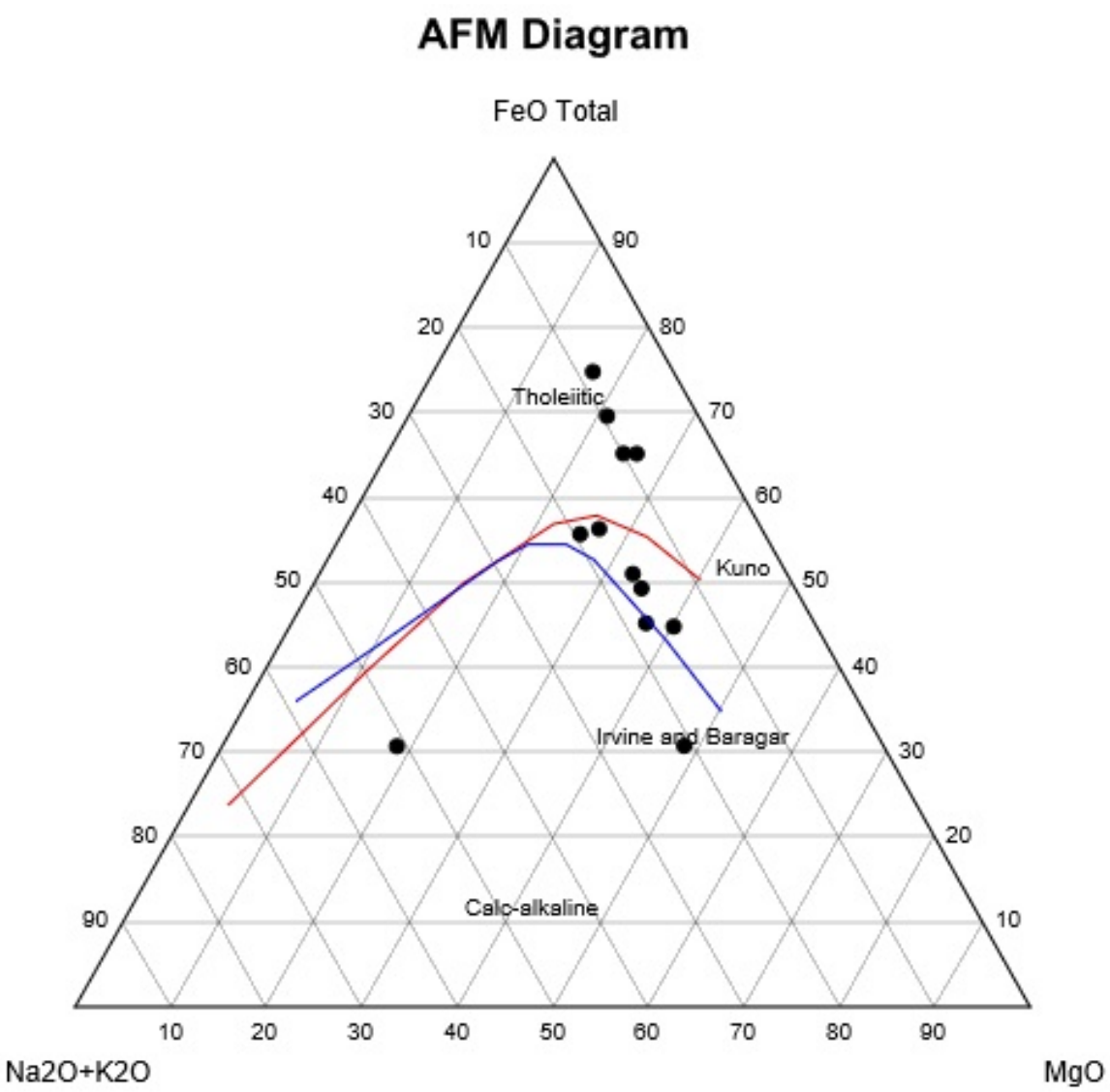

Figure 4.65: AFM diagram classifies the mafic hangingwall samples in Borden Mine into the tholeiitic and calc–alkaline series (Irvine and Baragar, 1971).

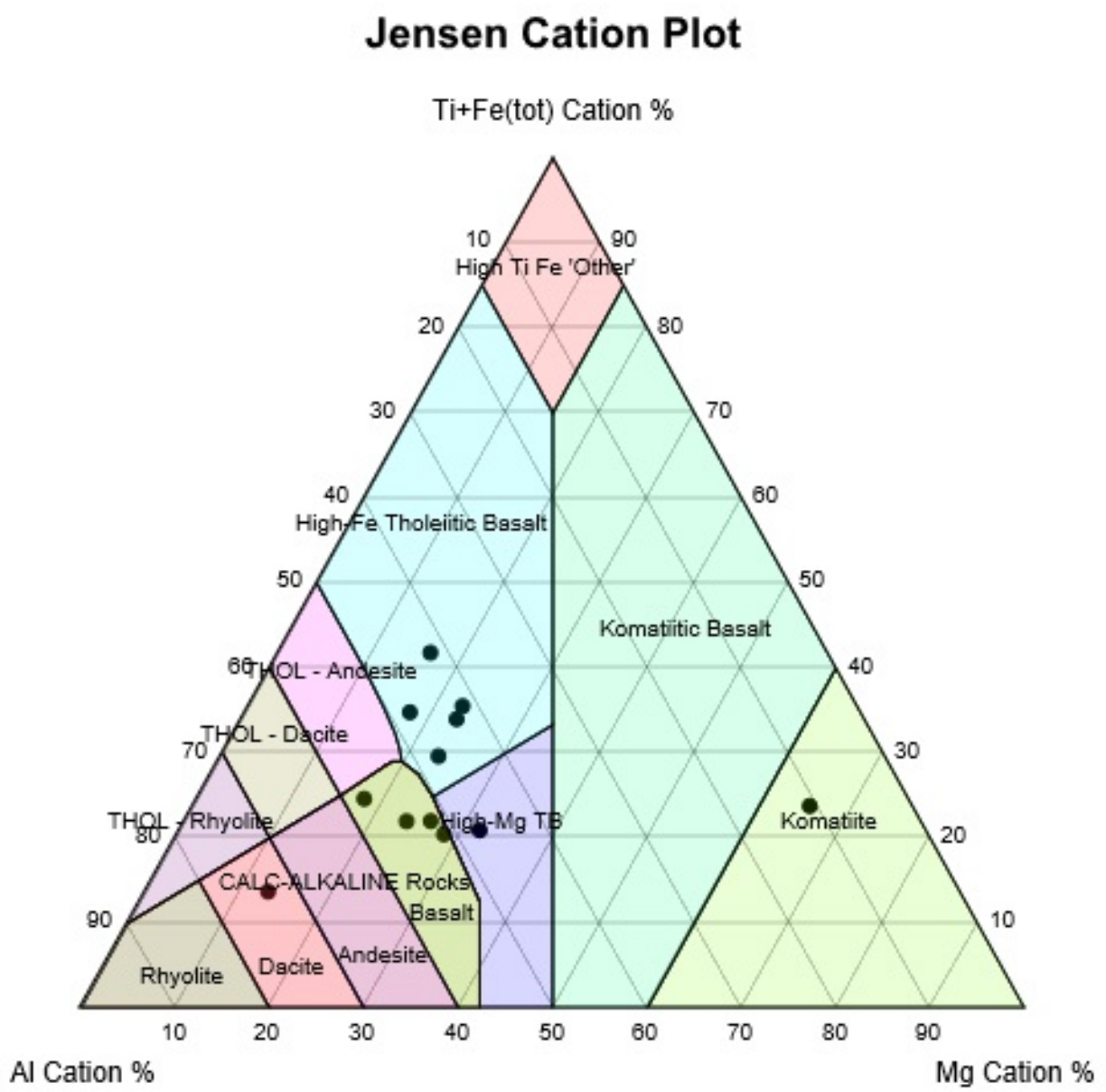

Figure 4.66: The Jensen cation plot categorizes the mafic hangingwall lithologies into komatiite, high–Fe tholeiitic basalt and calc–alkaline high–Mg basalt, basalt, and dacite (Jensen, 1976).

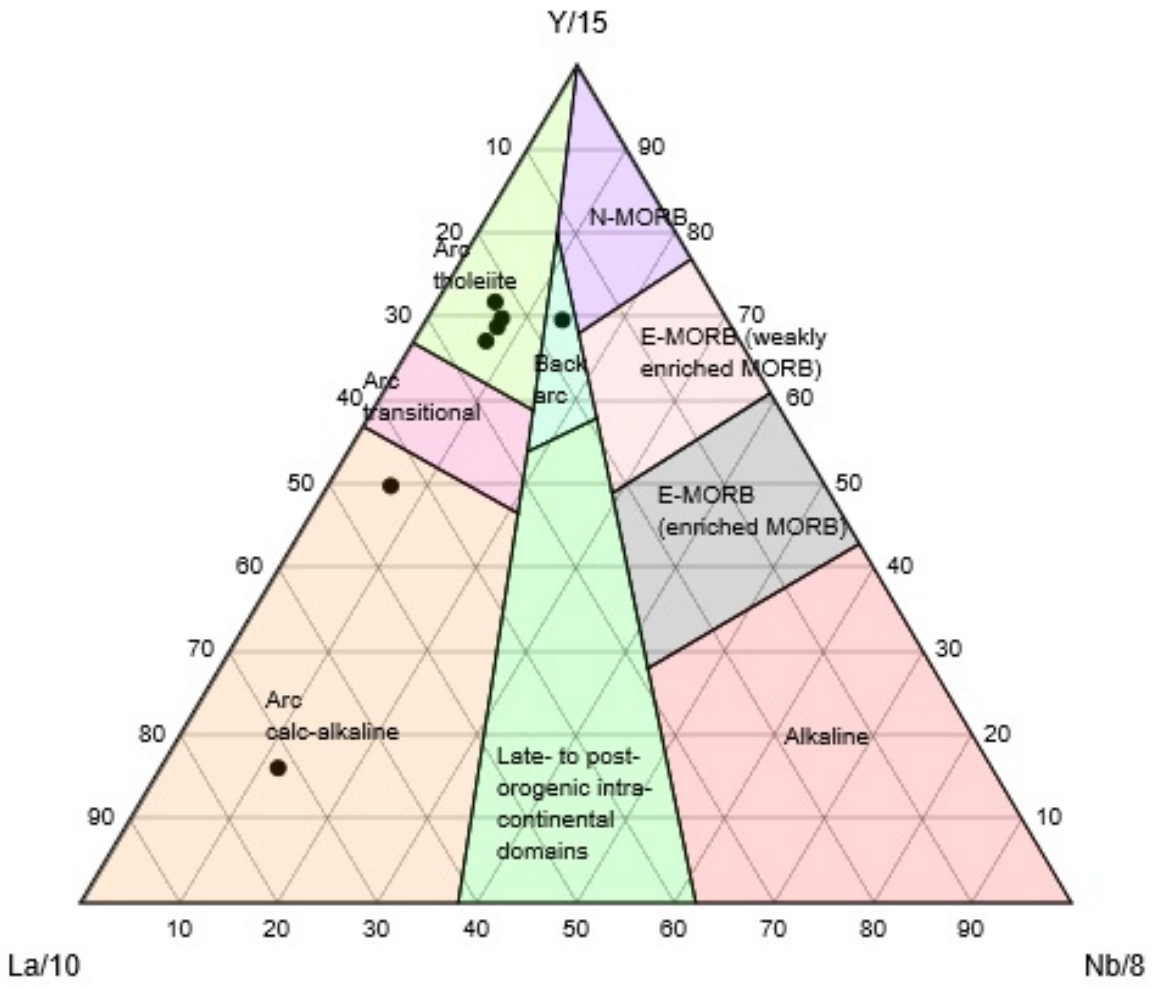

Figure 4.67: The tectonic classification of mafic igneous rocks using mafic hangingwall samples from Borden Mine classifies the majority of samples as arc tholeiite, two samples into the arc calc–alkaline, and one sample in the backarc region (Cabanis and Lecolle, 1989).

The hangingwall mafic lithologies plot in the arc tholeiite, arc calc–alkaline, and backarc fields in the tectonic classification of mafic igneous rocks diagram (Fig. 4.67) (Cabanis and Lecolle, 1989). This classification supports the AFM and Jenson plots and further supports MORB/BABB and arc magmatism. It also provides evidence of BABB in the hangingwall and footwall at Borden Mine. The MORB–normalized multi–element diagram of MORB–normalized multi–element diagram of footwall mafic lithologies clearly displays the enrichment of the most mobile elements (large ion lithophile (LIL) elements such as Sr, K_2O, Rb, Ba) and/or low field strength elements (LFSE such as Rb, K, Ba, Sr, Th) and relative to a depleted, flat pattern in the HFS (high field strength) elements (Nb, Ta, Zr, Hf, Ti, P) (Fig. 4.68). To account for potential enrichment of LIL and/or LFSE from alteration Th

may be represented the LFSE and defines a flat pattern relative to HFSE and REEs. All samples have low normalized abundances of Nb and Ta relative to LFSE and one samples has a Nb/Ta anomaly of 0 while the remainder are only slight, as is consistent with an arc geochemical signature (Li et al., 2017). There is minor variability in the enriched Rb, Ba, and Th and due to their mobility this is not unexpected in the hangingwall of Borden Mine. Similarly, the variability of enriched to depleted Ce is also attributed to the proximity to the gold mineralization. The majority of samples show a negative Nb anomaly, as would be typical of arc lithologies, while the the more tholeiitic samples have no anomaly. Enrichment of LIL elements paired with flat to depleted HFS elements are consistent with both MORB and arc settings (Taylor and Martinez, 2003).

This is consistent with the previous Cabanis and Lecolle (1989) classification. The MORB normalized multi–element REE patterns for hangingwall mafic lithologies use normalization values from Sun and McDonough (1989). The REE pattern is flat with variable enrichment in LREEs and generally flat HREEs (Fig. 4.69). One sample defines a more curved slope enriched in LREEs and depleted in HREEs which could represent a more intermediate composition and/or has been more greatly affected by gold mineralization. The flat, depleted sample is hypothesized to have experienced greater partial melting during migmatization than the other samples or a more ultramafic protolith.

The visually and petrographically indentical porphyroblastic amphibolite samples located above and below the ore zone in Borden Mine and are characterized by coarse–grained porphyroblastic hornblende and porphyroclastic plagioclase. The porphyroblastic amphibolite samples plot in both the tholeiitic and calc–alkaline series in the AFM plot, similar to both the footwall and hangingwall samples (Fig. 4.70). The Jensen cation plot further subdivides these samples into calc–alkaline basalt and tholeiitic dacite, similar to the footwall samples (Fig. 4.71).

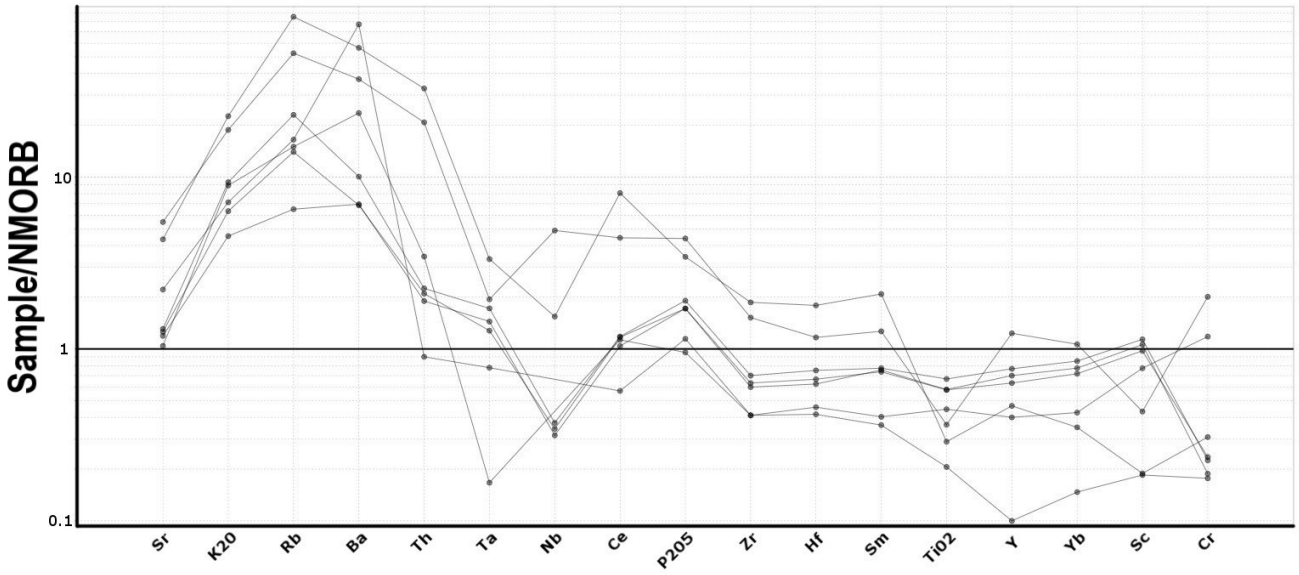

Figure 4.68: MORB–normalized multi–element diagram illustrating the whole–rock and trace element concentrations in the studied hangingwall mafic lithologies (Pearce, 1983).

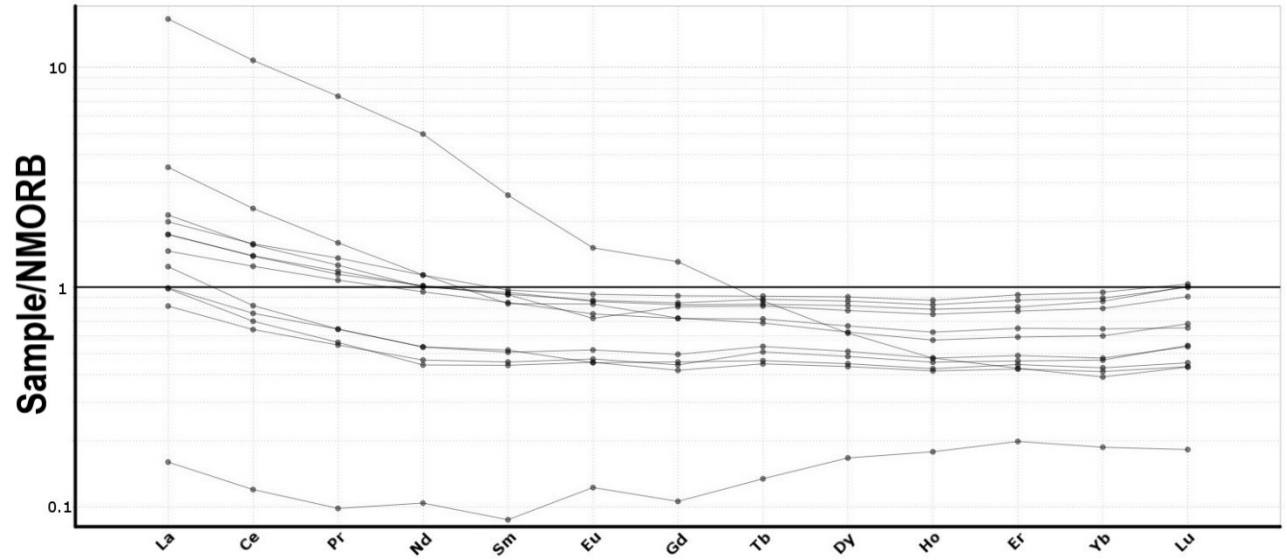

Figure 4.69: MORB–normalized rare earth element patterns in the studied hangingwall mafic lithologies are very flat with a slight enrichment in LREEs (Sun and McDonough, 1989).

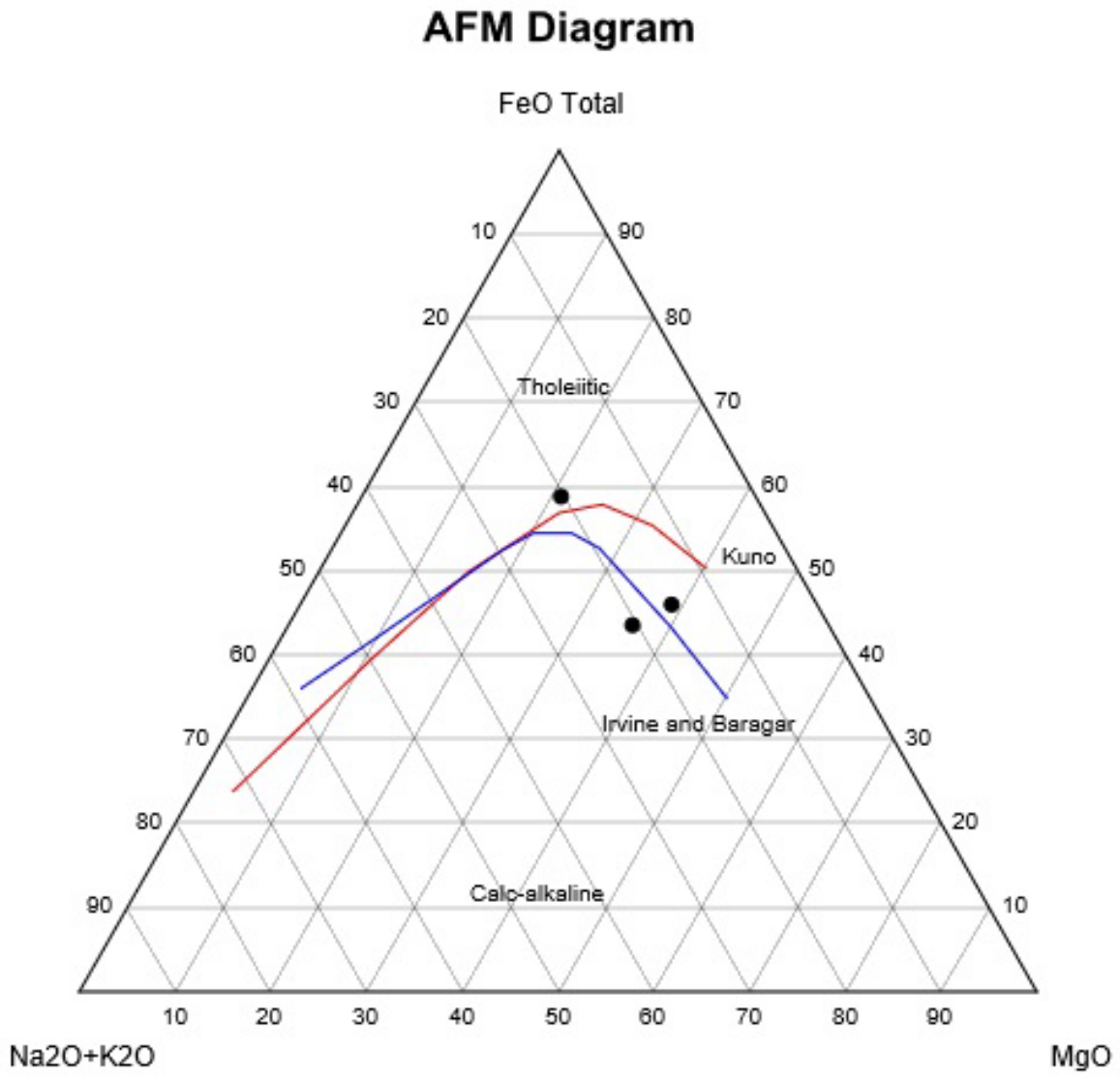

Figure 4.70: AFM diagram to classify porphyroblastic amphibolite samples in Borden Mine into the tholeiitic and calc–alkaline series (Irvine and Baragar, 1971).

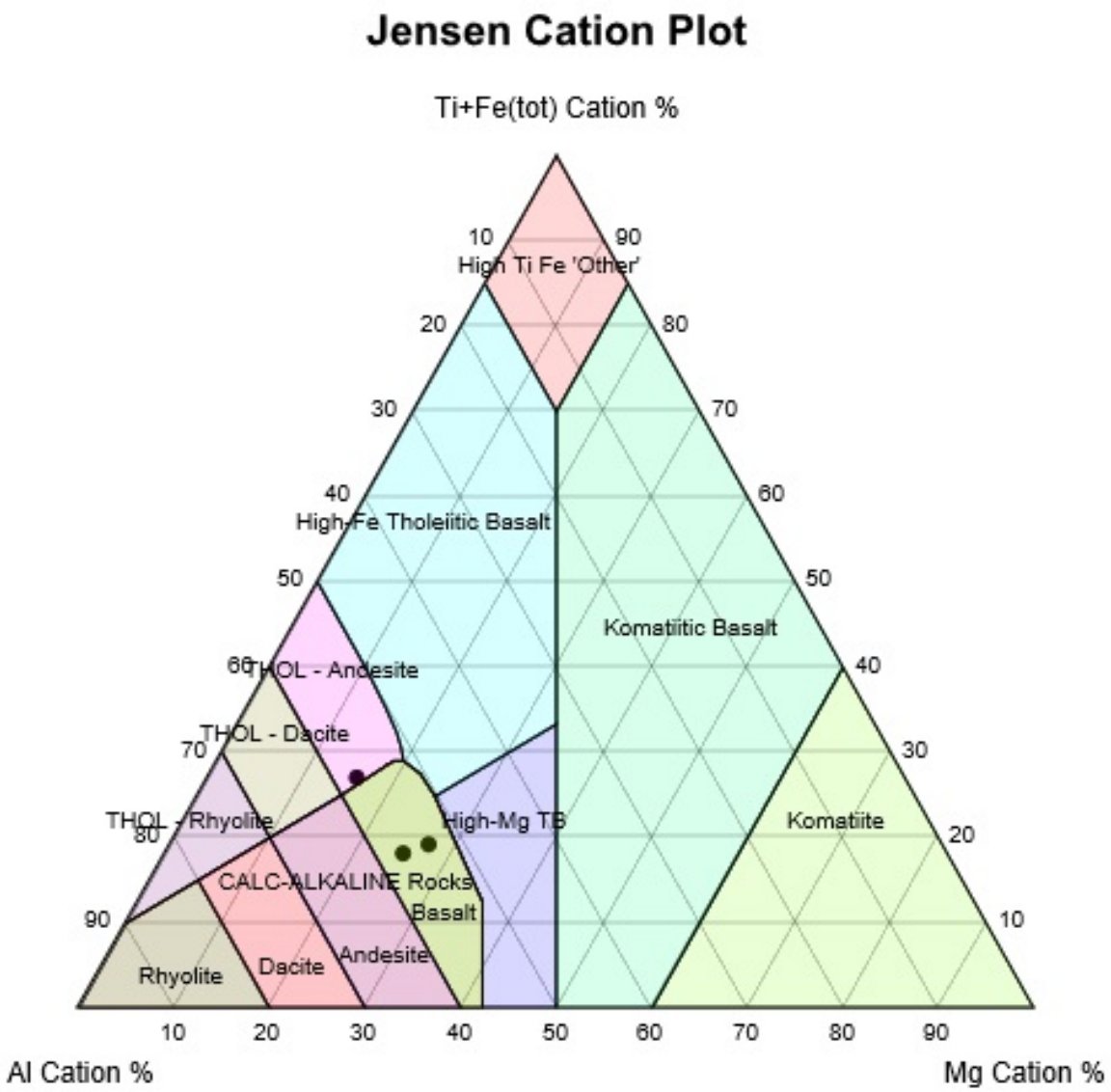

Figure 4.71: Jensen cation plot categorizes the porphyroblastic amphibolite as calc–alkaline basalt and tholeiitic dacite (Jensen, 1976).

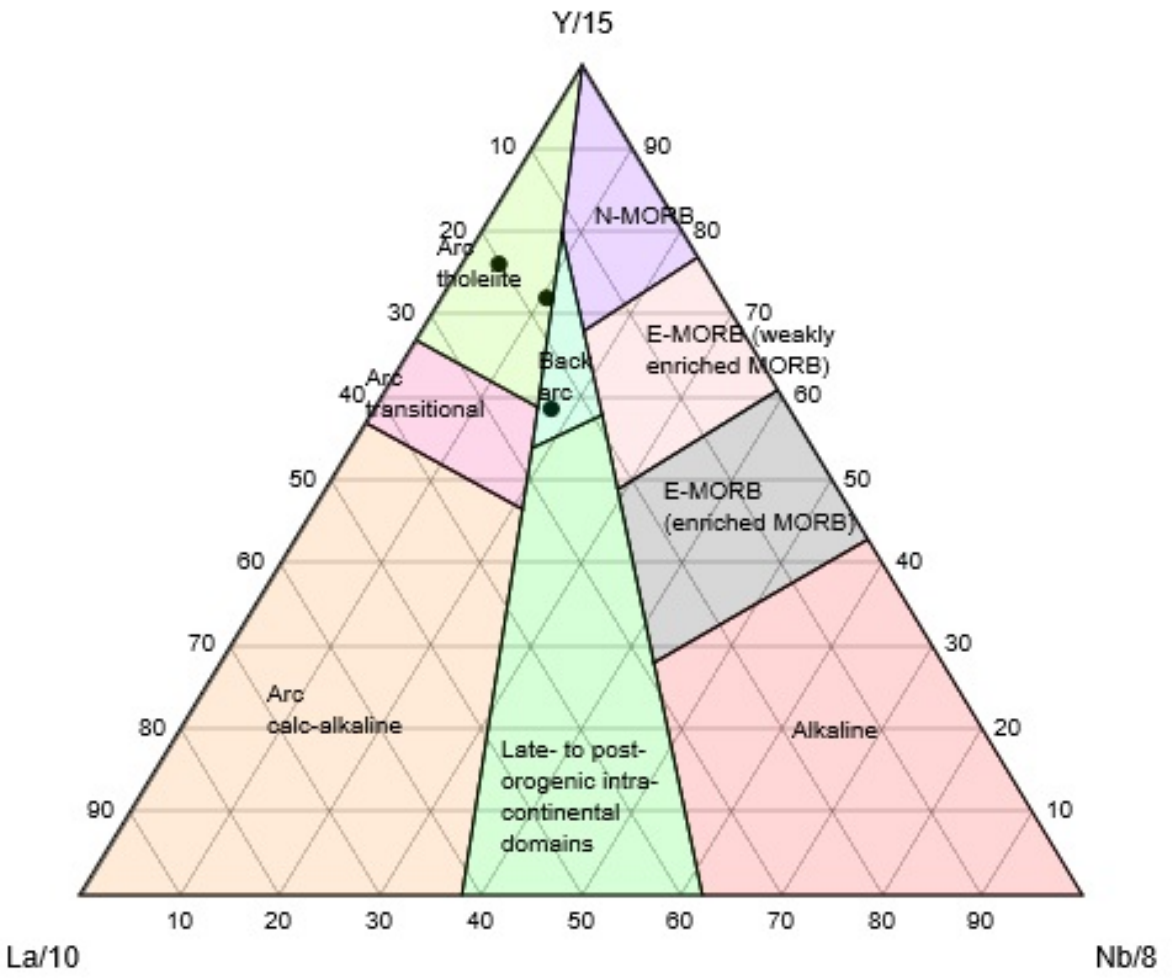

Figure 4.72: The tectonic classification of mafic igneous rocks categorizes the tectonic affinity of the porphyroblastic amphibolite from Borden Mine as backarc and arc tholeiite (Cabanis and Lecolle, 1989).

The tectonic classification of the porphyroblastic amphibolite plots the samples as arc tholeiite and backarc settings, similar to the footwall samples (Fig. 4.72) which is similar to both the hangingwall and footwall samples.

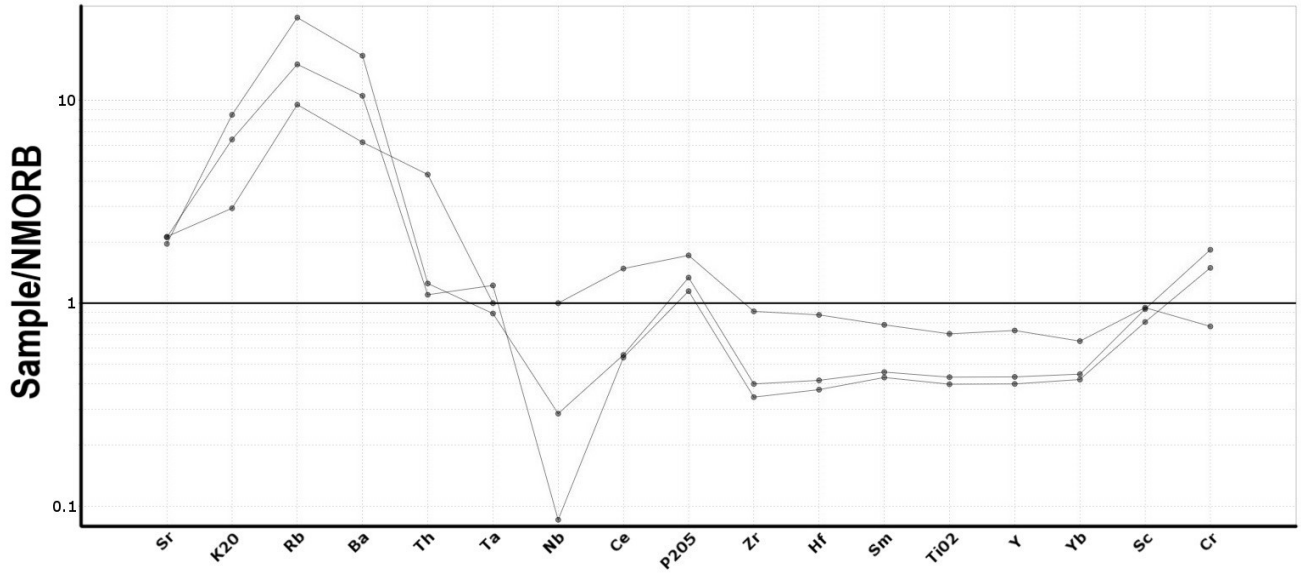

Figure 4.73: MORB–normalized multi–element diagram illustrating the whole–rock and trace element concentrations in the studied porphyroblastic amphibolite lithologies (Pearce, 1983).

The MORB–normalized multi–element diagram of MORB–normalized multi–element diagram of porphyroblastic amphibolite lithologies plots enriched LIL elements and relatively flat HFS elements (Fig. 4.73). There is minor variability in the enriched to flat Th and Ce, and flat to depleted Nb. The Th and Ce may be attributed to the proximity to the gold mineralization. The tholeiitic sample with a Nb/Ta ratio of 0 may reflect a more primitive magma source than the calc–alkaline samples with negative anomalies (Li et al., 2017). The MORB normalized multi–element REE patterns for hangingwall mafic lithologies use normalization values from Sun and McDonough (1989). The REE pattern is flat with variable enrichment in LREEs and generally flat HREEs. One sample defines a more curved slope enriched in LREEs and depleted in HREEs which could represent a more intermediate composition and/or has been more greatly affected by gold mineralization. The flat, depleted sample is hypothesized to have experienced greater partial melting during migmatization than the other samples or a more ultramafic protolith.

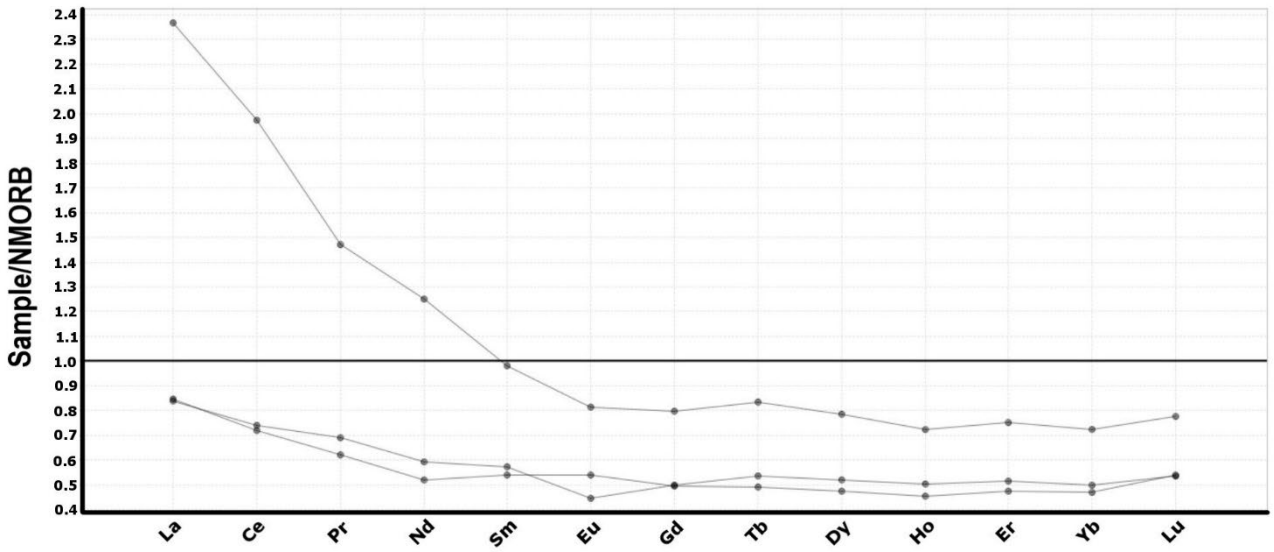

Figure 4.74: MORB–normalized rare earth element patterns in the studied porphyroblastic amphibolite is slightly enrichment in LREE and flat HREEs (Sun and McDonough, 1989).

The MORB normalized multi–element REE patterns for porphyroblastic amphibolite use normalization values from Sun and McDonough (Fig. 4.74) (1989). The REE pattern is curved to flat with minor, steep enrichment in LREEs by less than a factor of 1. The geochemical similarities of the porphyroblastic amphibolite to the footwall mafic lithologies are comparable and as such the porphyroblastic amphibolite should be classified into the category of footwall mafic lithologies.

The mafic lithologies located in the ore zone of the Borden Mine are variable but are typically schistose to mylonitic to migmatitic hangingwall mafic lithologies with minor footwall mafic lithologies. Due to the processes related to gold mineralization (i.e. hydrothermal alteration, high–temperature deformation) the whole rock geochemistry of the samples are variable (Figs. 4.47–4.48). Therefore, only trace element geochemistry as it has been less affected by these processes listed above due to the immobility HFS and REE elements (Figs. 4.75–4.76). The MORB normalized multi–element REE patterns for mafic lithologies in the ore zone are plotted following Sun and McDonough (1989). The REE pattern is curved to flat with steep enrichment in LREEs and a variable, relatively flat pattern in HREEs with minor anomalies. A negative anomaly is present in Ta and Nb, although one sample shows a positive anomaly in Nb. Ce displays both positive and negative anomalies, as is to be expected with variable hydrothermal input. Ti is variable as is to be expected with ilmenite after rutile, chlorite after hornblende, hornblende after pyroxenes, and variable titanite present in the ore zone. is present in Nb. Negative and positive anomalies include Y, Sc, and Cr although they are generally immobile elements supporting the hypothesis of element mobility during gold mineralization.

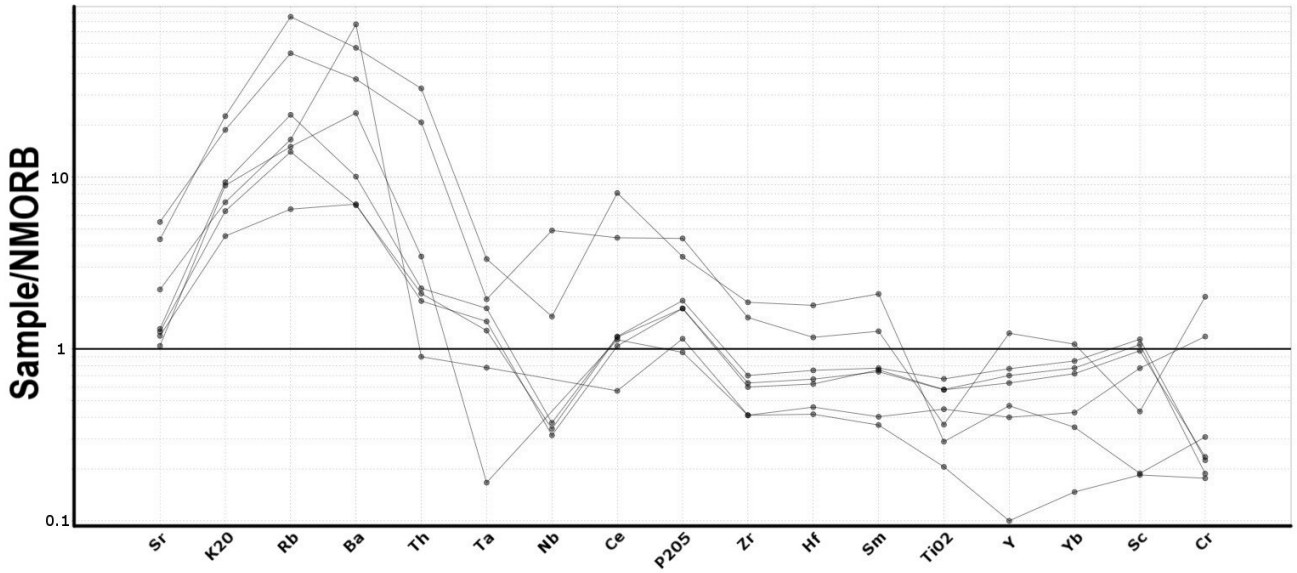

Figure 4.75: MORB–normalized multi–element diagram illustrating the whole–rock and trace element concentrations in the studied mafic lithologies within the ore zone (Pearce, 1983). Note the negative slope with enrichment in LIL.

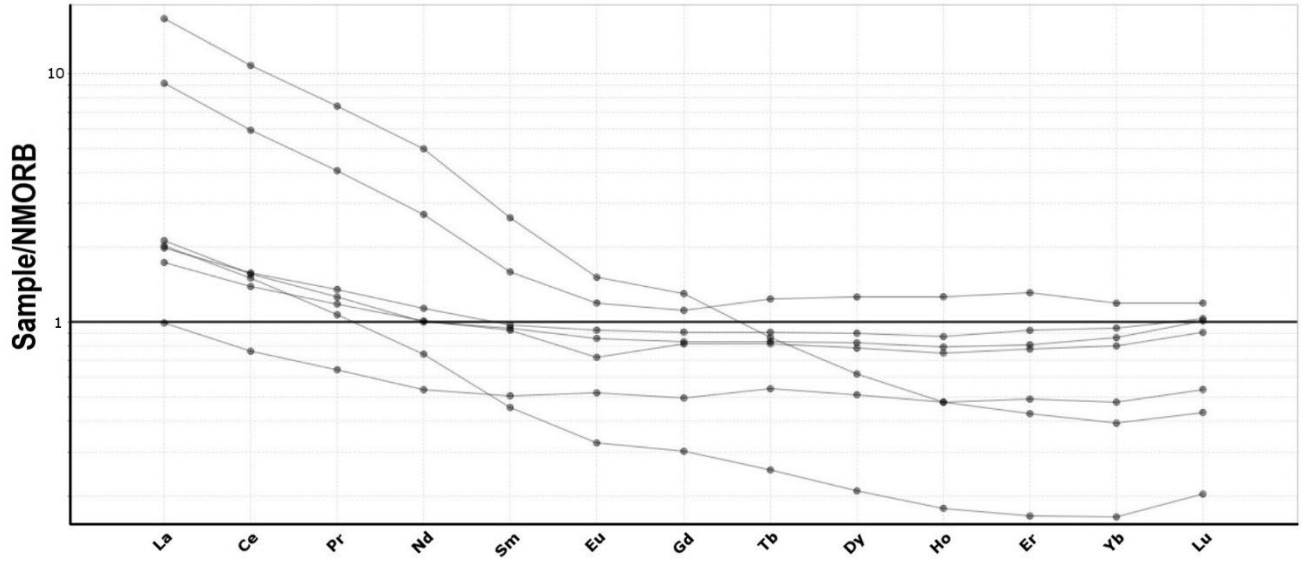

Figure 4.76: The MORB normalized multi–element REE patterns for mafic lithologies in the ore zone use normalization values from Sun and McDonough (1989). Note variability in the ore zone with flat patterns with some samples enriched in LREE and flat HREE, while others are depleted in HREE, and one sample is enriched in LREE and depleted in HREE.

The MORB normalized multi–element REE patterns for mafic lithologies in the ore zone are markedly different from outside the ore zone (Fig. 4.76). While the REE patterns for footwall, hangingwall, and porphyroblastic amphibolite samples displayed LREE curved, positive anomalies and flat HREE

patterns the ore zone defines a flat to negative slope. The LREEs range between slight enriched to slightly depleted compared to MORB values while the HREEs range from near MORB values to depleted. The REE patterns in the ore zone are compatible with the majority of the mafic lithologies in the footwall and hangingwall.

Mafic geochemistry from Chapleau belt (black circles) in the study area is displayed below to best compare to the adjacent Michipicoten greenstone belt of the Wawa subprovince (red triangles) (Figs. 4.77–4.81) (Turek et al., 1996a; Sage et al., 1996) and the Tisdale assemblage of the Abitibi subprovince (blue squares) (Fan and Kerrich, 1997). Ultramafic to intermediate lithologies from the Borden, Tisdale, and Mitchipicoten belts are plotted on a Pearce element ratio diagram, with Zr/Ti on the Y–axis acting as a proxy for silica, and Nb/Y on the X–axis acting as a proxy for total alkali content. The proxy elements are used due to the increased mobility of major and some minor elements during high–grade metamorphism and deformation. The majority of samples plot in the sub–alkaline region and are classified as basalt with some samples classified as intermediate with a single sample in the alkaline field (Fig. 4.76). Mafic to intermediate lithologies are also plotted on a Jenson cation plot which categorize the lithologies from all three belts into major volcanic rock types of sub–alkalic series and calc–alkaline, ranging from ultramafic to felsic (Fig. 4.77).

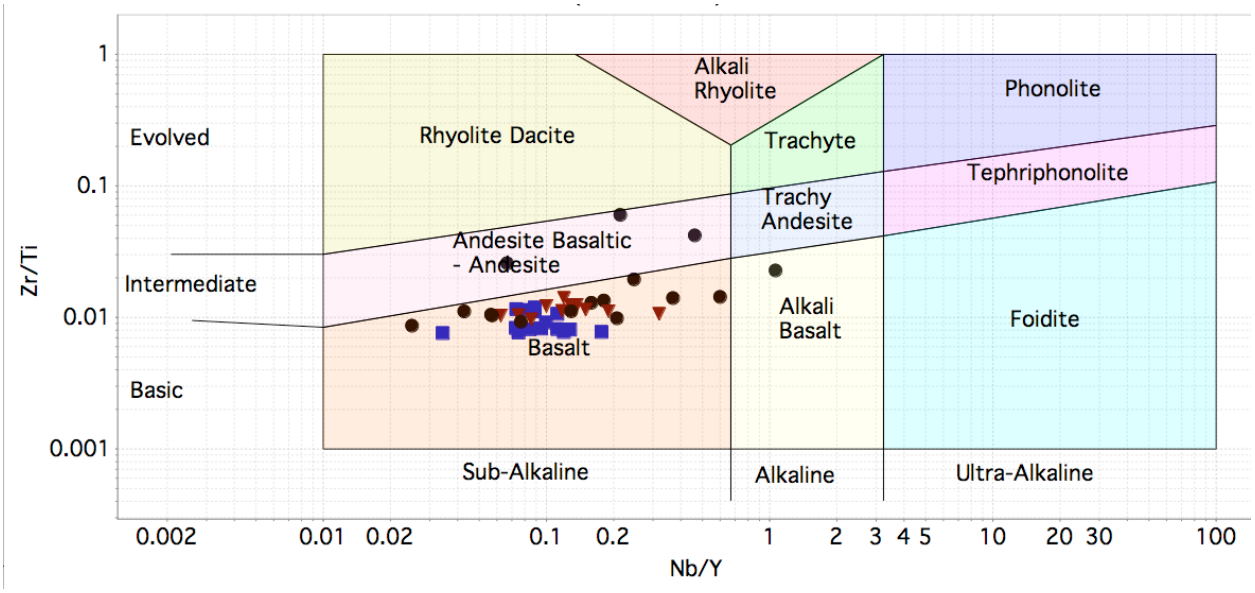

Figure 4.77: Pearce element ratio proxy diagram of mafic lithologies from Chapleau (black circles), Michipicoten (red triangles), and Abitibi (blue squares) greenstone belts show the sub–alkaline nature of the lithologies with the majority plotting as basalt, andesite basaltic–andesite, and one sample as alkali basalt (Modified after Pearce, 1996).

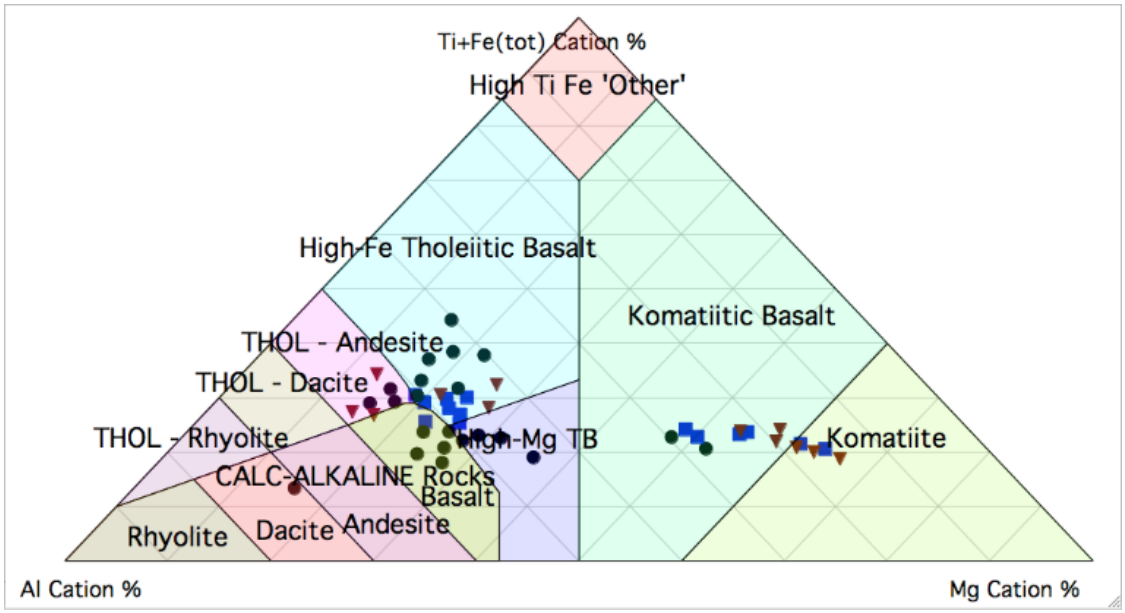

Figure 4.78: Jensen plot of ultramafic to mafic lithologies from Chapleau Belt (black circles) and Michipicoten (red squares) and Abitibi (blue squares) greenstone belts. The Chapleau Belt samples plot in the komatiitic basalt field, as well as in the tholeiitic series as high–Fe tholeiitic basalt, high–Mg tholeiitic basalt, andesite, and dacite, and in the calc–alkaline series with samples plotting as basalt and dacite. Note the similar nature of all three locations (Modified after Jensen, 1976; Capdevila et al., 1982; Sage, 1985; Turek et al., 1992, 1996a; Wyman and Kerrich, 2009b).

There are two large clusters of data with one straddling the tholeiitic and calc–alkaline series in the mafic to intermediate fields and another in the komatiitic basalt to komatiite fields. The samples collected in this study plot similarly to those from the Michipicoten and Abitibi greenstone belts, although there is more scatter in the Chapleau belt samples, particularly at the junction between the basaltic fields.

4.3.3 Geochemistry of intermediate to felsic lithologies

Preliminary studies of the newly discovered intermediate to felsic metavolcanic lithologies in the study area were conducted and compared to intermediate to felsic lithologies in the Michipicoten belt of the Wawa subprovince (Sage et al., 1995) and those in the Abitibi belt (Gaboury and Pearson, 2008) (Figs. 4.79–4.81). The majority of the intermediate to felsic lithologies in the Chapleau belt are classified as sub–alkaline, rhyolite dacite, similar to the majority of Michipicoten and Abitibi greenstone belt samples, with a few Chapleau samples in the andesite and basalt fields, including those in the alkaline field (Fig. 4.79). The scatter into the mafic fields may suggest many of the felsic lithologies had mafic protoliths and were modified during seafloor alteration.

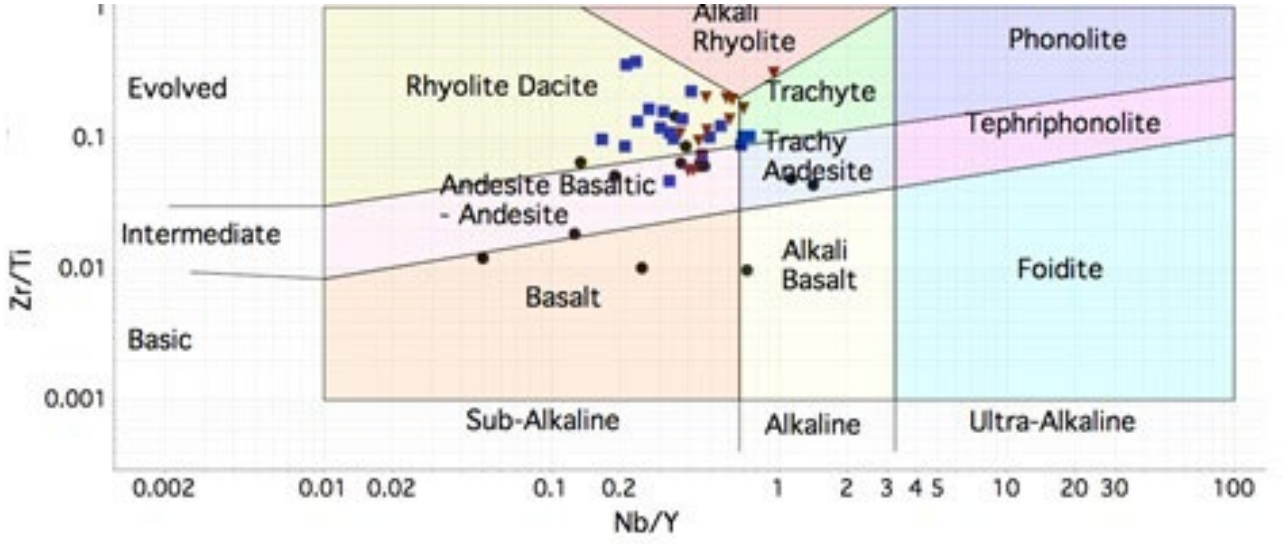

Figure 4.79: Pearce element ratio proxy diagram of intermediate to felsic lithologies from the Chapleau Belt (black circles) and Michipicoten (red triangles), and Abitibi (blue squares) greenstone belts. The Chapleau Belt samples plot in the sub–alkaline field in basalt, andesite basaltic–andesite, and rhyolite dacite fields with a few samples in the alkaline field as alkali basalt and trachy andesite. Note the similarities to the other localities. Note that some samples from the Chapleau Belt plot in the basalt field and may represent samples that experienced seafloor alteration and therefore had a mafic protolith (Modified after Jensen, 1976; Capdevila et al., 1982; Sage, 1985; Turek et al., 1992, 1996a; Pearce, 1996; Wyman and Kerrich, 2009b).

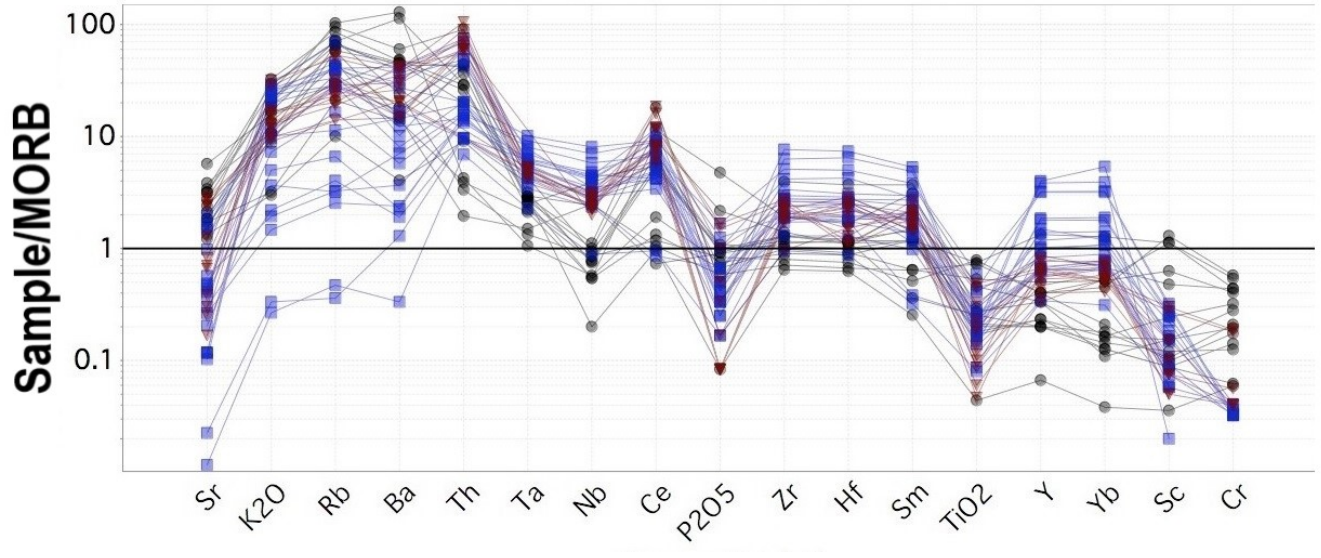

Figure 4.80: MORB–normalized multi–element diagram of Chapleau Belt (black) and Michipicoten (red) and Abitibi (blue) greenstone belts intermediate to felsic lithologies with overall similar patterns from all locations with the most similarity between the Michipicoten and Chapleau Belts (Modified after Pearce, 1983; Capdevila et al., 1982; Sage, 1985; Turek et al., 1992, 1996a; Wyman and Kerrich, 2009b).

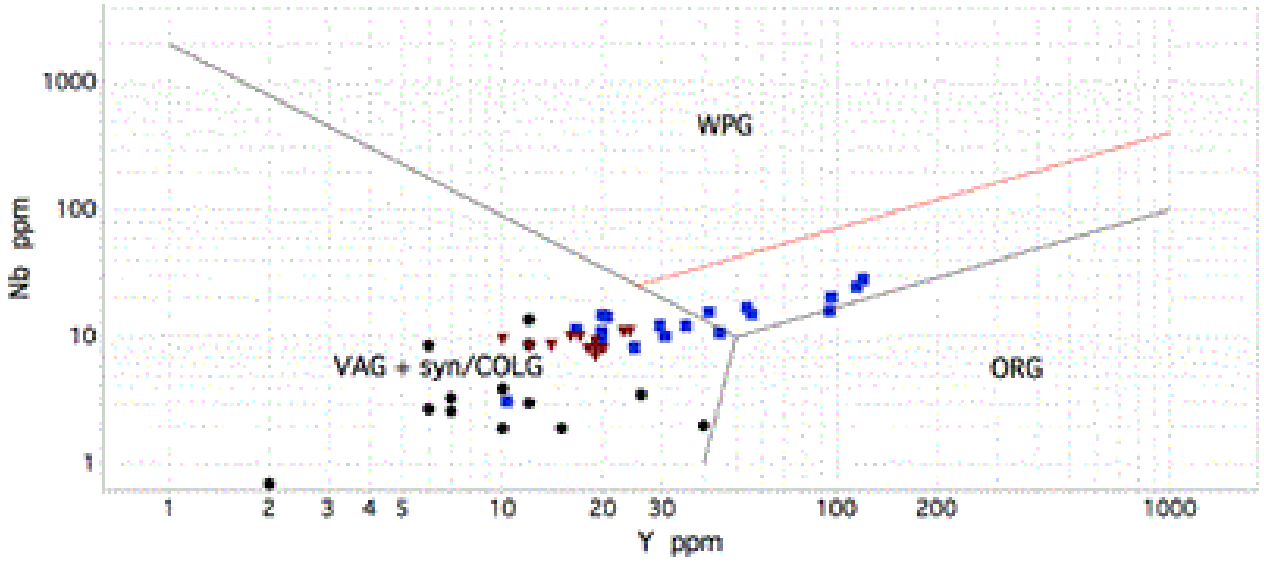

Figure 4.81: Trace element discrimination diagrams for the tectonic interpretation of felsic rocks of Chapleau Belt (black circles) and Michipicoten (red triangles) and Abitibi (blue squares) greenstone belts intermediate to felsic lithologies with the entirety of the Chapleau Belt samples falling within the volcanic arc granites and syn–collisional granite field. Note the similarity between the Chapleau and Michipicoten Belts with some overlap with the Abitibi samples (Modified after Jensen, 1976; Capdevila et al., 1982; Sage, 1985; Turek et al., 1992, 1996a; Pearce, 1983; Wyman and Kerrich, 2009b).

MORB–normalized multi–element diagram displaying the Chapleau belt intermediate to felsic lithologies share similarities with the Michipicoten and Abitibi greenstone belts, particularly the FI type rhyolites of the Abitibi greenstone belt as they are calc–alkaline and have strongly enriched LIL and LFS elements to HFS elements (Fig. 4.80). The samples from all three locations are generally in agreement with one another, however there is minor variability in the most mobile elements (LIL elements). There is some spread in Nb, Sc, Y, and Yb however the shape of the anomalies is similar. The tectonic discrimination diagram shows that the felsic to intermediate samples from this study and those of the Michipicoten and Abitibi greenstone belts plot predominantly in the VAG + syn–COLG region (or volcanic arc granites and syn–collisional granite fields), but numerous Abitibi greenstone samples plot in the WPG (within–plate granite) (Fig 4.81). These are consistent with the new tectonic hypothesis proposed in this thesis.

4.3.4 Unusual lithologies

Samples PVS044 and PVS096 have geochemical signatures resembling adakites and/or Archean high–Al TTG suites located throughout the Wawa subprovince (Polat and Kerrich, 2001). The adakite samples are similar to the high–Mg basalts although with greater SiO_2 and also relatively high Al_2O_3

contents, high La and low Yb contents resulting in fractionated REE, relatively high TiO_2, Fe_2O_3, Mg, Cr, and Ni contents (Polat and Kerrich, 2001).

Samples PVS016, PVS017, and PVS018 are newly identified lamprophyres that intruded into garnet–biotite schist, amphibolite, and banded iron formations. Mineralogically they are composed of metamorphic minerals of riebekite, chlorite, and biotite with few primary features typical of the lamprophyre facies as well as consistent geochemically with other lamprophyres (Mitchell, 1994) (Table 4.1).

Table 4.1: Whole rock and trace element geochemistry of lamprophyre samples. Note the low SiO_2, low total alkalis, and elevated Ba, Rb, Co, Cr, and Ni consistent with lamprophyre geochemistry (Mitchell, 1994).

Sample	PVS016	PVS017	PVS018
SiO_2 (wt pct)	60.93%	46.82%,	47.02%
Al_2O_3	13.84%	15.34%	14.56%
Fe_2O_3 (total)	10.78%	17.92%	15.51%
MgO	2.11%	4.52%	6.13%
Na_2O	0.75%	4.36%	3.13%
K_2O	4.51%	5.57%	5.04%
Ba (ppm)	2540	266	770
Co	67.2	76.4	63.3
Cr	59.8	347	55.2
Cs	11	20.5	24.5
Ni	55	170	55
Rb	167	258	260
LOI	3.64%	2.18%	5.29%

The lamprophyre samples are geochemically similar to the 2.7 to 2.67 Ga diamondiferous lamprophyres in the cycle 3 of the Michipicoten Greenstone belt and lamprophyres in the Abitibi subprovince (Table 4.1) (Lefèbvre et al., 2005). The lamprophyres in the Michipicoten greenstone belt have been interpreted to have been emplaced during the Kenoran orogeny in an area of local extension during subduction (Vaillancourt et al., 2004; Lefèbvre et al., 2005).

Gneisses, migmatites, and pegmatites in the study area generally have simple mineralogy and are composed predominantly of alkali feldspars and quartz, with more complex and evolved mineralogy including biotite, muscovite, garnet, sillimanite, tourmaline, beryl, and chrysoberyl (Figs. 4.8 A, 4.44 A). In contact with the migmatized, garnet–biotite schist ore are folded and boudinaged feldspar–quartz leucosome and pegmatite that hosts light green (tested on a sunny day, outdoors), translucent, euhedral, tabular to blocky chrysoberyl. In contact with the chrysoberyl are alkali feldspars (particularly perthite with bleb to flame lamella), albite, sillimanite (prismatic sillimanite partially replaced by fibrolite), biotite, muscovite, and tourmaline. Late pegmatites with straight, crosscutting contact boundaries are alkali–feldspar dominated with very–coarse grained, pegmatitic alkali feldspars (>3 cm) and trace quartz and quartz–rich pegmatite (>75% quartz) with pale blue, transparent, euhedral, prismatic hexagonal beryl. Beryllium values range 0–800 ppm in all lithologies and are >10 ppm in gneisses and pegmatites.

4.4 Sulphur isotopes

The sulphur isotope data have a range of δ^{34}S between –10.0‰ and 4.7‰ (Table 4.2). The pyrrhotite samples collected have a range between –3.2‰ to 4.7‰, including unmineralized pyrrhotite values between –0.2‰ and 4.7‰, and mineralized pyrrhotite values between –3.2‰ and 0.9‰. Pyrrhotite in the graphitic schist in the garnet–biotite schist has the heaviest value at 4.7‰, whereas pyrrhotite with the lightest value of –3.2‰ from amphibolite and oxide–facies banded iron formation with boudinaged pegmatite. Unmineralized, massive sulphide in amphibolite with lithons of granulite has a value of 3.1‰ and amphibolite with net–texture sulphides has a value of 4.1‰. Samples with macroscopic boudinage have values of –3.2‰ and –1.9‰. The sample of pyrrhotite at the contact between schistose meta–arenite and schistose meta–arkose sandstones has a value of –0.2‰. Samples of pyrrhotite in gold–mineralized amphibolite have values 0.9‰, –1.9‰, and –3.2‰ and samples of unmineralized amphibolite have values of 4.1‰ and 3.1‰.

The samples of pyrite range in δ^{34}S values from –7.2‰ to –0.3‰ with a sample of unmineralized, pyrite value of –0.3 ‰ and samples of mineralized, pyrite samples ranging between –7.2‰ to –3.0‰. Samples of pyrite in areas of boudinage with pegmatite range between –7.2‰ to –3.0‰. Samples of intergrown pyrite and pyrrhotite have a range of –10.0‰ to 0.8‰. Unmineralized, pyrrhotite and pyrite samples have δ^{34}S values between –1.1‰ and –1.5‰. An unmineralized sample collected from massive sulphide and stringers of intergrown pyrite and pyrrhotite collected from feldspar–biotite gneiss have values of –1.5‰ and –1.1‰ respectively. Mineralized, intergrown pyrrhotite and pyrite samples have δ^{34}S values ranging between –10.0‰ and 0.8‰. The sample of intergrown pyrite and pyrrhotite collected from amphibolite has the greatest value of the mineralized,

intergrown pyrite and pyrrhotite samples collected at 0.8‰. Samples of mineralized, intergrown pyrite and pyrrhotite in garnet–biotite schist, quartz–feldspar gneiss, and pegmatite have lower values ranging between –10.0‰ to 0.1‰.

Table 4.2: Sulphur isotope and their isotopic compositions from pyrrhotite (Po), pyrite (Py), and intergrown pyrrhotite and pyrite (Po+Py) collected from the Borden Mine in the Chapleau Belt.

Sample	Mineral	$\delta^{34}S$	Lithology
PVS170	Po	+4.7	Unmineralized biotite–garnet–graphite schist
PVS171	Po+Py	–1.5	Unmineralized biotite–plagioclase gneiss
PVS172	Po+Py	–1.1	Unmineralized biotite–plagioclase gneiss
PVS173	Po	+4.1	Unmineralized amphibolite
PVS174	Po	–1.5	Unmineralized biotite–feldspar gneiss
PVS178	Po	+4.1	Unmineralized amphibolite
PVS180	Po	+3.1	Unmineralized amphibolite
PVS181	Po	–1.9	Low–grade ore in felsic volcanic breccia
PVS183	Py	–0.3	Unmineralized biotite–feldspar gneiss
PVS186A	Po	+0.9	High–grade ore in garnet–biotite schist
PVS186B	Po+Py	+0.8	High–grade ore in garnet–biotite schist
PVS188	Po	–1.9	High–grade ore in garnet–biotite schist/pegmatite
PVS189	Py	–7.2	High–grade ore in garnet–biotite schist/pegmatite
PVS191	Po+Py	–4.5	High–grade ore in biotite–feldspar neosome
PVS192A	Po+Py	–3.1	High–grade ore in BIF boudin in amphibolite
PVS192B	Po+Py	–3.0	High–grade ore in BIF boudin in amphibolite
PVS192C	Po	–3.2	High–grade ore in BIF boudin in amphibolite
PVS192D	Py	–3.3	High–grade ore in BIF boudin in amphibolite
PVS193B	Po+Py	–4.4	High–grade ore in quartz–feldspar neosome
PVS194	Py	–3.0	High–grade ore in garnet–biotite schist
PVS195	Po+Py	–0.5	High–grade ore in garnet–biotite schist/neosome
PVS196	Po+Py	+0.6	High–grade ore quartz–feldspar–biotite gneiss
PVS198	Po	–1.4	High–grade ore in garnet–biotite schist
PVS199	Po+Py	–4.8	High–grade ore in sillimanite–garnet schist
PVS200	Po+Py	–10.0	High–grade ore quartz–feldspar pegmatite

PVS207	Po+Py	–2.2	High–grade ore in garnet–biotite schist/BIF
PVS214	Po	–1.9	High–grade ore in mylonitic amphibolite
PVS267	Po	–0.2	Unmineralized metasandstone

4.5 Lead isotopes

Lead isotope isotopic studies were carried out on six samples from ore and unmineralized zones (one of magnetite (Mt), two of pyrite (Py), and three of pyrrhotite (Po). PVS099 is anhedral magnetite from a low–grade ore, oxide BIF in the field at 16N 5306492/0327597. PVS165 is subhedral pyrite collected from a low–grade, sulphide BIF low–grade ore sample collected from the field at 16 N 5306440/0327710. Sample PVS186 is a high–grade sample of pyrrhotite in amphibolite from DDH#BL12–167 at 445.00 m. PVS192a and PVS192c are collected from high–grade ore collected from DDH# BL12–222 in quartz (BIF) boudins within pegmatite and migmatized amphibolite. Sample PVS192a is a stringer of euhedral pyrite that defines a boudin neck in at a contact with BIF, quartzofeldspathic gneiss, and pegmatite. PVS192c is pyrrhotite from the interior of the competent boudin and is not boudinaged. Sample PVS267 is pyrrhotite collected from an unmineralized contact between metasedimentary arkose and arenite lithologies in BL13–485 at 598.1 m. The data are displayed in Table 4.3. The lead isotopic data vary a considerable range as displayed in thorogenic and uranogenic covariation diagrams.

Table 4.3: Lead isotope samples and their isotopic compositions from magnetite (Mt), pyrite (Py), pyrrhotite (Po) collected from the Borden Mine in the Chapleau Belt.

Sample	Mineral	$^{206}Pb/^{204}Pb$	$^{207}Pb/^{204}Pb$	$^{208}Pb/^{204}Pb$	$^{207}Pb/^{206}Pb$	$^{208}Pb/^{206}Pb$
PVS099	Mt	19.825	15.689	44.483	0.79138	2.24375
PVS165	Py	17.419	15.435	39.399	0.88661	2.26160
PVS186	Po	14.734	15.004	35.058	1.01830	2.37930
PVS192a	Py	17.419	15.435	39.399	0.88661	2.26160
PVS192c	Po	13.737	14.745	33.930	1.07342	2.46993
PVS267	Po	16.143	15.250	36.036	0.94465	2.23221

4.6 Zircon geochronology and Hf isotopes

Zircon geochronology and Hf isotopic studies were conducted from one sample of sillimanite–garnet gneiss, interpreted from field relationships as a seafloor–altered felsic lithology, collected from the Discovery Trench of the Borden Mine property. The lack of detrital zircons, presence of both euhedral igneous and metamorphic textures, and U–Pb zircon geochronology ages are consistent with an igneous protolith followed by metamorphism. No features are consistent with a sedimentary protolith. The results have similarities to those reported by Moser (1994, 2008) for zircon in mafic lithologies of the Chapleau Belt and KSZ.

From the sillimanite–garnet–biotite gneiss of the Discovery Trench, four populations of zircon grains were identified using binocular microscopy, CL imaging, and U–Pb geochronology. The first population of zircon is characterized by stubby crystals and four to six pairs of oscillatory zones, sector zones, a light grey core with black melt inclusions, overgrowths, or annulus, and light grey rims in CL. The characteristics of the first population (n=34), including samples VS006–VS011, VS013–VS015, VS017–VS018, VS020–VS021, VS023–VS025, VS028–VS034, VS036, VS038–VS045, and VS047–VS049 are all identified as igneous zircons due to their distinct properties (Corfu et al., 2003). The second population of zircons are defined by an elongate, more prismatic crystal shape with patchy nebulous and fir–tree zones with dark, cloudy relict cores with a very low CL response, and light grey rims. The characteristics of the second population, including samples VS004, VS012, VS016, VS019, VS022, VS026–VS027, VS035, VS037, VS046, and VS050, are attributed to high–temperature and pressure metamorphic zircons (Corfu et al., 2003). The third population exhibits some characteristics of both the first and second populations, usually with stubby crystals with oscillatory zones that have dark, cloudy patches with very low CL response. The third population includes samples VS002, VS003 and VS005 and is attributed to partial, metamorphic overprint of igneous zircons and may preserve incomplete, metamorphic recrystallization (Corfu et al., 2003). The fourth population consists of only a single, large crystal, elongate and prismatic, with an elgonate, prismatic, bright, light grey, strong CL response, grey inner core, and thick, low–response CL response, medium–grey metamorphic rim. The fourth population is composed of only one sample, VS001, and represents metamorphic recrystallization (Corfu et al., 2003). The grains have a very low CL response, with sector and fir–tree zonation typical of high–temperature metamorphic zircons (Fig. 3.1) (Corfu et al., 2003).

Ages were determined using LA–ICP–MS and concordia and discordia diagrams were constructed for the two oldest populations (Figs. 4.82–4.85). The youngest population has only one zircon and is significantly younger than the other two populations with a $^{207}Pb/^{206}Pb$ age of 2598 ± 17 Ma and was not included in the two older concordia ages. The oldest age population has intercepts at 0 ± 0 and 2703.9 ± 2.8 Ma (or ± 7.3 Ma with 2 sigma and decay–constant errors included) and a mean

square weighted deviation (MSWD) = 0.89 (Fig. 4.83). The second–oldest population has a concordia age of 2667.1 ± 7.2 (2 Sigma, decay–constant errors included) and a MSWD (of concordance) = 5.1 and probability (of concordance) = 0.024 (Fig. 4.84). Discordia diagrams were also prepared as the discordant intercepts are also important, particularly for the metamorphic age data (Figs. 4.85). The most important lower intercept of the discordia diagram for our study is at 2598 ± 73.3 Ma as it defines the metamorphic events. An upper intercept at 2735 Ma is also an important discordia intercept in this study as it is approaching the upper age of known magmatism in the Wawa–Abitibi terrane.

Epsilon Hf (εHf) is plotted against the U–Pb crystallization ages and generalized populations (the younger and older populations) (Figs. 4.86–4.87). The depleted mantle growth line (DM) in red is modeled using $^{176}Lu/^{177}Hf = 0.0388$, present day $^{176}Hf/^{177}Hf = 0.28325$ (Griffin et al., 2000; Andersen et al., 2009) with a ^{176}Lu decay constant of 1.867x10–11 yr–1 (Söderlund et al., 2004). The DM model age is based on the $^{176}Hf/^{177}Hf$ ratio of mid–ocean ridge basalts (MORB). Epsilon Hf values for the first group of zircon at 2.70 Ga range from –3.7 to +4.1, indicating that mafic volcanism in the Chapleau Belt had a dominantly juvenile source with variable contributions from older crustal components. Depleted mantle model ages for the first population of zircon range between 2.99–3.47 Ga, also supportive of involvement of older crustal components for mafic volcanism in the Chapleau Belt (Figs. 4.86–4.87).

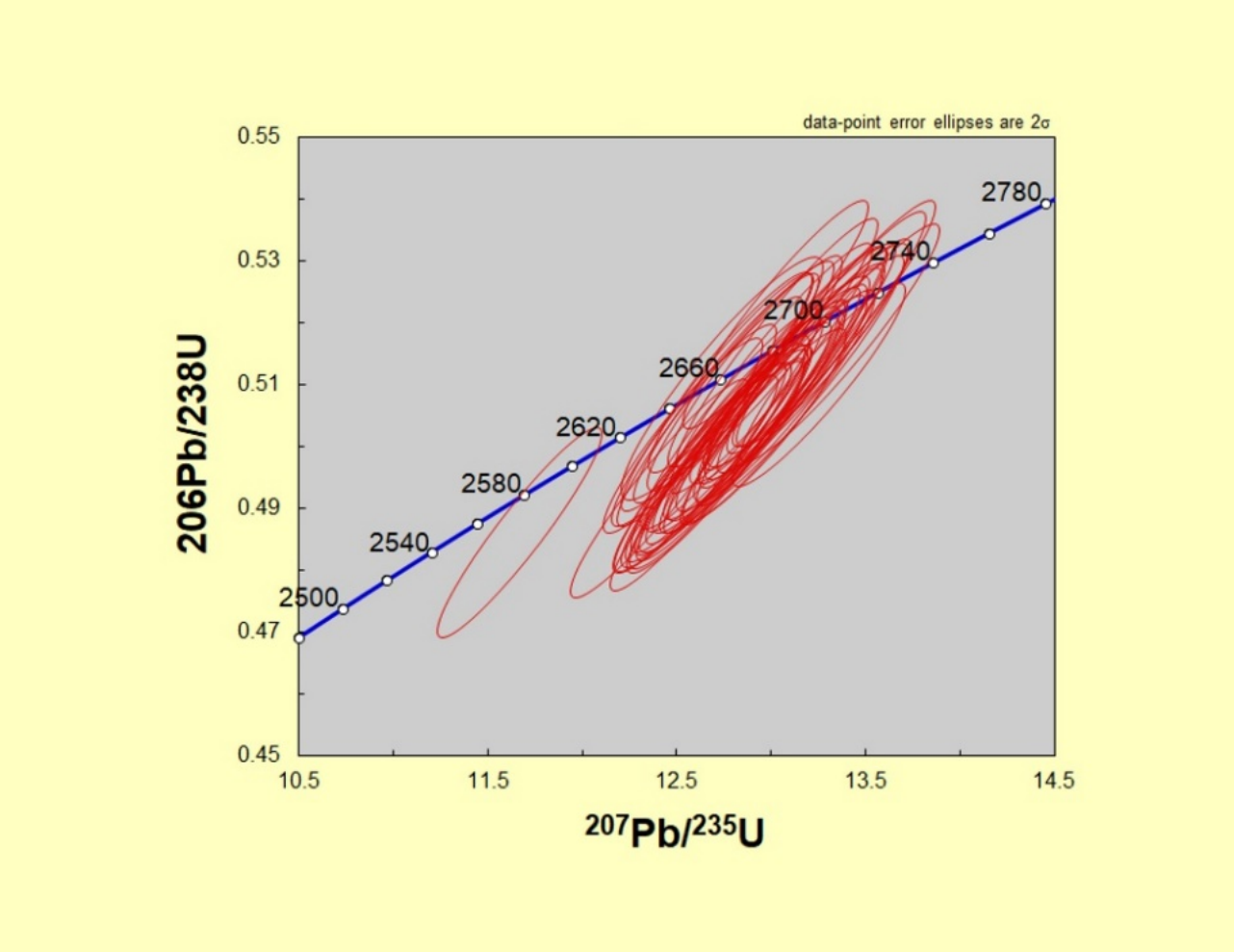

Figure 4.82: Concordia diagram of U–Pb LA–ICP–MS data of the zircon analyses collected from sillimanite–garnet–biotite gneiss and schist in the Discovery Trench in the Chapleau Belt.

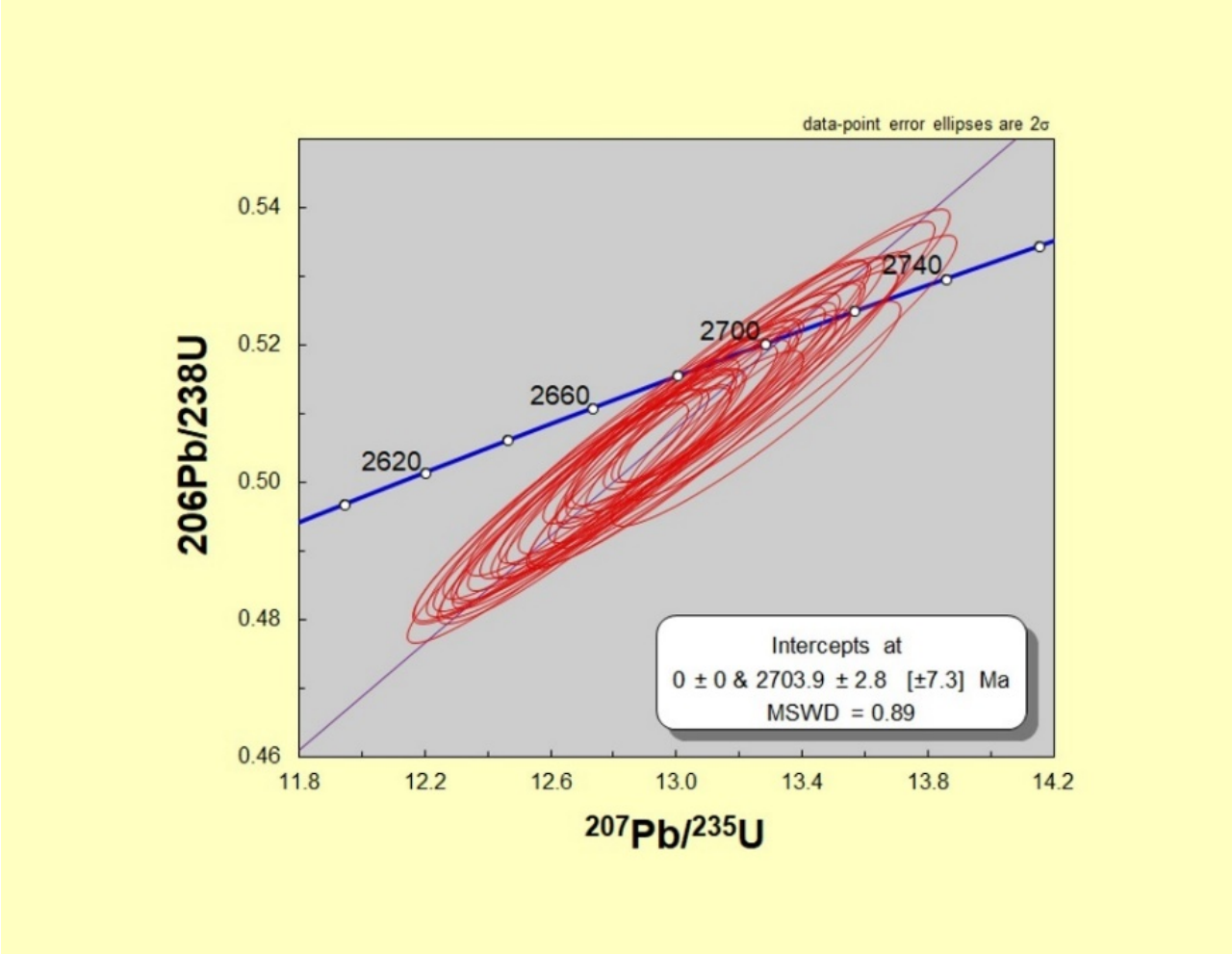

Figure 4.83: Concordia diagram of U–Pb LA–ICP–MS data of the oldest population of zircons collected from sillimanite–garnet–biotite gneiss and schist in the Discovery Trench in the Chapleau Belt with intercepts at 0 ± 0 and 2703.9 ± 2.8 (or ± 7.3 Ma with 2 sigma and decay–constant errors included) and an MSWD = 0.89.

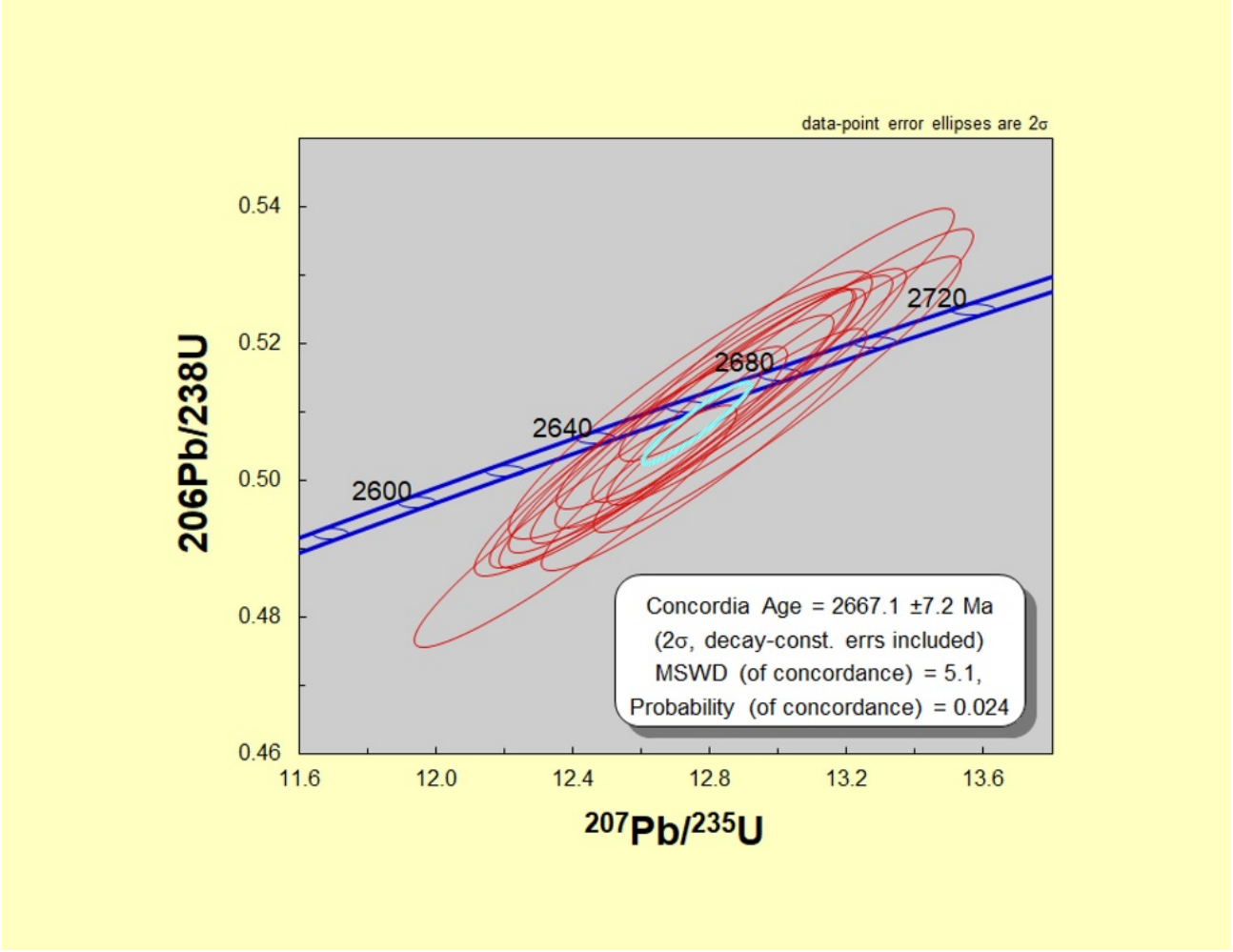

Figure 4.84: Concordia diagram displaying the U–Pb LA–ICP–MS data for the second–oldest population of zircon in sillimanite–garnet–biotite gneiss and schist in the Discovery Trench of the Chapleau Belt with intercepts at 2667.1 ± 7.2 (2 Sigma, decay–constant errors included) and a MSWD (of concordance) = 5.1 and probability (of concordance) = 0.024.

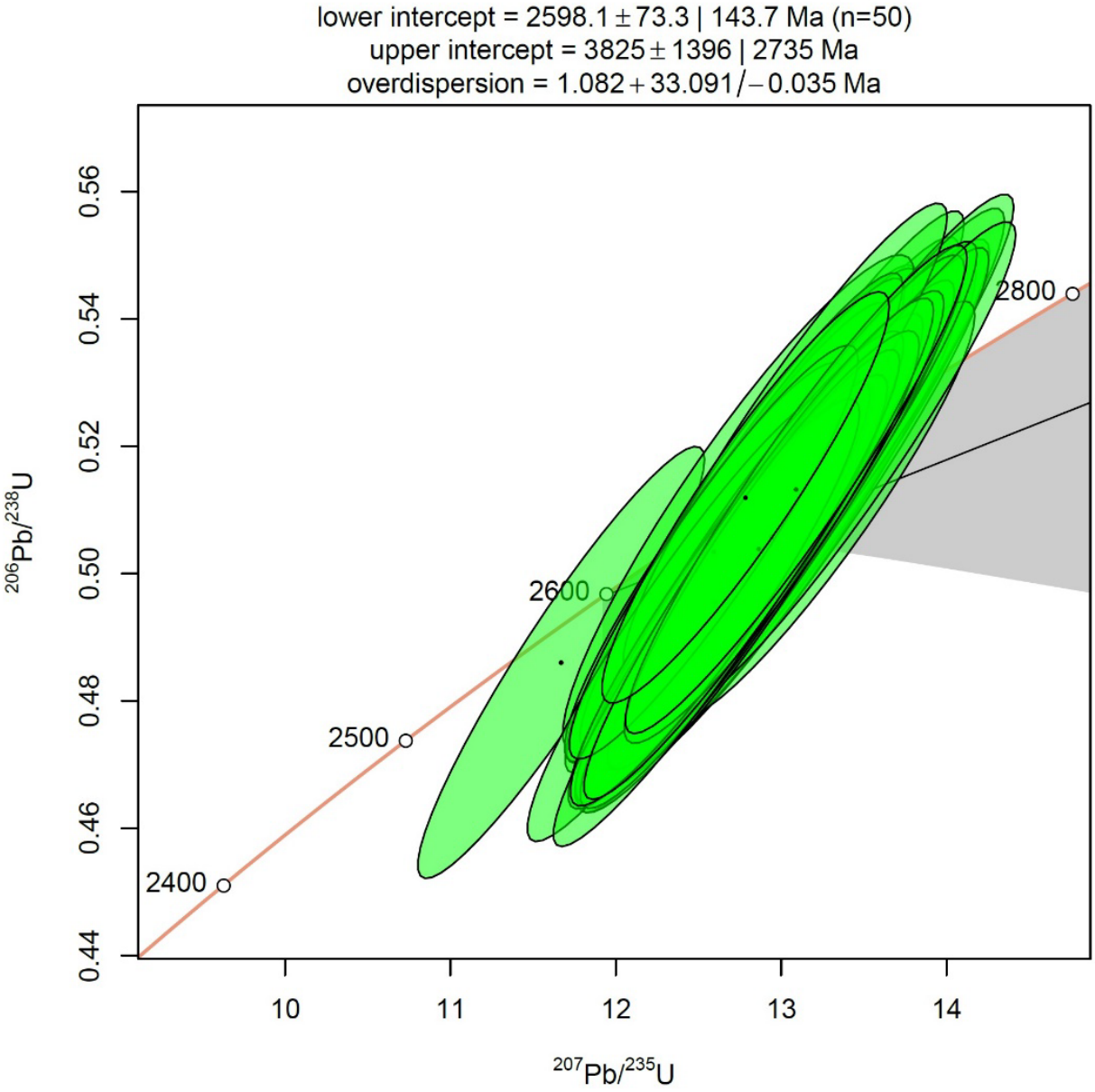

Figure 4.85: Discordia diagram displaying the U–Pb LA–ICP–MS data of all zircons collected from sillimanite–garnet–biotite gneiss and schist in the Discovery Trench in the Chapleau Belt with a lower intercept at 2598 ± 73.3 Ma consistent with the youngest zircon population.

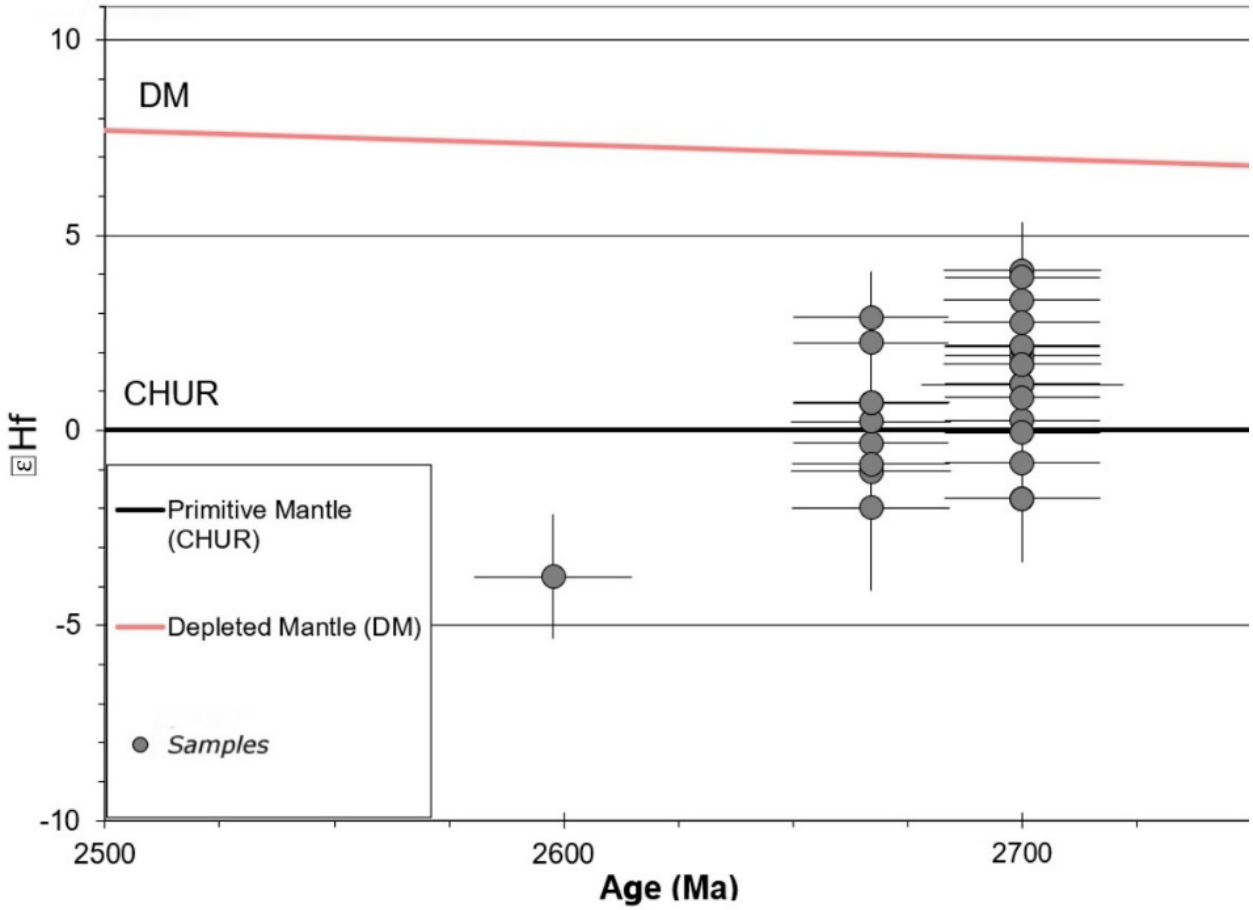

Figure 4.86: εHf values versus U–Pb crystallization ages grouped into the youngest (far left), young (middle), and oldest (far right) zircon populations from sillimanite–garnet–biotite gneiss and schist of the Discovery Trench in the Chapleau Belt (whiskers denote error) and are below the depleted mantle (DM) line and cross over the primitive mantle (CHUR) line, consistent with juvenile magmatism to an evolving system.

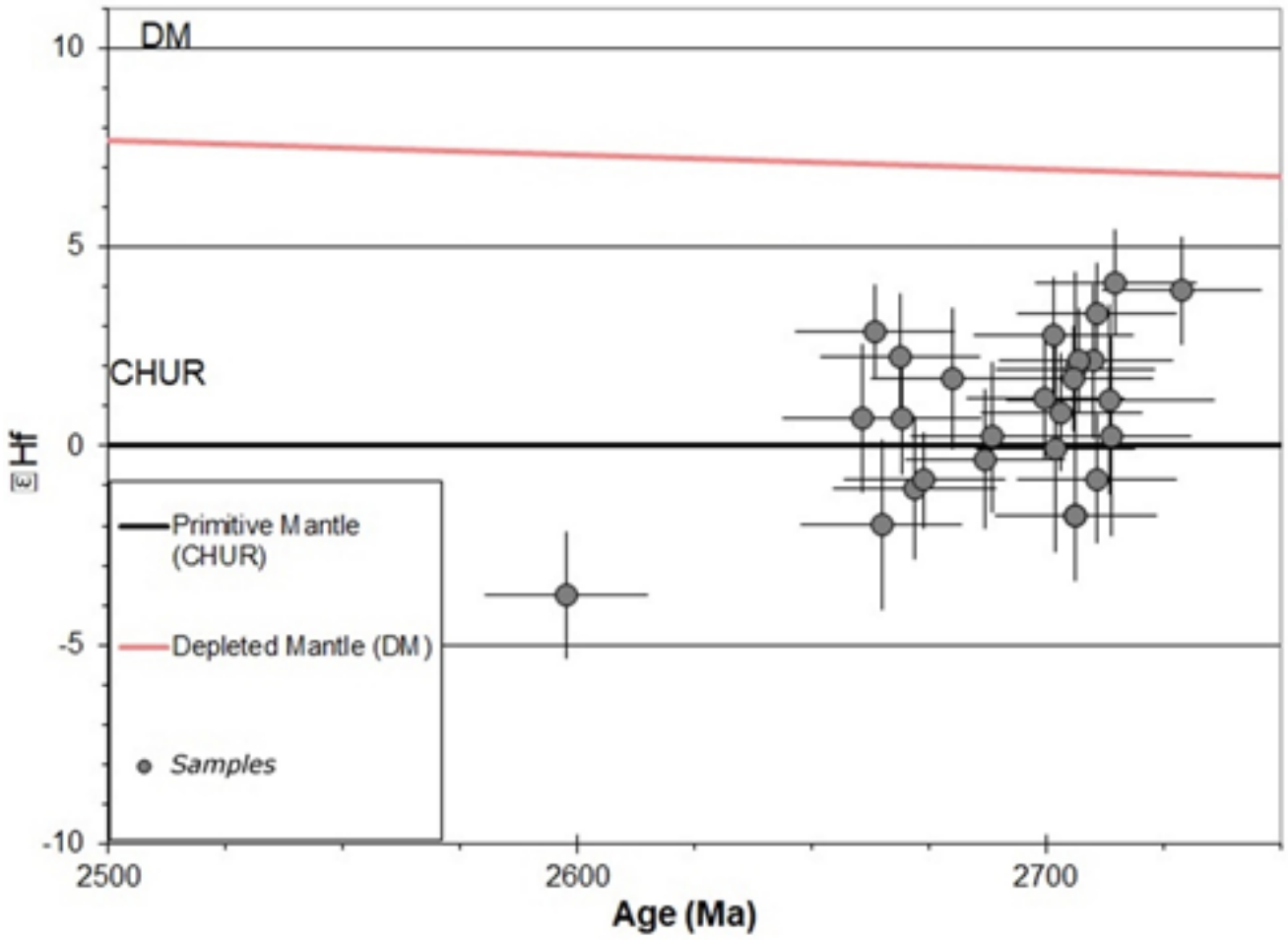

Figure 4.87: εHf values versus U–Pb crystallization ages for zircons from sillimanite–garnet–biotite gneiss and schist of the Discovery Trench in the Chapleau Belt (whiskers denote error) without grouping into the specific age categories and are below the DM line and cross over the CHUR line, consistent with an evolving system from juvenile magmatism to a more evolved system.

4.7 Field relationships, lithologies, and geochronology in the Chapleau Belt, WGD, and southern KSZ

The oldest and stratigraphically lowest lithologies in the study area are coarse–grained to porphyroblastic, massive to gneissic ultramafic to mafic amphibolite and metatexite (Figs. 4.2, 4.5, 4.6 E, 4.7 F, 4.9 B, 4.10 A–B; 4.13 B–C; 4.14 C–D, F–H; 4.15 C, E; 4.16 A–E; 4.17 A–C, E; 4.18 A–D). Interlayered in these lithologies are banded iron formations (BIF) and porphyroblastic hornblende ± garnet gneiss at the sharp, upper contact with fine–grained to medium–grained (± plagioclase porphyroclasts), gneissic to schistose mafic metavolcanic and volcaniclastic lithologies (Figs 4.7 D–E, 4.9 E). Interlayered are garnet–biotite and sillimanite–garnet–biotite gneisses and leucosomes (± chrysoberyl, beryl), schists, and migmatites with oxide– and sulphide–facies BIF and metasediments, muscovite quartzofeldspathic gneiss and migmatite, lamprophyre, and metavolcanic and volcaniclastic

mafic to felsic lithologies (Figs. 4.6 B; 4.7 A; 4.9 D–F; 4.10 C–F; 4.11 A–B, E–G; 4.13 A, F). At the highest stratigraphic level are metasandstones and metaconglomerates (Figs. 4.13 D–E, 4.16 C). Unique to the KSZ are high–pressure granulites and the Shawmere anorthosite complex (Fig. 4.15 D). The WGD is composed of all of the above lithologies (anorthosite has not been identified) at the lower to upper amphibolite facies although partially to completely assimilated in felsic plutonic lithologies and migmatitic leucosomes). U–Pb zircon ages of amphibolite and granulite from previous studies have dated the mafic lithologies between 2703 to 2680 Ma (Moser, 1994; Moser et al., 2008). The minimum age of mafic volcanism is dated at 2677 +5/–3 Ma (Percival and Krogh, 1983). All of these lithologies are continuous from the western WGD to the southern KSZ with an increasing metamorphic grade from amphibolite and patchy metatexite to granulite, stromatic and schollen metatexite, and diatexite.

Metaconglomerate and metasedimentary lithologies that have not experienced migmatization have an angular contact (defined by oblique–reverse and –normal sense shear zones) with the older lithologies described previously, and have a maximum depositional age 2667 ± 2 Ma (Krogh, 1993) and a lower age of burial and metamorphism in the lower crust at 2659 ± 8 Ma (Moser et al., 2008; Bowman et al., 2011). Crosscutting these older lithologies are pegmatitic to megacrystic, quartz–feldspar pegmatites in the Chapleau Belt and WGD and have U–Pb zircon ages of 2640 ± 2 to 2584 ± 2 Ma (Krogh, 1993). Pegmatitic dykes often define regional gneissosity, are commonly boudinaged, and much less commonly crosscut perpendicularly the regional fabric. The megacrystic pegmatites have straight contacts, are up to 1–meter–thick, and strike northwest–southeast to north–south with a vertical dip. The youngest lithology in the study area are diabase dykes of the Matachewan and Kapuskasing/Marathon mafic dyke swarms. The Matachewan mafic dykes (U–Pb baddeleyite age of 2459 ± 5 Ma (Heaman, 1997)) are typically <1 m thick, have straight to curved boundaries, strike northwest–southeast to north–south with subvertical dip, define vertical, upright open to gentle folds, or are perpendicular to extensional fabrics and green amphibole after pyroxene is common.

4.8 Zircon U–Pb geochronology and Lu–Hf isotope systematics

Four populations of zircon grains were identified using binocular microscopy, CL imaging (Fig. 3.1), and U–Pb geochronology (Fig. 4.82–4.85). The first population is defined by stubby crystals and four to six pairs of oscillatory zones, sector zones, light grey core with black melt inclusions, overgrowths, or annulus, and light grey rims in CL and are diagnostic of igneous zircons. The second population is defined by an elongate, more prismatic crystal shapes with patchy nebulous and fir–tree zones with dark, cloudy relict cores with a very low CL response, and light grey rims attributed to high–temperature and pressure metamorphic zircon. The third population exhibits some characteristics of both

the first and second populations, usually with stubby crystals with oscillatory zones that have dark, cloudy patches with very low CL response attributed to partial, metamorphic overprint of igneous zircon and may preserve incomplete, metamorphic recrystallization. The fourth population consists of only a single, large crystal, elongate and prismatic, with a light grey and strong CL core, and a thick, low CL rim. LA–ICP–MS analyses of the first three populations yielded two groups: an older, slightly discordant group of 34 spot analyses has the upper intercept at 2703.9 ± 7.3 Ma (2σ and including decay–constant uncertainty) and a mean square weighted deviation (MSWD) = 0.89, and the second and third groups of 15 analyses have a concordia age of 2667.1 ± 7.2 Ma and a MSWD = 5.1 and probability (of concordance) = 0.024. One single analysis for the fourth population zircon crystal has a much younger $^{207}Pb/^{206}Pb$ age of 2598 ± 17 Ma (spot VS–001).

The essentially uniform age of 2703.9 ± 7.3 Ma of the first group of LA–ICP–MS analyses (Fig. 4.83), with textures consistent with igneous zircon, supports our field hypothesis that the sillimanite–garnet–biotite gneiss from the Discovery Trench at the Borden Mine is a metamorphosed equivalent of seafloor hydrothermal alteration of the associated amphibolite. This age of 2703.9 ± 7.3 Ma is interpreted to represent the timing of mafic volcanism in the Chapleau Belt, similar to mafic volcanism in other parts of the Wawa–Abitibi terrane. The concordant age of 2667.1 ± 7.2 Ma from the second group of LA–ICP–MS analyses, with zircon textures consistent with granulite–facies metamorphism, is in close agreement with both the emplacement of the Shawmere anorthosite complex and the timing of the peak granulite–facies metamorphism in the KSZ (Fig. 4.84) (Moser et al., 2008; Bowman et al., 2011; Huang, H., pers. comm., 2015). Moreover, the younger $^{207}Pb/^{206}Pb$ age of 2598 ± 17 Ma from the single zircon grain of the fourth population is also consistent with the prolonged high–grade metamorphism of ~80 Ma in the KSZ (Moser et al., 2008; Bowman et al., 2011). Zircon ages between the 2703 Ma and 2667 Ma populations have characteristics of both groups and may suggest incomplete, metamorphic reactions. Epsilon Hf values provide evidence of a dominantly juvenile source with variable contributions from older crustal components in the Chapleau Belt. The tectonic evolution from juvenile to more evolved magmatism system is consistent with previous tectonic studies conducted in the Wawa–Abitibi terrane (Kerrich and Cassidy, 1994; Wyman and Kerrich, 2002; Ayer, 2005; Percival et al., 2006).

4.9 Structures, metamorphism, and fabric analysis

Previous field mapping in the WGD, Chapleau Belt, and southern, central, and northern KSZ by various workers have identified up to five stages of deformation (Percival and Card, 1983; Percival, 1989; Krogh, 1993; Bursall et al., 1994; Moser, 1994; Moser et al., 1996, 2008). This study has

identified these previously described structures and synthesized these results with newly identified structures and simplified the structural evolution into two stages.

Brittle–ductile to ductile, sinistral strike–slip shear zones strike east–west to northeast–south west and dip moderately to steeply to the northwest. Sinistral shear sense in mylonites, mineral fish, rotated foliation boudins, antithetic shear bands, S–C fabric, and isoclinal to sheath folds document the transfer structures in the region (Figs. 4.6–4.18, 4.25). Regional, ductile to brittle–ductile, sinistral shear zones define the northern and southern contacts of the Chapleau Belt with the WGD and continue into the central KSZ (Fig. 4.25). Similar shear zones are also within the interior of the Chapleau Belt and KSZ, all of which are defined as transfer shear zones in this study. Quartz ribbons, rotated and healed subgrains, and chessboard textures, feldspar ribbons, deformation twins, and subgrains, pyroxene deformation twins, and garnet subgrains provide evidence for sinistral, strike–slip deformation during at least the amphibolite to granulite facies metamorphism, and quartz c–axis fabrics are consistent with prism [c] slip systems during non–coaxial (sinistral) deformation (Figs. 4.6 A–D, 4.11 A–G, 4.12 C, 4.44 A–C, 4.45 A–C, 4.46) (Tullis, 1992; Okudaira, et al., 1995; Kruhl, 2003). The highest–strain shear zone in the interior of the Chapleau Belt can also be defined as a shear–related late Z–fold and parallels the open to gentle upright fold defining the Matachewan mafic dyke swarm (Figs. 2.2, 4.25). Other high–strain zones are located at the northern and southern boundaries with the WGD and the boundary also defines a Z–shape geometry. Similar regional– to local–scale, upright to vertical Z– and S–shaped folds are located throughout the Chapleau Belt and KSZ. Oblique structures (sinistral, reverse and sinistral, normal) are restricted to contacts along metaconglomerates with other lithologies. Overprinting structures are sinistral and dextral faults, cataclasites, breccia, and pseudotachylites, including the regional ILDZ.

Extensional shear zones are defined by gneissosity and located predominantly in the mafic metavolcanic lithologies and porphyroblastic mafic lithologies anastomoses around the younger plutons and domes in the WGD. Extensional structures in the WGD are defined by boudins and shear zones that have horizontal to vertical plunge to the east to northeast in the direction of greatest extension (Fig. 4.25). Extensional structures in the older lithologies, including the mafic metavolcanic and porphyroblastic mafic lithologies in the Chapleau Belt and KSZ, are defined by ductile, extensional horizontal to subhorizontal shear zones with the direction of greatest extension also to the northeast. Regional to outcrop scale amphibolite and granulite boudin trains with lengths 100 m to >1 km in length and outcrop–scale boudins, foliation boudins, chocolate–tablet structures, and mullions also define extensional structures and CCW rotation. Beneath the boudins and boudin trains are extensional ductile

shear zones that also extend to the northeast. Different types of boudin necks and shapes, particularly fish–mouth boudins and rotated foliation boudins, also support the extension direction.

The contact between the boudinaged amphibolite and granulite lithons and schistose to gneissic intermediate to felsic gneisses is complex. Schistose and gneissic intermediate to felsic gneisses anastomose and drape around the dense lithons defining doubly–plunging periclines. The periclinal anticlinal folds contour the shape of the mafic boudins with symmetrical limbs and near horizontal plunge. The boudin necks are infilled with felsic pegmatite and felsic gneisses with near vertical to vertical hornblende mineral lineation and the older near–horizontal lineation. Along the boudin–host lithology contact are near vertical, east–west to southeast–northwest striking, sinistral strike–slip ductile shear zones (Fig. 4.13 F, 4.16 B). Below the lithons are horizontal to subhorizontal extensional shear zones, commonly defined by felsic pegmatitic sills, perpendicular to boudin necks (Fig. 4.18 D).

The microstructures in the Borden Mine lithologies, including those in the ore zones, constrain the temperature, pressure, and strain rate conditions the lithologies experienced during formation and exhumation. Both basal <a> and prism [c] data form points and are subparallel to parallel to X and Y strain directions, not the Z strain direction. The CPOs of quartz with c–axis maxima sub–parallel to parallel to X are compatible with prism [c] slip at high metamorphic temperatures and microstructures that form at granulite facies temperatures (i.e., chessboard textures)(Kruhl, 2003). Other studies suggest that basal <a> slip and prism [c] CPOs imply formation at low–grade metamorphism after granulite or eclogite facies metamorphism (Barth et al., 2010). CPO data collected in quartz provide evidence for plane strain or flattening regimes. The highest–temperature deformation, denoted in prism [c], records a sinistral kinematic shear sense. Recrystallization, and perhaps progressive simple shear, can explain the single c–axis maxima due to orientation along the easier basal slip plane, parallel to the bulk shear plane (Bouchez and Duval, 1982), however that is a simple solution and the great spread of orientations may be due to rotation recrystallization or similar processes influencing heterogeneity in quartz boudins (Bouchez, 1977). Boudinage with subgrain formation in quartz, feldspars, and garnet provide evidence for possible dislocation creep during the amphibolite and granulite facies. This is particularly important as gold mineralization also survived these grades of metamorphism and can provide insight into solid–state remobilization of sulphide and native gold in addition to hydrothermal fluid remobilization.

Prograde metamorphic mineral assemblages are preserved in lithons in both strike–slip and extensional shear zones. However, in tightly–spaced, penetrative schistose to mylonitic fabric, boudin necks, and foliation boudins there is evidence of retrograde metamorphic reactions. In the Chapleau Belt there is an eastward increase in metamorphic grade as demonstrated by the blue–green hornblende–in and clinopyroxene–in isograds in Fig. 4.23, while the orthopyroxene–in isograd is just east of the map in

the southern KSZ (Percival, 1989). The first evidence of the prograde path of metamorphism in the KSZ (Fig. 4.88) is documented at 685°C–735°C, 9 kb (straight line with rectangles; Hartel and Pattison, 1996), crosses the muscovite dehydration reaction to 750°C–790°C, 10–11 kb (solid box; Mäder, 1994), reaches peak metamorphism at 850°C, 11 kb in the granulite facies at >2660 Ma (cross; Hartel and Pattison, 1996; Mäder et al. 1994), field observations of Bt + Grt to Bt + As (Sil) reactions in felsic granulite within the southern KSZ (dashed box), the retrograde path is documented at 685°C–735°C, 9 kb (line with circles; Hartel and Pattison, 1996), at lower pressure 770°C, 6 kb (Percival, 1983), observed Ch + Qtz to Be + As + Ms reactions in drill cores in the retrograde amphibolite facies at ca. 2620 Ma (medium grey field), and the path continues at 750°C, 6 kb (tilted cross, Percival, 1983).

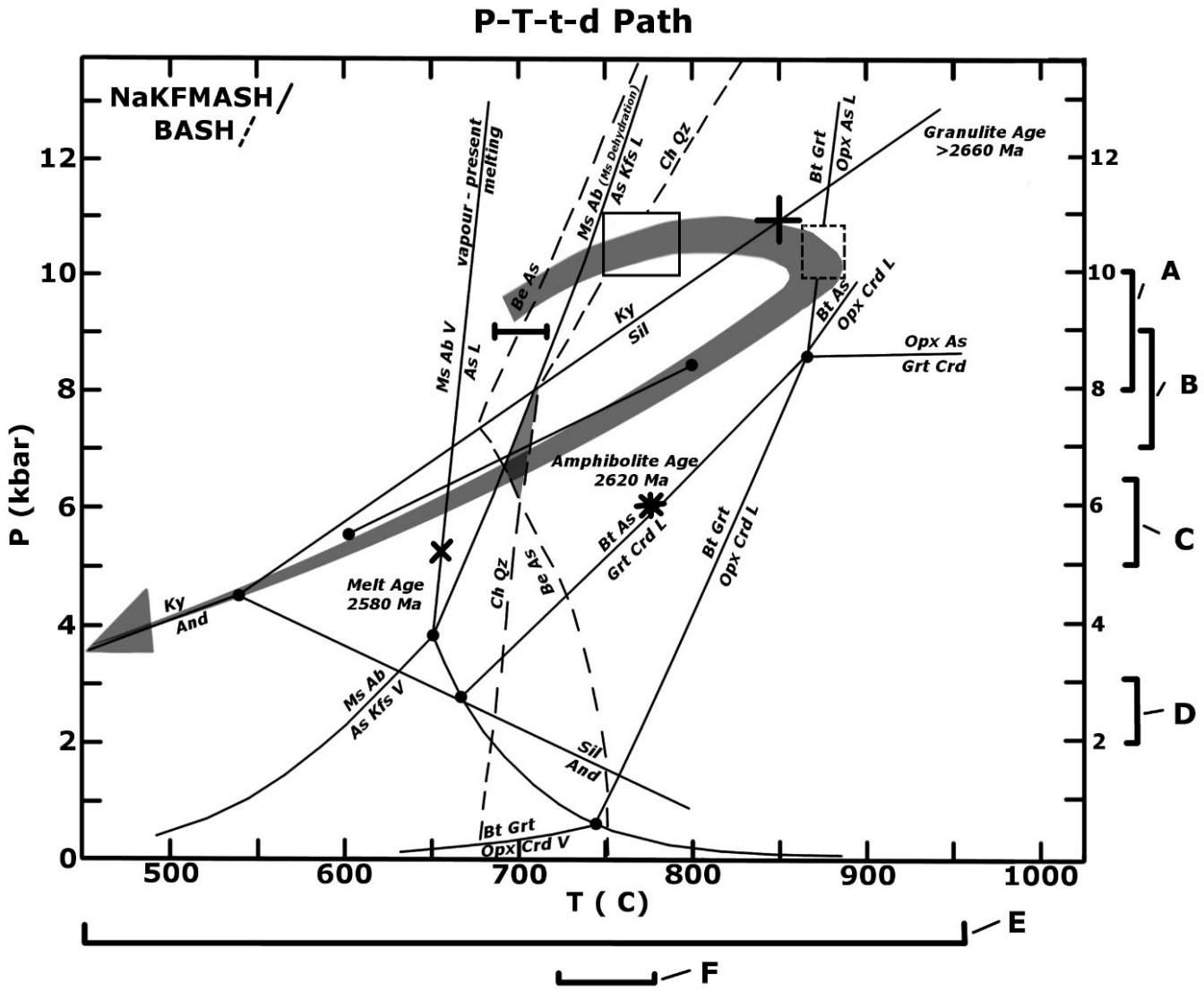

Figure 4.88: P–T–t–d path with NaKFMASH (solid lines) and BASH (dashed lines) petrogenetic grids displaying the hairpin tight, smooth, clockwise path in the Chapleau Belt and KSZ (modified after Robinson et al., 1982; Barton, 1986; White et al., 2001).

4.10 Correlation of the Wawa–Abitibi terrane across the WGD and KSZ

The tectonostratigraphy across the western WGD, the Chapleau Belt, and the southern KSZ can be correlated to the Catfish and Doré assemblages of the western Wawa subprovince and the Tisdale and Timiskaming assemblages of the southern Abitibi subprovince, albeit higher–grade equivalents (Fig. 4.89). Specifically, the stratigraphy of garnet–amphibolite and granulite, interlayered and topped with BIF and graphite schists, overlain by intermediate and quartzofeldspathic schists and gneisses, garnet–sillimanite–biotite schists and gneisses, topped with amphibolite, minor BIF and metasedimentary lithologies, and crosscut by diamond–bearing lamprophyre and pegmatites of the western WGD, Chapleau Belt, and southern KSZ are upper amphibolite to high–pressure granulites, metatexites, and diatexite equivalents of the youngest stratigraphy in the Wawa–Abitibi terrane (Figs. 3.89, 3.90). In particular, the U–Pb age of 2703.9 ± 7.3 Ma from the sillimanite–garnet–biotite gneiss from this study is within error with the 2710 ±7.7 to 2701 ± 7.7 Ma Catfish assemblage of the Michipicoten greenstone belt in the Wawa Subprovince (Smith, 1981; Turek, 1984; Corfu et al., 1989; Sage, 1985; Corfu and Sage, 1992; Turek et al., 1996) and the 2710 to 2704 Ma Tisdale and/or 2704 to 2695 Ma Blake River volcanic assemblages of the Abitibi Subprovince (Polat et al., 1998; Polat and Kerrich, 2000; Ayer et al., 2004, 2005; Benn and Moyen, 2008; McNicoll et al., 2014; Frieman et al., 2017; Monecke et al., 2017). Therefore, the correlation of any of these assemblages is geochronologically consistent with the new geochronology documented in the Chapleau Belt. The younger metasedimentary lithologies in the study area with a U–Pb detrital age of 2667 ± 2 Ma (Krogh, 1993) can also be correlated to the Doré metasediments in the Wawa subprovince with a <2680 ± 3 Ma detrial age and the ~2679–2669 Ma Timiskaming assemblage in the Abitibi subprovince (Corfu et al., 1991; Corfu, 1993, Ayer et al., 2002, 2005; Thurston et al., 2008; Smith, 1981; Turek, 1984; Corfu and Sage, 1992).

Overprinting, late Neoarchean metamorphism and plutonism can also be correlated across the study area into the Wawa and Abitibi subprovinces (Krogh and Turek, 1982; Corfu et al., 1989a, 1991; Turek et al., 1990a, 1996a; Pan et al., 1998; Pan and Fleet, 1999; Easton, 2000; Ayer et al., 2002, 2005; Percival and Easton, 2007; Benn and Moyen, 2008; Moser et al., 2008; Lodge et al., 2015; Frieman et al., 2017). However, the study area experienced a ~80 Ma high–grade metamorphism that the Wawa and Abitibi subprovinces did not and has been well documented in U–Pb geochronology using metamorphic zircon, monazite, and garnet (Frarey and Krogh, 1986; Percival, 1989; Corfu et al., 1989; Card, 1990; Turek et al., 1992; Moser, 1994; Krogh and Moser, 1994; Moser et al., 1996; 2008; LaFontaine, unpublished MSc. thesis, 2016; Kendrick et al., 2019). The high–grade metamorphism specific to the WGD and KSZ has been documented as a long–lasting high–temperature magmatic and metamorphic 80 Ma anomaly from 2660 Ma to 2585 Ma (Moser, 1994; Krogh and Moser, 1994; Moser et al., 1996,

2008; LaFontaine, unpublished MSc. thesis, 2016; Kendrick et al., 2019). While the high–temperature anomaly is a long–lived event the dominant mode of the U–Pb zircon, monazite, and titanite ages in the study area is 2.66 Ma (Krogh, 1993; Krogh and Moser, 1994), coinciding with the emplacement of the Shawmere anorthosite complex ca. 2.66 Ga (Huang, H., pers. comm., 2015).

The most distinctive correlative (or at a minimum, contemporaneous) stratigraphic markers across the southern Superior Province in the Wawa subprovince, WGD, Chapleau Belt, KSZ, and Abitibi subprovince include: (1) world–class gold mines hosted in mafic volcanism with evolving tectonic signatures from tholeiitic MORB (± BABB) to calc–alkaline arc and felsic volcanism in the ca. 2700 Ma mafic lithologies of the Chapleau Belt, WGD, and KSZ to the ca. 2700 Ma volcanic Tisdale and Blake River assemblages of the Abitibi subprovince (or within error of other formations including the Kinojevis, Krist and other minor assemblages) and Wawa and Catfish assemblages of the Wawa subprovince, (2) the <2667 ± 2 Ma metasedimentary lithologies in the study area with the <2680±3 Ma Doré metasediments in the Wawa subprovince and ~2679–2669 Ma Timiskaming assemblage in the Abitibi subprovince, and (3) the ca. 2.7–2.67 Ma diamondiferous lamprophyres that crosscut the Catfish assemblage of the Michipicoten greenstone belt, the mafic lithologies of the Chapleau Belt, and mafic lithologies in the Abitibi subprovince (Fig. 4.89).

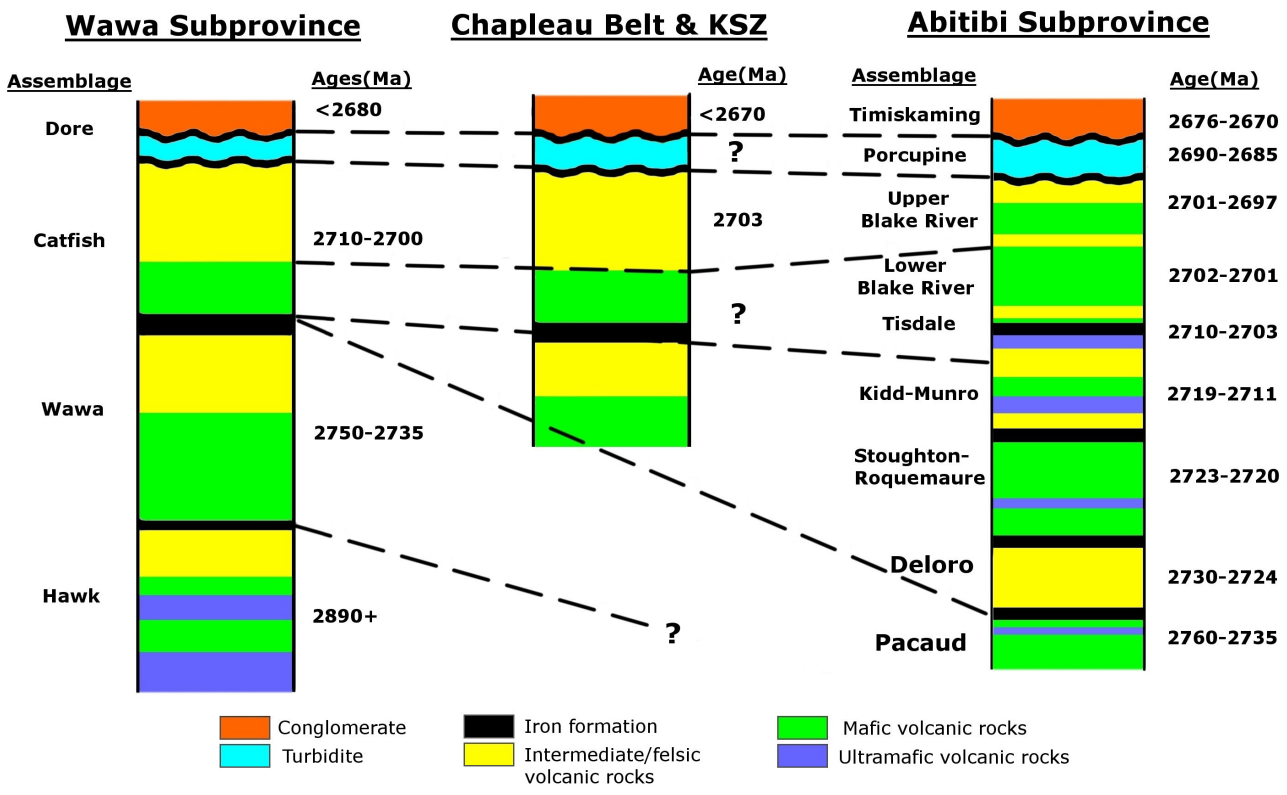

Figure 4.89: Proposed correlation and/or contemporaneous tectonostratigraphy across the Wawa subprovince, Chapleau Belt and southern KSZ, and Abitibi subprovince with major stratigraphic markers including metamorphosed conglomerate, turbidites, mafic and felsic lithologies, and BIF (after Moser, 1994; Ayer et al., 2010).

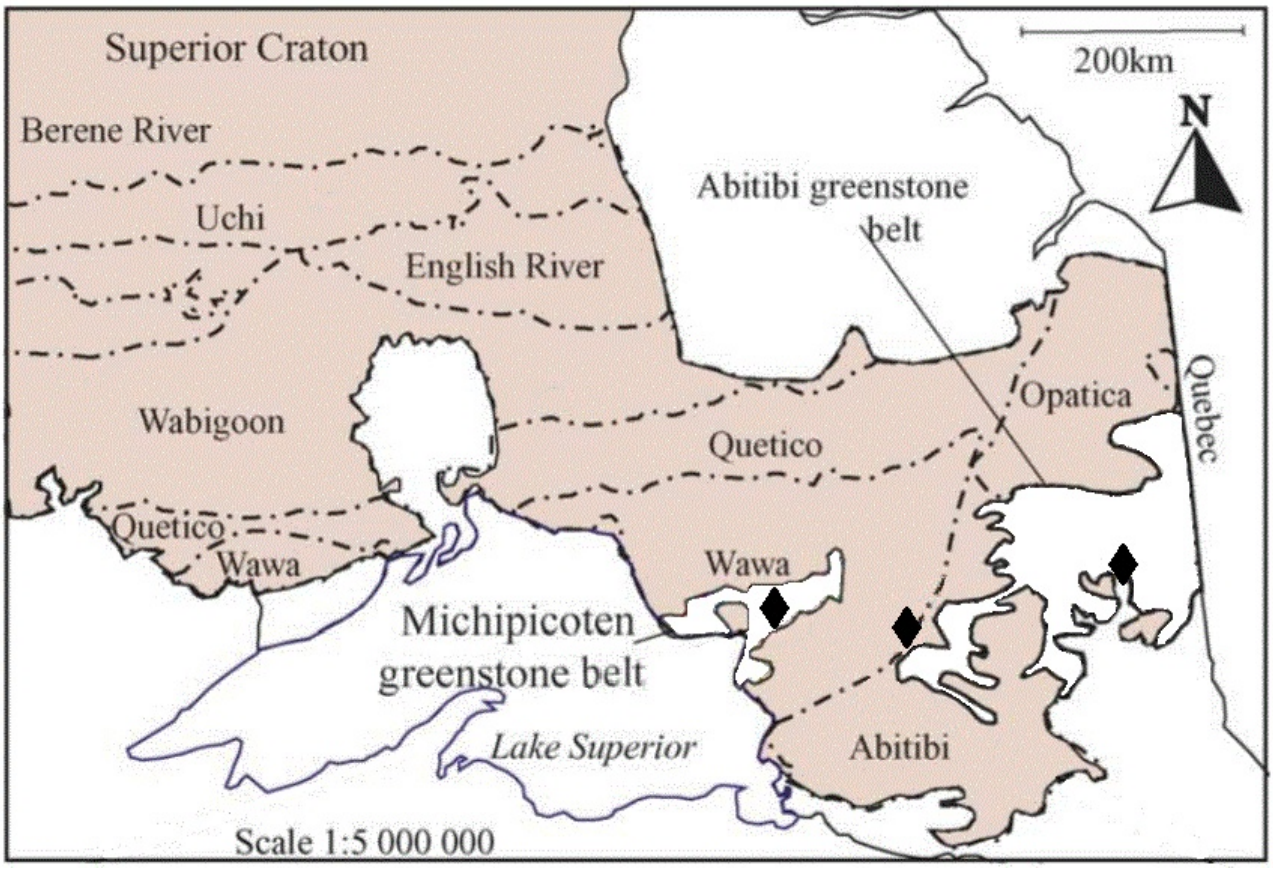

Figure 4.90: Location of diamondiferous lamprophyres in the Wawa and Abitibi subprovinces including the diamonds discovered in the Chapleau Belt (black diamonds) (Modified after Lefèbvre et al., 2005; Stachel et al., 2006; Wyman et al., 2006).

The ca. 2.7 to 2.67 Ga Mishibishu greenstone belt, or commonly accepted as an extension of the western Michipicoten greenstone belt, has the greatest similarity to the Chapleau Belt and southern KSZ as they share field relationships, stratigraphies, lithologies, whole rock and trace geochemistry, and geochronology, although have experienced different grades of metamorphism (Bennett and Thurston, 1977; Reid and Reilly, 1987; Turek et al., 1990a, 1996a). In particular, the metavolcanic lithologies include massive and pillowed magnesium and iron tholeiitic basalts, some of which have gabbroic textures including one with a "leopard" plagioclase–phyric basaltic flow. These lithologies are similar to the oldest tholeiitic magnesium and iron basalts in the Chapleau Belt (or commonly referred to as "footwall" lithologies) and porhpyroblastic amphibolite. Above these are tholeiitic andesite and calc–alkaline basalts, intermediate and felsic metavolcanic lithologies, and intercalated with iron tholeiitic basalts and iron formations. These lithologies are most similar to the younger iron tholeiitic basalt, iron formations, and calc–alkaline mafic, intermediate, and felsic metavolcanic and metavolcaniclastic rocks (or "hangingwall" lithologies). Metasedimentary rocks above the felsic metavolcanic rocks include chemical metasediments including oxide–facies and sulphide–BIF and clastic metasedimentary

lithologies including pebble– to boulder–sized polymictic conglomerates, sandstones, and mudstones. Crosscutting all previously described lithologies include syn– to post–tectonic intermediate to felsic plutonic lithologies that range from massive to gneissic and migmatitic with compositions ranging from granite, syenite, tonalite, granodiorite, and diorite. The mineralization in the Mishibishu greenstone belt occurs as native gold, pyrite, arsenopyrite, galena, and chalcopyrite in boudinaged quartz veins aligned parallel to the penetrative foliation or oblique to within schists (Bennett and Thurston, 1977; Bowen et al., 1986; Reid and Reilly, 1987; Turek et al., 1990a).

4.11 Synthesis of current and previous field mapping

The northern and southern boundaries between the WGD and Chapleau Belt are defined by east–west striking regional ductile, sinistral strike–slip shear zones dipping moderately to steeply to the north and define an orocline along the southern Chapleau Belt and KSZ, parallel to the ILDZ (Figs. 1.3–1.5, 2.11, 4.25). Parallel structures with greater sinistral–oblique components with more moderate dips to the north, and to a lesser degree the south, are continuous throughout the interior of the WGD, Chapleau Belt, and KSZ. These shear zones also generally define the orocline in the eastern Chapleau Belt and KSZ, parallel to the ILDZ, as well as define the boundaries of the shear–related late folds, including regional "Z–, M–, and S–shaped" folds (Bursall, 1990; Bursall et al., 1994; Moser, 1994; Carreras et al., 2005) (Figs. 4.24). The "Z–, M–, and S–shaped" boudin–related folds commonly represent boudin necks and their axes and the orocline overprints antithetic shearbands and shear zones. The regional–scale rotated boudins and foliation boudins are ductile to brittle–ductile structures that have the same geometries as the brittle structures in the ILDZ, including thrust faults (Percival and McGrath, 1986; Percival, 1989; Swoffer et al., 2011). Therefore, the most brittle structures in the ILDZ were formed and reactivated along the earlier structures and explains the dextral strike–slip and thrust fault geometries in the region.

Local– to microscopic–scale boudin necks and foliation boudin necks also define the same geometry of the orocline, with the long axes of the boudin neck perpendicular to the east–west to northeast–southwest strike with a shallow to moderate dip to the north to northwest. Regional– to local–scale, sinistral and dextral ductile to brittle–ductile shear zones have similar geometries to the larger structures, and have accommodated the CCW rotation in boudin necks, foliation boudins, upright (oroclinal) folds, and antithetic shear bands. Shear–related late folds and rotated boudins define CCW rotation and are fairly consistent with the hypothesis of Halls et al. (1993), that both sinistral shear zones or faults and dextral faults could account for the CCW rotation needed to deform Matachewan dyke swarms. However, in the case of the Chapleau Belt and southern KSZ the sinistral deformation was

localized in early, ductile, sinistral shear zones and the later, brittle–ductile to brittle deformation was accommodated in sinistral and brittle structures, including antithetic shear bands in the boudin necks. The dextral, brittle–ductile shear zones and antithetic shear bands have the same geometries as the dextral ± thrust faults in the ILDZ. The geometry of CCW rotated foliation boudin necks in the Chapleau Belt also north–south to northeast–southwest with shallow to moderate dips to the west to northwest, similar to the upright, oroclinal fold defined by the KSZ that parallels the ILDZ.

In the WGD, Chapleau Belt, and southern KSZ the areas of greatest extension are in the regional– to microscopic–scale boudins and boudin trains, and on the regional– to outcrop–scale these boudin necks define top to the northeast, horizontal to subhorizontal extensional shear zones. The sinistral and sinistral–oblique shear zones that parallel these boudin trains and boudins are proposed as transfer structures. Both vertical and Regional– to local–scale sinistral brittle–ductile shear zones define the schistose to gneissic fabric of upright Z–folds, periclines around boudin lithons, and oroclines and horizontal ductile shear zones are present at boudin necks contacts with syn–kinematic to post–kinematic felsic gneissic, plutonic, and pegmatitic host lithologies.

The subvertical to vertical shear zones are defined by high–temperature minerals and microstructures and were present during granulite facies metamorphism, which is consistent with the ca. 2700 to 2670 Ma dates of formation, folding, and thrusting proposed by Moser et al. (1996). The metamorphic age of ca. 2667 Ma is also consistent with previous work by Krogh and Moser (1994). The subhorizontal to horizontal shear zones in the study area are also consistent with the proposed east–west extension by ca. 2660 to 2637 Ma (Moser et al., 1996) and sedimentation followed by burial in areas of greatest dip–slip (Bowman et al., 2011). Although Moser et al. (1996) separated the stages of east–west extension and east–west shortening and fault reactivation (2630 to 2580 Ma), they could be contemporaneous in the transfer and extensional structures, respectively. Upright, near–vertical to vertical gentle to open folds in the proposed Kapuskasing orocline are also periclinal as they drape around boudinaged lithons between be transfer structures. Peak metamorphism, ca. 2.66 Ma, at upper amphibolite to granulite facies is preserved in lithons including boudin interiors. Retrograde lower–amphibolite facies metamorphism, alteration, and sedimentation (Bowman et al., 2011) are documented in ductile to brittle–ductile shear zones, and boudin necks throughout the Chapleau Belt and southern KSZ. Mineral assemblages of mainly epidote and calcite, indicative of low grade metamorphism and hydrothermal alteration, are also documented in dextral faults that overprint earlier ductile, sinistral shear zones. Other late features in the study area include faults, cataclasites, and pseudotachylites, including those well–studied in the ILDZ, that overprint earlier shear zones, foliation boudins, boudins, and antithetic shear bands. It is the youngest, brittle structures of the ILDZ that were reactivated along

older ductile structures in the Proterozoic (Figs. 1.3–1.5, 2.11). It is therefore more appropriate to constrain the onset of the formation and exhumation of the WGD and KSZ to the Neoarchean, rather than the Paleoproterozoic as is the more common practice. As the WGD, Chapleau Belt, KSZ, and ILDZ currently lack a tectonic mechanism for their formation a new model will be presented later in this section.

CHAPTER 5: NEW TECTONIC MODEL FOR THE WGD AND KSZ

5.1 Southern Superior Province tectonics

5.1.1 New Tectonic Model for the WGD and KSZ

Previous hypotheses for the exhumation of the KSZ, which included elements of intracratonic uplift, sinistral and dextral strike–slip structures, sutures, and mid–crustal exhumation of a gneissic terrain, cannot account a number of phenomena including an ~80 Ma high–temperature event nor the age discrepancies of the Archean–aged KSZ lithologies, and the seemingly incompatible Archean and Proterozoic structures, and geophysical features. The leading tectonic hypothesis for the KSZ proposes that the ILDZ is an Archean, cratonic–scale, sinistral–strike slip structure. However, the preferred structural hypothesis proposes that it formed in the Proterozoic as a thrust fault with minor dextral–strike slip components. These two hypotheses are contradictory, they focus on two different scales, they lack a tectonic mechanism for their formation, and do not account for other anomalies, particularly in geochronology and geophysics.

A new tectonic model includes the evolution from a mid–ocean ridge to arc setting (Wawa–Abitibi terrane) progressing to the Lakehead orogeny and the formation of MCCs, which account for all of these seemingly incompatible features. An orogeny accounts for the Neoarchean medium– to high–grade metamorphism along the boundary between the southern Superior Province and MRVT, orthogonal to oblique high–temperature structures with CCW rotation throughout the boundary between the MRVT and southern Superior Province, isotropic to boudinage structures throughout the lithosphere, low–angle to high–angle paleomagnetic fabrics, metamorphic and lithospheric–scale geophysical anomalies between the western and eastern southern Superior Province, and the high–temperature anomaly in the KSZ, among many other features listed in previous sections.

The mid–ocean ridge to arc settings in the Wawa–Abitibi terrane have been previously identified in numerous studies and have been amalgamated in this study for simplicity, however in the Abitibi subprovince, and to some extent the Wawa subprovince, further categorizations are well–described. The arc setting is generalized as the Kenora–Algoma accretion in this study as it incorporates the two names first identified and most commonly used to describe the terminal Archean accretion or orogeny in the Superior Province (Card and Ciesielski, 1986; Card, 1990; Phinney and Halls, 2001; Percival et al., 2006; Percival et al., 2012). The Kenora–Algoma accretion accounts for the tectonic evolution to an arc setting, early low– to medium–grade metamorphism, dextral strike–slip (arc–parallel structures), among other features listed in previous chapters.

Following the Kenora–Algoma accretion is the newly proposed Lakehead orogeny that accounts for Neoarchean, ductile to brittle–ductile, orthogonal to sinistral–oblique strike–slip with CCW rotational structures along the southern Superior Province and MRVT. The previous names used to describe the terminal tectonic event in the southern Superior Province include many names but all refer to the geographical area around the Great Lakes. The newly proposed Lakehead orogeny highlights this history and geography.

The new hypothesis proposes early strike–slip in the Neoarchean due to Lakehead orogeny, with plutonism, exhumation, and rotation facilitated by the development of a continental metamorphic core complex (MCC). Rotation created lower–angle structures (rotated boudins and foliation boudins) that were then reactivated in the Proterozoic. This new hypothesis provides the first tectonic mechanism for the formation of all of these features, including the enigmatic, isotropic to gneissic domal WGD, the contradictory Archean ductile deformation, and Proterozoic brittle deformation, as well as a long–lived high–temperature event.

The initial formation and exhumation of the KSZ can be explained by ca. 2.7 Ga MORB and ensuing arc formation, herein named the Kenora–Algoma accretion, underplating, followed by the proposed Lakehead orogeny prior to the granulite–facies metamorphism by at least ca. 2.67 Ga, and subsequent formation of a continental metamorphic core complex (MCC) and exhumation. Archean to Phanerozoic MCCs have been identified globally, although there is still ongoing debate about the end–member tectonic regimes (Coney, 1980; Lister and Davis, 1989). Characteristics of MCCs include gneissic to plutonic, domal to batholitic exposures of the middle– to lower–crust along mylonitic, extensional, ductile shear zones in the footwall and tilted, brittle–ductile to brittle structures on the upper hanging wall with younger, sedimentary cover above the metamorphic basement (Coney, 1980). Recent comprehensive studies (Whitney et al., 2012; Cooper et al., 2015; Lamont et al., 2020) provide the state of research in the field including the debates on certain processes, including tectonic styles, rheology, exhumation, and timing of emplacement.

The proposed MCC is consistent with other modern Cordilleran types, albeit of higher and deeper equivalents, and includes: (1) detachment, horizontal, extensional ductile shear zones and boudins in amphibolite, granulite, and migmatites, (2) exposure of exhumed, high–temperature and pressure lithologies and structures, (3) syn–kinematic to post–kinematic felsic plutons, (4) ductile, transfer, sinistral–oblique to strike–slip shear zones bounding the extensional structures, (5) metasedimentary, supracrustal lithologies in oblique shear zones perpendicular to extension, and (6) retrograde metamorphism during exhumation (Figs. 4.88, 5.1–5.5). The main difference from traditional MCCs is that the KSZ is located in a deeply eroded Archean terrain with high–grade metamorphic

lithologies and structures and lacks the unmetamorphosed to low–grade metamorphic host lithology (Coney, 1980). This discrepancy is attributed to the deeply eroded nature of the Archean craton and is similar to the adjacent, deeply–eroded Pontiac MCC.

The proposed Kapuskasing and Pontiac MCCs and Wawa and Quetico gneissic domes, as they are named and referred to in this study, host many of the requirements proposed by Coney (1980). Lacking from these MCCs are younger, sedimentary cover above the metamorphic basement (Coney, 1980). Instead, these MCCs have lower–grade, unmigmatized metamorphic sedimentary cover in the greenschist to lower–amphibolite facies which may be a reasonable equivalent in a deeply–eroded, Archean craton. In fact, the P–T–t–d curve of the KSZ (Fig. 4.88) is consistent with other compressional to transitional MCCs in the world (Figs. 5.1–5.2) (Lamont et al., 2020). Other characteristics include a footwall defined by the Wawa subprovince and WGD boundary identified by geophysical and field mapping studies (Percival and McGrath, 1986). The hanging wall is horizontal to moderately dipping towards the west with horizontal foliated and lineated mylonitic to gneissic fabrics, and corresponding meso– and microstructures, that indicate extensional shear zones, boudins, and transfer sinistral–oblique structures consistent with kinematics as a result of continental extension (Lister and Davis, 1989). Domal, felsic intrusions and assimilated host rock are present throughout the WGD and Quetico subprovince, and previous naming conventions used “domal” and “slate–gneiss” to describe these features, respectively (Card, 1990; Brun et al., 1994; Rey et al., 2009; Whitney et al., 2004).

In addition to evidence for the MCCs and gneissic domes there are also characteristics diagnostic of a compressional or transitional orogeny preserved in features that formed prior to and during the formation and exhumation of the MCC: (1) partial melting during regional, upper amphibolite to granulite facies of metamorphism, (2) thickened lithosphere and cratonic mantle keel, (3) early and steep structures that have been subsequently deformed by ductile, shallowly–dipping structures in a midcrustal décollement (Jamieson et al., 2004, 2011; Culshaw et al., 2006; Hodges, 2000; Royden et al., 2008). Adjacent to transitional orogenies are typically fold and thrust belts, which could include the southern Pontiac and Wawa subprovinces thrust components, and a foreland basin which may include the Huronian/Marquette Supergroup (Heather and Arias, 1992; Long, 2004; Jellicoe, 2019). Previous work has also documented potential for the formation of a MCCs during extension of the upper crust and upward flow of ductile channel materials during orogeny which is consistent with the findings in this study (Fig. 5.1) (Jamieson et al., 2006).

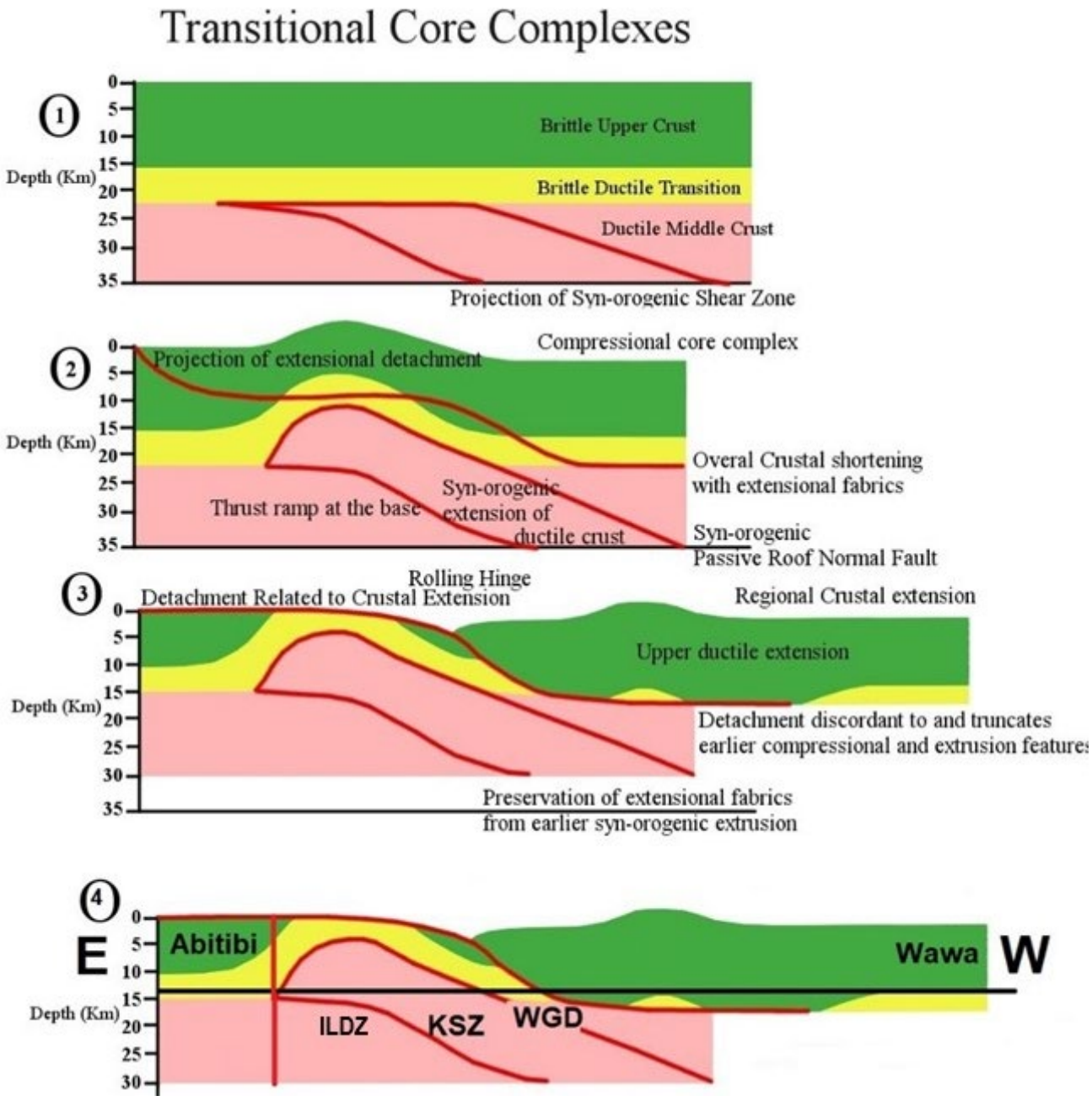

Figure 5.1: Common stages (1–3) of transitional metamorphic core complexes where compression and crustal thickening cause metamorphism and synorogenic extrusion followed by extension and exhumation. (4) Upper ductile extension and the detachment is consistent with the Wawa subprovince and WGD boundary and exhumation of the high–grade KSZ along the ILDZ and low–grade Abitibi subprovince (Modified after Lamont et al., 2020).

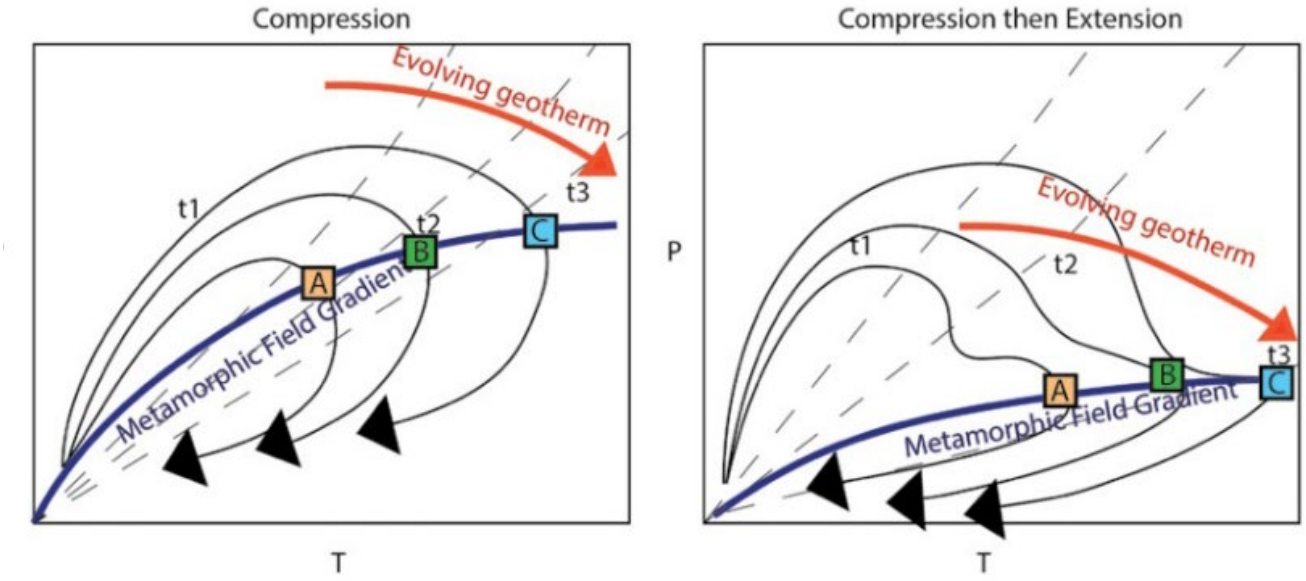

Figure 5.2: Common P–T paths in MCCs under different styles of deformation, metamorphic field gradients, and time. The P–T path that is most similar to the KSZ is the compression–dominated MCC due to the moderate metamorphic field gradient and smooth looped path, however further low–temperature retrograde metamorphic petrology is required to assess the compression then extension path. Three typical paths are displayed based on geothermal gradients, with t1 and A paths being the lowest temperature and fastest to form and the t3 and C paths the longest and hottest (Lamont et al, 2020).

Field mapping and seismic geophysical data, particularly seismic reflection data, support the hypothesis that the western Wawa subprovince is the hanging wall of the shallowly to moderately, westerly dipping MCC and the WGD and KSZ are the up thrown footwall exposing the primarily extensional, detachment shear zones (Figs. 5.3–5.5) (Gibb, 1978a; Fountain et al., 1990; Geis et al., 1990; Percival and West, 1994; Clowes et al., 1996; Percival et al., 2006). The structure of the MCC is consistent with Neoarchean lithospheric– to regional–scale listric extension with boudinage and CCW, documented in geochronology, seismic studies, and field mapping data, and may explain the early to late extension which the earlier proposed thrust fault and/or flower structures fail to do (Figs. 5.3–5.5) (Krogh, 1993; Moser, 1994; Borradaile et al., 2003). The faults in the ILDZ define only the late stage, brittle deformation along the detachment structure in the footwall, along the western boundary of the Abitibi subprovince. The dextral and thrust faults may have been reactivated along the late–stage foliation boudinage and boudinage during CCW rotation that over prints extensional and sinistral strike–slip structures. South of the KSZ the neighbouring Pontiac subprovince also hosts an MCC with similar geochronology, metamorphic and igneous petrology, migmatization, and structural geology (Camiré and Burg, 1993; Benn et al., 1994a). In addition to the gneissic and plutonic felsic domes in the WGD they have also been documented southwest of the KSZ in along the Quetico–Wawa subprovince boundary

with features similar to the Pontiac and KSZ MCCs that also lack a tectonic framework (Moser, 1994; Borradaile and Gauthier, 2003).

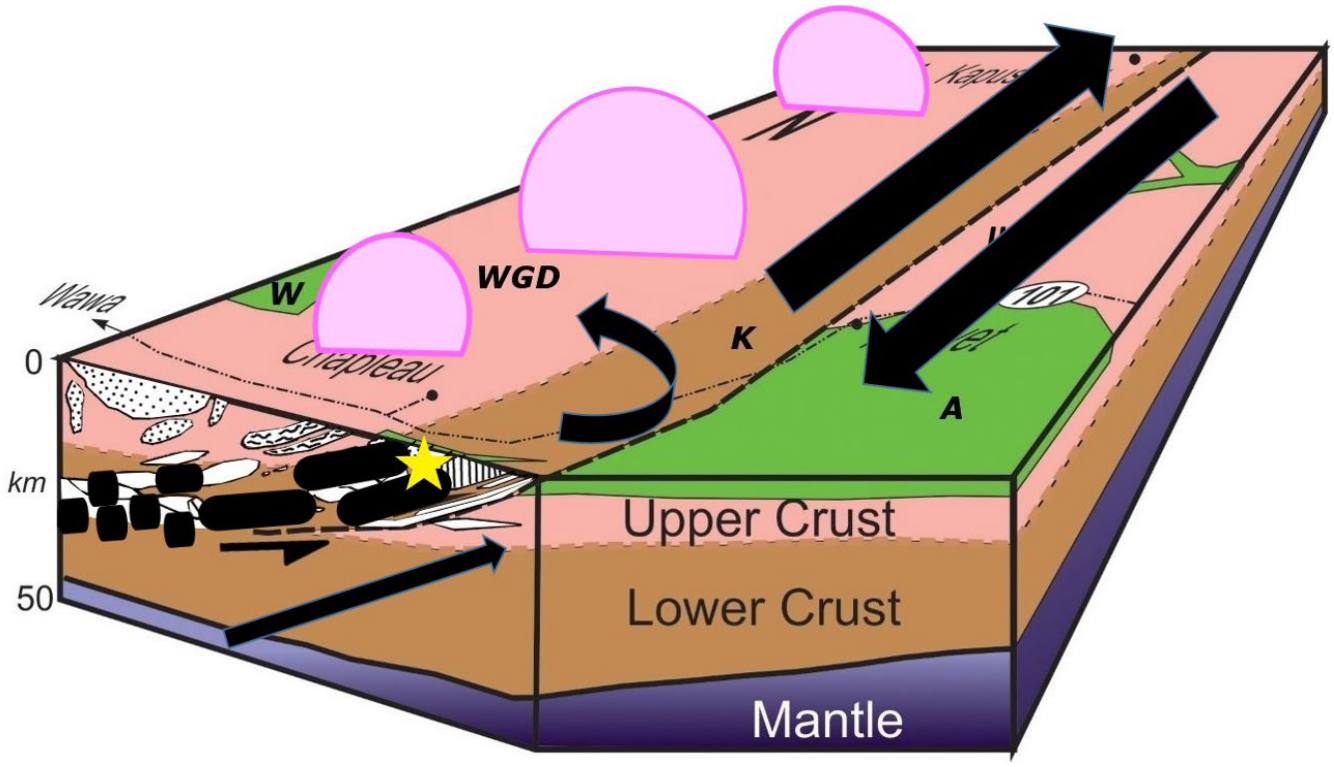

Figure 5.3: 3D seismic block model with the Wawa subprovince (W, green), WGD (pink), Chapleau Belt (south of the town of Chapleau, green), KSZ (K, brown), ILDZ (dashed line), and Abitibi subprovince (A, green) (Modified after Percival and McGrath, 1986; Bowland et al., 1988; Percival, 1989; Percival et al., 1989; Card, 1990; Moser, 1994, 1996). The transition from the vertical structures in the Wawa subprovince (W, dots) to the domal or shallowly– to moderately–dipping westerly extensional listric and boudinage structures in the WGD (isotropic black solid dots to boudinaged curved lines and undifferentiated boudins) are highlighted with the black arrow and bold dashed lines where they are exposed at surface at the Borden Mine (star) in the Chapleau Belt of the KSZ (K). Counterclockwise rotation and sinistral–strike slip structures are denoted by arrows.

The new tectonic model for the KSZ and WGD has a modern analogue in the Woodlark Rift and MCC in East Papua New Guinea (Abers et al., 2002). One proposed explanation for the development at Woodlark involves crustal thinning due to crust and mantle weakening due to the Trobriand volcanic arc formation, concentrating a zone of hot, weakened lithosphere that lead to thinning, MCC formation, and finally continental breakup (Abers et al., 2002). A recent study has provided evidence using mantle anisotropy to propose global mantle upwelling within oceanic transform plate boundaries connecting mid–ocean ridges (Eakin et al., 2018). The same type of processes may also have occurred in the study area, including the formation of mid–ocean ridges, and connecting oceanic transform plate boundaries offshore to the southern Superior Province, formed by ca. 2.70 Ga in the Wawa–Abitibi terrane. Mantle

upwelling may have occurred along the transform plate boundaries and mid–ocean ridges prior to subduction providing the source for juvenile mafic lithologies in the southern Superior Province. Subduction of one (or more) transform plate boundaries as a Subduction–Transform–Edge–Propagator (STEP) structure can explain the trigger for strike–slip components in the proposed MCCs (Grovers and Wortel, 2005; Hidas et al., 2019). The pattern of vertical to horizontal lineations, and opposing lineations, in the gneissic and plutonic domes in the WGD and Chapleau Belt are also present in other MCCs with large variability of in domes in the Naxos and Montagne Noire MCC (Charles et al., 2009; Kruckenberg et al., 2011; Rey et al., 2011). The role of metamorphic mineral growth in areas of boudinage may help to assist the understanding of this phenomenon.

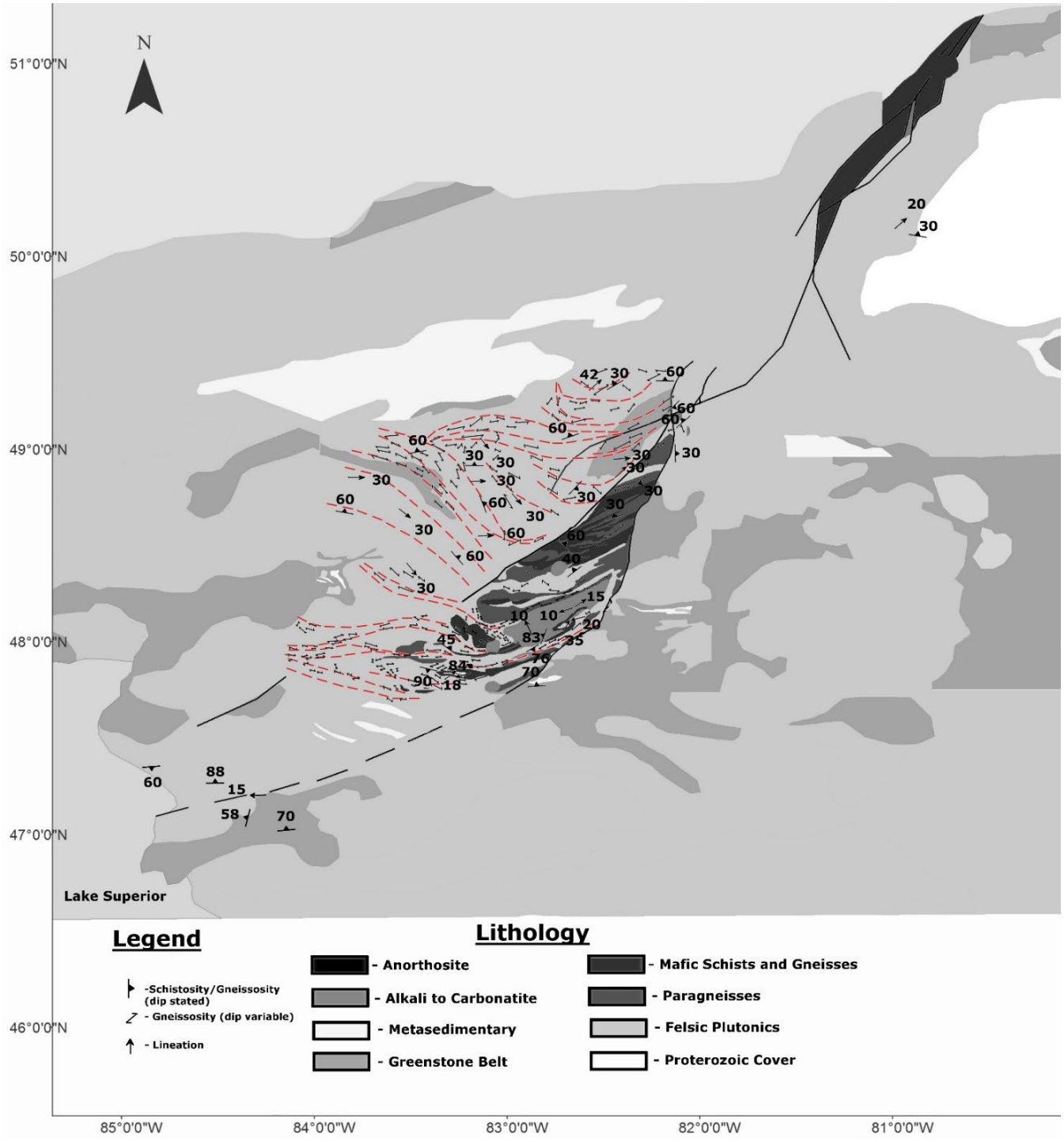

Figure 5.4: Regional gneissosity (red dashed lines) that define the strike–slip and extensional horizontal to vertical ductile shear zones that separate the western WGD and KSZ and define ductile, CCW rotation and the orocline in the eastern KSZ (Modified after Percival, 1989; Bursall, 1990; Bursall et al., 1994; Moser, 1994). The arcuate greenstone belts in the western Wawa subprovince also define the CCW. CCW rotation formed the ductile to brittle–ductile sinistral and dextral shear zones in the KSZ that were later overprinted by the later brittle structures in the ILDZ (westernmost dash and solid black line).

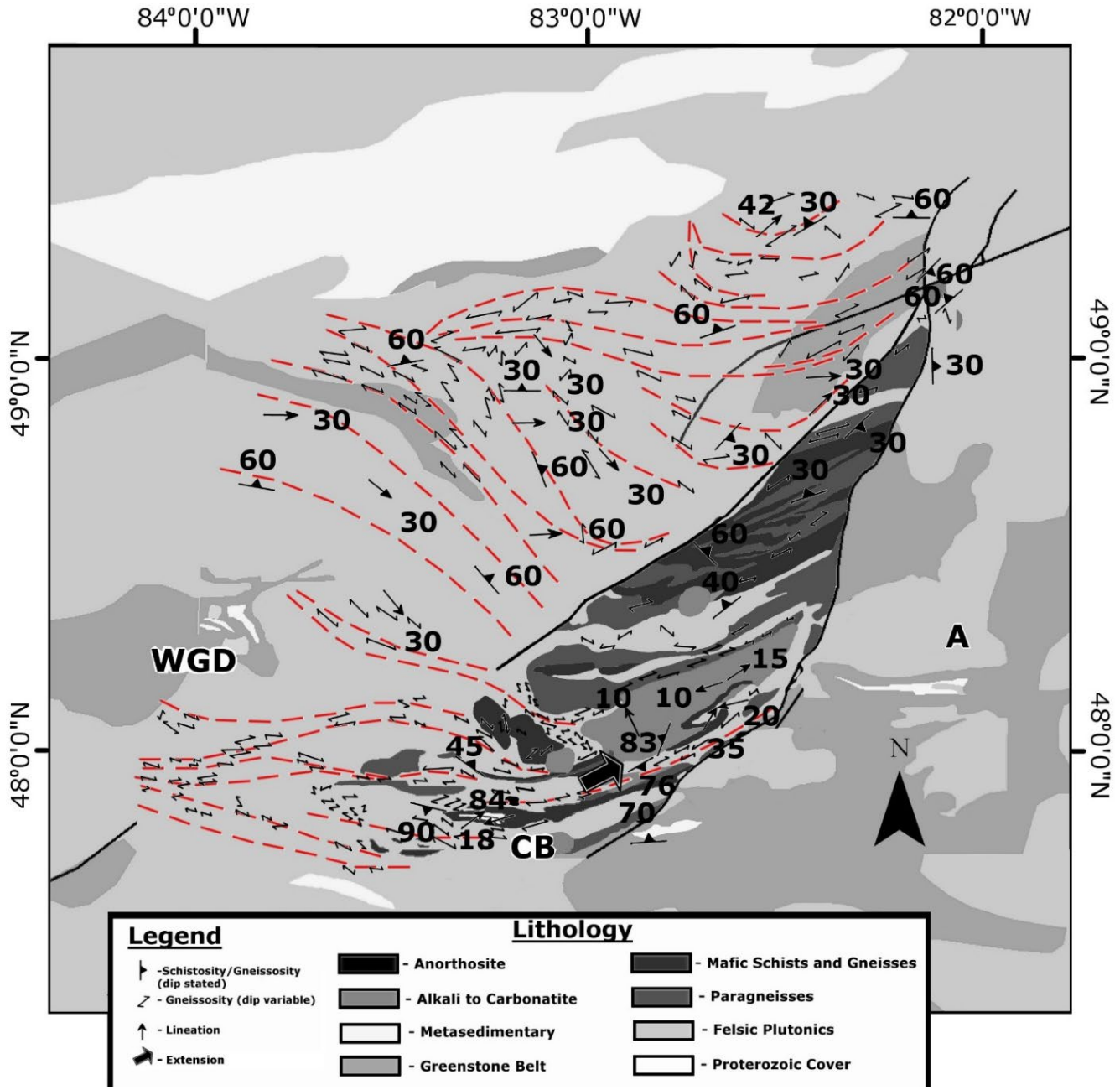

Figure 5.5: The western WGD, Chapleau Belt (CB), and KSZ are defined by gneissosity that defines the sigmoidal shape and documents CCW rotation in gneisses and domes as well as the orocline in the eastern KSZ–Abitibi subprovince boundary. Extension is directed to the northeast. Note the eastern to southeastern moderate plunges in the WGD defining extension in gneisses and the opposing plunges in the KSZ define boudins. The Abitibi subprovince (A) has been largely unaffected by these processes (Modified after Percival, 1989; Bursall, 1990; Bursall et al., 1994; Moser, 1994).

Neoarchean subduction to oblique orogeny followed by the formation of MCCs supports the evidence provided in this study as well as work of previous authors. Subduction during the accretion of the Wawa–Abitibi terrane to oblique collision along the southern margin of the Superior Province with the MRVT could account for the sinistral, oblique to strike–slip shear zones and exhumation of the high–grade metamorphic lithologies of the WGD and KSZ (Figs. 2.2, 2.3, 2.6–2.9, 5.3–5.5). Continued collision and subsequent exhumation, with migmatization and plutonism, can account for the formation of the presence and geometry of the domes, gneisses, and MCCs in the Quetico subprovince, WGD, KSZ, and Pontiac subprovince (and potential for the Ashuanipi subprovince also along the same plate boundary that also lacks a tectonic explanation) (Fig. 2.2, 2.3, 2.4, 5.5).

The oblique orogeny and MCC formation also solves numerous problems and provide a tectonic hypothesis for the dichotomy of the eastern and western Superior Province, including the cratonic–scale sinistral strike–slip displacement of the Wawa, Quetico, Wabigoon, and English River (and equivalents) subprovinces and northwest shear wave splitting transitions to east–west (Frederiksen et al., 2007). Anomalous sinistral strike–slip to oblique, northeast–southwest striking, west to southwest shallow to moderately dipping, ductile to brittle–ductile shear zones are also located in the study area, including the KSZ, and have similar geometries, ages, and exhumation histories to other northeast–striking shear zones along the southern Superior Province, including the Montreal River deformation zone, Burntside fault, Gravel River deformation zone, and Miniss River deformation zone, among others (Figs. 2.2, 2.6–2.9, 2.11, 2.13). The east–west striking structures in the Superior Province are referenced to have formed during accretion but no tectonic explanation has been hypothesized for the northeast–striking structures, including those that bound the curvilinear subprovince boundaries, although they are present in every southern subprovince. This study proposes the NE–striking structural zones, including the KSZ, many which expose high–grade metamorphic gneisses in curvilinear or indented subprovince boundaries, formed due to the proposed Lakehead orogeny.

According to the theory of indenter tectonics these sinistral, orthogonal to oblique structures are to be expected due to the older, more rigid MRVT colliding northeastward into the rheologically softer, younger southern Superior Province (Tapponnier and Molnar, 1975). In fact, a tectonic indenter has been previously proposed due to the structural complexity in the GLTZ defining the suture between the Wawa subprovince and southern Superior Province (Sims and Day, 1993a). The indenter in northern Wisconsin is also parallel to the irregular subprovince and terrane boundaries in the Quetico, Wabigoon, Bird River, Winnipeg River, and English River subprovinces. Other irregular boundaries require further study as well, including the eastern boundary of the Ashuanipi subprovince of the northeastern Superior Province (Figs. 2.4–2.5).

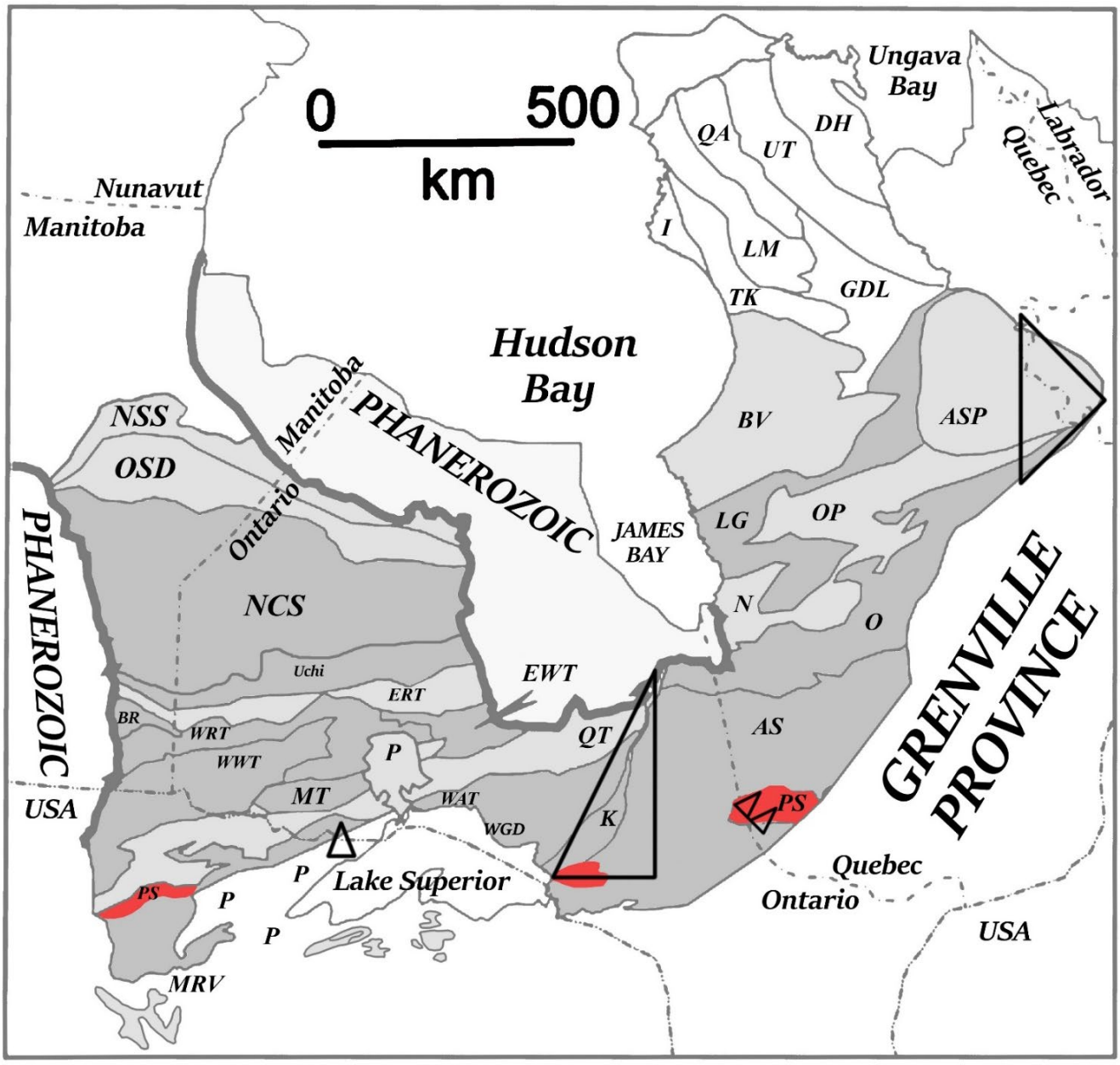

Figure 5.6: Previously identified and proposed metamorphic core complexes and gneiss–granite domes in the Quetico (QT), Pontiac (PS), Ashuanipi (ASP), and Kapuskasing Structural Zone (K) (triangles) and the Pontiac subprovince as a proposed accretionary prism and proposed equivalents (red) (Modified after Percival et al., 2012).

The presence of modern–day tectonics in the Precambrian is a popular debate in the geosciences. The complete cycle of arc, orogeny, and extensional tectonic settings in the Neoarchean provide evidence for modern tectonics. Previous authors have used a lack of high–pressure metamorphism in the southern Superior Province as evidence against subduction, however given the proposed data any earlier metamorphic high–pressure mineralogy and fabrics would have been destroyed by the overprinting

orogeny proposed. Late Neoarchean to early Paleoproterozoic stable metamorphic mineral assemblages and structural fabrics are congruent with oceanic–continental orogenesis between the MRVT colliding into the southern Superior Province. High–pressure and temperature schists, gneisses, and migmatites are present along the GLTZ suture zone (Peterson and Geiger, 1990). Regional, Barrovian isograds of staurolite, kyanite, and sillimanite have been mapped in the Pontiac subprovince and along the proposed western extension of the Pontiac subprovince accretionary wedge, in addition to reverse and thrust faults and nappes in the Wawa and Pontiac subprovinces (Feng and Kerrich, 1990; Camiré and Burg, 1993; Benn et al., 1994c; Goldner, 2013). Overprinting low–pressure metamorphism and variable unroofing is commonly referenced throughout the southern Superior Province and the proposed oblique orogeny could account for these features (Easton, 2000; Percival and Easton, 2007).

The proposed regions of the orogeny include: the subduction and accretion of the Wawa–Abitibi subprovince including underplating, northeast–directed collision (Lakehead orogeny) between the MRVT towards the Wawa–Abitibi terrane of the southern Superior Province, the foreland basin (basal layers of the Paleoproterozoic, sinistral transpressional to transtensional, transitional basin of the Marquette/Huronian Supergroups (Long, 2004), the suture zone (GLTZ), the accretionary prism (Pontiac subprovince and the proposed continuation) (Fig. 5.6), and the hinterland (the southern Superior Province where northeast–striking deformation zones and indenters are present with far field effects into the northern Superior Province) (Fig. 5.7).

Mid–ocean ridge and arc (± BABB) magmatism formed in the Wawa–Abitibi terrane, including the WGD, Chapleau Belt, and KSZ, between 2.703 Ga to 2.667 Ga, preceding subduction, underplating, and lamprophyre emplacement (Fig. 5.7) (Krogh, 1993). By ca. 2.67 Ma lamprophyre emplacement occurred during an extensional (± oblique) tectonic regime during subduction (Lefèbvre et al., 2005). The TTGs in the WGD and KSZ also require lower–crustal input, such as via subduction (Kendrick et al., 2019). Oblique collision between the MRVT and southern Superior Province with regional metamorphism is documented by ca. ≥2.66 Ga. Sedimentation occurred during extension to transtension by 2667 ± 2 Ma, and metasedimentary lithologies did not experience high–grade metamorphism and migmatization (Krogh, 1993). The lower age of burial, domal plutonism, and metamorphism in the lower crust is documented by at least 2659 ± 8 Ma (Moser et al., 2008; Bowman et al., 2011). Crosscutting these older lithologies, parallel and perpendicular to the orogenic front, are pegmatitic to megacrystic, quartz–feldspar pegmatites in the Chapleau Belt and WGD and have U–Pb zircon ages of 2640 ± 2 to 2584 ± 2 Ma. Exhumation of the MCCs and gneissic domes, migmatization, and oroclines formed by at least ca. >2.63 Ma during retrograde metamorphism (<2.63 Ga) (Percival, 1989; Moser, 1994, 1996; Krogh and Moser, 1994; Moser et al., 2008; LaFontaine, unpublished MSc. thesis, 2016;

Kendrik et al., 2019). Synchronously, the earliest extensional and sinistral ductile shear zones and folds in the KSZ were also formed by ca. 2630 Ma (Krogh, 1993). Felsic plutonism crosscutting earlier lithologies was continuous ca. 2.62–2.58 Ga with mafic dyke emplacement between ca. 2.55 to 2.45 Ga (Krogh, 1993; Moser, 1994, 1996; Moser, 2008; Bowman et al., 2011). Continued deformation and reactivation occurred along the ILDZ in the brittle deformation regime, overprinting earlier strike–slip to rotational/extensional ductile shear zones, boudins, and foliation boudins, into the Proterozoic (Easton, 1986; Krogh, 1993; Hanes et al., 1994; Percival and Peterman, 1994). The thrust and dextral strike–slip structures in the ILDZ mapped by previous authors post–date the earlier, ductile structures (Percival, 1989; Bursall et al., 1994; Moser, 1994, 1996). Previous work on the mafic dyke swarms throughout the Superior Province have focused on their location, petrology, folding, and geophysical properties (Evans and Halls, 2010). The proposed orogeny and subsequent transtension during MCC formation provide tectonic mechanisms, including extension and CCW rotation, to explain these cratonic– to regional–scale folds and oroclines, including those defined by mafic dykes (Fig. 5.8).

Previous paleomagnetism studies in the study area have evidence for pyrrhotite, magnetite, amphiboles, and micas that define foliations and lineations reaching their closure temperatures during exhumation through retrograde amphibolite facies and lower metamorphism between 2.55–2.2 Ga (Borradaile and Lagroix, 2000). Many of these minerals were produced or deformed during retrograde metamorphism and define the early steep foliations and lineations in ductile and brittle–ductile structures to the later shallower fabrics and therefore may be used to define the timing and tectonic processes of exhumation and the mafic dyke swarms. In the mafic dykes the formation of blue–green amphibole after subophitic to ophitic pyroxenes, cloudy feldspar, geochronology, and magnetite closure temperature support retrograde amphibolite facies temperatures in the least exhumed areas of the KSZ (Halls and Palmer, 1990; Halls and Zhang, 1998). It is therefore tectonically inconsistent to use the 2.5–2.4 Ga mafic dykes to define the brittle deformation in the KSZ between ca. 2070 to 1870 Ma (Bursnall, 1990; Evans and Halls, 2010).

Regionally, the various mafic dyke swarms intruded along crosscut all lithologies in the southern Superior Province and are also perpendicular to the Wawa–Abitibi terrane and GLTZ suture. On the outcrop–scale to local–scale in the WGD, Chapleau Belt and KSZ the mafic dykes outcrop perpendicular to boudinage and have been offset sinistrally or rotated into a sigmoidal or “Z–shape”. Extensional, sinistral–oblique strike–slip deformation, followed by CCW rotation occurred throughout the southern Superior Province and affected and formed the MCCs and oroclines in the southern Superior Province and mafic dyke swarms (Fig. 5.8) (Bates and Halls, 2001; Evans and Halls, 2010).

Neoarchean transtension began during the formation of the BABB, sedimentary basins, and continued during the formation of the MCCs. Neoarchean to Paleoproterozoic local extension occurred facilitated the emplacement of lamprophyres, mafic dyke swarms, and continued during the formation of the Huronian/Marquette Supergroup. The formation of the WGD, Chapleau Belt, and KSZ formed by transpressive tectonics and exhumation, and occurred prior to the retrograde metamorphism in the Matachewan dykes by 2.45 Ga (Percival and West, 1994; Bursall et al., 1994; Heaman, 1988). These mafic dyke studies have proposed the western portion of the Superior Province requires rigid body rotation of 10º–20º CCW to account for delineation differences in the 2500–2070 Ma Matachewan dyke swarm while taking into account the dextral–thrust components in the KSZ, specifically the ILDZ (Fig. 5.8) (Halls and Palmer, 1990; Ernst and Bleeker, 2010b; Evans and Halls, 2010). This study proposes that the sigmoidal geometry of the gneissic, sinistral, ductile to brittle–ductile shear zones and rotated foliation boudins throughout the WGD and western KSZ formed in transpressional and transtensional tectonic regimes, and accommodated 10s to 100s of kilometers of transcurrent–sense motion and 10º–20º CCW rotation. The KSZ orocline mirrors the proposed CCW rotation and defines the late–stage or reactivated thrust and dextral strike–slip faults. Dextral, transcurrent to transpressional structures throughout the southern Superior Province also deformed during this time and accommodated strain during orogeny and formation of MCCs. Continental transtensionl to rifting tectonic regimes occurred during dyke emplacement and early sedimentation in the Huronian/Marquette Supergroup (Long, 2004).

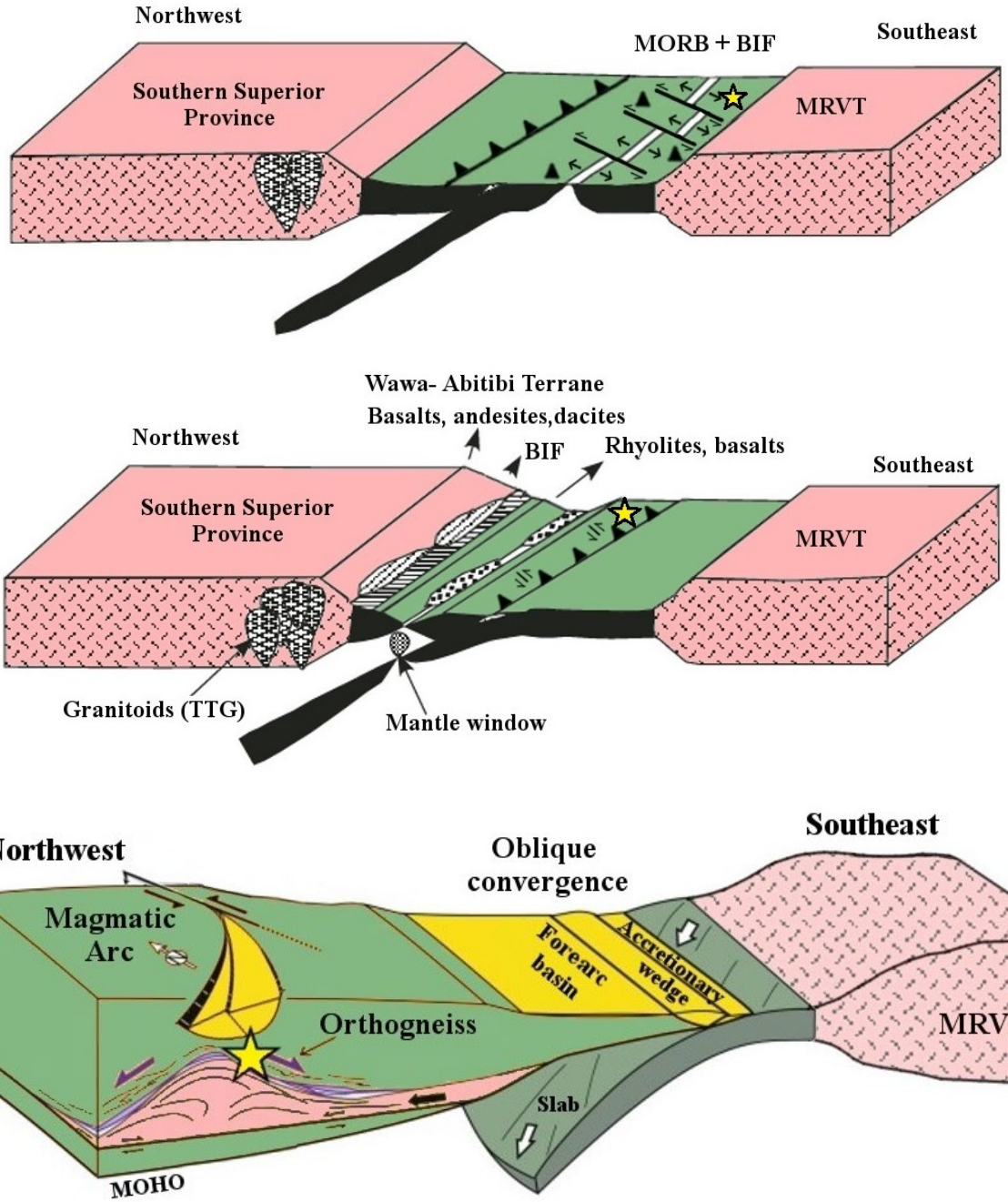

Figure 5.7: **(Top)** Mid–ocean ridge: Generalized tectonic evolution along the southern Superior Province including the formation of MORB and BIF in the Wawa–Abitibi Terrane (including the KSZ) ca. 2700 Ma. Low–grade gold mineralization (smallest star) is hosted in sulphide–facies BIF, **(Middle)** Kenora–Algoma accretion: Generalized tectonic evolution of an arc setting along the southern Superior Province including the formation of an arc in the Wawa–Abitibi Terrane (including the KSZ, green) ca. 2700 to 2670 Ma. Mineralization is buried by arc lithologies (medium star), **(Bottom)** Lakehead orogeny and MCC formation: Generalized tectonic evolution along the southern Superior Province including orogenesis by ca. 2660 Ma and the subsequent formation of the Pontiac subprovince, MCCs, and plutonism ceasing by ca. 2580 Ma. Orogenic gold mineralization is remobilized in high–temperature structures (large star).

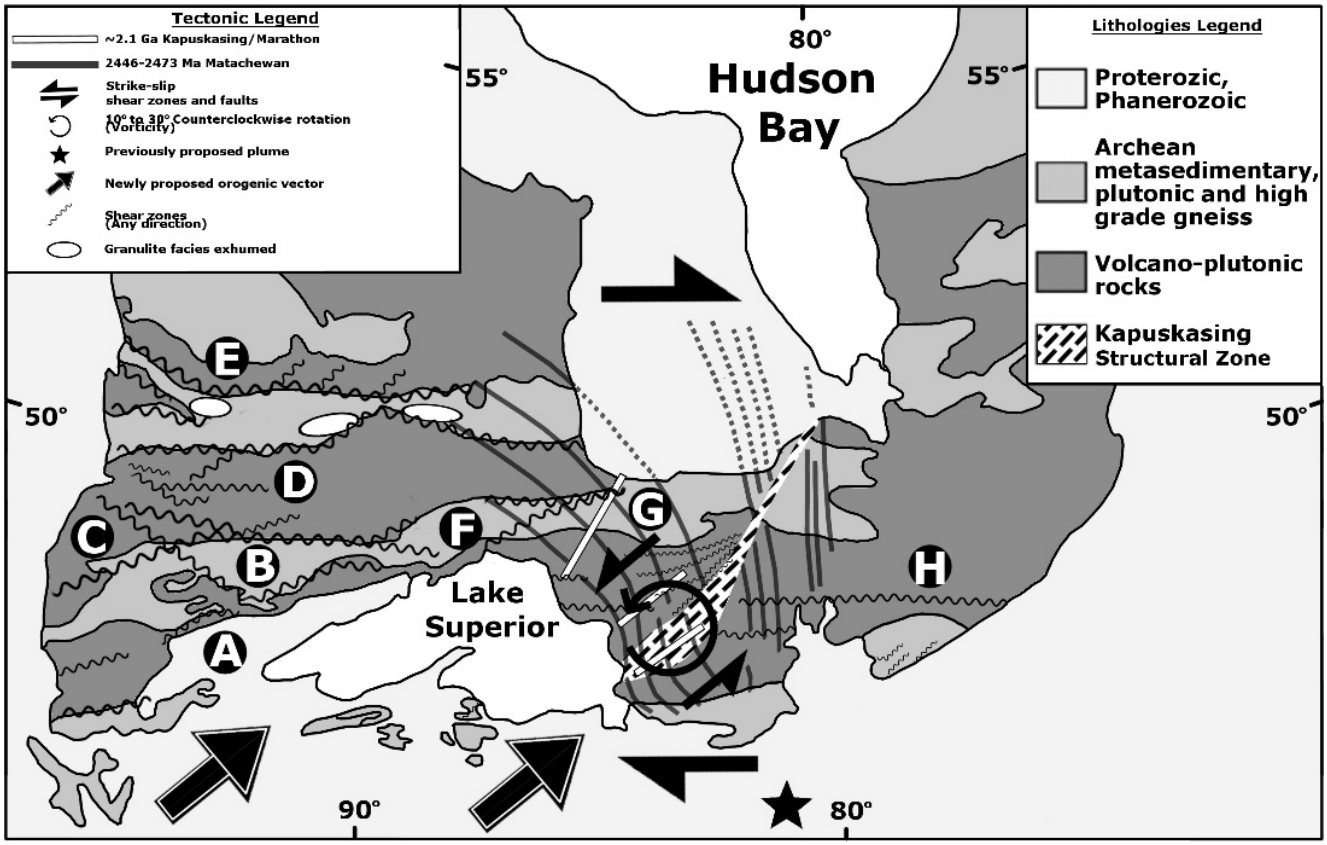

Figure 5.8: Regional tectonics, structure, and mafic dykes (dark grey and white lines) in the southern Superior Province (A) Vermilion, Burntside, and Minnesota River Valley structures, (B) Quetico, Eye–Dasha, Finlayson structures, (C) Cameron Lake, (D) Miniss River, Lake St. Joseph structures, (E) Red Lake structures, (F) Beardmore–Geralton, Hemlo, and other structures, (G) Gravel Lake, Chapleau Belt and other structures in the Kapuskasing Structural Zone, (H) Abitibi structures. The proposed orogeny along the southern Superior Province (black and grey arrows, southeast corner) created regional sinistral structures in KSZ with CCW rotation (small black arrows, centre), and cratonic– to regional–scale dextral structures throughout the Superior Province (large black arrows) (Modified after Card and Ciesielski, 1986; Percival et al., 2006 and additional references within thesis).

The new tectonic framework provides the first tectonic hypothesis for both the formation of the WGD, Chapleau Belt, and KSZ and provides evidence for the continuation of the Wawa–Abitibi terrane across the study area. The hypothesis clarifies and solves many outstanding issues in the study area, including the long–standing issues of an ~80 Ma high–temperature anomaly first documented by Moser et al. (1996, 2008), the crosscutting sinistral, northeast–striking ductile to brittle–ductile structures and horizontal extensional structures (Card, 1990; Sims and Day, 1993), metamorphic and geophysical discontinuity across between the eastern and western Superior Province (Easton, 2000), and CCW rotation across the southern Superior Province (Evans and Halls, 2010). The hypothesis also proposes that the Pontiac subprovince is not a minor, restricted subprovince with a MCC, but continues across the southern Superior Province and may include equivalents or extensions into the southern Batchawana greenstone belt of the Abitibi subprovince, the "Quiet Zone" between the MRVT and Wawa subprovince, and Neoarchean staurolite schist in North Dakota (Figs. 2.12–2.15) (McCormick, 2010; Southwick, 2014). This hypothesis also provides a tectonic mechanism for the exhumation of localized granulite regions throughout the southern Superior Province within areas of indenters, asymmetrical isograds, and irregularly shaped subprovince boundaries, and the very–low to low grade metamorphism in the Abitibi subprovince as it was protected by the decoupling along the KSZ during the orogeny in comparison to the western Superior Province (Fig. 2.3).

The new tectonic model can also be compared with previous models proposed for the WGD, KSZ, and southern Superior Province. For example, the previous intracratonic uplift structural model explains the Proterozoic dextral and thrust faults in the ILDZ and exposed Archean granulite but fails to provide an explanation for the earlier sinistral strike–slip and extensional ductile to brittle–ductile shear zones and boudins, prolonged high–temperature metamorphism, lack of Neoarchean thrust faults and flower structures, and a tectonic mechanism (Fig. 2.11) (Percival and Card, 1983; Ernst and Halls, 1984; Percival, 1989). The tectonic model proposed by Gibb (1978a) fails to explain the continuation between the eastern and western Superior Province and has no supporting geochronological data to support the suture hypothesis. The tectonic model of Watson (1980) focuses only on the cratonic–scale sinistral transcurrent fault zone and fails to account for the geochronology, metamorphic petrology, and thrust and dextral strike–slip faults and sinistral to extensional shear zones in the ILDZ (Watson, 1980). Other models have been more recently proposed and are based plume or vertical tectonic hypotheses, including models based on sagduction and fail to explain the overprinting structural fabrics and regional metamorphism throughout the study area and entire Superior Province (Mints, 2014; Lin et al., 2013; Bédard and Harris, 2014). These hypotheses are unnecessarily complicated and fail to explain the various types of lithospheric– to mantle–scale properties and geometry and lithospheric– to local–scale,

dextral, sinistral, and oblique ductile to brittle–ductile shear zones and boudins that formed during high–pressure, regional metamorphism and migmatization, overprinted by lower–pressure and temperature metamorphism throughout the Superior Province in the Neoarchean.

The new model involves no additional requirements. The new model proposed in this study includes components from previous workers, particularly from the models of Watson (1980), Percival and Card (1983), Ernst and Halls (1994), Moser (1994), and Percival (1989). The proposed model of the formation of the Kapuskasing and Pontiac MCCs as a result of a Neoarchean collision between the southern Superior Province and MRVT provides a tectonic mechanism for the decoupling of the western and eastern Superior Province to form and expose the WGD and KSZ mid– to lower–crustal equivalent of the Wawa–Abitibi terrane. It explains the formation of the early, sinistral, ductile shear zones, extension and rotation throughout the WGD and KSZ, oroclinal formation of the eastern KSZ, and overprinting faults in the ILDZ and the exposure of amphibolite, granulite, and migmatite, and felsic pluton magmatism. It also provides a tectonic explanation for the long–lived, high–grade metamorphic event in the KSZ proposed by Moser (1994), the late, regional low–pressure metamorphism throughout the southern Superior Province, the high–pressure granulite in the MRVT with Neoarchean zircon U–Pb metamorphic ages, the proposed extension of the Pontiac subprovince as an accretionary prism, abundant late Neoarchean plutonism, including complex pegmatites, throughout the southern Superior Province and MRVT, provides mechanism for thickened lithosphere for diamond emplacement, explains the general shape of the curvilinear subprovinces and overall fabric of the NE–striking southern Superior Province and NW–striking northeastern Superior Province, the gneissic domes and MCCs in the southern Superior Province, the various indenters in the southern Superior Province, transtensional to extensional regimes to emplace the mafic dyke warms, solves the contradictory seismic and paleomagnetism geophysical studies that defined both steeply dipping to horizontal fabrics in the study area and rotation in mafic dykes, and the initial Paleoproterozoic transtension to extensional depositional environments of the Huronian/Marquette Supergroup.

Due to the limited tectonic studies conducted in the southern Superior Province this proposal provides a cursory tectonic mechanism for many enigmatic lithological, structural, metamorphic, geophysical, and geochronological features. It offers a tectonic framework for the enigmatic WGD, Chapleau Belt, KSZ, Pontiac subprovince, and MRVT and bridges the Wawa and Abitibi subprovinces prior to this proposed Lakehead orogeny. The new tectonic framework may also be used to support the work by Van der Voo (Fig. 2.5) (2004). Van der Voo (2004) proposed a cratonic–scale oroclinal fold along the edge of the eastern Superior Province which was responsible for the marked change between the western Superior Province east–west striking subprovinces to northeast–southwest to north–south

striking subprovinces in the eastern and northeastern Superior Province. The new tectonic model proposed in this study has proposed the KSZ orocline which has a similar geometry, petrology, and geochronology to the northeastern Superior Province orocline defined by the Ashuanipi subprovince proposed by Van der Voo (Fig. 5.9). Therefore, similar tectonic processes could have operated along the entire southern Superior Province in the Neoarchean.

Even more importantly, this study can provide insight into the juxtaposition of high–metamorphic grade terrains and low–metamorphic grade and plutonic terrains, such as those in other Archean cratons. The striking similarity of northeast–directed Neoarchean orogeny, underplating, granulite facies metamorphism, exhumation, and felsic plutonism followed by Paleoproterozoic mafic dyke swarms in the southern Wyoming and Kola–Karelia cratons are of particular interest to be studied further (Fig. 2.2) (Frost et al., 2006; Grace et al., 2006; Dragovic et al., 2016).

5.1.2 Metamorphic Core Complexes as tectonic tools

This study proposed a new tectonic hypothesis for the southern Superior Province that explains many enigmatic features including the WGD, Chapleau Belt, KSZ, gneissic domes, irregular subprovince boundaries, and high–temperature metamorphism. MCCs commonly have components of transform, transpression, and/or transtension motion, and/or rotation which are underrepresented in paleotectonic reconstructions and may also provide context to many tectonics processes. The data most represented in paleotectonic reconstructions are convergent and divergent plate boundaries as the processes are well studied and preserved (Torsvik and Cocks, 2017). Due to the nature of the medium–to high–grade metamorphic and felsic plutonic lithologies in the hanging wall of MCCs they are generally well–preserved, yield robust minerals used in geochronology, and may provide evidence of transform (± transpression and/or transtension).

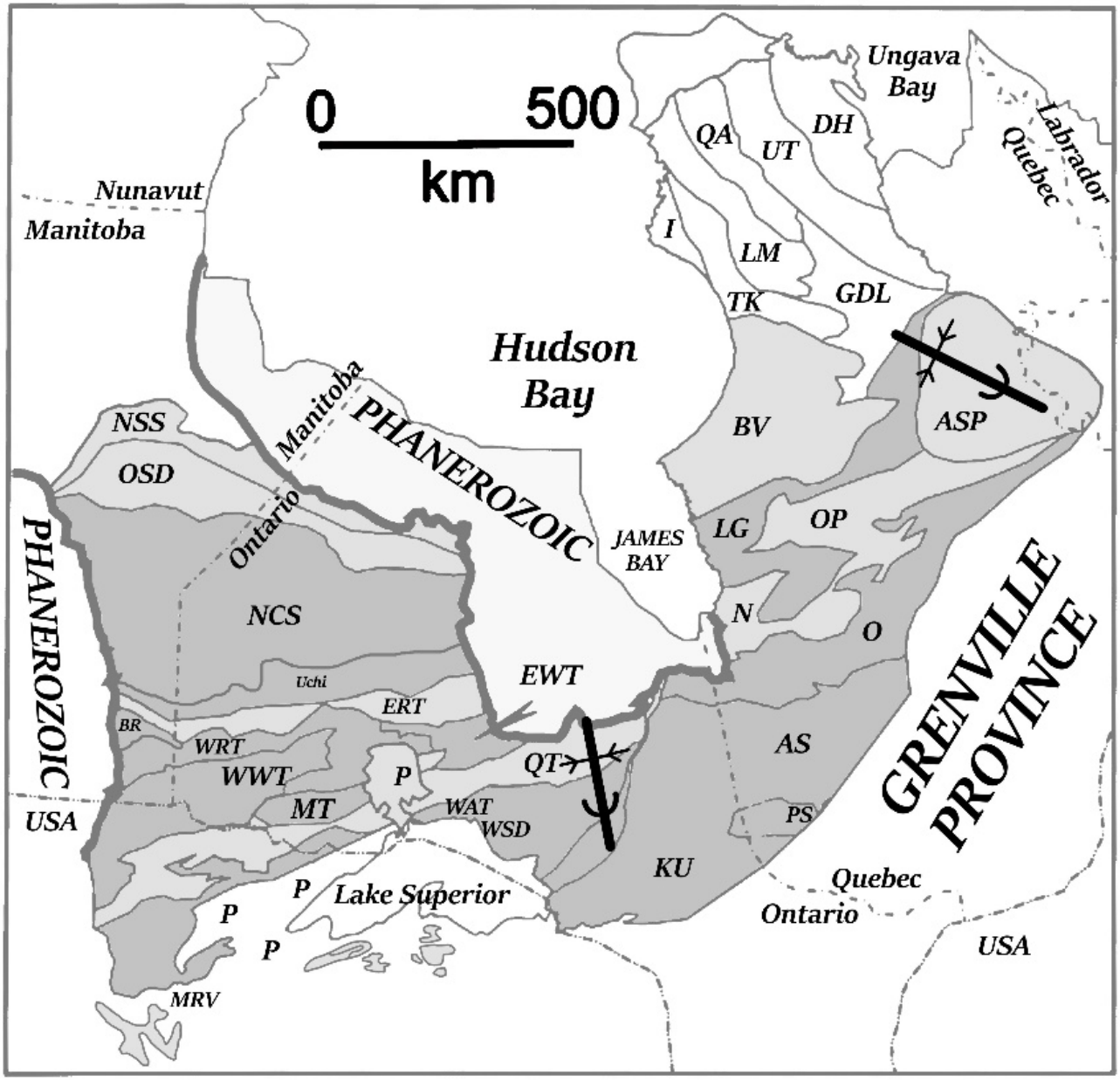

Figure 5.9: The proposed, regional–scale MCCs of the Superior Province have moderately to steeply plunging folds with gentle to open interlimb angles at the outcrop to regional scales and are defined as oroclines. At the cratonic scale the oroclines provide evidence for how the eastern and northern Superior Province was folded during the late Neoarchean to early Paleoproterozoic forming a cratonic–scale orocline. The CCW rotation documented in this study through the WGD, Chapleau Belt, and western KSZ and others in mafic dyke swarms may have been the trigger for oroclinal formation. Similar mafic dyke swarms are present in northeastern Superior Province and further investigation is required (Modified after Johnson, 1991; Bates and Halls, 1991; Bornhort and Johnson, 1998; Percival et al., 2012; Jirsa, 2016; van Nostrand et al., 2016).

The northeast–directed oblique collision between the MRVT with the southern Superior Province in the Neoarchean described in the previous section created predominantly dextral

transpression in the MRVT and sinistral transpression to local sinistral and dextral transtension throughout the southern Superior Province. The rigid, granulite, Paleoarchean to Neoarchean MRVT collided into the recently formed, and rheologically weaker, southern Superior Province creating oblique (sinistral–reverse) regional structures and gneissic domes in the western Superior Province and MCCs the eastern Superior Province. The progression from predominantly oblique, ductile to brittle–ductile, northeast–southwest striking, westerly to vertical shear zones, and gneissic domes in the western Superior Province to deformed gneissic domes and MCCs in the eastern Superior Province provide evidence of progressive transtension towards the east. Transpression to transtension, with regional– to local–extension, provided a tectonic mechanism for the exhumation and formation of KSZ and Pontiac MCCs and folded the mafic dyke swarms.

Continental convergent and divergent plate boundaries are commonly well preserved whereas oceanic and continental transform plate boundaries are less likely to be described or well preserved over geological time scales, due to many reasons including the lack of significant magmatism and related geochronology (Condie and Aster, 2010). MCCs commonly have transform, transcurrent, transpression, and transtension components and may also provide supportive paleotectonic evidence of subduction, collision, and exhumation (Whitney et al., 2012; Cooper et al., 2015). Due to the nature of the medium–to high–grade metamorphic and felsic plutonic lithologies in the hanging wall of MCCs they are typically well–preserved and yield robust minerals used in geochronology, including zircon and monazite. Therefore, there is high potential for preservation of transpressional to transtensional structures that can be precisely dated using many geochronological minerals (i.e., zircon, garnet) and systems (i.e. U–Th–Pb, Lu–Hf) hosted in magmatic to metamorphic lithologies. Therefore, this study recommends the use of MCCs as to document transform, transcurrent, transpressional to transtensional plate motions in paleotectonic studies, including reconstructions for the Proterozoic and Archean eons where data is sparse. Precambrian terranes are commonly deeply eroded and as such MCCs may lack typical features of recent and Phanerozoic metamorphic core complexes, similar to the KSZ and Pontiac MCCs. Deeply eroded MCCs may lack sedimentary cover, or may expose metamorphic lithologies from depths greater than the common greenschist to amphibolite facies.

The benefits of investigating non–convergent and divergent plate boundaries (i.e. transform) include improved understanding of complete tectonic cycles. The identification and study of MCCs may provide insight into these key components in addition to including useful transpressional to transform to transtensional tectonic components of paleotectonic plate reconstructions. Mantle–lithosphere interactions may also be collected from MCCs as coupling or decoupling can occur during formation. Oceanic and continental MCCs have been well–documented and studied from the present day to the end

of the Phanerozoic. Extensional, subhorizontal to horizontal, ductile to brittle–ductile shear zones in gneissic, migmatitic, and granitic lithologies are commonly mapped throughout Archean and Proterozoic cratons worldwide however few have been studied in regard to their tectonic context or proposed as MCCs (James and Mortensen, 1992; Sawyer and Barnes, 1994; Van Kranendonk and Collins, 1998; Zegers et al., 2001). By comparison, convergent plate boundaries, arcs and orogenies, and divergent plate boundaries, rift basins and back arcs, are readily identified using field mapping, structural, tectonic, and geophysical studies. By their very nature transform boundaries are limited in area by their width and may be easily missed or overlooked when compared to convergent and divergent plate boundaries with their characteristic regional structures, metamorphic grades, volcanism, plutonism, and geophysical anomalies over large, spatial areas. Transform and strike–slip structures are less commonly studied and typically identified only to account for problems in stratigraphy or structures during the field mapping and drafting processes. Although transform and strike–slip structures lack readily detectible regional–scale identifiers, particularly when compared to convergent and divergent plate boundaries, there are characteristics present in highly–eroded, Archean to Proterozoic metamorphic core complexes that can be utilized in paleotectonic reconstructions.

Archean cratons preserve paleotectonic information throughout their geological histories however their extensive geological ages and histories may be challenging to unravel. Despite their extensive study, the tectonic histories of many Archean cratons remain controversial. Controversy typically arises due to overprinting structural and metamorphic events during repeated tectonics events from the Archean into the Proterozoic. Another major difficulty is the lack of preservation and geochronology available in transform (± transpressive, transtensional) regimes to unravel the entire tectonic history.

The most well–preserved, exposed, and studied paleotectonic plate boundaries in Archean and Proterozoic cratons are typically continental convergent or divergent plate boundaries as they have regional– to local–scale diagnostic metamorphic, magmatic, structural, and geophysical characteristics. Typically transform plate boundaries, or those with transcurrent, transpressive, or transtensional components, lack these regional–scale characteristics or occur over smaller geographical areas. Therefore, due diligence must be taken by all researchers to investigate evidence of non–convergent and divergent plate motions, and must recognize it may take a concerted effort in studying other plate boundaries.

Current theories of paleoreconstructions of Neoarchean to Paleoproteroizic cratons and supercontinents are dominated by extensional tectonics, particularly the paleomagnetism and geochronology of mafic dyke swarms and document the tectonic processes of cratons, continents, and

supercontinents prior to breakup. Convergent tectonics typically support these extensional tectonic studies while tectonics involving components of transform motion are less studied. Extensional tectonic studies, including mafic dykes and basin formation, in the Neoarchean to Paleoproterozoic have proposed that numerous Archean cratons were part of one or more supercratons.

5.1.3 Similarities to other regions

Paleotectonic studies are instigated by identifying similarities between cratons, greenstone belts, high–grade gneisses, and mines have been proposed by various authors and indeed, the Neoarchean to Paleoproterzoic, regional, extensional or oblique shear zones and faults looked at in this study have been well–documented and studied in throughout many Archean and Proterozoic cratons. These structures documenting specific prograde and retrograde metamorphism is used to further document the paleotectonics and mineral potential of the region, and to reconstruct the paleotectonics of the cratons themselves and their mineral potential. The similarities of geological histories are remarkable and this study proposes a tectonic framework that supports previous authors reconnaissance to detailed field and mine mapping, petrological, and geochronological studies.

The tectonic evolution of the southern Superior Province proposed in this study supports early formation of an immature arc, arc to subduction, and accretion between 2.70 to 2.67 Ga to oblique collision with the Paleo– to Mesoarchean MRVT by 2.667 to 2.30 Ga, to exhumation and formation of MCCs ca. 2.62 to 2.58 Ga, and transtension, extension, and ultramafic to mafic magmatism into the Paleoproterozoic is present in the southern Superior Province. Evidence of this tectonic evolution, including accretion, collision, and exhumation, is preserved in the Paleo– to Mesoarchean MRVT that strikes predominantly east–west with moderate to steep, variable northward and southward dips (Group 1), Neoarchean WGD, KSZ, and Pontiac subprovince of the southern Superior Province with predominantly northeast–striking, variable moderate to steep dips (Group 2), and the Mesoarchean to Neoarchean Wawa and Abitibi subprovinces with predominantly east–west striking, steep dips to the north and host world–class gold mines (Group 3). North to northeast–striking and vertical, transtensional to extensional structures host ultramafic to mafic dyke swarms and intrusions (± Ni–Cu PGE deposits) throughout the southern Superior Province (Group 4) and parallel the earlier Group 2 structures.

5.1.4 Wyoming Province and Minnesota River Valley Terrane

Evidence of collision is well preserved in Group 1 of the Paleoarchean to Neoarchean MRVT with proposed extension into the Paleoarchean to Nearchean Wyoming craton with gneisses and migmatites that have experienced high temperature and pressure regional metamorphism and plutonism

in the Neoarchean. Neoarchean transpression to transtension is preserved in Group 2 of the southern Superior Province in the WGD, KSZ, and Pontiac subprovince, particularly sinistral transtension in the Kapuskasing and Pontiac MCCs that experienced regional metamorphism, and SAT, Sweetwater, Teton, and Wind River of the Wyoming craton. Neoarchean magmatism, very low–grade metamorphism, and only localized areas of transpression and transtension is preserved in Group 3 metavolcanic and sedimentary lithologies. Group 4 ultramafic to mafic magmatism and dyke swarms strike north to northeast that formed during transtension to extension following the Lakehead orogeny (or similar collision along the same plate boundary), and exhumation and/or MCC formation and are hosted throughout the southern Superior Province and extend into the Wyoming Province.

The southern Superior and northern Wyoming Provinces have extensive geochronological evidence for an orogeny in the Neoarchean (Figs. 1.2, 2.15)(Bickford et al., 2006; Schmitz et al., 2006; Moser et al., 2008; Dragovic et al., 2016). The southern boundaries of the Wyoming Province and MRVT have similar geological histories extending from the Paleo– to Neoarchean including a suture of high–pressure and temperature metamorphic gneisses and schist in contact with Meso– to Neoarchean mafic to bimodal volcanism in MORB to arc tectonic settings (Peterson and Geiger, 1990; Sims and Day, 1993b; Bickford et al., 2006; Schmitz et al., 2006; Dragovic et al., 2016). A suture in the Wyoming and Superior Provinces has been previously proposed by Dragovic et al., (2016) in the Wyoming Province using stratigraphy and geochronology and by Ojakangas et al., (2001), drill cores McCormick (2010) and Ernst and Bleeker, (2010) in the Superior through stratigraphy and mafic swarm studies, respectfully. Other workers have proposed the connection between the Wyoming and Superior Province (Chamberlain et al., 2015) and we propose the ca. 2670 Ma Lakehead orogeny with the GTLZ suture in the Superior Province continuous into the Black Hills of North Dakota, Great Falls Tectonic Zone, Powder River Pass shear zone, and OTSB in Wyoming. This orogeny (or similar along the same plate boundary) created the GLTZ suture and the extension in the Wyoming Province that strikes predominantly east–west striking in the Wyoming Province and southwestern Superior Province and changes to northwest–southeast striking in the southeastern Superior Province (Fig. 5.10).

The similarities of this proposed extension across the southern Superior and Wyoming Provinces is particularly striking and has been previously suggested by many authors from various areas of the geosciences. Roscoe and Card (1993) proposed the Huronian/Marquette Supergroup of the Superior Province and the Snowy Pass Supergroup of the Wyoming craton were continuous and proposed the breakup of a pre–2.5 Ga supercontinent at 2.1 Ga and similar work by Ojakangas et al. (2001). The global mafic magmatic event at ca. 2.45 Ga in Superior, Wyoming, and Kola–Karelia Provinces was first proposed Heaman (1997) and proposed it was an abortive breakup of the supercontinent of

Kenorland and placed the Baltica Shield to the south of the Canadian Shield. Paleomagnetic studies by Halls et al. (1998) using paleomagnetic evidence placed it on the eastern side of the Canadian Shield.

5.1.5 Requirements for the proposed paleotectonic reconstruction

To simplify the tectonic history of the paleotectonics of the previously described section they can be categorized into three category: 1) the oldest category involves ridged, cold Paleo– to Mesoarchean (with minor components younger and older) craton(s) that have initiated the tectonic collision with northeast–dipping subduction followed by continental collision, 2) the second category involves warm, plastic Mesoarchean to Neoarchean craton(s) with economically endowed terranes and subprovinces striking east–west along strike and is the craton that craton 1 collides into, and 3) is the youngest category and crosscuts category 1 perpendicularly and category 2 obliquely due to the Neoarchean to Paleoproterozoic structures exposed as a result of the collision between category 1 and 2 which triggers mafic dyke swarms (some being economically endowed) and sedimentation during exhumation.

The Superior and Wyoming Provinces have evidence of continental transpressional to transtensional tectonic history during the Neoarchean as do other Archean cratons (i.e. Kola–Karelia), although some have greater components of transtension or extension. The lithologies, geochronology, structural geology, geophysical geology, and igneous and metamorphic petrology, described in the above section categorizes all of the regions into four main groups to better recognize their Neoarchean to Paleoproterozoic tectonic similarities.

The proposed orogeny, exhumation/MCCs, and gneissic domes (or similar high–grade gneisses, migmatites, and felsic plutonic geological features) experienced significant transcurrent, transpressive, and transtensional tectonic regimes. This tectonic information can be used in combination with other studies can help in discerning and refining paleotectonic reconstructions where extensional settings, dominated by mafic dyke swarm and sedimentary studies, fail to explain other earlier tectonic components, including compressive to transcurrent regimes. The tectonic and paleotectonic reconstructions can they be used in understanding supercontinental cycles.

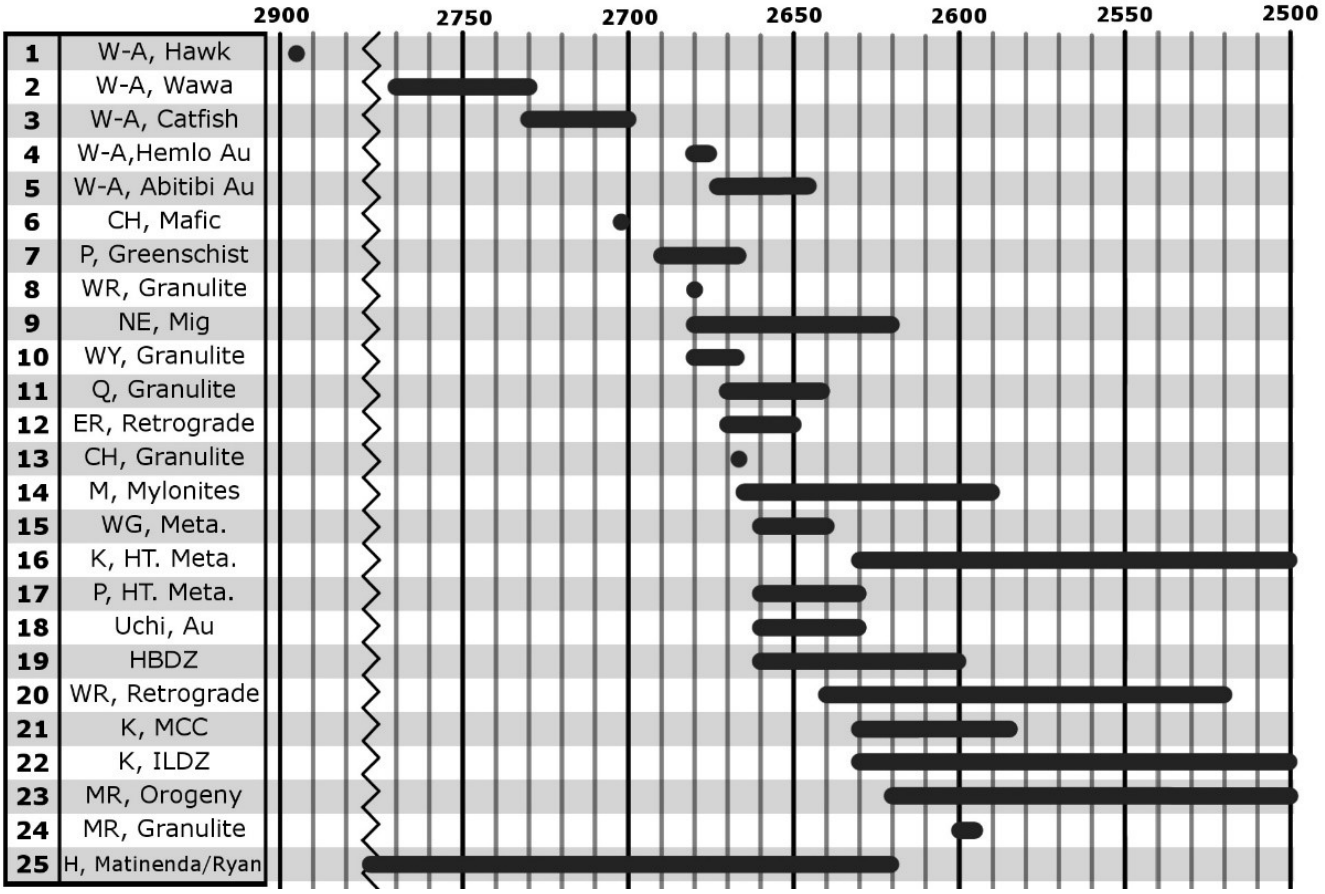

Figure 5.10: Generalized geochronological events in the Superior and Wyoming Provinces and MRVT: (1) Wawa, Abitibi Subprovinces (W–A), Hawk formation; (2) Wawa, Abitibi Subprovinces (W–A), Wawa formation; (3) Wawa, Abitibi Subprovinces (W–A), Catfish formation; (4) Wawa, Abitibi Subprovinces (W–A), gold mineralization at the Hemlo Mine; (5) Wawa, Abitibi Subprovinces (W–A), gold mineralization in the Abitibi subprovince; (6) Chapleau Belt (CH), zircon U–Pb age of sillimanite–garnet gneiss and mafic lithologies, this study; (7) Pontiac subprovince (P), greenschist facies metamorphism; (8) Winnipeg River subprovince (WR), granulite facies metamorphism (Corfu, 1988); (9) Northeastern Superior Province (NE), migmatization during high–grade metamorphism; (10) Wyoming Province (WY), granulite facies metamorphism; (11) Quetico subprovince (Q), granulite facies metamorphism; (12) English River subprovince (ER) and adjacent subprovinces, retrograde metamorphism after granulite facies; (13) Chapleau Belt (CH), age of granulite facies metamorphism; (14) Marmion terrane (M), age of NE–striking mylonites; (15) Wawa Gneiss Domain (WG), age of metamorphism; (16) KSZ (K), high– temperature and pressure metamorphism; (17) Pontiac (P), high–grade metamorphism and migmatization, (18) Uchi, gold mineralization and remobilization, (19) Wabigoon, Humboldt Bay Deformation Zone (HBDZ), age of retrograde metamorphism, (20) Winnipeg River (WR), retrograde metamorphism, (21) Kapuskasing Structural Zone (K), formation of MCCs; (22) Kapuskasing Structural Zone (K), formation of the ductile structures in the Ivanhoe Lake Deformation Zone, (23) MRVT, (MR), proposed orogeny with the Superior Province, (24) MRVT (MR), granulite facies, (25) Huronian (H), detrital age of Matinenda and Ryan formations (Turek et al., 1984, 1992; Davis and Lin, 2003; Beakhouse, 2007; Feng and Kerrich, 1992; van Nostrand and Broughm, 2016; Souders and Frost, 2006; Pan et al., 1994; Pan and Fleet, 1998; Moukhsil et al., 2003; Kamineni et al, 1990; Corfu, 1988; Moser, 1996; Easton, 2000; Ma; Feng and Kerrich, 1990, 1991; Dubé et al., 2004; Culshaw et al., 2006; Corfu, 1988; Moser et al., 2008; Schmitz et al., 2006; Bickford et al., 2006; Easton and Heaman, 2011).

5.1.6 Final considerations of paleotectonic reconstructions

The tectonic history is presented as: 1) Neoarchean subduction of an oceanic transform plate boundary (or boundaries), 2) subsequent oblique collision between rigid, older continental lithosphere and weak, younger arc and continental lithosphere, 3) transpressional to transtensional plate movements as exhumation syn– to post–orogeny along the southern Superior and Wyoming Provinces, 4), mafic dyke swarms and magmatism along previous transtensional to extensional structures, 5) Snowy Pass and Huronian/Marquette sedimentation, including uranium mineralization.

New methods to reconstruct the southern Superior and Wyoming Provinces during the Neoarchean to Paleoproterozoic are limited to the studies of paleomagnetism of mafic dyke swarms and sedimentary basins that both formed through extensional tectonics. This study recommends the use of orogeny, exhumation/MCCs, gneissic domes, and similar features as evidence for transpressional to transtensional plate motions in paleotectonic plate reconstructions including reconstructions for the Proterozoic and Archean eons where data is sparse or poorly preserved. Further multi–disciplinary tectonic studies are necessary to improve our understanding of Archean tectonics and uniformitarianism and by using MCCs as analogues for transform plate boundaries we may greatly enhance paleotectonic reconstructions. Smaller–scale geological features must also become more common in paleoreconstructions as unique or signature features may prove to be important, such as metamorphosed, diamond–bearing, calc–alkaline breccias, lamporphyres, and kimberlites in this study.

CHAPTER 6: MODEL FOR GOLD MINERALIZATION IN BORDEN MINE

6.1 Introduction

The original focus of this thesis was to provide the first model to constrain the gold mineralization in upper amphibolite to granulite facies lithologies in the Borden Mine. The Borden Mine is located in the Chapleau Belt that neighbours the WGD and KSZ and lacks features common to other orogenic gold deposits and adjacent gold deposits in the Wawa–Abitibi terrane. As this study is the first in the Chapleau Belt it focused on high–level data collection to support future detailed research. Trench mapping, drill core logging, geochronological, and geochemical analyses conducted for this thesis focused primarily at the Borden Mine site in the Chapleau Belt and neighbouring WGD and KSZ (Figs. 4.19–4.25, 6.1–6.3).

The data support the hypothesis of early, Neoarchean mineralization along the BIF contact with "footwall" and "hanging wall" seafloor–altered mafic volcanic lithologies and remobilized during subsequent metamorphism (Figs. 4.9 A–F). The mineralization survived, albeit modified and remobilized, during accretion, orogenies, and MCC formation during exhumation from the Neoarchean to Paleoproterozoic. The remobilization at high–metamorphic grades during high–temperature deformation resulted in features uncommon to lower–metamorphic grade orogenic gold deposits in the adjacent Wawa–Abitibi terrane. The Borden Mine in the Chapleau Belt is an outstanding example of gold mineralization that has persisted and remobilized throughout high–temperature metamorphism and deformation.

6.2 Regional Geology

The Wawa and Abitibi subprovinces of the Superior Province host numerous world–class gold mines and deposits (Kerrich and Cassidy, 1994). Despite the proximity to these gold mines the WGD and KSZ have been underexplored due to their high–grade metamorphism. The limited prospecting and field mapping conducted in the region may have not recognized the remobilized, high–grade metamorphic and high–temperature structures and textures that host the mineralization as it differs from the mineralization in the Wawa–Abitibi terrane. The adjacent Michipicoten, Mishibishu, Gamitagama greenstone belts of the Wawa subprovince and Blake River and Tisdale Groups of the Abitibi subprovince experienced very–low grade to medium–grade metamorphic histories with mineralization localized in quartz veins within transpressional to transtensional strike–slip brittle–ductile shear zones and faults (Figs. 2.2, 2.3, 2.7–2.9) (Jemielita et al., 1990; Kerrich and Cassidy, 1994; Jellicoe et al., 2019; Mercier–Langevin et al., 2020; Tuba et al., 2021).

Field mapping, drill core logging, petrography, and geochemical analyses provide evidence of the BIF and mafic protolith ore and host lithologies that reached prograde upper amphibolite to granulite facies, migmatized to metatexites or diatexites, and experienced retrograde lower amphibolite facies and greenschist to sub–greenschist facies metamorphism. The gold mineralization is hosted in ductile sinistral–strike slip to oblique (sinistral–reverse) shear zones that are overprinted by brittle–ductile sinistral and dextral strike–slip to oblique shear zones that remobilized during boudinage into areas of regional– to microscopic–scale boudin necks, foliation boudins, and mullions during 10–15ºCCW rotation (Figs. 4.9A, E; 4.12 C–D; 4.24–4.25). The rotation accounts for the sigmoidal "Z–shape" and shallow to moderate plunge of the deposit (Figs. 2.1, 4.9 C, 4.24–4.25). The partial melting of mafic lithologies triggered remobilization into leucosomes and pegmatites in these boudin necks and foliation boudins. The protoliths and mineralization at the Borden Mine and Chapleau Belt are comparable to those in the Michipicoten (Mishibishu) and Abitibi greenstone belts, however, they have experienced higher–temperature metamorphic and deformation histories.

6.3 Borden Mine geology

The gold mineralization at the Borden Mine is atypical as it is hosted in high–grade metamorphic lithologies and lack quartz veins and appreciable sulphide mineralization (typically trace to 2% pyrite and pyrrhotite, except in semi–massive to massive sulphide–facies banded iron formations adjacent to ore zones) compared to more typical orogenic gold deposits (Goldfarb et al., 2005). The host lithologies in the Borden Mine and Chapleau Belt are predominantly mafic lithologies with massive, schistose, mylonitic, gneissic, metatexite and diatexite migmatitic textures. The gold mineralization is generally localized to the boundary between the "footwall" and "hangingwall" mafic lithologies with interlayered sillimanite–garnet–biotite schist and newly discovered BIF. The structurally and stratigraphically lowest assemblage of mafic lithologies (or "footwall" mafic lithologies) have protoliths with tholeiitic, ultramafic to intermediate geochemical signatures and affinities to MORB (± BABB) (Fig. 6.2). The upper mafic lithologies (or "hangingwall" mafic lithologies) are predominantly amphibolite with minor intermediate to felsic metavolcanic and volcaniclastic lithologies, BIF, sillimanite–garnet–biotite schist, garnet–muscovite–garnet schist, schists and gneisses, garnet–sillimanite–perthitic feldspar gneiss, and graphitic schists. An angular unconformity separates the metamorphosed ultramafic to felsic plutonic, volcanic, and volcaniclastic lithologies with the younger metasedimentary lithologies above. Quartz–feldspar and complex pegmatites form in low–strain zones throughout migmatized mafic lithologies. Megacrystic quartz–feldspar pegmatites are the only pegmatites that do not form in low–strain zones and crosscut all of the older lithologies. The youngest lithology in the study area are diabase dykes.

At the mine–site scale the ore is hosted in a rotated and boudinaged, regional–scale ductile, sinistral strike–slip shear zone along the boundaries between gneissic amphibolite at the contact between the lower "footwall" amphibolites and the upper "hangingwall" amphibolites and sillimanite–garnet–biotite schist and BIF (Fig. 6.2). At the mine–site to drill–core scale the mineralization is constrained to the schistose to mylonitic fabrics that anastomose around rotated boudins and foliation boudins, and overprint earlier gneissosity and metatexite migmatites in mafic to felsic plutonic, volcanic, and volcaniclastic lithologies, and oxide– and sulphide–facies BIF (Figs. 4.9 A, C, E, F, 4.10–4.12, 4.19–4.26). Subeconomic (<0.2 g/t Au) gold mineralization is located outside of regional to local brittle–ductile shear zones that lack rotated boudins and rotated foliation boudins in massive, sulphide–facies BIF and interlayered "hangingwall" amphibolite and garnet gneiss, and along the lithological boundary between the mafic to felsic volcanic and volcaniclastic breccia with euhedral, medium–grained pyrite and pyrrhotite.

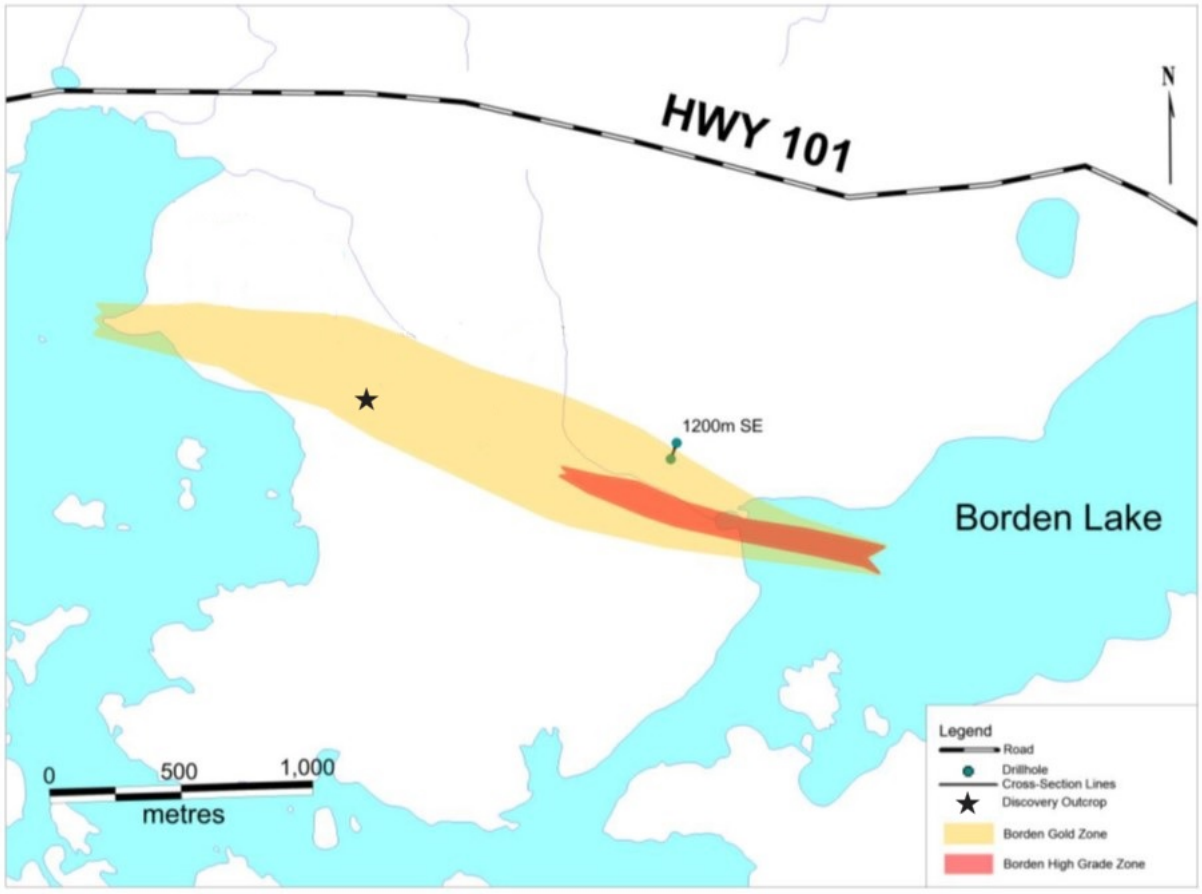

Figure 6.1: The high–grade ore zone (red), mineralized envelope (yellow), Discovery Trench (low–grade mineralization at surface and location of geochronology sample, star), and drill core section line 1200 m SE of the Borden Mine (Modified after LaFontaine, unpublished MSc. thesis, 2016).

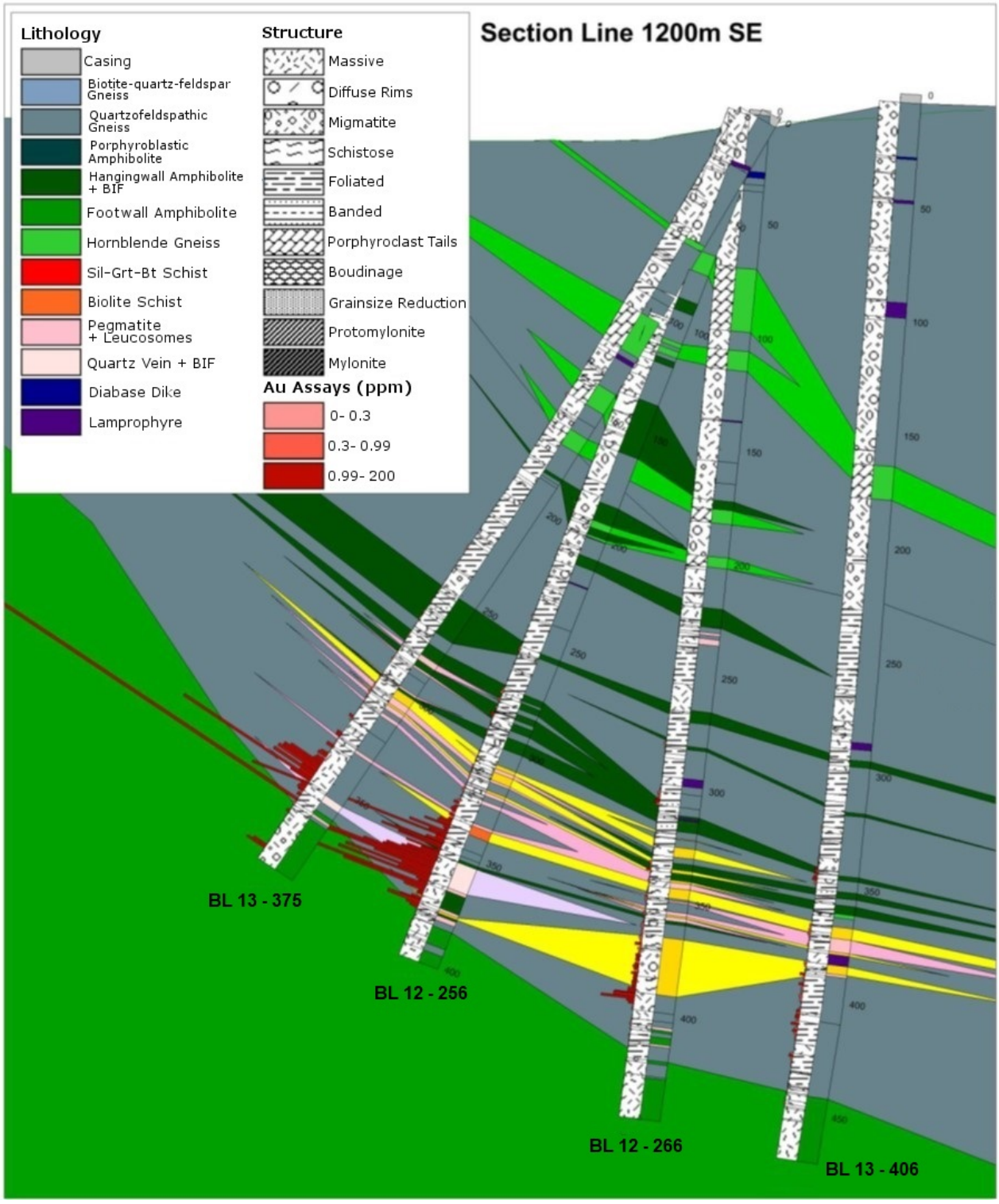

Figure 6.2: Section line 1200 m SE cross section, including high–grade BL–12–256 diamond drill hole. Lithological and structural re–interpretations were conducted in collaboration with D. LaFontaine and K. Jellicoe (Jellicoe, 2014, unpublished Honours BSc. Thesis, and LaFontaine, 2016, unpublished MSc. thesis) (Modified after LaFontaine, unpublished MSc. thesis, 2016).

6.4 Structural characteristics

Field mapping extended the Chapleau Belt into the western WGD where it has been partially to completely assimilated. Mapping also defined belt– to regional–scale ductile sinistral–strike slip to oblique (sinistral–reverse) shear zones that are overprinted by local– to outcrop–scale brittle–ductile sinistral and dextral strike–slip to oblique shear zones in antithetic shearbands. Antithetic shear bands are localized to 10–15ºCCW rotated boudin necks (Fig. 4.21, 4.24). Migmatitic structures were also mapped and follow the general trend of increasing metamorphic grade and higher–temperature deformation towards the east into the southern KSZ (Fig. 4.23). The mineralization style progressively increases eastward with higher–grade lithologies in higher–temperature structures from lower–grade WGD to higher–grade Chapleau Belt and KSZ. The mineralization in the WGD is hosted in zones of abundant pyrrhotite and pyrite in recognizable quartz veins in brittle–ductile shear zones while the minor to trace amounts of sulphide mineralization in the Chapleau Belt and KSZ is hosted in quartz veins that have been obliterated by mylonitization and rotational boudinage in high–temperature, sinistral shear zones. Also obscuring the high–temperature mineralization are leucosomes developed through partial melting of mafic lithologies where remobilization of native gold is present in leucosomes and pegmatites in boudin necks and foliation boudins within high–grade ore zones. No gold mineralization is present in the youngest, brittle Proterozoic faults.

The high–temperature deformation during metamorphism concentrated the ore in belt– to regional–scale ductile to brittle–ductile shear zones, boudin necks, foliation boudins, shear bands, chocolate–tablet structures, along mullions, and folded fractures. Competency contrasts in the region are documented between lithologies that preserved their prograde amphibolite to granulite facies mineralogy and gneissic textures and those in schistose to mylonitic retrograded granulite and amphibolite in boudin necks. Competency contrasts are able to be semi–quantified based on boudin types with medium– to coarse–grained ultramafic to mafic lithologies as the most rheologically competent lithologies followed by mafic and felsic metavolcanics and banded iron formation lithologies, coarse–grained to pegmatitic pegmatites, and the least competent schistose and flattened lithologies.

6.5 Petrography

The high–temperature structures mapped on the belt– to outcrop–scale are prominent on the microscopic scale (Figs. 4.9–4.12, 4.23, 4.44–4.45). Folded, boudinaged, and sheared quartz veins are also identifiable in thin section, although they are generally unidentifiable on the outcrop– to hand sample–scale. Sulphides and native gold are also identifiable in thin section in areas that appear to be

unmineralized in drill cores or outcrops. The very low modal percentages of sulphides in the Borden Mine (outside of sulphide–facies BIF) range between trace to 2%.

The sulphide and gold mineralization on the microscopic scale is localized in zones of sulphide–facies BIF in garnet–sillimanite–biotite schists between the “footwall” and “hangingwall” amphibolites. These ore zones exhibit microstructures that are consistent with crystal plastic deformation during upper amphibolite to granulite facies metamorphism, including as inclusions and folded fractures in garnet, pyroxene, and chessboard–texture quartz. Mineralization is also present in microfaults and boudins in zones that have undergone ductile to brittle deformation in areas that experienced retrograde amphibolite facies and lower metamorphic reactions, including native gold inclusions in muscovite. Minerals more typical of VMS deposits, including sphalerite, are present in garnet and pyroxenes as inclusions and may provide insight into mineralization at the seafloor.

In zones of highest strain, such as mylonites, the native gold commonly defines subgrain boundaries which suggests it experienced crystal plastic deformation and also defines boudin necks, providing evidence that it behaved as a solid during high–temperature ductile deformation (Figs. 4.9–4.12). In areas of lower strain, such as in lithons and boudin interiors, the sulphides have been partially melted with daughter minerals of euhedral pyrite, arsenopyrite, and löllengite inside coronas of anhedral pyrrhotite, and native gold (Figs. 4.10 A–B, 4.12). Sulphide melts and have been remobilized to areas of lower strain and preserved in microscopic fractures, strain shadows, boudin necks, foliation boudins, mullions, and cataclasites with overprinted schistosity (Figs. 4.12 C–D, 4.44 A). Therefore, there may be a relationship between strain rate, rheology, and the style of gold mineralization and remobilization.

Felsic plutonic, pegmatitic, and migmatitic leucosomes concentrated in regional– to microscopic–scale rotated boudin and foliation boudin necks may have formed during retrograde metamorphism as documented by the presence of retrograde muscovite, biotite, tourmaline, and Be–rich minerals. These mineralized areas also experienced the greatest plane strain during prograde amphibolite to granulite facies metamorphism and flattening during retrograde metamorphism and therefore were the most easily rotated and remobilize mineralization. Flattening and the formation of a more schistose fabric due to the presence of white mica after alkali feldspar further increased the rheological and enhanced boudinage and rotation. The introduction of fluid to trigger retrograde metamorphic reactions occurred in these rotated boudin necks and host the greatest amount of white mica, biotite, and tourmaline. Areas of greatest rotation provided space for felsic leucosomes and intrusions and subsequent remobilization of gold mineralization.

6.6 Geochronology

U–Pb laser ablation ICP–MS zircon geochronology confirmed an igneous crystallization age ca. 2.700 Ga, a metamorphic event ca. 2.670 Ga in the sillimanite–garnet–biotite schists and gneisses, and one zircon age ca. 2.580 Ga at the Borden Mine (see Chapter 3). The age of the sillimanite–garnet–biotite schist defines the upper limit on the age of gold mineralization. Other studies at the Borden Mine have further constrained the age of garnet growth to 2630 Ma to 2623 Ma (LaFontaine, unpublished MSc. thesis, 2016).

6.7 Sulphur and Lead Isotopic studies

Isotopic studies were conducted to further constrain the style of mineralization at the Borden Mine (Tables 4.2–4.3; Figs. 6.3–6.4). Sulphur isotopic analyses was conducted on pyrite, pyrrhotite, intergrown pyrite–pyrrhotite, and magnetite samples collected from barren and ore zones. The barren samples were analyzed and have an isotopic range between –1.5 ‰ and +4.7 ‰. The samples collected from low–grade ore in drill cores and outcrops range between –5 ‰ and +1 ‰ and economic ores range between –8 ‰ to –10 ‰. The structural, metamorphic, and petrographical evidence of high–strain during retrograde metamorphism, and partial melting the ^{34}S–depletion in ore samples may suggest an evolving hydrothermal system and remobilization compared to the most ^{34}S–enriched values in the lowest grade and barren samples.

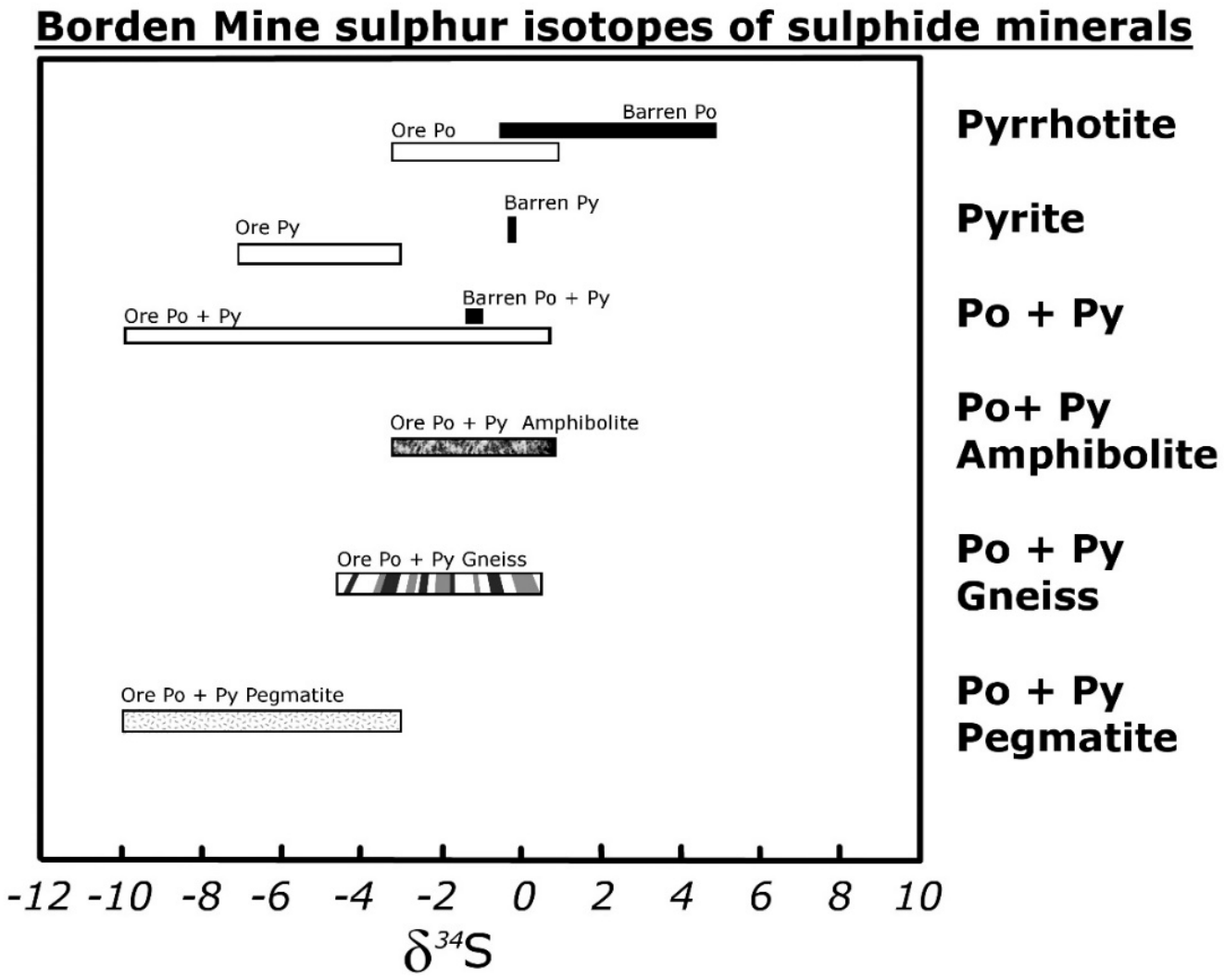

Figure 6.3: Sulphur isotopic data of pyrite (Py), pyrrhotite (Po), and mixtures of both collected from ore and barren zones in the Chapleau Belt and Borden Mine. Barren samples of all sulphides are heavier than ore samples in all sulphides. Ore collected from different host lithologies (amphibolite, gneiss, and pegmatite) can also be differentiated with pegmatite having the lightest signatures. The populations of barren and ore pyrrhotite have minor overlap while the barren and ore pyrite have none making these excellent isotopic tools for exploration. The pyrite and pyrrhotite is commonly intergrown and has also been assessed for use as an exploration tool. The light isotopic signatures in ore suggest remobilization of gold and sulphide minerals is important to mineralization at the Borden Mine and Chapleau Belt.

Similar light sulphur isotopic signatures are also present at the nearby Hemlo Mine in the Wawa subprovince, with signatures as low as –17.5 ‰, that have been attributed to isotopic fractionation between oxidized and reduced sulphur species (Cameron and Hattori, 1985). The pyrite related to gold mineralization at Hemlo Mine is depleted in $\delta^{34}S$ with eight samples –5.7 ‰ ± 0.9 (Fig. 1.5). The lead isotopic analyses show that the highest–grade samples have the least radiogenic lead isotopic compositions and narrowest ranges of $^{206}Pb/^{204}Pb$ ratios of all the samples (Fig. 6.4). The samples that are located in the most competent zones have lowest $^{206}Pb/^{204}Pb$ ratios and older Neoarchean Pb–Pb model ages while the sample that experienced boudinage has the greatest $^{206}Pb/^{204}Pb$ ratio and the youngest Proterozoic Pb–Pb model age. This isotopic, mineralogical, and textural relationship may suggest an evolving style of mineralization from the Neoarchean into the Proterozoic. Although the samples collected were from metavolcanic, BIF, and metasedimentary samples they have similar isotopic signatures, suggesting that the mineralization is from a single reservoir. In fact, the samples provide a single–stage Pb–Pb model age of 2760 Ma with $\mu = 8.113$ is remarkably similar to the Wawa subprovince and comparable to the Abitibi subprovince (Vervoort et al., 1994; Sage et al., 1987; Bornhorst et al., 1998; Thorpe et al., 1987; Thorpe, 1999). The younger samples are also similar to the lead isotopes from whole rock in the WGD (Smith et al., 1992).

Previous authors have proposed the gold and sulphide mineralization in the Wawa and Abitibi subprovinces formed in volcanic and subvolcanic lithologies is also true in the Chapleau Belt, although at lower grade metamorphic equivalents (Vervoort et al., 1994; Sage et al., 1987; Bornhorst et al., 1998; Thorpe et al., 1987; Thorpe, 1999).

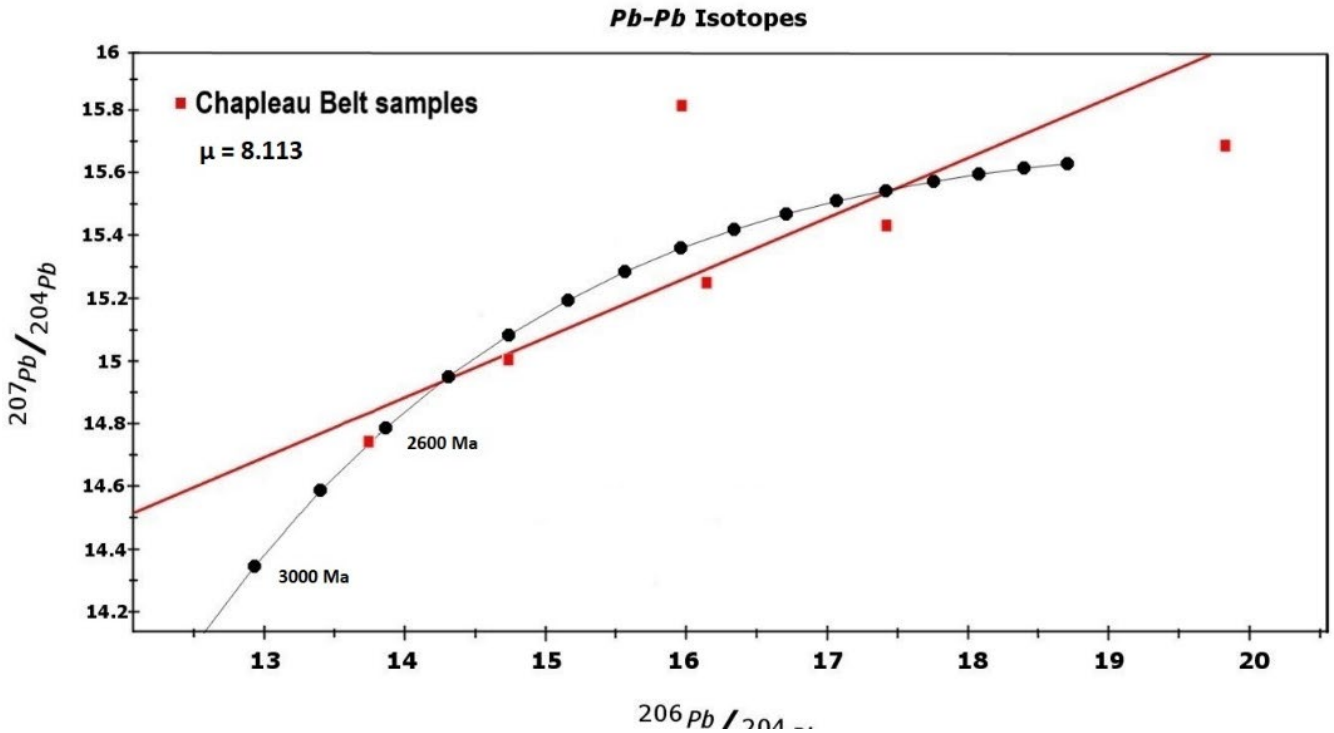

Figure 6.4: Single–stage lead isotopic ratios in pyrite, pyrrhotite, and magnetite samples collected from the Borden Mine and Chapleau Belt (red boxes). The analyses generally fall on or near the isochron (red line) except for the Proterozoic pyrite sample (above the line). The growth curve of the Borden Mine and Chapleau Belt samples (circles, μ=8.113) is similar to other studies conducted in the Wawa and Abitibi subprovinces, and WGD (Sage et al., 1987; Thorpe et al., 1987; Kerrich and Kyser, 1994; Vervoort et al., 1994; Bornhorst et al., 1998; Thorpe, 1999 and references therein). Areas of field Superior Province gold and VMS deposits are also plotted to highlight that at least one sample plots within the field Superior Province gold (light black line and stars) and not the VMS field (thick black line and stars). The Stacey and Kramers (1975) evolution curve is plotted in black with black circles.

6.8 New prospecting tools for the Wawa Gneiss Domain and Kapuskasing Structural Zone

Based on the field mapping, drill core logging, petrography, sulphur and lead isotopic geochemistry, and geochemistry the vectors for gold mineralization in the Chapleau Belt and adjacent WGD and KSZ should include: (1) Field mapping for rotated boudinage in schistose to mylonitic sinistral strike–slip shear zones and corresponding, abrupt >45º change in mineral lineations defined by dark green to black hornblende, green augite pyroxene, red garnets, or clast lineations in boudin necks, (2) Geophysical magnetic susceptibility and resistivity surveys for magnetite and pyrrhotite, (3) Light sulphur isotopes in sulphides (–10 ‰ to +1 ‰), (4) $^{206}Pb/^{204}Pb$ ratios and with Neoarchean Pb–Pb model ages (13.737 $^{206}Pb/^{204}Pb$, 14.745 $^{207}Pb/^{204}Pb$, 33.930 $^{208}Pb/^{204}Pb$), (5) Assaying mylonitized, migmatized mafic lithologies with euhedral pyrite, muscovite, and Be–rich minerals. Inclusions of sphalerite, pyrrhotite, and other sulphide and related elevated trace elements in the ore zone include Ge, Ga, Gd,

Hg, S, etc. in high–grade metamorphic minerals formed prior to prograde amphibolite facies metamorphism and thus formed early, potentially with the primary gold mineralization.

6.9 Formation and remobilization of ores

The gold mineralization in the Borden Mine is proposed to have formed at an oceanic seafloor setting hosted in MORB and BIF, including subeconomic gold mineralization in sulphide–facies BIF. The tectonic regime developed and evolved into to an arc to orogenic setting which formed a more orogenic–style deposit. An orogeny with corresponding regional, prograde amphibolite to granulite facies metamorphism, and migmatization created high–temperature sulphide minerals in the ore zones, including löllengite. Exhumation and retrograde amphibolite facies metamorphism, oblique (sinistral–reverse) ductile to brittle–ductile shear zones, and regional to microscopic–scale rotated boudins have aided in the concentration and remobilization of gold mineralization, including sulphide melts, in the Chapleau Belt along the shallow to moderate plunging, lineation of mullions, and boudin necks in shear zones (Figs. 6.2, 6.5). Remobilization of native gold into leucosome, felsic plutonic and pegmatitic lithologies overprint the earlier orogenic gold mineralization (Fig. 4.9 F). The felsic intrusive lithologies in mineralized boudin necks further influenced the rheological contrasts and fluids in the region, as demonstrated in the presence of muscovite, biotite, amphiboles, beryl, and tourmalines (Figs. 4.10 C–D, 4.15 B, 4.44 A). The youngest sulphides to form that no do contain gold mineralization are anhedral pyrite and subhedral, magnetic pyrrhotite, both of which further constrain the mineralization history.

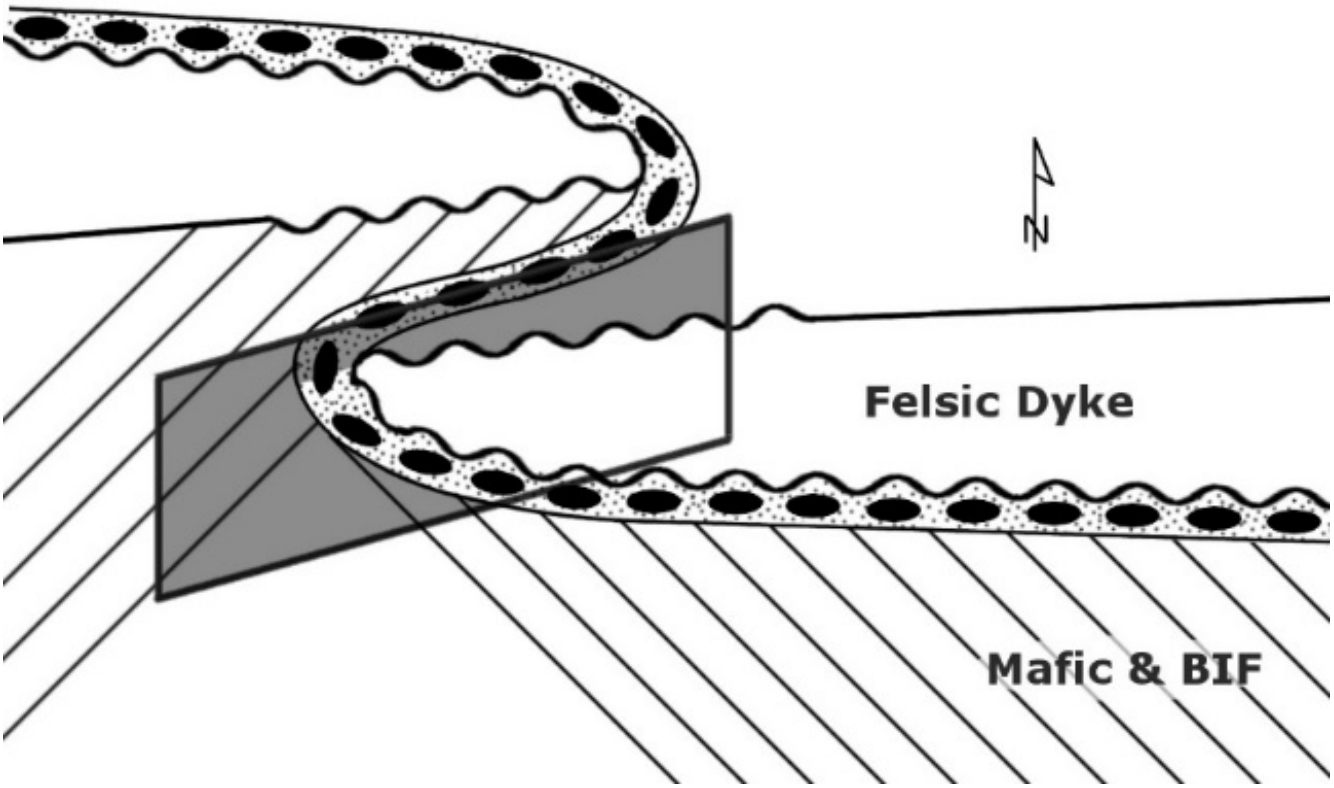

Figure 6.5: Simplified schematic of the lithologies and structures that host the gold mineralization at the Borden Mine. The boundary between the "footwall" and "hangingwall" mafic protoliths (lined, defining mullions) host the BIF (black, boudinaged) and sillimanite–garnet–biotite schist (dots) and felsic, pegmatitic dykes and leucosomes (white, waves defining mullions) that host gold mineralization in the boudins and mullions. Note that the sillimanite–garnet–biotite schist and gneiss along this boundary has a mafic protolith. Rotated, foliation boudinage overprinted by dextral brittle–ductile shear zones, dextral antithetic shear bands, and later faults are defined along the northeast–southwest striking plane (medium grey) with shallow to steep dips and plunges along contacts. Late Proterozoic faults do not host gold mineralization.

The gold deposits and mines in the Wawa and Abitibi subprovinces are lower–metamorphic grade with lower–temperature structural equivalents to the Borden Mine of the Chapleau Belt of the KSZ. In fact, the ongoing deformation in the WGD and KSZ is attributed to the synchronous reactivation documented by Kerrich and Kyser (1994) in the Abitibi subprovince.

6.10 Gold mineralization and remobilization in the Borden Mine and implications for other high–grade terrains

The Borden Mine is an example of long–lived gold mineralization and remobilization from an early seafloor hydrothermal setting to orogenesis and subsequent exhumation. Remobilization and upgrade of gold mineralization formed in prograde and retrograde ductile to brittle–ductile shear zones with rotated regional– to microscopic–boudin necks. High–grade ore remobilized from amphibolite and

BIF into boudins necks, lineations of mullions, and along the shallow– to moderate–plunging boundaries of quartz–alkali feldspar ± biotite, ± muscovite, ± garnet, ± chrysoberyl, ± beryl leucosomes and intrusions. Petrographically the sulphide melt inclusions in amphibolites, granulites, and BIF host euhedral daughter minerals of pyrite, arsenopyrite, and löllengite with coronas of native gold and a secondary corona of pyrrhotite further confirming high–temperature crystal plastic and melt remobilization (Figs. 4.10 A–B, 4.12 A–F).

Due to the high–grade metamorphism and deformation in the WGD, Chapleau Belt and KSZ have many features, or high–grade equivalents, that are not present in the adjacent Wawa and Abitibi subprovinces. The best exploration tools for field mapping and drill core logging in the Borden Mine and Chapleau Belt are locating muscovite in sillimanite–garnet–biotite schist after earlier alkali feldspars with folded alkali–feldspar pegmatite with biotite, chrysoberyl, and tourmaline in fractured garnet adjacent to sulphide–facies BIF in amphibolite gneisses (Fig. 4.44 A). The most sensitive mineralogical and geochemical indicator of gold mineralization at these scales is the presence beryllium–rich minerals in leucosomes of sillimanite–garnet–biotite schist and amphibolite. The presence of coarse–grained muscovite is also a fair mineralogical and geochemical indicator to gold mineralization in schists and gneisses however it fails in felsic to intermediate metavolcanic lithologies and less evolved pegmatites in the study area (Fig. 4.7 D). Modal percentages of sulphides in the WGD, Chapleau Belt, and KSZ are poor indicators for exploration in the WGD, Chapleau Belt, and KSZ as they are lower than in the Wawa and Abitibi subprovinces except in sulphide–facies BIF where they are identical. Quartz veins are also a poor exploration vector as they are nearly obliterated in the Chapleau Belt at the outcrop scale and are best identified in drill core and thin section as quartz boudins. Useful isotopic exploration vectors include light sulphur isotopic signatures between –10.0‰ and 0.8‰ and low (~0.93 to 1.00) $^{206}Pb/^{204}Pb$ isotopic ratios in subhedral to euhedral pyrite, pyrrhotite, and intergrown pyrite and pyrrhotite.

The higher–temperature deformation and metamorphism in the Chapleau Belt formed ore zones in lithons within regional, east–west striking shear zones and sheath folds, and local, east–west– to northeast–southwest striking boudin necks, and east–west– to northeast–southwest striking and shallow to vertical extension defined by boudins, foliation boudins, chocolate tablet structures, and mullions on the regional–, outcrop–, and microscopic scales. On the microscopic scale the gold mineralization is localized to zones of sulphide–facies BIF in sillimanite–garnet–biotite schists and gneisses. Overprinting brittle–ductile microfaults and boudins host the gold mineralization in zones that have undergone retrograde amphibolite and lower reactions with microstructures consistent with deformation at these temperatures. Native gold defines subgrain boundaries and foliation boudinage suggesting it was present during these styles of crystal plastic deformation and behaved as a solid during these processes at the

microscopic scale. In the high–temperature shear zones of the Chapleau Belt the sulphides have been partially melted with daughter minerals of euhedral pyrite, arsenopyrite, and löllengite inside coronas of anhedral pyrrhotite, and native gold, similar to other deposits (McClay and Ellis, 1983; Tomkins et al., 2007). Gold mineralization is present in the sulphide melts and have been remobilized to areas of lower strain and preserved in microscopic fractures, strain shadows, boudin necks, foliation boudins, mullions, and schistose cataclasites. Outside the areas of highest strain in shear zones, the least deformed sulphide minerals are preserved in massive sulphide BIF, lithons, and in competent, boudin interiors. In these more competent areas the most primary sulphur and lead isotopes are preserved.

CHAPTER 7: SUMMARY

The study on gold mineralization at Borden Mine and Chapleau Belt developed into field visits and mapping in the neighbouring WGD, KSZ, MRVT, and Pontiac, Wawa, and Abitibi subprovinces as the role of tectonics became important to the mineralization history in the original study area. Due to the lack of tectonic mechanisms for the formation of the Chapleau Belt between the WGD and KSZ a more tectonic approach was required to constrain the original hypotheses on the gold mineralization. The new tectonic model solves the previous inconsistences and supports the gold mineralization model for the Borden Mine. It also explains the 100 Ma timing paradox of gold mineralization in the Wawa and Abitibi subprovinces of the southern Superior Province and far–field affects throughout the Superior Province.

The new tectonic model proposed in this study connects the Wawa–Abitibi terrane across the WGD, Chapleau belt, and KSZ based on tectonostratigraphy from field mapping, geochemistry, and geochronology of the Chapleau Belt, Michipicoten (Mishibishu) greenstone Belt, and the southern Abitibi greenstone belt. This study provides a tectonic framework for the divide between the western and eastern Superior Province and builds on previous geological and geophysical studies. The new tectonic model proposes the WGD and KSZ were exhumed in the Neoarchean as a continental MCC with the high–grade footwall of the KSZ exhumed in comparison to the southern Superior Province and the WGD as the hanging–wall, high–strain listric regional structure. The southern KSZ exposes a gneissic to migmatitic, steeply– to moderately–plunging orocline in the KSZ.

CCW rotation is documented in the geometry of the Wawa subprovince–WGD boundary (and greenstone belts therein), WGD gneissosity, and Chapleau belt, regional folds, rotated and asymmetric boudins, foliation boudins, and antithetic shear bands, in the gneissic fabric of the western WGD, and the Matachewan mafic dyke swarms parallel and perpendicular to the orogenic front. The ductile sinistral strike–slip shear zones, KSZ oroclinal fold, anithetic shear bands, and foliation boudins in the WGD, Chapleau Belt, and KSZ predate the later thrust and dextral faults and pseudotachylites, including the ILDZ, and have similar geometries.

Oblique collision between the MRVT and southern Superior Province formed the Pontiac subprovince accretionary prism (including equivalent extensions) causing the new, Lakehead orogeny and regional, prograde high–pressure metamorphism by ca. ≥2.667 Ga, following mid–ocean ridge magmatism, arc formation, and subduction by ca. 2.703 Ga. The formation and exhumation of MCCs and an orocline were synchronous with retrograde upper amphibolite facies metamorphism throughout the southern Superior Province by at least ca. >2.63 Ga (Moser et al., 1996). Plutonism and continued extension, transtension, rotation, and related folding occurred between ca. 2.63 Ga in felsic plutons with

magmatism ceasing by ca. 2.58 Ga (Krogh, 1993; Moser, 1994). The Matachewan mafic dyke swarm was emplaced perpendicular to boundinage and affected by cratonic– to outcrop–scale CCW rotation in the Neoarchean and continued into the Paleoproterozoic.

Some of the inconsistencies this new model solves are the contrasting work by previous workers, particularly from the models of Watson (1980), Percival and Card (1983), Ernst and Halls (1994), Percival (1989b), and Moser (1994, 1996, 2008). Indeed, the formation model of the Kapuskasing, Pontiac, and Ashuanipi MCCs due to predominantly sinistral–oblique shear zones and boudinage as a result of a Neoarchean collision between the southern Superior Province and MRVT provides a tectonic explanation for the formation of the early, sinistral, ductile shear zones, rotated boudins, and overprinting faults in the ILDZ, the exposure of amphibolite, granulite, and migmatite, and felsic pluton magmatism. It also provides a tectonic explanation for the long–lived, high–grade metamorphic event in the KSZ proposed by Moser (1994), the regional low–pressure metamorphism throughout the southern Superior Province (Easton, 2000; Percival and Easton, 2007), the Neoarchean high–pressure granulite in Minnesota, Michigan, and Wisconsin (Sims and Day, 1993; Peterson, and Geiger, 1990), the proposed extension of the Pontiac subprovince as an accretionary prism (Southwick, 1991; McCormick, 2010), abundant late Neoarchean plutonism, including complex pegmatites, throughout the southern Superior Province and MRVT (Bickford et al., 2006; Schmitz et al., 2006), provides a thickened lithosphere for diamond emplacement, explains the general shape of the curvilinear subprovinces and overall fabric of the NE–striking southern Superior Province and NW–striking northeastern Superior Province, the gneissic domes in the southern Superior Province (Borradaile and Gauthier, 2003; Liodas, 2010), and the various indenters in the southern Superior Province (Sims et al., 1980; Sims and Day, 1993). Perhaps most importantly, this study can provide tectonic mechanisms for the juxtaposition of high–metamorphic grade terrains with low–metamorphic grade and plutonic terrains such as those in other Archean cratons. There are numerous similarities between many Archean cratons, including the Kola–Karelia, Kaapvaal, Zimbabwe, and Dharwar, and especially the Wyoming Province, and their tectonic relationship and proximity during the Neoarchean to Paleoproterozoic requires further study (Roscoe and Card, 1993; Heaman, 1997; Halls et al., 1998; Ojakangas et al., 2001a, 2001b; Bleeker, 2003b; Daly et al., 2006; Kramers et al., 2006; Ernst and Bleeker, 2010b; Kramers et al., 2011; Doyle, 2015; Mints, 2015).

The research on the Borden Mine and Chapleau Belt provides many new exploration tools for the area as other high–grade metamorphic terrains that have historically been ignored by prospecting and mineral exploration projects. Future prospecting and exploration in high–grade metamorphic terrains should be encouraged, regardless of the widely held belief that gold mineralization is absent in these

types of regions, particularly those that lack sulphides and quartz veins. The gold mineralization in the Borden Mine and Chapleau Belt are high–grade metamorphic equivalents of those in the Wawa–Abitibi terrane and hosted in higher–temperature lithologies and structures. Ductile to brittle–ductile, sinistral–strike slip shear zones that formed during prograde and retrograde metamorphism document remobilization and upgrade of gold mineralization, and only occur in the high–grade ore zone. The region's greatest strain, retrograde metamorphism, boudinage, and rotation is located in the high–grade ore zone at the Borden Mine. The ore has been remobilized into rotated regional boudin necks defined by vertical lineation and retrograde mineralogy. These features support the hypothesis of remobilization of ore that originally formed as low–grade mineralization in sulphide–facies banded iron formation. Sulphur isotopic data is also consistent with magmatic Sulphur as part of seafloor alteration and stratibound mineralization. The Proterozoic structures, including sinistral and dextral strike–slip faults and thrust faults have no gold mineralization and have heavier sulphur isotopic signatures. These findings could be used throughout the region and in other high–grade metamorphic terrains to better explore for gold mineralization.

Future studies could include expanding the new tectonic model and gold mineralization studies at the Borden Mine. Other future work should include exploration for beryl and diamonds in the study area and update the work being done on heat generation and radioactivity in the Archean as they were calculated based on the assumption of the last Archean orogeny having occurred by 2.7 Ga (Burov et al., 1998; Frederiksen et al., 2013; Jaupart et al., 2014).

In summary, the WGD and KSZ are a natural window into the mid– to lower–crust that is now correlated across to the Wawa and Abitibi subprovinces. The new model provides the first tectonic framework for the region, integrating previously incongruent data. Collision followed by exhumation of a continental metamorphic core complex account for all of the contradictory data in previous studies. The terminal tectonic event in the southern Superior Province occurred long after the 2680 Ma date previously reported. And lastly, gold mineralization in the Borden Mine formed initially as part of syn–volcanic seafloor hydrothermal alteration and was remobilized, and reconcentrated, during prograde and retrograde metamorphism from 2667 Ma to 2580 Ma.

REFERENCES

Abers, G.A., Ferris, A., Craig, M., Davies, H.L., Lerner–Lam, A.L., Mutter, J.C., and Taylor, B., 2002, Mantle compensation of active metamorphic core complexes at Woodlark rift in Papua New Guinea: Nature, v. 418, p. 862–865, doi: 10.1038/nature00990.

Andersen, T., Andersson, U.B., Graham, S., Aberg, G., and Simonsen, S.L., 2009, Granitic magmatism by melting of juvenile continental crust: new constraints on the source of Palaeoproterozoic granitoids in Fennoscandia from Hf isotopes in zircon: Journal of the Geological Society, v. 166, p. 233–247, doi:10.1144/0016–76492007–166.

Ashton, K., Heaman, L., Lewry, J., Hartlaub, R., and Shi, R., 1999, Age and origin of the Jan Lake Complex: A glimpse at the buried Archean craton of the Trans–Hudson orogen: Canadian Journal of Earth Sciences, v. 36, p. 185–208.

Atkinson, B.T., Bousquet, P., Pace, A., Debicki, R.L., Daniels, C.M., Wilson, A.C., Halet, S.E., Beauchamp, S., and McMillan, R., 2014, Report of Activities 2013, Resident Geologist Program, Timmins Regional Resident Geologist Report: Timmins and Sault Ste. Marie Districts: Report of Activities 2013, Resident Geologist Program, Timmins Regional Resident Geologist Report: Timmins and Sault Ste. Marie Districts; Ontario Geological Survey Open File Report 6294, 121p.

Ayer, J.A., Thurston, P.C., Bateman, R., Dubé, B., Gibson, H.L., Hamilton, M.A., Hathway, B., Hocker, S.M., Houlé, M.G., Hudak, G., Lafrance, B., Lesher, C.M., Ispolatov, V.O., MacDonald, P.J., Péloquin, A.S., Piercey, S.J., Reed, L.E. and Thompson, P.H. 2005. Overview of results from the Greenstone Architecture Project: Discover Abitibi initiative; Ontario Geological Survey, Open File Report 6154, 146p.

Ayer, J., Amelin, Y., Corfu, F., Kamo, S., Ketchum, J., Kwok, K., and Trowell, N., 2002, Evolution of the southern Abitibi greenstone belt based on U–Pb geochronology: Autochthonous volcanic construction followed by plutonism, regional deformation and sedimentation: Precambrian Research, v. 115, p. 63–95.

Ayer, J.A., and Davis, D.W., 1997, Neoarchean evolution of differing convergent margin assemblages in the Wabigoon Subprovince: geochemical and geochronological evidence from the Lake of the Woods greenstone belt, Superior Province, Northwestern Ontario: Precambrian Research, v. 81, p. 155–178, doi:10.1016/S0301–9268(96)00033–2.

Ayres, L.D., 1978, Metamorphism in the Superior Province of northwestern Ontario and its relationship to crustal development; in, Metamorphism in the Canadian Shield; Fraser, J.A. (ed.); Heywood, W.W. (ed.). Geological Survey of Canada, Paper 78–10, 1978, p. 25–36,

Barth, N.C., Hacker, B.R., Seward, G.G.E., Walsh, E.O., Young, D., and Johnston, S., 2010, Strain within the ultrahigh–pressure Western Gneiss region of Norway recorded by quartz CPOs: Geological Society, London, Special Publications, v. 335, p. 663–685, doi:10.1144/SP335.27.

Barton, M.D., 1986, Phase equilibria and thermodynamic properties of minerals in the BeO–Al_2O_3 –SiO_2–H_2O (BASH) system, with petrologic applications: Am. Mineral., v. 71, p. 277–300.

Bates, M.P., and Halls, H.C., 1991a, Broad–scale Proterozoic deformation of the central Superior Province revealed by paleomagnetism of the 2.45 Ga Matachewan dyke swarm: Canadian Journal of Earth Sciences, v. 28, p. 1780–1796, doi:10.1139/e91–159.

Bates, M.P., and Halls, H.C., 1991b, Paleomagnetism of dykes from the Groundhog River Block, northern Ontario: implications for the uplift history of the Kapuskasing Structural Zone: Canadian Journal of Earth Sciences, v. 28, p. 1424–1428, doi:10.1139/e91–125.

Beakhouse, G.P., Lin, S. and Kamo, S.L. 2011. Magmatic and tectonic emplacement of the Pukaskwa batholith, Superior Province, Ontario, Canada: Canadian Journal of Earth Sciences, v.48, p.187–204.

Beakhouse, G.P., and McNutt, R.H., 1991, Contrasting types of Late Archean plutonic rocks in northwestern Ontario: implications for crustal evolution in the Superior Province: Precambrian Research, v. 49, p. 141–165, doi:10.1016/0301–9268(91)90060–N.

Beakhouse, G.P., McNutt, R.H., and Krogh, T.E., 1988, Comparative Rb–Sr and U–Pb zircon geochronology of late– to post–tectonic plutons in the Winnipeg River belt, Northwestern Ontario, Canada: Chemical Geology: Isotope Geoscience section, v. 72, p. 337–351, doi:10.1016/0168–9622(88)90046–2.

Bédard, J.H and Harris, L.B., 2014, Neoarchean disaggregation and reassembly of the Superior craton: Geology, v. 42, n. 11, p. 951–954.

Bedeaux, P., Mathieu, L., Pilote, P., Rafini, S., and Daigneault, R., 2018, Origin of the Piché Structural Complex and implications for the early evolution of the Archean crustal–scale Cadillac – Larder Lake Fault Zone, Canada: Canadian Journal of Earth Sciences, p. 1–18, doi:10.1139/cjes–2017 0270.

Belyanin, G.A., Kramers, J.D., Vorster, C., and Knoper, M.W., 2014, The timing of successive fluid events in the Southern Marginal Zone of the Limpopo Complex, South Africa: Constraints from 40Ar–39Ar geochronology: Precambrian Research, v. 254, p 169–193, https://doi.org/10.1016/j.precamres.2014.08.014.

Benn, K. and Kamber, B.S., 2009, In Situ U/Pb Granulite-Hosted Zircon Dates, Kapuskasing Structural Zone, Ontario: A Late Archean Large Igneous Province (LIP) as a Substrate for Juvenile Crust: The Journal of Geology, v. 117, p. 519–541, doi:10.1086/600864.

Benn, K., Miles, W., Ghassemi, M.R., and Gillett, J., 1994b, Crustal structure and kinematic framework of the northwestern Pontiac Subprovince, Quebec: an integrated structural and geophysical study: Canadian Journal of Earth Sciences, v. 31, p. 271–281, doi:10.1139/e94–026.

Benn, K., and Moyen, J.–F., 2008, The Late Archean Abitibi–Opatica terrane, Superior Province: A modified oceanic plateau, in Special Paper 440: When Did Plate Tectonics Begin on Planet Earth?, Geological Society of America, v. 440, p. 173–197, doi:10.1130/2008.2440(09).

Bennett, G., and Thurston, P.C., 1977, Geology of the Pukaskwa River–University River Area; Districts of Algoma and Thunder Bay: Ontario Division of Mines, v. GR153, p. 60.

Berclaz, A., Leclair, A., David, J., and Maurice, C., 2004, Structural evolution of the Northeastern Superior Province (NESP) over 1 billion years, with emphasis on greenstone belts and their relation with enclosing granitoids [abstract]: Eos Transactions, CGU/AGU/SEG/EEGS Joint Assembly, Abstract no. V31A–03.

Bethune, K.M., Helmstaedt, H.H. and McNicoll, V.J. 2006. Structural analysis of the Miniss River and related faults, western Superior Province: Post–collisional displacement initiated at terrane boundaries: Canadian Journal of Earth Sciences, v.43, p.1031–1054.

Bickford, M.E., Wooden, J.L., and Bauer, R.L., 2006, SHRIMP study of zircons from Early Archean rocks in the Minnesota River Valley: Implications for the tectonic history of the Superior Province: Geological Society of America Bulletin, v. 118, p. 94–108, doi:10.1130/B25741.1.

Bleeker, W., 2003a, The late Archean record: a puzzle in ca. 35 pieces: Lithos, v. 71, p. 99–134, doi:10.1016/j.lithos.2003.07.003.

Blenkinsop, T.G., and Frei, R., 1996, Archean and Proterozoic mineralization and tectonics at the Renco Mine (northern marginal zone, Limpopo Belt, Zimbabwe): Economic Geology, v. 91, p. 1225 1238, doi:10.2113/gsecongeo.91.7.1225.

Blenkinsop, T.G. and Doyle, M.G., 2014, Structural controls on gold mineralization on the margin of the Yilgarn craton, Albany–Fraser orogeny: The Tropicana deposit, Western Australia: Journal of Structural Geology, v. 67, n. 189–204.

Boerner, D.E., Kurtz, R.D., and Craven, J.A., 2000, A summary of electromagnetic studies on the Abitibi –Grenville transect: Canadian Journal of Earth Sciences, v. 37, p. 427–437.

Böhlke, J.K., 1989, Comparison of metasomatic reactions between a common CO_2–rich vein fluid and diverse wall rocks: Intensive variables, mass transfers and gold mineralization at Alleghany, California: Economic Geology, v. 84, p. 291–327.

Böhlke, J.K., 1982, Orogenic (metamorphic–hosted) gold quartz veins: In Erickson, R.L. (compiler), Characteristics of mineral deposit occurrences: U.S. Geological Survey Open–File Report 82 795, p. 70–76.

Boily, M., Leclair, A., Maurice, C., Berclaz, A. et David, J., 2006, Étude géochimique et isotopique du Nd des assemblages volcaniques et plutoniques du nord–est de la Province du Supieur (NEPS): Ministère des Ressources naturelles, Québec, GM62031.

Boily, M., Leclair, A., Maurice, C., Bédard, J.H., and David, J., 2009, Paleo– to Mesoarchean basement recycling and terrane definition in the Northeastern Superior Province, Québec, Canada: Precambrian Research, 168: 23–44.

Bornhorst, T.J., Thorpe, R.I., and Johnson, R.C., 1998, Lead isotope study of veins in the Archean Ishpeming Greenstone belt, Michigan: Economic Geology, v. 93, p. 102–107.

Bornhorst, T.J., and Johnson, R.C., 1998, Archean tectonic evolution of the southern edge of the Superior Province in Michigan: Abstracts with Programs – Geological Society of America, v. 30, p. 159.

Borowik, A., 1998, Structural analysis in the footwall of the Uchi–English River subprovince boundary, Red Lake region, northwestern Ontario [MSc. thesis]: University of Toronto, 266 p.

Borradaile, G.J., and Gauthier, D., 2003, Emplacement of an Archean gneiss dome, northern Ontario, Canada: Inflation inferred from magnetic fabrics: Gneissic diapirism and magnetic fabrics: Tectonics, v. 22, p. n/a–n/a, doi:10.1029/2002TC001443.

Borradaile, G.J., and Lagroix, F., 2000, Thermal Enhancement of Magnetic Fabrics in High Grade Gneisses: Geophysical Research Letters, v. 27, p. 2413–2416, doi:10.1029/2000GL008522.

Borradaile, G.J., Werner, T., and Lagroix, F., 2003, Differences in paleomagnetic interpretations due to the choice of statistical, demagnetization and correction techniques: Kapuskasing Structural Zone, northern Ontario, Canada: Tectonophysics, v. 363, p. 103–125, doi:10.1016/S0040 1951(02)00667–4.

Bouchez, J.L., 1977, Plastic deformation of quartzites at low temperature in an area of natural strain gradient, Tectonophysics, v. 39, p. 25–50.

Bouchez, J.L. and Duval, P., 1982, The fabric of polycrystalline ice deformed in simple shear: experiments in torsion, natural deformation and geometrical interpretation: Journal of Textures and Microstructures, v. 5., p. 1–17.

Bowen, R.P., Logothetis, J., and Heather, K.B., 1986, Precambrian geology of the Mishibishu Lake area, northeastern section, Districts of Thunder Bay and Algoma: Ontario Geological Survey Map P.2970, Geological Series– Preliminary Map, scale 1:15 840 or 1 inch to ¼ mile.

Bowman, J.R., Moser, D.E., Valley, J.W., Wooden, J.L., Kita, N.T., and Mazdab, F.K., 2011, Zircon U Pb isotope, 18O and trace element response to 80 m.y. of high temperature metamorphism in the lower crust: Sluggish diffusion and new records of Archean craton formation: American Journal of Science, v. 311, p. 719–772, doi:10.2475/09.2011.01.

Breaks, F.W. and Bond, W.D. 1993. The English River Subprovince–An Archean Gneiss Belt: Geology, Geochemistry and associated mineralization: Ontario Geological Survey, Open File Report5846, v.1, p.1–483, 884p.

Beakhouse, G.P., 2007, Structurally controlled, magmatic hydrothermal model for Archean lode gold deposits: a working hypothesis: Ontario Geological Survey, Open File Report 6193, 133p.

Brun, J.–P., Sokoutis, D., Tirel, C., Gueydan, F., Van Den Driessche, J., and Beslier, M.–O., 2017, Crustal versus mantle core complexes: Tectonophysics, doi:10.1016/j.tecto.2017.09.017.

Burke, K., and Dewey, J.F., 1973, Plume–Generated Triple Junctions: Key Indicators in Applying Plate Tectonics to Old Rocks: The Journal of Geology, v. 81, p. 406–433.

Burov, E., Jaupart, C., and Mareschal, J.C., 1998, Large–scale crustal heterogeneities and lithospheric strength in cratons: Earth and Planetary Science Letters, v. 164, p. 205–219, doi:10.1016/S0012 821X(98)00205–2.

Bursnall, J.T., 1990, Deformation sequence in the southeastern Kapuskasing structural zone Ivanhoe Lake, Ontario, Canada: Exposed cross–sections of the continental crust, p. 469–484.

Bursnall, J.T., Leclair, A.D., Moser, D.E., and Percival, J.A., 1994, Structural correlation within the Kapuskasing uplift: Canadian Journal of Earth Sciences, v. 31, p. 1081–1095, doi:10.1139/e94 097.

Cabanis, B. and Lecolle, M., 1989, Le diagramme La/10 – Y/15 – Nb/8: Un outil pour la discrimination des series volcaniques et en evidence des mélange et/ot de vontamination curstale: Comptes Rendus de l'Academie des Sciences, Serie II, v. 309, p. 2023–2029.

Callan, N.J. 1991. Syn–deformational shear zone–hosted Au–quartz vein mineralization in TTG host rocks, Renabi Mine area, North Ontario: structural analysis, microstructural characteristics and vein paragenesis: Ontario Geological Survey, Open File Report 5759, 194p.

Cameron, E.M., and Hattori, K., 1985, The Hemlo gold deposit, Ontario: A geochemical and isotopic study: Geochimica et Cosmochimica Acta, v. 49, p. 2041–2050, doi:10.1016/0016 7037(85)90062–6.

Camiré, G.E., and Burg, J.–P., 1993, Late Archaean thrusting in the northwestern Pontiac Subprovince, Canadian Shield: Precambrian Research, v. 61, p. 51–66, doi:10.1016/0301–9268(93)90057–9.

Capdevila, R., Goodwin, A.M., Ujike, O., and Gorton, M.P., 1982, Trace–element geochemistry of Archean volcanic rocks and crystal growth in southwestern Abitibi Belt, Canada: Geology, v. 10, p. 418, doi:10.1130/0091–7613(1982)10<418:TGOAVR>2.0.CO;2.

Card, K.D., 1990, A review of the Superior Province of the Canadian Shield, a product of Archean accretion: Precambrian Research, v. 48, p. 99–156, doi:10.1016/0301–9268(90)90059–Y.

Card, K.D. and Cielsielski, A. 1986. DNAG 1: subdivisions of the Superior Province of the Canadian Shield: Geoscience Canada, v.813–p.5–13.

Carreras, J., Druguet, E., and Griera, A., 2005, Shear zone–related folds: Journal of Structural Geology: v. 27, p. 1229–1251, doi:10.1016/j.jsg.2004.08.004.

Černý, P., and Manitoba. Mineral Resources Division, 1981, The Cat Lake–Winnipeg River and the Wekusko Lake pegmatite fields, Manitoba: Winnipeg, Manitoba Dept. of Energy and Mines, Mineral Resources Division, 216 p.

Chamberlain, K.R., Frost, C.D., and Frost, B.R., 2003, Early Archean to Mesoproterozoic evolution of the Wyoming Province: Archean origins to modern lithospheric architecture: Canadian Journal of Earth Sciences, v. 40, p. 1357–1374, doi:10.1139/e03–054.

Chamberlain, K.R., Kilian, T., Evans, D.A.D., and Bleeker, W., 2015, Late Archean to Proterozoic reconstructions of Wyoming and Superior cratons: Abstracts with Programs – Geological Society of America, v. 47, p. 447.

Charles, N., Faure, M., and Chen, Y., 2009, The Montagne Noire migmatitic dome emplacement (French Massif Central): new insights from petrofabric and AMS studies: Journal of Structural Geology, v. 31, p. 1423–1440, doi:10.1016/j.jsg.2009.08.007.

Chipera, S.J. and Perkins, D., 1988, Evaluation of biotite–garnet geothermometers: Application to the English River subprovince, Ontario: Contributions to Mineralogy and Petrology, 98, 40–48.

Chipera, S.J., and Perkins, D. 1988. Evaluation of biotite–garnet geothermometers: application to the English River Subprovince: Contributions to Mineralogy and Petrology, 98, 40–48.

Claoué, J.C., Compston, W., and Cowden, A., 1988, The age of the Kambalda greenstones resolved by ion–microprobe: implications for Archean dating methods: Earth and Planetary Science Letters, v. 89, p. 239–259.

Clowes, R.M., Calvert, A.J., Eaton, D.W., Hajnal, Z., Hall, J., and Ross, G.M., 1996, LITHOPROBE reflection studies of Archean and Proterozoic crust in Canada: Tectonophysics, v. 264, p. 65–88.

Colvine, A.C., 1984, An integrated model for the origin of Archean lode gold deposits, Ontario: Geological Survey Open File Report 5524, 98 p.

Colvine, A.C., 1989, An empirical model for the formation of Archean gold deposits Products of final cratonization of the Superior Province, Canada, in Keays, R.R., and Skinner, B.J., eds., The geology of gold deposits– the perspective in 1988: Economic Geology Monograph 6, p. 37–53.

Committee Guides Metrology, J, 2008. Evaluation of Measurement Data – Guide to the expression of Uncertainty in Measurement (GUM 2008).

Condie, K.C., and Aster, R.C., 2010, Episodic zircon age spectra of orogenic granitoids: The supercontinent connection and continental growth: Precambrian Research, v. 180, p. 227–236, doi:10.1016/j.precamres.2010.03.008.

Corfu, F. and Sage, R.P. 1992. U–Pb age constraints for the deposition of clastic metasedimentary rocks and late–tectonic plutonism, Michipicoten Belt, Superior Province: Canadian Journal of Earth Sciences, v. 29, p. 1640–1651.

Corfu, F., and Stott, G.M., 1996, Hf isotopic composition and age constraints on the evolution of the Archean central Uchi Subprovince, Ontario, Canada: Precambrian Research, v. 78, p. 53–63, doi:10.1016/0301–9268(95)00068–2.

Corfu, F., and Stott, G.M., 1986, U–Pb ages for late magmatism and regional deformation in the Shebandowan Belt, Superior Province, Canada: Canadian Journal of Earth Sciences, v. 23, p. 1075–1082, doi:10.1139/e86–108.

Corfu, F., and Grunsky, E.C., 1987, Igneous and Tectonic Evolution of the Batchawana Greenstone Belt, Superior Province: A U–Pb Zircon and Titanite Study: The Journal of Geology, v. 95, p. 87–105.

Corfu, F., 1988, Differential response of U–Pb systems in coexisting accessory minerals, Winnipeg River Subprovince, Canadian Shield: implications for Archean crustal growth and stabilization: Contributions to Mineralogy and Petrology, v. 98, p. 312–325, doi:10.1007/BF00375182.

Corfu, F., Krogh, T.E., Kwok, Y.Y., and Jensen, L.S., 1989a, U–Pb zircon geochronology in the southwestern Abitibi greenstone belt, Superior Province: Canadian Journal of Earth Sciences, v. 26, p. 1747–1763, doi:10.1139/e89–148.

Corfu, F., Krogh, T.E., Kwok, Y.Y., and Jensen, L.S., 1989b, U–Pb zircon geochronology in the southwestern Abitibi greenstone belt, Superior Province: Canadian Journal of Earth Sciences, v. 26, p. 1747–1763, doi:10.1139/e89–148.

Corfu, F., and Muir, T.L. 1989b. The Hemlo – Heron Bay greenstone belt and Hemlo Au–Mo deposit, Superior Province, Ontario, Canada: 2. Timing of metamorphism, alteration and Au mineralization from titanite, rutile and monazite U–Pb geochronology: Chemical Geology, 79: 201–223.

Corfu, F., and Davis, D.W., 1991, A U–Pb geochronological framework for the western Superior Province, Ontario, In Geology of Ontario. (Williams, H.R., P. C. Thurston, Sutcliffe, R.H., & Stott, G.M., Eds.): Toronto: Ontario Ministry of Northern Development and Mines, Ontario Geological Survey, v. Special Vol. 4, Part 2, 1335–1346.

Corfu, F., Jackson, S.L., and Sutcliffe, R.H., 1991, U–Pb ages and tectonic significance of late Archean alkalic magmatism and nonmarine sedimentation: Timiskaming Group, southern Abitibi belt, Ontario: Canadian Journal of Earth Sciences, v. 28, p. 489–503, doi:10.1139/e91–043.

Corfu, F., Stott, G.M., and Breaks, F.W., 1995, U–Pb geoehronology and evolution of the English River Subprovince, an Archean low P–high T metasedimentary belt in the Superior Province: Tectonics, v. 14, p. 1220–1233, doi:10.1029/95TC01452.

Cox, S.F., Knackstedt, M.A., Braun, J., 2001, Principles of structural control on permeability and fluid flow in hydrothermal systems: Reviews in Economic Geology, 14, 1–24.

Corfu, F., Hanchar, J.M., Paul, W.O., and Kinny, P., 2003, Atlas of zircon textures: Reviews in Mineralogy and Geochemistry, v. 53, 1, p. 469–500.

Craddock, J.P., Anziano, J., Wirth, K., Vervoort, J.D., Singer, B., and Zhang, X., 2007, Structure, geochemistry and geochronology of a Penokean Lamprophyre Dike Swarm, Archean Wawa Terrane, Little Presque Isle, Michigan, USA: Precambrian Research, v. 157, p. 50–70, doi:10.1016/j.precamres.2007.02.010.

Crawford, A.J., and Doyle, M.G., 2016, Granulite–Hosted Gold: Tectonic Setting and Lithogeochemistry of the Tropicana Deposit, Western Australia: Economic Geology, v. 111, p. 395–420, doi:10.2113/econgeo.111.2.395.

Culshaw, N., Purves, M., Reynolds, P., and Stott, G., 2006, Post–collisional upper crustal faulting and deep crustal flow in the eastern Wabigoon subprovince of the Superior Province, Ontario: Evidence from structural and 40Ar/39Ar data from the Humboldt Bay High Strain Zone: Precambrian Research, v. 145, p. 272–288, doi:10.1016/j.precamres.2005.12.006.

Czeck, D., 2003, Testing models for obliquely plunging lineations in transpression: a natural example and theoretical discussion: Journal of Structural Geology, v. 25, p. 959–982, doi:10.1016/S0191 8141(02)00079–2.

Czeck, D.M., Fissler, D.A., Horsman, E., and Tikoff, B., 2009, Strain analysis and rheology contrasts in polymictic conglomerates: An example from the Seine metaconglomerates, Superior Province, Canada: Journal of Structural Geology, v. 31, p. 1365–1376, doi:10.1016/j.jsg.2009.08.004.

Czeck, D.M., Maes, S.M., Sturm, C.L., and Fein, E.M., 2006, Assessment of the relationship between emplacement of the Algoman plutons and regional deformation in the Rainy Lake region, Ontario: Canadian Journal of Earth Sciences, v. 43, p. 1653–1671, doi:10.1139/e06–061.

David, J., Godin, L., Stevenson, R., O'Neil, J. and Francis, D., 2009, U–Pb ages (3.8–2.7 Ga) and Nd isotope data from the newly identified Eoarchean Nuvvuagittuq supracrustal belt, Superior Craton, Canada: Geological Society of America Bulletin, 121: 150–163.

Davis, D.W., and Jackson, M.C., 1988, Geochronology of the Lumby Lake greenstone belt: A 3 Ga complex within the Wabigoon subprovince, northwest Ontario: Geological Society of America Bulletin, v. 100, p. 818–824, doi:10.1130/0016–7606(1988)100<0818:GOTLLG>2.3.CO;2.

Davis, D.W., Poulsen, K.H., and Kamo, S.L., 1989, New Insights into Archean Crustal Development from Geochronology in the Rainy Lake Area, Superior Province, Canada: The Journal of Geology, v. 97, p. 379–398.

Davis, D.W. and Lin, S., 2003, Unraveling the geologic history of the Hemlo Archean gold deposit, Superior province, Canada: a U–Pb geochronological study: Econ. Geol. 98, 51–67.

Dahl, P.S., Hamilton, M.A., Wooden, J.L., Foland, K.A., Frei, R., McCombs, J.A., and Holm, D.K., 2006, 2480 Ma mafic magmatism in the northern Black Hills, South Dakota: a new link connecting the Wyoming and Superior cratons: Canadian Journal of Earth Sciences, v. 43, p. 1579–1600, doi:10.1139/e06–066.

Daigneault, R., Mueller, W.U., and Chown, E.H., 2002, Oblique Archean subduction: accretion and exhumation of an oceanic arc during dextral transpression, Southern Volcanic Zone, Abitibi Subprovince Canada: Precambrian Research, v. 115, p. 261–290, doi:10.1016/S0301 9268(02)00012–8.

Daly, J.S., Balagansky, V.V., Timmerman, M.J., and Whitehouse, M.J., 2006, The Lapland–Kola orogen: Palaeoproterozoic collision and accretion of the northern Fennoscandian lithosphere: Geological Society, London, Memoirs, v. 32, p. 579–598, doi:10.1144/GSL.MEM.2006.032.01.35.

Desrochers, J.–P., and Hubert, C., 1996, Structural evolution and early accretion of the Archean Malartic Composite Block, southern Abitibi greenstone belt, Quebec, Canada: Canadian Journal of Earth Sciences, v. 33, p. 1556–1569, doi:10.1139/e96–118.

Devaney, J.R., and Williams, H.R., 1989, Evolution of an Archean subprovince boundary: a sedimentological and structural study of part of the Wabigoon–Quetico boundary in northern Ontario: Canadian Journal of Earth Sciences, v. 26, p. 1013–1026, doi:10.1139/e89–082.

DeWolfe, J.C., Lafrance, B., and Stott, G.M., 2007, Geology of the shear–hosted Brookbank gold prospect in the Beardmore–Geraldton belt, Wabigoon subprovince, Ontario: Canadian Journal of Earth Sciences, v. 44, p. 925–946, doi:10.1139/e06–118.

Doyle, M.G., Fletcher, I.R., Foster, J., Large, R.R., Mathur, R., McNaughton, N.J., Meffre, S., Muhling, J.R., Phillips, D., and Rasmussen, B., 2015, Geochronological Constraints on the Tropicana Gold Deposit and Albany–Fraser Orogen, Western Australia: Economic Geology, v. 110, p. 355–386, doi:10.2113/econgeo.110.2.355.

Doyon, 2004. Comparaison de la composition des roches métasédimentaires archéennes dans les bassins de la Province du Supérieur; une étude géochimique et statistique. Université du Québec à Chicoutimi; mémoire de maîtrise, 214 pages.

Dragovic, B., Guevara, V.E., Caddick, M.J., Baxter, E.F., and Kylander–Clark, A.R.C., 2016, A pulse of cryptic granulite–facies metamorphism in the Archean Wyoming Craton revealed by Sm–Nd garnet and U–Pb monazite geochronology: Precambrian Research, v. 283, p. 24–49, doi:10.1016/j.precamres.2016.07.010.

Dubé, B., Williamson, K., McNicoll, V., Malo, M., Skulski, T., Twomey, T., and Sanborn–Barrie, M., 2004, Timing of Gold Mineralization at Red Lake, Northwestern Ontario, Canada: New Constraints from U–Pb Geochronology at the Goldcorp High–Grade Zone, Red Lake Mine, and the Madsen Mine: Economic Geology, v. 99, 8, 1611–1641.

Dubé B., Gosselin P, Mercier–Langevin P., Hannington M, Galley A., 2007, Gold–rich volcanogenic massive sulphide deposits. In Goodfellow WD (ed) Mineral deposits of Canada: a synthesis of major deposit–types, disctict metallogeny, the evolution of geological provinces, and exploration methods, Geological Association of Canada, Mineral Deposits Division, Special Publication 5, p. 75–94

Duguet, M., Lin, S., Davis, D.W., Corkery, M.T., and McDonald, J., 2009, Long–lived transpression in the Archean Bird River greenstone belt, western Superior Province, Southeastern Manitoba: Precambrian Research, v. 174, p. 381–407, doi:10.1016/j.precamres.2009.09.001.

Duguet, M. and Szumylo, N., 2016, Archean and Proterozoic geology of the Borden Lake area, Kapuskasing Structural Zone, Abitibi–Wawa terrane; in Summary of Field Work and Other Activities, 2016: Ontario Geological Survey, Open File Report 6223, p. 4–1 to 4 20.

Dyess, J.E., Hansen, V.L., and Goscinak, C., 2015, Constrains on vorticity and non–coaxial shear direction in Neoarchean L–S tectonites, an example from northern Minnesota, USA: Precambrian Research, v. 256, p. 189–200, doi:10.1016/j.precamres.2014.11.010.

Easton, R.M., 1986, Geochronology Compliation Map For Ontario: Sheet 3: East–Central Ontario, All Isotopic Systems: Ontario Geological Survey Map P.2842, Compilation Series – Preliminary Map.

Easton, R.M., 2000, Metamorphism of the Canadian Shield, Ontario, Canada. I. The Superior Province: The Canadian Mineralogist, v. 38, p. 287–317, doi:10.2113/gscanmin.38.2.287.

Easton, R.M., and Heaman, L.M., 2011, Detrital zircon geochronology of the uraniferous Paleoproterozoic Matinenda Formation (Huronian Supergroup), Elliot Lake, Ontario: Abstracts with Programs – Geological Society of America, v. 43, p. 41–42.

Edwards, G.R. and Stauffer, M.R., 1999, Polyphase deformation and crustal evolution in the Pipestone Lake area of the Archean Wabigoon subprovince, Superior Province, Canada: Canadian Journal of Earth Sciences, v. 36, p. 459–477.

Eglington, B.M. and Harmer, R.E., 1999, GEODATE for Windows version 1: Isotope regression and modelling software: Council for Geoscience Open–file report 1999–0206 O, 24pp.

Emmons, W. H., 1937, Gold Deposits of the World. McGraw–Hill, New York, 562 p.

Erikson, E.J., 2010, Structural and kinematic analysis of the Shagawa Lake shear zone, Superior Province, northern Minnesota: implications for the role of vertical versus horizontal tectonics in the Archean (K. Bethune, Ed.): Canadian Journal of Earth Sciences, v. 47, p. 1463–1479, doi:10.1139/E10–054.

Ernst, R., and Bleeker, W., 2010a, Large igneous provinces (LIPs), giant dyke swarms, and mantle plumes: significance for breakup events within Canada and adjacent regions from 2.5 Ga to the Present, Lithoprobe—parameters, processes, and the evolution of a continent, Lithoprobe Contribution 1482, Geological Survey of Canada Contribution 20100072. (R. Clowes, Ed.): Canadian Journal of Earth Sciences, v. 47, p. 695–739, doi:10.1139/E10–025.

Ernst, R., and Bleeker, W., 2010b, Large igneous provinces (LIPs), giant dyke swarms, and mantle plumes: significance for breakup events within Canada and adjacent regions from 2.5 Ga to the Present, Lithoprobe—parameters, processes, and the evolution of a continent, Lithoprobe Contribution 1482. Geological Survey of Canada Contribution 20100072. (R. Clowes, Ed.): Canadian Journal of Earth Sciences, v. 47, p. 695–739, doi:10.1139/E10–025.

Ernst, R., and Bleeker, W., 2010c, Large igneous provinces (LIPs), giant dyke swarms, and mantle plumes: significance for breakup events within Canada and adjacent regions from 2.5 Ga to the Present, Lithoprobe—parameters, processes, and the evolution of a continent, Lithoprobe Contribution 1482. Geological Survey of Canada Contribution 20100072. (R. Clowes, Ed.): Canadian Journal of Earth Sciences, v. 47, p. 695–739, doi:10.1139/E10–025.

Ernst, R.E., and Halls, H.C., 1984, Paleomagnetism of the Hearst dike swarm and implications for the tectonic history of the Kapuskasing Structural Zone, northern Ontario: Canadian Journal of Earth Sciences, v. 21, p. 1499–1506, doi:10.1139/e84–155.

Evans, D.A.D., and Halls, H.C., 2010, Restoring Proterozoic deformation within the Superior craton: Precambrian Research, v. 183, p. 474–489, doi:10.1016/j.precamres.2010.02.007.

Fan, J., and Kerrich, R., 1997, Geochemical charactenstics of Al–depleted and undepleted komatiites and HREE–enriched tholeiites, western Abitibi greenstone belt: variable HFS/REE systematics in a heterogeneous mantle plume: Geochern. Cosmochim. Acta, 61, 4723–4744 p.

Feng, R., and Kerrich, R., 1990, Geobarometry, differential block movements, and crustal, structure of the southwestern Abitibi greenstone belt, Canada: Geology, v. 18, p. 870, doi:10.1130/0091 7613(1990)018<0870:GDBMAC>2.3.CO;2.

Feng, R., and Kerrich, R., 1991, Single zircon age constraints on the tectonic juxtaposition of the Archean Abitibi greenstone belt and Pontiac subprovince, Quebec, Canada: Geochimica et Cosmochimica Acta, v. 55, p. 3437–3441.

Feng, R., Kerrich, McBride, S., and Farrar, E., 1992, 40Ar39Ar age constraints on the thermal history of the Archean Abitibi greenstone belt and the Pontiac Subprovince: Implications for terrane collision, differential uplift, and overprinting of gold deposits: Canadian Journal of Earth Sciences, 29, 1389–1411 p.

Ferré, E.C., Gébelin, A., Conder, J.A., Christensen, N., Wood, J.D., and Teyssier, C., 2014, Seismic anisotropy of the Archean crust in the Minnesota River Valley, Superior Province: Geophysical Research Letters, v. 41, p. 1514–1522, doi:10.1002/2013GL059116.

Festa, V., 2009, C–axis fabrics of quartz–ribbons during high–temperature deformation of syn–tectonic granitoids (Sila Massif, Calabria, Italy): Comptes Rendus Geoscience, v. 341, p. 557–567, doi:10.1016/j.crte.2009.06.008.

Foster, D., Mueller, P.A., Mogk, D., Wooden, J.L, and Vogl, J., 2006. Proterozoic evolution of the western margin of the Wyoming craton: implications for the tectonic and magmatic evolution of the northern Rocky Mountains: Canadian Journal of Earth Sciences, 43, 1601–1619.

Fountain, D.M., Salisbury, M.H., and Percival, J., 1990, Seismic structure of the continental crust based on rock velocity measurements from the Kapuskasing Uplift: Journal of Geophysical Research, v. 95, p. 1167, doi:10.1029/JB095iB02p01167.

Fralick, P., Purdon, R.H., and Davis, D.W., 2006, Neoarchean trans–subprovince sediment transport in southwestern Superior Province: sedimentological, geochemical, and geochronological evidence: Canadian Journal of Earth Sciences, v. 43, p. 1055–1070, doi:10.1139/e06–059.

Frarey, M.J., and Krogh, T.E., 1986, U–Pb zircon ages of late internal plutons of the Abitibi and eastern Wawa subprovinces, Ontario and Quebec: Paper – Geological Survey of Canada, v. 86–1A, 43 48 p.

Frederiksen, A.W., Deniset, I., Ola, O., and Toni, D., 2013, Lithospheric fabric variations in central North America: Influence of rifting and Archean tectonic styles: Lithospheric fabric in Central North America: Geophysical Research Letters, v. 40, p. 4583–4587, doi:10.1002/grl.50879.

Frederiksen, A.W., Miong, S.–K., Darbyshire, F.A., Eaton, D.W., Rondenay, S., and Sol, S., 2007, Lithospheric variations across the Superior Province, Ontario, Canada: Evidence from tomography and shear wave splitting: Journal of Geophysical Research, v. 112, doi:10.1029/2006JB004861.

Frieman, B.M., Kuiper, Y.D., Kelly, N.M., Monecke, T., and Kylander–Clark, A., 2017, Constraints on the geodynamic evolution of the southern Superior Province: U–Pb LA–ICP–MS analysis of detrital zircon in successor basins of the Archean Abitibi and Pontiac subprovinces of Ontario and Quebec, Canada: Precambrian Research, v. 292, p. 398–416, doi:10.1016/j.precamres.2017.01.027.

Frost, C.D., and Frost, B.R., 1993, The Archean history of the Wyoming Province (A. W. Snoke, J. R. Steidtmann, & S. M. Roberts, Eds.): Memoir – Geological Survey of Wyoming, p. 58–76.

Frost, B.R., Frost, C.D., Cornia, M., Chamberlain, K.R., and Kirkwood, R., 2006, The Teton – Wind River domain: a 2.68–2.67 Ga active margin in the western Wyoming Province: Canadian Journal of Earth Sciences, v. 43, p. 1489–1510, doi:10.1139/e06–102.

Fyfe, W.S., and Henley, R.W., 1973, Some thoughts on chemical transport processes, with particular reference to gold: Miner. Sci. Eng., v. 5, p. 295–303.

Gamelin, G. 2015. A comparative study of the mafic lithologies from the Borden Belt gold deposit area, and adjacent greenstone belts in the Wawa–Abitibi Terrane of the Kapuskasing Structural Zone [BSc. thesis]: University of Saskatchewan, 67 p.

Geis, W.T., Cook, F.A., Green, A.G., Milkereit, B., Percival, J.A., and West, G.F., 1990, Thin thrust sheet formation of the Kapuskasing structural zone revealed by Lithoprobe seismic reflection data: Geology, v. 18, p. 513–516, doi:10.1130/0091–7613(1990)018<0513:TTSFOT>2.3.CO;2.

Gibb, R.A., 1978a, A gravity survey of James Bay and its bearing on the Kapuskasing Gneiss Belt, Ontario: Tectonophysics, v. 45, p. T7–T13, doi:10.1016/0040–1951(78)90002–1.

Gibb, R.A., 1978b, A gravity survey of James Bay and its bearing on the Kapuskasing Gneiss Belt, Ontario: Tectonophysics, v. 45, p. T7–T13, doi:10.1016/0040–1951(78)90002–1.

Giblin, P.E., and Armburst, G.A., 1973, Batchawana, Algoma District, Ontario; Ontario Division of Mines, Map 2251, scale 1 inch to 1 mile.

Gilbert, H.P., 2006, Geological investigations in the Bird River area, southeastern Manitoba (NTS 52L5N and 6); in Report of Activities 2006, Manitoba Science, Technology, Energy and Mines, Manitoba Geological Survey, p. 184–205.

Goldfarb, R.J., Baker, T., Dubé, B., Groves, D.I., Hart, C.J.R., and Gosselin, P. 2005. Distribution, Character, and Genesis of Gold Deposits in Metamorphic Terranes: Economic Geology 100th Anniversary Volume, 407–450p.

Goldfarb, R.J., and Groves, D.I., 2015, Orogenic gold: Common or evolving fluid and metal sources through time: Lithos, v. 233, p. 2–26, doi:10.1016/j.lithos.2015.07.011.

Goldfarb, R.J., Groves, D.I., and Gardoll, S., 2001, Rotund versus skinny orogens: Well–nourished or malnourished gold?: Geology, v. 29, p. 539, doi:10.1130/0091 7613(2001)029<0539:RVSOWN>2.0.CO;2.

Goldner, J.N., 2013, Structure and metamorphism along the Burntside Lake Shear Zone near Ely, MN [MSc. thesis]: University of Minnesota, 92 p.

Goldcorp Inc. (2016) Borden deposit 3D block model. Retrieved October 09, 2018 from https://www.goldcorp.com/English/portfolio/development–projects/borden

Goodings, C.R., and Brookfield, M.E., 1992, Proterozoic transcurrent movements along the Kapuskasing lineament (Superior Province, Canada) and their relationship to surrounding structures: Earth Science Reviews, v. 32, p. 147–185, doi:10.1016/0012–8252(92)90024–N.

Goodwin, A.M., 1965, Volcanism and gold deposition in the Birch–Uchi Lakes area: Canadian Mining and Metallurgical Bulletin (Canadian Institute of Mining and Metallurgy), Montréal, v. 58, p. 304–314.

Goscombe, B.D., Passchier, C.W., and Hand, M., 2004, Boudinage classification: end–member boudin types and modified boudin structures: Journal of Structural Geology, v. 26, p. 739–763, doi:10.1016/j.jsg.2003.08.015.

Govers, R. and Wortel, M.J.R., 2005, Lithosphere tearing at STEP faults: Response to edges of subduction zones, Earth Plant. Sci. Letter., 236, p. 505–523.

Gower, C.F., and Clifford, P.M., 1981, The structural geometry and geological history of Archean rocks at Kenora, north–western Ontario—a proposed type area for the Kenoran Orogeny: Canadian Journal of Earth Sciences, v. 18, p. 1075–1091, doi:10.1139/e81–103.

Grace, R.L., Chamberlain, K.R., Frost, B.R., and Frost, C.D., 2006, Tectonic histories of the Paleo– to Mesoarchean Sacawee block and Neoarchean Oregon Trail structural belt of the south–central Wyoming Province: Canadian Journal of Earth Sciences, v. 43, p. 1445–1466, doi:10.1139/e06 083.

Griffin, W.L., Pearson, N.J., Belousova, E., Jackson, S.E., van Achterbergh, E., O'Reilly, S.Y., and Shee, S.R., 2000, The Hf isotope composition of cratonic mantle: LAM–MC–ICPMS analysis of zircon megacrysts in kimberlites: Geochimica et Cosmochimica Acta, v. 64, p. 133–147, doi:10.1016/S0016–7037(99)00343–9.

Guernina, S. and Sawyer, E.W. 2003. Large–scale melt depletion in granulite terranes: an example from the Archean Ashuanipi Subprovince of Quebec: Journal of Metamorphic Geology, v. 21, p. 181 201.

Hagemann, S.G., and Cassidy, K.F., 2000, Archean orogenic lode gold deposits (S. G. Hagemann & P. E. Brown, Eds.): Reviews in Economic Geology, v. 13, p. 9–68.

Halls, H.C., Cheney, E.S., and Heaman, L.M., 1998, Global mafic magmatism at 2.5 Ga: Remnants of an ancient large igneous province?: Comments and Reply: Geology, v. 26, p. 93, doi:10.1130/00917613(1998)026<0093:GMMAGR>2.3.CO;2.

Halls, H.C., and Palmer, H.C., 1990, The tectonic relationship of two Early Proterozoic dyke swarms to the Kapuskasing Structural Zone: a paleomagnetic and petrographic study: Canadian Journal of Earth Sciences, v. 27, p. 87–103, doi:10.1139/e90–007.

Halls, H.C., Stott, G.M. and Davis, D.W. 2005. Paleomagnetism, geochronology and geochemistry of several Proterozoic mafic dike swarms in northwestern Ontario: Ontario Geological Survey, Open File Report 6171, 59p.

Halls, H.C., and Zhang, B., 1998, Uplift structure of the southern Kapuskasing zone from 2.45 Ga dike swarm displacement: Geology, v. 26, p. 67, doi:10.1130/0091 7613(1998)026<0067:USOTSK>2.3.CO;2.

Hamdy, M.M., Abd El–Wahed, M.A., Gamal El Dien, H., and Morishita, T., 2017, Garnet hornblendite in the Meatiq Core Complex, Central Eastern Desert of Egypt: Implications for crustal thickening preceding the ~600 Ma extensional regime in the Arabian–Nubian Shield: Precambrian Research, v. 298, p. 593–614, doi:10.1016/j.precamres.2017.07.002.

Hanes, J.A., and Archibald, D.A., 1998, Post–orogenic tectonothermal history of the Archean western Superior Province of the Canadian Shield as determined by conventional and laser Ar–Ar dating (H. Helmstaedt & R. Harrap, Eds.): Lithoprobe Report, p. 12–16.

Hanes, J.A., Archibald, D.A., Hodgson, C.J., and Robert, F., 1992a, Dating of Archean auriferous quartz vein deposits in the Abitibi greenstone belt, Canada: Economic Geology and the Bulletin of the Society of Economic Geologists, v. 87, p. 1849–1861, doi:10.2113/gsecongeo.87.7.1849.

Hanes, J.A., Archibald, D.A., Hodgson, C.J., and Robert, F., 1992b, Dating of Archean auriferous quartz vein deposits in the Abitibi greenstone belt, Canada: Economic Geology and the Bulletin of the Society of Economic Geologists, v. 87, p. 1849–1861, doi:10.2113/gsecongeo.87.7.1849.

Hanes, J.A., Archibald, D.A., Queen, M., and Farrar, E., 1994, Constraints from 40 Ar/ 39 Ar geochronology on the tectonothermal history of the Kapuskasing uplift in the Canadian Superior Province: Canadian Journal of Earth Sciences, v. 31, p. 1146–1171, doi:10.1139/e94–102.

Hanes, J.A., Archibald, D.A., Ullrich, T.D., Grant, J.W., and Ortega–Rivera, A., 2003, Regional–scale variations in post–orogenic thermal histories of tectonic domains in the western Superior Province of the Canadian Shield as revealed by Ar–Ar geochronology: Program with Abstracts – Geological Association of Canada, v. 28.

Hartel, T.H.D., and Pattison, D.R.M., 2003, Genesis of the Kapuskasing (Ontario) migmatitic mafic granulites by dehydration melting of amphibolite: the importance of quartz to reaction progress: Journal of Metamorphic Geology, v. 14, p. 591–611, doi:10.1046/j.1525–1314.1996.00404.x.

Heaman, L.M., 1997, Global mafic magmatism at 2.45 Ga: Remnants of an ancient large igneous province?: Geology, v. 25, p. 299, doi:10.1130/00917613(1997)025<0299:GMMAGR>2.3.CO;2.

Heaman, L.M., Machado, N., and Krogh, T.E., 1988, Combined U–Pb and Sr–Nd studies on carbonatites, lamprophyre and diabase dykes, and mafic gneisses from the KSZ and vicinity: Lithoprobe Report, p. 21.

Heather, K.B., and Arias, Z., 1992, Geological and structural setting of gold mineralization in the Goudreau–Lochalsh area, Wawa gold camp: Ontario Geological Survey 5832 Open File Report 5832, 159 p.

Hidas, K., Garrido, C. J., Booth–Rea, G., Marchesi, C., Bodinier, J.–L., Dautria, J.–M., Louni Hacini, A., and Azzouni–Sekkal, A., 2019, Lithosphere tearing along STEP faults and synkinematic formation of lherzolite and wehrlite in the shallow subcontinental mantle: Solid Earth Discuss., https://doi.org/10.5194/se–2019–32

Hildebrand, R.S., 2009, Did Westward Subduction Cause Cretaceous–Tertiary Orogeny in the North American Cordillera?: Geological Society of America Special Papers, v. 457, p. 71.

Hill, M.L., Kolb, M.J., Stinson, V.R., and Scott, R.J., 2011, Structural control of mineralization in shear zone–hosted gold deposits [abs.]: Geological Society of America, Abstracts with Programs, v. 43, n. 5., p. 513.

Hodkiewicz, P.F., Groves, D.I., Davidson, G.J., Weinberg, R.F., and Hagemann, S.G., 2009, Influence of structural setting on sulphur isotopes in Archean orogenic gold deposits, Eastern Goldfields Province, Yilgarn, Western Australia: Mineralium Deposita, v. 44, p. 129–150, doi:10.1007/s00126–008–0211–5.

Hoffman, P.F., 1989, Precambrian geology and tectonic history of North America, in Bally, A.W., and Palmer, A.R., eds., The Geology of North America – An Overview: Geological Society of America, Boulder, Colorado, A, p. 447–512.

Hoffman, E.L., 1992, Instrumental neutron activation in geoanalysis: Journal of Geochemical Exploration, v. 44, p. 297–319, doi:10.1016/0375–6742(92)90053–B.

Holubec, J., 1972, Lithostratigraphy, structure and deep crustal relations of Archean rocks of the Canadian Shield, Rouyn–Noranda area, Quebec: Krystalinikum, v. 9, p. 63–88.

Hrabi, R.B., and Cruden, A.R., 2006, Structure of the Archean English River subprovince: implications or the tectonic evolution of the western Superior Province, Canada: Canadian Journal of Earth Sciences, v. 43, p. 947–966, doi:10.1139/e06–023.

Hynes, A., and Song, Z., 2006, Variable unroofing in the western Superior Province – metamorphic evidence and possible origin: Canadian Journal of Earth Sciences, v. 43, p. 805–819, doi:10.1139/e06–049.

Hrabi, R.B., and Cruden, A.R., 2006, Structure of the Archean English River subprovince: implications for the tectonic evolution of the western Superior Province, Canada: Canadian Journal of Earth Sciences, v. 43, p. 947–966, doi:10.1139/e06–023.

Hutchinson, R.W., Burlington, J.L., 1984, Some broad characteristics of greenstone belt gold lodes. In: Foster, R.P. (ed.), Gold'82: The geology, geochemistry and genesis of gold deposits, Balkema, Rotterdam, p. 339–372.

Hutchinson, R.W., 1987, Metallogeny of Precambrian gold deposits: Space and time relationships: Economic geology, v. 82, 8, p. 1993–2007.

Hutchinson, 1993, A multi–stage, multi–process genetic hypothesis for greenstone–hosted gold lodes, Ore Geology Reviews, v. 8, p. 349–382.

Hynes, A., and Song, Z., 2006, Variable unroofing in the western Superior Province – metamorphic evidence and possible origin: Canadian Journal of Earth Sciences, v. 43, p. 805–819, doi:10.1139/e06–049.

Ickert, R.B., 2013. Algorithms for estimating uncertainties in initial radiogenic isotope ratios and model ages: Chem. Geol. 340, 131–138.

Imreh, L., 1973, Relations Stratigraphiques entre le Groupe de Pontiac et le Sillon Métavolcanique de Baby au Témiscamingue, Québec: Canadian Journal of Earth Sciences, v. 10, p. 1350–1353, doi:10.1139/e73–121.

Irvine, T. N. & Baragar, W. R. A., 1971, A guide to the chemical classification of the common volcanic rocks, Canadian Journal of Earth Sciences, v. 8, p. 523–548.

Ispolatov, V., Lafrance, B., and Dube, B., 2004, Summary of field work and other activities 2004: Ontario Geological Survey, Toronto, ON, Canada, p. 42.1–42.6

Jackson, S.L., Fyon, J.A., 1991, The western Abitibi subprovince in Ontario. In: Geology of Ontario Special Volume 4, Part 1, Ontario Geological Survey, pp. 405–484

James, D.T., and Mortensen, J.K., 1992, An Archean metamorphic core complex in the southern Slave Province: basement–cover structural relations between the Sleepy Dragon Complex and the Yellowknife Supergroup: Canadian Journal of Earth Sciences, v. 29, p. 2133–2145.

Jaupart, C., Mareschal, J.–C., Bouquerel, H., and Phaneuf, C., 2014, The building and stabilization of an Archean Craton in the Superior Province, Canada, from a heat flow perspective: Journal of Geophysical Research: Solid Earth, v. 119, p. 9130–9155, doi:10.1002/2014JB011018.

Jayananda, M., Moyen, J.–F., Martin, H., Peucat, J.–J., Auvray, B., and Mahabaleswar, B., 2000, Late Archaean (2550–2520 Ma) juvenile magmatism in the Eastern Dharwar craton, southern India: constraints from geochronology, Nd–Sr isotopes and whole rock geochemistry: Precambrian Research, v. 99, p. 225–254, doi:10.1016/S0301–9268(99)00063–7.

Jellicoe, K. 2014. Petrographic study of amphibolites in Chapleau, Ontario [BSc. thesis]: University of Saskatchewan, 32 p.

Jellicoe, K. M., Lin, S., Ciufo, T.J., Yakymchuk, C., and Mercier–Langevin, P. 2018. Structural controls and relative timing of events at the orogenic Island Gold deposit, Michipicoten Greenstone Belt, Wawa, Ontario In: Rogers, N. (Ed.),Targeted Geoscience Initiative: 2017 report of activities, volume 1: Geological Survey of Canada, Open File 8358, 254 p. https://doi.org/10.4095/306391

Jemielita, R.A., Davis, D.W., and Krogh, T.E., 1990, U–Pb evidence for Abitibi gold mineralization postdating greenstone magmatism and metamorphism: Nature, v. 346, p. 831–834.

Jensen, L.S., 1976, A new cation plot for classifying subalkalic volcanic rocks: Ministry of Natural Resources, MP. 66, 22 p.

Johnson, R.C., 1991, Archean geology of the northern block of the Ishpeming Greenstone Belt, Marquette County, Michigan / by R.C. Johnson and T.J. Bornhorst. p. cm. (Contributions to Precambrian geology of Lake Superior region; ch. F) (U.S. Geological Survey bulletin; 1904–F)

Kamineni, D.C., Stone, D., and Peterman, Z.E., 1990, Early Proterozoic deformation in the western Superior province, Canadian Shield: Geological Society of America Bulletin, v. 102, p. 1623 1634, doi:10.1130/0016–7606(1990)102<1623:EPDITW>2.3.CO;2.

Kendrick, J., Yakymchuk, C., Duguet, M., and Moser, D., 2019, American Geophysical Union, Fall Meeting 2019, abstract #V31G–0142.

Kendrick, J., Yakymchuk, C., Duguet, M., and Vervoort, J., 2019, The Kapuskasing Structure revisited: new insights into reworking of Neoarchean crust from garnet geochronology: GAC MAC, p. 118–119.

Kerrich, R. and Hodder, R.W., 1982, Archean lodge gold and base metal deposits: evidence for metal separation into independent hydrothermal systems; in R.W. Hodder and W. Petruk (editors), Gold Deposits, CIM, Spec. Vol. 24, p. 144–160.

Kerrich, R. and Cassidy, K.F., 1994, Temporal relationships of lode gold mineralization to accretion magmatism, metamorphism and deformation Archean to present: A review: Ore Geology Reviews, v. 9, p. 263–310.

Kerrich, R. and Kyser, T.K., 1994, 100 Ma timing paradox of Archean gold, Abitibi greenstone belt (Canada): new evidence from U–Pb and Pb–Pb evaporation ages of hydrothermal zircons: Geology, v. 22, n. 12, p. 1131–1134.

Kerrich, R., Polat, A., and Xie, Q., 2008, Geochemical systematics of 2.7 Ga Kinojevis Group (Abitibi), and Manitouwadge and Winston Lake (Wawa) Fe–rich basalt–rhyolite associations: Backarc rift oceanic crust?: Lithos, v. 101, p. 1–23, doi:10.1016/j.lithos.2007.07.009.

Kington, J.D., and Goodliffe, A.M., 2008, Plate motions and continental extension at the rifting to spreading transition in Woodlark Basin, Papua New Guinea: Can oceanic plate kinematics be extended into continental rifts?: Tectonophysics, v. 458, p. 82 – 95, doi:10.1016/j.tecto.2007.11.027.

Kramers, J.D., McCourt, S., Roering, C., Smit, C.A., van Reenen, D.D., 2011. Origin and evolution of Precambrian high–grade Gneiss terranes, with special emphasis on the Limpopo Complex of Southern Africa. In: van Reenen, D.D., Kramers, J.D., McCourt, S., Perchuk, L.L (Eds.): Geological Society of America Memoirs, vol. 207. Geological Society of America, pp. 311–324.

Kremer, P.D. and Lin, S., 2006: Structural geology of the Bernic Lake area, Bird River greenstone belt, southeastern Manitoba (NTS 52L6): implications for rare element pegmatite emplacement; in Report of Activities 2006, Manitoba Science, Technology, Energy and Mines, Manitoba Geological Survey, p. 206–213.

Kretz, R., 1983, Symbols for rock–forming minerals: American Mineralogist, v. 68, p. 277–279.

Krogh, T.E., 1993, High precision U–Pb ages for granulite metamorphism and deformation in the Archean Kapuskasing structural zone, Ontario: implications for structure and development of the lower crust: Earth and Planetary Science Letters, v. 119, p. 1–18, doi:10.1016/0012 821X(93)90002–Q.

Krogh, T.E., Kamo, S.L., Hanley, T.B., Hess, D.F., Dahl, P.S., and Johnson, R.E., 2011, Geochronology and geochemistry of Precambrian gneisses, metabasites, and pegmatite from the Tobacco Root Mountains, northwestern Wyoming craton, Montana, (W. J. Davis, Ed.): Canadian Journal of Earth Sciences, v. 48, p. 161–185, doi:10.1139/E10–095.

Krogh, T.E., and Moser, D.E., 1994, U–Pb zircon and monazite ages from the Kapuskasing uplift: age constraints on deformation within the Ivanhoe Lake fault zone: Canadian Journal of Earth Sciences, v. 31, p. 1096–1103, doi:10.1139/e94–098.

Krogh, T.E., and Turek, A., 1982, Precise U–Pb zircon ages from the Gamitagama greenstone belt, southern Superior Province: Canadian Journal of Earth Sciences, v. 19, p. 859–867, doi:10.1139/e82–071.

Kruckenberg, S.C., Vanderhaeghe, O., Ferré, E.C., Teyssier, C., and Whitney, D.L., 2011, Flow of partially molten crust and the internal dynamics of a migmatite dome, Naxos, Greece: Internal dynamics of the Naxos Dome: Tectonics, v. 30, TC3001, doi:10.1029/2010TC002751.

Kruhl, J.H., 2003, Prism– and basal–plane parallel subgrain boundaries in quartz: a microstructural geothermobarometer: Journal of Metamorphic Geology, v. 14, p. 581–589, doi:10.1046/j.1525 1314.1996.00413.x.

LaFontaine, D., 2016, Structural and metamorphic control on the Borden gold deposit, Chapleau, Ontario [MSc. thesis]: Lakehead University, 184 p.

Lafrance, B., 2015, Geology of the orogenic Cheminis gold deposit along the Larder Lake – Cadillac deformation zone, Ontario (K. M. Bethune, Ed.): Canadian Journal of Earth Sciences, v. 52, p. 1093–1108, doi:10.1139/cjes–2015–0067.

Lamont, T.N., Searle, M.P., Waters, D.J., Roberts, N.M.W., Palin, R.M., Smye, A., Dyck, B., Gopon, P., Weller, O.M., and St–Onge, M.R., 2020, Compressional origin of the Naxos metamorphic core complex, Greece: Structure, petrography, and thermobarometry: GSA Bulletin, 132, 1–2, p. 149 197.

Langford, F.F., and Morin, J.A., 1976, The development of the Superior Province of northwestern Ontario by merging island arcs: American Journal of Science, v. 276, p. 1023–1034.

Lawson, A.C., 1888, Report on the geology of the Rainy Lake region, In Geological and Natural History Survey of Canada, 1898, Reports and maps of investigations and surveys, 1887–1888, Geological Survey of Canada, Annual report vol. 3., pt. F, p. 182.

Leclair, A.D., Ernst, R.E., and Hattori, K., 1993, Crustal–scale auriferous shear zones in the central Superior province, Canada: Geology, v. 21, p. 399, doi:10.1130/0091 7613(1993)021<0399:CSASZI>2.3.CO;2.

Leclerc, F. 2004. Évolution tectonostratigraphique et méta–morphique de la ceinture volcano sédimentaire de Qalluviartuuq–Payne, nord–est de la Province du Supérieur [thèse]. Université du Québec à Montréal.

Lefèbvre, N., Kopylova, M., and Kivi, K., 2005, Archean calc–alkaline lamprophyres of Wawa, Ontario, Canada: Unconventional diamondiferous volcaniclastic rocks: Precambrian Research, v. 138, p. 57–87, doi:10.1016/j.precamres.2005.04.005.

Li, L., Xiong, X.L., Liu, X.C., 2017, Nb/Ta Fractionation by Amphibole in Hydrous Basaltic Systems: Implications for Arc Magma Evolution and Continental Crust Formation: Journal of Petrology, v. 58, 1, p. 3–28, https://doi.org/10.1093/petrology/egw070.

Lin, S., 2001, Stratigraphic and Structural Setting of the Hemlo Gold Deposit, Ontario, Canada: Economic Geology, v. 96, p. 477–507, doi:10.2113/gsecongeo.96.3.477.

Lin, S., Parks, J., Heaman, L.M., Simonetti, A., Corkery, M.T., 2013, Diapirism and sagduction as a mechanism for deposition and burial of "Timiskaming–type" sedimentary sequences, Superior Province: Evidence from detrital zircon geochronology and implications for the Borden Lake conglomerate in the exposed middle to lower crust in the Kapuskasing uplift, Precambrian Research, v. 238, p. 148–157, doi.org/10.1016/j.precamres.2013.09.012.

Liodas, N.T., 2010, Gneiss dome development & transcurrent tectonics in the Archean: Example of the Pukaskwa batholith and Hemlo shear zone, Superior Province, Canada, [MSc. thesis]: Southern Illinois University Carbondale, 266 p.

Lodge, R.W.D., Gibson, H.L., Stott, G.M., Franklin, J.M., and Hudak, G.J., 2015, Geodynamic setting, crustal architecture, and VMS metallogeny of ca. 2720 Ma greenstone belt assemblages of the northern Wawa subprovince, Superior Province (J. Hanley, Ed.): Canadian Journal of Earth Sciences, v. 52, p. 196–214, doi:10.1139/cjes–2014–0163.

Long, D.G.F., 1984, Tectonic setting of early Aphebian strata in the Southern Province: sedimentation in an elongate pull–apart basin related to oblique subduction: Geol. Assoc. Can. Miner. Assoc. Can, 9, 84 (program with abstracts).

Long, D.G.F., 1995, Huronian sandstone thickness and paleocurrent trends as a clue to the tectonic evolution of the Southern Province: Can. Miner., 33, 922–923.

Long, D.G.F., 2004, The tectonostatigraphic evolution of the Huronian basement and the subsequent basin fill: geological constraints on impact models of the Sudbury event: Precambrian Research, v. 129, p. 203–223, doi:10.1016/j.precamres.2003.10.003.

Long, D.G.F. and Lloyd, T.R., 1983, Placer gold potential of basal Huronian strate of the Elliot Lake Group in the Sudbury Area, Ontario: Ontario Geological Survey, Misc. Pap. 116, 256–258.

Loucks, R.R. and Mangrogenes, J.A., 1999, Gold solubility in supercritical hydrothermal brines measured in synthetic fluid inclusions: Science, v. 284, p. 2159–2163.

Ludden, J., Hubert, C., and Gariepy, C., 1986, The tectonic evolution of the Abitibi greenstone belt of Canada: Geological Magazine, v. 123, p. 153–166.

MacDonald, D.L., 1992, Contrasting styles of alteration and metamorphism in shear zones at Wawa, Ontario [MSc. thesis]: University of Windsor, p. 160.

Mackasey, W.O., Blackburn, C.E., Trowell, N.F., 1974 A regional approach to the Wabigoon Quetico Belts and its bearing on exploration in northwestern Ontario: Ontario Division of Mines, Miscellaneous Paper 58, 30 p.

Mäder, U., Percival, J.A., and Berman, R.G., 1994, Recalculated geothermobarometry estimates for the Kapuskasing uplift: Can. J. Earth Sci. 31, 1134–1145.

Martinez, M.L., and York, D., 1990, A comparative $^{40}Ar/^{39}Ar$ study of the Kapuskasing structural zone and the Wawa gneiss terrane: thermal and tectonic implications: Canadian Journal of Earth Sciences, v. 27, p. 787–793, doi:10.1139/e90–080.

Maurice, C., David, J., Bedard, J.H. and Francis, D., 2009, Evidence for a widespread mafic cover sequence and its implications for continental growth in the Northeastern Superior Province: Precambrian Research, 168: 45–65.

Meschede, M., 1986, A method of discriminating between different types of mid–ocean ridge basalts and continental tholeiites with the Nb–Zr–Y diagram: Chemical Geology, v. 56, 3–4, p. 207–218.

Mercier–Langevin, P., Dubé, B., Lafrance, B., Hannington, M., Galley, A., Moorhead, J., and Gosselin, P., 2007, Metallogeny of the Doyon–Bousquet–LaRonde mining camp, Abitibi greenstone belt,

Quebec, In Goodfellow, W.D., ed., Mineral Deposits of Canada: A Synthesis of Major Deposit Types, District Metallogeny, the Evolution of Geological Provinces, and Exploration Methods: Geological Association of Canada, Mineral Deposits Division, Special Publication No. 5, p. 673 701.

Mercier–Langevin P., Lawley, C.J.M., and Castonguay, S., (ed.), 2020, Targeted Geoscience Initiative 5: Contributions to the Understanding of Canadian Gold Systems: Geological Survey of Canada, Open File 8712, 328 p. https://doi.org/10.4095/323661

McClay, K.R. and Ellis, P.G., 1983, Deformation and recrystallization of pyrite: Mineralogical Magazine, 47, 527–538.

McCormick, Kelli A., 2010, Precambrian Basement Terrane of South Dakota, Bulletin 41, Department of Environment and Natural Resources; Geological Survey Program, University of South Dakota, Vermillion, SD.

McDonough, W.F. and Sun, S.–S, 1995, The composition of the Earth: Chemical Geology, v. 120, p. 223–253.

McGill, G.E., 1992, Structure and kinematics of a major tectonic contact, Michipicoten greenstone belt, Ontario: Canadian Journal of Earth Sciences, v. 29, p. 2118–2132, doi:10.1139/e92–168.

McNicoll, V., Goutier, J., Dube, Benoit, Mercier–Langevin, P., Ross, P–S., Dion, C., Monecke, T., Legault, M., Percival, J., Gibson, H.L, 2014, U–Pb geochronology of the Blake River Group, Abitibi greenstone belt, Quebec, and implications for base metal exploration: Economic Geology, v. 109, n. 1., p. 27–59.

McNicoll, V., Dubé, B., Castonguay, S., Oswald, W., Biczok, J., Mercier–Langevin, P., Skulski, T., and Malo, M., 2016, The world–class Musselwhite BIF–hosted gold deposit, Superior Province, Canada: New high–precision U–Pb geochronology and implications for the geological setting of the deposit and gold exploration: Precambrian Research, v. 272, p. 133–149, doi:10.1016/j.precamres.2015.09.029.

McWilliams, G.M., 1998, Operation Ignace–Armstrong, Mine Centre–Entwine Lake area: Geology of Area IV: Ontario Geological Survey, p. 49.

Melnyk, M., Davis, D.W., Cruden, A.R., and Stern, R.A., 2006, U–Pb ages constraining structural development of an Archean terrane boundary in the Lake of the Woods area, western Superior Province, Canada: Canadian Journal of Earth Sciences, v. 43, p. 967–993, doi:10.1139/e06–035.

Meyer, G., Grabowski, G.P.B., Guindon, D.L. and Chaloux, E.C. 2005. Report of Activities 2004, Resident Geologist Program, Kirkland Lake Regional Resident Geologist Report: Kirkland Lake District: Ontario Geological Survey, Open File Report 6150, 56p.

Milkereit, B., Canada. Natural Resources Canada issuing body, Geological Survey of Canada issuing body, and Geological Survey (U.S.) issuing body, 1988, 1986 Great Lakes seismic reflection survey, migrated data: Great Lakes seismic reflection survey, migrated data.

Mints, M.V., 2015, 3. Neoarchean intracontinental areas of sedimentation, magmatism, and high temperature metamorphism (hot regions) in eastern Fennoscandia, in Geological Society of America Special Papers, Geological Society of America, v. 510, p. 89–123, doi:10.1130/2015.2510(03).

Mitchell, R.H., 1994, The lamprophyre facies: Mineralogy and Petrology, v. 51, p. 137–146, doi:10.1007/BF01159724.

Mole, D.R., Thurston, J.H., Marsh, R.A., Stern, J.A., Ayer, J.A., Martin, L.A.J., and Lu, Y.J., 2021, The formation of Neoarchean continental crust in the south–east Superior Craton by two distinct geodynamic processes: Precambrian Research, v. 356, 106104, https://doi.org/10.1016/j.precamres.2021.106104.

Morin, D., Jébrak, M., Bardoux, M., and Goulet, N., 1993, Pontiac metavolcanic rocks within the Cadillac tectonic zone, McWatters, Abitibi Belt, Quebec: Canadian Journal of Earth Sciences, v. 30, p. 1521–1531, doi:10.1139/e93–130.

Montsion, R., Thurston, P., Ayer, J., 2018, 1:2 000 000 Scale Geological Compilation of the Superior Craton – Version 1: Mineral Exploration Research Centre, Harquail School of Earth Sciences, Laurentian University Document Number MERC–ME–2018–017

Mortensen, J.K., and Card, K.D., 1993, U–Pb age constraints for the magmatic and tectonic evolution of the Pontiac Subprovince, Quebec: Canadian Journal of Earth Sciences, v. 30, p. 1970–1980, doi:10.1139/e93–173.

Moukhsil, A., Legault, M., Boily, M., Doyon, J., Sawyer, E.W., and Davis, D.W. 2003.Synthèse géologique et métallogénique de la ceinture de roches vertes de la Moyenne et de la Basse Eastmain (Baie–James). Ministère des Ressources Naturelles, de la Faune et des Parcs, Québec; ET 2002–06, 57 pages, 1 plan.

Moser, D.E., 1994, The geology and structure of the mid–crustal Wawa gneiss domain: a key to understanding tectonic variation with depth and time in the late Archean Abitibi – Wawa orogen: Canadian Journal of Earth Sciences, v. 31, p. 1064–1080.

Moser, D.E. and Heaman, L.M., 1997, Proterozoic zircon growth in Archean lower crustal xenoliths, southern Superior craton – a consequence of Matachewan ocean opening: Contributions to Mineralogy and Petrology, v. 128, n. 2/3, p. 164–175.

Moser, D.E., Bowman, J.R., Wooden, J., Valley, J.W., Mazdab, F., and Kita, N., 2008, Creation of a continent recorded in zircon zoning: Geology, v. 36, p. 239–242.

Moser, D.E., Heaman, L.M., Krogh, T.E., and Hanes, J.A., 1996, Intracrustal extension of an Archean orogen revealed using single–grain U–Pb zircon geochronology: Tectonics, v. 15, p. 1093–1109, doi:10.1029/96TC00130.

Mueller, P.A. and Frost, C.D., 2006, The Wyoming Province: a distinctive Archean craton in Laurentian North America: Canadian Journal of Earth Sciences, 43, 10, 1391.

Mueller, P.A., Peterman, Z.E., and Granath, J.W., 1985, A Bimodal Archean Volcanic Series, Owl Creek Mountains, Wyoming: The Journal of Geology, v. 93, p. 701–712.

Muir, T.L., 2003, Structural evolution of the Hemlo greenstone belt in the vicinity of the world–class Hemlo gold deposit: Canadian Journal of Earth Sciences, v. 40, p. 395–430, doi:10.1139/e03 004.

Musacchio, G., 2004, Lithospheric structure and composition of the Archean western Superior Province from seismic refraction/wide–angle reflection and gravity modeling: Journal of Geophysical Research, v. 109, doi:10.1029/2003JB002427.

Nadeau, M. 2016. Chemistry of garnets in the Borden Belt: Ionic diffusion resulting in chemical homogenization, [BSc. thesis]: University of Saskatchewan, 79 p.

Nitescu, B., and Halls, H.C., 2002, A gravity profile across southern Saganash Lake fault: implications for the origin of the Kapuskasing Structural Zone: Canadian Journal of Earth Sciences, v. 39, p. 469–480, doi:10.1139/e01–100.

Occhipinti, S.A., Tyler, I.M., Spaggiari, C.V., Korsch, R.J., Kirkland, C.L., Smithies, R.H., Martin, K., and Wingate, M.T.D., 2017, Tropicana translated: a foreland thrust system imbricate fan setting for ca. 2520 Ma orogenic gold mineralization at the northern margin of the Albany–Fraser Orogen, Western Australia: Geological Society, London, Special Publications, p. SP453.6, doi:10.1144/SP453.6.

Ojakangas, R.W., Marmo, J.S., and Heiskanen, K.I., 2001a, Basin evolution of the Paleoproterozoic Karelian Supergroup of the Fennoscandian (Baltic) Shield: Sedimentary Geology, v. 141–142, p. 255–285, doi:10.1016/S0037–0738(01)00079–3.

Ojakangas, R.W., Morey, G.B., and Southwick, D.L., 2001b, Paleoproterozoic basin development and sedimentation in the Lake Superior region, North America: Sedimentary Geology, v. 141–142, p. 319–341, doi:10.1016/S0037–0738(01)00081–1.

Oliver, J., Ayer, J., Dubé, B., Aubertin, R., Burson, M., Panneton, G., Friedman, R., and Hamilton, M., 2012, Structure, Stratigraphy, U–Pb Geochronology and Alteration Characteristics of Gold

Mineralization at the Detour Lake Gold Deposit, Ontario, Canada: Exploration and Mining Geology, v. 20, p. 1–30.

Osmani, I.A., and Stott, G.M., 1988, Regional–scale shear zones in Sachigo Subprovince and their economic significance (A. C. Colvine, M. E. Cherry, B. O. Dressler, P. C. Thurston, C. L. Baker, R. B. Barlow, & C. Riddle, Eds.): Ontario Geological Survey Miscellaneous Paper, p. 53–67.

Pan, Y., E. Fleet, M., and Heaman, L., 1998a, Thermo–tectonic evolution of an Archean accretionary complex: U–Pb geochronological constraints on granulites from the Quetico Subprovince, Ontario, Canada: Precambrian Research, v. 92, p. 117–128, doi:10.1016/S0301–9268(98)00070 9.

Pan, Y., and Fleet, M.E., 1995, Geochemistry and origin of cordierite–orthoamphibole gneiss and associated rocks at an Archaean volcanogenic massive sulphide camp: Manitouwadge, Ontario, Canada: Precambrian Research, v. 74, p. 73–89, doi:10.1016/0301–9268(95)00010–3.

Pan, Y., and Fleet, 1999, Kyanite in the western Superior Province of Ontario: Implication for Archean accretionary tectonics: Canadian Mineralogist, v. 37, p. 359–373.

Pan, Y., Fleet, M.E., and Williams, H.R., 1994, Granulite–facies metamorphism in the Quetico Subprovince, north of Manitouwadge, Ontario: Canadian Journal of Earth Sciences, v. 31, p. 1427–1439, doi:10.1139/e94–126.

Pan, Y., Heaman, L.M., and Breaks, F.W., 1999, Thermo–tectonic evolution of the Umfreville–Conifer Lake granulite zone and the English River–Winnipeg River boundary zone (R. M. Harrap & H. H. Helmstaedt, Eds.): Lithoprobe Report, p. 104–108.

Pan, Y., Therens, C., and Ansdell, K., 1998b, Geochemistry of mafic–ultramafic rocks from the Werner Gordon Lake area (H. Helmstaedt & R. Harrap, Eds.): Lithoprobe Report, p. 29–34.

Passchier, C.W., Trouw, R.A.J., 2006, Microtectonics, 2nd ed. xvi, 366 p. CD–ROM. Berlin, Heidelberg, New York: Springer–Verlag.

Pearce, J.A., 1983, Role of the sub–continental lithosphere in magma genesis at active continental margins, In Hawkesworth, C.J. and Norry, M.J. eds. Continental basalts and mantle xenoliths, Nantwich, Cheshire: Shiva Publications, pp. 230–249.

Pearce, J.A., 1996, A User's Guide to Basalt Discrimination Diagrams. In: Wyman, D.A., Ed., Trace Element Geochemistry of Volcanic Rocks: Applications for Massive Sulphide Exploration, Geological Association of Canada, Short Course Notes, Vol. 12, 79–113.

Pearce, J. A., 2008, Geochemical fingerprinting of oceanic basalts with applications to ophiolite classification and the search for Archean oceanic crust: Lithos, v. 100, p. 14–48.

Percival, J.A., 1981, Geological evolution of part of the central Superior Province based on relationships among the Abitibi and Wawa subprovinces and the Kapuskasing Structural Zone [Ph.D. thesis]: Queen’s University.

Percival, J.A. (Ed.), 1994, The Kapuskasing transect of Lithoprobe [Special Volume]: Canadian Journal of Earth Sciences, v. 31, n. 7, p. 1013–1286.

Percival, J.A., and Card, K.D., 1983, Archean crust as revealed in the Kapuskasing uplift, Superior province, Canada: Geology, v. 11, p. 323–326, doi:10.1130/0091 7613(1983)11<323:ACARIT>2.0.CO;2.

Percival, J.A., and McGrath, P.H., 1986, Deep crustal structure and tectonic history of the Northern Kapuskasing Uplift of Ontario: An integrated petrological–geophysical study: Tectonics, v. 5, p. 553–572, doi:10.1029/TC005i004p00553.

Percival, J.A., and Sullivan, R.W., 1988, Age constraints on the evolution of the Quetico Belt, Superior Province, Ontario.: Geological Survey of Canada, Paper 88–2 In Radiogenic age and isotopic studies, report 2, 97–107 p.

Percival, J.A., 1989a, A regional perspective of the Quetico metasedimentary belt, Superior Province, Canada: Canadian Journal of Earth Sciences, v. 26, p. 677–693, doi:10.1139/e89–058.

Percival, J.A., 1989b, Granulite terranes and the lower crust of the Superior Province (R. F. Mereu, S. Mueller, & D. M. Fountain, Eds.): Geophysical Monograph, v. 51, p. 301–310, doi:10.1029/GM051p0301.

Percival, J.A., and Williams, H.R., 1989, Late Archean Quetico accretionary complex, Superior province, Canada: Geology, v. 17, p. 23, doi:10.1130/0091 7613(1989)017<0023:LAQACS>2.3.CO;2.

Percival, J.A., Stern, R.A., Skulski, T., Card, K.D., Mortensen, J.K., and Begin, N.J. 1994. Minto block, Superior Province: Missing link in deciphering assembly of the craton at 2.7 Ga: Geology, v. 9, p. 839–842.

Percival, J.A., and Peterman, Z.E., 1994, Rb–Sr biotite and whole–rock data from the Kapuskasing uplift and their bearing on the cooling and exhumation history: Canadian Journal of Earth Sciences, v. 31, p. 1172–1181, doi:10.1139/e94–103.

Percival, J.A., and West, G.F., 1994, The Kapuskasing uplift: a geological and geophysical synthesis: Canadian Journal of Earth Sciences, v. 31, p. 1256–1286.

Percival, J.A. and Skulski, T. 2000, Tectonothermal evolution of the northern Minto block, Superior Province, Quebec, Canada: The Canadian Mineralogist, v. 38, p. 45–378.

Percival, J.A., Stern, R.A., and Rayner, N. 2002. Archean adakites from the Ashuanipi complex, eastern Superior Province, Canada: geochemistry, geochronology and tectonic significance: Contributions to Mineralogy and Petrology, v. 145, 3, p. 265–280.

Percival, J.A., Sanborn–Barrie, M., Skulski, T., Stott, G.M., Helmstaedt, H., and White, D.J., 2006, Tectonic evolution of the western Superior Province from NATMAP and Lithoprobe studies: Canadian Journal of Earth Sciences, v. 43, p. 1085–1117, doi:10.1139/e06–062.

Percival, J.A., and Easton, R.M., 2007, Geology of the Canadian Shield in Ontario: an update, Geological Survey of Canada, Open File 5511, 67 p., doi:10.4095/223891.

Percival, J.A., Skulski, T., Sanbon–Barrie, M., Stott, G.M., Leclair, A.D., Corkery, M.T., and Boily, M. 2012. Geology and tectonic evolution of the Superior Province, Canada. In: Tectonic Styles in Canada: The Lithoprobe Perspective (Percival, J.A., Cook, F.A, and Clowes R.M., editors). Geological Association of Canada; Special Paper 49, pages 321–378.

Peschler, A.P., Benn, K., and Roest, W.R., 2006, Gold–bearing fault zones related to Late Archean orogenic folding of upper and middle crust in the Abitibi granite–greenstone belt, Ontario: Precambrian Research, v. 151, p. 143–159, doi:10.1016/j.precamres.2006.08.013.

Peterman, Z.E., and Day, W., 1989, Early Proterozoic activity on Archean faults in the western Superior province— Evidence from pseudotachylite: Geology, v. 17, p. 1089, doi:10.1130/0091 7613(1989)017<1089:EPAOAF>2.3.CO;2.

Peters, S. G. and Golding, S. D. (1989) Geologic, fluid inclusion and stable isotope studies of granitoid hosted gold bearing quartz veins, Charters Towers, northeastern Australia, The Geology of Gold Deposits: The Perspective in 1988 (Keays, R. R. et al., eds.): Econ. Geol. Monogr., 6, 260 273.

Peterson, J.W., and Geiger, C.A., 1990, The Hardwood Gneiss: Evidence for High P–T Archean Metamorphism in the Southern Province of the Lake Superior Region: The Journal of Geology, v. 98, p. 273–281, doi:10.1086/629398.

Phinney, W.C., and Halls, H.C., 2001, Petrogenesis of the Early Proterozoic Matachewan dyke swarm, Canada, and implications for magma emplacement and subsequent deformation: Canadian Journal of Earth Sciences, v. 38, p. 1541–1563, doi:10.1139/cjes–38–11–1541.

Pilkington, M. and Percival, J.A., 1999, Crustal magnetization and long–wavelength aeromagnetic anomalies of the Minto block, Quebec: Journal of Geophysical Research Solid Earth, 104, B4, 7513–7526.

Pirie, J., and Mackasey, W.O., 1978, Preliminary examination of regional metamorphism in parts of Quetico metasedimentary belt, Superior Province, Ontario (J. A. Fraser & W. W. Heywood, Eds.): Paper – Geological Survey of Canada, p. 37–48.

Pisarevskiy, S. and Waele, B. and Jones, S. and Soderlund, U. and Ernst, R. 2015. Paleomagnetism and U–Pb age of the 2.4 Ga Erayinia mafic dykes in the south–western Yilgarn, Western Australia: Paleogeographic and geodynamic implications: Precambrian Research. 259: pp. 222–231.

Platzman, E., and Platt, J.P., 2004, Kinematics of a twisted core complex: Oblique axis rotation in an extended terrane (Betic Cordillera, southern Spain): Kinematics of a twisted core complex: Tectonics, v. 23, p. n/a–n/a, doi:10.1029/2003TC001549.

Polat, A., Kerrich, R., and Wyman, D.A., 1998, The late Archean Schreiber–Hemlo and White River Dayohessarah greenstone belts, Superior Province: collages of oceanic plateaus, oceanic arcs, and subduction–accretion complexes: Tectonophysics, v. 294, p. 295–326.

Polat, A. and Kerrich, R., 1999, Formation of an Archean tectonic mélange in the Schreiber–Hemlo greenstone belt, Superior Province, Canada: Implications for Archean subduction–accretion process: Tectonics, v. 18, p. 733–755, doi:10.1029/1999TC900032.

Polat, A, and Kerrich, R., 2000, Archean greenstone belt magmatism and the continental growth mantle evolution connection: constraints from Th–U–Nb–LREE systematics of the 2.7 Ga Wawa subprovince, Superior Province, Canada: Earth Planet. Sci. Lett., v. 175, p. 41–54.

Polat, A. and Kerrich, R., 2001, Magnesian andesites, Nb–enriched basalt–andesites, and adakites from late Archean 2.7 Ga Wawa greenstone belts, Superior Province, Canada: implications for late Archean subduction zone petrogenetic processes: Contributions to Mineralogy and Petrology, v. 141, 1, p. 36–52.

Powell, W.G., Carmichael, D.M., and Hodgson, C.J., 1995, Conditions and timing of metamorphism in the southern Abitibi greenstone belt, Quebec: Canadian Journal of Earth Sciences, v. 32, p. 787 805, doi:10.1139/e95–067.

Powell, W.G., Carmichael, D.M., and Hodgson, C.J., 1993, Thermobarometry in a subgreenschist to greenschist transition in metabasites of the Abitibi greenstone belt, Superior Province, Canada: Journal of Metamorphic Geology, v. 11, p. 165–178, doi:10.1111/j.1525–1314.1993.tb00138.x.

Puffett, W.P., 1974, Geology of the Negaunee Quadrangle, Marquette County, Michigan: United States Government Printing Office, 53 p.

Reid, R.G., and Reilly, B.A., 1987, Mishibishu Lake Area, Districts of Algoma and Thunder Bay: Summary of Field Work and Other Activities 1987 Miscellaneous Paper 137, 429 p.

Rey, P.F., Teyssier, C., Kruckenberg, S.C., and Whitney, D.L., 2011, Viscous collision in channel explains double domes in metamorphic core complexes: Geology, v. 39, p. 387–390, doi:10.1130/G31587.1.

Ridler, R.H., 1970, Relationship of mineralization to volcanic stratigraphy in the Kirkland–Larder Lake Area, Ontario, Proc. Geol. Assoc. Can., v. 21, p. 33–42.

Robert, F. and Brown, A.C., 1986. Archean gold bearing quartz veins at the sigma mine, Abitibi greenstone belt, Quebec: Part I. Geological relations and formation of the vein system: Economic Geology, v. 81, p.578–592.

Robert, F. and Poulsen, K.H, 2001. Vein formation and deformation in greenstone gold deposits: Soc. Econ. Geol. Rev., 14, 111–155.

Robert, F., Poulsen, K. H., and Dubé, B., 1994, Structural analysis of lode gold deposits in deformed terranes: Geological Survey of Canada, Open File 2850, 140 p.

Robinson, B.W., 1995, Sulphur isotope standards, Reference and intercomparison materials for stable isotopes of light elements; Proceedings of a consultants meeting held in Vienna, 1–3. Dec. 1993, IAEA–TECDOC–825, 39–45 p.

Rocheleau, M., and Dimroth, E., 1985, Petrology of the Archean Pontiac and Kewagama sediments and implications for the stratigraphy of the southern Abitibi belt: Discussion: Canadian Journal of Earth Sciences, v. 22, p. 1374–1377, doi:10.1139/e85–142.

Roscoe, S.M., and Card, K.D., 1993, The reappearance of the Huronian in Wyoming: rifting and drifting of ancient continents: Canadian Journal of Earth Sciences, v. 30, p. 2475–2480, doi:10.1139/e93 214.

Rosenbaum, G., and Lister, G.S., 2004, Neogene and Quaternary rollback evolution of the Tyrrhenian Sea, the Apennines, and the Sicilian Maghrebides: Tectonics, v. 23, TC1013, doi: 10.1029/2003TC001518.

Rosenbaum, G., Gasparon, M., Lucente, F.P., Peccarillo, A., and Miller, M.S., 2008, Kinematics of slab tear faults during subduction segmentation and implications for Italian magmatism: Tectonics, v. 27, TC2008, doi: 10.1029/2007TC002143.

Royden, L.H., 1993a, Evolution of retreating subduction boundaries formed during continental collision: Tectonics, v. 12, p. 629–638, doi: 10.1029/ 92TC02641.

Royden, L.H., 1993b, The tectonic expression of slab pull at continental convergent boundaries: Tectonics, v. 12, p. 303–325, doi: 10.1029/92TC02248.

Sage, R.P., 1985, Goudreau–Lochalsh Area, District of Algoma; p. 90–94 in Summary of Fieldwork and Other Activities 1985, Ontario Geological Survey, edited by John Wood, Owen L. White, R.B. Barlow, and A.C. Colvine, Ontario Geological Survey, Miscellaneous Paper 126, 351 p.

Sage, R.P., Thorpe, R., and Berdusco, E., 1987, Geology of the Michipicoten Iron Formation: Institute on Lake Superior Geology, Field Trip Guidebook, v. 33., pt. 3, p. 93.

Sage, R.P., Lightfoot, P.C., and Doherty, W., 1996, Geochemical characteristics of granitoid rocks from within the Archean Michipicoten Greenstone Belt, Wawa Subprovince, Superior Province, Canada: implications for source regions and tectonic evolution: Precambrian Research, v. 76, p. 155–190, doi:10.1016/0301–9268(95)00021–6.

Samson, I.M., Bas, B., and Holm, P.E., 1997, Hydrothermal evolution of auriferous shear zones, Wawa, Ontario: Economic Geology, v. 92, p. 325–342, doi:10.2113/gsecongeo.92.3.325.

Sanborn–Barrie, M., and Skulski, T., 2006, Sedimentary and structural evidence for 2.7 Ga continental arc–oceanic–arc collision in the Savant–Sturgeon greenstone belt, western Superior Province, Canada: Canadian Journal of Earth Sciences, v. 43, p. 995–1030, doi:10.1139/e06–060.

Saunders, A.D. and Tarney, J., 1984, Geochemical characteristics of basaltic volcanism within back–arc basins, Geological Society, London, Special Publications, v. 16, p. 59–76.

Sawyer, E.W., and Barnes, S.–J., 1994, Thrusting, magmatic intraplating, and metamorphic core complex development in the Archaean Belleterre–Angliers Greenstone Belt, Superior Province, Quebec, Canada: Precambrian Research, v. 68, p. 183–200, doi:10.1016/0301–9268(94)90029 9.

Sawyer, E.W., 2008, Atlas of Migmatites. Canadian Mineralogist Special Publication 9, NRC Research Press, Ottawa, Ontario, Canada.

Schmitz, M.D., Bowring, S.A., Southwick, D.L., Boerboom, T.J., and Wirth, K.R., 2006, High precision U–Pb geochronology in the Minnesota River Valley subprovince and its bearing on the Neoarchean to Paleoproterozoic evolution of the southern Superior Province: Geological Society of America Bulletin, v. 118, p. 82–93, doi:10.1130/B25725.1.

Schneiderhöhn, H., 1941, Lehrbuch der Erzlagerstättenkunde. Fischer–Verlag, Jena, p. 858.

Shaw, D.M., 1956. Geochemistry of pelitic rocks. Part III: Major elements and general geochemistry: Bulletin of the Geological Society of America, Vol. 67, pp. 919–934.

Sibson, R. H., Robert, F., & Poulsen, K. H, (1988), High–angle reverse faults, fluid–pressure cycling, and mesothermal gold–quartz deposits: Geology, 16 (6), 551–555.

Simonetti, A., Heaman, L.M., Chacko, T., and Banerjee, N.R., 2006, In situ petrographic thin section U Pb dating of zircon, monazite, and titanite using laser ablation–MC–ICP–MS: International Journal of Mass Spectrometry, v. 253, p. 87–97, doi:10.1016/j.ijms.2006.03.003.

Simonetti, A., Heaman, L.M., Hartlaub, R.P., Creaser, R.A., MacHattie, T.G., and Böhm, C., 2005, U Pb zircon dating by laser ablation–MC–ICP–MS using a new multiple ion counting Faraday collector array: Journal of Analytical Atomic Spectrometry, v. 20, p. 677, doi:10.1039/b504465k.

Sims, P.K., Card, K.D., Morey, G.B., and Peterman, Z.E., 1980, The Great Lakes tectonic zone — A major crustal structure in central North America: Geological Society of America Bulletin, v. 91, p. 690, doi:10.1130/0016–7606(1980)91<690:TGLTZA>2.0.CO;2.

Sims, P.K., and Day, W.C., 1993, The Great Lakes Tectonic Zone– Revisited, US Geological Survey Bulletin, 1904–S, p. 11.

Simmons, C.E., Hanson, G.N., and Lumbers, S.B., 1980, Geochemistry of the Shawmere anorthosite complex, Kapuskasing structural zone, Ontario: Precambrian Research, v. 11, p. 43–71, doi:10.1016/0301–9268(80)90080–7.

Siragusa, G.M., 1986, Geology of the Batchewana–Pangis area, district of Algoma: Toronto, Ministry of Northern Development and Mines, Ontario, Ontario Geological Survey report 243, 56 p.

Smith, P.E. 1981. Rb–Sr whole rock and U–Pb zircon geochronology of the Michipicoten greenstone belt, Wawa area, northwestern Ontario: [MSc. thesis] University of Windsor, Windsor ON.

Smith, P.E., Farquhar, R.M., and Halls, H.C., 1992, U–Th–Pb isotope study of mafic dykes in the superior Province, Ontario, Canada: uniformity of initial Pb isotope ratios of the Hearst dykes: Chemical Geology (Isotope Geoscience Section, v. 94, p. 261–280.

Smith, S.R., Foster, G.L., Romer, R.L., Tindle, A.G., Kelley, S.P., Noble, S.R., Horstwood, M., and Breaks, F.W., 2004, U–Pb columbite–tantalite chronology of rare–element pegmatites using TIMS and Laser Ablation–Multi Collector–ICP–MS: Contributions to Mineralogy and Petrology, v. 147, p. 549–564, doi:10.1007/s00410–003–0538–y.

Söderlund, U., Patchett, P.J., Vervoort, J.D., and Isachsen, C.E., 2004, The 176Lu decay constant determined by Lu–Hf and U–Pb isotope systematics of Precambrian mafic intrusions: Earth and Planetary Science Letters, v. 219, p. 311–324, doi:10.1016/S0012–821X(04)00012–3.

Sol, S., Thomson, C.J., Kendall, J.–M., White, D., VanDecar, J.C., and Asudeh, I., 2002, Seismic tomographic images of the cratonic upper mantle beneath the Western Superior Province of the Canadian Shield—a remnant Archean slab?: Physics of the Earth and Planetary Interiors, v. 134, p. 53–69, doi:10.1016/S0031–9201(02)00081–X.

Souders, A.K., and Frost, C.D., 2006, In suspect terrane? Provenance of the late Archean Phantom Lake metamorphic suite, Sierra Madre, Wyoming: Canadian Journal of Earth Sciences, v. 43, p. 1557 1577, doi:10.1139/e06–114.

Southwick, D.L., 1991, On the genesis of Archean granite through two–stage melting of the Quetico accretionary prism at a transpressional plate boundary: Geological Society of America Bulletin, v. 103, p. 1385, doi:10.1130/0016–7606(1991)103<1385:OTGOAG>2.3.CO;2.

Southwick, D.L., 2014, Reexamination of the Minnesota River valley subprovince with emphasis on Neoarchean and Paleoproterozoic events: Minnesota Geological Survey Report of Investigations 69, 52 p.

Stachel, T., Banas, A., Muehlenbachs, K., Kurszlaukis, S., and Walker, E.C., 2006, Archean diamonds from Wawa (Canada): samples from deep cratonic roots predating cratonization of the Superior Province: Contributions to Mineralogy and Petrology, v. 151, p. 737–750, doi:10.1007/s00410 006–0090–7.

Stacey, J.C., Kramers, J.D., 1975, Approximation of terrestrial lead isotope evolution by a two–stage model: Earth Planet. Sci. Lett. 26, 207–221.

Stern, R.A., Bodorkos, S., Kamo, S.L., Hickman, A.H., and Corfu, F., 2009, Measurement of SIMS instrumental mass fractionation of Pb isotopes during zircon dating: Geostandards and Geoanalytical Research, v. 33, p. 145–168.

Stern, R.A., Hanson, G.N., and Shirey, S.B., 1989, Petrogenesis of mantle–derived, LILE –enriched Archean monzodiorites and trachyandesites (sanukitoids) in southwestern Superior Province: Canadian Journal of Earth Sciences, v. 26, p. 1688–1712, doi:10.1139/e89–145.

Stevens, L.M., Bendick, R., and Baldwin, J.A., 2017, Synconvergent exhumation of metamorphic core complexes in the northern North American Cordillera: Geology, v. 45, p. 495–498, doi:10.1130/G38802.1.

Stewart, J.W., 1984, The auriferous carbonate exhalite concept re–examined, [abs.]: Geological Society of America, Reno, November 4–7, 1984.

Stichler, W., Gonfiantini, R., and Rozanski, K., 1995, "Summary", Reference and intercomparison materials for stable isotopes of light elements, 7–11 p.

Stinson, V.R., Kolb, M. J., and Hill, M. L., 2009, Metamorphism and Deformation at Musselwhite Mine [abstract]: Institute on Lake Superior Geology Proceedings, 55th Annual Meeting, Ely, MN, v. 55, part 1, p. 74.

Stinson, V.R., and Hill, M.L., 2010, Structural control at Hammond Reef gold deposit north of Atikokan, Ontario [abstract]: Institute on Lake Superior Geology Proceedings, 56th Annual Meeting, International Falls, MN, v. 56, part 1, p. 64.

Stinson, V.R., 2013, An investigation on the control of gold mineralization in the Beardmore–Geraldton greenstone belt and surrounding Quetico–Wabigoon subprovince boundary area [MSc. thesis]: Lakehead University, Thunder Bay, 143 p.

Stone, D., 2010, Precambrian Geology of the Central Wabigoon Subprovince Area, Northwestern Ontario: Open File Report 5422, 130 p.

Stone, D. 1981, The Sydney Lake Fault Zone in Ontario and Manitoba Canada [Ph.D. thesis]: University of Toronto, 146 p.

Stone, D., Corkery, M.T., Halle, J., Ketchum, J., Lange, M., Skulski, T., and Whalen, J., 2004, Geology and tectonostratigraphic assemblages, eastern Sachigo Subprovince, Ontario and Manitoba: Calgary, AB, Canada: Geological Survey of Canada.

Stott, G.M., Davis, D.W., Parker, J.R., Straub, K.J., and Tomlinson, K.Y., 2002, Geology and tectonostratigraphic assemblages, eastern Wabigoon Subprovince, Ontario: Geological Survey of Canada, Open File 4285, Ontario Geological Survey, Preliminary Map P.3449.

Stott, G.M., 1996, The geology and tectonic history of the Central Uchi Subprovince; Ontario Geological Survey, Open Fire Report 5952, 179 p.

Studemeister, P.A., 1985, The greenschist metamorphism of Archaean synvolcanic stocks near Wawa, Ontario, Canada: Journal of Metamorphic Geology, v. 3, p. 79–90, doi:10.1111/j.1525 1314.1985.tb00306.x.

Sun, W. and McDonough, W., 1989, Chemical and isotopic systematics of oceanic basalts: Implications for mantle composition and processes, Geological Society, London, Special Publications, v. 42, n. 1.

Swoffer, B., Hill, M.L., and Fitz, T., 2011, A deformation history of the Ivanhoe Lake Fault [abs.]: Institute on Lake Superior Geology Meeting, v. 57, p. 78.

Symons, D.T.A., Lewchuk, M.T., Dunlop, D.J., Costanzo–Alvarez, V., Halls, H.C., Bates, M.P., Palmer, H.C., and Vandall, T.A., 1994, Synopsis of paleomagnetic studies in the Kapuskasing structural zone: Canadian Journal of Earth Sciences, v. 31, p. 1206–1217, doi:10.1139/e94–106.

Taylor, B. and Martinez, F., 2003, Back–arc basin basalt systematics: Earth and Planetary Science Letters, v. 210, p. 481 497.

Thorpe, R.I., Sage, R.P, and Franklin, J.M., 1987, Lead isotope evidence for an old crustal source for many ore leads in the Wawa region [abs.]: Institute on Lake Superior Geology, Proceedings and Abstracts, v. 33, pt. I, p. 76–77.

Thorpe, R.., 1999, The Pb isotope linear array for volcanogenic massive sulphide deposits of the Abitibi and Wawa subprovinces, Canadian Shield: Economic Geology Monograph, v. 10, p. 555–576, doi:10.1007/3–540–27946–6.

Thurston, P.C., Osmani, I.A., and Stone, D., 1991, Northwestern Superior Province (P. C. Thurston, H. R. Williams, R. H. Sutcliffe, & G. M. Stott, Eds.): Ontario Geological Survey Special Volume, p. 81–142.

Thurston, P.C., Ayer, J.A., Goutier, J., Hamilton, M.A., 2008. Depositional gaps in Abitibi greenstone belt stratigraphy: A key to exploration for syngenetic mineralization: Economic Geology 103, 1097–1134. doi:10.2113/gsecongeo.103.6.1097.

Tomkins, A.G., Pattison, D.R.M., and Frost, B.R., 2007, On the initiation of metamorphic sulphide anataxis: Journal of Petrology, 48, 3, 511–535.

Tomlinson, K.Y., and Dickin, A.P., 2003, Project Unit 02–036 (C. L. Baker, R. I. Kelly, J. A. Ayer, & R. M. Easton, Eds.): Open File Report – Ontario Geological Survey, p. 13.1–13.8.

Tomlinson, K.Y., Hall, R.P., Hughes, D.J., and Thurston, P.C., 1996, Geochemistry and assemblage accretion of metavolcanic rocks in the Beardmore–Geraldton greenstone belt, Superior Province: Canadian Journal of Earth Sciences, v. 33, p. 1520–1533, doi:10.1139/e96–115.

Tomlinson, K.Y., Stott, G.M., Percival, J.A., and Stone, D., 2004, Basement terrane correlations and crustal recycling in the western Superior Province: Nd isotopic character of granitoid and felsic volcanic rocks in the Wabigoon subprovince, N. Ontario, Canada: Precambrian Research, v. 132, p. 245–274, doi:10.1016/j.precamres.2003.12.017.

Torsvik, T.H. and Cocks, L.R.M., 2017, Earth history and palaeogeography; Cambridge, Cambridge University Press, https://doi.org/10.1017/ 9781316225523.

Tuba, Györgyi, Kontak, D.J., Choquette, B.G., Pfister, J., Hastie, E.C.G., and va Hees, E.H.P., 2021, Fluid diversity in the gold–endowed Archean orogenic systems of the Abitibi greenstone belt (Canada) I: Constraining the PTZ of prolonged hydrothermal systems, v. 135, 104221.

Tullis, J., 1992, Dislocation creep regimes in quartz aggregates: Journal of Structural Geology, v. 14, p. 145–159.

Turek, A., 1984, U–Pb zircon ages and the evolution of the Michipicoten plutonic–volcanic terrane of the Superior Province, Ontario: Canadian Journal of Earth Sciences, 21: 457–464.

Turek, A., Sage, R.P. and van Schmus, W.R., 1992. Advances in the geochronology of the Michipicoten greenstone belt, Superior Province, Ontario: Canadian Journal of Earth Sciences, v.29, p.1154 1165.

Turek, A., Heather, K.B., Sage, R.P., and Van Schmus, W.R., 1996a, U Pb zircon ages for the Missanabie Renabie area and their relation to the rest of the Michipicoten greenstone belt, Superior Province, Ontario, Canada: Precambrian Research, v. 76, p. 191–211.

Turek, A., Keller, R., and Schmus, W.R.V., 1990, U–Pb zircon ages of volcanism and plutonism in the Mishibishu greenstone belt near Wawa, Ontario: Canadian Journal of Earth Sciences, v. 27, p. 649–656, doi:10.1139/e90–062.

Vaillancourt, C., Ayer, J.A., Zubowski, S.M., Kamo, S.L., Baker, C.L., Debicki, E.J., Parker, J.R., Kelly, R.I., and Easton, R.M., 2004, Project Unit 03–002: Open File Report – Ontario Geological Survey, p. 6.1–6.9.

Valli, F., Guillot, S., and Hattori, K.H., 2004, Source and tectono–metamorphic evolution of mafic and pelitic metasedimentary rocks from the central Quetico metasedimentary belt, Archean Superior Province of Canada: Precambrian Research, v. 132, p. 155–177, doi:10.1016/j.precamres.2004.03.002.

Van der Voo, R., 2004, GSA Today, v. 14, no. 12, doi: 10.1130/1052–5173(2004)0142.0.CO;2

Van Kranendonk, M.J., and Collins, W.J., 1998, Timing and tectonic significance of Late Archean, sinistral strike–slip deformation in the Central Pilbara Structural Corridor, Pilbara Craton, Western Australia: Precambrian Research, v. 88, p. 207–232.

Van Lankvelt, A., Schneider, D.A., Biczok, J., McFarlane, C.R.M., and Hattori, K., 2016, Decoding Zircon Geochronology of Igneous and Alteration Events Based on Chemical and Microstructural

Features: a Study from the Western Superior Province, Canada: Journal of Petrology, v. 57, p. 1309–1334, doi:10.1093/petrology/egw041.

van Nostrand, T.S., Westhues, A., and Broughm, S. 2016., Geology of the northeastern Ashuanipi Complex, Western Labrador (Parts of NTS 23J/05, 06, 07 and 11), Current Research, Newfoundland and Labrador, Department of Natural Resources Geological Survey, Report 16–1, p. 173–196.

Vandall, T.A., and Symons, D.T.A., 1990, Paleomagnetism of Archean granites and Matachewan dikes in the Wawa Subprovince, Ontario: reevaluation of the Archean apparent polar wander path: Canadian Journal of Earth Sciences, v. 27, p. 1031–1039, doi:10.1139/e90–107.

Vervoort, J.D., White, W.M., and Thorpe, R.I., 1994, Nd and Pb isotope ratios of the Abitibi greenstone belt: new evidence for very early differentiation of the Earth: Earth Planetary Science Letters, v. 125: 215–229. DOI: 10.1016/0012–821X(94)90146–5.

Wagner, T., Boyce, A.J., Jonsson, E., and Fallick, A.E., 2004, Laser microprobe sulphur isotope analysis of arsenopyrite: experimental calibration and application to the Boliden Au–Cu–As massive sulphide deposit: Ore Geology Reviews, v. 25, p. 311–325, doi:10.1016/j.oregeorev.2004.05.002.

Wang, X., 1993, U–Pb zircon geochronology study of the Bird River greenstone belt, southeastern Manitoba.: National Library of Canada = Bibliothèque nationale du Canada.

Wang, X., 1993, U–Pb zircon geochronology study of the Bird River greenstone belt, southeastern Manitoba [M.Sc. thesis]: University of Windsor, Windsor, 96 p.

Warr, L.N., 2021, IMA–CNMNC approved mineral symbols, Mineralogical Magazine, v. 85, p. 291 320.

Watkinson, D.H., Thurston, P., and Shafiqullah, M., 1972, The Shawmere Anorthosite of Archean Age in the Kapuskasing Belt, Ontario: The Journal of Geology, v. 80, p. 736–739, doi:10.1086/627799.

Watson, J., 1980, The origin and history of the Kapuskasing structural zone, Ontario, Canada: Canadian Journal of Earth Sciences, v. 17, p. 866–875.

Wells, M.L. and Hoisch, T.D., 2008, The role of mantle delamination in widespread Late Cretaceous extension and magmatism in the Cordilleran orogen, western United States: GSA Bulletin, v. 120, n. 5–6, p. 515–530. doi: https://doi–org.cyber.usask.ca/10.1130/B26006.1.

Weinburg, R.F., Hodkiewicz, P.F., and Groves, D.I., 2004, What controls gold distribution in Archean Terranes: Geology, v. 32, p. 545–548.

West, G.F., and Ernst, R.E., 1991, Evidence from aeromagnetics on the configuration of Matachewan dykes and the tectonic evolution of the Kapuskasing Structural Zone, Ontario, Canada: Canadian Journal of Earth Sciences, v. 28, p. 1797–1811, doi:10.1139/e91–160.

Wheeler, J.O., Hoffman, P.F., Card, K.D., Davidson, A., Sanford, B.V., Okulitch, A.V. and Roest, W.R. (compilers). 1996: Geological Map of Canada, Geological Survey of Canada, Map 1860A, scale 1:5 000 000.

Williams, H.R., 1989, Geological studies in the Wabigoon, Quetico and Abitibi–Wawa subprovinces, Superior Province of Ontario, with emphasis on the structural development of the Beardmore Geraldton Belt: Ontario Geological Survey, Open File Report 5724, 189p.

Williams, H.R., Stott, G.M., Thurston, P.C., Sutcliffe, R.H., Bennett, G., Easton, R.M., and Armstrong, D.K., 1992, Tectonic evolution of Ontario (P. C. Thurston, H. R. Williams, R. H. Sutcliffe, & G. M. Stott, Eds.): Ontario Geological Survey Special Volume, p. 1255–1332.

Wilson, C.J.L., Russell–Head, D.S., Kunze, K., and Viola, G., 2007, The analysis of quartz c–axis fabrics using a modified optical microscope: Journal of Microscopy, v. 227, p. 30–41, doi:10.1111/j.1365–2818.2007.01784.x.

Wyman, D.A., Ayer, J.A., Conceição, R.V., and Sage, R.P., 2006, Mantle processes in an Archean orogen: Evidence from 2.67 Ga diamond–bearing lamprophyres and xenoliths: Lithos, v. 89, p. 300–328, doi:10.1016/j.lithos.2005.12.005.

Wyman, D.A., Ayer, J.A., and Devaney, J.R., 2000, Niobium–enriched basalts from the Wabigoon subprovince, Canada: evidence for adakitic metasomatism above an Archean subduction zone: Earth and Planetary Science Letters, v. 179, p. 21–30, doi:10.1016/S0012–821X(00)00106–0.

Wyman, D.A., and Kerrich, R., 2002, Formation of Archean continental lithospheric roots: The role of mantle plumes: Geology, v. 30, p. 543, doi:10.1130/0091 7613(2002)030<0543:FOACLR>2.0.CO;2.

Wyman, D., and Kerrich, R., 2009a, Plume and arc magmatism in the Abitibi subprovince: Implications for the origin of Archean continental lithospheric mantle: Precambrian Research, v. 168, p. 4–22, doi:10.1016/j.precamres.2008.07.008.

Wyman, D., and Kerrich, R., 2009b, Plume and arc magmatism in the Abitibi subprovince: Implications for the origin of Archean continental lithospheric mantle: Precambrian Research, v. 168, p. 4–22, doi:10.1016/j.precamres.2008.07.008.

Wyman, D., and Kerrich, R., 2010a, Mantle plume – volcanic arc interaction: consequencemagmatism, metallogeny, and cratonization in the Abitibi and Wawa subprovinces, Lithoprobe parameters, processes, and the evolution of a continent . (R. Clowes, Ed.): Canadian Journal of Earth Sciences, v. 47, p. 565–589, doi:10.1139/E09–049.

Wyman, D.A., Kerrich, R., and Polat, A., 2002a, Assembly of Archean cratonic mantle lithosphere and crust: plume–arc interaction in the Abitibi–Wawa subduction–accretion complex: Precambrian Research, v. 115, p. 37–62, doi:10.1016/S0301–9268(02)00005–0.

Wyman, D.A. and Kerrich, R., 2010, Mantle plume – volcanic arc interaction: consequences for magmatism, metallogeny, and cratonization in the Abitibi and Wawa subprovinces, Canada: Canadian Journal of Earth Science, v. 47, p. 565–589.

Young, G.M., 2015, Did prolonged two–stage fragmentation of the supercontinent Kenorland lead to arrested orogenesis on the southern margin of the Superior province?: Geoscience Frontiers, 6, 419–435.

Zaleski, E., 1999, Geological evolution of the Manitouwadge greenstone belt and Wawa–Quetico subprovince boundary, Superior Province, Ontario, constrained by U–Pb zircon dates of supracrustal and plutonic rocks: Canadian Journal of Earth Sciences, v. 36, n. 6, p. 945–966.

Zegers, T.E., Nelson, D.R., Wijbrans, J.R., and White, S.H., 2001, SHRIMP U–Pb zircon dating of Archean core complex formation and pancratonic strike–slip deformation in the East Pilbara Granite–Greenstone Terrain: Tectonics, v. 20, p. 883–908.

Zhou, S., Polat, A., Longstaffe, F.J., Yang, K., Fryer, B.J., and Weisener, C., 2016, Formation of the Neoarchean Bad Vermilion Lake Anorthosite Complex and spatially associated granitic rocks at a convergent plate margin, Superior Province, Western Ontario, Canada: Gondwana Research, v. 33, p. 134–159, doi:10.1016/j.gr.2015.08.014.

Zweng, P.L., Mortensen, J.K., and Dalrymple, G.B., 1993, Thermochronology of the Camflo gold deposit, Malartic, Quebec; implications for magmatic underplating and the formation of gold bearing quartz veins: Economic Geology, v. 88, p. 1700–1721, doi:10.2113/gsecongeo.88.6.1700.

6247 **APPENDIX A: WHOLE ROCK AND TRACE ELEMENT GEOCHEMISTRY**

6248

Sample ID	VS001	VS002	VS003	VS004	VS005	VS006	VS007	VS008	VS009	VS010
SiO2 (%)	45.09	47.21	47.33	45.07	64.8	66.33	71.89	56.06	48.46	43.58
Al2O3	13.93	14.06	15.8	16.04	15.42	15.52	15.13	16.44	18.92	19.24
Fe2O3(T)	17.02	12.47	12.8	11.91	4.95	3.88	1.98	8.34	8.85	10.12
MnO	0.695	0.304	0.375	0.402	0.081	0.092	0.04	0.189	0.137	0.156
MgO	4.74	4.12	4.72	4.15	3.34	2.28	0.89	3.9	6.53	7.64
CaO	13.05	12.7	12.16	15.57	3.01	3.81	2.46	7.24	10.92	10.76
Na2O	1.25	1.47	2.63	1.43	4.3	4.16	4.24	4.31	2.78	1.73
K2O	0.68	1.51	0.65	0.43	2.19	0.81	2.26	0.33	0.96	1.27
TiO2	0.593	1.139	0.638	0.575	0.482	0.416	0.255	0.88	0.598	0.648
P205	0.05	0.02	0.09	0.01	< 0.01	0.01	0.06	< 0.01	0.1	0.02
LOI	2.44	5.65	3.59	3.74	1.75	2.81	1.16	0.61	2.15	3.12
Total	99.54	100.8	100.7	99.36	100.6	100.3	100.4	98.4	100.3	98.33
Au (ppb)	42	43	5	< 1	< 1	< 1	5	< 1	< 1	< 1
Ag (ppm)	< 0.5	< 0.5	< 0.5	< 0.5	< 0.5	< 0.5	< 0.5	< 0.5	< 0.5	< 0.5
As	3	3	3	1	1	2	3	< 1	< 1	1
Ba	189	481	294	112	1645	379	781	131	210	331
Be	< 1	1	< 1	< 1	3	2	2	< 1	< 1	< 1
Bi	< 0.1	0.2	0.1	< 0.1	0.3	< 0.1	0.2	< 0.1	0.2	0.1
Br	< 0.5	3.8	< 0.5	32.9	< 0.5	< 0.5	< 0.5	< 0.5	< 0.5	< 0.5
Cd	< 0.5	< 0.5	< 0.5	< 0.5	< 0.5	< 0.5	< 0.5	< 0.5	< 0.5	< 0.5
Co	82.4	66.4	94.7	96.8	32.8	44	16.7	51.2	58.6	45.4
Cr	372	35.7	398	380	151	59.3	13.7	131	373	458
Cs	0.5	4.3	1	1.3	9.1	1.9	2.8	0.3	1.5	1.9
Cu	96	368	48	89	33	91	21	33	22	58
Ga	15	18	16	16	20	21	21	22	15	18
Ge	1.6	0.6	1	0.7	0.8	< 0.5	0.7	1.7	1.1	0.9
Hf	1	2.3	0.9	0.9	5.3	3.6	3.3	2.7	0.9	1
Hg	< 1	< 1	< 1	< 1	< 1	< 1	< 1	< 1	< 1	< 1
In	< 0.1	< 0.1	< 0.1	< 0.1	< 0.1	< 0.1	< 0.1	< 0.1	< 0.1	< 0.1

Ir	< 1	< 1	< 1	< 1	< 1	< 1	< 1	< 1	< 1	< 1
Mo	< 2	< 2	< 2	< 2	< 2	< 2	< 2	< 2	< 2	< 2
Nb	2.9	3.1	< 0.2	< 0.2	7.8	4.9	2.9	2	0.3	1
Ni	128	40	149	171	58	45	17	70	87	94
Pb	< 5	11	5	< 5	16	7	20	< 5	< 5	< 5
Rb	16	35	19	14	69	34	46	8	30	51
S (%)	0.435	1.18	0.12	0.245	0.057	0.165	0.49	0.049	0.038	0.089
Sb (ppm)	0.3	0.3	0.3	0.3	< 0.1	< 0.1	0.1	< 0.1	< 0.1	0.1
Sc	40.3	45.3	41.8	38.9	10.4	6.7	2.91	29.9	32.3	37.4
Se	< 0.5	< 0.5	< 0.5	< 0.5	< 0.5	< 0.5	< 0.5	< 0.5	< 0.5	< 0.5
Sample ID	VS001	VS002	VS003	VS004	VS005	VS006	VS007	VS008	VS009	VS010
Sn	< 1	< 1	< 1	< 1	< 1	< 1	< 1	< 1	< 1	< 1
Sr	344	427	389	290	1159	466	533	209	253	235
Ta	0.41	0.32	0.24	0.23	0.66	0.75	0.41	0.32	0.22	0.16
Th	2	0.72	0.2	0.12	10.6	7.97	5.3	0.92	0.22	0.25
U	0.11	0.14	0.04	0.02	2.07	1.89	1.78	0.22	0.05	0.07
V	243	331	255	238	88	61	31	224	204	252
W	280	179	202	230	179	368	135	105	198	42
Y	14	24	13	14	28	10	6	17	12	13
Zn	84	74	81	49	74	42	58	73	52	64
Zr	35	76	32	28	183	139	115	93	31	36
La	2.85	5.97	2.61	2.93	59	48.9	26.8	6.03	2.12	2.1
Ce	7.78	14.3	6.05	5.28	115	96.9	53.7	13.8	5.4	5.56
Pr	1.21	2.06	0.9	0.96	14.1	11.6	6.4	1.91	0.82	0.91
Nd	5.92	9.53	4.31	4.59	52.4	41.3	22.6	8.05	3.8	4.33
Sm	1.77	3	1.61	1.67	11.1	6.83	3.77	2.56	1.42	1.51
Eu	0.664	1.16	0.522	0.54	2.48	1.46	0.924	0.84	0.55	0.454
Gd	2.77	3.58	2.14	1.95	8.24	4.03	2.25	2.82	1.82	1.84
Tb	0.45	0.69	0.4	0.36	1.12	0.46	0.23	0.5	0.33	0.36
Dy	2.8	4.54	2.65	2.4	5.87	2.15	1.03	3.16	2.16	2.37
Ho	0.58	0.96	0.57	0.52	1.02	0.34	0.17	0.64	0.46	0.51
Er	1.68	2.91	1.75	1.57	2.66	0.89	0.43	1.85	1.41	1.53

Tl	0.07	0.22	0.15	0.13	0.54	0.2	0.3	< 0.05	0.09	0.16
Tm	0.254	0.43	0.261	0.234	0.361	0.116	0.059	0.277	0.213	0.232
Yb	1.67	2.77	1.72	1.52	2.23	0.72	0.37	1.89	1.43	1.52
Lu	0.277	0.424	0.278	0.238	0.345	0.119	0.058	0.316	0.245	0.243
Mass (g)	1.079	1.029	1.061	1.051	1.07	1.075	1.041	1.032	1.027	1.037
Sample ID	VS011	VS012	VS013	VS014	VS015	VS016	VS017	VS018	VS019	VS020
SiO2 (%)	52.06	66.51	59.41	53.28	71.76	60.93	46.82	47.02	56.52	68.02
Al2O3	12.97	14.34	16	12.32	11.05	13.84	15.34	14.56	14.95	15.74
Fe2O3(T)	19.68	6.92	14.47	14.32	8.55	10.78	17.92	15.51	6.52	3.95
MnO	1.097	0.098	0.303	0.487	0.121	0.112	0.334	0.394	0.147	0.059
MgO	3.93	2.97	4	5.14	1	2.11	4.52	6.13	6.02	0.95
CaO	8.48	2.76	0.18	8.75	0.28	0.35	0.71	2.73	5.03	0.82
Na2O	1.15	4.22	0.19	1.03	0.67	0.75	4.36	3.13	3.54	4.04
K2O	0.84	1.18	2.4	0.68	3.28	4.51	5.57	5.04	2.82	4.62
TiO2	0.511	0.622	0.921	0.867	0.355	1.063	0.879	1.033	0.544	0.468
P205	0.06	0.14	0.03	0.09	0.16	0.04	0.05	0.14	0.23	0.2
LOI	–0.02	0.9	1.79	2.8	2.93	3.64	2.18	5.29	4.02	1.5
Total	100.7	100.7	99.68	99.78	100.2	98.14	98.67	101	100.3	100.4
Au (ppb)	< 1	5	499	300	649	683	159	355	10	462
Ag (ppm)	< 0.5	< 0.5	1.2	0.6	1.4	1.5	< 0.5	0.8	< 0.5	0.5
As	< 1	< 1	< 1	3	2	2	4	< 1	2	1
Ba	120	462	381	139	2575	2540	266	770	742	1282
Be	< 1	< 1	2	2	3	3	6	3	4	4
Bi	< 0.1	< 0.1	0.2	4.7	0.5	1.2	0.1	0.3	0.6	< 0.1
Br	< 0.5	< 0.5	< 0.5	< 0.5	< 0.5	< 0.5	< 0.5	< 0.5	< 0.5	< 0.5
Cd	0.7	< 0.5	< 0.5	< 0.5	< 0.5	< 0.5	< 0.5	0.7	< 0.5	< 0.5
Co	38.7	34	80.9	50.9	52.6	67.2	76.4	63.3	60	30.8
Cr	102	137	132	58.8	86.2	59.8	347	55.2	503	61.2
Cs	2.2	2.8	13.2	1	4.8	11	20.5	24.5	10.3	4.3
Cu	22	43	241	105	102	91	54	177	21	13
Ga	13	19	24	15	15	21	23	19	19	21
Ge	0.6	1.2	1.9	0.9	1.1	1.9	3.6	1.8	1.4	1.8

Hf	2.2	3.3	2.3	1.6	1.9	2.2	1.1	1.7	2.8	4
Hg	< 1	< 1	< 1	< 1	< 1	< 1	< 1	< 1	< 1	< 1
In	< 0.1	< 0.1	< 0.1	< 0.1	< 0.1	< 0.1	< 0.1	< 0.1	< 0.1	< 0.1
Ir	< 1	< 1	< 1	< 1	< 1	< 1	< 1	< 1	< 1	< 1
Mo	< 2	< 2	< 2	< 2	< 2	< 2	< 2	< 2	< 2	< 2
Nb	1	2.4	1.9	1.1	< 0.2	8.7	6.8	1.7	17.1	3.7
Ni	47	63	80	49	54	55	170	55	159	48
Pb	5	< 5	12	11	12	< 5	5	7	< 5	10
Rb	31	27	110	13	110	167	258	260	105	120
S (%)	0.024	0.065	1.45	2.33	3.26	4.35	0.986	2.35	0.14	0.458
Sb (ppm)	< 0.1	< 0.1	0.4	1.4	0.4	1.3	0.5	0.4	0.4	0.2
Sc	22.9	17.5	56.8	39	18	41.8	44.7	49	17.3	7.78
Se	< 0.5	< 0.5	< 0.5	< 0.5	< 0.5	< 0.5	< 0.5	< 0.5	< 0.5	< 0.5
Sample ID	VS011	VS012	VS013	VS014	VS015	VS016	VS017	VS018	VS019	VS020
Sn	< 1	< 1	2	< 1	< 1	< 1	2	< 1	< 1	< 1
Sr	75	399	41	143	214	183	188	418	657	378
Ta	0.48	0.4	0.31	0.26	0.45	2.69	0.68	0.16	0.35	0.46
Th	0.97	2.75	1.22	0.38	4.17	2.68	9.86	6.17	4.16	8.62
U	0.22	0.59	0.27	0.09	0.57	0.83	0.83	0.58	1.43	1.82
V	143	137	354	272	150	360	337	337	142	81
W	157	180	173	147	293	515	91	130	278	121
Y	15	12	22	19	6	13	43	52	37	12
Zn	187	83	248	167	77	124	207	193	78	63
Zr	79	133	86	57	72	77	46	64	137	151
La	8.78	18.9	7.19	4.34	5.18	5.09	12.5	4.67	22.8	51.3
Ce	17.1	40.1	16.1	10.4	9.93	11.3	25.4	11	44.3	102
Pr	2.1	4.67	2.15	1.56	1.22	1.57	3.22	1.59	5.37	12.4
Nd	8.3	17.6	9.31	7.37	4.68	6.86	12.7	7.45	19.8	44.5
Sm	2.21	3.57	2.59	2.43	1.17	2	3.15	2.72	4.18	7.94
Eu	0.854	0.93	0.775	0.736	0.344	0.583	0.622	0.924	1.22	1.75
Gd	2.66	2.81	2.64	3	1.25	2.1	3.3	3.89	4.1	5.01
Tb	0.46	0.39	0.56	0.55	0.21	0.39	0.87	1.04	0.83	0.56

Dy	2.84	2.21	3.95	3.56	1.28	2.38	6.68	8.35	5.73	2.53
Ho	0.58	0.41	0.93	0.76	0.25	0.49	1.5	1.92	1.28	0.42
Er	1.76	1.17	2.99	2.31	0.7	1.47	4.56	6.13	3.89	1.08
Tl	0.06	0.16	5.52	0.6	11.1	21.7	5.05	4.76	4.35	4.94
Tm	0.269	0.171	0.477	0.357	0.099	0.227	0.697	0.943	0.572	0.145
Yb	1.83	1.17	3.21	2.44	0.64	1.53	4.61	6.34	3.62	0.95
Lu	0.31	0.2	0.521	0.412	0.104	0.259	0.745	0.978	0.543	0.159
Mass (g)	1.03	1.055	1.059	1.039	1.02	1.078	1.036	1.056	1.033	1.096

6249

Sample ID	VS021	VS022	VS023	VS024	VS025	VS026	VS027	VS028	VS029	VS030
SiO2 (%)	65.51	57.02	19.39	55.67	65.94	49.74	46.95	66.29	43.23	72.75
Al2O3	22.18	16.03	5.24	16.91	15.08	14.27	12.76	15.55	15.78	13.73
Fe2O3(T)	5.4	14.23	59.04	13.12	3.98	13	16.11	3.5	17.04	1.96
MnO	0.055	0.442	0.055	0.416	0.12	0.434	0.49	0.1	0.543	0.048
MgO	1.61	4.29	0.57	2.14	2.11	5.5	5.47	1.94	4.56	0.76
CaO	0.51	2.67	1.63	0.79	4.64	10.08	10.65	3.88	12.03	2.23
Na2O	1.11	1.73	1.44	2.68	2.54	2.13	1.28	3.32	1.15	2.44
K2O	2.24	2.09	1.34	4.54	3.39	1.4	0.95	2.18	0.95	5
TiO2	1.021	0.628	0.309	0.808	0.433	1.003	0.87	0.398	0.977	0.252
P205	0.07	0.25	0.05	0.04	0.18	0.1	0.09	0.16	0.08	0.09
LOI	0.95	0.09	9.5	3.1	1.38	2.9	2.82	1.2	2.03	1.28
Total	100.7	99.47	98.55	100.2	99.79	100.6	98.44	98.52	98.38	100.5
Au (ppb)	14	41	57	447	50	283	655	31	534	46
Ag (ppm)	< 0.5	< 0.5	0.8	0.9	< 0.5	< 0.5	0.8	0.6	0.8	< 0.5
As	318	760	< 1	7	6	2	3	2	< 1	2
Ba	893	696	471	329	1129	201	137	1656	518	1199
Be	4	3	< 1	4	2	2	1	2	3	2
Bi	< 0.1	< 0.1	1.8	0.6	0.1	2.4	4.8	0.9	3.4	< 0.1
Br	< 0.5	< 0.5	< 0.5	< 0.5	< 0.5	< 0.5	< 0.5	< 0.5	< 0.5	< 0.5
Cd	< 0.5	0.6	0.9	< 0.5	< 0.5	< 0.5	< 0.5	< 0.5	< 0.5	< 0.5
Co	89.4	92.6	153	84.3	40.8	53.9	95.7	44.7	72.9	57.9
Cr	456	1000	44.2	428	76.8	56.3	47	66.3	138	22.8

Cs	12.1	15.5	0.7	16.1	27.6	2.3	2.2	11.2	1.8	6.9
Cu	9	33	596	98	20	100	143	41	164	17
Ga	24	20	6	22	23	19	16	22	19	19
Ge	1.5	2.4	0.6	2.6	< 0.5	0.9	0.9	< 0.5	0.7	< 0.5
Hf	1.8	3.9	1	1.1	4.3	1.8	1.5	3.5	1.9	2.9
Hg	< 1	< 1	< 1	< 1	< 1	< 1	< 1	< 1	< 1	< 1
In	< 0.1	< 0.1	< 0.1	< 0.1	< 0.1	< 0.1	< 0.1	< 0.1	< 0.1	< 0.1
Ir	< 1	< 1	< 1	< 1	< 1	< 1	< 1	< 1	< 1	< 1
Mo	< 2	5	3	< 2	< 2	< 2	< 2	< 2	< 2	17
Nb	< 0.2	6.6	< 0.2	13.4	5.4	1.3	1.2	3	0.9	4
Ni	158	233	228	181	39	53	67	46	84	24
Pb	< 5	< 5	26	13	13	< 5	5	20	8	33
Rb	86	74	30	207	171	46	28	94	22	130
S (%)	0.008	0.216	7.75	1.39	0.471	2.31	3.79	0.944	3.61	0.545
Sb (ppm)	2.3	0.8	< 0.1	1.4	2	3.2	3.7	0.4	1.8	0.7
Sc	45	34.3	7.39	48.6	7.55	45.5	42.4	6.6	54.6	3.68
Se	< 0.5	< 0.5	< 0.5	< 0.5	< 0.5	< 0.5	< 0.5	< 0.5	< 0.5	< 0.5
Sample ID	VS021	VS022	VS023	VS024	VS025	VS026	VS027	VS028	VS029	VS030
Sn	< 1	< 1	< 1	< 1	< 1	< 1	< 1	< 1	< 1	< 1
Sr	196	502	125	97	521	157	151	496	228	352
Ta	0.24	0.54	0.03	0.15	0.6	0.31	0.23	0.66	0.23	0.75
Th	0.39	6.52	0.69	0.37	6.55	0.45	0.42	6.52	0.4	4.61
U	0.09	2.03	0.32	0.12	2.97	0.13	0.1	1.85	0.09	2.01
V	362	201	57	305	69	330	286	60	345	47
W	242	217	6	130	323	145	187	367	139	579
Y	12	27	3	16	14	23	21	10	21	7
Zn	57	168	58	173	89	162	165	76	162	41
Zr	62	148	37	41	168	63	54	133	65	109
La	4.03	39.6	5.06	2.49	41.5	4.96	5.32	39.6	4.34	27.7
Ce	10.3	78.5	11.3	5.96	80.7	11.8	11.7	78.5	10.4	54.4
Pr	1.53	9.79	1.41	0.88	9.75	1.79	1.66	9.28	1.51	6.57
Nd	7.27	37.5	5.43	4.03	36.3	8.28	7.3	33.3	7.42	23.3

Sm	2.21	8.05	1.19	1.44	6.89	2.55	2.49	5.89	2.44	4.16
Eu	0.43	1.56	0.332	0.486	1.54	0.947	0.878	1.32	0.889	1.06
Gd	2.33	6.44	1.11	1.72	4.8	3.36	3.06	3.87	3.12	2.65
Tb	0.39	0.94	0.17	0.38	0.58	0.61	0.56	0.42	0.59	0.28
Dy	2.21	5.24	0.95	2.76	2.81	4.11	3.75	2.02	3.93	1.24
Ho	0.43	0.95	0.18	0.62	0.48	0.88	0.8	0.34	0.84	0.22
Er	1.2	2.67	0.49	1.89	1.27	2.74	2.41	0.88	2.59	0.58
Tl	2.37	2.08	0.22	7.9	2.73	0.87	0.64	1.23	0.41	1.17
Tm	0.172	0.389	0.072	0.291	0.181	0.423	0.38	0.118	0.397	0.083
Yb	1.14	2.65	0.5	1.92	1.19	2.89	2.63	0.76	2.72	0.55
Lu	0.185	0.447	0.092	0.311	0.197	0.47	0.459	0.126	0.454	0.091
Mass (g)	1.042	1.015	1.057	1.021	1.036	1.002	1.059	1.052	1.003	1.036

6250

6251

Sample ID	VS031	VS032	VS033	VS034	VS035	VS036	VS037	VS039	VS040
SiO2 (%)	45.16	57.38	54.24	55.61	53.87	71.32	59.79	63.26	50.25
Al2O3	13.65	13.62	15.37	12.93	14	10.4	13.64	12.14	12.05
Fe2O3(T)	18.86	12.97	12.9	18.12	15.58	5.84	12.58	9.4	10.04
MnO	0.296	0.189	0.264	0.809	0.292	0.358	0.607	0.16	0.306
MgO	4.34	1.07	1.32	2.11	3.82	2.47	1.86	1.09	3.59
CaO	7.14	0.98	1.93	2.05	2.6	3.76	1.54	1.8	13.73
Na2O	1.21	1.4	1.81	1.62	1.85	0.67	1.64	1.98	1.26
K2O	2.94	7.44	6.7	3.67	3.68	2.32	5.23	5.12	1.35
TiO2	1.108	0.979	1.063	0.972	0.868	0.179	1.023	0.46	0.773
P205	0.12	0.09	0.1	0.12	0.09	0.07	0.11	0.28	0.06
LOI	4.08	2.89	2.88	2.73	2.84	1.65	1.68	2.4	5.14
Total	98.9	99.02	98.58	100.7	99.5	99.04	99.69	98.09	98.57
Au (ppb)	1270	968	1030	1270	835	1050	1060	2010	1240
Ag (ppm)	1.2	1.4	1.1	2.2	1.4	0.8	1.2	2	1.5
As	4	< 1	< 1	< 1	3	7	< 1	< 1	17
Ba	667	761	803	118	168	457	306	6171	583
Be	4	4	7	9	11	25	4	18	6

Bi	3.1	0.5	0.2	1.8	1.6	0.6	0.3	0.3	< 0.1
Br	< 0.5	< 0.5	< 0.5	< 0.5	< 0.5	< 0.5	< 0.5	< 0.5	4.7
Cd	0.6	< 0.5	< 0.5	< 0.5	0.5	< 0.5	< 0.5	< 0.5	< 0.5
Co	225	86.8	72.6	92.8	58.8	31	53.7	32.7	55.8
Cr	60	54.9	62.9	58	113	9.6	76.3	48.5	180
Cs	31.4	11.9	16.3	19.5	29.4	11.4	12.6	6.5	2.7
Cu	324	159	151	213	115	36	174	69	98
Ga	18	18	20	18	19	15	21	19	16
Ge	0.6	1.5	1.6	4.1	1.8	1.7	4.7	2	< 0.5
Hf	2	1.6	1.8	1.6	1.6	2	1.8	2.5	1.5
Hg	< 1	< 1	< 1	< 1	< 1	< 1	< 1	< 1	< 1
In	< 0.1	< 0.1	< 0.1	< 0.1	< 0.1	< 0.1	< 0.1	< 0.1	< 0.1
Ir	< 1	< 1	< 1	< 1	< 1	< 1	< 1	< 1	< 1
Mo	< 2	< 2	< 2	< 2	< 2	3	< 2	< 2	3
Nb	2.7	1.1	22	< 0.2	1.5	1.4	0.8	2.7	< 0.2
Ni	77	70	59	92	64	18	68	39	70
Pb	15	24	10	10	8	5	16	16	6
Rb	137	263	255	172	236	133	256	181	46
S (%)	5.25	3.21	2.24	4.07	2.86	1.14	2.07	2.93	3.05
Sb (ppm)	2.5	0.7	0.7	4.2	2.9	3.4	0.5	0.5	4.7
Sc	46.6	39.8	47.4	54.3	45.6	10.3	48.7	15.7	44.3
Se	< 0.5	< 0.5	< 0.5	< 0.5	< 0.5	< 0.5	< 0.5	< 0.5	< 0.5
Sample ID	VS031	VS032	VS033	VS034	VS035	VS036	VS037	VS039	VS040
Sn	< 1	< 1	< 1	< 1	< 1	2	< 1	< 1	< 1
Sr	213	229	290	195	193	209	260	610	254
Ta	0.64	0.21	0.31	0.34	0.14	0.51	0.17	0.34	0.31
Th	0.64	0.74	0.49	0.37	0.47	2.86	0.32	3.68	0.31
U	5.01	0.33	0.26	0.1	0.23	1.93	0.19	0.97	0.33
V	327	302	341	320	312	67	357	129	253
W	273	133	424	333	81	272	124	132	195
Y	33	9	23	56	14	11	24	15	19
Zn	112	128	150	143	209	92	152	114	74

Zr	69	58	67	58	59	76	62	95	55
La	6.85	4.66	5.38	4.17	5.11	16.6	3.72	19.8	5.45
Ce	16.3	9.99	12.6	9.71	11.5	32.7	8.1	39.5	11.7
Pr	2.48	1.39	2.12	1.41	1.68	3.97	1.17	4.87	1.65
Nd	11.6	6.23	8.69	6.78	7.23	13.8	5.18	18	7.31
Sm	3.86	1.89	2.67	2.26	2.31	2.62	1.51	3.59	2.26
Eu	1.31	0.71	0.954	0.734	0.664	0.717	0.717	0.939	1.16
Gd	4.84	2.28	3.4	3.31	2.59	2.22	2.47	3.01	2.9
Tb	0.91	0.35	0.64	0.95	0.45	0.34	0.58	0.46	0.53
Dy	6.05	1.92	4.23	8.76	2.84	1.87	4.22	2.59	3.35
Ho	1.3	0.36	0.91	2.14	0.59	0.36	0.92	0.52	0.69
Er	3.95	1.03	2.75	6.99	1.79	1.04	2.78	1.49	2.05
Tl	2.57	8.68	9.57	8.12	14.2	7.15	5.46	10.3	1.3
Tm	0.618	0.155	0.425	1.09	0.28	0.154	0.418	0.221	0.316
Yb	4.31	1.1	2.9	7.38	1.98	1.06	2.74	1.43	2.18
Lu	0.723	0.193	0.481	1.18	0.357	0.179	0.429	0.233	0.381
Mass (g)	1.071	1	1.035	1.034	1.041	1.068	1.008	1.072	1.065

6252

Sample ID	VS041	VS042	VS043	VS044	VS045	VS046	VS047	VS048	VS049	VS050
SiO2 (%)	64.07	64.92	49.9	46.4	68.86	47.53	47.35	47.42	67.18	59.54
Al2O3	14.4	14.94	9.69	17.12	13.05	15.17	16.03	15.98	12.78	15.32
Fe2O3(T)	3.79	3.73	7.47	10.14	3.2	10.03	10.13	9.46	9.74	11.51
MnO	0.067	0.068	0.279	0.359	0.076	0.249	0.204	0.253	0.073	0.361
MgO	2.04	1.6	5.93	5.84	2.27	8.06	6.36	6.95	1.05	2.27
CaO	4.39	4.22	14.31	14.19	4.22	12.7	14.02	11.6	0.86	1.35
Na2O	3.92	3.97	2.21	1.81	3.16	2.13	2.35	2.7	0.56	0.93
K2O	2.66	2.44	1.47	1.07	2.37	0.88	0.62	0.62	4.14	4.7
TiO2	0.41	0.422	0.289	0.669	0.291	0.472	0.501	0.508	0.852	0.77
P205	0.2	0.18	0.13	0.06	0.16	0.05	0.04	0.04	0.13	0.07
LOI	3.42	2.65	6.72	1.3	1.58	1.35	1.25	2.81	2.41	1.83
Total	99.38	99.13	98.4	98.94	99.25	98.6	98.85	98.34	99.77	98.66
Au (ppb)	49	45	638	20	1170	10	16	< 1	1680	769

Ag (ppm)	< 0.5	< 0.5	1.6	< 0.5	0.7	< 0.5	< 0.5	< 0.5	1.3	0.8
As	6	6	5	6	7	3	2	< 1	< 1	< 1
Ba	1188	774	413	1546	571	1446	1008	1659	223	289
Be	3	3	7	< 1	5	3	1	< 1	9	12
Bi	0.2	0.3	1.3	0.1	< 0.1	< 0.1	0.1	< 0.1	< 0.1	0.2
Br	< 0.5	< 0.5	< 0.5	3.4	< 0.5	< 0.5	< 0.5	< 0.5	< 0.5	< 0.5
Cd	< 0.5	< 0.5	0.8	< 0.5	< 0.5	< 0.5	< 0.5	< 0.5	< 0.5	< 0.5
Co	30.1	38.9	30.9	67.4	23.8	84.9	73.1	69	47.6	54.9
Cr	59	67.3	53.6	295	44.7	244	237	218	74	435
Cs	6.5	6.9	13.7	4.6	8	1.5	0.9	2.2	10	18.1
Cu	26	39	61	48	20	41	163	23	103	54
Ga	21	21	15	17	17	14	14	14	19	21
Ge	1.1	1.4	1.9	0.6	1	1.7	1.1	1	1.7	3.6
Hf	3.5	3.7	2.3	1.1	2.7	0.7	0.8	0.7	1.4	0.9
Hg	< 1	< 1	< 1	< 1	< 1	< 1	< 1	< 1	< 1	< 1
In	< 0.1	< 0.1	< 0.1	< 0.1	< 0.1	< 0.1	< 0.1	< 0.1	< 0.1	< 0.1
Ir	< 1	< 1	< 1	< 1	< 1	< 1	< 1	< 1	< 1	< 1
Mo	< 2	< 2	< 2	< 2	< 2	< 2	< 2	< 2	< 2	< 2
Nb	5.6	25.4	3.2	< 0.2	1.5	< 0.2	< 0.2	< 0.2	< 0.2	< 0.2
Ni	47	48	72	147	42	261	274	218	57	121
Pb	< 5	11	9	< 5	7	< 5	< 5	< 5	< 5	< 5
Rb	83	84	59	33	89	21	6	10	179	241
S (%)	0.329	0.282	1.08	0.106	0.268	0.062	0.508	0.08	2.18	1.12
Sb (ppm)	0.4	0.5	0.6	0.6	0.3	0.4	0.4	0.3	0.2	0.6
Sc	7.25	6.97	11.4	30.9	4.82	31.8	32.2	32.3	39.3	46.7
Se	< 0.5	< 0.5	< 0.5	< 0.5	< 0.5	< 0.5	< 0.5	< 0.5	< 0.5	< 0.5
Sample ID	VS041	VS042	VS043	VS044	VS045	VS046	VS047	VS048	VS049	VS050
Sn	< 1	< 1	< 1	< 1	< 1	< 1	< 1	< 1	< 1	< 1
Sr	605	837	320	266	493	261	377	309	122	248
Ta	0.57	0.71	0.48	0.14	0.38	0.17	0.09	0.1	0.22	0.08
Th	7.2	9.05	4.17	0.18	5.27	0.2	0.2	0.15	0.42	0.05
U	2.03	2.11	2.65	0.04	2.78	0.03	0.04	0.04	0.1	0.06

V	67	68	133	239	76	191	195	198	327	307
W	172	258	72	141	168	180	90	106	169	100
Y	12	12	15	12	7	14	11	12	4	13
Zn	39	62	96	61	66	84	59	60	96	136
Zr	141	144	95	37	105	29	27	28	48	33
La	44.9	45.2	23.8	2.48	33.3	2.05	2.46	3.1	4.8	1.64
Ce	89.6	90.9	48.8	5.7	65.8	4.81	5.25	6.18	11	3.34
Pr	10.9	11.2	5.96	0.85	7.91	0.72	0.74	0.85	1.61	0.46
Nd	40.1	40.3	21.6	3.9	28.3	3.4	3.23	3.9	7.19	1.99
Sm	7.13	7.08	4.33	1.33	4.53	1.2	1.16	1.36	2.38	0.69
Eu	1.57	1.78	1.03	0.528	1.06	0.48	0.464	0.462	0.529	0.549
Gd	4.65	4.92	3.32	1.82	2.98	1.63	1.54	1.68	2.53	1.38
Tb	0.51	0.56	0.43	0.36	0.31	0.34	0.3	0.31	0.31	0.34
Dy	2.37	2.5	2.55	2.32	1.4	2.2	1.98	2.04	1.38	2.5
Ho	0.41	0.4	0.46	0.48	0.22	0.46	0.42	0.43	0.21	0.58
Er	1	1.02	1.31	1.45	0.56	1.37	1.26	1.32	0.49	1.8
Tl	1.28	1.07	1	0.43	1.05	0.24	0.7	0.09	12.6	24.2
Tm	0.136	0.143	0.199	0.215	0.076	0.205	0.193	0.199	0.066	0.271
Yb	0.88	0.93	1.36	1.45	0.51	1.42	1.26	1.31	0.43	1.71
Lu	0.15	0.155	0.225	0.244	0.083	0.247	0.198	0.206	0.072	0.264
Mass (g)	1.016	1.049	1.05	1.062	1.023	1.018	1.071	1.086	1.041	1.041

Sample ID	PVS051	PVS052	PVS053	PVS054	PVS054B	PVS055	PVS056	PVS057	PVS058	PVS096
SiO2 (%)	59.85	63.48	55.3	54.71	48.54	65.21	36.94	65.7	79.18	79.21
Al2O3	14.64	12.88	14.7	13.94	15.36	10.86	9.87	4.95	9.59	4.45
Fe2O3t	11.27	10.95	10.87	15.06	10.36	1.34	28.41	17.25	2.12	5.6
MnO	0.281	0.379	0.315	0.296	0.255	0.123	1.196	2.143	0.038	0.148
MgO	2.01	2.11	5.94	3.85	8	0.65	5.1	0.92	0.41	3.63
CaO	3.15	3.06	3.59	2.75	13.07	7.41	14.77	2.19	0.53	0.89
Na2O	1.29	1.86	0.81	1.94	2.2	2.38	0.52	0.48	0.78	0.29
K2O	3.57	2.57	4.8	3.62	0.89	5.52	0.2	0.54	6.11	1.93
TiO2	0.895	0.768	1.025	0.904	0.494	0.173	0.329	0.216	0.227	0.208
P205	0.15	0.13	0.76	0.12	0.04	0.15	0.05	0.15	0.06	0.26
LOI	2.51	1.78	2.48	2.88	1.37	6.08	2.77	3.33	1.85	1.95
Total	99.62	99.97	100.6	100.1	100.6	99.9	100.1	97.87	100.9	98.57
Au (ppb)	1910	2440	710	1010	7	182	357	18700	441	> 30000
Ag (ppm)	1.4	1.4	0.6	1.5	< 0.5	< 0.5	1.6	5.6	< 0.5	5.9
As	< 1	< 1	7	< 1	< 1	2	6	< 1	2	6
Ba	440	235	845	166	1476	1440	36	298	903	240
Be	27	24	14	11	3	3	< 1	826	31	109
Bi	0.5	0.4	< 0.1	2.4	< 0.1	0.2	0.4	0.7	< 0.1	0.2
Br	< 0.5	< 0.5	< 0.5	< 0.5	< 0.5	< 0.5	< 0.5	< 0.5	< 0.5	< 0.5
Cd	< 0.5	< 0.5	< 0.5	< 0.5	< 0.5	< 0.5	0.8	0.9	< 0.5	< 0.5
Co	83.7	81.7	35	55.8	83.6	34.9	137	47.8	64	52.5
Cr	66.2	69.1	160	112	229	24.4	132	25.6	33	34.5
Cs	14.5	12.9	22.7	28.8	1.6	0.9	0.2	3.5	2.7	9.9
Cu	101	167	45	105	34	95	1040	214	22	55
Ga	24	18	23	19	14	14	9	6	10	9
Ge	3.5	3.9	1.5	1.9	1.4	1.1	2.3	2.8	2.6	3
Hf	1.8	1.3	6.2	1.5	0.7	1.6	0.5	0.3	1.2	0.3

Hg	< 1	< 1	< 1	< 1	< 1	< 1	< 1	< 1	< 1	< 1
In	< 0.1	< 0.1	< 0.1	< 0.1	< 0.1	< 0.1	< 0.1	< 0.1	< 0.1	< 0.1
Ir	< 1	< 1	< 1	< 1	< 1	< 1	< 1	< 1	< 1	< 1
Mo	< 2	< 2	< 2	< 2	< 2	8	< 2	4	< 2	< 2
Nb	0.9	< 0.2	7.7	1.3	< 0.2	23	0.4	3.1	1.1	1.5
Ni	55	59	43	61	262	9	288	95	20	23
Pb	< 5	< 5	6	7	< 5	12	21	8	44	9
Rb	177	151	304	230	21	123	4	37	155	126
S (%)	2.13	2.26	0.854	2.83	0.065	0.39	4.49	4.9	0.459	0.945
Sb (ppm)	0.6	0.7	0.8	3.2	0.4	0.2	0.3	0.2	0.5	0.7
Sc	41.3	39.9	29.8	47.5	31.5	3.48	35.5	30.8	4.88	8.84
Se	< 0.5	< 0.5	< 0.5	< 0.5	< 0.5	< 0.5	< 0.5	< 0.5	< 0.5	< 0.5
Sample ID	PVS051	PVS052	PVS053	PVS054	PVS054B	PVS055	PVS056	PVS057	PVS058	PVS096
Sn	< 1	< 1	< 1	< 1	< 1	1	1	< 1	< 1	1
Sr	476	577	385	205	269	272	35	198	605	50
Ta	0.87	0.4	0.52	0.14	0.13	0.37	0.14	0.27	0.82	0.63
Th	0.81	0.45	10.9	0.45	0.23	8.07	0.14	0.73	2.27	1.64
U	0.32	0.2	2.36	0.22	0.03	0.54	0.06	0.26	0.43	0.57
V	278	288	248	317	196	17	202	147	47	127
W	500	447	58	61	182	317	267	389	875	703
Y	17	20	34	13	12	11	22	23	2	6
Zn	115	121	263	198	85	6	100	52	121	123
Zr	69	50	238	58	28	69	21	15	57	15
La	6.76	4.34	84.5	4.77	2.23	15.3	2.02	5.22	13.7	3.68
Ce	15	10.3	175	10.5	5.25	30.4	4.28	10.1	27.3	7.66
Pr	2.14	1.49	22.5	1.47	0.77	3.72	0.67	1.37	3.28	0.97
Nd	9.08	6.65	87.9	6.95	3.6	14	2.98	5.99	11.9	3.77
Sm	2.56	2.27	18.6	2.1	1.28	3.19	1.21	2.01	1.92	0.87
Eu	0.743	0.571	3.34	0.65	0.491	1.49	0.491	0.586	0.668	0.167
Gd	2.76	2.79	14.3	2.46	1.63	4.07	1.95	2.48	0.91	0.98

Tb	0.47	0.54	1.77	0.44	0.33	0.61	0.44	0.46	0.1	0.17
Dy	3.03	3.72	8.35	2.79	2.29	2.78	3.24	2.97	0.48	0.98
Ho	0.65	0.84	1.34	0.59	0.51	0.38	0.73	0.63	0.07	0.17
Er	1.98	2.68	3.35	1.75	1.61	0.77	2.49	1.94	0.16	0.44
Tl	35.8	31.5	54.3	16.1	1.25	0.93	0.24	0.89	2.99	3.06
Tm	0.307	0.424	0.453	0.271	0.244	0.077	0.433	0.332	0.02	0.057
Yb	2.1	2.88	2.83	1.89	1.58	0.43	3.09	2.25	0.11	0.35
Lu	0.353	0.489	0.458	0.327	0.242	0.058	0.471	0.313	0.017	0.049
Mass (g)	1.041	1.005	1.057	1.059	1.084	1.185	1.727	1.377	1.13	1.119

6264

Sample ID	PVS097	PVS098	PVS099	PVS100	PVS101	PVS102	PVS103	PVS104	PVS105	PVS106
SiO2 (%)	69.76	47.75	34.01	62.72	54.64	58.72	51.2	50.77	47.21	68.01
Al2O3	16.14	19.1	8.52	2.98	5.38	15.79	16.01	13.97	31.83	17.75
Fe2O3(T)	2.56	9.23	38.37	29.16	34.08	9.03	11.85	14.65	0.85	2.14
MnO	0.035	0.153	0.955	0.099	0.136	0.217	0.328	0.239	0.011	0.036
MgO	1.04	6.48	3.23	0.96	1.5	3.48	3.46	5.71	0.19	0.73
CaO	2.59	10.47	10.91	2.65	4.07	6.52	11.93	10.02	16.34	3.21
Na2O	4.81	2.74	0.4	0.27	0.54	3.7	2.13	2.63	2.21	4.85
K2O	2.36	1.33	0.19	0.21	0.39	0.48	0.3	0.53	0.03	1.58
TiO2	0.318	0.64	0.725	0.073	0.125	0.799	1.115	1.054	0.038	0.271
P205	0.11	0.05	0.04	0.12	0.13	0.08	0.08	0.08	< 0.01	0.07
LOI	1.14	2.87	1.55	–0.08	–0.01	0.75	1.39	1.13	0.57	1.11
Total	100.9	100.8	98.89	99.16	101	99.57	99.8	100.8	99.28	99.75
Au (ppb)	< 1	25	< 1	26	14	< 1	< 1	< 1	< 1	13
Ag (ppm)	< 0.5	< 0.5	< 0.5	< 0.5	< 0.5	< 0.5	< 0.5	< 0.5	< 0.5	0.5
As	< 1	< 1	< 1	2	< 1	< 1	< 1	< 1	< 1	< 1
Ba	972	309	51	23	37	276	82	62	23	488
Be	2	< 1	< 1	3	3	< 1	< 1	< 1	< 1	3

Bi	0.1	0.2	0.2	0.1	0.1	< 0.1	< 0.1	< 0.1	< 0.1	< 0.1
Br	< 0.5	< 0.5	< 0.5	< 0.5	< 0.5	< 0.5	10.8	< 0.5	< 0.5	< 0.5
Cd	< 0.5	< 0.5	1.2	0.8	0.9	< 0.5	< 0.5	< 0.5	< 0.5	< 0.5
Co	40.6	63.9	36.5	31.4	20.4	62.2	78.9	63.4	19.4	40.3
Cr	15.5	320	32	14	16.5	101	290	47.8	< 0.5	8.7
Cs	2	2	1.5	0.6	1.4	5.2	1.7	0.4	< 0.1	4.2
Cu	12	30	14	93	76	14	134	139	5	5
Ga	21	15	16	5	7	17	18	16	20	24
Ge	1.3	2	2.4	7.9	9	1.8	2.1	3	0.8	1.3
Hf	2.8	0.8	1	0.6	1	2.2	1.6	1.4	< 0.1	3.5
Hg	< 1	< 1	< 1	< 1	< 1	< 1	< 1	< 1	< 1	< 1
In	< 0.1	< 0.1	< 0.1	< 0.1	< 0.1	< 0.1	< 0.1	< 0.1	< 0.1	< 0.1
Ir	< 1	< 1	< 1	< 1	< 1	< 1	< 1	< 1	< 1	< 1
Mo	< 2	< 2	< 2	< 2	3	< 2	< 2	< 2	< 2	< 2
Nb	2.7	2.6	1	0.3	0.7	1.9	1.5	1.3	< 0.2	2.3
Ni	21	97	40	9	7	64	139	52	3	12
Pb	12	< 5	< 5	< 5	< 5	< 5	< 5	< 5	< 5	17
Rb	59	43	12	5	10	42	12	8	< 1	57
S (%)	0.025	0.066	0.045	0.069	0.074	0.025	0.317	0.161	0.05	0.065
Sb (ppm)	< 0.1	< 0.1	0.3	0.4	0.5	< 0.1	< 0.1	< 0.1	0.2	1
Sc	3.51	30.5	11.6	2.18	3.41	25.2	42.4	45.2	0.77	2.89
Se	< 0.5	< 0.5	< 0.5	< 0.5	< 0.5	< 0.5	< 0.5	< 0.5	< 0.5	< 0.5
Sample ID	PVS097	PVS098	PVS099	PVS100	PVS101	PVS102	PVS103	PVS104	PVS105	PVS106
Sn	1	< 1	1	2	2	2	1	< 1	< 1	< 1
Sr	684	369	13	6	11	205	178	179	201	633
Ta	0.52	0.15	0.17	0.21	0.14	0.38	0.34	0.16	0.12	0.51
Th	5.74	0.24	0.61	0.34	0.86	0.78	0.26	0.36	< 0.05	6.03
U	1.14	0.08	0.16	0.12	0.27	0.22	0.1	0.11	< 0.01	1.49
V	38	214	202	23	34	212	314	327	8	26
W	353	250	152	242	134	269	207	94	152	325

Y	6	11	11	3	5	15	22	19	< 1	5
Zn	56	65	146	38	42	103	87	87	6	42
Zr	116	33	45	31	49	89	60	54	3	139
La	27.5	2.18	4.78	2.91	5.22	5.76	4.18	3.85	0.43	32.8
Ce	56.5	5.49	9.46	8.09	12.6	13.3	10.1	10.1	0.76	66.2
Pr	6.8	0.85	1.16	0.98	1.62	1.79	1.61	1.56	0.09	7.78
Nd	24.9	3.95	4.67	3.52	6.02	8.01	7.08	7.2	< 0.05	28.4
Sm	3.88	1.32	1.37	1.1	1.51	2.13	2.51	2.38	0.08	4.27
Eu	1.02	0.551	0.637	0.999	1.27	0.819	1.01	0.879	0.239	1.11
Gd	2.23	1.68	1.53	1.14	1.57	2.41	3.05	2.83	0.07	2.21
Tb	0.28	0.32	0.26	0.2	0.27	0.44	0.55	0.57	0.01	0.24
Dy	1.17	2.01	1.59	1.17	1.57	2.7	3.6	3.41	0.05	0.92
Ho	0.2	0.4	0.35	0.23	0.32	0.53	0.77	0.77	< 0.01	0.16
Er	0.56	1.22	1.14	0.68	0.96	1.61	2.25	2.2	0.02	0.41
Tl	0.69	0.35	0.17	0.09	0.11	0.18	0.1	0.09	< 0.05	0.36
Tm	0.08	0.205	0.19	0.109	0.162	0.262	0.357	0.366	< 0.005	0.051
Yb	0.43	1.39	1.3	0.7	1.05	1.75	2.36	2.24	0.02	0.31
Lu	0.055	0.195	0.207	0.1	0.148	0.244	0.351	0.321	< 0.002	0.044
Mass (g)	1.241	1.36	1.899	1.478	1.605	1.441	1.336	1.441	1.324	1.351

6265

Sample ID	PVS107	PVS108	PVS109	PVS110	PVS111	PVS112	PVS113	PVS114	PVS115	PVS116
SiO2 (%)	66.81	66.66	92.36	50.46	63.97	55.61	46.6	46.64	49.7	70.55
Al2O3	15.72	15.41	1.47	12.61	21.42	21.39	14.6	17.56	18.58	14.66
Fe2O3(T)	4.48	4.21	1.87	18.68	6.97	9.32	14.88	13	10.33	3.05
MnO	0.105	0.109	0.02	0.251	0.043	0.22	0.48	0.337	0.191	0.046
MgO	1.85	2.43	0.3	3.93	1.65	4.22	7.49	5.27	4.38	1.03
CaO	3.63	3.22	0.23	8.34	0.56	1.06	10.46	8.07	5.24	1.42

Na2O	3.76	3.29	0.27	2.56	1.15	1.26	2.29	3.34	3.18	3.35
K2O	1.64	2.28	0.27	0.74	1.51	3.25	0.83	1.9	3.01	4.42
TiO2	0.394	0.381	0.056	2.072	1.481	0.762	1.076	1.191	1.118	0.301
P205	0.22	0.21	0.02	0.27	0.03	0.34	0.08	0.09	0.09	0.12
LOI	1.41	1.58	2.78	0.1	1.73	1.86	1.45	3.51	4.74	1
Total	100	99.78	99.66	100	100.5	99.29	100.2	100.9	100.6	99.94
Au (ppb)	69	43	73	< 1	21	2	233	616	345	117
Ag (ppm)	< 0.5	< 0.5	< 0.5	< 0.5	< 0.5	< 0.5	< 0.5	< 0.5	< 0.5	< 0.5
As	< 1	< 1	< 1	2	5	5	< 1	< 1	< 1	< 1
Ba	404	657	50	230	288	522	236	1402	2578	2263
Be	2	2	< 1	1	4	5	3	4	3	1
Bi	0.3	0.4	0.3	< 0.1	< 0.1	< 0.1	1.3	0.8	0.6	0.2
Br	< 0.5	< 0.5	< 0.5	< 0.5	< 0.5	< 0.5	< 0.5	< 0.5	< 0.5	< 0.5
Cd	< 0.5	< 0.5	< 0.5	0.5	< 0.5	< 0.5	0.7	0.5	< 0.5	< 0.5
Co	42.1	35.8	82.1	79.2	59.8	58.5	47.4	71.4	47.4	37.9
Cr	72.4	82.7	21.2	29.1	111	118	48.3	67.6	110	31.3
Cs	14.2	21.5	3.2	1.1	6.9	17.1	0.8	14.9	32.3	9.4
Cu	25	13	33	160	25	18	50	70	86	22
Ga	19	19	2	20	25	30	20	21	22	18
Ge	1.1	1	0.5	2.5	1.6	2.2	3.2	2.3	1.8	1.4
Hf	3.1	3	0.3	4.5	2.2	4.6	1.8	1.7	2.1	2.7
Hg	< 1	< 1	< 1	< 1	< 1	< 1	< 1	< 1	< 1	< 1
In	< 0.1	< 0.1	< 0.1	< 0.1	< 0.1	< 0.1	< 0.1	< 0.1	< 0.1	< 0.1
Ir	< 1	< 1	< 1	< 1	< 1	< 1	< 1	< 1	< 1	< 1
Mo	< 2	< 2	< 2	< 2	< 2	< 2	< 2	< 2	2	< 2
Nb	2.7	3.2	< 0.2	7.3	3.1	4.4	1.4	10	2	2.7
Ni	58	22	31	33	55	46	32	35	38	31
Pb	17	18	< 5	< 5	31	13	< 5	7	8	32
Rb	92	131	18	23	66	136	9	100	206	141
S (%)	0.436	0.05	0.305	0.173	0.324	0.138	0.906	1.96	1.71	0.342

Sb (ppm)	0.9	1	0.4	0.7	1.3	1.1	2.1	1.9	1.5	0.4
Sc	6.87	6.37	1.05	41.9	48.3	24.9	50.3	61.7	44.9	4.82
Se	< 0.5	< 0.5	< 0.5	< 0.5	< 0.5	< 0.5	< 0.5	< 0.5	< 0.5	< 0.5
Sample ID	PVS107	PVS108	PVS109	PVS110	PVS111	PVS112	PVS113	PVS114	PVS115	PVS116
Sn	< 1	< 1	< 1	2	1	1	1	1	< 1	2
Sr	414	413	30	136	440	304	238	354	380	407
Ta	0.51	0.51	0.64	0.74	0.42	0.61	0.3	0.28	0.19	0.4
Th	7.44	7.2	0.71	2.76	0.57	9.84	0.42	2.35	0.85	5.82
U	1.59	0.95	0.12	0.74	0.4	2.18	0.21	0.63	0.63	1.19
V	61	55	14	439	355	202	464	371	293	50
W	287	238	948	309	341	329	190	154	104	263
Y	6	5	< 1	47	34	23	25	34	40	6
Zn	112	86	17	146	91	109	232	182	166	70
Zr	131	128	12	182	85	184	64	70	81	116
La	16.9	10	0.36	18.1	6.97	58.8	4.44	5.63	8.04	34.5
Ce	33.9	19.2	0.76	40.6	16.1	123	11.8	14.6	19	70.5
Pr	3.97	2.25	0.09	5.51	2.35	15.4	1.81	2.34	2.71	8.58
Nd	14.7	8.27	< 0.05	24	11.1	59.7	8.42	11.5	12.3	32.4
Sm	2.62	1.48	0.07	6.3	3.01	9.92	2.65	3.56	3.91	4.95
Eu	0.781	0.663	0.05	1.91	1.15	2.88	0.984	1.67	1.45	1.28
Gd	1.68	0.97	0.08	6.68	3.85	6.34	3.19	4.38	5.21	2.76
Tb	0.23	0.14	0.01	1.2	0.78	0.86	0.6	0.84	1.04	0.33
Dy	1.11	0.82	0.06	7.57	5.13	4.02	3.96	5.38	6.93	1.37
Ho	0.2	0.17	0.01	1.53	1.07	0.75	0.89	1.14	1.4	0.23
Er	0.6	0.47	0.03	4.79	3.22	2.11	2.66	3.48	4.25	0.62
Tl	1.17	1.98	0.53	0.3	3.55	5.25	0.84	1.62	3.32	1.89
Tm	0.089	0.077	0.005	0.753	0.489	0.326	0.448	0.601	0.675	0.08
Yb	0.54	0.49	0.03	4.92	3.04	1.95	2.85	3.68	4.31	0.49
Lu	0.073	0.066	< 0.002	0.72	0.416	0.261	0.396	0.55	0.578	0.058

Mass (g)	1.237	1.311	1.311	1.473	1.316	1.326	1.346	1.269	1.303	1.352

6266

Sample ID	PVS117	PVS118	PVS119	PVS120	PVS121	PVS122	PVS123	PVS124	PVS125	PVS126
SiO2 (%)	84.3	69.81	73.65	58.22	56.39	50.89	69.27	63.75	72.54	55.78
Al2O3	7.9	15.77	13.98	12.18	13.97	14.06	14.78	17.11	14.03	12.88
Fe2O3t	1.82	2.62	2	10.16	10.22	15.91	2.91	4.9	1.11	9.59
MnO	0.017	0.068	0.055	0.303	0.406	0.32	0.069	0.13	0.024	0.221
MgO	0.21	1.41	1.04	3.22	3.15	5.16	0.93	1.82	0.27	6.58
CaO	1.5	2.71	2.23	6.64	10.61	3.47	2.26	3.6	1.03	7.5
Na2O	2.54	3.87	3.14	1.5	1.76	1.78	2.79	4.16	2.16	1.43
K2O	0.45	3.22	3.64	1.52	0.44	3.39	4.89	3.12	7.07	3.43
TiO2	0.066	0.27	0.215	0.695	0.679	0.985	0.254	0.529	0.088	0.92
P205	0.01	0.12	0.09	0.11	0.11	0.09	0.13	0.34	0.02	0.83
LOI	0.95	1.11	0.92	6.08	1.82	4.21	1.18	1.15	1.7	1.6
Total	99.75	101	101	100.6	99.55	100.3	99.46	100.6	100	100.8
Au (ppb)	73	45	36	512	378	698	89	43	42	18
Ag (ppm)	< 0.5	< 0.5	< 0.5	0.5	< 0.5	0.9	< 0.5	< 0.5	< 0.5	< 0.5
As	3	< 1	< 1	2	2	< 1	4	3	3	11
Ba	81	911	1084	277	74	908	948	257	985	2359
Be	1	3	2	4	3	2	2	3	1	3
Bi	0.1	0.1	< 0.1	1	0.7	1.1	0.1	0.1	< 0.1	1
Br	< 0.5	< 0.5	< 0.5	< 0.5	< 0.5	< 0.5	< 0.5	< 0.5	< 0.5	< 0.5
Cd	< 0.5	< 0.5	< 0.5	< 0.5	< 0.5	< 0.5	< 0.5	< 0.5	< 0.5	< 0.5
Co	54.6	35.9	34.7	64.8	63.9	108	42.6	49.9	36.9	53.7
Cr	14.8	35.3	22.9	39.2	51.7	55.2	48.8	32.9	14.1	216
Cs	1.1	9.3	8.3	12.2	1.4	31.7	10.6	18.4	7.6	9.3
Cu	20	14	11	96	88	184	20	18	8	5
Ga	11	20	18	17	17	20	18	28	14	19
Ge	1	1.3	1.6	2	1.6	1.8	1.9	1.9	1.4	1.9

Hf	1.5	2.7	2.3	1.5	2	1.6	2.4	2.9	5.4	5.6
Hg	< 1	< 1	< 1	< 1	< 1	< 1	< 1	< 1	< 1	< 1
In	< 0.1	< 0.1	< 0.1	< 0.1	< 0.1	< 0.1	< 0.1	< 0.1	< 0.1	< 0.1
Ir	< 1	< 1	< 1	< 1	< 1	< 1	< 1	34	< 1	< 1
Mo	< 2	< 2	< 2	< 2	< 2	3	< 2	< 2	< 2	< 2
Nb	0.7	2.6	2.1	2.1	2	2.4	3.3	19.3	0.7	18.5
Ni	22	21	20	53	40	65	36	24	7	52
Pb	17	24	29	< 5	6	< 5	38	28	43	20
Rb	20	131	129	91	6	248	171	181	209	118
S (%)	0.593	0.394	0.224	2.37	2.39	3.8	0.359	0.253	0.118	0.055
Sb (ppm)	0.5	0.7	0.5	2.1	2	2.1	1	< 0.1	0.5	2.3
Sc	1.43	3.51	3.39	32.4	26.7	37.9	6.16	11.3	2.58	23.1
Se	< 0.5	< 0.5	< 0.5	< 0.5	< 0.5	< 0.5	< 0.5	< 0.5	< 0.5	< 0.5
Sample ID	PVS117	PVS118	PVS119	PVS120	PVS121	PVS122	PVS123	PVS124	PVS125	PVS126
Sn	< 1	3	2	3	1	2	3	5	1	2
Sr	160	331	302	217	290	219	255	248	255	1435
Ta	0.51	0.57	0.52	0.44	0.41	0.53	0.77	1.76	0.44	0.7
Th	1.82	5.19	7.08	1.45	2.58	0.52	8.28	8.08	22.6	10.7
U	1.97	2.38	10.6	1.29	0.6	0.66	4.76	18.8	1.83	3.07
V	16	35	29	237	220	274	50	120	23	187
W	510	271	313	338	345	486	339	386	306	167
Y	2	7	6	21	17	15	7	15	4	42
Zn	46	90	70	130	129	206	85	151	28	149
Zr	58	104	90	57	85	64	93	106	182	250
La	4.98	24.9	22.2	11.9	15	5.26	26.7	12.7	30.8	87.3
Ce	9.67	51.3	45.6	25.1	31.1	12.4	53.8	25.8	60.1	193
Pr	1.1	6.25	5.48	3.32	3.92	1.68	6.44	3.29	6.83	23.8
Nd	3.63	23.6	21	14.2	15.4	6.81	24.3	13.5	23.5	97.1
Sm	0.84	3.75	3.35	3.36	3.17	1.93	3.95	3.1	3.45	18.8
Eu	0.464	0.885	0.661	1.13	0.888	0.716	0.675	0.568	0.622	4.95

Gd	0.52	2.27	1.99	3.17	2.84	2.01	2.45	2.87	1.61	13.8
Tb	0.07	0.28	0.25	0.6	0.47	0.4	0.28	0.4	0.18	1.83
Dy	0.35	1.23	1.16	3.7	2.55	2.6	1.31	2.43	0.79	8.53
Ho	0.05	0.2	0.2	0.71	0.52	0.52	0.22	0.46	0.14	1.45
Er	0.15	0.55	0.55	2.03	1.5	1.58	0.6	1.28	0.43	3.73
Tl	0.56	1.36	1.35	1.19	0.31	2.71	2.01	1.9	2.2	1.34
Tm	0.022	0.072	0.082	0.328	0.231	0.262	0.089	0.188	0.066	0.521
Yb	0.13	0.43	0.43	2.08	1.53	1.67	0.55	1.26	0.43	3.05
Lu	0.015	0.062	0.051	0.299	0.223	0.233	0.081	0.189	0.064	0.426
Mass (g)	1.242	1.144	1.236	1.524	1.335	1.302	1.216	1.172	1.09	1.314

6267

Sample ID	PVS127	PVS128	PVS129	PVS130	PVS131	PVS132	PVS133	PVS134	PVS135	PVS136
SiO2 (%)	53.59	68.42	62.6	68.28	66.87	68.51	68.04	45.03	46.39	45.88
Al2O3	13.51	15.37	14.63	15.47	16.15	16.41	16.1	13.14	13.39	12.33
Fe2O3(T)	9.68	3.57	6.58	3.13	3.79	3.19	4.56	17.57	17.44	14.88
MnO	0.287	0.087	0.178	0.09	0.139	0.109	0.087	0.541	0.648	0.43
MgO	6.93	1.54	4.87	2.21	2.51	1.63	1.48	5.79	5.72	5.56
CaO	8.11	2.83	2.79	2.92	4.42	4.7	4.75	13.87	11.53	15.21
Na2O	1.6	3.23	2.44	3.31	3.16	3.17	2.89	0.83	0.92	0.4
K2O	2.43	3.57	3.52	3.55	2.15	1.63	1.3	0.37	0.5	0.1
TiO2	0.919	0.391	0.529	0.394	0.421	0.393	0.381	0.904	0.968	0.864
P205	0.83	0.21	0.4	0.21	0.26	0.11	< 0.01	0.08	0.08	0.1
LOI	1.24	0.94	1.88	1.07	0.76	0.64	1.21	2.55	2.49	3.16
Total	99.12	100.2	100.4	100.6	100.6	100.5	100.8	100.7	100.1	98.91
Au (ppb)	< 1	25	33	38	25	< 1	< 1	1660	398	245
Ag (ppm)	0.5	< 0.5	< 0.5	< 0.5	< 0.5	< 0.5	< 0.5	0.9	0.7	< 0.5
As	8	2	4	< 1	< 1	< 1	< 1	< 1	< 1	< 1
Ba	1053	1902	365	1091	857	855	896	73	77	79

Be	4	1	1	2	3	8	3	1	2	< 1
Bi	1.4	0.2	0.5	0.4	0.2	0.2	0.1	3.2	3.3	2.2
Br	< 0.5	< 0.5	< 0.5	< 0.5	< 0.5	< 0.5	< 0.5	< 0.5	< 0.5	< 0.5
Cd	< 0.5	< 0.5	< 0.5	< 0.5	< 0.5	< 0.5	< 0.5	< 0.5	< 0.5	< 0.5
Co	52.9	52.3	58.6	47.8	34.3	32	61.2	53.9	52.7	98.8
Cr	222	73.7	210	73	85.2	43.7	52.2	48.9	54.4	49.2
Cs	12.3	12.6	32.4	18.2	21.5	14.5	12.3	0.3	0.9	0.3
Cu	4	33	18	12	2	4	5	175	155	42
Ga	20	20	22	20	21	25	18	17	16	18
Ge	2.4	1.1	1.4	1	1.5	0.8	0.9	2.1	2.3	2.5
Hf	6.4	3.1	3.2	3.1	3.3	2.9	2.8	1.4	1.4	1.3
Hg	< 1	< 1	< 1	< 1	< 1	< 1	< 1	< 1	< 1	< 1
In	< 0.1	< 0.1	< 0.1	< 0.1	< 0.1	< 0.1	< 0.1	< 0.1	< 0.1	< 0.1
Ir	< 1	< 1	< 1	< 1	< 1	< 1	< 1	< 1	< 1	< 1
Mo	< 2	< 2	< 2	< 2	< 2	< 2	< 2	< 2	< 2	< 2
Nb	9.9	3.1	5.6	3	5.2	13.6	8.5	1.3	1.2	7.9
Ni	48	55	118	54	55	28	26	61	57	57
Pb	13	25	11	21	17	19	15	< 5	< 5	< 5
Rb	117	124	221	141	164	131	117	4	6	1
S (%)	0.094	0.483	0.265	0.329	0.021	0.034	0.065	4	3.43	2.21
Sb (ppm)	2.2	0.7	1.1	1.5	0.6	0.4	1	2.9	3.1	3.3
Sc	23.6	6.82	10.3	5.94	6.39	3.93	4.21	39.9	43.3	41.3
Se	< 0.5	< 0.5	< 0.5	< 0.5	< 0.5	< 0.5	< 0.5	< 0.5	< 0.5	< 0.5
Sample ID	PVS127	PVS128	PVS129	PVS130	PVS131	PVS132	PVS133	PVS134	PVS135	PVS136
Sn	3	< 1	2	< 1	< 1	< 1	< 1	< 1	1	< 1
Sr	965	466	249	331	399	461	288	199	182	371
Ta	0.72	0.53	0.7	0.49	0.56	0.45	0.53	0.3	0.19	0.47
Th	12.6	7.78	10.7	7.61	7.96	8.73	4.01	0.33	0.4	0.43
U	3.19	2.07	2.04	1.76	1.69	3.26	0.76	0.12	0.12	0.11
V	190	58	86	55	62	50	51	304	310	318

W	260	318	341	258	250	250	490	322	157	461
Y	44	7	12	10	11	12	6	24	22	22
Zn	173	67	127	57	75	71	44	131	154	113
Zr	270	134	144	137	151	115	100	53	56	54
La	91.1	11.3	24.4	46.2	51.5	31.1	2.96	4.88	4.5	7.17
Ce	195	24.5	55.9	96.9	105	61	7.31	11.4	10.7	13.9
Pr	25	3.01	7.61	12.1	13.1	7.7	1.02	1.68	1.62	2.04
Nd	101	11.1	33.3	45.1	48.2	28.6	4.44	7.82	7.44	9.26
Sm	19.5	2.13	5.46	7.17	7.95	4.76	1.19	2.39	2.34	2.54
Eu	4.79	0.793	1.24	1.85	1.84	1.31	0.402	0.864	0.869	0.907
Gd	13.7	1.58	3.29	4	4.46	3.41	1.14	3.01	3.01	3.08
Tb	1.79	0.25	0.42	0.46	0.5	0.46	0.17	0.58	0.55	0.59
Dy	8.09	1.22	2.02	1.89	2.19	2.24	0.96	3.66	3.6	3.69
Ho	1.4	0.23	0.38	0.34	0.35	0.39	0.2	0.8	0.78	0.77
Er	3.54	0.63	1.05	0.88	0.85	0.96	0.59	2.41	2.36	2.28
Tl	1.45	1.59	3.18	2.31	2.3	2	1.87	0.42	0.28	0.29
Tm	0.495	0.089	0.155	0.112	0.108	0.126	0.095	0.399	0.386	0.361
Yb	2.81	0.62	0.94	0.64	0.65	0.71	0.61	2.63	2.54	2.35
Lu	0.398	0.094	0.121	0.089	0.086	0.093	0.085	0.383	0.373	0.354
Mass (g)	1.372	1.3	1.115	1.264	1.404	1.381	1.153	1.485	1.433	1.554

6268

Sample ID	PVS137	PVS138	PVS139	PVS140	PVS141	PVS142	PVS143	PVS144	PVS145	PVS146
SiO2 (%)	54.61	55.39	57.9	91.65	49.5	60.51	59.15	69.74	59.14	56.18
Al2O3	14.5	17.95	16.59	2.41	17.34	15.9	18.41	15.94	15.98	17.5
Fe2O3(T)	10.91	7.93	7.28	2.32	12.22	7.95	8.92	4.18	14.25	15.66
MnO	0.434	0.246	0.17	0.051	0.252	0.111	0.862	0.048	0.562	0.593
MgO	5.05	5.62	5	0.98	7.2	2.59	2.75	1.79	4.04	4.25
CaO	8.12	3.98	3.96	0.81	3.45	1.59	1.44	1.02	0.46	0.29
Na2O	1.16	1.17	2.11	0.31	1.67	0.63	1.58	2.12	0.32	0.28

K2O	0.96	2.97	2.52	0.23	3.54	2.42	2.02	1.6	2.88	3.18
TiO2	1.084	1.179	1.091	0.147	1.125	0.64	0.438	0.409	1.05	1.117
P205	0.06	0.1	0.07	0.02	0.09	0.96	0.57	0.26	0.19	0.1
LOI	3.35	4.4	3.35	0.75	4.47	5.61	2.64	3.31	2.02	1.61
Total	100.2	100.9	100	99.68	100.9	98.91	98.78	100.4	100.9	100.7
Au (ppb)	274	89	118	29	216	186	68	1	115	123
Ag (ppm)	< 0.5	< 0.5	0.5	< 0.5	1.1	1	1.2	< 0.5	1.2	1
As	< 1	< 1	< 1	< 1	< 1	1	2	< 1	3	3
Ba	151	481	294	38	438	613	365	298	337	389
Be	1	1	2	< 1	2	3	4	4	3	3
Bi	0.7	0.2	0.1	< 0.1	0.3	0.2	< 0.1	< 0.1	< 0.1	< 0.1
Br	< 0.5	< 0.5	< 0.5	9.1	< 0.5	< 0.5	< 0.5	< 0.5	< 0.5	< 0.5
Cd	< 0.5	< 0.5	< 0.5	< 0.5	< 0.5	< 0.5	< 0.5	< 0.5	1.1	1.4
Co	110	53.9	77.9	66.2	72.4	46.4	57.8	49.2	81.2	102
Cr	114	144	135	23.8	139	213	109	69.9	129	134
Cs	0.9	10.6	15.1	0.9	13.8	14.4	9.6	6.7	15.6	16.1
Cu	177	61	103	29	160	142	58	16	127	143
Ga	16	20	20	3	18	23	23	19	18	19
Ge	2.1	1.4	1.3	0.7	1.5	1.5	3	1.5	2.3	3.1
Hf	1.7	1.8	1.6	0.2	1.6	3.4	4	2.6	1.5	1.7
Hg	< 1	< 1	< 1	< 1	< 1	< 1	< 1	< 1	< 1	< 1
In	< 0.1	< 0.1	< 0.1	< 0.1	< 0.1	< 0.1	< 0.1	< 0.1	< 0.1	< 0.1
Ir	< 1	< 1	< 1	< 1	< 1	< 1	< 1	< 1	< 1	< 1
Mo	< 2	< 2	< 2	< 2	< 2	< 2	< 2	< 2	< 2	< 2
Nb	1	3	8.7	0.4	2.7	5.9	3.5	1.9	1.7	2.6
Ni	81	64	79	23	79	120	42	37	91	82
Pb	< 5	52	26	< 5	< 5	6	37	13	84	137
Rb	48	145	116	9	147	109	87	72	123	128
S (%)	1.4	0.326	0.595	0.219	1.79	1.71	0.485	0.028	1.35	1.3
Sb (ppm)	1	0.5	0.4	0.3	0.6	1	0.8	0.8	0.8	1.1

Sc	49.9	51.9	44.9	6.13	44.3	16.3	19.1	6.15	49	46.3
Se	< 0.5	< 0.5	< 0.5	< 0.5	< 0.5	< 0.5	< 0.5	< 0.5	< 0.5	< 0.5
Sample ID	PVS137	PVS138	PVS139	PVS140	PVS141	PVS142	PVS143	PVS144	PVS145	PVS146
Sn	< 1	< 1	< 1	< 1	< 1	< 1	< 1	< 1	< 1	1
Sr	194	146	221	23	112	75	183	220	51	37
Ta	0.35	0.24	0.27	0.49	0.18	0.6	0.48	0.47	0.34	0.46
Th	0.51	0.67	0.39	0.08	0.7	11.3	8.85	7.32	0.34	0.49
U	0.11	0.18	0.14	0.02	0.14	4.6	2.39	1.9	0.21	0.2
V	318	263	328	43	261	118	173	159	330	386
W	366	124	223	655	97	143	247	348	312	370
Y	24	12	12	3	16	52	26	10	21	21
Zn	135	124	96	24	159	111	108	65	264	346
Zr	67	72	64	10	65	152	171	126	61	70
La	5.55	5.43	4.28	0.62	5.16	95.7	53.7	44.9	4.11	4.97
Ce	13.3	11.8	10.4	1.56	10.8	196	114	92.1	10.3	11.9
Pr	1.92	1.42	1.57	0.26	1.48	24.9	14.2	11.6	1.58	1.82
Nd	8.93	6.29	7.24	1.26	6.62	98.8	57.6	43.5	8.32	8.05
Sm	2.71	1.69	2.11	0.39	1.78	17.9	10.2	7.4	2.81	2.45
Eu	0.99	0.487	0.667	0.094	0.679	3.73	2.68	1.91	0.685	0.608
Gd	3.29	2.17	2.11	0.39	2.11	12.4	6.45	4.8	3.07	2.85
Tb	0.61	0.37	0.32	0.07	0.4	1.7	0.84	0.57	0.57	0.55
Dy	3.92	2.3	1.9	0.43	2.55	8.09	4.21	2.3	3.5	3.58
Ho	0.82	0.47	0.43	0.09	0.51	1.45	0.81	0.33	0.7	0.73
Er	2.42	1.5	1.58	0.27	1.59	4.18	2.38	0.71	1.98	2.09
Tl	0.5	2.72	2.94	0.61	3.47	2.97	3.08	1.64	3.77	4.24
Tm	0.385	0.234	0.278	0.039	0.276	0.641	0.363	0.076	0.315	0.315
Yb	2.56	1.53	1.78	0.25	1.72	3.86	2.3	0.37	2.05	2.03
Lu	0.364	0.212	0.253	0.034	0.239	0.567	0.318	0.05	0.284	0.277
Mass (g)	1.326	1.289	1.433	1.274	1.547	1.298	1.322	1.342	1.537	1.353

Sample ID	PVS147	PVS148	PVS149	PVS150	PVS151	PVS152	PVS153	PVS154	PVS155	PVS156
SiO2 (%)	60.19	56.4	48.58	56.18	57.03	46.28	58.34	59.29	55.96	56.94
Al2O3	17.29	16.68	18.29	18.06	17.15	16.47	18.79	14.02	14.09	17.14
Fe2O3(T)	12.12	14.94	23.35	15.62	13.23	21.35	12.1	14.59	15.83	15.82
MnO	0.58	0.259	0.494	0.23	0.235	1.107	0.351	0.276	0.24	0.431
MgO	3.88	4.57	3.91	4.23	3.88	5.63	3.89	3.69	4.38	4.78
CaO	0.46	0.4	0.18	0.12	0.07	0.31	0.1	0.15	0.29	0.23
Na2O	0.23	0.88	0.15	0.19	0.16	0.3	0.26	0.37	0.98	0.23
K2O	2.67	3.11	2.34	2.81	3.23	4.33	3.39	3.06	3.57	2.55
TiO2	0.967	1.075	1.211	1.189	1.116	1.26	1.305	0.887	1.01	0.848
P205	0.23	0.04	0.04	0.04	< 0.01	0.03	0.02	0.03	0.05	0.02
LOI	2.37	2.47	1.91	1.47	2.38	1.37	1.48	4.49	4.52	1.4
Total	101	100.8	100.5	100.1	98.48	98.45	100	100.9	100.9	100.4
Au (ppb)	21	154	121	262	189	213	76	250	270	77
Ag (ppm)	< 0.5	1	0.7	0.8	1.3	1.3	< 0.5	1.6	1.5	< 0.5
As	2	< 1	< 1	< 1	1	< 1	< 1	< 1	< 1	< 1
Ba	343	342	304	315	469	694	638	285	339	223
Be	3	3	2	3	3	2	3	2	3	3
Bi	< 0.1	0.1	< 0.1	< 0.1	< 0.1	< 0.1	< 0.1	< 0.1	0.1	< 0.1
Br	< 0.5	< 0.5	< 0.5	< 0.5	< 0.5	< 0.5	< 0.5	< 0.5	< 0.5	< 0.5
Cd	< 0.5	< 0.5	0.7	< 0.5	< 0.5	0.7	< 0.5	< 0.5	< 0.5	1
Co	42	114	81.7	95.9	77.3	95.5	74.4	108	105	110
Cr	114	122	153	145	123	93.8	81.3	78.5	70.6	83.1
Cs	14.2	15.8	13.3	15.8	16.9	20.6	15.3	14.6	15.6	11.3
Cu	34	245	142	164	195	256	116	233	321	116
Ga	17	20	27	24	24	20	25	19	18	19
Ge	3.6	2.4	3.1	2.1	2.1	5.7	2.9	2.6	2.4	3.3
Hf	1.8	1.6	1.8	1.7	1.8	1.4	2.1	1.2	1.4	2.2

Hg	< 1	< 1	< 1	< 1	< 1	< 1	1	< 1	< 1	< 1
In	< 0.1	< 0.1	< 0.1	< 0.1	< 0.1	< 0.1	< 0.1	< 0.1	< 0.1	< 0.1
Ir	< 1	< 1	< 1	< 1	< 1	< 1	< 1	< 1	< 1	< 1
Mo	< 2	< 2	< 2	< 2	< 2	< 2	< 2	< 2	< 2	< 2
Nb	1.1	3.6	1.5	1.7	2.2	2.5	3.3	1.8	14.2	1.6
Ni	34	100	70	63	59	101	73	83	85	83
Pb	5	14	< 5	< 5	< 5	9	6	9	11	48
Rb	104	115	98	115	136	181	146	134	141	92
S (%)	0.122	1.72	1.81	1.1	1.56	2.36	0.907	2.92	3.04	0.675
Sb (ppm)	1	1.4	0.9	1.3	1.1	0.8	1.2	1.6	0.8	0.8
Sc	40.1	57.4	59	38.5	53.8	68.8	52.1	34	39.9	68
Se	< 0.5	< 0.5	< 0.5	< 0.5	< 0.5	< 0.5	< 0.5	< 0.5	< 0.5	< 0.5
Sample ID	PVS147	PVS148	PVS149	PVS150	PVS151	PVS152	PVS153	PVS154	PVS155	PVS156
Sn	< 1	1	< 1	< 1	1	1	1	< 1	1	< 1
Sr	41	329	18	20	20	81	72	71	267	124
Ta	0.22	0.4	0.24	0.49	0.28	0.24	0.31	0.37	0.35	0.33
Th	1.24	0.47	0.41	0.48	0.88	0.36	0.6	0.4	0.64	2.21
U	0.38	0.2	0.19	0.18	0.32	0.26	0.29	0.17	0.19	0.34
V	260	383	546	383	344	423	445	293	342	365
W	183	376	267	480	217	187	164	363	248	325
Y	20	37	20	13	31	34	25	16	31	46
Zn	104	155	179	171	161	195	150	124	158	289
Zr	73	66	70	66	74	56	82	56	59	91
La	7.81	5.19	5.02	5.82	5.91	4.52	5.88	3.76	6.1	12.3
Ce	17.9	12.5	12.2	14	13.4	11	14.2	8.35	13.6	29.4
Pr	2.5	1.84	1.84	2.12	1.94	1.66	2.11	1.21	1.98	4.23
Nd	11.4	8.78	8.59	10.6	8.89	8.15	9.93	5.31	9.48	19.2
Sm	2.82	2.61	2.58	2.79	2.44	2.45	2.82	1.28	2.67	5.17
Eu	0.848	0.935	0.742	0.916	0.812	0.656	0.64	0.464	0.883	1.75
Gd	3.03	3.37	2.7	2.57	2.94	3.55	2.99	1.38	3.23	5.23

Tb	0.56	0.71	0.53	0.38	0.58	0.75	0.59	0.3	0.66	1
Dy	3.45	5.2	3.6	2.21	4.2	5.39	3.88	2.12	4.61	7.02
Ho	0.68	1.19	0.76	0.48	0.98	1.12	0.82	0.5	1.01	1.53
Er	1.93	3.82	2.34	1.55	3.33	3.29	2.59	1.69	3.1	4.45
Tl	4.03	4.38	4.04	4.89	6.33	9.03	7.91	7.75	8.67	5.85
Tm	0.296	0.627	0.377	0.261	0.58	0.529	0.427	0.285	0.496	0.672
Yb	1.91	4.07	2.5	1.85	4.06	3.69	2.91	1.95	3.31	4.37
Lu	0.26	0.592	0.371	0.284	0.614	0.544	0.431	0.305	0.498	0.637
Mass (g)	1.5	1.29	1.546	1.539	1.472	1.547	1.448	1.296	1.456	1.388

6272

6273

Sample ID	PVS157	PVS158	PVS159	PVS160	PVS161	PVS162	PVS163	PVS165	PVS166
SiO2 (%)	68.28	40.69	92.6	73.48	72.95	79.52	48.39	37.32	55.63
Al2O3	5.59	2.28	0.35	12.26	9	5.12	17.58	2	16.07
Fe2O3(T)	15.3	7.68	1.3	2.69	7.97	7.6	9.4	40.91	9.73
MnO	0.104	0.32	0.083	0.043	0.108	0.068	0.157	0.265	0.26
MgO	2.36	10.8	1.51	0.61	1.87	1.62	6.58	4.81	3.9
CaO	4.64	18.57	2.5	0.48	2.34	0.98	11.93	6.45	10.37
Na2O	0.46	2.93	0.09	1.13	0.88	0.92	2.84	0.2	2.43
K2O	0.16	1.75	0.06	8.33	2.31	1.22	0.57	0.14	0.6
TiO2	0.789	0.107	0.011	0.177	0.632	0.377	0.688	0.109	1.017
P205	0.09	0.01	< 0.01	0.01	0.06	< 0.01	0.1	0.02	0.08
LOI	0.85	13.84	1.11	0.96	1.74	2.17	2.65	6.38	0.68
Total	98.62	98.96	99.61	100.2	99.87	99.61	100.9	98.59	100.8
Au (ppb)	< 1	20	> 30000	2320	1550	12500	< 1	131	< 1
Ag (ppm)	< 0.5	< 0.5	1.4	< 0.5	0.6	2.5	< 0.5	1.3	< 0.5
As	< 1	16	4	< 1	< 1	< 1	< 1	4	2
Ba	11	91	15	1718	216	90	165	13	77
Be	1	3	65	5	47	10	< 1	< 1	< 1
Bi	< 0.1	0.2	< 0.1	< 0.1	0.1	0.3	0.2	2.7	3

Br	< 0.5	< 0.5	< 0.5	< 0.5	< 0.5	< 0.5	< 0.5	< 0.5	< 0.5
Cd	< 0.5	0.7	< 0.5	< 0.5	< 0.5	< 0.5	< 0.5	0.9	< 0.5
Co	78.2	84.8	62.4	55.8	88.1	90.2	33.9	85.4	35.5
Cr	28.4	1350	< 0.5	44.9	40.1	23.4	677	32.3	321
Cs	0.4	0.3	0.1	7.2	7.6	6.6	0.8	0.5	0.7
Cu	198	15	3	24	108	82	52	1740	26
Ga	11	4	5	11	12	10	15	7	15
Ge	6.5	2	2.5	1.8	3.3	2	1.8	3.9	2.1
Hf	1.1	0.2	< 0.1	1.9	0.9	1.1	0.9	0.3	1.5
Hg	< 1	< 1	< 1	< 1	< 1	1	< 1	< 1	< 1
In	< 0.1	< 0.1	< 0.1	< 0.1	< 0.1	< 0.1	< 0.1	< 0.1	< 0.1
Ir	< 1	< 1	< 1	< 1	< 1	< 1	< 1	< 1	< 1
Mo	< 2	5	< 2	< 2	< 2	92	< 2	< 2	< 2
Nb	0.8	< 0.2	0.4	8.5	0.9	4.9	1.6	< 0.2	2.4
Ni	31	793	5	21	49	31	76	212	170
Pb	< 5	< 5	< 5	30	< 5	< 5	< 5	7	< 5
Rb	2	5	2	228	128	82	19	5	20
S (%)	0.412	0.137	0.018	0.438	1.7	2.2	0.107	9.37	0.168
Sb (ppm)	0.5	0.5	1.2	0.5	< 0.1	0.4	0.4	0.5	0.5
Sc	11.9	7.41	0.81	2.41	23.1	6.48	31.1	5.63	35
Se	< 0.5	< 0.5	< 0.5	< 0.5	< 0.5	< 0.5	< 0.5	9	< 0.5
Sample ID	PVS157	PVS158	PVS159	PVS160	PVS161	PVS162	PVS163	PVS165	PVS166
Sn	< 1	< 1	< 1	2	< 1	4	< 1	< 1	< 1
Sr	18	133	35	366	159	78	242	6	157
Ta	0.46	< 0.01	0.49	0.65	0.48	0.88	0.12	< 0.01	0.16
Th	0.26	6.15	0.25	1.37	0.42	4.49	0.17	0.07	0.24
U	0.1	0.1	0.07	0.68	0.4	1.32	0.06	0.04	0.08
V	168	61	34	68	214	476	232	62	278
W	484	106	614	432	529	637	< 1	< 1	< 1
Y	15	6	2	2	5	2	14	12	23
Zn	95	101	16	41	60	83	77	60	50

Zr	49	7	5	86	40	44	36	13	64
La	4.66	0.4	0.13	1.12	3.89	5.76	2.74	2.58	3.65
Ce	11.3	0.9	0.23	1.91	9.18	11.2	6.69	5.4	9.33
Pr	1.69	0.13	0.04	0.22	1.33	1.26	1	0.7	1.42
Nd	8.08	0.76	0.2	0.81	6.08	4.49	5.23	3.43	6.95
Sm	2.33	0.23	0.11	0.11	1.78	0.75	1.58	0.94	2.24
Eu	0.987	0.125	0.055	0.392	0.364	0.123	0.604	0.212	0.77
Gd	2.38	0.39	0.17	0.15	1.9	0.5	1.89	1.04	2.65
Tb	0.43	0.09	0.04	0.03	0.27	0.07	0.36	0.21	0.48
Dy	2.63	0.76	0.31	0.18	1.19	0.31	2.37	1.46	3.03
Ho	0.51	0.18	0.07	0.04	0.16	0.05	0.49	0.33	0.63
Er	1.45	0.59	0.18	0.13	0.35	0.16	1.42	1.09	1.93
Tl	0.77	0.4	0.98	2.38	3.64	1.37	0.15	0.13	0.19
Tm	0.22	0.087	0.028	0.021	0.037	0.025	0.221	0.189	0.308
Yb	1.45	0.57	0.19	0.18	0.19	0.15	1.48	1.39	1.97
Lu	0.224	0.083	0.028	0.03	0.027	0.02	0.227	0.244	0.297
Mass (g)	1.259	1.106	1.163	1.147	1.137	1.179	1.45	1.708	1.829

APPENDIX B: U–PB ZIRCON GEOCHRONOLOGY AND HF ISOTOPE GEOCHEMISTRY

Identifier	$^{176}Hf/^{177}Hf$	Error (2 se)	$^{180}Hf/^{177}Hf$	Error (2 se)	$^{176}Lu/^{177}Hf$	Error (2 se)	$^{176}Yb/^{177}Hf$	Error (2 se)	$^{207}Pb/^{206}Pb$ Age (Ma)	2 s Error (Ma)	T_{DM} Hf (Ma)	εHf (t)	Error (2 s)
VS-Hf-1	0.281050	0.000044	1.886086	0.000249	0.000801	0.000047	0.028116	0.001585	2598	17	3.58	-3.7	1.6
VS-Hf-2	0.281088	0.000049	1.886128	0.000455	0.000791	0.000019	0.026736	0.000620	2687	17	3.34	-0.3	1.7
VS-Hf-3	0.281107	0.000053	1.886461	0.000655	0.000868	0.000046	0.029444	0.001480	2688	17	3.29	0.2	1.9
VS-Hf-4	0.281089	0.000050	1.886037	0.000496	0.001026	0.000058	0.034655	0.003191	2672	17	3.40	-1.0	1.8
VS-Hf-5	0.281155	0.000049	1.886112	0.000304	0.000897	0.000026	0.031508	0.001306	2680	17	3.16	1.7	1.8
VS-Hf-6	0.281099	0.000070	1.886114	0.000430	0.001030	0.000024	0.033364	0.001313	2714	17	3.31	0.3	2.5
VS-Hf-8	0.281142	0.000069	1.886106	0.000245	0.000860	0.000056	0.027347	0.001968	2706	17	3.16	1.9	2.5
VS-Hf-10	0.281146	0.000054	1.886091	0.000236	0.000869	0.000039	0.027592	0.001620	2710	17	3.14	2.1	1.9
VS-Hf-12	0.281067	0.000046	1.885693	0.000248	0.001399	0.000071	0.046176	0.003465	2706	17	3.48	-1.7	1.6
VS-Hf-13	0.281083	0.000037	1.886023	0.000218	0.001266	0.000052	0.042216	0.002167	2711	17	3.40	-0.8	1.3
VS-Hf-14	0.281099	0.000045	1.886096	0.000264	0.001044	0.000098	0.032219	0.003315	2702	17	3.33	-0.1	1.6
VS-Hf-15	0.281114	0.000073	1.886273	0.000653	0.001432	0.000078	0.045776	0.002386	2674	17	3.38	-0.9	2.6
VS-Hf-16	0.281175	0.000034	1.886036	0.000353	0.000781	0.000027	0.025632	0.001481	2711	17	3.03	3.3	1.2
VS-Hf-17	0.281149	0.000036	1.886025	0.000235	0.000876	0.000040	0.027657	0.001315	2707	17	3.13	2.2	1.3
VS-Hf-18	0.281115	0.000037	1.886274	0.000223	0.000829	0.000062	0.024722	0.001890	2714	17	3.23	1.2	1.3
VS-Hf-19	0.281144	0.000067	1.886070	0.000301	0.000999	0.000022	0.032300	0.000977	2661	22	3.23	0.7	2.4
VS-Hf-21	0.281139	0.000052	1.886186	0.000312	0.000837	0.000018	0.026562	0.000624	2707	17	3.16	1.9	1.9
VS-Hf-22	0.281182	0.000037	1.886831	0.000503	0.000548	0.000055	0.018319	0.001722	2715	17	2.97	4.1	1.3
VS-Hf-24	0.281133	0.000040	1.886309	0.000193	0.000879	0.000042	0.027896	0.001236	2669	17	3.24	0.7	1.4
VS-Hf-23	0.281135	0.000044	1.886062	0.000433	0.001035	0.000037	0.031655	0.001360	2700	17	3.21	1.2	1.5
VS-Hf-25	0.281193	0.000038	1.886250	0.000294	0.001031	0.000037	0.032570	0.000980	2729	17	2.99	3.9	1.3
VS-Hf-30	0.281165	0.000044	1.886066	0.000315	0.000659	0.000061	0.020005	0.001263	2669	17	3.10	2.2	1.6
VS-Hf-31	0.281141	0.000042	1.886233	0.000225	0.001377	0.000162	0.044565	0.006419	2703	17	3.25	0.9	1.5
VS-Hf-36	0.281193	0.000042	1.886239	0.000184	0.001313	0.000151	0.042758	0.005432	2702	17	3.08	2.8	1.5
VS-Hf-41	0.281148	0.000037	1.886235	0.000227	0.001094	0.000014	0.036026	0.000507	2706	17	3.17	1.7	1.3
VS-Hf-45	0.281131	0.000060	1.886265	0.000336	0.002276	0.000099	0.078977	0.004971	2665	17	3.47	-2.0	2.1
VS-Hf-46	0.281182	0.000033	1.886192	0.000165	0.000570	0.000013	0.018418	0.000618	2664	17	3.04	2.9	1.2

Identifier	$^{176}Hf/^{177}Hf$	Error (2 se)	$^{180}Hf/^{177}Hf$	Error (2 se)	$^{176}Lu/^{177}Hf$	Error (2 se)	$^{176}Yb/^{177}Hf$	Error (2 se)	$^{207}Pb/^{206}Pb$ Age (Ma)	2 s Error (Ma)	T_{DM} Hf (Ma)	εHf (t)	Error (2 s)
MUDTANK-1	0.282483	0.000028	1.886484	0.000187	0.000035	0.000001	0.001272	0.000020					
MUDTANK-2	0.282511	0.000032	1.886498	0.000175	0.000035	0.000001	0.001290	0.000026					
MUDTANK-3	0.282504	0.000033	1.886450	0.000172	0.000035	0.000001	0.001269	0.000018					
MUDTANK-4	0.282505	0.000028	1.886470	0.000167	0.000034	0.000000	0.001254	0.000018					
MUDTANK-6	0.282503	0.000027	1.886131	0.000141	0.000030	0.000001	0.001317	0.000015					
MUDTANK-5	0.282506	0.000034	1.885908	0.000228	0.000030	0.000001	0.001342	0.000019					
MUDTANK-7	0.282501	0.000028	1.886022	0.000216	0.000030	0.000000	0.001343	0.000012					
91500-1	0.282300	0.000038	1.886573	0.000172	0.000291	0.000000	0.008059	0.000034					
91500-2	0.282272	0.000030	1.886733	0.000198	0.000291	0.000001	0.008105	0.000030					
91500-3	0.282296	0.000039	1.886542	0.000239	0.000290	0.000001	0.008154	0.000029					
91500-4	0.282318	0.000035	1.886615	0.000209	0.000290	0.000000	0.008163	0.000022					
91500-5	0.282269	0.000035	1.884918	0.000172	0.000336	0.000001	0.011674	0.000043					
91500-6	0.282313	0.000029	1.886245	0.000193	0.000329	0.000001	0.010994	0.000082					
91500-7	0.282273	0.000036	1.886337	0.000231	0.000330	0.000000	0.011126	0.000056					

^{176}Lu decay constant (1.867×10^{-11}/yr) (Söderlund et al. 2004)

Chondritic values of $^{176}Lu/^{177}Hf$=0.0336 and $^{176}Hf/^{177}Hf$= 0.282785 (Bouvier et al., 2008)

$^{176}Lu/^{177}Hf$ ratios of mafic crust (Pietranik et al., 2008)

Model depleted mantle with $^{176}Lu/^{177}Hf$ ratio of 0.0388; present day $^{176}Hf/^{177}Hf$ ratio of 0.28325 (Griffin et al., 2000; Andersen et al., 2009)

Identifier	^{206}Pb (cps)	^{204}Pb (cps)	$^{207}Pb/^{206}Pb$	2 s	$^{207}Pb/^{235}U$	2 s	$^{206}Pb/^{238}U$	2 s	Rho	$^{207}Pb^*/^{206}Pb^*$ age (Ma)	2 s error (Ma)	$^{206}Pb^*/^{238}U$ age (Ma)	2 s error (Ma)	$^{207}Pb^*/^{235}U$ age (Ma)	2 s error (Ma)	% discordance
Standard																
OG1-1	655505	92	0.30082	0.00311	29.53970	0.85473	0.71219	0.01925	0.934	3474	16	3467	72	3472	28	0.2
OG1-2	633993	91	0.29826	0.00308	29.38698	0.86300	0.71459	0.01965	0.936	3461	16	3476	73	3467	28	-0.4
OG1-3	558782	35	0.29768	0.00309	28.75601	0.85747	0.70061	0.01959	0.938	3458	16	3423	74	3445	29	1.0
OG1-4	554012	12	0.29652	0.00307	28.75408	0.81932	0.70330	0.01867	0.932	3452	16	3433	70	3445	28	0.6
OG1-5	574939	70	0.29622	0.00307	26.13104	0.72812	0.63979	0.01655	0.928	3451	16	3188	65	3351	27	8.2
Samples																
VS-001	510741	69	0.17413	0.00181	11.66954	0.35417	0.48604	0.01386	0.940	2598	17	2554	60	2578	28	1.7
VS-002	1437559	104	0.18376	0.00189	12.78196	0.38961	0.50448	0.01447	0.941	2687	17	2633	62	2664	28	2.1
VS-003	870537	107	0.18391	0.00194	12.99774	0.43965	0.51259	0.01647	0.950	2688	17	2668	70	2679	31	0.8
VS-004	2394294	129	0.18208	0.00192	12.84040	0.40333	0.51146	0.01513	0.942	2672	17	2663	64	2668	29	0.3
VS-005	2184966	75	0.18298	0.00191	13.03299	0.43795	0.51658	0.01650	0.950	2680	17	2685	70	2682	31	-0.2
VS-006	568128	35	0.18679	0.00194	12.96745	0.35511	0.50350	0.01276	0.926	2714	17	2629	54	2677	25	3.2
VS-007	1013016	75	0.18590	0.00191	13.11910	0.38214	0.51184	0.01395	0.936	2706	17	2664	59	2688	27	1.6
VS-008	539072	70	0.18635	0.00193	13.27007	0.37067	0.51645	0.01340	0.929	2710	17	2684	57	2699	26	1.0
VS-009	757568	41	0.18592	0.00192	13.10969	0.40043	0.51140	0.01470	0.941	2706	17	2663	62	2688	28	1.6
VS-010	272641	41	0.18642	0.00194	13.22804	0.42107	0.51464	0.01549	0.945	2711	17	2676	66	2696	30	1.3
VS-011	1197845	62	0.18545	0.00191	13.09487	0.34931	0.51212	0.01260	0.923	2702	17	2666	54	2687	25	1.4
VS-012	1016424	19	0.18232	0.00188	12.91606	0.37533	0.51379	0.01396	0.935	2674	17	2673	59	2674	27	0.0
VS-013	595061	82	0.18643	0.00196	13.05253	0.37448	0.50777	0.01355	0.930	2711	17	2647	58	2683	27	2.4
VS-014	500741	105	0.18600	0.00193	13.29487	0.43114	0.51840	0.01593	0.947	2707	17	2692	67	2701	30	0.5
VS-015	280759	28	0.18675	0.00194	13.03627	0.42056	0.50629	0.01547	0.947	2714	17	2641	66	2682	30	2.8
VS-016	1313198	136	0.18088	0.00243	12.74175	0.43410	0.51091	0.01600	0.919	2661	22	2661	68	2661	32	0.0
VS-017	403727	19	0.18601	0.00192	13.33160	0.43887	0.51981	0.01625	0.949	2707	17	2698	69	2703	31	0.3
VS-018	193658	14	0.18688	0.00195	13.15785	0.44848	0.51064	0.01657	0.952	2715	17	2659	70	2691	32	2.1
VS-019	1840831	60	0.18180	0.00188	12.67389	0.40056	0.50562	0.01510	0.945	2669	17	2638	64	2656	29	1.2
VS-020	966212	34	0.18519	0.00191	12.91956	0.39562	0.50597	0.01459	0.942	2700	17	2639	62	2674	28	2.3
VS-021	333971	16	0.18848	0.00195	13.25324	0.37464	0.50998	0.01341	0.931	2729	17	2657	57	2698	26	2.7
VS-022	1393260	12	0.18174	0.00186	12.76465	0.40099	0.50939	0.01512	0.945	2669	17	2654	64	2662	29	0.6
VS-023	853721	7	0.18558	0.00192	13.13706	0.42742	0.51342	0.01584	0.948	2703	17	2671	67	2690	30	1.2
VS-024	453352	4	0.18539	0.00192	12.80244	0.42218	0.50084	0.01568	0.949	2702	17	2617	67	2665	31	3.2

6292

Identifier	^{206}Pb (cps)	^{204}Pb (cps)	$^{207}Pb/^{206}Pb$	2 s	$^{207}Pb/^{235}U$	2 s	$^{206}Pb/^{238}U$	2 s	Rho	$^{207}Pb^*/^{206}Pb^*$ age (Ma)	2 s error (Ma)	$^{206}Pb^*/^{238}U$ age (Ma)	2 s error (Ma)	$^{207}Pb^*/^{235}U$ age (Ma)	2 s error (Ma)	% discordance
VS-025	390248	139	0.18588	0.00192	12.97068	0.43988	0.50609	0.01635	0.952	2706	17	2640	70	2678	31	2.5
VS-026	1821933	15	0.18133	0.00189	12.71816	0.41536	0.50870	0.01574	0.948	2665	17	2651	67	2659	30	0.5
VS-027	3142235	14	0.18117	0.00186	12.53429	0.34490	0.50179	0.01281	0.928	2664	17	2621	55	2645	26	1.6
VS-028	340417	4	0.18511	0.00194	12.74708	0.37899	0.49945	0.01390	0.936	2699	17	2611	59	2661	28	3.4
VS-029	200588	1	0.18447	0.00193	12.72802	0.38614	0.50042	0.01425	0.939	2693	17	2616	61	2660	28	3.0
VS-030	501792	2	0.18524	0.00192	13.13203	0.39841	0.51417	0.01466	0.940	2700	17	2674	62	2689	28	1.0
VS-031	497331	0	0.18564	0.00195	12.88409	0.38829	0.50337	0.01421	0.937	2704	17	2628	61	2671	28	2.9
VS-032	343759	0	0.18524	0.00194	12.76182	0.37482	0.49966	0.01371	0.934	2700	17	2612	59	2662	27	3.4
VS-033	481840	0	0.18507	0.00191	12.86909	0.40369	0.50433	0.01493	0.944	2699	17	2632	64	2670	29	2.5
VS-034	505527	1	0.18759	0.00194	13.36472	0.43025	0.51670	0.01575	0.947	2721	17	2685	67	2706	30	1.3
VS-035	1681190	1	0.18121	0.00186	13.02353	0.40014	0.52124	0.01509	0.943	2664	17	2704	64	2681	29	-1.5
VS-036	257030	1	0.18558	0.00197	12.70613	0.38180	0.49658	0.01396	0.935	2703	17	2599	60	2658	28	4.0
VS-037	624674	9	0.18245	0.00190	12.40854	0.38548	0.49325	0.01444	0.942	2675	17	2585	62	2636	29	3.5
VS-038	420792	0	0.18470	0.00191	12.70513	0.38995	0.49891	0.01442	0.942	2695	17	2609	62	2658	28	3.3
VS-039	671669	2	0.18442	0.00190	12.80481	0.38206	0.50359	0.01410	0.939	2693	17	2629	60	2665	28	2.4
VS-040	503189	0	0.18468	0.00192	12.65531	0.36753	0.49699	0.01348	0.934	2695	17	2601	58	2654	27	3.6
VS-041	613811	68	0.18555	0.00193	12.96621	0.41577	0.50681	0.01537	0.946	2703	17	2643	65	2677	30	2.3
VS-042	1362436	61	0.18435	0.00190	12.62403	0.37270	0.49665	0.01374	0.937	2692	17	2599	59	2652	27	3.6
VS-043	417751	72	0.18545	0.00192	12.71293	0.37955	0.49718	0.01392	0.938	2702	17	2602	60	2659	28	3.9
VS-044	596738	68	0.18519	0.00191	12.66895	0.42780	0.49616	0.01595	0.952	2700	17	2597	68	2655	31	4.0
VS-045	957311	54	0.18443	0.00192	12.59946	0.35722	0.49548	0.01307	0.930	2693	17	2594	56	2650	26	3.8
VS-046	740584	68	0.18142	0.00187	12.59162	0.35675	0.50337	0.01328	0.931	2666	17	2628	57	2650	26	1.4
VS-047	530188	60	0.18560	0.00192	12.94253	0.36433	0.50574	0.01324	0.930	2704	17	2638	56	2675	26	2.5
VS-048	540674	56	0.18515	0.00193	12.86389	0.43195	0.50390	0.01609	0.951	2700	17	2631	69	2670	31	2.6
VS-049	670677	100	0.18498	0.00191	13.09026	0.42217	0.51323	0.01568	0.947	2698	17	2670	66	2686	30	1.0
VS-050	1155347	60	0.18111	0.00187	12.78417	0.35495	0.51195	0.01320	0.928	2663	17	2665	56	2664	26	-0.1

*Not common lead calculated

bd= below detection

N/A= Not applicable

Standard= Owen's Gully Diorite (OG 1), East Pilbara Terrane of the Archean (3.6-2.8 Ga) Pilbara Craton, Western Australia at (Kloppenburg 2003; Van Kranendonk et al., 2006; Hickman and Van Kranendonk 2008)

6293

APPENDIX C: CONDENSED REGIONAL FIELD NOTES SUMMERS 2014–2016 (including UTM 16N Northing and Easting, lithology name, strike, dip, dip direction, additional notes including plunge and trend and detailed descriptions (unedited))

5304708	331080	Metaconglomerate	85	80	N	
5304711	331080	Metaconglomerate	103.5	66.7	NE	
5304691	331138	Metaconglomerate	267	61	S	
5304737	331023	Metaconglomerate	265	73	S	
5304885	330649	Metaconglomerate	72	72	N	
5304899	330650	Metaconglomerate	95	72	N	
5304905	330470	QFG	75	66	N	
5304899	330440	Metaconglomerate	101	64	N	
5304890	330432	QFG	85	72	N	
5304908	330397	Metaconglomerate	92	77	N	
5304910	330376	Metaconglomerate	71	60	N	
5304912	330365	Metaconglomerate	69	71	N	
5304915	330331	Metaconglomerate	75	79	N	
5304893	330335	Metaconglomerate	76	64	N	
5304910	330286	Metaconglomerate	70	68	N	
5304839	330286	Metaconglomerate	90	71	N	
5304927	330270	QFG	69	65	N	
5304943	330287	QFG	80	63	N	
5305225	328354	Amphibolite	80	75	N	
5306229	328611	Amphibolite	263	80	N	
5302880	325595	Intermediate	109	83	N	
5302891	325614	Intermediate	118	74	N	
5302878	32590	Intermediate	100	74	N	
5302083	325330	QFG	92	86	N	
5302082	325338	QFG	181.5	86	N	
5302093	325346	Assimilated Gneiss	80	79	N	
5307405	327369	Amphibolite	108.5	75.5	N	
5307349	327390	Assimilated Gneiss	125	78	N	
5307084	327541	Amphibolite	65	67	N	

5302736	340902	Intermediate	245	59.5	SE	
5302695	341075	Intermediate	245	73	S	
5302676	341223	Amphibolite	286	79.5	S	
5302457	341408	Intermediate	80	69.5	NE	
5302415	341516	Intermediate	73	70.5	N	
5302468	341749	Intermediate	77.5	78	N	
5302542	341948	Intermediate	84	72	NE	
5302590	342582	Amphibolite	245	82.5	S	
5303370	339307	Amphibolite	107.5	65	NE	
5302449	340029	Pegmatite	73	79	N	
5302196	340102	Pegmatite	60	85	N	
5303116	340773	Intermediate	45	80	NW	
5303129	340790	Intermediate	59	73	NW	
5302294	342763	Intermediate	85	71	N	
5302297	342775	Intermediate	68	76	N	
5305865	332598	Amphibolite	85	85	N	
5305863	332589	Amphibolite	90	79	N	
5306001	332570	Intermediate	105	78	NE	
5305222	330067	Intermediate	70	77	N	
5303627	326876	Intermediate	130	66	NE	
5303623	326870	Intermediate	119	74	NE	
5303628	326883	Intermediate	290	72.5	S	
5303635	326892	Metaconglomerate	107.5	72.75	NW	
5303641	326895	Intermediate	94	73.5	N	
5302526	325709	Intermediate	105	77.5	NE	
5309909	340145	Migmatitic Gneiss	225	64	S	
5304636	331338	QFG	84	57.5	N	
5304485	331729	QFG	94	67.5	N	
5304611	331330	Metaconglomerate	251	61	S	

6298

5307082	327561	Amphibolite	88	82	N	
5306836	327103	Metaconglomerate	188.5	76	S	
5306842	327112	Amphibolite	76	82	N	
5306842	327104	Amphibolite	284	80	S	
5306831	327084	Metaconglomerate	107	45	N	
5306662	326940	Metaconglomerate	88	74	N	
5306371	327108	Metaconglomerate	70	84	N	
5306359	327082	Amphibolite	65	79	N	
5303736	330119	garnet_biotite_schist_qfg_trench_g	265	64	S	
5303015	330359	Metaconglomerate_northernmetaconglomerate_a	212	68	S	
5303024	330363	Metaconglomerate_northernmetaconglomerate_a	245	70	S	
5302930	330451	Metaconglomerate_northernmetaconglomerate_b	117	82	N	
5303728	330155	garnet_biotite_schist_qfg_trench_f	296	71	S	
5302931	330450	Metaconglomerate_metaconglomerate_a	113	75	N	
5303385	330941	qfg_pegmatite_large_pegmatite_trench	148	74	N	
5303216	330955	Metaconglomerate_foldedmetaconglomerate_a	125	61	N	
5303211	330949	Metaconglomerate_foldedmetaconglomerate_b	162	57	N	
5303725	330303	QFG_trench_a	160	69	N	
5303709	330325	QFG_trench_b	108	56	N	
5306519	327622	intermediate_amphibolite_garnet_boudin_trench	82	73	N	
5304164	327170	felsic/amph	92	79	S	
5304175	327180	felsic/amph	0	0		
5304199	327200	felsic/amph	0	0		
5304806	329576	felsic with qtz eyes	92	84	N	
5304239	327187	felsic/amph	94	74	S	
5304249	327186	amph/felsic	64	80	S	
5304249	327186	felsic/amph	84	90		
5304804	329551	metaconglomerate	80	57	N	
5304802	329545	metaconglomerate	97	52	N	

6299

5307601	327896	pegmatite	294	90		
5307600	327696	2 pegmatites	42	90		
5307624	327596	amphibolite	93	52	NNE	
5307605	327576	feldspar gneiss, gneissosity	102	79	N	
5307084	327544	amphibolite	75	76	N	
5307084	327544	amphibolite	75	76	N	
5306951	327482	stripper/amph	70	85	S	
5306733	327877	patchy mig (amphibolite)	0	0		
5306501	327623	amphibolite	104	89	NNE	
5306500	327623	amphibolite	88	89	NNE	
5306500	327623	amphibolite	0	0		
5306800	326800	Wawa Gneiss	95	75	N	boulder?
5307132	326887	Wawa Gneiss	0	0		
5307128	326888	Wawa Gneiss	264	79	S	
5307125	326888	Wawa Gneiss	97	74	S	
5307120	326889	Stripper/amph	58	86	N	
5306324	328570	Amph	285	86	S	
5306542	327859	felsic/amph	244	78.5	S	
5306547	327860	transition to amphibolite	0	0		
5306500	327850	Intensely deformed amphiboolite	93	78	S	
5306470	327843	contact peg/amph	76	66	S	
5306475	327825	peg/amph contact	76	44	S	
5306497	327814	felsic quartz eyes	79.5	44		
5306525	328000	felsic quartz eyes	72	51	N	
5306564	328348	felsic quartz eyes	83	84	N	
5302364	332013	metaconglomerate	97	65	N	
5302380	332025	peg	75	61	N	
5302429	332049	peg	102	76	N	
5302445	332049	metaconglomerate	101	85	N	

6300

5304763	329589	metaconglomerate	80	52	N	
5304763	329589	metaconglomerate	100	52	N	
5307801	328916	amphibolite (migmatized)	105	82	N	
5307837	328880	migmatite	103	73	NNE	
5307837	328880	pegmatite boudin train	290	63	SW	
5307837	328880	transition between gneisses?	271	62.5	N	
5307821	328808	Possible metaconglomerate	0	0		
5307822	328809	gniess	103	90		
5307820	328810	gneiss	91	90		
5307784	328682	amphibolite	291	59.5	N	
5307779	328692	amph and felsic melt	0	0		
5307780	328693	amph and felsic melt	0	0		
5307781	328694	amph and peg	94	55	N	
5307784	328696	gneiss	131	54.5	NNE	
5307785	328697	int and peg	0	0		
5307785	328697	pegmatite	0	0		
5307790	328690	amphibolite in felsic	131	77	N	
5307800	328580	felsic gneiss	0	0		
5307805	328580	felsic gneiss	0	0		
5307809	328439	felsic gneiss	0	0		
5307757	328213	top of S, peg	104	75	N	
5307757	328213	middle of S	205	54	S	
5307757	328213	bottom of S	109	74	N	
5307777	328210	felsic with amph	0	0		
5307708	328149	felsic with peg	0	0		
5307674	328131	felsic with ribbons	0	0		
5307490	328096	re-xstal, amphibolite	94	69	N	
5307500	327896	felsic gneissosity	115	65	N	
5307550	327896	re-xstal, amphibolite	99	63	N	

6301

5302464	332052	felsic/amph gneiss	0	0		
5302480	332053	peg/congl contact	101	99	N	
5302504	332054	amphibolite between 2 metaconglomerates	0	0		
2302600	332056	peg, bio-musc	0	0		
5302621	332059	metaconglomerate	107	76.5	S	
5302619	331957	strained pegmatite/felsic gneiss	0	0		
5302609	331912	peg on peninsula	0	0		
5302595	331877	metaconglomerate	0	0		
5302574	331844	metaconglomerate	108	81	N	
5302489	331829	metaconglomerate	0	0		
5302358	331616	metaconglomerate	103	85	N	
5302265	331585	metaconglomerate	0	0		
5302225	331538	amphibolite to hornblende gneiss	105	64	S	
5302236	331506	metaconglomerate/amphibolite	103	90		
5306489	319328	amphibolite	0	0		
5306500	319400	amphibolite	78	78	S	
5306600	319500	peg	70	66	S	
5306674	319600	Pegmatite	82	65	N	
5306960	320010	Stripper	115	74	S	
5307277	320442	Pegmatite	104	90		
5307276	320441	Pegmatite	77	59.5	S	
5307338	320490	Pegmatite	110	78	S	Migmatized pegmatite; Schillern
5306875	321413	Metaconglomerate	95	78.5	S	
5303655	319378	Felsic amph gneiss	94	90		
5303500	319400	Metaconglomerate to sandy layer	107	90	N	East side of lake along road, dip angle goes from 77 degrees to 90 degrees
5303000	319500	Metaconglomerate	104	77	N	
5302336	331634	metaconglomerate	106	85	N	Peninsual with metaconglomerate and sandstone (highest strain here)
5302000	332000	metaconglomerate	0	0		
5301701	332167	pegmatite	35	38		

6302

5302336	331634	metaconglomerate	106	85	N	
5301701	332167	pegmatite	55	38		
5299909	333148	pegmatite	35	90		
5299950	333060	pegmatite	58	90		
5299968	333017	felsic gneiss and stripper	83	82.5	N	
5300210	332679	restite, amphibolite	98	90		No dip measurement indicated
5309914	340172	Pegmatite/amphibolite	61	18	S	
5345091	397178	Amphibolite	0	0		
5341034	391609	Quartzite metaconglomerate	147.5	83	E	
5339936	385722	Mafic	2	49	SW	
5346883	381515	Shawmere	55	74	S	
5346883	381515	Shawmere	57	64	N	
5301128	324883	Felsic gneiss	146	90		No dip measurement indicated
5301385	324962	Felsic gneiss	100	90		No dip measurement indicated
5301476	324073	Felsic gneiss	98	90		No dip measurement indicated
5303456	327168	Metaconglomerate	160	84		
5303405	327314	Metaconglomerate	109	71	S	
5303394	327346	Metaconglomerate	107	70	N	
5303350	327400		92	90		No dip measurement indicated
5303300	327415	amph-meta contact	94	86	N	
5303245	327421	amphibolite	88	80	N	
5303200	327450	amph and peg	85	71	N	
5303175	327485	metaconglomerate	98	80	N	
5303155	327495	metaconglomerate	89	82	N	
5303154	327496	metaconglomerate	91	73	N	Tightest foliation in Chapleau
5303163	327575	metaconglomerate	87	68	S	
5303137	327720	amphbolite/felsic/meta	94	78	S	
5303003	327810	amphibolite-int	100	70	N	
5302713	328057	felsic-mafic contact	95	70	S	

6303

5302700	328100	amphibolic OC?	99	73	S	
5302693	328137	amphibolite	102	90		No dip measurement indicated
5302649	328163	amph-int	0	0		
5302789	328241	amphibolite	98	85	N	
5302780	328260	amphibolite	97.5	88	N	
5302760	328290	amphibolite	99.5	86	S	
5302751	328311	amphibolite	0	0		
5302603	328294	metaconglomerate	102	82	S	peg on south, metaconglomerate, and then amph to int on north side
5303109	326195	amphibolite contact/intermediate gneiss	0	0		
5303100	326191	int/amphibolite	0	0		
5303095	326187	amph/int contact	124	89		
5303141	326234	Int gneiss, Quartz vein	97.5	71.5	N	
5303151	326237	Ends int gneiss to felsic	101	77	N	
5303151	326237	int-felsic gneiss	78	82	S	
5301814	325390	peg in metaconglomerate or mafic?	6	90		
5301773	325341	peg	0	0		North side of Hwy 101
5301577	325237	mig	87	80	N	
5301521	325193	Wawa gneiss, peg	0	0		
5301412	325129	Amphibolite/peg	8	90		
5301386	325115	Wawa gneiss	0	0		
5301349	325111	Wawa gneiss	0	0		
5301355	325121	Wawa gneiss	0	0		
5301377	325131	Wawa gneiss	0	0		
5301440	325160	New Trench, NW of boudin trench	0	0		New trench NW of boudin trench, WRONG UTM
5306378	327095	Metaconglomerate	69	90	S	
5306366	327108	Felsic breccia	0	0		
5306366	327108	Felsic breccia	69	82	S	
5306359	327081	amph, felsic breccia, metaconglomerate	0	0		west side of new south trench
5306374	327115	amph, felsic breccia, metaconglomerate	0	0		east side of new south trench

6304

5306380	327103	amphibolite	0	0		north, new east trench
5306372	327072	amphibolite, qtz eyes	70	82	S	north, new west side
5307287	327418	migmatite, Wawa Gneiss	94	80	N	
5307348	327392	migmatite, Wawa Gneiss	0	0		
5298015	321023	Amphibolite migmatite	349	39	S	
5298015	321030	Wawa gneiss	83	90	SW	
5298009	321025	Amphibolite, peg, siliceous feldspar-qtz gneiss	90	90		Fold city!!!No dip measurement indicated
5298014	321029	Wawa gneiss	90	90		HOriztonal to shallow. No dip measurement indicated
5298000	321032	Wawa gneiss	90	90	N	No dip measurement indicated
5297988	321035	Wawa gneiss	90	90		Shallow to horizontal, No dip measurement indicated
5297982	321036	Wawa gneiss	90	90	N	Moderate,No dip measurement indicated
5297974	321037	Wawa gneiss	90	90	NW	Steep to NW, No dip measurement indicated
5297955	321041	Wawa gneiss	90	90	NW	Steep, No dip measurement indicated
5297555	321150	Wawa gneiss	90	90		Near horiztonal, No dip measurement indicated
5297159	321303	Wawa gneiss	90	90		End, No dip measurement indicated
5298294	321138	Mig, peg	63	71.5	N	
5298346	321240	Amphibolite	90	90	N	
5298745	322159	mig	87	72	N	
5298700	322000	peg	141	69	E	
5298600	322000	Amphibolite, boudinaged	68.5	74	N	
5298580	321900	hbl in mig	100	76	N	
5298561	321869	pegmatite	145	90		
5298600	321890	Felsic to int bands	100	60	S	
5298675	322000	Felsic to int	78.5	62	N	
5298696	322134	Amph to intermediate, peg	89	82	S	
5310163	340518	Wawa gneiss	97	90	N	
5310581	341193	Amphibolite	66	90	NW	No dip measurement indicated
5303015	330359	Metaconglomerate	75	63	N	Northern Metaconglomerate A
5303013	330363	Metaconglomerate	287	70	S	Northern Metaconglomerate A

6305

5303024	330363	Metaconglomerate	110	69	N	Northern Metaconglomerate B
5304164	327170	felsic/amph	92	79	S	Little amphibolite and mostly felsic, lithology is continous NW up tp UTMN 5304199 and UTME 3271200
5304199	327200	felsic/amph	92	79	S	Little amphibolite and mostly felsic
5304806	329576	felsic with qtz eyes	92	84	N	Foliation in OC ranges from 90-101 as it anastomoses around c.g. quartz (vein?) Qtz eyes are foliated parallel to E-W and are stretched 1.5-2x.
5304239	327187	felsic/amph	94	74	S	Felsic with amphibole and quartz-rich (c.g. areas)
5304249	327186	amph/felsic	64	80	S	Amphibolite to felsic porphyry. Intermediate with amphibole-rich layers, with <10cm wide amphibolite areas. Feldspar and quartz eye rich layer next to amphibolite has tails on all of them. Stretch 1:2.
5304249	327186	felsic/amph	84	90		Contact between feldspar-qtz porphyry and amphibolite is 104.
5304249	327186	felsic/amph	104	90		Contact between feldspar-qtz porphyry and amphibolite
5304249	329552	metaconglomerate	100	57	N	Deans brother RV park
5304804	329551	metaconglomerate	80	57	N	Allowed onto Dean's brother's RV park!!!
5304802	329545	metaconglomerate	97	52	N	
5304763	329589	metaconglomerate	80	52	N	Magnetic iron formation clast in metaconglomerate!
5304763	329590	metaconglomerate	100	52	N	
5307801	328916	amphibolite (migmatized)	105	82	N	Edge of belt? Transition from amphibolite-rich area into transition zone with very coarse-grained plagioclase amphibolite and areas of m.g.-c.g. amphibolite migmatized. Vein migmatite with 1-3cm wide qtz-feldspar
5307803	328923	wawa gneiss	125	82	N	Edge of belt? Transition from amphibolite-rich area into transition zone with very coarse-grained plagioclase amphibolite and areas of m.g.-c.g. amphibolite migmatized. Vein migmatite with 1-3cm wide qtz-feldspar veins. Bands 125/82N. OC 7m W-E x 1.5m N-S on hill. (photo)
5307837	328880	wawa gneiss	103	73	NNE	Transition again between felsic and amphibolite.
5307836	328881	wawa gniess	123	73	NNE	Gneissic amphibolite rich bands, no true amphibolite.Epidote vein parallel to foliation, probably replacing hornblende.
5307830	328845	pegmatite boudin train	290	63	SW	10x10m2. 310/63SW pegmatite boudin train. Stripper area is small in the transitional area of OC. One small area (photo) of deformed pegmatite is the transition between felsic gneiss and transitional area. Oriented sample 291/62.5N (**Sample 1***)
5307830	328840	pegmatite boudin train	310	63	SW	10x10m2. 310/63SW pegmatite boudin train. Stripper area is small in the transitional area of OC. One small area (photo) of deformed pegmatite is the transition between felsic gneiss and transitional area.
5307825	328815	transition between gneisses?	271	62.5	N	(**Sample 1***)
5307821	328808	transitional gneiss?	0	0		Possible metaconglomerate? Transitional gneiss. Dyke that follows gneissosity. Repeating

6306

						layers of different lithologies. Areas of pegmatite lithons are protected and able to recrystallize hornblende amphibole.
5307820	328810	gneiss	91	90		Isoclinal, recumbant, sheath folds, parallel to foliation. Some showing dextral and some showing sinistral kinematics. (some pointing towards 111 degrees (towards west) and another 123 degrees (towards east)
5307819	328820	gneiss	103	90		Isoclinal, recumbant, sheath folds, parallel to foliation. Some showing dextral and some showing sinistral kinematics. (some pointing towards 111 degrees (towards west) and another 123 degrees (towards east)
5307784	328682	amphibolite	291	59.5	N	Strained bands of amphibolite
5307779	328692	amph and felsic melt	0	0		Amphoblite boudins with qtz and f.g. felsic melt in boudin neck
5307780	328693	amph and felsic melt	0	0		Small folds of felsic melt with axial planes of 119, 098 (139, 118). Similar crystal structures of qtz/feldspars around lithon/boudins (<1m x 1m)
5307781	328695	amph and peg	94	55	N	5m N-S x 1m wide OC Mainly gneiss with minor pegmatite and amphibolite. Amphibolite in gneiss 094/55N similar to pegmatite.
5307782	328696	gneiss	131	54.5	NNE	Large stripped gneissic OC.
5307785	328697	int and peg	0	0		tight minor folds in intermediate feldspar-qtz-amphibolite gneiss with minor pegmatite. Feldspar clasts of pegmatite are randomly oriented to defining the lineation.
5307785	328697	wawa gneiss	0	0		Qtz-feldspar pegmatite within random sub-angular to angular blocks of amphibolite.
5307790	328620		131	77	N to 90	Slivers of amphibolite in felsic melt.
5307795	328550		0	0		5m N-S x 4 m E-W. Felspar-rich gneiss with amphbole-rich areas. One amphibolite and a few peg, one with biotite (e.g. pegmatite).
5307800	328450	pegmatite	120	90		Feldspar-rich gneiss 8m E-W x 4m N-S.
5307809	328439	pegmatite	135	62		Feldspar-rich gneiss, alkali-fedlspar boudin train! Photo. Peg is 135/62N
NO UTM						Banded, less gneissic than previous ones, amphibole-rich. Large pegmatite, at least 1m wide. Possible metaconglomerate. Certainly mafic, int and felsic bands. Xenolith of amphibolite in metaconglomerate or? 141/44-90
5307757	328213	Feldspar-qrtz-hornblende gneiss	104	75	N	Northern end of S-fold in pegmatite, 104(124)/75N
5307757	328213	Feldspar-qrtz-hornblende gneiss	205	54	S	Bottom/southern end of S-fold in pegmatite.The qtz elevages in the middle of the "S" 205 (225)/54S.
5307757	328213	Feldspar-qrtz-hornblende gneiss	109	74	N	Middle of S-fold in pegmatite, 109(129)/74N
5307777	328210	felsic with amph	0	0		Across the road. Feldspar-qtz-amphibole gneiss with recrystallized hbl (e.g. and euhedral). 3x3m2
5307708	328149	felsic with peg	0	0		White OC with pink alkali fedlspar, quartz and minor xenolith of amphibolite. Feldspars have undergone grain size reduction. Qtz has a blue-grey colour. Feldspars are 1.25 cm to 2-3 mm showing the grain size reduction in the field.
5307674	328131	felsic with ribbons	0	0		Less pegmatite-rich than previous outcrops. Repeating bands of feldspars-rich areas and

6307

6308

						amphibole-rich areas. Deformed pegmatite is present. Quartz ribbons are present and beginning. 2m E-W x 4m N-S. Photo of grain sized reduction in qtz and feldspars. Transitional area.
5307490	328096	re-xstal, amphibolite	94	69	N	Felsic-rich OC with 2x2m2 mafic xenolith. (***Sample 2***)
5307491	328096	felsic with mafic xenolith	135	65	N	Felsic-rich OC with 2x2m2 mafic xenolith
5307493	328096	re-xstal, amphibolite	119	63	N	Recrystallized amphibolite. Felsic-rich OC with 2x2m2 mafic xenolith
5307495	328099	re-xstal, amphibolite	114	69	N	Felsic-rich OC with 2x2m2 mafic xenolith, recrystallize amphibolite
5307500	328100	re-xstal, amphibolite	135	65	N	Gneissosity in recrystallized amphibolite. Felsic-rich OC with 2x2m2 mafic xenolith
5307550	328250	felsic gneissosity	115	65	N	M.g.-c.g. feldspars-qtz gneiss with xenoliths of partially amphibolite. White rock. Some xenoliths, potentially have older (greener?) centres that are not f.g. and not recrystallized. 10m N-S x 3m E-W. Matt noticed orthoclase (pegmatitic) with areas of darkre and lighter zones in the mineral (strain?)
5307575	328400	re-xstal, amphibolite	99	63	N	contains two sets of pegmatite
5307580	328450	pegmatite	62	90		re-xstal amphibolite with pegmatite
5307585	3284500	pegmatite	314	90		re-xstal amphibolite with pegmatite, is foliated and boudinaged
5307600	328550	homogeneous gneiss	119	81	N	Homogeneous gneiss with very minor hornblende. One spot of epidote alteration and minor pegmatics. No recrystallization of amphibolites. Gneissosity 119/81N
5307600	328550	pegmatite	294	90		Homogeneous gneiss with very minor hornblende. One spot of epidote alteration and minor pegmatics. No recrystallization of amphibolites. Gneissosity 119/81N
5307610	328560	pegmatite	42	90		Homogeneous gneiss with very minor hornblende. One spot of epidote alteration and minor pegmatics. No recrystallization of amphibolites. Gneissosity 119/81N
5307624	327596	pegmatite	93	52	NNE	Pegmatite, amphibolite xenoliths strained, less common feldspar gneiss. 113/52NNE amphibole-rich layer (3x3m2)
5307624	327596	Amphibolite	113	52	NNE	Amphibolite layer in pegmatite (3x3 m2) less common feldspar gneiss
5307605	327576	feldspar gneiss, gneissosity	102	79	N	Feldspar gneiss with recrystallized hornblende in minor areas and minor peg. 102(122)/79N gneissosity.
5307084	327544	amphibolite	75	76	N	Intermediate gneiss? Probably metaconglomerate. Flattened and stretched. 5% is qtz veins! 3mm wide, possible beginning of migmatite? Patchy migmatite then/or during strain? (***Sample 3***) Boudin. 075(095)/76N foliation of amphibolite.
5307084	327544	amphibolite	75	76	N	Intermediate gneiss? Probably metaconglomerate. Flattened and stretched. 5% is qtz veins! 3mm wide, possible beginning of migmatite? Patchy migmatite then/or during strain? (***Sample 3***) Boudin. 075(095)/76N foliation of amphibolite.
5306951	327482	stripper/amph	70	85	S	Stripper rock but with mainly m.g. hornblende. (some areas are vertical)
5306952	327483	stripper/amph	30	90		stripper rock with m.g. hornblende lineation.
5306953	327484	stripper/amph	90	85	S	stripper rock with m.g. hornblende. Some areas are near vertical

6309

5306733	327877	amphibolite/migmitite				Patchy migmatite in amphibolite (greyer, smaller). 1mm wide and 10-16cm long plagioclase-qtz and recrystallized amphibole. Photo! Start of migmatitization.
						Amphibolite pinches out within felsic! Therefore the felsic dykes crosscut the amphibolite. And thinner felsic dykes coming into amphibolite. Photo.
						Foliation boudinage in deformed amphibolite. Qtz and pink alkali feldspar in amphibolite, foliation boudin! Migmatite? Pegmatite? Photo.
						Ideas: banana peel=octopus qtz vein=foliation boudinage shapes. Photos of qtz in.
						10mm long x 4mm wide plagioclase in amphibolite.
5306500	327623		104	89	NE	Area of hornblende + gar, less deformed (foliation: 068(088)/89N) and an area of deformed hornblende + garnet oblique to foliation 104(124)/81NE).
5306501	327623		88	89	N	Area of hornblende + gar, less deformed (foliation: 068(088)/89N) and an area of deformed hornblende + garnet oblique to foliation 104(124)/81NE).
5306500	327623					Amazing boudinage and foliation boudinage! Photo of close up.
						Oblique angle from above sample and regular strike/dip too.
						Elongated garnet parallel to foliation in feldspar phenocryst mafic gneiss. Sample might be too thin?
						Phenocryst of plagioclase and no phenocryst contact show minor vein to patchy migmatite with anhedral garnet and hornblende and qtz and feldspar. No elongated garnet! Photo
						Deformed and less deformed garnet in between BIF layers. Photo of BIF dilation zone.
		boulder?	95	75	N	Northern OC at end of Road. No good outcrop, maybe a boulder?
5307132	326887					Recrystallized hornblende layers, feldspar-rich layers. Diabase dykes E-W (boulder??). Wawa Gneiss.
		Wawa Gneiss	264	79	S	Gneiss with 60% feldspar and 40% quartz and layers of stripper rock/recrystallized hornblende. Some folds, but only a couple small ones. (284)/79S.
		Wawa Gneiss	97	74	S	Gneissic, some N-dipping folds. Complex. Pegmatite, granitic and recrystallized hornblende. (117)/74S.
5307120	326889	Stripper/amph	58	86	N	Amphibolite. No foliation, weird! 2 dykes (diabase). Gneissic stripper amphibolite.(078)/86N.
5306324	328570	Amph	285	86	S	Amphibolite with minor felsic-intermediate bands parallel to foliation. Very f.g. amphibolite (grain size reduction) 305/86S. Near area of intese deformation with N&S dipping anastomosing SZ. 20mx20m2
5306542	327859		244	78.5	S	Feldspar-rich and hornblende matrix. 2-3mm long feldspar. 5x5m2. 244 (264)/78.5S.
5306547	327860	moderate lineation				Transition to amphibolite, v.f.g. to fine-grained. 1x1m2
			93	78	S	Long, sandy hill. Foliated intensely. 093(113)/78S. Strongly foliateed and lineated hornblende amphiboles.
5306470	327843	contact peg/amph	76	66	S	Other side of hill is pegmatite? M.g. pegmatite striking similarly.

6310

		peg	76	44	S	Other side of hill has pegmatite/amphibolite contact at 096/66S and a little pegmatite striking at 096/44S.
						There is one "cross cutting" quartz vein in the pegmatite (which is in amphibolite) looks like extensional gash. Photo!
5306497	327814	felsic quartz eyes	79.5	44		Weathered surface is pink to white, quartz eyes defining foliation, up to 3 cm long and 1-2 mm wide. Fresh surface is light to medium grey. Qtz eyes, hornblende, biotite, and feldspar define the foliation.
		felsic quartz eyes	72	51	N	Lineation is defined by quartz eyes. Felsic dyke? Felsic-intermediate? Intrusive? 092/51N foliation. 44/099.5E quartz eye lineation.
5306564	328348	felsic quartz eyes	83	84	N	Quartz eyes, biotite-rich, feldspar, no hornblende. Foliation defined by qtz and biotite. Lineation is defined by quartz eyes 5-7mm long by 1-2mm wide. Foliation: 103/84N. Lineation (qtz eyes): 41/095E
5302364	332013	metaconglomerate	97	65	N	097(117)/65N. Intermediate to felsic gneiss (metaconglomerate). Pegmatite pinching and swelling same as above. The gneissic bands/clasts are ~5cm wide. 6x6m2. Pegmatite in metacgonlomerate anastomosing SZ around bouin: 075(095)/61N, 141(161)/62.5N
to		peg	75	61	N	Pegmatite with pinch and swell are 40cm long (E-W) and 16 cm and 12cm wide (N-S). They are fractured 45 to each of those directions.
5302429	332049	peg	102	76	N	102(122)/76N Stretched pegmatite that has been boudinaged. Pegmatite is <10cm wide in intermediate gneiss or metaconglomerate.
5302445	332049	metaconglomerate	101	85	N	1-5mm wide gneissosity (multiple!) Another pegmatite boudinaged. 10cm thick, verifiable clasts!
5302464	332052					Pegmatite contact with metaconglomerate (photo through water). Mineralization! Muscovite!
to		peg/congl contact	101	99	N	101(121)/99N. 0.75m wide quartz peg in metaconglomerate. Clast is lineated horizontal?
5302504	332054					Contact between amphibolite (<0.5m wide) and two metaconglomerate. Quartz (or peg) at each contact and are boudinaged. Horizontal to <10 degree plunge east (clasts in metaconglomerate).
						>5x5m2 pegmatite with HUGE biotite and muscovite!!! Metre-scale folds around the v.c.g.-pegmatite with micas. Micas only In areas of boundinage! Very deformed pegmatite! All c.g. but in mica-boudin ares are pegmatite size crystals (dilation zones?). Foliation is (104)124/81S!!! "Fold" axis due to boudinage is striking 023 degrees. Folds perpindicular to foliation are related to boudinage. **Sample 8***
5302621	332059	metaconglomerate	107	76.5	S	South side, felsic gneiss with small quartz veins like in the trenches. North side is metaconglomerate. Metaconglomerate has c.g. pegmatite dipping south. South side is vertical (felsic). Metaconglomerate is 107 (127)/76.5S
5302619	331957					Strained pegmatite and felsic gneiss (deformed pegmatite) is 2x2m2.
5302609	331912					Continuation of pegmatitc/felsic gneiss on peninsula point.

6311

5302595	331877					Metaconglomerate again!
5302574	331844	metaconglomerate	108	81	N	Metaconglomerate, 15x15m2. 108 (128)/81N. Pegmatite boudin as a sinistral tension fracture OR rotated and boudinaged? Horizontal lineation.
5302489	331829					Metaconglomerate con't on. Tight foliation, spacing is 1-2mm wide. Horizontal to <1 degree E plunging clasts again.
5302358	331616		103	85	N	Flattened AND stretched metaconglomerate. More flattened here than usual! <2cm thick clasts. (drawing)
5302265	331585					Metaconlgomerate.
5302225	331538		105	64	S	Amphibolite to hornblende gneiss with 0.25 sliver of more felsic? Area. Qtz boudins along contact at 105(125)/64S. 101 (121)/78N is the foliation in amphibolite.
5302236	331506		103	90		Contact between amphibolite and metaconglomerate. 103 (123)/near vertical.
5306489	319328					Local areas of recrystallization of amphibole (hornblende). Gneissic. Areas of pegmatite. Areas of amphibolite or patchy migmatized amphibolite. Photo.
			78	78	S	Beginning of vein-type migmatites! Boudinaged (or new melt) strikes 028 (048)/90 between amphibolite pods.
			70	66	S	Granitic to pegmatite with minor veins and chillera striking 100 (120)/90. 20m N-S x 7 m E-W. The schilleran are straight N-S and strikes E-W. 350 to 354 to 004 fold axis (330 to 334 to 344)
5306674	319600	Pegmatite	82	65	N	Side of forestry road. Pegmatite is quartz-rich at strikes 082 (102)/65N.
5306960	320010	Stripper	115	74	S	Recrystallized amphibolite (stripper rock) defines a foliation 095 (115)/074S. Vein-type migmatite and recrystallized amphibolite (f.g. amphibolite) with felsic plag veins.
5307277	320442	Pegmatitc	104	90 (c.g. peg)	077/59.5S	5m (E-W) x 15 m (N-S). Nearly all m.g. to c.g. pegmatite, no pegmatitic sizes. Pegmatite is near competency differences. 1 amphibolite xenolith in pegmatite outcrop. Schistose amphibolitc, intensely deformed, <1mm foliation spacing. 077 (097)/59.5S
5307338	320490	Pegmatite	110	78	S	20m (N-S) x 5 m (E-W). Migmatitic felsic gneiss with pegmatite and wisps of amphibolite. Schilleran? 110/78S. Spotty areas of real pegmatitic crystal sizes.Migmatite Schilleran
5306875	321413	Metaconglomerate	95	78.5	S	BEST OUTCROP EVER! 15 m (N-S) x 5 m (E-W). Corner Street OC! Many areas of v.c.g. reerstyallized hornblende. Felsic areas elongated, intermediate areas elongated, amphibolite is tear dropped shapped to eye shaped. Pegmatite to feldspar (pink) bands are throughout (<2cm wide). Most probably a metaconglomerate! Migmatized.
5303655	319378	QFG	94	90		Feldspar-quartz-hornblende gneiss
			107	90	N	East side of Borden Lake along long road. Metaconglomerate to sandy layer (sandy layer is 0.5 m wide). Secondary measurement 77
			104	77	N	1-5mm wide metaconglomerate , with some gentle folds in tightly spaced areas.
5302336	331634	metaconglomerate	106	85	N	Peninsula with metaconglomerate and sandstone. Highest strain is where measurement was taken.
						Photo of highest strain in metaconglomerate 1-3 mm wide schistosity

6312

						Rotated quartz clast/boudin with anti-clockwise rottion or sinistral deformation after dextral (photo of delta kinematic indicator)
5301701	332167	pegmatite	35	38		Pegmatite parallel to foliation. 7 m E-W x 2 m N-S, all pegmatitic pegmatite
5302336	331634	metaconglomerate	106	85	N	Peninsula with metaconglomerate and sandstone. Highest strain is where measurement was taken.
						Photo of highest strain in metaconglomerate 1-3 mm wide schistosity
						Rotated quartz clast/boudin with anti-clockwise rottion or sinistral deformation after dextral (photo of delta kinematic indicator)
						Amphibolite clast, partial melt in folded plagioclase areas.
5301701	332167	pegmatite	55	38		Pegmatite paraellel to foliation. 7 m E-W x 2 m N-S, all pegmatitic pegmatite
5299909	333148	pegmatite	35	90		55/vertical is the highest strain area and 78/vertical is the boudinaged area. Amphibolite with migmatitic vein to net-structured migmatite.
		pegmatite	58	90		15m N-S x 3 m E-W, pegmatite areas & pods
5299968	333017	felsic gneiss and stripper	83	82.5	N	Felsic gneiss, more "stripper gneiss" look as 2 stripes of amphibole-rich lines are present. Trace pyrite. Anhedral, v.f.g. Tightly spaced gneissosity, ~2cm.
5300210	332679	restite, amphibolite	98			Huge, amazing, beautiful outcrop! Bleach worthy!!!! General strike of restite amphibolite clasts (eye shapes) are 118.
		felsic gneiss (Wawa)		90		Felsic, quartz-feldspar gneiss (neosome) also generally simiular, however multiple mesocopic folds in sinistral, sheath and dextral (very soupy). 30-40cm wide megacrystic pegmatite crosscuts outcrop.
						Unstrained, quartz-feldspar scholen textures, higher deformation? ENE plugning mini-folds. 35m N-S x 5 m E-W
5309914	340172	Pegmatite/amphibolite	61	18	S	Pegmatite leucosome, feldspar-rich (c.g. to m.g.). 10 similar gneissic bands in 1m2 area. Larger amphibolite is striking E-W with vertical to horizontal dip. Smaller clasts are also variable, one instance of fracture granulite. CPX in field east of 1st occurance on Adam's Rd South. CPX is only in recrystallized amphibolite pods. First instance of OPX+GAR in field?
		gar+cpx+hbl_ opx?	74	85	S	Mafic pod in felsic gneiss. Second dipping measurement 31
5345091	397178	Amphibolite				East of Foleyet: Black amphibolite, white plagioclase, green epidote, pegmatite dykes. Very irregular shaped ampihbolite clast/xenolith. Amphibolite has sulphides, 0.01%, Py is 0.3mm wide, cubic, chalcopyrite is 0.1mm wide. Feldspar shows minor eyes in E-W plane, potential stripper rock? NO migmatization, not even patchy.
5341034	391609	Quartzite metaconglomerate	147.5	83	E	Quartzite on a little hill on road side. The majority of the hill is weathered. Metasandstone to metaconglomerate. Extremely siliceous. Restricted provinence? Only quartize! Sample of metaconglomerate
5339936	385722	Mafic	2	49	SW	The stripper rock IIbl+Cpx gneiss is well foliated and lineated. Mafic- IIbl+Cpx, biotite. Very strange lithology. Biotite next to pegmatite. Biotite in pegmatite, soupy pegmatite. Areas of cpx+opx_plag; cpx+plag; cpx+hbl+hbl+cpx+biotite (near pegmatite). Stripper rock

6313

						to mafic gneiss. Biotite gneiss is next to pegmatite. Mafic area has more random orientation as it is deformed near pegmatite. Middle of OC between 20m long E-W, 2m N-S
5346883	381515	Shawmere	55	74	S	Shawmere Anorthosite Rd Area: Mylonite! Photo. North side: 075/74S, 077/64N. Sample of strange, recrystallized pink minerals ontop of gar+cpx (zeolites? Carbonates? OH?)
		Shawmere	57	64	N	
5301128	324883	Felsic gneiss	146			Felsic gneiss with amphibole in some 3cm wide gneissic sections.
5301385	324962	Felsic gneiss	100			Same as above, roughly 120 degrees, 1x1m2 outcrop
5301476	324073	Felsic gneiss	98			Felsic gneiss to intermediate gneiss. M.g., feldspar, hornblende, very weakly gneissic. Side of the road.
5303456	327168	Metaconglomerate	173	88		Metaconglomerate or amphibolite. Probably metaconglomerate. 1x1m2. Second measurement 158/83
5303405	327314	Metaconglomerate	109	71	S	quartz-veins in intermediate to amphibolite? Probably metaconglomerate.
5303394	327346	Metaconglomerate	107	70	N	Metaconglomerate (definite) with 7-8 cm wide to 3-4 cm wide clasts
			92			Amphibolite 112
		amph-meta contact	94	86	N	Amphibolite contact with metaconglomerate 114/86N
5303245	327421	amphibolite	88	80	N	Dark, f.g.-m.g; light is m.g.-c.g., amphibolite with peg (deformed to m.g.), metaconglomerate 108/80N, Tightly spaced foliation 2-3mm spacing
		amph and peg	85	71	N	Amphibolite lens 105/71N
		metaconglomerate	98	80	N	
5303155	327495		89	82	N	Quartz veins up to 10cm wide; sinistral and dextral kinematic indicators in veins; 7m N-S, 5m E-W
5303154	327496		91	73	N	Boudinage E-W in quartz veins shows dextral movement. Tightest foliation in Chapleau area? <1mm foliation spacing.
5303163	327575	metaconglomerate	87	68	S	1x1m2, amphibolite and felsic & intermediate bands (metaconglomerate?) Bad dip angle.
5303137	327720		94	78	S	072/48N gently folded fault breccia. Striped amphibolite wall! Boudinage in pegmatite, clasts of intermediate to mafic. Foliation boudinage. Very tightly spaced foliation. Intermediate to amphibolite. 10 m E-W x 5 m N-S
5303003	327810		100	70	N	Intermediate to amphibolite schist (very schistose) on tiny hill. 2x2m2
5302713	328057	felsic-mafic contact	95	70	S	Striped area with amphibolite, felsic and quartz veins at contact. Contact is very irregular and folded (photo). Felsic is hbl-rich near amphibolite.
		amphibolie OC?	99	73	S	Felsic with amphibolite (iron stained) and c.g. felsic pegmatite? Qtz voudins in amphibolite. North side: amphibolite, South side: felsic
5302693	328137	amphibolite	102			16-20m: amphibolite, hornblende gneiss (minor), pegmatite (<2cm wide), finger grained amphibolite. Beautiful intermediate gneiss with amphibolite (photo).
5302649	328163					Peg: 122/90, qtz: 093.5/84.5S. Axial trace of intermediate and m.g. amphibolite folds is 124.

6314

5302789	328241	amphibolite	98	79 to 90	N	New Road #2. Amphibolite (v.f.g., mylonitic) with mullion, and 2 peg intruded.Quartz veins are boudinaged in the amphibolite and crosscut pegmatite. 4mx4m2
con't			97.5	88	N	2 peg intrusions, amphibolite
con't			99.5	86	S	Multiple waves of folds
5302751	328311					Multiple waves of folds again.
5302603	328294		102	82	S	New Road #3. 4 m N-S x 1 m E-W. Peg south side, metaconglomerate, then amphibolite to intermeidate gneiss in the north side. Mainly metaconglomerate.
5303109	326195					Hwy 101 near Chapleau Hill OC. Contact between intermediate gneiss (feldspar, hbl, qtz and muscovite near pegmatites) and amphibolite is irregular, not igneous due to change in foliations and cut off quartz vein (drawing).
to						
5303095	326187	amph/int contact	124	86.5S to 90		Intermediate gneiss next to amphibolite. Photo of qtz vein folded and mica along contact. Diabase surrounding it all. Vertical boudinage. Intermediate gneiss has folded qtz veins. Amphibolite is schistose with multiple veins. 30cm wide quartz vein with amphibolite wall rock inside intermediate gneiss parallel to foliation.
5303141	326234	Quartz vein	97.5	71.5	N	End of intermediate gneiss
5303151	326237	int gneiss	101	77	N	Intermediate gneiss with clockwise rotation and assymetircal straight boudins/chocolate tablet. Amphibolite pinch and swell (vertical, both directions)
		felsic gneiss	78	82S		Feldspar-quartz gneiss (pegmatitic areas, kpsar strung out into gneiss)
5301814	325390	peg in metaconglomerate or mafic?	6	90		Pegmatite 15cm striking 006(026)/90?. Round to flattened "clasts" of granulite, some moved from pegmatite mafic enclaves. Mafic or metaconglomerate protolith?
5301773	325341	peg				Across road (Hwy 101) the same deformed pegmatite, granitic.
5301577	325237					Diabase
		mig	87	80	N, various	Wawa gneiss! Maybe metaconglomerate? Photo.
		peg	352.5	90		
		peg	4	90		
			352.5	90		Photo of squished veins. Across Hwy 101 is the same feslic Wawa gneiss with c.g.-peg and mafic. Compressed vein direction
5301463	325189	peg				Folded peg vein (photo)
to		peg	2	90		Sinistral SZ in peg? Flattened peg (squishy) 022 direction of compression
5301521	325193	Wawa gneiss, peg				Wawa Gneiss with many bands of amphibolite, melted amphibolite and peg 028/vertical
5301412	325129	Amphibolite/peg	8	90		amphibolite/peg melted
5301386	325115	Wawa gneiss				Wawa Gneiss

6315

6316

5301349	325111					Wawa Gneiss
to						
5301377	325131	Wawa gneiss				Wawa Gneiss
5301440	325160					New Trench NW of Boudin Trench
5306378	327095	Metaconglomerate	69	90	S?	Metaconglomerate with mafic with garnet
		mafic with gar	66	80	S	Garnet amphibolite (sample 15)
5306366	327108	Felsic breccia	random?			Felsic breccia, quartz veins, 3% pyrite cubic, chalcopyrite.
5306366	327108	Felsic breccia				Felsic breccia, quartz veins, DPO & CPO for quartz sample?
		Felsic breccia	69	82	S	New Trench South, NW of Boudin Trench, most "breccia" are <45 in foliation direction (quartz veins)
5306359	327081	west side of new trench				
5306374	327115	east side of new trench				
5306380	327103					East side of trench of north trenches end to end
5306372	327072					West side of trench
5306365	327080	qtz vein	348			Evidence of compression with flattened epidote/qtz veins
5306350	327100	qtz vein/peg in amphibolite	098 Seahorse			Pegmatite? Alkali felspar and qtz in amphibolite, wispy (migmatite); see pic movement along 098(118)?
5306340	327150	amphibolite				Amphibolite- patchy to net migmatite (beginning stages)
5306340	327200	amphibolite				Amphibolite: within amphibolite itself and not just at contacts. The "fault" has QV, straight and boxy amphibolite pieces.
5306290	327380	qtz eye/amph contact	70	82	S	Contact between amphibolite and qtz-feldspar schist (qtz eye gneiss/schist)
5306290	327418	migmatite, Wawa Gneiss	94	80	N	Wawa Gneiss, migmatite. All different lithologies present, black recrystallized migmatite, pegmatite, intermediate, felsic, and all other lithos? Light and dark samples collected. Vein-type migmatite? Photos on Matt's phone. "augen gneiss" with feldspar present.
5307287	327392					Vein to schollen? Still amphibolite-rich areas.
5307348	327392					Hill Outcrop South
		Diabase				0-6.5m: Diabase
		Qtz/py				6.5-9.9m: Qtz and pyrite
		Amphibolite				9.9-15.0m: amphibolite
		Qtz-rich host rock				15-28m: qv with py mineralization at edge of quartz-rich hostrock. Granulite wrapped around qtz areas.
		Amphibolite				28-32.2: Amphibolite. Patchy migmatite. Quartz, plag, biotite, and pyrite present. 072 epidote

6317

5298015	321025	Amphibolite, peg, siliceous feldspar-qtz gneiss	E-W Fold City!!! Axial planes E-W			Fold city is amphibolite to pegmatite to silciouos feldspar-qtz gneiss with recrystallized CPX and HBL in plag+qtz patchy mig. Coherent folds unlike anywehre we've seen. Vertical dip.
5298009	321029				Horiztonal to shallow	Blocks and rafts, horizontal to shallow dipping
5298014	321032				N	Steeply dipping north
5298000	321035				Shallow to horizontal	Blocks and rafts, shallow to horizontal
5297988					Moderate	Moderately dipping
	321037				Steep to NW	Steeply dipping northwest
5297974	321041				Steep	Steeply dipping
5297955					Near horiztonal	Gently folded and near horizontal areas, in amphibolite and pegmatite. Photos of peg from vertical to horizontal with qtz vein.
5297159	321303					End
						Wawa Gneiss
	321138	Mig, peg	63	71.5	N	Wawa Gneiss. Gneiss (plag/amph and qtz/feldspar areas). Plag-amphibole gneiss with pegmatite (alkali felspar and qtz) with pinch and swell. Photo of layers.
5298294	321240	Amphibolite	270	87	N	Amphibolite (80%) and migmatite (20%) and lots of hornblende. Striking roughly E-W and dipping north, with patches to veins of mig.
5298346	322159	mig	87	72	N	Bands of c.g. peg, f.g. plag-hornblende, etc. Amphibolite pod 1x1m2. Net texture mig at most.
5298745	322165	peg	141	69	E	Peg 30cm wide with pegmatitic to megacrystic. Biotite near amphibolite contact.
5298750	322170	Amphibolite, boudinaged	68.5	74	N	Recrystallized hbl in amphibolite, boudinaged amphibolite
5298750	322170	hbl in mig	100	76	N	Vein texture migmatite in amphibolite, see photo for schollen?
5298775	321869	pegmatite	145	90		Felsic to intermediate lithologies are now completely melted and felsic gneiss with pegmatite.
5298561	321850	Felsic to int bands	100	60	S	
5298566	321830	Felsic to int	78.5	62	N	Felsic to intermediate mostly melted, few CPX-rich and Hbl-rich pods. Photo of felsic.
5298590	322134	Amph to intermediate, peg	89	82	S	Across Hwy 101. Amphibolite and intermediate gneiss & crosscutting peg. Photo.
5298696	322135	Amph to intermediate, peg				
						Desmond Moser's horizontal outcrops
5310581	340518		planar view			Intermediate to felsic gneiss with feldspars and quartz with CPX+Hbl+peg (mig)

						vein
		Amph				32.2-45.2m: Metamorphic, cubic Py in schistose amphibolite as "rafts" in qtz-rich gneiss
		Qtz-rich felsic gneiss				45.2-59m: Qtz-felsic gneiss with minor amphibolite and P
						Plag+CPX+Gar+Py
		Amphibolite				59-73.6m: amphibolite with green CPX+gar+py+small felsic pods
		Qtz-feldspar gneiss				73.6-76.6m: qtz-feldspar gneiss (more feldspar than previous areas)
		Peg				76.6-77.6m: pegmatite
		Amphi				77.6-89.6m: mafic
		Qtz-feldspar gneiss				89.6m-92.9m: felsic with mafic pod
		Qtz-feldspar gneiss				92.9-94.9m:
		Qtz-feldspar gneiss				94.9-96.9m: quartz-feldspar gneiss
		Felsic upper, amphibolite lower				96.9-104.6m: felsic at the highest portion, mafic near the ground
		Qtz-feldspar gneiss				104.6-111.1m: felsic unit again
		Amphibolite				111.1-122.1m: mafic and net-textured amphibolite migmatite
		Qtz-feldspar gneiss				122.1-125.1m: felsic
		Amphibolite/Peg				125.1-128.4: mafic and peg contact
		Muscovite felsic gneiss				128.4-131.0m: felsic with muscovite (up to c.g.!)
		Amphibolite				131.0-133.3: Mafic with deformed pyrite (m.g.-c.g. Py and f.g. py in epidote or cpx alteration in patchy migmatite)
		Feldspar gneiss				133.3-145.3m: Felspar-rich area in felsic unit
		Amphibolite migmatite				145.3-156.0m: mafic to intermediate with migmatite
		Felsic gneiss				156.0-172.5m: felsic unit
		Amphibolite				172.5-187.9m: intermediate to mafic
		Felsic gneiss				187.9-192.3: felsic
5304387	327875	End of Hill OC North				End of Hill OC north (epidote, hbl, py, mig? Alt?)
Wawa Gneiss at Wawa/Chapleau Hwy sign area	321023	Amphibolite migmatite	349	39	S	CPX in plag and qtz amphibolite migmatite, Edge of gneiss, NW dipping
5298015	321030		103	90	SW dipping	SW dipping

			from top of OC			clasts/xenoliths/restites
5310163	340520	cpx+hbl pod	42	30	NE	Horizontal to shallow to moderate dip (NE dip)
5310164	340522	cpx+hbl pod	49	90		Boudinage E-W in CPX+HBL pods. Photos. No dip measured
5310166	340525	foliation & fish in vein mig, feldspar gneisses	97	90		Alkali feldspar+qtz "peg" is vein migmaties (metatexites here). F.g. py in feldspar gneisses. Feldspar eyes show sinistral movement. Picture.No dip measured
5310166	341193	Amphibolite	66	75	NW	Amphibolite with garnet. Huge area on Hwy with moderate dips to NW. 20x20 and opposite of HwY 101.

APPENDIX D: CONDENSED NOTES ON SAMPLES AND PETROGRAPHY

Sample #: PVS001 **SCMR/IUGS name: Garnet amphibolite, regional boudin** **Location: Hwy 101, D. Moser's Hill Outcrop at** 5301760/325341 (16N UTM) "Footwall" amphibolite with garnet(rotated); Sulphides visible within garnet; Handsample, no thin section, geochemistry
Sample #: PVS002 **SCMR/IUGS name: Garnet amphibolite, regional boudin** **Location: Hwy 101** "Footwall" amphibolite with rare garnet; Pyrrhotite present, anhedral, disseminated, trace; some calcite veins crosscutting gneissosity; Handsample, no thin section, geochemistry
Sample #: PVS003 **SCMR/IUGS name: Garnet amphibolite, regional boudin** **Location: Hwy 101** "Footwall" amphibolite, little garnet present; Handsample, no thin section, geochemistry
Sample #: PVS004 **SCMR/IUGS name: Garnet amphibolite, regional boudin** **Location: Hwy 101** "Footwall" amphibolite, little mm-size red garnet present; but with calcite veins present; Handsample, no thin section, geochemistry
Sample #: PVS005 **SCMR/IUGS name: Feldspar-quartz leucosome to neosome, regional boudin neck** **Location: Hwy 101** "Feldspar porphyry" or diorite? next to garnet-amphibolite PVS004, least deformed; Handsample, no thin section, geochemistry
Sample #: PVS006 **SCMR/IUGS name: Feldspar-quartz leucosome to neosome, regional boudin neck** **Location: Hwy 101** "Feldspar porphyry" 2nd least deformed; Handsample, no thin section, geochemistry
Sample #: PVS007 **SCMR/IUGS name: Feldspar-quartz leucosome to neosome, regional boudin neck** **Location: Hwy 101** "Feldspar porphyry" most deformed, silica rich; Handsample, no thin section, geochemistry
Sample #: PVS008 **SCMR/IUGS name: Amphibolite, mylontite** **Location: Boudin Outcorp, Probe Mine Inc. Boudin Outcrop at** 5305232/320828 (16N UTM) Amphibolite with plagioclase porphyroclasts; blastomylonite, areas of grain size reduction visible; Handsample, no thin section, geochemistry
Sample #: PVS009 **SCMR/IUGS name: Amphibolite mylonite** **Location: Boudin Outcorp** Amphibolite with c.g. porphyroblasts of green-blue amphiboles. Partially rplaced by chlorite, blastomylonite; Handsample, no thin section, geochemistry
Sample #: PVS010 **SCMR/IUGS name: Amphibolite, mylonitic** **Location: Boudin Outcorp**

Amphibolite with c.g. porphyroblasts of green-blue amphiboles. Same as PVS009, ultramylonite; Handsample, no thin section, geochemistry
Sample #: PVS011 **SCMR/IUGS name: Garnet amphibolite, mylonitic** **Location: Boudin Outcorp** "Hanging wall amphibolite" at camp name. Boudinaged garnet-amphibolite gneiss; Handsample, no thin section, geochemistry
Sample #: PVS012 **SCMR/IUGS name: Metaconglomerate** **Location: Conglomerate Outcorp 5305058/330439 (16N UTM)** Metaconglomerate, flattened and elongated clasts (ultramafic, mafic, intermediate, felsic); Handsample, no thin section, geochemistry
Sample #: PVS013 **SCMR/IUGS name: Garnet-biotite gneiss** **Location: Discovery Zone Trench, 5303700/330306 (16N UTM)** Garnet-biotite gneiss ore or termed "garnet-biotite felsic gneiss" at camp, lower discovery outcrop; Handsample, no thin section, geochemistry
Sample #: PVS014 **SCMR/IUGS name: Garnet-biotite gneiss** **Location: Discovery Zone Trench** Amphibolite ore, trace euhedral pyrite and anhedral pyrrhotite, south side of upper discovery outcrop. Contact with felsic gneiss to the north; Handsample, no thin section, geochemistry
Sample #: PVS015 **SCMR/IUGS name: Sillimanite-garnet-muscovite gneiss** **Location:** BL62; 4-5m Sillimanite (2^{nd} isograd), garnet (m.g., euhedral), biotite, and muscovite in the same sample. Sillimanite and muscovite in the same area of the trench! Named "Felsic gneiss" at camp. Handsample, no thin section, geochemistry
Sample #: PVS016 **SCMR/IUGS name: Garnet-sillimanite-biotite gneiss** **Location: Drill core BL62 at 32.5 m depth** V.c.g., pegmatitic. Quartz (anhedral) matrix and boudinaged quartz vein porphyroclasts with tails of muscovite, pyrite, pyrrhotite) (30%), feldspars (subhedral to euhedral, microcline, perthite) (30%), fibrolite (euhedral) (15%), unstable prismatic sillimanite (subhedral to euhedral) (5%), biotite (subhedral) (10%), muscovite (subhedral to euhedral) (8%), sulphides (2%, pyrite, pyrrhotite), rutile (trace, euhedral), chlorite (trace, anhedral), tourmaline (trace, anhedral), carbonate (trace, anhedral). The quartz and felspars display undulose extinction and evidence for subgrains. Biotite in boudin necks is rotated and kinked while the muscovite and fibrolite define the boudin necks. Fibrolite has grown in the late muscovite. The matrix quartz displays checkerboard microstructures and provides a minimum temperature of deformation of 850C. Quartz and feldspar ribbons provide evidence of diffusion creep during amphibolite facies. The sulphides define kinematic indicators and have been boudinaged and quartz and carbonates have filled the boudin necks.
Sample #: PVS017 **SCMR/IUGS name: Riebeckite-phlogopite-chlorite lamprophyre** **Location: Drill core BL63 at 153-155 m depth**

6328

6329

6330

V.c.g. to c.g. Preodminantly metamorphosed lamprophyre and minor garnet-biotite schist host rock. The lamprophyre is c.g. to v.c.g. and dominated by euhedral, v.c.g. biotite (40%, tan to brown pleochroism), anthophyllite (10%), riebeckite (10%), epidote (10%), talc (10%), carbonate (5%), garnet (10%), prehnite (5%), chlorite (5%), oxides (magnetite, 1%), and albite (4%). The feldspar is only in equilibrium with the garnet. Biotite is extremely coarse grained and dominates the lithology. The amphiboles, epidote, talc, prehnite, and chlorite have completely replaced earlier mineralogy and the blue amphibole also occurs in biotite cleavage planes. Even with working with lamprophyres in my MSc. I have never seen such a strange mineralogical assemblage except in metamorphosed lamprophyres in the Wabigoon subprovince.
Sample #: PVS018 **SCMR/IUGS name: Riebeckite-phlogopite-chlorite lamprophyre and healed breccia** **Location: Drill core BL70 at 103-104 m** Sampled for the blue mineral observed in drill core. V.c.g. to v.f.g. Clasts visible in sample. Garnet (anhedral, 10%) fractured, biotite (subhedral to euhedral, 30%), amphibole (subhedral to euhedral, clear, anthophyllite, radiating) 20%, blue amphibole (anhedral to subhedral, blue-violet pleochroism, riebeckite interior to the other clear amphiboles) (10%), prismatic clear anthophyllite, epidote (tr), carbonate matrix (20%), feldspar clasts (10%), and opaques (trace). The Garnet is fractured an anhedral, biotite, felspars, define the foliation. Feldspars are completely replaced. Numerous plucked areas. Pyrites have quartz fringes. The anthophyllite pseudomorphs earlier pyroxene or olivine. (Photo: 10x, blue amphiboles and biotite).
Sample #: PVS019 **SCMR/IUGS name: Glaucophane-biotite amphibolite** **Location: Drill core BL70 at 132-133 m** F.g. to m.g. Biotite-glaucophane amphibolite. Hornblende (subhedral to euhedral, green pleochroism) defines the lineation and foliation (40%), plagioclase (subhedral, weakly to moderately altered to sericite, 35%), quartz-carbonate veins (10%), biotite (very coarse grained, 10%), glaucophane (4%, euhedral, replaced earlier hornblende where stable with biotite), and sulphides (1%). (Photo: 20x, blue amphibole after hornblende next to biotite).
Sample #: PVS020 **SCMR/IUGS name: Biotite-perthite gneiss** **Location: Drill core BL70 at 172-173m** V.c.g., equigranular. Quartz (anhedral, 30%), alkali feldspars (subhedral to euhedral, perthite, microcline, 30%), plagioclase (subhedral, 10%), biotite (15%), muscovite (15%), and opaques (trace). Deformation twins are present in all feldspars. Perthite has flame lamellae. Subgrains in all feldspars. Pyroxene crystals are out of equilibrium and are replaced with amphibole, carbonate, and biotite. Undulose extinction, subgrains, and grain shape bulging is present in quartz and feldspars. Weak to moderate sericite alteration in plagioclase. Gentle to open folds in perthitic flame lamalle!
Sample #: PVS021 **SCMR/IUGS name: Sillimanite-chrysoberyl-biotite gneiss** **Location: Drill core BL174 at 109 m** C.g. to v.c.g. Sillimanite (euhedral, prismatic and fibrolite, 10%), alkali feldspars (subhedral to euhedral, 30%), albite (euhedral, 10%), biotite (subhedral, 10%), garnet (anhedral, 5%), quartz (20%), chrysoberyl (10%), opaques (4%), tourmaline (trace) and carbonate (1%). No

6331

muscovite is present in thin section. Prismatic sillimanite exhibits undulatory extinction and is openly folded. Chrysoberyl is in equilibrium with quartz and biotite. Prismatic sillimanite is present as inclusions in porphryoblastic and poikiolitic garnet and in strain shadows around garnet. Plagioclase coronas around garnet. Fibrolite is located everywhere else in cleavage and crystal boundaries of quartz-feldspar. Carbonate is also located in strain shadows and in fractures in garnet. Quartz exhibits undulatory extinction, subgrains, bulging, and ribbons. The garnet is inclusion zoned in the core and nearly inclusion-free at the rims.
Sample #: PVS022 **SCMR/IUGS name: Tourmaline-garnet-biotite schist** **Location: Drill core BL174 at 109.5 m** C.g. to v.c.g. The general fabric of the sample is a schistose, healed breccia after gneissosity. The garnet (fractured, subhedral, 10%), biotite (20%), quartz (30%), alkali feldspars (30%), plagioclase (5%), tourmaline (5%), and opaques (sulphides and magnetite; lollengite, pyrite, gold, and pyrrhotite, 5%). Schistosity and boudinage overprint the earlier gneissosity and brecciation. The intensely fractured garnet and matrix is infilled with quartz, biotite, carbonate, and tourmaline. Microfaults and quartz veins crosscut all minerals. The interior of a quartz-only vein is composed entirely of carbonate suggesting the carbonate phase was latest if the syntaxial features are valid. The quartz exhibits undulatory extinction, subgrains, and bulging in the quartz veins and undulatory extinction in the matrix. Tourmaline as smaller brecciated fragments in garnet and biotite define brecciated areas with quartz veins. Pyrite, lollengite, pyrrhotite in garnet as inclusions. Lollengite in healed breccias. Tourmaline is olive to army green with sector zoned interiors of a turquoise green. (Photo: 10x, tourmaline in garnet fractures).
Sample #: PVS023 **SCMR/IUGS name: Amphibolite in ore zone with cm-thick pyrrhotite with net textures** **Location: Drill core BL308 at 465.9 m depth** Greatest amount of sulphides at Borden (modal 3-5%). Stringers of sulphide displaying net-textures at contact between footwall amphibolite and gold zone; Handsample, no thin section, geochemistry
Sample #: PVS024 **SCMR/IUGS name: Sillimanite-garnet-muscovite gneiss** **Location: Drill core BL12-311 at 251.2 m** C.g. to v.c.g. Quartz (20%), alkali feldspars (20%), albite (5%), garnet (10%), biotite (20%), muscovite (10%), sillimanite (fibrolite and prismatic, 10%), and opaques (5%). Fibrolite is located in c.g. muscovite, biotite, and quartz with prismatic sillimanite in the interiors of the fibrolite mats. Prismatic sillimanite is also preserved as inclusions in garnet and biotite. Photos of prismatic sillimanite and garnet and k-spar, 10x.
Sample #: PVS025 **SCMR/IUGS name: Amphibolite and leucosome contact** **Location: Drill core BL10-11 at 34 m** Amphibolite and "felsic gneiss" boundary, maybe also QFP? Sheared with 246 ppb Au, 7ppb Ag; Handsample, no thin section, geochemistry
Sample #: PVS026 **SCMR/IUGS name: Amphibolite** **Location: Drill core BL10-11 at 38.4 m** Amphibolite, 509 ppb Au, 9 ppb Ag; Handsample, no thin section, geochemistry

6332
6333

Sample #: PVS027 **SCMR/IUGS name: Amphibolite** **Location: Drill core BL10-11 at 43 m** F.g. to m.g. amphibolite, equigranular, lacks schistosity or gneissosity. Plagioclase feldspar (subhedral to euhedral, 40%), hornblende (green to tan pleochroism, euhedral, 50%), opaques (pyrite, pyrrhotite, 5%), and quartz veins (5%). Undulatory extinction exhibited in plagioclase feldspar and quartz. Zircon minerals are >trace, perhaps 0.0125%. Probe Mines Inc. gold fire assay value of 371 ppb.
Sample #: PVS028 **SCMR/IUGS name: Biotite gneiss, neosome** **Location: Drill core BL10-12 at 5.5 m depth** C.g. to v.c.g. Quartz (anhedral, 40%), alkali feldspars (microcline and perthite, 30%), albite feldspar (subhedral, 10%), chrysoberyl (euhedral, 4%), biotite (subhedral, 15%), sulphides (1%, pyrite), and zircon (trace). Biotite and zircon define the foliation of this lithology. The plagioclase albite feldspar is moderately to intensely altered to sericite. Photo: 10x Chrysoberyl with penetration twins. Contact between amphibolite and feldspar-rich gneisses. Probe Mines Inc. gold fire assay value of 501 ppb.
Sample #: PVS029 **SCMR/IUGS name: Garnet-pyroxenes Amphibolite** **Location: Drill core BL10-12 and 12m depth** F.g. to m.g. amphibolite. Hornblende (euhedral, m.g., porphyroblastic, poikioblastic with plagioclase inclusions, defines schistosity, previous gneissosity, and lineations, 40%), plagioclase (euhedral, 30%), pyroxene (one population of m.g., subhedral to euhedral, green cpx augite 20% and a second population, v.c.g., skeletal, opx with no pleochroism, 2%), garnet (anhedral, skeletal, 8%), quartz (quartz vein that displays undulose extinction, subgrains, serrated edges, regime 3), and sulphides and gold (pyrite and arsenopyrite as daughter minerals with coronas of gold and pyrrhotite, trace). Garnet, cpx, and hornblende in or near the quartz vein are v.f.g. and anhedral. Probe Mines Inc. gold fire assay value of 1860 ppb.
Sample #: PVS030 **SCMR/IUGS name: Amphibolite** **Location: Drill core BL10-12 at 32 m depth** M.g. Plagioclase (euhedral, 40%), hornblende (35%), biotite (10%), microcline (5%), titanite (euhedral, 5%), quartz (quartz veins, 5%), plagioclase myermykite (trace), sericite (trace), epidote (trace), and opaques (trace). Sericite defines zoning in plagioclase with the interiors of the plagioclase moderately to intensely altered and the rims unaltered, particularly where mymekite is present. Feldspars display deformation twins, undulose extinction, and subgrains. Photo of deformed and twinned plagioclase and microcline 10x. Probe Mines Inc. gold fire assay value of 82 ppb.
Sample #: PVS031 **SCMR/IUGS name: Augite-biotite amphibolite** **Location: Drill core BL10-12 at 53 m** F.g. to v.c.g. Plagioclase feldspar (subhedral to euhedral, weakly sericitized, 25%), hornblende (f.g., euhedral, 25%), cpx augite (subhedral, 10%), scapolite (15%), and biotite (subhedral, 25%). Probe Mines Inc. gold fire assay value of 903 ppb.
Sample #: PVS032 **SCMR/IUGS name: Biotite-perthite schist**

6334
6335

Location: Drill core BL10-12 at 65.4 m M.g. to c.g. Alkali feldspars (euhedral, microcline and perthite, 40%), biotite (subhedral, brown to tan pleochroism, 20%), plagioclase (10%), quartz (15%), hornblende (10%), carbonate (5%), sulphides (trace), muscovite (trace), titanite (trace), and garnet (trace). All sulphides are rimmed by carbonate. All quartz and feldspars exhibit undulose extinction, subgrains, and deformation twins. Probe Mines Inc. gold fire assay value of 1531 ppb.
Sample #: PVS033 **SCMR/IUGS name: Garnet-biotite schist** **Location**: **Drill core BL10-12 at 70 m** C.g. to v.c.g. Alkali feldspars (euhedral, microcline and perthite, 40%, biotite (subhedral, m.g., 20%), garnet (euhedral, 10%), quartz (20%), plagioclase (subhedral, moderately sericitized, 5%), muscovite (euhedral, c.g., adjacent to sulphides, 4%), sulphides (anhedral, disseminated gold, 1%). Biotite defines the intense foliation. Probe Mines Inc. gold fire assay value of 5199 ppb.
Sample #: PVS034 **SCMR/IUGS name: Garnet-biotite-muscovite schist** **Location: Drill core BL10-12 at 79.9 m depth** C.g. to v.c.g.Alkali feldspars (euhedral, 30%), quartz (anhedral, 20%), plagioclase (anhedral, intensely sercitized, 10%), biotite (subhedral, 30%), muscovite (euhedral, 5%), and garnet (anhedral to subhedral, adjacent to sulphides, 5%). The quartz is generally polygonal with only a few instances of undulatory extinction and subgrains. The plagioclase is too altered to detect any internal deformation. Probe Mines Inc. gold fire assay value of 800 ppb.
Sample #: PVS035 **SCMR/IUGS name: Chyrosberyl-garnet-biotite gneiss** **Location: Drill core BL10-12 at 92.4 m depth** C.g. to v.c.g. Garnet (anhedral, poikiloblastic and porphyroblastic, 10%), biotite (subhedral, 20%), quartz (anhedral, 30%), plagioclase (subhedral, 10%), alkali feldspars (euhedral, 22%), chrysoberyl (euhedral, 5%), sulphides (3%, pyrrhotite, pyrite, gold disseminated throughout particularly in biotite cleavage planes and defining boudins). Quartz and feldspars exhibit undulose extinction, subgrain boundaries, serrated grain boundaries, and deformation twins. Probe Mines Inc. gold fire assay value of 8439 ppb.
Sample #: PVS036 **SCMR/IUGS name: Garnet-biotite schist** **Location: Drill core BL10-12 at 102.5 m depth** C.g. Alkali feldspar (euhedral, c.g. microcline and perthite, 30%), quartz (c.g. porphyroclasts, 30%), plagioclase (moderately to intensely sericitized, 10%), biotite (subhedral, 20%), garnet (10%), carbonate (trace), sulphides (anhedral to euhedral, trace), oxides (titanomagnetite, trace), muscovite (euhedral, trace), opx (anhedral, skeletal, trace). Opx is stable with carbonate, biotite, and sulphide and as inclusions in anhedral sulphide in trace amounts. Weak foliation defined by biotite. Probe Mines Inc. gold fire assay value of 2480 ppb.
Sample #: PVS037 **SCMR/IUGS name: Biotite-muscovite schist to amphibolite with gradual contact** **Location: Drill core** BL10-12 at 122.5 m C.g. Alkali feldspars (subhedral to euhedral, microcline, perthite, 30%), plagioclase (subhedral to euhedral, weak sericite alteration 10%), quartz (20%), hornblende (subhedral to euhedral, 10%), opx (anhedral, skeletal, trace), biotite (subhedral, 20%), muscovite (after biotite, 10%),

6336

6337

6338

and sulphides (pyrrhotite, pyrite, gold, defining foliation, trace). Biotite defines the foliation. Quartz in quartz veins exhibits undulose extinction, subgrains, healed and folded fractures, and serrated grain boundaries. Boudinaged sulphides with recrystallized subgrains of quartz in the neck. Xenotime after zircon. Probe Mines Inc. gold fire assay value of 6611 ppb.
Sample #: PVS038 **SCMR/IUGS name: Quartz-perthite neosome** **Location: Drill core BL10-12 at 134.1 m** C.g. to v.c.g. Alkali feldspars (euhedral, microcline, perthite, and mymekitic textures, 30%), quartz (anhedra, graophyricl, 30%), plagioclase (subhedral to euhedral, weak sericite alteration, 20%), biotite (subhedral, weak foliation, 20%). Pegmatitic textures. Quartz and feldspars exhibit undulose extinction with chessboard extinctions in a few grains, subgrains, and bulging. Probe Mines Inc. gold fire assay value of 1261 ppb
Sample #: PVS039 **SCMR/IUGS name: Calc-silicate and amphibolite contact** **Location: Drill core** BL10-12 at 141 m F.g. to m.g. Calc-silicate layer in amphibolite. Plagioclase (subhedral, 20%), scapolite (anhedral, 20%), hornblende (subhedral to euhedral, 30%), cpx augite (5%), titanite (euhedral, 5%), carbonate (20%), quartz (trace), and sulphides (trace). The lithology is predominantly amphibolite with limited sections of calc-silicate. The weak foliation is defined by hornblende. Lineations are also defined by hornblende. Probe Mines Inc. gold fire assay value of 923 ppb.
Sample #: PVS040 **SCMR/IUGS name: Chlorite-biotite amphibolite** **Location: Drill core BL10-12 at 146.25 m depth** C.g. Biotite amphibolite intrusive Plagioclase (25%), alkali feldspars (20%), quartz (10%), biotite (25%), zoisite (5%), chlorite (5%), carbonate (10%). Weakly foliated with biotite and chlorite after biotite defining the foliation. The plagioclase feldspars are weakly to moderately altered to sericite. The zoicite, chlorite, and carbonate have replaced earlier hornblende. Probe Mines Inc. gold fire assay value of 39 ppb.
Sample #: PVS041 **SCMR/IUGS name: Chlorite-biotite amphibolite** **Location: Drill core BL10-12 at 190.5 m depth** F.g. to m.g. Plagioclase (subhedral, moderate to intense sericite alteration, 20%), alkali feldspars (subhedral to euhedral, 20%), quartz (10%), biotite (subhedral, 20%), chlorite (subhedral, 10%), actinolite (subhedral, acicular after chlorite, 10%), and carbonate (anhedral, 10%). Probe Mines Inc. gold fire assay value of 86 ppb.
Sample #: PVS042 **SCMR/IUGS name: Augite amphibolite** **Location: Drill core BL10-12 at 198 m depth** Cpx augite (c.g., subhedral, 30%), hornblende (euhedral, 20%), plagioclase (euhedral, 30%), scapolite (10%), titanite (euhedral, c.g., deformation twins, quartz (5%), sulphides (anhedral, 5%), carbonate (trace), and opx (trace, one instance of opx inclusion in sulphide). The chlorite is predominantly adjacent to sulphide. Probe Mines Inc. gold fire assay value of 414 ppb.
Sample #: PVS043 **SCMR/IUGS name: Amphibolite**

6339

Location: Drill core BL10-12 at 208.0 m depth M.g. Amphibolite. Equigranular, lacks foliation. Hornblende (tan to green pleochroism, f.g.-m.g., euhedral, 45%), plagioclase (subhedral to euhedral, 45%), cpx (anhedral, skeletal, 5%), carbonate (anhedral, 5%), and sulphides (trace). The chlorite is predominantly adjacent to sulphide. Probe Mines Inc. gold fire assay value of 16 ppb.
Sample #: PVS044 **SCMR/IUGS name: Biotite schist into amphibolite** **Location: Drill core BL10-12 at 208.56 m depth** M.g. to c.g. The Biotite schist (intermediate) sample grades into an amphibolite (mafic). The biotite schist is composed of alkali feldspars (euhedral to subhedral, 30%), plagioclase (subhedral, weak sericite alteration, 20%), quartz (30%), and biotite (20%) with biotite and quartz defining the foliation. The mafic side of the sample is composed of plagioclase (40%), hornblende (euhedral, green to tan pleochroism, 30%), cpx augite (anhedral, 20%), titanite (euhedral, 5%), carbonate (5%), and sulphides (trace). Probe Mines Inc. gold fire assay value of 24 ppb.
Sample #: PVS045 **SCMR/IUGS name: Amphibolite** **Location: Drill core BL10-12 at 216m depth** M.g. to c.g. amphibolite. Hornblende (euhedral, m.g., green pleochroism, 30%), cpx augite (m.g. to c.g., anhedral to euhedral, 30%), plagioclase (euhedral, moderately altered by sericite, 40%), titanite (clear to pink pleochroism, euhedral, 5%), carbonate (anhedral, 5%), chlorite (subhedral, 5%), and sulphides (trace). Probe Mines Inc. gold fire assay value of 21 ppb.
Sample #: PVS046 **SCMR/IUGS name: Amphibolite** **Location: Drill core BL10-12 at 221 m depth** M.g. amphibolite. Hornblende (euhedral, m.g., green pleochroism, 30%), cpx augite (c.g., anhedral to subhedral, 20%), plagioclase (euhedral, moderately sericite altered, 30%), carbonate (anhedral, 10%), opx (clear, parallel extinctions, poikioblastic, 5%), rutile (trace), and sulphides (trace). The pyroxenes define one lineation and the later amphibole defines a second and intersect at nearly 90 degrees. Probe Mines Inc. gold fire assay value of 8 ppb.
Sample #: PVS047 **SCMR/IUGS name: Amphibolite** **Location: Drill core BL10-12 at 233 m depth** M.g. Amphibolite. Hornblende (euhedral, green to yellow pleochroism, 50%), plagioclase (euhedral, weak to moderate sericite alteration, 40%), carbonate (crosscutting carbonate veins, 10%). The hornblende defines the lineation. Only locally do a few plagioclase crystals display undulatory extinction, subgrains, and deformation twins. Probe Mines Inc. gold fire assay value of 2.5 ppb.
Sample #: PVS048 **SCMR/IUGS name: Garnet-biotite gneiss** **Location: Drill core BL10-13 at 108.5 depth** Garnet-biotite gneiss or “Garnet biotite felsic gneiss” at camp, 1540 ppb Au, geochemistry
Sample #: PVS049 **SCMR/IUGS name: Garnet-fibrolite-biotite schist** **Location: Drill core BL10-13 at 109.5 m depth**

6340
6341

C.g. to v.c.g. Alkali feldspars (subhedral to euhedral, 20%), plagioclase (euhedral, 15%), quartz (anhedral, 20%), biotite (subhedral, 20%), muscovite (subhedral, 10%), garnet (anhedral to subhedral, 5%), fibrolite sillimanite (9%), sulphides (1%). The biotite, muscovite, and fibrolite define the foliation. Probe Mines Inc. gold fire assay value of 920 ppb.
Sample #: PVS050 **SCMR/IUGS name: Garnet-biotite gneiss** **Location: Drill core BL10-13 at 113 m depth** Alkali feldspars (f.g. to c.g., subhedral to euhedral, 40%), quartz (anhedral, m.g., 15%), biotite (subhedral, m.g. to c.g., brown pleochroism, 20%), garnet (f.g. to m.g., euhedral, 10%), muscovite (m.g., subhedral, 10%), oxides (magnetite and ilmenite, trace), and sulphides (anhedral pyrrhotite infilling fractures and as coronas around pyrite and gold, gold is anhedral in anhedral pyrrhotite, pyrite and lollengite daughter inclusions in pyrrhotite with gold coronas, sulphides define foliation and boudinage, including healed fractures in boudin necks, 5%). (Photo: Quartz and alkali feldspar inclusions in sulphides exhibit evidence of undulatory extinction, serrated grain boundaries, and subgrains while the matrix crystals do not and have recovered almost completely.) Probe Mines Inc. gold fire assay value of 7476 ppb.
Sample #: PVS051 **SCMR/IUGS name: Garnet-biotite gneiss** **Location: Drill core BL10-13 at 113.5 m depth** Garnet biotite felsic gneiss, 1380 ppb Au, geochemistry
Sample #: PVS052 **SCMR/IUGS name: Garnet-biotite gneiss** **Location: Drill core BL10-13 at 115 m depth** Alkali feldspars (f.g. to c.g., subhedral to euhedral, microcline and perthite, 35%), quartz (anhedral, m.g., 15%), biotite (subhedral, m.g. to c.g., brown pleochroism, 20%), garnet (f.g. to m.g., euhedral, with <20 µm anhedral monazite inclusions, 15%), muscovite (m.g., subhedral, 10%), and sulphides (anhedral pyrrhotite infilling fractures and as coronas around pyrite and gold, gold is anhedral in anhedral pyrrhotite, pyrite and lollengite daughter inclusions in pyrrhotite with gold coronas, sulphides define foliation and boudinage, 5%). Probe Mines Inc. gold fire assay value of 4325 ppb.
Sample #: PVS053 **SCMR/IUGS name: Garnet-biotite gneiss** **Location: BL10-13 at 115.5 m depth** Sample collected from drill core and left in core shack during field mapping. Disappeared in summer 2013 and found again in 2014 in Sarah's room after Probe Mines Inc. geologist Sarah quit and Gleceria Gamelin moved in for summer lodging.
Sample #: PVS054 **SCMR/IUGS name: Healed, schistose cataclasite, fault zone** **Location: Drill core BL13-474 at 372.5 m depth** V.c.g. to aphanitic (Healed breccia to pseudotachylite). The rock is composed of quartz (30%), alkali feldspars (30%), plagioclase (30%), carbonate (10%), hematite (trace), and talc (trace). The clasts are angular to very angular. The grain size ranges from v.c.g. pegmatitic textures to aphantitic pseudotachylite.
Sample #: PVS055 **SCMR/IUGS name: Healed, schistose cataclasite, fault zone in Garnet-clinopyroxene-hornblende gneiss or Plagioclase-free restite**

6342
6343

Location: Drill core BL13-474 at 372.9 m depth Garnet (c.g. to v.c.g., subhedral, 30%), cpx pyroxene (subhedral to euhedral, clear to green pleochroism, 30%), horblende (subhedral, light green to dark green pleochroism, 30%), carbonates (5%), opaques (5%). Bands of hornblende (and trace zoicite) in mylontitic areas. No plagioclase in sample (photo: 5x, cpx-gar only). Plagioclase-only dykes, sills, and intrusives are adjacent to samples and concentrate in low-pressure areas in the field. Ivanhoe Lake Deformation Zone in Chapleau Belt.
Sample #: PVS056 **SCMR/IUGS name: Garnet-biotite gneiss** **Location: Drill core BL12-256 at 340 m depth** Quartz (anhedral, v.f.g. to c.g., anhedral, 30%), biotite (subhedral, 30%), garnet (anhedral to euhedral, f.g. to m.g., 15%), plagioclase (anhedral, completely sericitized, 20%), sulphides (pyrite, pyrrhotite, gold located predominantly in boudinaged quartz veins and native gold is disseminated throughout, 5%), alkali feldspars (trace), carbonate (crosscutting vein). Photo: 5x, Sulphides and garnet define the quartz vein boundaries and "pin" many subgrains. They are located along the grain boundaries and healed fractures. Garnet, sulphides, and biotite define the foliation in this sample. Quartz is nearly polygonal with relatively few remaining subgrains showing it recovered almost completely. Ore zone sampled.
Sample #: PVS057 **SCMR/IUGS name: Neosome; Beryl-perthite pegmatite** **Location: Drill core BL12-256 at 341.4 m depth.** C.g. to v.c.g.Alkali feldspars (anhedral to euhedral, perthite, microcline, myrmekitic textures, 40%), quartz (anhedral, granophyric textures, 30%), plagioclase (subhedral, interiors intensely zoned with sericite, exterior graphitic, 30%), biotite (subhedral, 10%), chlorite (anhedral, after biotite, 5%), muscovite (subhedral, 5%), sulphides (5%), and trace beryl (bright green colour, no pleochroism, euhedral). Alkali feldspars and plagioclase feldspars exhibit evidence of subgrain formation, bulging, and deformation twins. V.c.g. quartz exhibits undulose extinction, serrated grain boundaries, and bulging. No chessboard textures or significant grain size reduction. Photo at 5x. Ore zone sampled.
Sample #: PVS058 **SCMR/IUGS name: Neosome; Biotite-chlorite gneiss** **Location: Drill core BL12-256 at 345.2 m depth** C.g. to v.c.g. Altered biotite intrusive. Quartz (anhedral, 40%), biotite (subhedral, m.g. and as inclusions in sulphides otherwise v.c.g., 30%), chlorite (after biotite, 15%), muscovite (subhedral, 5%), carbonate (anhedral, 5%), and sulphides (euhedral, pyrite, 5%). Carbonate-rich zones are composed of v.f.g. from grain size reduction, Regime 3 quartz, and limited biotite. Biotite and chlorite may have replaced pyroxenes due to faint, prismatic crystal shapes they have polymorphed. Ore zone sampled.
Sample #: PVS059 **SCMR/IUGS name:** Restite; amphibolite with 25% modal quartz veins **Location: Drill core BL12-256 at 348.6 m depth** C.g. to v.c.g. Quartz veins in amphibolite. Restite of of PVS058 neosome. Quartz (anhedral, 25%), plagioclase (25%), augite clinopyroxene (subhedral to euhedral, 40%), carbonate (10%), opaques (trace), chlorite (trace), alkali feldspars (trace), and titanite (trace). Blue amphibole is located along the crystal boundaries of clinopyroxene and carbonate. The quartz

6344
6345

veins are v.c.g., anhedral, exhibit undulatory extinction, have serrated edges, and minor subgrains. They are regime 2. Ore zone sampled.
Sample #: PVS060 **SCMR/IUGS name: SCMR/IUGS name: Restite; amphibolite with 40% modal quartz veins** **Location: Drill core BL12-256 at 350.4 m depth** C.g. to v.c.g. amphibolite and quartz veins. A more altered version of PVS059. Quartz (anhedral to subhedral, 40%), augite clinopyroxene (subhedral to euhedral, light green pleochroism, 40%), blue-green amphibole (upper amphibolite blue-green amphibole, after hornblende, not defining the earlier foliation and lineation like tan-brown pleochroic hornblende but defining the second foliation and lineation of the foliation boudinage, 10%), carbonate 9anhedral, 5%), zoicite (after pyroxenes and plagioclase, 5%), chlorite (trace), epidote (matrix, trace), and opaques (pyrrhotite, magnetite, trace). The quartz exhibits more instances of subgrains, bulging, and smaller grain sized reduced grains. Ore zone sampled.
Sample #: PVS061 **SCMR/IUGS name: Neosome; Quartz-biotite-muscovite pegmatite** **Location: Drill core BL12-256 at 360.9 m** Pegmatite, some undulatory extinction and serrated grains but less than previous samples. Quartz (anhedral, v.c.g, 50%), biotite (subhedral, 10%), muscovite (subhedral, after plagioclase, 10%), plagioclase (subhedral, v.c.g., 30%), carbonate (trace), chlorite (trace), opaques (trace). The plagioclase is has healed fractures and faults. No subgrains are noted in thin section so this must be late in the petrogenetic sequence. Photo: Serrated quartz grain boundaries (5X). Ore zone sampled.
Sample #: PVS062 **SCMR/IUGS name: Amphibolite** **Location: Drill core BL13-479 at 482.6 m depth** Ore zone, 5% pyrrhotite, and heavily altered with carbonate and chlorite. Has not been returned from Vicki at GSC in Ottawa.
Sample #: PVS063 **SCMR/IUGS name: Chrysoberyl-perthite-quartz leucosome** **Location: Drill core BL13-481 at 534.3 m depth** Pegmatitic leucosome with a mm-bleb of visible gold at crystal boundaries
Sample #: PVS064 **SCMR/IUGS name: Leucosome and melanosome in amphibolite** **Location: Drill core BL13-13 at 20.3 m** Amphibolite with both melanosome (garnet, pyroxenes) and leucosome (perthite, quartz, plagioclase).
Sample #: PVS065 **SCMR/IUGS name: Leucosome in garnet-biotite amphibolite (BIF/quartz vein)** **Location: Drill core BL13-13 at 21.8 m depth** Early oxide facies BIF/quartz veins in amphibolite. M.g. to c.g. Quartz (anhedral, predominantly veins, 30%), plagioclase (subhedral to euhedral, m.g., moderately sericitized, 30%), hornblende (subhedral to euhedral, tan-green pleochroism, 20%), garnet (anhedral, fractured, f.g., 10%), biotite (anhedral to subhedral, 10%), and carbonate (anhedral, trace%). Undulatory extinction sweeping OVER earlier chessboard in quartz vein (photo, 5x). Plagioclase is typically exhibits deformation twins. Ore zone sampled.

6346

6347

6348

Sample #: PVS066 **SCMR/IUGS name: Tightly folded leucosome in garnet-biotite amphibolite (BIF/quartz vein)** **Location: Drill core BL13-13 at 26.7 m depth** M.g. to c.g. Quartz (anhedral, c.g., veins, 30%), hornblende (subhedral, tan-green pleochrosim, 20%), plagioclase (subhedral, moderately to intensely sericitized, 30%), biotite (subhedral, 15%), carbonate (5%), opaques (trace). The biotite appears to aligned with the amphibole cleavage planes. The quartz and feldspar are more deformed than PVS065 with quartz and feldspar displaying subgrains. Quartz exhibits serrated grain boundaries. Near ore zone sampled.
Sample #: PVS067 **SCMR/IUGS name: Pegmatitic perthite-quartz-plagioclase leucosome in garnet-biotite amphibolite melanosome** **Location: Drill core BL13-13 at 34.3 m** M.g. to v.c.g. Quartz (c.g. to pegmatitic, anhedral, 30%), alkali feldspars (c.g. to pegmatititc, subhedral to euhedral, microcline, perthite, 30%), plagioclase (c.g. to pegmatitic, subhedral to euhedral, no sericite alteration to weak alteration, 30%), biotite (c.g. to pegmatitic, anhedral to subhedral, after hornblende 5%), hornblende (c.g. to pegmatitic, subhedral, light green to dark green pleochroism, blue-green at boundaries with biotite, 5%), and sulphides (trace). The non-altered feldspars display deformation twins while the quartz crystals exhibit undulatory extinction, subgrains, and serrated grains. Photo: serrated quartz grains. Near ore zone.
Sample #: PVS068 **SCMR/IUGS name: Schistose, mylonititc cataclasite in amphibolite** **Location: Drill core BL13-13 at 50.3 m** Plagioclase (subhedral, f.g. to m.g., completely replaced by sericite except for a few crystals, 40%), quartz (anhedral, f.g. to c.g., veins, 30%), hornblende (subhedral, defining lineation and foliation, tan-green pleochroism, 20%), biotite (subhedral, 10%), chlorite (trace), carbonate (trace), and opaques (pyrite, anhedral to euhedral, trace). The quartz exhibits undulatory extinction, subgrains, bulging, and grain size reduction while the plagioclase may only exhibit a few instances of subgrains. As the plagioclase is completely altered it is difficult to assess.
Sample #: PVS069 **SCMR/IUGS name: Amphibolite** **Location: Drill core BL13-13 at 50.18 m** M.g. to c.g. amphibolite. Hornblende (subhedral to euhedral, tan to dark green pleochroism, 30%), plagioclase (anhedral to subhedral, f.g. to c.g., f.g. are subgrains within larger areas of plagioclase with deformation twins and no alteration, c.g. plagioclase is completely altered to sericite, 40%), biotite (subhedral, c.g., and as an inclusion in sulphides, 10%), carbonate (veins, crosscut earlier quartz veins, anhedral to euhedral, deformation twins and thick high-temperature twins, 10%), quartz (earlier, boudinaged quartz veins, anhedral, subgrains, undulatory extinction, brecciated in areas of carbonate veins, 10%), and sulphides (trace, located in hornblende cleavage planes, in matrix). The latest vein that crosscuts earlier veins and amphibolite is carbonate-only and at an oblique angle to that are earlier, boudinaged quartz veins. Healed breccias are present in areas of carbonate veins. Biotite is greatest adjacent to carbonate and quartz veins. Healed, gently folded fractures in plagioclase are visible in hand sample.
Sample #: PVS070

6349

SCMR/IUGS name: Garnet amphibolite and BIF/quartz veins **Location: Drill core BLS12-01 at 37.25 m** Plagioclase (f.g. to m.g., subhedral to euhedral, moderate to intense sericitie alteration, 40%), hornblende (f.g. to m.g., euhedral, light green to dark green teal pleochroism, 40%), garnet (m.g. to c.g., porphyroblastic, poikiloblastic, coronas of plagioclase, 10%), biotite (subhedral, after hornblende, 4%), actinolite (trace), quartz (anhedral, boudinaged quartz veins, exhibits undulose extinction, subgrains, serrated grain boundaries, and checkerboard microstructures 5%), and sulphides (anhedral to euhedral, 1%).
Sample #: PVS071 **SCMR/IUGS name: Garnet amphibolite** **Location: Drill core BLS12-01 at 38.65 m** M.g. to c.g. Garnet (c.g., anhedral, poikiloblastic with plagioclase and hornblende in only outer inclusions near rim, porphyroblastic, out of equilibrium, 10%), hornblende (f.g. to m.g., euhedral, light green to medium teal-green pleochroism, 45%), plagioclase (f.g., subhedral, 43%), and sulphides (euhedral, pyrite and pyrrhotite, 2%). Weak to moderate mylontitic texture with well-defined foliations and lineation defined by plagioclase and hornblende unlike most samples which are moderately to strongly foliated, lineated, and mylontitic.
Sample #: PVS072 **SCMR/IUGS name: Pegmatite, leucosome** **Location: Drill core BLS12-01 at 56.31 m** C.g. to pegmatitic. Plagioclase (pegmatitic, euhedral, moderately to intensely altered to zoicite, 30%), quartz (pegmatitic, anhedral, 30%), alkali feldspars (pegmatitic, subhedral to euhedral, 30%), muscovite (alteration as sericite, 5%), zoicite (alteration in plagioclase, 5%), and beryl (euhedral, green colour, radiating fractures into surrounding matrix, trace). Healed fractures in plagioclase infilled with plagioclase and hematite. (Photos: 10x, zoicite and beryl).
Sample #: PVS073 **SCMR/IUGS name: Garnet amphibolite with BIF/quartz veins** **Location: Drill core BLS12-01 at 98.8 m depth** Garnet (m.g. to c.g., pink-orange pleochroism, anhedral to subhedral, rotated, 10%), hornblende (f.g. to m.g., subhedral to euhedral, medium green to dark teal-green pleochroism, 35%), plagioclase (f.g., subhedral to euhedral, 35%), biotite (subhedral, after hornblende, 5%), carbonate (formed after quartz in boudin necks, followed by prehnite in carbonate, 5%), prehnite (located in carbonate vein, trace), actinolite (after hornblende and adjacent to biotite, trace), epidote (in plagioclase, trace), and sulphides (trace). Earlier quartz vein is present across the entire thin section. The quartz vein does not have straight boundaries but slightly wavy boundaries and is boudinaged and en echelon. The quartz in the vein is m.g. to c.g. and displays checkerboard microstructures. The largest boudin is surrounded by garnet. (Photos: quartz boudins, 5x). Carbonate-prenhite vein is parallel to foliation.
Sample #: PVS074 **SCMR/IUGS name: Chlorite-riebeckite amphibolite next to lamprophyre** **Location: Drill core BLS12-01 at 103.5 m** Green and blue alteration (amphiboles) next to kimberlite/lamprophyre.
Sample #: PVS075 **SCMR/IUGS name: Biotite amphibolite, boudin neck** **Location: Drill core BLS12-01 at 99.6 m depth**

6350
6351

Plagioclase (f.g. to m.g., subhedral, weak to no sericite alteration, 30%), quartz (anhedral, 10%, strain shadows), hornblende (euhedral, light green to dark green pleiochroism, blue glaucophane after hornblende when touching carbonate, 35%), biotite (subhedral, brown pleochroism, 20%), carbonate (anhedral, 4%), and sulphides (disseminated, euhedral, define foliation and lineation as hornblende, 1%). Plagioclase exhibits deformation twins and a few instances of undulatory extinction.
Sample #: PVS076 **SCMR/IUGS name: Amphibolite and BIF/quartz vein boudin with pyrite, pyrrhotite, magnetite in boudin necks** **Location: Drill core BLS12-01 at 87.67 m depth** Plagioclase (f.g. to m.g., subhedral, weak to no sericite alteration, 50%), hornblende (euhedral, light green to dark green pleiochroism, 50%), biotite (anhedral, trace), carbonate (anhedral, trace), and sulphides (disseminated, euhedral, define foliation and lineation as hornblende, trace). Plagioclase displays no deformation twinning and nearly no polysynthetic and albitic twinning. The plagioclase has been completely recovered except in a few single crystals.
Sample #: PVS077 **SCMR/IUGS name: Lamporphyre** **Location: Drill core BLS12-01 at 107.8 m depth** Chlorite and riebeckite in lamporphyre; on hold for geochemistry.
Sample #: PVS078 **SCMR/IUGS name: Biotite gneiss** **Location: Drill core BLS12-256 at 10.8 m depth** Biotite gneiss or “Felsic biotite gneiss”, on hold for geochemistry.
Sample #: PVS079 **SCMR/IUGS name: Fault breccia and gouge** **Location: Drill core BL12-256 at 23.4 m depth** Ivanhoe Lake Deformation Zone at a low angle (~30 degrees) to foliation and lineation with potassic alteration, on hold for geochemistry.
Sample #: PVS080 **SCMR/IUGS name: Biotite-quartz-feldspar granofel** **Location: Drill core BL12-256 at 29 m depth** Quartz-feldspar porphyry, biotite rich, on hold for geochemistry
Sample #: PVS081 **SCMR/IUGS name: Biotite gneiss** **Location: Drill core BL12-256 at 51.3 m depth** Biotite gneiss or “Felsic biotite gneiss”, on hold for geochemistry
Sample #: PVS082 **SCMR/IUGS name: Biotite gneiss** **Location: Drill core BL12-256 at 78.0 m depth** Biotite gneiss or “Felsic gneiss”, on hold for geochemistry
Sample #: PVS083 **SCMR/IUGS name: Biotite-feldspars gneiss** **Location: Drill core BL12-256 at 64.8 m depth** Two feldspars, biotite gneiss or “felsic gneiss porphyry”, on hold for geochemistry
Sample #: PVS084 **SCMR/IUGS name: Garnet-biotite-feldspars gneiss**

6352
6353

Location: Drill core BL12-256 at 91.8 m depth Garnet-biotite gneiss or "Felsic gneiss with garnet", on hold for geochemistry
Sample #: PVS085 **SCMR/IUGS name: Biotite-feldspars gneiss** **Location: Drill core BL12-256 at 133.8 m depth** Biotite gneiss or "Felsic gneiss", on hold for geochemistry
Sample #: PVS086 **SCMR/IUGS name: Biotite-feldspars gneiss** **Location: Drill core BL12-256 at 157.8 m depth** Biotite-feldspar gneiss (trace corderite) or "felsic gneiss", on hold for geochemistry
Sample #: PVS087 **SCMR/IUGS name: Biotite-feldspars gneiss** **Location: Drill core BL12-256 at 178.7 m depth** Biotite gneiss or "Felsic gneiss", on hold for geochemistry
Sample #: PVS088 **SCMR/IUGS name: Biotite-feldspars gneiss, leucosome** **Location: Drill core BL12-256 at 201.0 m depth** Pink, c.g., biotite-feldspars gneiss or "Felsic gneiss",on hold for geochemistry
Sample #: PVS089 **SCMR/IUGS name: Biotite-feldspars gneiss, leucosome** **Location: Drill core BL12-256 at 235.7 m depth** Biotite-feldspars gneiss or "Felsic gneiss",on hold for geochemistry
Sample #: PVS090 **SCMR/IUGS name: Biotite-feldspars gneiss and microcline-perthite-quartz gneiss contact, leucosome and neosome** **Location: Drill core BL12-256 at 250.7 m depth** Biotite gneisses or "Felsic gneiss/porphyry", on hold for geochemistry
Sample #: PVS091 **SCMR/IUGS name: Quartz-feldspar dyke** **Location: Boudin Outcrop** Deformed quartz (grey to blue) eyes in quartz-feldspar felsic dyke with contact with intermediate to mafic gneiss at 296/84. The eyes are elongated and flattened, on hold for geochemistry
Sample #: PVS092 **SCMR/IUGS name: Amphibolite** **Location: Boudin Outcrop** Porphyroblastic amphibolite or "Deformed stripper rock". The amphibolite has anastomosing meso-scale shear zones, on hold for geochemistry.
Sample #: PVS093 **SCMR/IUGS name: Garnet amphibolite** **Location: Boudin Outcrop** Garnet gneiss boudin area across the road, on hold for geochemistry
Sample #: PVS094 **SCMR/IUGS name: Magnetite-quartz BIF (Algoma-type oxide facies banded iron formation)** **Location: Boudin Outcrop**

6354
6355

Iron formation, garnet-biotite schist layered between lean iron formation, on hold for geochemistry
Sample #: PVS095 **SCMR/IUGS name: Garnet-biotite schist (Algoma-type silicate facies banded iron formation)** **Location: Boudin Outcrop** Garnet-biotite Schist layer and BIF, on hold for geochemistry
Sample #: PVS096 **SCMR/IUGS name: Amphibolite** **Location: Boudin Outcrop** "Andesite" sample, geochemistry
Sample #: PVS097 **SCMR/IUGS name: Amphibolite in contact with garnet-rich layer in BIF** **Location: Boudin Outcrop** Amphibolite and garnet-rich layer beside BIF, geochemistry (test for Au &VMS, and other heavy elements against seafloor geochem)
Sample #: PVS098 **SCMR/IUGS name: Biotite schist** **Location: Boudin Outcrop** Biotite schist layer near BIF at garnet-amphibole and amphibole-only boudins, geochemistry (test for Au and other heavy elements against seafloor geochem)
Sample #: PVS099 **SCMR/IUGS name: Garnet-biotite schist** **Location: Boudin Outcrop** Iron formation (327/75), Garnet-biotite shist layered between lean iron formation, geochemistry (test for Au and other heavy elements against seafloor geochem)
Sample #: PVS100 **SCMR/IUGS name: Garnet-biotite schist and BIF** **Location: Boudin Outcrop** Garnet-biotite layers and BIF, geochemistry (stable metamorphic mineral assemblage, Fe-rich? Different stability & minerals? Fe=amphibole?, test for Au and other heavy e
Sample #: PVS101 **SCMR/IUGS name: Amphibolite** **Location: Boudin Outcrop** Andesite , geochemistry (test the evolution of volcanics, check against Glecy's samples)
Sample #: PVS102 **SCMR/IUGS name: Amphibolite** **Location: Boudin Outcrop** Hornblende and garnet-rich layers beside BIF, geochemistry (test for Au and other heavy elements against seafloor geochem)
Sample #: PVS103 **SCMR/IUGS name: Garnet-hornblende-biotite schist** **Location: Boudin Outcrop** Garnet-amphibole boudins and amphibole-only boudins (test for Au and other heavy elements against seafloor geochem, and mobilization)
Sample #: PVS104

6356

SCMR/IUGS name: Garnet-hornblende-biotite schist **Location: Shawmere Anorthosite** Homogeneous anorthosite in eastern antiform (the site where Dr. Hua Huang sampled)
Sample #: PVS105 **SCMR/IUGS name: Feldspars gneiss** **Location: Discovery Outcrop** Quartz, Feldspar gneiss or "porphyry" at camp; geochemistry.
Sample #: PVS106 **SCMR/IUGS name: Biotite gneiss** **Location: Discovery Outcrop** 315/80 foliation defined by biotite, geochemistry (test trace elements across mineralization strike
Sample #: PVS107 **SCMR/IUGS name: Biotite gneiss anastomosing around BIF/quartz boudin train** **Location: Discovery Outcrop** 2 foliations wrapping around quartz boudin, earlier hornblende lineation is horizontal and at boudin it drops to vertical!, geochemistry (test trace elements & alteration across mineralization strike)
Sample #: PVS108 **SCMR/IUGS name: Biotite gneiss anastomosing around BIF/quartz boudin train** **Location: Discovery Outcrop** Quartz- rich BIF boudins and biotite-rich tails
Sample #: PVS109 **SCMR/IUGS name: Diabase** **Location: Discovery Outcrop** Diabase contact, geochemistry (test for remobilization)
Sample #: PVS110 **SCMR/IUGS name: Sillimanite-garnet-biotite gneiss** **Location: Discovery Outcrop** Quartz rods and sillimanite at the west side of OC, 319/68 trending parallel to foliation, no plunge, geochemistry (test trace elements & alteration across mineralization strike)
Sample #: PVS111 **SCMR/IUGS name: Sillimanite-garnet-biotite gneiss** **Location: Discovery Outcrop** Sillimanite gneiss, geochemistry (test trace elements & alteration across mineralization strike). This sample was given to GSC for SHRIMP dating but was ignored in favour of a non-crosscutting felsic dyke that I allowed them to take earlier even though I specifically described to them the reasons they should not use it.
Sample #: PVS112 **SCMR/IUGS name: Amphibolite** **Location: Discovery Outcrop Channel Sample** Amphibolite, geochemistry (test trace elements & alteration across mineralization strike). Discovery OC-Trench-FD01301
Sample #: PVS113 **SCMR/IUGS name: Amphibolite**

6357

Location: Discovery Outcrop Channel Sample Plagioclase-rich amphibolite, geochemistry (test trace elements & alteration across mineralization strike). Daniel LaFontaine's sample series for his MSc. thesis: FD01302
Sample #: PVS114 **SCMR/IUGS name: Biotite gneiss** **Location: Discovery Outcrop Channel Sample** Biotite gneiss, geochemistry (test trace elements & alteration across mineralization strike). FD01303A
Sample #: PVS115 **SCMR/IUGS name: Biotite gneiss** **Location: Discovery Outcrop Channel Sample** "Felsic Biotite Gneiss", geochemistry (test trace elements & alteration across mineralization strike). FD01303B
Sample #: PVS116 **SCMR/IUGS name: Biotite gneiss** **Location: Discovery Outcrop Channel Sample** "Felsic Biotite Gneiss", geochemistry (test trace elements & alteration across mineralization strike). FD01304
Sample #: PVS117 **SCMR/IUGS name: Quartz-feldspar neosome, pegmatitic** **Location: Discovery Outcrop Channel Sample** Pegmatitic leucosome, geochemistry (test trace elements & alteration across mineralization strike), FD01305
Sample #: PVS118 **SCMR/IUGS name: Biotite gneiss** **Location: Discovery Outcrop Channel Sample** Biotite gneiss, "Felsic gneiss/contact", geochemistry (test trace elements & alteration across mineralization strike), FD01305B
Sample #: PVS119 **SCMR/IUGS name: Biotite gneiss** **Location: Discovery Outcrop Channel Sample** Biotite gneiss, "Felsic gneiss", geochemistry, (test trace elements & alteration across mineralization strike), FD013506. Gave GSC permission to collaborate with me but they chose this sample for SHRIMP dating and unfortunately it does not actually crosscut the ore zone as it is a leucosome that is flattened and then chose not to collaborate. FD01306.
Sample #: PVS120 **SCMR/IUGS name: Biotite gneiss** **Location: Discovery Outcrop Channel Sample** Garnet-biotite-feldspar gneiss or "felsic gneiss", geochemistry (test trace elements & alteration across mineralization strike). FD01307.
Sample #: PVS121 **SCMR/IUGS name: Amphibolite** **Location: Discovery Outcrop Channel Sample** 5% pyrite disseminated in gneissic amphibolite, geochemistry (test trace elements & alteration across mineralization strike, Au-increase related to sulphides?) FD01308.
Sample #: PVS122

6358
6359

SCMR/IUGS name: Amphibolite **Location: Discovery Outcrop Channel Sample** 5% pyrite and pyrrhotite disseminated in gneissic amphibolite, geochemistry (test trace elements & alteration across mineralization strike, Au-increase related to sulphides?). FD01309.
Sample #: PVS123 **SCMR/IUGS name: Biotite-feldspar gneiss** **Location: Discovery Outcrop Channel Sample** Felsic Gneiss, geochemistry (test trace elements & alteration across mineralization strike). FD01310.
Sample #: PVS124 **SCMR/IUGS name: Quartz-feldspar pegmatitic neosome** **Location: Discovery Outcrop Channel Sample** Pegmatite, geochemistry (test trace elements & alteration across mineralization strike), thin section needed, FD01311.
Sample #: PVS125 **SCMR/IUGS name: Quartz-feldspar pegmatitic neosome** **Location: Discovery Outcrop Channel Sample** Pegmatite, geochemistry (test trace elements & alteration across mineralization strike), thin section needed.FD01312.
Sample #: PVS126 **SCMR/IUGS name: Amphibolite** **Location: Discovery Outcrop Channel Sample** Amphibolite, geochemistry (test trace elements & alteration across mineralization strike). FD01313
Sample #: PVS127 **SCMR/IUGS name: Amphibolite** **Location: Discovery Outcrop Channel Sample** Amphibolite, geochemistry (test trace elements & alteration across mineralization strike). FD01314.
Sample #: PVS128 **SCMR/IUGS name: Amphibolite** **Location: Discovery Outcrop Channel Sample** Amphibolite, geochemistry (test trace elements & alteration across mineralization strike). FD01315.
Sample #: PVS129 **SCMR/IUGS name: Feldspar-quartz gneiss** **Location: Discovery Outcrop Channel Sample** Feldspar-quartz gneiss or “Porphyry”, geochemistry (test trace elements & alteration across mineralization strike). FD01316
Sample #: PVS130 **SCMR/IUGS name: Feldspar-quartz gneiss** **Location: Discovery Outcrop Channel Sample** Feldspar-quartz gneiss or “Porphyry”, geochemistry (test trace elements & alteration across mineralization strike). FD01317.
Sample #: PVS131

6360

6361

6362

SCMR/IUGS name: Feldspar-quartz gneiss **Location: Discovery Outcrop Channel Sample** Feldspar-quartz geniss, or "Felsic gneiss" at camp, geochemistry (test trace elements & alteration across mineralization strike) FD01318.
Sample #: PVS132 **SCMR/IUGS name: Feldspar-quartz gneiss** **Location: Discovery Outcrop Channel Sample** Feldspar-quartz gneiss or "Porphyry", geochemistry (test trace elements & alteration across mineralization strike). FD01319.
Sample #: PVS133 **SCMR/IUGS name: Feldspar-hornblende-feldspar gneiss** **Location: Discovery Outcrop Channel Sample** Amphibolite with abundance of feldspars or "Felsic Amphiolite gneiss", geochemistry (test trace elements & alteration across mineralization strike, compare to felsic gneisses & amphibolite and see if assimilation is the cause of the mineralogy). FD01320.
Sample #: PVS134 **SCMR/IUGS name: Amphibolite** **Location: Discovery Outcrop Channel Sample** Amphibolite, geochemistry (test trace elements & alteration across mineralization strike). FD01321.
Sample #: PVS135 **SCMR/IUGS name: Amphibolite** **Location: Discovery Outcrop Channel Sample** Amphibolite, geochemistry (test trace elements & alteration across mineralization strike) FD01322.
Sample #: PVS136 **SCMR/IUGS name: Amphibolite** **Location: Discovery Outcrop Channel Sample** Amphibolite, geochemistry (test trace elements & alteration across mineralization strike) FD013223
Sample #: PVS137 **SCMR/IUGS name: Amphibolite** **Location: Discovery Outcrop Channel Sample** Amphibolite with 1% disseminated pyrite, geochemistry (test trace elements & alteration across mineralization strike) FD01324
Sample #: PVS138 **SCMR/IUGS name: Biotite-feldspar gneiss** **Location: Discovery Outcrop Channel Sample** Biotite-feldspar gneiss or "Felsic gneiss", geochemistry (test trace elements & alteration across mineralization strike). FD01325.
Sample #: PVS139 **SCMR/IUGS name: Amphibolite** **Location: Discovery Outcrop Channel Sample** Amphibolite with abundant feldspars or "Felsic/Amphibolite gneisses", geochemistry (test trace elements & alteration across mineralization strike) FD01326.

6363

Sample #: PVS140 **SCMR/IUGS name: Amphibolite with BIF/quartz boudin train** **Location: Discovery Outcrop Channel Sample** Quartz?, geochemistry (test trace elements & alteration across mineralization strike and in boudins). FD01327.
Sample #: PVS141 **SCMR/IUGS name: Amphibolite** **Location: Discovery Outcrop Channel Sample** Amphibolite (test trace elements & alteration across mineralization strike). FD01328.
Sample #: PVS142 **SCMR/IUGS name: Amphibolite** **Location: Discovery Outcrop Channel Sample** Amphibolite (test trace elements & alteration across mineralization strike). FD01329.
Sample #: PVS143 **SCMR/IUGS name: Biotite-feldspar gneiss** **Location: Discovery Outcrop Channel Sample** Biotite-feldspar gneiss or "Felsic gneiss", geochemistry (test trace elements & alteration across mineralization strike) FD01330.
Sample #: PVS144 **SCMR/IUGS name: Biotite-feldspar gneiss** **Location: Discovery Outcrop Channel Sample** Biotite-feldspar gneiss or "Felsic gneiss", geochemistry (test trace elements & alteration across mineralization strike) FD01331.
Sample #: PVS145 **SCMR/IUGS name: Biotite-feldspar gneiss** **Location: Discovery Outcrop Channel Sample** Porphyry, geochemistry (test trace elements & alteration across mineralization strike, volcanic?). FD01332.
Sample #: PVS146 **SCMR/IUGS name: Garnet-biotite gneiss** **Location: Discovery Outcrop Channel Sample** Garnet-rich gneiss, geochemistry (test trace elements & alteration across mineralization strike, strongest seafloor alteration?). FD01333.
Sample #: PVS147 **SCMR/IUGS name: Garnet-sillimanite-biotite gneiss and schist** **Location: Discovery Outcrop Channel Sample** Garnet-sillimanite-biotite gneiss and schists, geochemistry (test trace elements & alteration across mineralization strike, strongest seafloor alteration?). FD01334.
Sample #: PVS148 **SCMR/IUGS name: Garnet-sillimanite-biotite gneiss and schist** **Location: Discovery Outcrop Channel Sample** Garnet-sillimanite-biotite gneiss and schists, geochemistry (test trace elements & alteration across mineralization strike, strongest seafloor alteration?). FD01335.
Sample #: PVS149 **SCMR/IUGS name: Garnet-sillimanite-biotite gneiss and schist** **Location: Discovery Outcrop Channel Sample**

6364
6365

Garnet-sillimanite-biotite gneiss and schists, geochemistry (test trace elements & alteration across mineralization strike, strongest seafloor alteration?). FD01336.
Sample #: PVS150 **SCMR/IUGS name: Garnet-sillimanite-biotite gneiss and schist** **Location: Discovery Outcrop Channel Sample** Garnet-sillimanite-biotite gneiss and schists, geochemistry (test trace elements & alteration across mineralization strike, strongest seafloor alteration?). FD01337.
Sample #: PVS151 **SCMR/IUGS name: Garnet-sillimanite-biotite gneiss and schist** **Location: Discovery Outcrop Channel Sample** Garnet-sillimanite-biotite gneiss and schists, geochemistry (test trace elements & alteration across mineralization strike, strongest seafloor alteration?). FD01338.
Sample #: PVS152 **SCMR/IUGS name: Garnet-biotite schist** **Location: Discovery Outcrop Channel Sample** Garnet-Biotite schist, geochemistry (test trace elements & alteration across mineralization strike, difference in major oxides from Gar-Bt-Sil?). FD01339.
Sample #: PVS153 **SCMR/IUGS name: Garnet-sillimanite-biotite schist** **Location: Discovery Outcrop Channel Sample** Garnet-Sillimanite-biotite schist, geochemistry (test trace elements & alteration across mineralization strike). FD01340.
Sample #: PVS154 **SCMR/IUGS name: Garnet-sillimanite-biotite schist** **Location: Discovery Outcrop Channel Sample** Garnet-Sillimanite-biotite schist, geochemistry (test trace elements & alteration across mineralization strike). FD01341.
Sample #: PVS155 **SCMR/IUGS name: Garnet-sillimanite-biotite schist** **Location: Discovery Outcrop Channel Sample** Garnet-Sillimanite-biotite schist, geochemistry (test trace elements & alteration across mineralization strike). FD01342.
Sample #: PVS156 **SCMR/IUGS name: Garnet-sillimanite-biotite schist** **Location: Discovery Outcrop Channel Sample** Garnet-Sillimanite-biotite schist, geochemistry (test trace elements & alteration across mineralization strike). FD01343.
Sample #: PVS157 **SCMR/IUGS name: Garnet amphibolite adjacent to BIF** **Location: Boudin Outcrop** Garnet amphibolite, (test trace elements & alteration across mineralization strike). FD01344.
Sample #: PVS158 **SCMR/IUGS name: Amphibolite** **Location: Drill core BL13-384 at 437.2 m depth** Amphibolite, nil gold fire assay value.
Sample #: PVS159

6366
6367

SCMR/IUGS name: Biotite-feldspar gneiss with quartz boudins **Location: Drill core BL12-256 at 358.9-359.0 m depth** Biotite-feldspar gneiss or "Altered biotite-felsic-gneiss" at camp with quartz flooding, geochemistry, (test trace element and alteration, quartz flooding related to mineralization or alteration)
Sample #: PVS160 **SCMR/IUGS name: Quartz-feldspars neosome, pegmatitic** **Location: Drill core BL12-256 at 376.7 m depth** Pegmatite, geochemistry, thin section needed, (Test for Au and other heavy elements present in true pegmatite)
Sample #: PVS161 **SCMR/IUGS name: Garnet-biotite schist with BIF and quartz veins** **Location: Drill core BL12-268 at 375.2-375.3 m depth** Garnet-biotite schist with folded, fractured BIF and quartz veins or "Garnet-biotite-felsic gneiss with quartz flooding" at camp, geochemistry, thin section needed (test trace element and alteration, quartz flooding related to alteration).
Sample #: PVS162 **SCMR/IUGS name: Feldspars-biotite gneiss** **Location: BL12-268 at 391.3-391.4 m depth** Feldspars-biotite gneiss or "Altered sedimentary felsic gneiss with siliceous alteration" at camp, geochemistry, (test trace element and alteration, quartz flooding related to alteration, other elements moblized?).
Sample #: PVS163 **SCMR/IUGS name: Amphibolite** **Location: Plagioclase-hornblende gneiss and amphibolite** Amphibolite gneiss with porphyritic plagioclase; geochemistry (compare mobilization and alteration to high-grade zone)
Sample #: PVS164 **SCMR/IUGS name: Quartz-feldspar gneiss with blue-grey quartz eyes** **Location: Boudin Outcrop** Felsic dykes that source the dacite to rhyodacite breccia and pyroclastics that host mineralization above the ore zone. Taken to GSC to use for SHRIMP as it better dates the mineralization than the sample they collected with my permission and still there.
Sample #: PVS165 **SCMR/IUGS name: Sulphide facies banded iron formation** **Location: 5306440/0327710 (UTM 16N)** Sulphide facies banded iron formation lens with massive, euhedral pyrite within amphibolite; geochemistry (test for other heavy elements and alteration).
Sample #: PVS166 **SCMR/IUGS name: Sulphide facies banded iron formation** **Location: 5306440/0327710 (UTM 16N)** Amphibolite host rock to Sample PVS165.
Sample #: PVS167 **SCMR/IUGS name: Plagioclase-biotite gneiss** **Location: 5302891/0325614 (UTM 16N)** Highly-strained intermediate intrusive, plagioclase-biotite gneiss, foliation 298/74N.

6368
6369

Sample #: PVS168 **SCMR/IUGS name: Garnet-biotite-graphite schist** **Location: Drill core BL11-37 at 205.55 to 205.65 m depth** Garnet-biotite schist to garnet-biotite-graphite schist.
Sample #: PVS169 **SCMR/IUGS name: Garnet-biotite schist** **Location: Drill core BL11-37 at 202.3 to 202.3 m depth** Garnet-biotite schist adjacent to graphitic-rich schist
Sample #: PVS170 **SCMR/IUGS name: Garnet-biotite-graphite schist** **Location: Drill core BL11-37 at 205.55 to 205.65 m depth** Graphite-rich schist sampled from PVS168 for use in sulphur isotope analysis.
Sample #: PVS171 **SCMR/IUGS name: Biotite-plagioclase gneiss** **Location: Drill core BL14-642 at 131.20 to 131.25 m depth** Biotite-plagioclase gneiss with semi-massive to massive pyrrhotite and pyrite mineralization. Unmineralized with gold. "'Dead'.Biotite felsic gneiss with Massive sulphide mineralization Py+Po rich" at camp.
Sample #: PVS172 **SCMR/IUGS name: Biotite-plagioclase gneiss** **Location: Drill core BL14-642 at 131.1 to 131.2 m depth** Biotite-plagioclase gneiss with semi-massive to massive pyrrhotite and pyrite mineralization. Unmineralized with gold. "'Dead'.Biotite felsic gneiss with Massive sulphide mineralization Py+Po rich" at camp.
Sample #: PVS172 **SCMR/IUGS name: Biotite-plagioclase gneiss** **Location: Drill core BL14-642 at 131.20 to 131.25 m depth** 131.2 to 131.1m :Felsic biotite schist. 'Dead'. Stringer sulphides Po+Py rich. SULFUR ISOTOPE TEST
Sample #: PVS173 **SCMR/IUGS name: Amphibolite** **Location: Drill core BL11-48 at 361.5 to 361.5 m depth** Schistose amphibolite. 'Dead' Au mineralization possible. Collected for SULFUR ISOTOPE TEST
Sample #: PVS174 **SCMR/IUGS name: Biotite-feldspar gneiss** **Location: Drill core BL11-22 at 38.9 to 40.0 m depth** Biotite-feldspar gneiss or "Biotite Felsic Gneiss. 'Dead'" at camp. SULFUR ISOTOPE TEST
Sample #: PVS175 **SCMR/IUGS name: Amphibolite with boudins of granulite** **Location: Drill core BL13-413 at 354.0 to 350.9 m depth** Amphibolite with granulite boudins with the granulite sampled or "Footwall amphibolite 'Dead'" at camp. 2%, euhedral, f.g. pyrite. SULFUR ISOTOPE
Sample #: PVS176 **SCMR/IUGS name: Amphibolite** **Location: Drill core BL12-171 at 83.2 to 83.3 m depth**

6370
6371

Leuco-amphibolite or "Dead, Bleached amphibolite" at camp. 2%, anhedral, pyrrhotite. SULFUR ISOTOPE
Sample #: PVS177 **SCMR/IUGS name: Amphibolite** **Location: Drill core BL10-11 28.6 to 28.7 m depth** Amphibolite with trace anhedrl pyrrhotite or "'Dead'. Amphibolite" at camp. Po rich. SULFUR ISOTOPE
Sample #: PVS178 **SCMR/IUGS name: Amphibolite** **Location: Drill core BL11-131 at 248.5 to 248.6 m depth** BL12-236 Amphibolite with trace sulphides or "'Dead' amphibolite" at camp. SULFUR ISOTOPE
Sample #: PVS179 **SCMR/IUGS name: Amphibolite** **Location: Drill core BL12-236 at 344.05 to 344.7 5m depth** Amphibolite or "'Dead amphibolite'" at camp. SULFUR ISOTOPE
Sample #: PVS180 **SCMR/IUGS name: Amphibolite with granulite boudins** **Location: Drill core BL12-115 at 509.6 to 509.65 m depth** Amphibolite with granulite boudins and semi-massive to massive, anhedral pyrrhotite or 'Dead' amphibolite at camp. SULFUR ISOTOPE
Sample #: PVS181 **SCMR/IUGS name: Quartz-feldspar rhyodacite volcanic breccia** **Location:** 5306367,0327107 (UTM 16N) Volcanic breccia mineralized with disseminated to blebs of 1% euhedral pyrite and trace chalcopyrite.
Sample #: PVS182 **SCMR/IUGS name: Quartz-feldspar neosome, pegmatitic** **Location: Discovery Outcrop Trench** C.g. to pegmatitic quartz-feldspar neosome collected from trench. Similar to the sample GSC collected with my permission. FD01312
Sample #: PVS183 **SCMR/IUGS name: Biotite-feldspar gneiss** **Location: BL11-128 at 118.5 to 118.4 m depth** Biotite-feldspar gneiess or "'Dead' Felsic Gneiss" at camp. 1% epidote and 1% anhedral, pyrite. SULFUR ISOTOPE.
Sample #: PVS184 **SCMR/IUGS name: Quartz-feldspar-biotite gneiss, neosome, pegmatitic** **Location: BL11-132 at 229.7 to 229.6 m depth** Quartz-feldspar-biotite gneiss or "'Dead'.QFG bitotite with pegmatite" at camp with 2% euhedral pyrite and pyrrhotite. SULFUR ISOTOPE
Sample #: PVS185 **SCMR/IUGS name: Amphibolite** **Location: BL12-180 at 345.2 to 355.3 m depth** Amphibolite with trace pyrrhotite or "'Dead' amphibolite at camp". SULFUR ISOTOPE. Pyrite and Pyrrotite

6372
6373

Sample #: PVS186A **SCMR/IUGS name: Garnet-biotite schist** **Location: BL12-167 at 455.0 to 455.05 m depth** Garnet-biotite schist in high-grade ore zone, 1% disseminated pyrrhotite. SULFUR ISOTOPE.
Sample #: PVS186B **SCMR/IUGS name: Garnet-biotite schist** **Location: BL12-167 at 455.0 to 455.05 m depth** Garnet-biotite schist in high-grade ore zone, 1% disseminated anhedral pyrrhotite and euhedral pyrite. SULFUR ISOTOPE.
Sample #: PVS187 **SCMR/IUGS name: Garnet-biotite schist** **Location: BL11-130 at 95.3 to 95.4 m depth** Garnet-biotite schist in high-grade ore zone with 1% disseminated, euhedral pyrite and anheadl pyrrhotite.
Sample #: PVS188 **SCMR/IUGS name: Garnet-biotite schist** **Location: BL11-139 at 212.3 to 212.4 m depth** Garnet-biotite schist near fold and contact with pegmatite in high-grade ore zone, 1% disseminated anhedral pyrrhotite and euhedral pyrite. SULFUR ISOTOPE.
Sample #: PVS189 **SCMR/IUGS name: Quartz-feldspar gneiss, neosome** **Location: BL11-034 at 173 to 174.5 m depth** Quartz-feldspar gneiss, neosome transition into pegmatite in high-grade ore zone, 1% disseminated anhedral pyrrhotite and euhedral pyrite. SULFUR ISOTOPE
Sample #: PVS190 **SCMR/IUGS name: Garnet-biotite schist** **Location: BL11-130 at 284.6 to 284.7 m depth** Garnet-biotite schist in high-grade ore zone, 1% disseminated anhedral pyrrhotite and euhedral pyrite. SULFUR ISOTOPE
Sample #: PVS191 **SCMR/IUGS name: Biotite-feldspar gneiss, neosome** **Location: BL11-133at 297.6 to 297.8 m depth** Feldspar-biotite gneiss or "'High Au' biotite felsic gneiss" with pyrite and pyrrhotite lens. SULPHUR ISOTOPE
Sample #: PVS192A **SCMR/IUGS name: BIF/quartz and sulphide facies BIF boudin in garnet-biotite schist** **Location: BL12-222 at 321.1 to 321.2 m depth** Tail of euhedral pyrite boudinaged that is within the pyrrhotite-pyrite boudin. SULPHUR ISOTOPE
Sample #: PVS192B **SCMR/IUGS name: Feldspar-biotite gneiss, neosome, pegmatitic** **Location: BL12-222 at 361.65 to 361.8 m depth** Feldspar-biotite gneiss, neosome with transition into pegmatitic texture. 1 cm, euhedral, pyrite in pyrite-pyrrhotite lens. SULPHUR ISOTOPE
Sample #: PVS192C **SCMR/IUGS name: Amphibolite with BIF/quartz boudin next to pegmatite**

6374

6375

6376

Location: BL12-222 at 321.05 to 321.2 m depth Amphibolite with BIF/quartz boudin adjacent to pegmatite in high=grade ore zone. Anhedral, pyrrhotite-rich section. SULPHUR ISOTOPE
Sample #: PVS192D **SCMR/IUGS name: Amphibolite with BIF/quartz boudin next to pegmatite** **Location: BL12-222 at 321.05 to 321.2 m depth**. Amphibolite with BIF/quartz boudin adjacent to pegmatite in high=grade ore zone. Euhedral, pyrite-rich section. SULPHUR ISOTOPE SULFUR ISOTOPE
Sample #: PVS192E **SCMR/IUGS name: Amphibolite with BIF/quartz boudin next to pegmatite** **Location: BL12-222 at 321.05 to 321.2 m depth**. Amphibolite with BIF/quartz boudin adjacent to pegmatite in high=grade ore zone. Euhedral, pyrite and anhedral, pyrrhotite section. SULPHUR ISOTOPE SULFUR ISOTOPE
Sample #: PVS193A **SCMR/IUGS name: Quartz-feldspar-biotite gneiss, neosome, pegmatititc** **Location: BL11-028 at 85.95 to 86.0 m depth**. Quartz-feldspar gneiss, neosome with pegmatitic crystal sizes or "QFG with biotite" at camp. High=grade ore zone.. SULPHUR ISOTOPE SULFUR ISOTOPE
Sample #: PVS193B **SCMR/IUGS name: Quartz-feldspar-biotite gneiss, neosome, pegmatititc** **Location: BL11-028 at 81.4 to 81.5 m depth**. Quartz-feldspar-biotite gneiss, neosome with pegmatitic crystals or "QFG with Biotite and Pegmatite at camp. High-grade ore zone. Euhedral, pyrite and anhedral, pyrrhotite section. SULFUR ISOTOPE
Sample #: PVS194 **SCMR/IUGS name: Garnet-biotite schist** **Location: BL12-222 at 322.0 to 322.05 m depth** Garnet-biotite schist in high-grade ore zone, 1% disseminated euhedral pyrite. SULFUR ISOTOPE
Sample #: PVS195 **SCMR/IUGS name: Quartz-feldspar-biotite gneiss, neosome** **Location: BL11-028 at 85.95 to 86.0 m depth** Quartz-feldspar-biotite gneiss, neosome in high-grade ore zone, 1% disseminated euhedral pyrite. SULFUR ISOTOPE
Sample #: PVS196 **SCMR/IUGS name: Quartz-feldspar-biotite gneiss, neosome, pegmatitic** **Location: BL11-028 at 81.4 to 81.5 m depth** Quartz-feldspar-biotite gneiss, neosome with pegmatitic crystals or "Quartz-feldspar gneiss" at camp in high-grade ore zone, 1% disseminated euhedral pyrite. SULFUR ISOTOPE
Sample #: PVS197 **SCMR/IUGS name: Sillimanite-garnet-biotite schist** **Location: BL11-029 at 115.5 to 115.55 m depth** Sillimanite-biotite-garnet schist after gneiss or "Garnet-biotite ore" at camp with 1% euhedral pyrite and anhedral pyrrhotite defining foliation. High-grade ore zone. SULFUR ISOTOPE
Sample #: PVS198 **SCMR/IUGS name: Garnet-biotite schist**

6377
6378

Location: BL11-034 at 163.6 to 163.7 m depth Garnet-biotite schist or "garnet-biotite ore" at camp. High=grade ore zone. SULFUR ISOTOPE
Sample #: PVS199 **SCMR/IUGS name: Sillimanite-garnet-perthite schist** **Location: BL11-034 at 164.03 to 164.13 m depth** Sillimanite-garnet-perthite schist o "garnet-biotite ore" at camp. Strange to see stable alkali feldspars in a schistose rock with prismatic, 2nd isograd sillimanite! No muscovite or corderite visible. High=grade ore zone. Disseminated, 1% euhedral pyrite and anhedral pyrrhotite. SULFUR ISOTOPE
Sample #: PVS200 **SCMR/IUGS name: Quartz-feldspar neosome, pegmatitic** **Location: BL11-062 at 39.82 to 39.83 m depth** Pegmatitic neosome of quartz and feldspars or "pegmatite" at camp. High-grade ore zone. Disseminated pyrite. SULPHUR ISOTOPE.
Sample #: PVS201 **SCMR/IUGS name: Amphibolite with sulphide facies BIF** **Location: BL12-256 at 344.23 to 344.33 m depth** Amphibolite with sulphide BIF. Massive, euhedral pyrite. High-grade ore zone. SULPHUR ISOTOPE.
Sample #: PVS202 **SCMR/IUGS name: Garnet-biotite schist with pegmatite** **Location: BL12-174 at 45.4 to 45.5 m depth** Garnet-biotite schist with adjacent pegmatite or "garnet-biotite ore" at camp. High=grade ore zone. 1% disseminated euhedral pyrite and pyrrhotite. SULFUR ISOTOPE
Sample #: PVS203 **SCMR/IUGS name: Felsic volcanic breccia** **Location: BL12-178 at 41.7 to 41.8 m depth** Felsic volcanic breccia with overprinted schistose fabric. High=grade ore zone. 2% disseminated euhedral pyrite and pyrrhotite. SULFUR ISOTOPE
Sample #: PVS204 **SCMR/IUGS name: Quartz-feldspar gneiss** **Location: BL11-22 at 38.6 to 38.8 m depth** Pyrite-pyrrhotite sulphide facies BIF boudinaged High=grade ore zone. 2% disseminated euhedral pyrite and pyrrhotite. SULFUR ISOTOPE
Sample #: PVS205 **Mineral name: Pyrrhotite** **Location: BL11-131 at 248.5 to 248.6 m depth** Pyrrhotite sample from PVS178. Po net textures. SULPHUR ISOTPE
Sample #: PVS206 **SCMR/IUGS name: Pyrrhotite** **Location: BL11-139 at 212.3 to 212.4 m depth** Pyrrhotite sample from PVS188. SULPHUR ISOTOPE
Sample #: PVS207 **SCMR/IUGS name: Garnet-biotite schist with oxide and sulphide facies BIF** **Location: BL11-139 at 95.3 to 95.4 m depth**

6379

Pyrrhotite, pyrite, and magnetite samples from PVS187. SULPHUR ISOTOPE
Sample #: PVS208 **SCMR/IUGS name: Garnet-biotite schist with oxide and sulphide facies BIF** **Location: BL11-133 at 297.6 to 297.8 m depth** Biotite-feldspar gneiss with sulphide and oxide BIF or "Biotite felsic Gneiss" at camp. From sample PVS191; make into TS; SULPHUR ISOTOPE
Sample #: PVS209 **SCMR/IUGS name: Felsic volcanic breccia** **Location: BL12-178 at 41.7 to 41.8 m depth** Schistose quartz-feldspar volcanic breccia (with "blue-grey quartz eyes") with 3% euhedral, f.g. to m.g. pyrite. From sample PVS200; to make into TS
Sample #: PVS210 **SCMR/IUGS name: Garnet-biotite schist** **Location: BL11-034 at 164.03 to 164.13 m depth** Garnet-biotite schist with 1% euhedral pyrite and anhedral pyrrhotite from sample PVS195; make into TS
Sample #: PVS211 **SCMR/IUGS name: Garnet-biotite schist** **Location: BL11-034 at 163.6 to 163.7 m depth** Garnet-biotite schist with 1% euhedral pyrite and anhedral pyrrhotite from sample PVS196; make into TS
Sample #: PVS212 **SCMR/IUGS name: Biotite-feldspar gneiss, melanosome** **Location: BL11-034 at 164.03 to 164.13 m depth** Biotite-feldspar gneissic melanosome with pyrrhotite anastomosing around feldspar porphyroclasts
Sample #: PVS213 **SCMR/IUGS name: Quartz-feldspar gneiss** **Location: BL11-062 at 30.85 to 30.95 m depth** Schistose, brecciated quartz-feldspar gneiss with sulphides defining schistose and brecciated fabrics.
Sample #: PVS214 **SCMR/IUGS name: Amphibolite** **Location: BL10-10 at 57.3 to 57.35 m depth** Mylontitic amphibolite with 3% euhedral, f.g. to m.g. pyrite and anhedral, f.g. pyrrhotite. High=grade ore zone.ISOPTOPE SULFUR
Sample #: PVS215 **SCMR/IUGS name: Quartz-feldspar neosome, pegmatitic** **Location: BL11-062 at 13.1 to 13.2 m depth** Pegmatitic quartz-feldspar neosome with gneissic fabric overprinting earlier breccia, 1% anhedral pyrrhotite
Sample #: PVS216 **SCMR/IUGS name: Amphibolite and sulphide-facies BIF** **Location: BL12-256 at 344.23 to 344.33 m depth** Amphibolite with sulphide-facies BIF lens from sample PVS198; SULPHUR ISOTOPE
Sample #: PVS217

6380
6381

SCMR/IUGS name: Amphibolite **Location: BL10-10 at 344.23 to 344.33 m depth** Mylontitic amphibolite with 1% euhedral, f.g. to m.g. pyrite and anhedral, f.g. pyrrhotite. SULPHUR ISOTOPE
Sample #: PVS218 **SCMR/IUGS name: Garnet-magnetite-biotite schist** **Location: BL11-62 at 59.85 to 59.90 m depth** Garnet-magnetite-biotite schist; make into TS
Sample #: PVS219 **SCMR/IUGS name: Garnet amphibolite and tourmaline-garnet-biotite schist contact, mylonitized** **Location: BL11-62 at 54.5 to 55.45 m depth** Garnet-biotite schist. 1% pyrite and pyrrhotite with full corona of Po around Py. V.f.g. to c.g. mylontized garnet amphibolite-tourmaline garnet-biotite schist contact. Amphibolite:. Hornblende (subhedral to euhedral, f.g. to m.g., light green to green pleochroism, 30%), plagioclase (v.f.g. to c.g., anhedral to subhedral, 30%), garnet (f.g. to c.g., anhedral, intensely fractured, flattened and elgonated, defines lineations and foliations, silicate and sulphide inclusions are rotated, garnet has been rotated counterclockwise and boudinaged with biotite defining the boudin necks, 10%), and sulphides (trace). Hornblende psuedomorphs earlier cpx and garnet is out of equilibrium (photo) with irregular crystal boundaries, anhedral crystal shapes (photo). Hornblende defines two lineations at nearly 90 degrees, biotite, garnet, and hornblende define foliation. Anastomosing foliation in boudin necks is defined by biotite. Garnet-biotite schist: Gradual transition from amphibolite on the cm-scale into areas that are richer in garnet, biotite, and with no hornblende, and have tourmaline. Plagioclase, quartz, and hornblende exhibit evidence of intense grain size reduction and exhibit no undulatory extinction. Only a few m.g. plagioclase crystals display deformation twins. Hornblende exhibits simple twinning parallel to foliation and primary lineation. Plagioclase (v.f.g. to m.g., subhedral, 34%), garnet (c.g., anhedral to subhedral, poikiloblastic and porphyroblastic, 15%), biotite (subhedral, brown to red pleochroism, 20%), tourmaline (subhedral to euhedral, trigonal and pseudohexagonal, olivine green to beige-brown pleochroism and visible sector zoning, defines foliation and defines two lineations, one parallel to foliation and another 90 degrees normal, 20%), quartz (anhedral, 10%), and sulphides (1%). Photo: 5x boudinaged garnets, deformation twins in plagioclase.
Sample #: PVS220 **SCMR/IUGS name: Metaconglomerate or Quartz-feldspar-biotite gneiss** **Location: BL11-32 at 120.13 to 120.2 m depth** Protomylonite. Metaconglomerate; make into TS
Sample #: PVS221 **SCMR/IUGS name: Amphibolite with oxide-facies BIF** **Location: BL11-48 from 361.6 to 361.7 m depth** Amphibolite with oxide-facies BIF. Quartz boudin and pyrrhotite in amphibolite. From sample PVS173. SULPHUR ISOTOPE.
Sample #: PVS222 **SCMR/IUGS name: Garnet-amphibolite** **Location: BL10-12 from 272-272.1 m depth**

6382
6383

Amphibolite with garnet boudinaged with pyrrhotite boudin necks. Maake into TS, send for geochemistry
Sample #: PVS223 **SCMR/IUGS name: Amphibolite with oxide-facies BIF** **Location: BL12-236 from 344.65 to 344.7 m depth** Amphibolite with quartz boudin with pyrrhotite boudin neck. From sample PVS179. SULPHIDE ISOTOPE
Sample #: PVS224 **SCMR/IUGS name: Hornblende-biotite-feldspar metatexite** **Location: BL12-236 from 344.65 to 344.7 m depth** Hornblende-biotite-feldspar metatexite with assimilated granitoid
Sample #: PVS225 **SCMR/IUGS name: Quartz-feldspar volcanic breccia** **Location:** 5306367/0327107 (16N Zone, UTM) Gneissic overprinting felsic breccia with sulphides from Sample PVS143; make into TS, send for geochemistry
Sample #: PVS226 **SCMR/IUGS name: Augite-garnet metatexite and quartz-feldspar neosome** **Location: BL13-473 at 522 to 522.1 m depth** Melanosome of pyroxene-garnet metatexite, gneissic and pegmatitic, quartz-feldspar neosome. Make into TS, send for geochemistry
Sample #: PVS227 **SCMR/IUGS name: Pegmatitic quartz-feldspar neosome** **Location: BL13-397 at 428.74 to 428.75 m depth** Quartz-felspar neosome, pegmatitic crystal size. Make into TS, send for geochemistry
Sample #: PVS228 **SCMR/IUGS name: Garnet-pyroxenes granulite** **Location: BL13-397 at 438.8 to 438.9 m depth** Garnet-pyroxene granulite partially retrograded to amphibolite with 2% f.g., anhedral pyrrhotite.
Sample #: PVS229 **SCMR/IUGS name: Quartz-feldspar neosome** **Location: BL13-397 at 428.2 to 428.3 m depth** Quartz-feldspar neosome, pegmatitic. Make into TS, send for geochemistry.
Sample #: PVS230 **SCMR/IUGS name: Muscovite-quartz-feldspar neosome** **Location: BL13-409 at 30.0 to 30.1 m depth** Muscovite-quartz-feldspar neosome, pegmatitic and gneissic fabric. Make into TS, send for geochemistry. Muscovite geochemistry.
Sample #: PVS231 **SCMR/IUGS name: Muscovite-quartz-feldspar neosome** **Location: BL13-409 at 45.1 to 45.2 m depth** Muscovite-quartz-feldspar neosome, pegmatitic and gneissic fabric, 1% m.g., euhedral pyrite. Make into TS, send for geochemistry. Muscovite geochemistry.
Sample #: PVS232 **SCMR/IUGS name: Muscovite-quartz-feldspar neosome**

6384
6385

Location: BL13-409 at 57.1 to 57.2 m depth Muscovite-quartz-feldspar neosome, pegmatitic and gneissic fabric, 1% m.g., euhedral pyrite. Make into TS, send for geochemistry. Muscovite geochemistry.
Sample #: PVS233 **SCMR/IUGS name: Muscovite-quartz-feldspar neosome, biotite schist, and quartz-feldspar neosome, pegmatitic** **Location: BL13-409 at 65.6 to 65.7 m depth** Muscovite-quartz-feldspar neosome, biotite schist, and quartz-feldspar neosome, pegmatitic or "QFG and Mica Schist with Pegmatite"; make into TS, send for geochemistry
Sample #: PVS234 **SCMR/IUGS name: Muscovite-quartz-feldspar neosome, pegmatitic** **Location: BL13-409 at 71.0 to 71.1 m depth** Muscovite-quartz-feldspar neosome, pegmatitic crystal size with 1% m.g., euhedral pyrite within quartz boudins.
Sample #: PVS235 **SCMR/IUGS name: Hornblende-plagioclase-biotite gneiss** **Location: BL13-409 at 77.7 to 77.8 m depth** Amphibolite partially melted and altered to hornblende-plagioclase-biotite gneiss or "stripper rock" at camp.
Sample #: PVS236 **SCMR/IUGS name: Biotite-muscovite schist contact with quartz-feldspar neosome, pegmatite** **Location: BL13-409 at 86.8 to 86.9 m depth** Biotite- muscovite schist and pegmatite with 1% f.g. to m.g., euhedral pyrite and anheadl pyrrhotite.
Sample #: PVS237 **SCMR/IUGS name: Quartz-feldspar neosome, pegmatite** **Location: BL13-409 at 88.4 to 88.5 m depth** Boudinaged quartz-feldspar nesome with pegmatitic crystal size. 1% f.g. to m.g., euhedral pyrite and anheadl pyrrhotite in boudin necks in pegmatite.
Sample #: PVS238 **SCMR/IUGS name: Muscovite-quartz-feldspar schist with quartz-feldspar neosome, pegmatitic** **Location: BL13-409 at 99.4 to 99.5 m depth** Muscovite-quartz-feldspar schist with nesome, pegmatitic; 1% f.g. to m.g., euhedral pyrite and pyrrhotite.
Sample #: PVS239 **SCMR/IUGS name: Biotite-quartz-feldspar schist with quartz-feldspar neosome, pegmatite** **Location: BL13-409 at 104.7 to 104.8 m depth** Biotite-quartz-feldspar schist with quartz-feldspar neosome with pegmatitic crystal size; 1% f.g. to m.g., euhedral pyrite and pyrrhotite.
Sample #: PVS240 **SCMR/IUGS name: Biotite schist with quartz-feldspar neosome, pegmatite** **Location: BL13-409 at 129.1 to 129.2 m depth**

6386
6387

Biotite schist with quartz-feldspar neosome, pegmatite; 1% f.g. to m.g., euhedral pyrite and pyrrhotite.
Sample #: PVS241 **SCMR/IUGS name: Quartz-feldspar gneiss** **Location: BL13-409 at 143.8 to 143.9 m depth** Quartz-feldspar gneiss with 1% f.g. to m.g., euhedral pyrite and pyrrhotite.
Sample #: PVS242 **SCMR/IUGS name: Amphibolite** **Location: BL11-133 at 354.9 to 355.0 m depth** Amphibolite with overprinting schistose fabric; potential for Glecy's geochemistry.
Sample #: PVS243 **SCMR/IUGS name: Amphibolite** **Location: BL13-409 at 151.2 to 151.3 m depth** Amphibolite with overprinting schistose fabric; potential for Glecy's geochemistry
Sample #: PVS244 **SCMR/IUGS name: Garnet-biotite schist with oxide BIF/quartz boudin** **Location: BL13-409 at 152.1 to 152.2 m depth** Garnet-biotite schist with oxide-facies BIF/quartz boudin with 2% m.g., euhedral pyrite and pyrrhotite in boudin neck.
Sample #: PVS245 **SCMR/IUGS name: Muscovite-quartz-feldspar schist** **Location: BL13-409 at 152.8 to 152.9 m depth** Garnet-biotite schist with oxide-facies BIF/quartz boudin with 2% m.g., euhedral pyrite and pyrrhotite in boudin neck.
Sample #: PVS246 **SCMR/IUGS name: Garnet-augite amphibolite** **Location: Boudin Outcrop** Garnet-augite amphibolite with garnet-rich layers. Send for geochemistry for Glecy?
Sample #: PVS247 **SCMR/IUGS name: Muscovite schist and quartz-feldspar neosome, pegmatitic** **Location: BL12-268 at 368.83 to 368.90 m depth** Muscovite schist contact with quartz-feldspar neosome (pegmatite).
Sample #: PVS248 **SCMR/IUGS name: Muscovite-biotite schist and quartz-feldspar neosome, pegmatitic** **Location: BL13-409 at 160.1 to 160.2 m depth** Biotite-muscovite schist contact with quartz-feldspar neosome (pegmatitic). 2%, f.g. to m.g., euhedral pyrite and pyrrhotite.
Sample #: PVS249 **SCMR/IUGS name: Biotite schist with semi-massive sulphide** **Location: BL13-409 at 163.6 to 163.7 m depth** Biotite schist with 10% semi-massive sulphides grading to 3% disseminated pyrrhotite defining foliation.
Sample #: PVS250 **SCMR/IUGS name: Biotite schist with quartz-feldspar neosome, pegmatitic** **Location: BL13-409 at 168 to 168.5 m depth**

6388
6389

Biotite schist and quartz-feldspar neosome, pegmatite with 2%, f.g. to m.g., euhedral pyrite and pyrrhotite.
Sample #: PVS251 **SCMR/IUGS name: Quartz-amphibolite to hornblende-biotite-plagioclase gneiss** **Location: BL13-409 at 172.0 to 172.1 m depth** Siliceous amphibolite gradual transitions into hornblende-biotite-plagioclase gneiss or "'stripper' amphibolite" at camp.
Sample #: PVS252 **SCMR/IUGS name: Biotite-feldspar schist and quartz-feldspar neosome, pegmatitic** **Location: BL13-409 at 183.0 to 183.4 m depth** Biotite-feldspar schist transitions gradually into quartz-feldspar neosome (pegmatite) with 2%, f.g. to m.g., euhedral pyrite and pyrrhotite.
Sample #: PVS253 **SCMR/IUGS name: Muscovite-biotite-feldspar gneiss** **Location: BL13-409 at 183.0 to 183.1 m depth** Muscovite-biotite-feldspar gneiss with porphyroblasts of muscovite >1 cm.
Sample #: PVS254 **SCMR/IUGS name: Garnet-biotite schist with oxide-facies BIF/quartz boudin and quartz-feldspar neosome, pegmatitic** **Location: BL13-409 at 192.7 to 192.8 m depth** Garnet-biotite schist with boudinaged quartz and neosome of quratz-feldspar pegmatite.
Sample #: PVS255 **SCMR/IUGS name: Quartz-feldspar volcanic breccia** **Location: BL13-409 at 199.9 to 200.0 m depth** Schistose fabric overprinting earlier gneissic and breccia fabrics in quartz-feldspar volcanic breccia with 3%, f.g. to m.g., disseminated, euhedral pyrite.
Sample #: PVS256 **SCMR/IUGS name: Quartz-feldspar-biotite neosome, pegmatitic** **Location: BL13-409 at 105.4 to 105.6 m depth** Quartz-feldspar-biotite neosome, pegmatitic with 1%, f.g. to m.g. disseminated, euhedral pyrite.
Sample #: PVS257 **SCMR/IUGS name: Muscovite-quartz-feldspar schist** **Location: BL13-409 at 210.0 to 210.1 m depth** Muscovite-quartz-feldspar schist 2%, f.g. to m.g. disseminated, euhedral pyrite and pyrrhotite.
Sample #: PVS258 **SCMR/IUGS name: Garnet-biotite mylonite** **Location: BL13-409 at 215.75 to 215.8 m depth** V.f.g to f.g., ultramylontitic garnet-biotite schist, ore zone.
Sample #: PVS259 **SCMR/IUGS name: Biotite-plagioclase schist** **Location: BL13-409 at 219.0 to 219.1 m depth** Biotite-plagioclase schist
Sample #: PVS260 **SCMR/IUGS name: Biotite-chlorite schist and quartz-feldspar neosome, pegmatitic** **Location: BL13-409 at 221.1 to 222.2 m depth**

6390

6391

6392

Biotite-chlorite schist with boudin of quartz-feldspar neosome, pegmatite. 2%, f.g. to m.g., disseminated, euhedral pyrite and pyrrhotite.
Sample #: PVS261 **SCMR/IUGS name: Amphibolite** **Location: BL13-409 at 225.05 to 225.2 m depth** Amphibolite with porphyroclastic plagioclase in mylontitic fabric.
Sample #: PVS262 **SCMR/IUGS name: Amphibolite** **Location: BL13-409 at 237.1 to 237.2 m depth** Amphibolite, patchy metatexite with 3%, f.g. to m.g., disseminated, euhedral pyrite and pyrrhotite ore zone.
Sample #: PVS263 **SCMR/IUGS name: Garnet amphibolite** **Location: BL13-409 at 242.9 to 243.0 m depth** Garnet-amphibolite with trace disseminated sulphides.
Sample #: PVS264 **SCMR/IUGS name: Garnet amphibolite** **Location: BL13-409 at 243.2 to 243.3 m depth** Garnet-amphibolite
Sample #: PVS265 **SCMR/IUGS name: Garnet amphibolite** **Location: BL13-409 at 246.8 to 246.9 m depth** Schistose garnet-amphibolite with schistose overprinting brecciated quartz-feldspar neosome (pegmatite)
Sample #: PVS266 **SCMR/IUGS name: Garnet amphibolite boudinaged** **Location: Boudin Outcrop** Garnet amphibolite with boudinaged shear-banded foliation boudinage!
Sample #: Katia Jellicoe's Sample KJ014 Amphibolite "footwall amphibolite" Hornblende (40%), plagioclase (30%), clinopyroxene (20%), biotite (with chlorite, prenhite after biotite 10%). Chlorite after biotite
Sample #: Matthew Nadeau's Sample 4 **5306733/327877 (UTM 16N)** **Garnet-rich amphibolite** Hornblende (subhedral to euhedral, tan to brown and second population is light green to dark green pleochroism, 40%), plagioclase (subhedral, 30%), garnet (anhedral to subhedral, 15%), clinozoicite (10%), titanite (euhedral, 5%), and sulphides (trace). The hornblende and garnet define the lineation and foliation. Garnet has been boudinaged and hornblende near the garnet is green, not brown, and defines a second lineation related to boudinage. Subgrains are located in low-strain areas of garnet. Deformation twins are present in hornblende and titanite. Foliation boudinage.
Sample #: Matthew Nadeau's Sample 11 **5346883/ 381515 (UTM 16N)** **Garnet-opx-cpxy mylonite** (photo),

6393

Opx (m.g., euhedral, 20%), cpx (m.g., subhedral to euhedral, 30%), garnet (subhedral to euhedral, 30%), plagioclase (f.g., subhedral, 20%), sulphides (trace), and carbonates (trace). The pyroxenes, garnets, and plagioclase define the foliation and lineation. Undulatory extinction is present in plagioclase and opx. Garnet coronas around opx.

*Please see Honours theses by Katia Jellicoe (2013), Gleceria Gamelin (2014), and Matthew
6394 Nadeau (2015) for further information about their samples collected or additional samples.

6395

Sample #: PVS267 SCMR/IUGS name: Metasandstone Location: BL13–485 at 598.1 m Contact between metamorphosed arkose and arenite sandstones with 2% pyrrhotite mineralization, used for Pb–isotopic study.

6396

APPENDIX E: REGIONAL MAP